# Neoproterozoic source rocks and analogue microbial reservoir characterisation: from outcrop to dynamic reservoir simulation

Gerd Winterleitner

Thesis submitted to Royal Holloway, University of London

for the degree of Doctor of Philosophy

Earth Sciences Department

Royal Holloway, University of London

September 2014

## Declaration of Authorship

I, Gerd Winterleitner hereby declare that this thesis and the work presented in it is entirely my own. Where I have consulted the work of others, this is always clearly stated.

Gerd Winterleitner

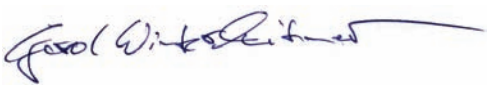

September 2014

## Abstract

This research project presents an integrated study of selected aspects of Neoproterozoic carbonate sedimentology in Namibia from a petroleum point of view. In recent years petroleum companies started to explore Neoproterozoic frontier petroleum plays due to the global steady increase for the demand of oil and gas. However, despite an enormous research effort over the last two decades, little is yet known about Neoproterozoic geology and in particular about Precambrian petroleum geology. From a petroleum exploration point of view, the search for Neoproterozoic hydrocarbon systems is a new frontier in petroleum geology.

The focus of the first part of this research project has been on the evaluation of potential source rocks along strike of the southern edge of the Owambo Basin in North Namibia. This includes detailed sedimentological characterisation of four transects of the more than 4 km-thick Otavi carbonate platform. 40 samples were collected in the field and subsequently analysed for total organic carbon (TOC) content. None of these samples could be classified as potential source rock due to the low total organic carbon content (< 0.5% TOC). However, 2 samples from the Halali Waterhole showed elevated TOC values and might have acted as source rocks during the Neoproterozoic. Further investigations of these sequences were, however, hampered due to the unclear stratigraphic position in the succession. A key observation is the absence of organic-enriched sediments in the Keilberg Member, north of Tsumeb, which is regarded as potential source rock interval for the Owambo Basin. This shows that the Keilberg Member is not a basin-wide source rock horizon. These results suggest that organic-enriched sediments were deposited during post-glacial flooding in tectonically controlled anoxic sub-basins with restricted water circulation. A potential analogue system for the Otavi carbonate platform is the early Silurian-Ordovician post-glacial source rock system of North Africa.

The second part of the thesis presents a multidisciplinary, outcrop-based analogue hydrocarbon reservoir characterisation of a microbial carbonate system in the Nama Basin of South Namibia. The incentive for this investigation was to better understand potential microbial carbonate reservoirs in the subsurface of the Owambo Basin and elsewhere. The terminal Neoproterozoic Kuibis ramp carbonates are superbly exposed in the Zebra River canyon system, providing the opportunity to study this system in three dimensions from micro- to macro-scale. Reservoir characterisation includes detailed sedimentological and structural field observations and

interpretations. The microbial bioherm evolution has been analysed in detail and a generic model describing bioherm evolution has been proposed. Consequently, a new bioherm nomenclature to describe bioherm geometries has been introduced, including merged, composite and stacked bioherm complexes. Structural characterisation of the microbial carbonate system revealed an important phase of fracture development. Syn-depositional fractures are *intrinsic* to the microbial carbonates due to body forces of an early lithified, fragile microbial framework. This has an important implication for microbial reservoir characterisation because fractures have to be considered in microbial reservoirs independent form the regional setting. Thin-section analyses were used to determine petrophysical properties of the reservoir and non-reservoir facies. Subsequently, terrestrial laser scanning (lidar) was used to acquire high-resolution digital outcrop data of the canyon system in order to construct a static geocellular analogue reservoir model. Object-based and multiple-point statistics facies modelling were chosen to develop a detailed facies model of the microbial carbonates. These facies models served subsequently as basis for dynamic performance studies. The final step of the reservoir characterisation constitutes a streamline fluid flow forecasting analysis, following a top-down modelling philosophy. Based on the integrated reservoir characterisation the analogue microbial carbonate system of the Omkyk Sequence 2 in the Nama Basin is classified as hybrid 3 type reservoir after the carbonate reservoir classification of Ahr (2008). Reservoir heterogeneity and geometry is constrained by depositional processes in combination with syn-depositional fractures. However, the diagenetic history of the Omkyk Sequence 2 has not been studied. Selective dolomitisation of microbialites indicate that diagenetic alterations have affected the carbonate system. Therefore, future research might refine or overturn this classification.

## Acknowledgements

The last four years have been a remarkable journey. It was truly fantastic to work at Royal Holloway University on such an amazing project and in an inspiring research environment. I got to know wonderful people, colleagues and friends.

First of all I want to thank my supervisors, Dan Le Heron and Bernie Vining. I cannot remember any day coming to Dan's office, finding him too busy to talk to me. Always patient, listening and guiding me through this research project. Most importantly, providing me with coffee during early hours. I have great memories of stimulating discussions with Dan at bonfires in the Namibian desert over a pint. I want to thank Bernie for his help and guidance during the entire PhD. Bernie's enthusiasm, his passion for geoscience research and positive attitude was very inspiring. I also want to thank him for setting up the Neoproterozoic Research Programme, my internship with Baker Hughes in Rio de Janeiro and his ongoing support. I want to thank NAMCOR and Sonangol for funding this project. From the department I want to thank Pete, Margaret, Ian, Jürgen, Frank, Mark, Kevin and Neil for all their help over the last four years.

I want to express my gratitude to Dan Bosence, Kate Gibbons, Fred Kamona, Ben Mapani, Leonardo Borghi, Frances Abbot and Mary Raigosa for discussions and help in the field, which significantly improved my understanding of carbonate sedimentology and reservoir modelling.

One of the most important things to me over the last four years has been the friends I got to know. Foremost my former housemates, Eldert, Giovanni, Oris and Seb. Also all the friends I got to know at Royal Holloway and London, Sila, Miguel, Jorge, Ivan, Moises, Guy, Dave, Lorenzo, Hugo, Mauro, Maria, Tim, Juliane, Viola and Arnaud. We had great times and lots of fun in our house, great nights out in the pubs of Egham and London. It was an amazing time and I will always look back on this time with very fond memories. I want to thank Emi and Erwan from my research group for good times in the field and their support.

I want to express my gratitude to my family, my parents Josef and Roswitha, my sisters Anna and Petra, my nephew Lucas and niece Alba for their unconditional love and support.

Above all, I want to thank Celine for all her love over the last years. The most important part of my PhD, my wife-to-be. The most wonderful person I know.

I want to dedicate this thesis to my grandparents.
I would not have come so far without them.

Josef and Josefa Winterleitner and Ernestine Windegger.

In loving memory.

# Table of contents

# Table of Figures

## List of Tables



## List of Equations

# 1 The Neoproterozoic Research Programme in Namibia

## 1.1 Introduction

This project presents an integrated assessment of selected aspects of Neoproterozoic carbonate sedimentology in Namibia from a petroleum systems perspective. The global, steady increase for the demand of oil has forced petroleum companies to evaluate frontier petroleum plays such as offshore deep-water, potential Arctic and also Neoproterozoic hydrocarbon systems in recent years (e.g. Craig *et al.*, 2009). However, despite an enormous research effort over the last two decades, little is yet known about Neoproterozoic geology and in particular about Precambrian petroleum geology.

From a petroleum exploration point of view, the search for Neoproterozoic hydrocarbon systems is a new frontier in petroleum geology (Ghori *et al.*, 2009). The search for these 'old' petroleum systems comprises significantly higher risks as for the Phanerozoic counterparts. For instance the timing of hydrocarbon generation and subsequent migration versus trap-formation are far more difficult to constrain given the enormous timespan, as compared to conventional Phanerozoic petroleum systems. Regarding the immense time period, potential Neoproterozoic hydrocarbon plays have to outlast for hundreds of million years. Thus, risks arise from the preservation of hydrocarbon accumulations, in terms of leakage through later tectonic activity or through bio degradation.

From a source rock perspective it is intriguing that we actually can find potential organic-rich sediments before the Cambrian radiation and the onset of animal life. The oldest 'life' oil has been found in the McArthur Basin in Australia and has an age of approximately 1.4 Ga (Ghori *et al.*, 2009) (see Figure 1). But little is known about the involved organism and source rock evaluation of these old sediments is still in early stages (Craig *et al.*, 2013; Olcott, 2005). Considering Neoproterozoic petroleum plays means to look for systems with high uncertainties and risks.

One might ask why are we looking at these high-risk and thus eventually expansive and uneconomic petroleum plays? The simple answer is because we have to. Many of the world's 'traditional' proven petroliferous basins are approaching

exploration maturity and much of the 'easy oil' has now been found. As a result, significant exploration effort is now being devoted to the Neoproterozoic systems (Aziz and Ghnia, 2009; Bhat *et al.*, 2009; Craig *et al.*, 2009).

The Neoproterozoic, which is almost as long as the entire Phanerozoic, is relatively poorly known from a petroleum perspective, despite the existence of producing, proven and potential plays in many parts of the world (see Figure 2). Potential Precambrian hydrocarbon systems are expected across northern Africa, USA, South America, India and the Middle East (Ghori *et al.*, 2009). Producing fields are in Russia (Ural province, Siberia), China and in the São Francisco Basin of Brazil (Craig *et al.*, 2013). The Huqf Supergroup in Oman is one example, which demonstrates the economic viability of these 'old' petroleum systems. More than 90% of Oman's oil production is directly related to the Neoproterozoic source rocks (Grosjean *et al.*, 2009). However, a better understanding of the stratigraphy and structural history of Proterozoic sequences worldwide is required to encourage future exploration. Furthermore, detailed studies of potential source and reservoir rocks have to be carried out in order to ensure a deeper understanding of Neoproterozoic petroleum plays.

## 1.2 The Neoproterozoic Research Programme

The Neoproterozoic research group in Royal Holloway, University of London comprises three postgraduate research students, who focused on proven and potential petroleum plays in the Precambrian of Southwest Africa and Brazil. Because of the enormous expanse of the project area, the mega region was divided into three separate field areas and every researcher was working on one area. The areas are (1) the São Francisco Basin in Brazil, (2) the Neoproterozoic successions of Congo and Zambia and (3) the Precambrian rock record of Namibia (see Figure 3). The principle idea of this strategy was to study the proven and producing Neoproterozoic petroleum system in the São Francisco Basin and subsequently transfer and apply the gained knowledge to the Southwest African successions in order to identify potential petroleum plays.

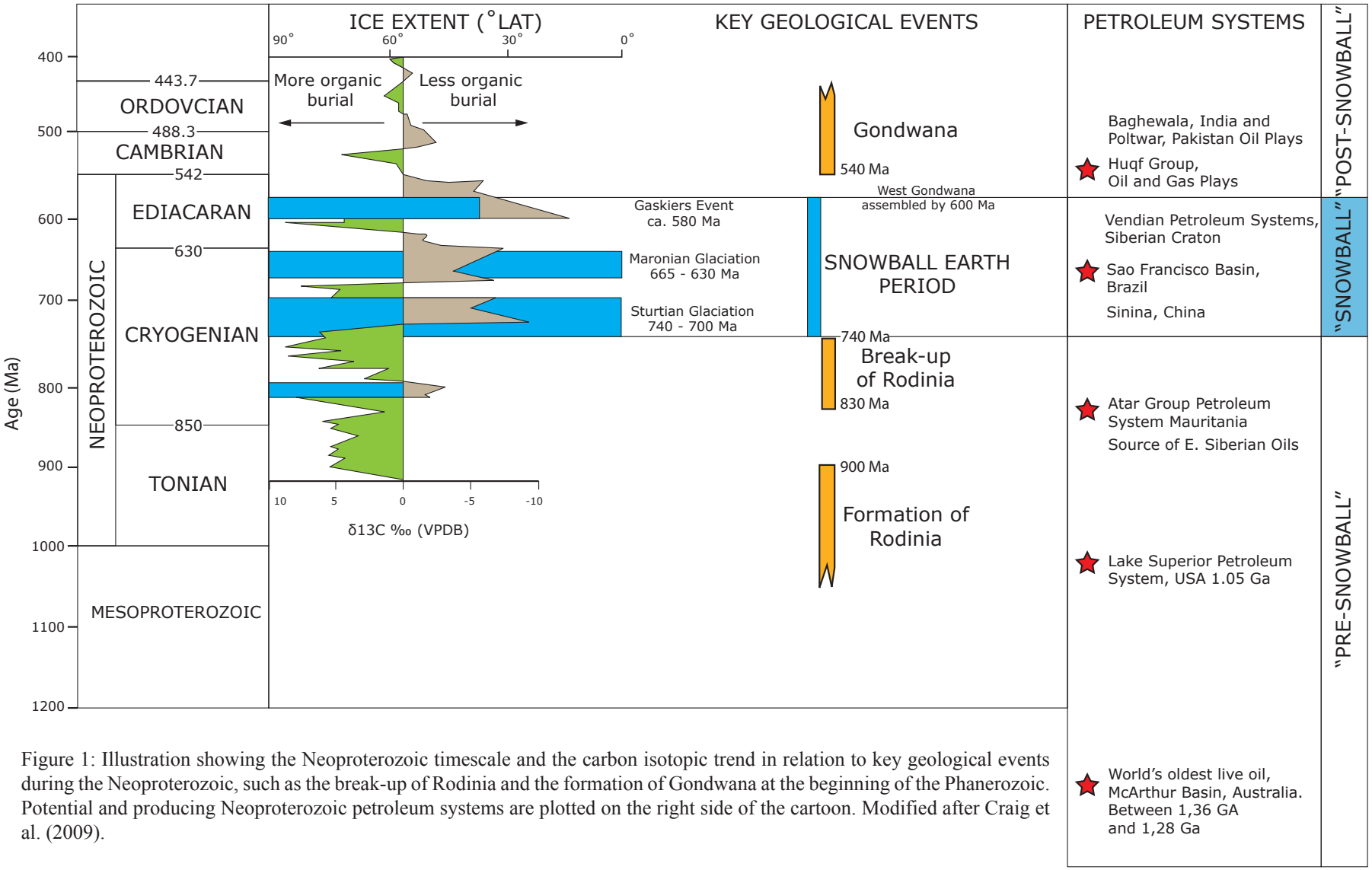


Figure 1: Illustration showing the Neoproterozoic timescale and the carbon isotopic trend in relation to key geological events during the Neoproterozoic, such as the break-up of Rodinia and the formation of Gondwana at the beginning of the Phanerozoic. Potential and producing Neoproterozoic petroleum systems are plotted on the right side of the cartoon. Modified after Craig et al. (2009).

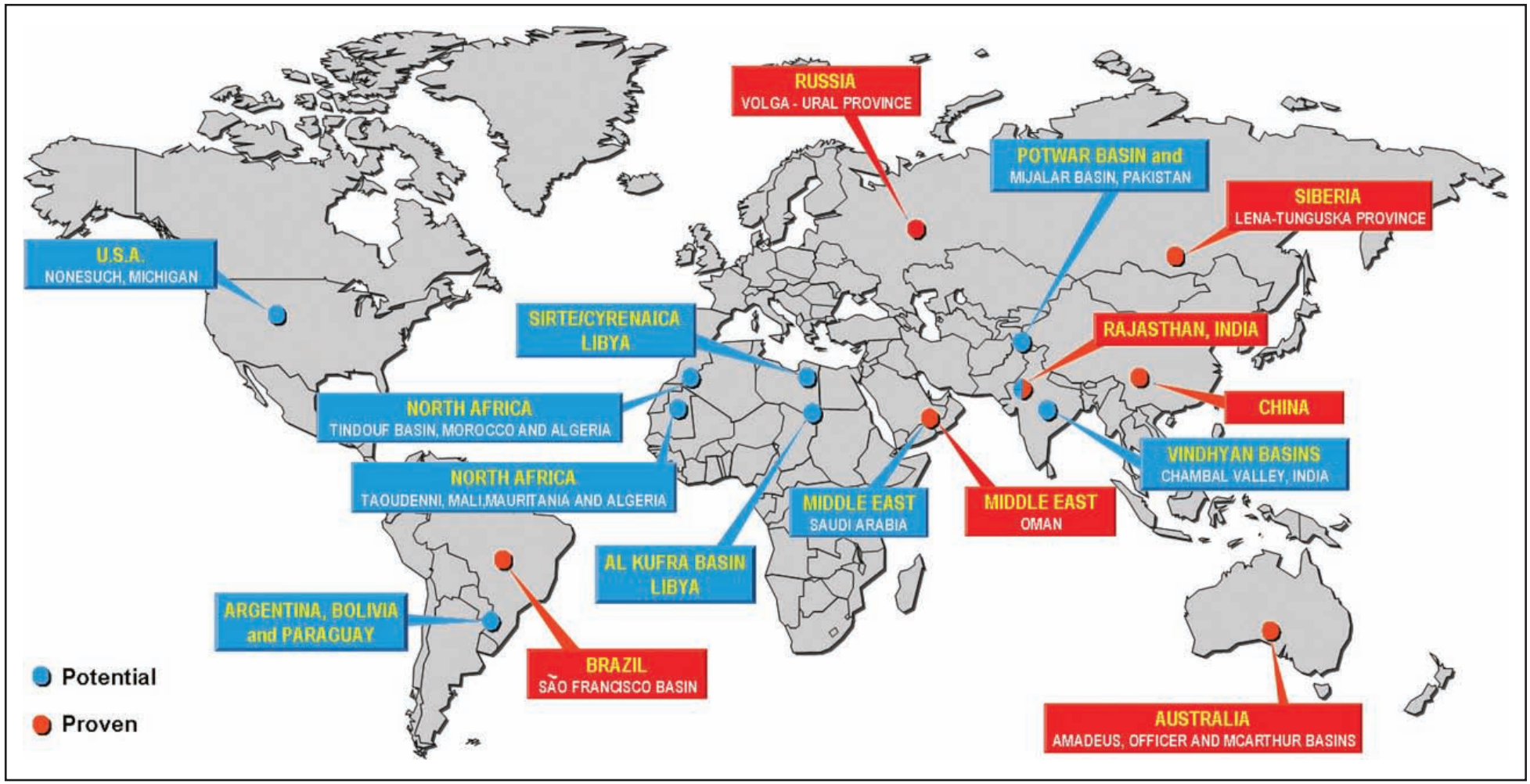


Figure 2: Global distribution of proven and potential Neoproterozoic petroleum systems. Modified after Craig et al. (2009).

The São Francisco basin developed during the Pan African orogeny on the western part of the Congo São-Francisco Craton (see Figure 3) (Alkmim *et al.*, 2006; Sial *et al.*, 2009). The corresponding basins on the eastern part of the Congo-São Francisco Craton (including the Angola block) are the Central Cuvette in Congo and the Owambo Basin in North Namibia and Angola, respectively (Frimmel, 2009; Miller *et al.*, 2009b). The basic idea behind our research effort is to get a better understanding of the petroleum system in the São Francisco basin in terms of source rock horizon, trap and seal geometries and potential reservoirs. Subsequently the gained expertise can be applied to the basins in Southwest Africa, due to assumed similarities in basin evolution in terms of potential source rock horizons, timing of hydrocarbon expulsion, reservoirs and trap and seal geometries.

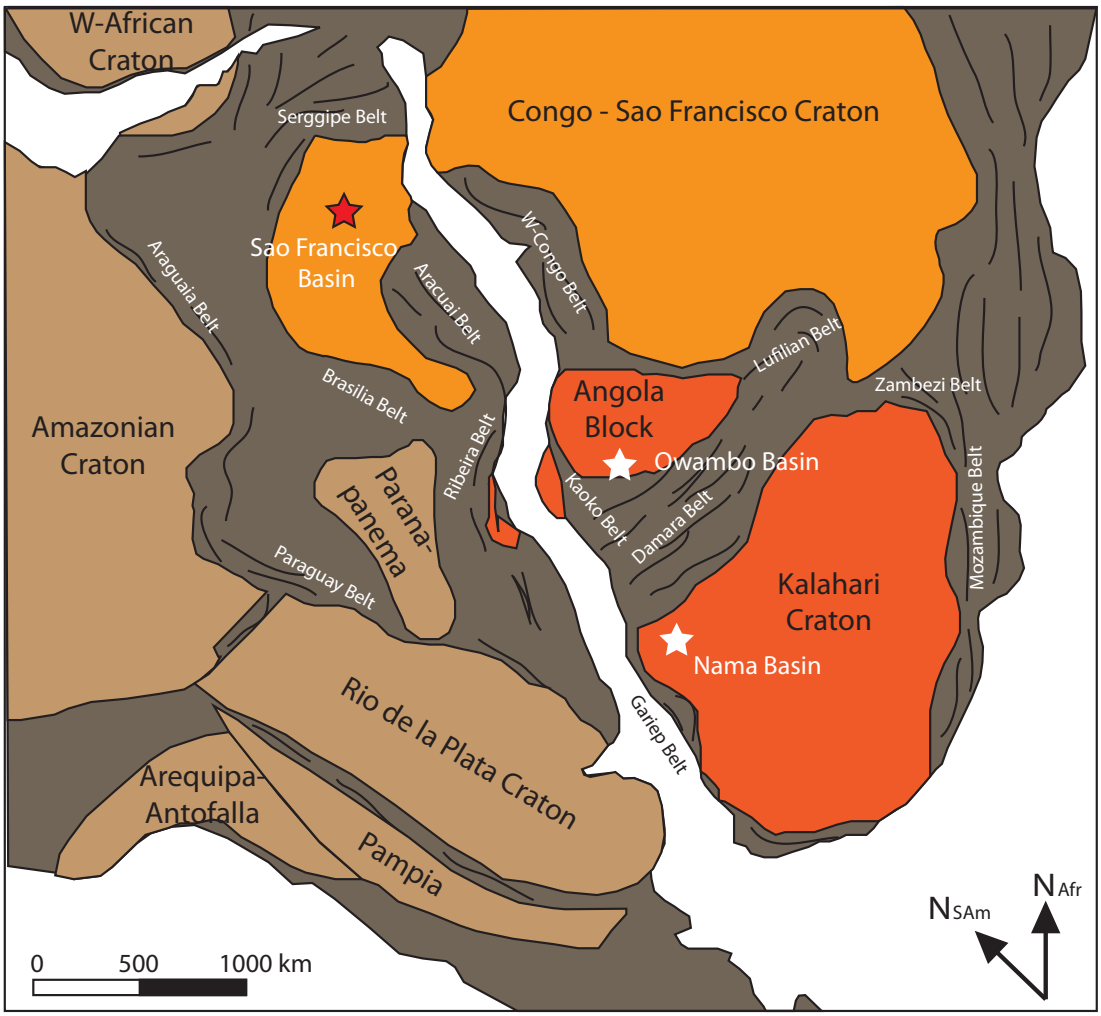


Figure 3: Block configuration of Southwest Africa and South America. The orange highlighted cratons (Congo-São Francisco and Kalahari cratons) constitute the mega region of the Neoproterozoic research programme. Dark grey area and black lines indicate location of Pan-African orogenic belts. The white stars highlight the locations of the Owambo and Nama Basins, the field areas visited during the course of this research project. Red star marks the proven Neoproterozoic petroleum system in the São Francisco basin of Brazil. Modified after Frimmel *et al.*(2010).

This thesis represents the efforts undertaken by the author to better understand potential Neoproterozoic petroleum plays in Namibia. The project was funded by NAMCOR and Sonangol, the national Namibian and Angolan petroleum companies, which are currently actively exploring the Neoproterozoic succession of the Owambo Basin, onshore Namibia and Angola for potential petroleum plays. The motivation for NAMCOR and Sonangol is the occurrence of oil and gas shows in wells in the Owambo Basin of North Namibia and South Angola (personal communications with staff of NAMCOR and Sonangol). Furthermore, the recent discovery of a potential economically viable Neoproterozoic source rock at the southern rim of the Owambo Basin raised expectations to discover a petroleum play in the basin (Bechstädt *et al.*, 2009). However, very little is known about the basin stratigraphy, evolution and in particular about the potential source rock horizons and the expected hydrocarbon reservoirs. Thus, the two main focal points in this research project are:

1. The investigation of **potential source rocks in North Namibia** along the southern rim of the Owambo Basin.
2. The development of an **analogue reservoir model in the Nama Basin of South Namibia**, in order to better understand potential reservoirs in the subsurface of the Owambo Basin.

### 1.2.1 Thesis structure

The first part of this thesis deals with the investigation of possible source rocks along the southern edge of the Owambo Basin. The objective was to obtain multiple transects of exposed Neoproterozoic strata along the rim of the basin and subsequent total organic carbon analyses of organic rich sediments. The initial aim was to link the findings to core descriptions and seismic lines of the Owambo Basin. The source rock part of this research project is covered in **chapter 2**.

The main part of the thesis (**chapter 3-7**) covers the development of a static geocellular reservoir analogue model of a microbial carbonate system. Craig *et al.* (2009) compared producing Neoproterozoic fields worldwide and defined two groups of hydrocarbon systems and associated reservoir rocks for the Neoproterozoic: (1) “glacial” and (2) “pre- and post-glacial” systems. Reservoir rocks of the first group are predominantly glacial siliciclastic. Carbonates, and in particular microbial carbonates constitute the main reservoir rocks of the pre- and

post-glacial systems. The main part of the Owambo Basin, the Otavi group, is carbonate dominated (Miller, 1997) and therefore NAMCOR and Sonangol assume that potential hydrocarbon reservoirs are most likely situated within microbialites. Additionally, a seismic survey, carried out in the late 1970's in the Owambo Basin, identified the presence of potential microbial carbonates within the basin, due to the presence of giant mound-like structures, which were interpreted to represent microbial bioherms (Miller, 1997).

Superbly exposed microbial carbonates are disclosed in the Ediacaran Nama Basin of the Kuibis Subgroup in South Namibia. The carbonate ramp system is deeply dissected by dendritic canyon systems, providing an opportunity to study the ramp system in detail and in three dimensions from a sedimentological and structural point of view. Thus, the sections of the Nama Basin were chosen for the development of a reservoir analogue model to study microbial reservoir characteristics. Microbial reservoir characterisation is a fairly recent development in carbonate research. A new impulse to this field is coming from Brazil with the recent discovery of huge hydrocarbon reservoirs offshore Rio de Janeiro. These reservoirs are situated in the Pre-salt formations within microbial carbonates (Beglinger *et al.*, 2012; Gomes *et al.*, 2009). However, very little is yet known about the sub-seismic reservoir characteristics of microbial carbonates. In order to better understand the internal architecture and sub-seismic heterogeneities of a microbial carbonate system, a high detailed three-dimensional reservoir analogue model was constructed. This includes detailed sedimentological studies of the microbialite system **(chapter 3)** and their structural characteristics **(chapter 5)**. Terrestrial laser scanning (lidar) was used to capture the reservoir architecture and heterogeneities **(chapter 4)**. The virtual outcrop model from the lidar survey served as basis for the development of a geocellular analogue model, including detailed facies models of the microbial carbonate system **(chapter 6)**. The dynamic behaviour of the reservoir model was studied by performing a streamline forecasting analysis. Since the geocellular model is an analogue model for potential subsurface reservoirs in the Owambo Basin, no actual production data was available and therefore history matching of well production rates was not possible. However, through hypothetically simulating fluid flow by choosing standard reservoir conditions, the basic dynamic behaviour of the microbial system could be studied. This is described and presented in **chapter 7** of the thesis. **Chapter 8** provides a synthesis of the research outcomes and puts the

findings into a broader context. Furthermore, recommendations for future research are given in **chapter 8**.

All digital data acquired and generated during the course of this research project, including lidar point-cloud data, virtual outcrop models, geocellular reservoir models and streamline fluid flow simulations are attached in APPENDIX VIII. Data are stored on one DVD (lidar raw data) and one USB pen-drive for virtual outcrop models and static and dynamic reservoir models.

## 1.3 The Neoproterozoic era

The Neoproterozoic Era is the time period in earth history, which begins 1000 Ma years ago and lasts until the beginning of the Cambrian. The Precambrian-Cambrian boundary is currently set at around 542 ± 0.3 Ma years (Gradstein *et al.*, 2004) and the Neoproterozoic Era is thus almost as long as the entire Phanerozoic. During this interval, Earth experienced some of the most severe orogenic events known to men, like the entire geodynamic cycle of the ancient supercontinent Rodinia and possibly a second orogenic supercycle of the supercontinent Pannotia (Li *et al.*, 2008; Scotese, 2009). The Neoproterozoic ends with the onset of the formation of Gondwana, the first supercontinent in the Phanerozoic (see Figure 1).

The Neoproterozoic is the youngest Precambrian era and is divided into three periods, which are from oldest to youngest: Tonian, Cryogenian and Ediacaran. This subdivision is closely related to the lifecycle of Rodinia (see Figure 1). The Tonian (1000 Ma – 850 Ma), named after the Greek word for stretching or tension *tonos*, comprises the first 150 Ma years in the Neoproterozoic. It is the time when Rodinia is still a supercontinent but already started to disperse (De Waele *et al.*, 2008; Li *et al.*, 2004).

The Cryogenian, after the Greek words *cryos* (ice) and *genesis* (birth) is the middle period of the Neoproterozoic. There is no actual GSSP point (Global Boundary Stratotype Section and Point), which defines the base of the Cryogenian, but at the moment the base is defined by a fixed rock age of 850 Ma years (Gradstein *et al.*, 2012). The Cryogenian comprises the time of the break-up of Rodinia (Li *et al.*, 2008, and references therein). It is a time of intense geodynamic events and severe climate changes. The association with the name-giving *cryos* is derived from the worldwide occurrence of glacial sediments, which led to the formulation of the

"Snowball Earth" hypothesis (Hoffman, 1998; Kirschvink, 1992) (see below). This hypothesis proposes at least two global glaciations, where the entire planet was frozen over. The Sturtian glaciation at around 750 to 700 Ma is the older super-icehouse event and some authors consider the onset of this glaciation as the base of the Cryogenian (Smith, 2009). The younger global glaciation, known as Marinoan, took place around 665 Ma – 635 Ma (Allen and Etienne, 2008; Hoffmann *et al.*, 2004).

The base of the Marinoan cap carbonate marks the transition to the Ediacaran. The Ediacaran, named after the town Ediacara in the Flinders Range of Australia, is the youngest period of the Neoproterozoic and starts around 635-630 Ma ago. The type section of the lower boundary is within the Nuccaleena Formation at the Flinders Range and the GSSP spike directly above the Elatina diamictites (Knoll, 2000; Rose and Maloof, 2010; Shields, 2005). Direct radiometric ages from the type section could not be obtained and age constraints are derived from the correlative equivalents in Namibia based on U-Pb zircon age dates of 635.5±1.2 Ma (Hoffmann *et al.*, 2004). The Ediacaran is characterized by the ongoing intense orogenic events derived from the break-up of Rodinia. The Pan African orogeny lasted during the entire period, which formed a number of mobile belts, eventually amalgamating the southern continents to Gondwana in the early Cambrian (Alkmim, 2001; Alkmim *et al.*, 2006; Deynoux *et al.*, 2006; Frimmel *et al.*, 2010). It is still under dispute if there has been a second short-lived Neoproterozoic supercontinent, Pannotia, which might have assembled around 600 Ma (Meert and Lieberman, 2004; Scotese, 2009).

Following the Marinoan global glaciation, life recovered on earth again and the Ediacaran-biota appeared in these latest stages of the Precambrian. This enigmatic biota marks the first appearance of larger, multicellular and architecturally complex organism on Earth (Narbonne, 2005). The biota is represented by mostly sessile tubular to frond-shaped organisms which started to appear at around 575 Ma, following the Avalon radiation (Shen *et al.*, 2008; Xiao and Laflamme, 2009). In particular, a lot of research on the Ediacaran biota has been done in Namibia, in the Kuibis and Schwarzrand Subgroups of the Nama Basin where the majority of the field work for this research project was carried out (Germs *et al.*, 1986; Glaessner, 1963). The biota in the Nama basin is described as Nama-assemblage. Specimens of Ediacaran biota are exceptionally well preserved in the terminal Proterozoic succession, known as Nama-type preservation (Narbonne, 2005). This Ediacaran

type fossil preservation encapsulates fossils within fine-grained sediments (mud to fine-grained sandstones), typically deposited on one single storm or mudflow and preserves the fossils in three dimensions. A prominent example for the Nama-type preservation is *Ausia fenestrata,* a coral like fossil described from successions of the Nama Basin (Hahn and Pflug, 1985). Only one specimen has been found so far but due to its preservation in 3D a detailed reconstruction of *Ausia* was possible.

As introduced above, the Neoproterozoic is almost as long as the entire Phanerozoic Era and Precambrian research is at its infancy. In the last two decades a huge effort in Precambrian research has been undertaken but still very little is yet known about this time period in Earth's history. Challenges arise simply from the availability of suitable outcrops. Less than 3% of todays mapped outcrops are of Neoproterozoic age (Lowe, 1992). Most of these formations are highly deformed and/or metamorphosed, which makes it incredible difficult to obtain reliable data. Given the fact that the advent of life, as we know it today, happened in the latest Precambrian, biostratigraphic methods in order to obtain age constrains cannot be applied for most the Neoproterozoic except for the latest Ediacaran. Absolute radiometric age dates and palaeomagnetic data are sparse. Consequently, global correlations are difficult and often within huge error margins (Allen and Etienne, 2008). Therefore, palaeogeographic reconstructions and the position and configuration of ancient continents are a challenging task and at the present state of knowledge highly speculative (Li *et al.*, 2009; Piper, 2009).

### 1.3.1 The Snowball Earth hypothesis

The "Snowball Earth" hypothesis proposes at least two global glaciations during the Cryogenian, where the entire planet was frozen over (Hoffman, 1998; Kirschvink, 1992). The Sturtian glaciation is the older one, and lasted from about 750 to 700 Ma (Hoffman, 1996; Hoffman and Li, 2009; Macdonald, 2010). The second global glaciation, from approximately 660 to 635 is called Marinoan (Halverson *et al.*, 2004; Hoffmann *et al.*, 2004; Mahan *et al.*, 2010) (see Figure 1). The hypothesis is mainly based on the worldwide occurrence of diamictites, interpreted as glacial deposits in approximately the same stratigraphic horizons. Furthermore, glacial deposits have been found in low latitude and near equator positions. This leads to the assumption that the entire planet was completely frozen. However, it is not always straightforward to identify diamictites as glacial sediments and some researchers are

actually questioning the "Snowball Earth" hypothesis based on the occurrence of glacial diamictites (Eyles, 1993; Eyles and Januszczak, 2004). Their main argument is that not all diamictites are necessarily formed by glacial processes. The term diamictites is purely descriptive and refers to a sedimentary rock, characterised by a fine-grained sandy to muddy matrix with poorly sorted intra and/or extra clasts. Eyles and Januszczak (2007) compiled a comprehensive list regarding processes involved forming diamictites, which ranges from volcanic activity, fault gouges, marine debris flows and turbiditic olistostromes to impact breccias. In order to identify diamictites to be of glacial origin several key characteristics have to be present such as striated clasts or dropstones. The authors argue that in fact most of the worldwide-interpreted Cryogenian Snowball diamictites might be in fact not of glacial origin and are better interpreted in the context of regional and global geodynamic evolution. In particular the Sturtian glaciation, which coincides with the break-up of the Neoproterozoic supercontinent Rodinia and extensive tectonic activity on a global scale (Figure 1). An additional challenge to explain a completely frozen Earth is the recognition of active fluvial and marine sedimentation, which requires an hydrogeological cycle and therefore ice free conditions (Allen and Etienne, 2008; Le Heron *et al.*, 2011). Furthermore, ironstones of North Namibia at the base and within Snowball glacial sediments show evidence for microbial precipitation and therefore potential interglacial intervals and the survival of life (Le Heron *et al.*, 2013a).

However, next to the glacial diamictites there is another, even more enigmatic characteristic related to the global glaciation during the Cryogenian: cap carbonates (Kennedy *et al.*, 2001; Nedelec *et al.*, 2007; Pruss *et al.*, 2010; Rose and Maloof, 2010; Shields, 2005; Vieira *et al.*, 2007). As their name implies, these carbonates cap, normally with a knife sharp contact (see Figure 4), the glacial sediments and comprise one of the most negative $\delta C^{13}$ excursion, of up to -48 ‰, in the geological record. The formation of cap carbonates is not yet understood. It is assumed that these carbonates formed due to chemical precipitation directly on the ocean floor during intense flooding and transgression events, following deglaciation of the "Snowball Earth" (Hoffman *et al.*, 2007). The origin of the $\delta C^{13}$ anomaly is still a matter of debate and several hypotheses have been brought forward. They range from a massive methane release during deglaciation (Ganqing *et al.*, 2003; Kennedy *et al.*, 2008; Kennedy, 2001) until the proposal of a stratified ocean with a dissolved

organic carbon (DOC) reservoir with highly depleted $C^{13}$ content due to the absence of life in the aftermath of the global glaciations (Jiang *et al.*, 2010).

Despite the ongoing debate about the validity of the 'Snowball Earth' hypothesis and the origin and nature of cap carbonates, it is evident that we can find two horizons of glacial sediments and related cap carbonates in similar stratigraphic positions all over the world. These sequences are used as global marker horizons, either through stratigraphic correlation of the couplet diamictites–cap carbonates or through correlation of the unique isotope signatures of the cap carbonates.

Figure 4: Outcrop photo showing the knife-sharp contact of Sturtian diamictites and overlying cap carbonates. Chuos Formation at Varianto Farm, NW Namibia. Courtesy of Dan Le Heron.

### 1.3.2 Neoproterozoic petroleum systems

The Neoproterozoic is the era before the Cambrian radiation and animal life as we know it today. It is the time of the enigmatic Ediacaran fauna and the era of microorganisms. Even though we can assume that physical and chemical processes during the Neoproterozoic were the same as today, Precambrian strata influenced by biological process (e.g.: organosedimentary deposits) might exhibit significant differences as compared to the Phanerozoic rock record (Butterfield, 2009). Thus, potential source rocks, enriched with organic matter might have different characteristics than the Phanerozoic counterparts (Craig *et al.*, 2013). Similar questions arise when investigating potential reservoir rocks. In particular carbonate reservoirs, which comprise the majority of host rocks worldwide (Lucia, 2007b). The carbonate factory is strongly influenced by the organism, which precipitates calcium

carbonate. Therefore, Neoproterozoic carbonates, built-up by poorly understood organisms, might have significant different reservoir characteristics and heterogeneities from micro to macro scale. Neoproterozoic siliciclastic reservoirs are often situated within glacial deposits, which are found globally at several key horizons in the Neoproterozoic strata. They are linked to the Snowball Earth global glaciations during the mid-Neoproterozoic and depositions of extensive glacial sediments. However, a better understanding of the reservoir characteristics and global correlation is still needed. Key questions to address, in order to better understand these ancient petroleum plays are: What are the characteristics of potential source and reservoir rocks? Once identified, how can we correlate these findings on a regional and possibly on a global scale in order to define potential worldwide source rock and reservoir horizons?

The connection between global climate and source rock deposition is a well understood phenomenon (Tissot and Welte, 1978c). Figure 5 illustrates the overall global climate conditions and sea-level curve during the Neoproterozoic and Phanerozoic. This timespan in earth history is divided into a series of cyclic greenhouse (250 Ma) and icehouse (150 Ma) periods. Greenhouse periods are characterised by a relatively warm climate, high sea levels and favourable conditions for life and thus source rock deposition. The figure furthermore illustrates global source rock distribution and shows that major global source rocks were deposited during greenhouse periods and global transgression events. For instance the source rocks, responsible for more than 50% of the global oil production were deposited during late Jurassic and mid-Cretaceous greenhouse periods, including the economically important Kimmeridge clay, being the main source rock of the North Sea oil fields (e.g.: Myers and Wignall, 1987). Understanding this relationship from the Phanerozoic, allows extrapolation into the Neoproterozoic to search for globally distributed source rock horizons. Suitable source rock periods should preferentially comprise, a warm climate, high sea levels compared with transgressional events. Exactly these conditions are present after the Snowball Earth glaciations. Two warm periods are present in the middle of the Neoproterozoic, which is illustrated in Figure 5. The super-icehouse conditions during Sturtian and Marinoan times are followed by a super-greenhouse climate, which is characterised by an assumed rapid deglaciation, major flooding events and post-glacial marine transgression. Large shelf areas were flooded with the development of intrashelf and restricted basins and

in many areas anoxic conditions developed (Bechstädt *et al.*, 2009; Craig *et al.*, 2009). Furthermore, the two global glaciations coincide with main geodynamic phase during the Neoproterozoic (e.g.: break-up of Rodinia during Sturtian times) leading to source rock deposition in rift systems and during basin development (Kendall *et al.*, 2009; Kendall *et al.*, 2006). An additional important factor, making post-glacial successions potential global source rock horizons is the recovery of life. During the Snowball Earth periods, life was practically shut down or survived only in oases.

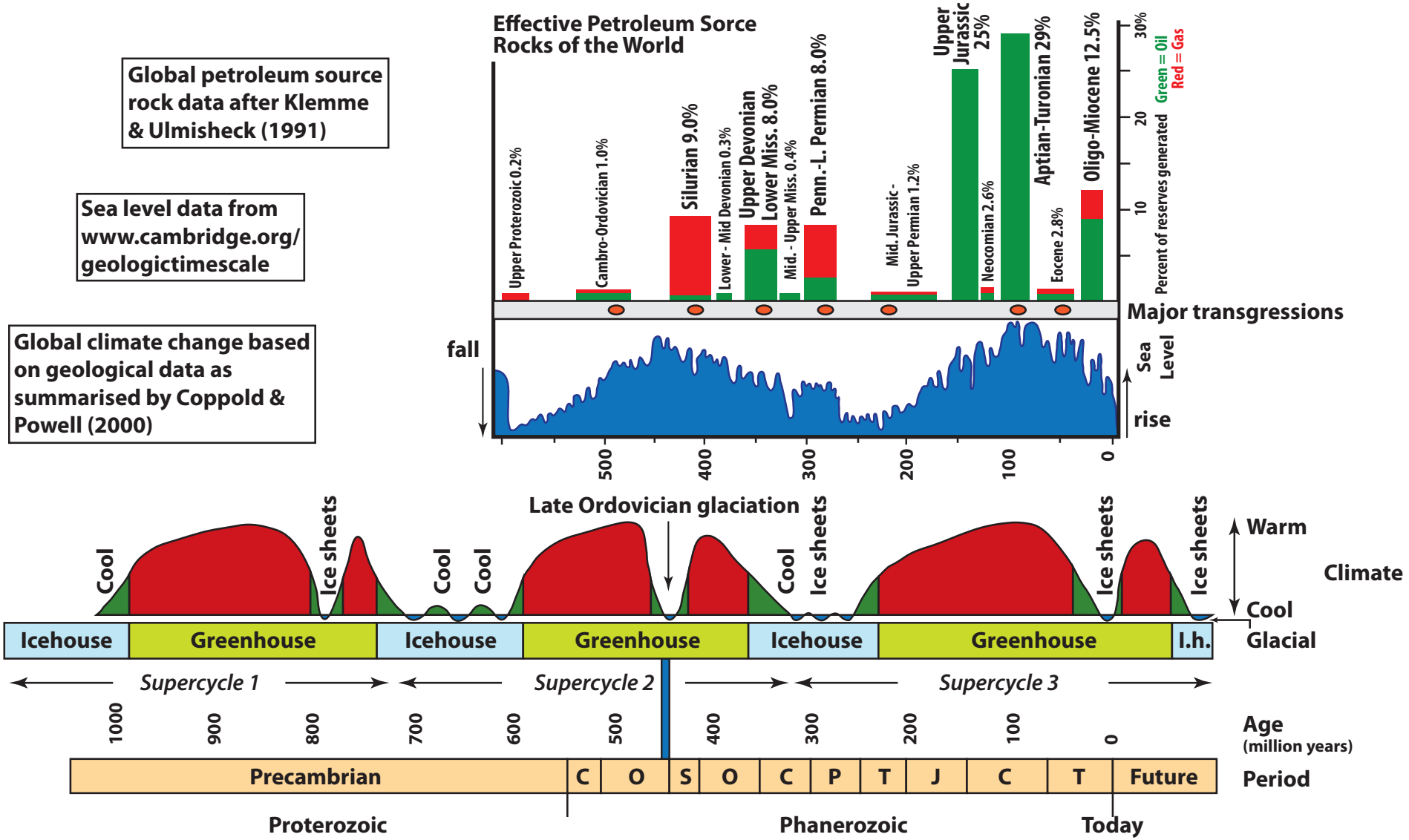


Figure 5: Cartoon illustrating the global climate during the Neoproterozoic and Phanerozoic. This timespan is divided into 3 supercycles, each lasting for about 400 Ma, in turn sub-divided in greenhouse periods (250 Ma) and icehouse periods (150 Ma). The global sea level curve is illustrated in the upper half of the cartoon in relation to the major global source rock horizons. Modified after Craig et al. (2009) and references therein.

With the deglaciation and climate change, life evolved again, subsequently providing the possibility for deposition of organic enriched sediments. Figure 1 shows the carbon isotopic trend for the Neoproterozoic and positive excursions are located after the global glaciation. Organisms preferentially incorporate $C_{12}$ during their lifecycle due to a better energy efficiency. Thus a positive carbon excursion indicates high primary productivity and the burial of organic matter since the lighter $C_{12}$ is removed from the carbon cycle. The above described characteristics make the postglacial horizons preferred source rock habitats.

Connected to the re-awakening of life on earth, is the rise of carbonate production and extensive carbonate platforms formed in the interglacial intervals. The main reef-builder in the Precambrian are microbialites (Penny *et al.*, 2014). Microbialites are the sedimentological products of microorganisms such as cyanobacteria and algae. Microbial carbonates form through a combination of binding, trapping and agglutination of sediment grains and in situ carbonate precipitation (Riding, 2000; Riding, 2011). The appearance of microbial carbonates range from their well-known layered stromatolitic texture to a chaotic clotted texture, so-called thrombolites (Shapiro, 2000). The macrostructure of microbialites ranges from dome-shaped, columnar to goblet-shaped varieties. The two end-members of microbial carbonate megastructures are biostromes and bioherms (see Figure 6). Biostromes are characterised by a laterally extensive, tabular appearance, whereas bioherms are represented by mound like, laterally discontinuous bodies.

These carbonate sequences are of special interest for petroleum geologists because they represent prospective hydrocarbon reservoirs and the megastructures are within seismic resolution. However, a better understanding of their sub-seismic characteristics is still needed to better understand and predict reservoir quality and performance.

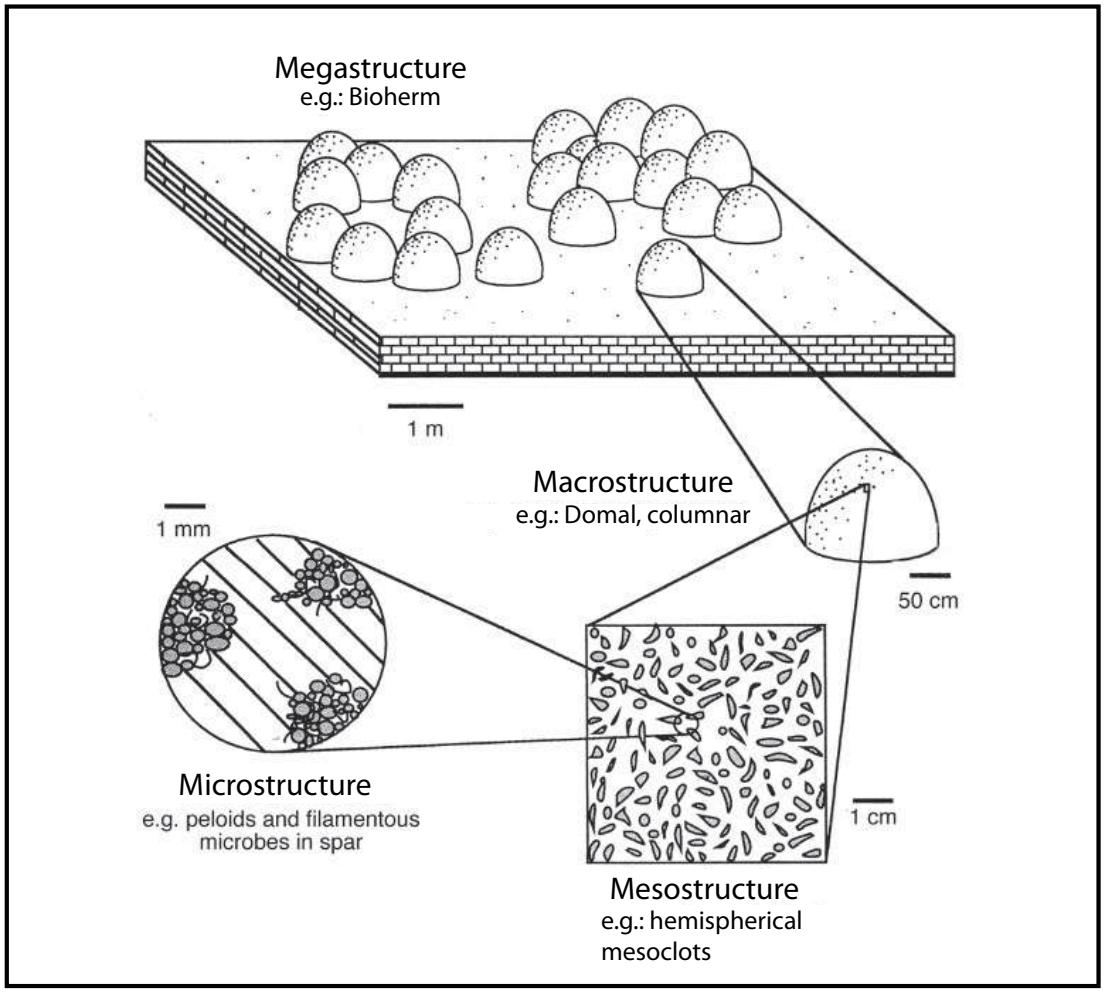


Figure 6: The four scales of microbialite investigation from microstructure to macrostructure. Modified after Flügel (2004).

## 1.4 Geodynamic Evolution during the Neoproterozoic

### 1.4.1 Assembly and break-up of Rodinia

The first half of the Neoproterozoic is characterized by the initial stages of Rodinias break-up. Rodinia, the first identified supercontinent in Earth's history (see Figure 7), formed during the Grenville orogenic cycle (1100-900 Ma) during the latest stages of the Mesoproterozoic and earliest Neoproterozoic (Li *et al.*, 2008). A central problem is the exact configuration of the cratons in Rodinia due to the problems described in the paragraph 1.3. For a detailed compilation and description of possible Rodinia configurations see Li et al. (2008). Not only is the configuration of the cratons within Rodinia under debate, but also which cratons actually contributed to the assembly of the supercontinent (Li *et al.*, 2009; Piper, 2009). One of the central questions in this debate is the history of the Congo-Sao Francisco (hereafter as CSFC) craton. Whilst Li et al. (2008) place the CSFC at the western margin of the

core of Rodinia, other authors see the CSFC as separated from the supercontinent, possibly by an ocean greater than 10000 km (De Waele *et al.*, 2008; Johnson *et al.*, 2005; Scotese, 2009). Scotese (2009) actually regards the collision of the CSFC with Rodinia at around 780-750 Ma as the initial cause for the break-up of Rodinia (see discussion below).

During the Tonian, Rodinia was still intact, although the first continental rifting occurred in this time period (Li *et al.*, 2004). The final break-up of Rodinia took place at around 750 Ma (see Figure 7). The reason for the break-up is still under debate and at the moment two models are proposed: (1) the superplume model after (Li *et al.*, 2008) and (2) a model proposing that the driving force for the break-up is due to slab pull of subducted oceanic lithosphere (Scotese, 2009).

The superplume model is based on the assumption that heat will build up under large insulating continental landmasses. 'Mantle-avalanches' are proposed to occur beneath the subduction zones surrounding the large landmass. Mantle-avalanches are thought to be the result of down welling of dense material following subduction of colder oceanic material (Li *et al.*, 2008). An avalanche push-up effect of the mantle in conjunction with the heat build-up triggers the formation of superplumes. These superplumes then occur as clusters or plume-swarms at Earth's surface and are regarded to be the reason for the initial break-up of Rodinia.

The 'slab pull' model, proposed by Scotese (2009), considers slab pull as the driving force during the Neoproterozoic global tectonic events. Slab pull is the consequence of the negative buoyancy of subducted oceanic crust, which in turn leads to the situation that continental plates get pulled towards subduction zones. The model proposes that Rodinia collided at around 750 Ma with the Congo Craton, approximately at the position of the Kalahari Craton (at the western centre of Rodinia). Scotese (2009) proposes that the Congo Craton was completely surrounded by subduction zones. After the collision of the CSFC with Rodinia these subduction zones split up in a northern and a southern arm respectively. This had the effect that Rodinia eventually split up into two parts: North- and South-Rodinia. Both parts were pulled towards the subduction zones around the Congo-Craton and North-Rodinia rotated counter-clockwise, South-Rodinia rotated clockwise, towards the trench axis. The model is based on two significant assumptions: Firstly, there was no true polar wander (TPW) during the Neoproterozoic and secondly that the

Neoproterozoic plate tectonic mechanisms are the same as Phanerozoic tectonic principles.

The first case is of special interest for the history of North-Rodinia. It shows a rapid rotation over the North Pole after the break-up of Rodinia. Scotese (2009) sees the reason solely in rapid plate movement. However, there are opposing hypotheses, which regard this quick rotation due to true polar movement (Li *et al.*, 2004).

The second assumption is that the plate tectonic mechanisms are the same as in the Phanerozoic. New evidence shows, however, that the Neoproterozoic mantle composition was different to that in the Phanerozoic, which might have affected the tectonic dynamic during the Neoproterozoic (Stern, 2008). Nevertheless, in both models Rodinia starts to break up at around 750 Ma in the lower Cryogenian.

### 1.4.2 The birth of Gondwana and the Pan-African orogenic cycle

Similar to the uncertainties regarding the block configuration of Rodinia, is the geodynamic evolution after the break-up of Rodinia. Still under debate is the possibility of the formation of a second, short lived supercontinent, called Pannotia or Greater Gondwanaland (Hoffman, 1991). Pannotia might have formed at around 600 Ma years, but lasted only for about 40-50 Ma years (Scotese, 2009).

The complexity in resolving the geodynamic evolution after the break-up of Rodinia lies again in the uncertainties of the block configuration of Rodinia. As described above, Scotese (2009) assumes that the CSFC was not part of Rodinia and its collision is the reason for the break-up of Rodinia, in North- and South-Rodinia. Both parts presumably rotated during the next 150 Ma years over the North- and South Pole, respectively. At around 600 Ma years they collided with the CSFC to form the supercontinent Pannotia. Rodinia turned itself “inside-out” (Hoffman, 1991). Soon after its assembly, Pannotia started to drift apart at around 560-550 Ma into four main blocks: Gondwana, Laurentia, Baltic and Siberia

Li et al. (2008), who argued that Rodinia contained all continental blocks, suggest a prolonged break-up process for Rodinia. After the break-up of Rodinia, continental blocks drifted away around Laurentia (proposed centre-craton of Rodinia) to form Gondwana on the other side of the Earth. At around 600 Ma West-Gondwana, comprising the Congo-Sao Francisco, West Sahara (WS), Rio de la Plata (RDP) and Amazonia (AM) cratons were already assembled. The Kalahari (KH) craton was still separated from West-Gondwana at that time (see Figure 7). The final

amalgamation of Gondwana took place by the closure of the 'Mozambique Ocean' and the collision of West- and East-Gondwana (India, Australia, Antarctica) and the docking of the Kalahari Craton at the Congo and Rio de la Plata cratons at around 550 Ma (Basei *et al.*, 2009; Mantovani and Brito Neves, 2009; Miller *et al.*, 2009b).

In both possible models for the geodynamic evolution after the break-up of Rodinia there is a peak in orogenic events at ~600 Ma years (see Figure 7). This event is part of the Pan-African Event. The term Pan-African Event describes a series of orogenic events following the break-up of Rodinia, rather than one single orogeny (Alkmim, 2001; Frimmel *et al.*, 2010; Johnson *et al.*, 2005; Pedrosa-Soares *et al.*, 2008). These series of collision of the continental fragments of Rodinia started after the rifting of the supercontinent and lasted probably until the early Cambrian. The peak at ~600 Ma refers to the formation of West-Gondwana (Li *et al.*, 2008). The mobile belts, which formed during the amalgamation of the cratons are the Pan-African orogens and mainly refer to the suture zones in the Gondwana continents. These are for instance the, Kaoko, Lufilian, Zambezi and West-Congo belt in present day Africa (Frimmel *et al.*, 2010). On the South American side are for example the Araçuai, the Araguaia or the Dom Feliciano belt (Gaucher *et al.*, 2009). The latest Pan-African belts are the Damara and Gariep belts in Namibia and northern South Africa, which formed during the collision of the KH craton with the CSFC and RDP cratons (Frimmel *et al.*, 2010; Frimmel *et al.*, 2002).

## 1.5 The Neoproterozoic of Namibia

The Neoproterozoic geology and geodynamic evolution of Namibia is closely related to the lifecycle of Rodinia and the evolution of three Pan-African orogenic belts in Southwest Africa, which are: the NW-SE trending Kaoko belt in NW Namibia and south Angola, the ENE-WSW striking Damara belt in central Namibia and the Grip belt in southernmost Namibia which, extends further into South Africa (see Figure 3 and Figure 8).

The following resume of the Neoproterozoic geodynamic development of Namibia focuses predominately on the evolution of the Damara orogen because both field areas investigated during the course of this research project are located within the Damara Supergroup. The Damara Supergroup comprises the geological record of the entire evolution of the Damara orogen, starting with the initial rift sediments at

the end of the Tonian until the final molasses sediments deposited in the Mulden and Nama foreland basins at the Cambrian boundary with the formation of Gondwana (Miller *et al.*, 2009b). A schematic cross-section through the Damara belt, illustrating the main geological groups and formations is illustrated in Figure 9.

The initial intracratonic rifting, coinciding with the break-up of Rodinia, started around 900-850 Ma ago (Frimmel and Miller, 2009; Miller *et al.*, 2009b). The exact timing of the onset of the rifting is not yet constrained. The triple junction of the three-pronged Damara rift system lies in Swakopmund, on the western coast of Namibia (see Figure 8). The northern arm extents into the Kaoko belt and the southern arm into the Gariep belt. The NE-trending arm comprises the rift system forming the Damara orogen. Within the latter rift system, two rifts developed: (1) the Northern Rift and the (2) Southern Rift. These rift systems separated the Congo Craton (including the Angola Block) to the north and the Kalahari Craton to the south (present day coordinates).

Continental rift sediments are summarised in the Nosib Group, which forms the basal unit of the Damara Supergroup. They are characterised by polymict breccias, conglomerates and coarse-grained, feldspathic sandstones (Miller *et al.*, 2009a). The transition from rifting to drifting is represented by the Ombombo and Ugab subgroups and is marked by the occurrence of volcanic rocks (Naauwpoort and Askevold Formations), which have an U-Pb single zircon age of 746±2 Ma (Hoffman, 1996). With the ongoing drifting both rift systems evolved into deep oceanic troughs, forming the Damara Ocean, comprised of the Outjo Sea in the north and the Khomas Sea in the south. The Adamastor Ocean (proto-Atlantic) developed at the Kaoko and Gariep spreading zones. Rift shoulder uplift in the Damara rift system occurred in the latest stages of Ombombo Subgroup and triggered the evolution of extensive carbonate platforms on palaeohighs, such as the Northern Platform of the Otavi Group (see Figure 9) (Hoffman and Halverson, 2008).

The following Chuos Formation represents the first “Snowball Earth” glaciation in Namibia and it is a Sturtian equivalent. The Chuos Formation directly overlies the volcanic rocks of the Naauwpoort formation and therefore the base of Sturtian Snowball glaciation in Namibia is constrained by 746±2 Ma. The Chuos Formation is represented by massive deposition of diamictites, which have been interpreted as glacial deposits due to the occurrence of dropstones and striated clasts (Busfield and Le Heron, 2013; Hoffman and Halverson, 2008; Le Heron *et al.*, 2013b). A

dropdown of sea level, exposure of the rift shoulders and the formation of deep-cutting palaeovalleys, eroding the underlying Ombombo Subgroup and Nosib Group, accompany the Chuos glaciation (Miller *et al.*, 2009a). The Chuos glaciation is followed by continental break-up and large-scale transgression due to the melt down of the "Snowball Earth".

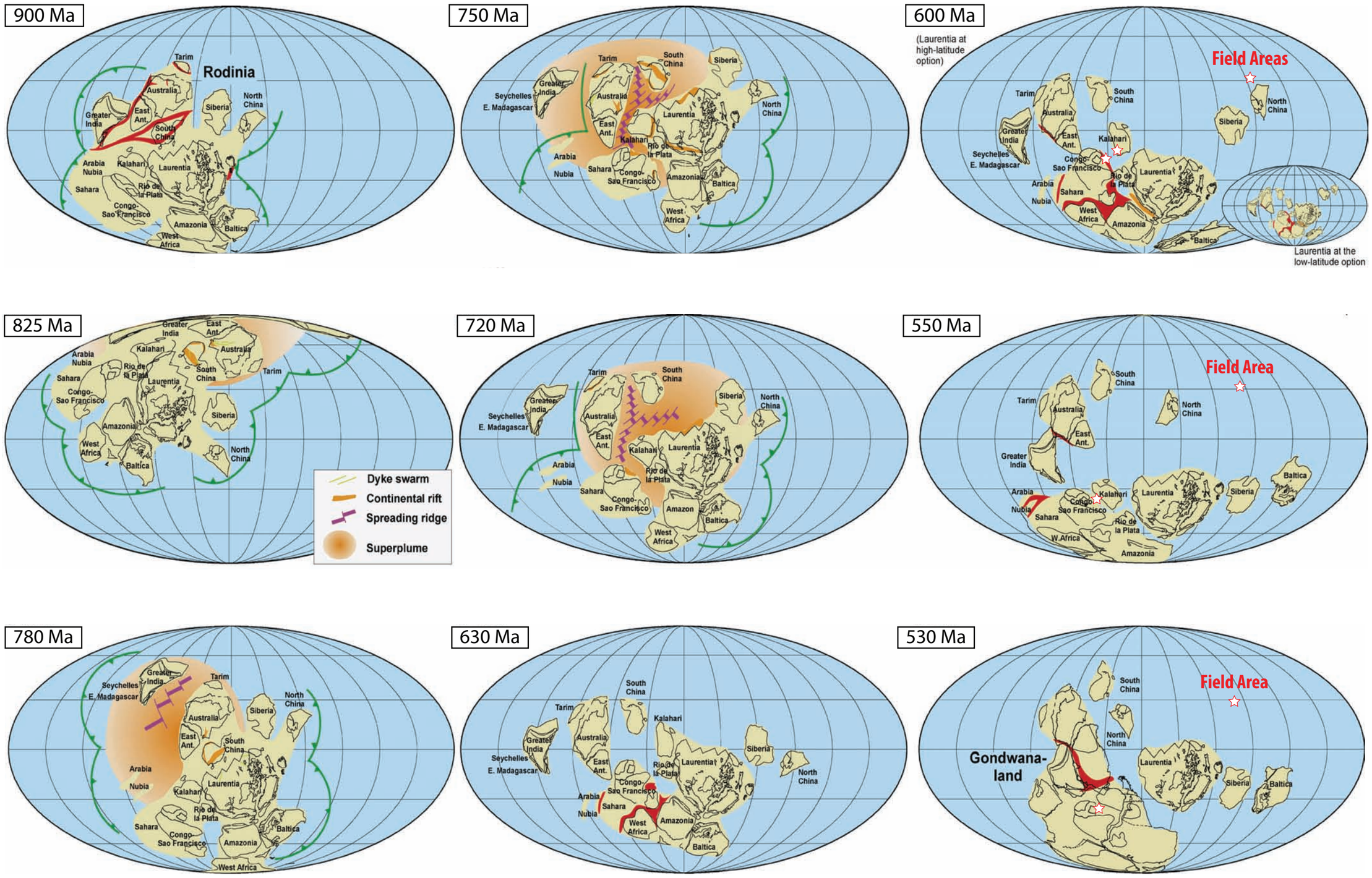


Figure 7: Geodynamic evolution from the beginning of the Neoproterozoic and the break-up of Rodinia until the formation of Gondwana in the early Cambrian. Note the location of the field areas in the last 3 globes, on the Kalahari Craton and West-Gondwana. The illustration is based on the model after Li et al. (2008). Modified after Li et al. (2008).

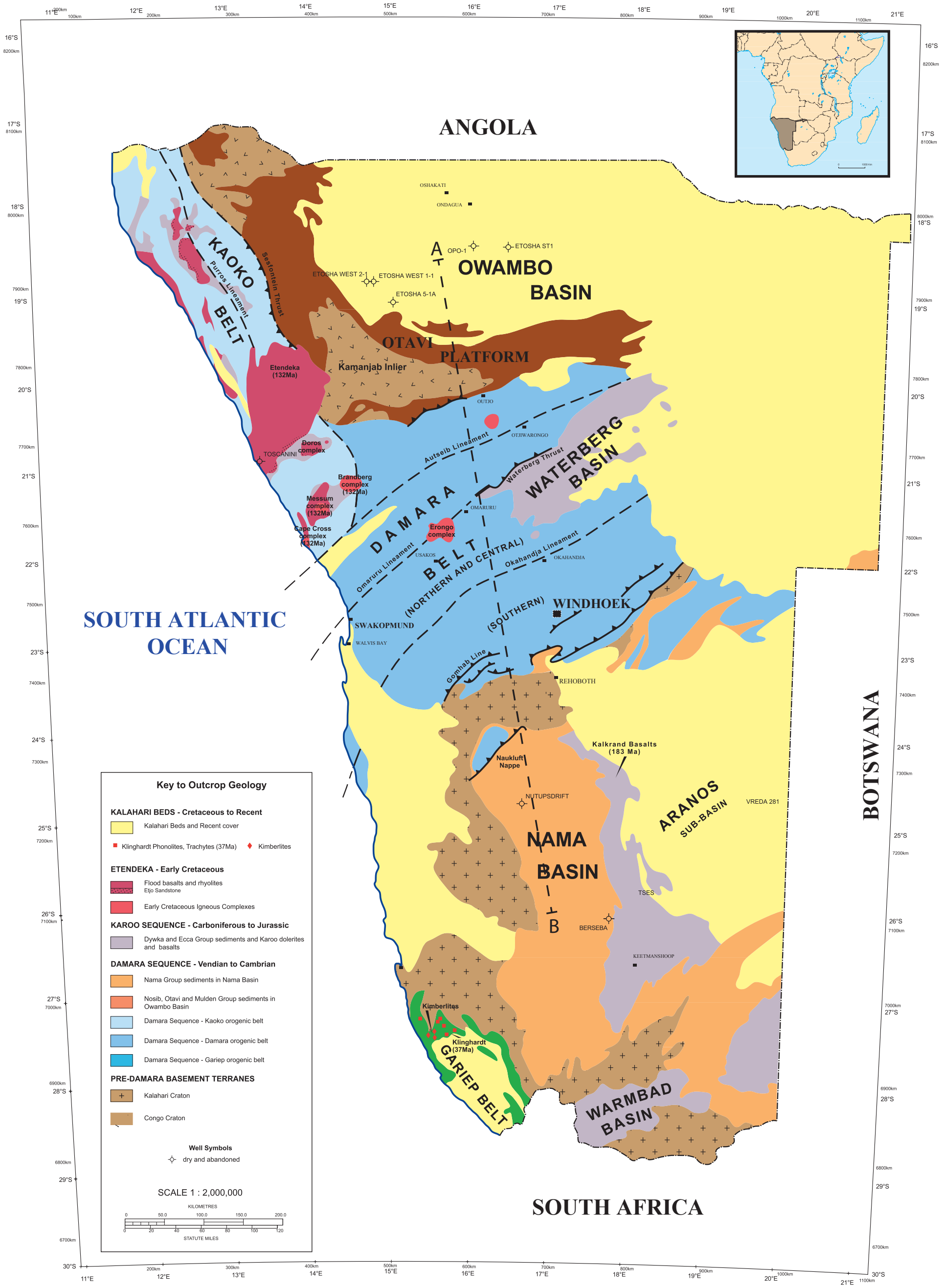


Figure 8: 1: 2 000 000 geological map of Namibia illustrating main tectono-stratigraphic units. Black dotted line indicates location of cross-section in Figure 9. Source: Geological survey of Namibia.

During this time the onset of the Otavi carbonate platform at the Northern Platform of the Outjo Sea occurred (Miller *et al.*, 2009b). The Otavi platform is a 4 km thick carbonate-dominated succession, which developed on an active foreland fold and thrust belt and comprises the main part of the Otavi Group (Hoffman and Halverson, 2008; Miller, 1997). It is distributed along the southern rim of the Owambo Basin and is exposed along strike for over 700 km in north Namibia (see Figure 8). The platform is subdivided into a Western Platform along the Kamanjab Inlier and Sesfontein Thrust fault facing the Kaoko Belt. The Eastern Platform is located in the Otavi Mountainland, in the area around Tsumeb and Grootfontein with palaeoslopes towards the Otju Sea and Owambo Basin.

The second global Snowball glaciation, the Marinoan glaciation, is represented by glacial diamictites of the Ghaub Formation at 635±1.2 Ma, constrained by U-Pb zircon age date obtained from an interbedded ash bed (Hoffmann *et al.*, 2004). Diamictites are followed by tan to pink-coloured cap carbonates of the Keilberg Member forming the base of the post-glacial Maieberg Formation. Simultaneously with the Marinoan cap carbonates appear the first MORB-basalts in the Khomas Sea, representing final continental break-up and ocean floor spreading in the Southern Rift. The Northern Rift subsequently developed as a failed arm (Frimmel *et al.*, 2010).

The Ghaub glaciation occurs stratigraphically approximately in the middle of the Northern Platform and the second half of the carbonate platform developed on a passive margin (Elandshoek – Hüttenberg Fm.) (Hoffman and Halverson, 2008). The equivalent in the Southern Rift to the Otavi Group in the Northern Rift is the Witveli group (Miller, 2008). The Witveli Group comprises a mixed carbonate siliciclastic succession, which developed on the passive margins of the Khomas Sea. However due to the high grade deformation and metamorphism during the closure of the Khomas Sea the Witveli Group has not been subject of detail investigation. Furthermore, the Sturtian and Marinoan marker horizon are sparse and over wide areas absent in the southern rift, which makes correlation to the northern platform difficult. The Blaubecker Formation is regarded as Chuos and the Bildah Member as Maieberg cap carbonates equivalents, respectively (see Figure 9).

The change from drifting to subduction started first in the Kaoko Zone and might have already started at around 700 Ma (Dürr and Dingeldey, 1996). The final closure of the northern Adamastor Ocean and continental collision of the Kaoko belt

occurred at around 595-575 (Frimmel, 2009). This is followed by exhumation of the Kaoko orogeny and the deposition of the molasse sediments of the basal Mulden Group in the Owambo Basin. North directed subduction of oceanic lithosphere in the Khomas Sea started around 580 Ma. The overriding Congo Craton submerged the Kalahari plate and initiated deposition of the lower Nama foreland sediments at around 550 Ma, marked by the development of extensive carbonate platforms and flysch sediments (e.g.: Kuibis carbonate platform, compare chapter 3 for detail overview). The final continent collision between Kalahari and Congo cratons occurred at around 542 Ma and the closure of the Damara Ocean (Blanco *et al.*, 2011). This coincides with the closure of the southern Adamastor Ocean and the evolution of the Gariep orogeny (Frimmel *et al.*, 2002). Continental collisions are followed by exhumation of the Damara and Gariep belts and the deposition of the upper Nama Group molasse sediments in the Nama foreland basin.

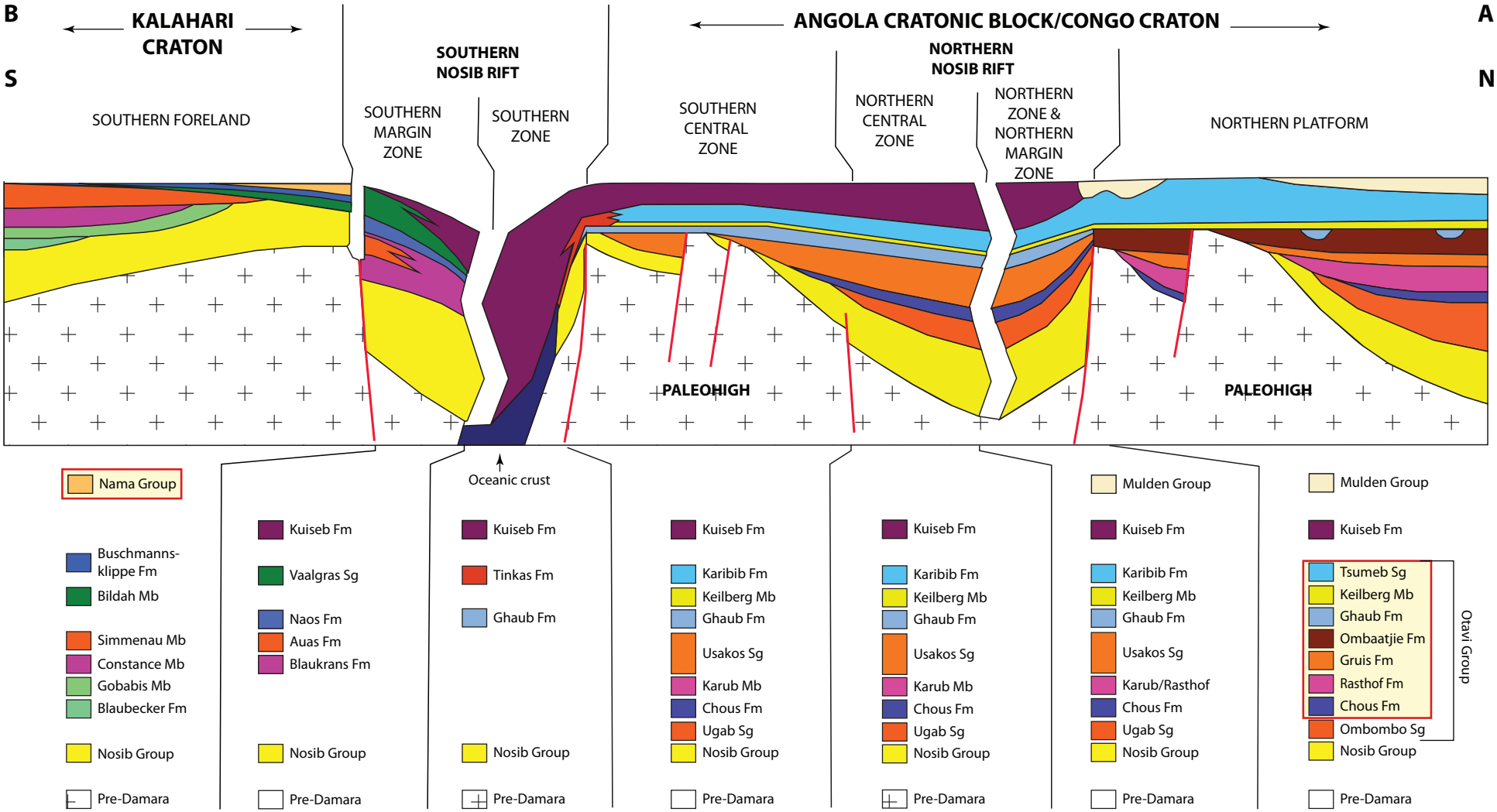


Figure 9: Schematic north-south cross-section through the Damara belt illustrating the main stratigraphic units of the Damara Supergroup and spatial distribution. See Figure 8 for location of cross-section. Red rectangles indicate visited section during the course of this research project. Modified after Frimmel et al. (2010).

# 2 Source rock evaluation of the Otavi carbonate platform

## 2.1 Introduction

Hydrocarbons, trapped in subsurface reservoirs are the end product of phyisco-chemical transformations of organic material. In order to accumulate and preserve organic matter in the rock record, special conditions are required. High bio-productivity is essential, and a preservation mechanism such as anoxic conditions, which inhibit the degradation of organic material, is needed. During burial, with increasing temperature, organic-rich sediments may enter the oil window, which represents the temperature ranges under which carbon chains begin to crack and start to produce petroleum and gas, respectively. The fluid and gaseous hydrocarbons are subsequently expelled and migrate through the sediment succession until they get trapped and stored in a hydrocarbon reservoir.

Source rocks are an integral part of a petroleum play because without a source rock there is no hydrocarbon system. Thus, the study and recognition of potential source rock horizons is often the first part of petroleum exploration. Potential source rock facies are preferentially deposited during times of relatively high sea levels and warm temperatures. High sea levels lead to flooding of shelf areas (e.g. flooded estuaries), and restricted basins may potentially develop, with anoxic conditions, due to a lack of water circulation. High temperatures promote high bio-productivity, and hence deposition of organic matter. Source rock studies on a basinal scale therefore especially target horizons with these characteristics, such as major transgressional sequences.

The aim of this chapter is to present the results of the investigation of the Otavi carbonate platform- a post-glacial succession of early Cryogenian age- from a source rock point of view. Firstly, detailed sedimentological description of four “targeted” potential source rock horizons along strike of the platform margin is provided. Secondly, these rocks are investigated in terms of total organic carbon (TOC) analysis. The TOC content is the main criterion in order to identify organic matter-enriched sediments as potential source rocks. The chapter concludes with the interpretation and discussion of the results.

## 2.2 The Otavi carbonate platform

The Otavi carbonate platform is exposed along strike for more than 700 km on the southern rim of the Owambo Basin (see Figure 10). The carbonate platform developed on the southern edge of the Congo Craton during the Neoproterozoic and is represented by the Otavi Group of the Damara Supergroup (see Figure 11) (Miller, 2008). The Otavi Group is subdivided into the Ombombo, Abenab and Tsumeb Subgroups. A schematic cross-section through the western part, illustrating platform architecture, formations and stratal ages is given in Figure 11. The Ombombo Subgroup is a mixed clastic and carbonate sequence. It marks the transition from rifting to drifting stage in the Damara rift system (Miller *et al.*, 2009a). The Abenab and Tsumeb Subgroups constitute the main part of the Otavi carbonate platform. The platform started to develop on palaeohighs and exhumed rift shoulders of the northern Otju rift and subsequently evolved into a well-developed platform with palaeoslopes towards the south to the Otju Sea and to north towards the Owambo Basin, respectively (Hoffman and Halverson, 2008; Miller *et al.*, 2009a). The platform has a thickness of approximately 4 km, but it is assumed to reach up to 6 km in the subsurface of the Owambo Basin (Miller, 1997).

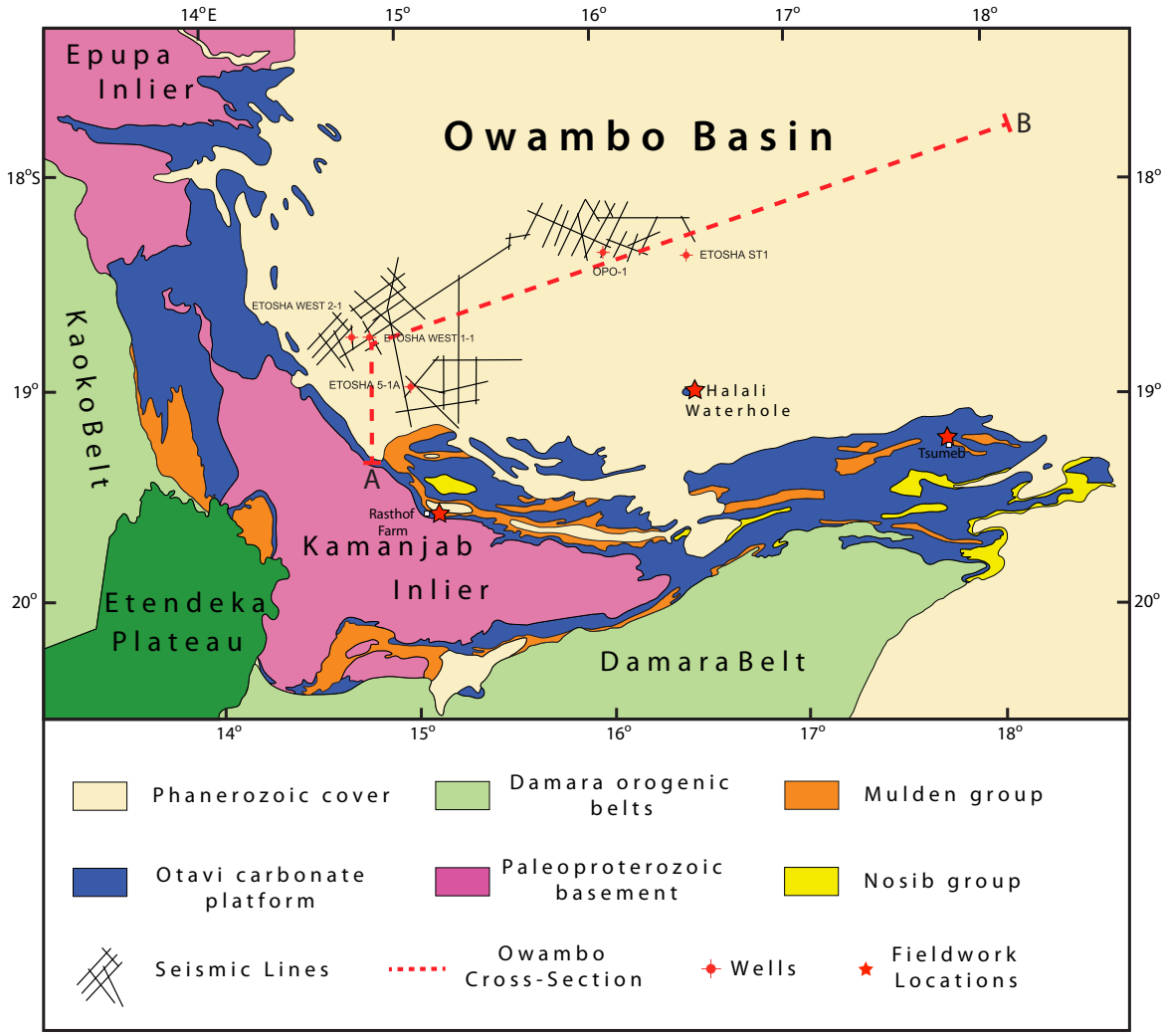


Figure 10: Generalised geological map of the Otavi carbonate platform and Owambo Basin showing seismic lines and well locations. Note the distribution of the platform on the southern rim of the Owambo Basin, between the Pan-African Damara and Kaoko belts. Modified after (Hoffman, 2011).

The Otavi group is punctuated twice by two diamictite intervals, which define the basal formations of the (lower) Abenab and (upper) Tsumeb subgroups. The Chuos formation, overlying the Ombombo Subgroup represents the first glacial event and is the equivalent of Sturtian 'Snowball Earth' glacial event. The Chuos diamictites have been intensively studied within the Snowball Earth community and have been vigorously debated in terms of glacial or not (Eyles and Januszczak, 2004; Eyles and Januszczak, 2007). However, subsequent detailed investigations of the Chuos Formation proved that the diamictites are of glacial origin (Busfield and Le Heron, 2013; Le Heron *et al.*, 2013a; Le Heron *et al.*, 2013b). The overlying Rasthof Formation represents the cap carbonate sequence, with 10-15 m thick cap carbonates followed by up to 300 m thick grey to black dolomites. The top of the Rasthof Formation is marked by a subaerial exposure surface and palaeokarst, which

represents the transition to carbonates of the Gruis and Ombaatjie formations at the top of the Abenab Subgroup (Miller *et al.*, 2009a).

The Ghaub Formation, interpreted as the equivalent of the Marinoan Snowball event, forms the base of the Tsumeb Subgroup (Hoffman, 2011; Hoffmann *et al.*, 2004). It is represented by reddish to brown clast-bearing diamictites, which have been interpreted as glacial deposits, although this interpretation has been questioned (Eyles and Januszczak, 2007). The overlying Maieberg Formation contains the cap carbonate facies, represented by the Keilberg Member. The overlying Elandshoek and Hüttenberg formations are shallow water carbonate sequences, forming the top of the Otavi carbonate platform (Miller *et al.*, 2009a). The continuation of the Otavi platform into the subsurface is not well understood owing to the paucity of seismic data, and the fact that only one well (Etosha 5-1A) has penetrated the uppermost levels of the Neoproterozoic. A schematic cross-section through the Owambo Basin is illustrated in Figure 12. It is assumed that the couplet of Snowball Earth glacial diamictites and cap carbonates are continuous throughout the basin (Miller, 1997). If they have source rock potential, then they have wide lateral extent.

### 2.2.1 Depositional settings for source rocks within the Otavi carbonate platform

As mentioned in the introduction (see paragraph 1.3.2), deposition of source rocks requires specific environmental conditions. The two main factors are high organic productivity, in order to generate sufficient enough organic material, and anoxia to preserve the organic matter from oxygenation and degradation upon deposition. The three main depositional settings for source rock horizons in the Phanerozoic which provide these conditions are lakes, deltas and marine basins (Demaison and Moore, 1980).

Organic-enriched sediments deposited in lakes constitute the majority of source rocks derived from continental settings. Source rock deposition occurs preferentially in deep lakes where water stratification occurs and bottom waters are not affected by wave activity. Furthermore, lakes in low latitudes are preferred source rock habitats due to little seasonal variation of climate and therefore generally no overturn of the water column occurs leading. Thus, anoxic conditions may develop in deeper parts of the lakes. A prominent example for source rocks deposited in a lake is the Eocene Green River Formation of Utah and Colorado, USA (Horsfield *et al.*, 1994).

Deltas also constitute a favourable setting for source rock deposition. Organic-enriched sediments are deposited in low-energy settings of deltas (e.g.: swamps or abundant delta channels). Organic matter is primarily derived from freshwater alga and bacteria, marine biota and terrigenous plant material from the hinterland.

The majority of the world's oil has, however, been sourced from marine source rocks. Marine organic-enriched sediments are deposited in two principle depositional settings: (1) restricted marine basins and (2) upwelling zones at continental slopes and shelves (Demaison and Moore, 1980). Restricted marine basins are characterised by a limited exchange of water with the open sea. Thus, these basins are prone to water-stratification and development of anoxia in deeper parts of the basin.

Upwelling of deep, nutrient-rich bottom waters preferentially occurs on the western side of continental landmasses (Parrish and Curtis, 1982). Water currents are forced to ascend due to Earth rotational force (Coriolis force). This results in extremely high bio-productivity in the photic zone of shelf and slope areas. Subsequent biodegradation of organic matter needs high amount of oxygen and anoxic conditions may therefore occur in bottom waters. A modern day example for source rock deposition in an upwelling zone is the west coast of Namibia, where organic-enriched sediments are deposited with up to 26% TOC (Demaison and Moore, 1980).

Neoproterozoic source rock evaluation is still at its infancy and little is yet known about source rock characteristics and principle depositional setting. A comprehensive review of Precambrian source rocks with special focus on geochemistry and palaeobiology is given in Craig, *et al.* (2013). As described in the introduction chapter (compare paragraph 1.3), two major transgressional events in the Cryogenian coincide with rapid deglaciation of Snowball Earth. These Neoproterozoic post-glacial sequences are increasingly recognised as potential source rock horizons worldwide (Gorter *et al.*, 2007; Heijlen *et al.*, 2008; Le Heron, 2012; Le Heron and Craig, 2012; Olcott, 2005). Thus, these sequences constitute preferred target horizons for source rock studies in underexplored Neoproterozoic basins.

Two post-glacial sequences are recognised in the Otavi Group, the Rasthof and Maieberg cap carbonate sequences, respectively (compare paragraph 1.5). Post-glacial sea level rise for both sequences has been estimated to be several hundreds of metres (Domack and Hoffman, 2011; Halverson, 2002; Le Heron *et al.*, 2013b),

resulting in the flooding of the glacial-overprinted palaeorelief. Furthermore, Hoffman (2011) showed that the Marinoan post-glacial flooding of the Otavi carbonate platform was accompanied by the development of anoxia in restricted basins due to water-stratification of sea and melt water.

The reoccurrence of animal life after the meltdown of Snowball Earth might constitute a source for potential organic matter in these sequences. Figure 11 illustrates the carbon isotopic signature of the Otavi carbonates. Note that two negative excursions are contemporaneous with the glaciations but quickly regain positive values in the overlying post-glacial successions. This indicates the removal of $C_{12}$ and organic burial in the post Snowball Earth successions of the Otavi carbonate platform.

Thus, potential settings for the deposition of organic-enriched sediments in the Otavi carbonate platform are restricted, anoxic marine basins, which formed during post-glacial flooding of the platform. Therefore, this model was used to identify potential source rock horizons within the Otavi platform and consequently field work locations were defined accordingly. Lakes and deltas as depositional models were excluded from consideration because the Otavi platform is interpreted to have formed in an open marine setting, on palaeo-highs at the southern rim of the Angola Block (see paragraph 2.2) and no lake or delta successions have been identified within the Otavi Group. The prediction of upwelling zones needs accurate reconstruction of the palaeogeography of a given target area. This was, however, hampered due to the unknown palaeogeographic setting of the Angola Block.

Evidence for organic-enriched sediments in the Marinoan post-glacial formations of the Otavi carbonate platform in north Namibia has been published by Bechstädt *et al.,* (2009). The authors concluded that these sections have the potential to represent an economically viable source rock for potential Neoproterozoic hydrocarbon plays in the Owambo Basin. However, a better understanding of these source rock horizons in the Otavi carbonate platform, in terms of lateral distribution and stratigraphic position, is needed.

Based on the above-described considerations regarding potential depositional settings for organic-enriched sediments and in concert with published data, the source rock evaluation targeted post-glacial sequences along the southern rim of the Owambo Basin, along strike the Otavi carbonate platform.

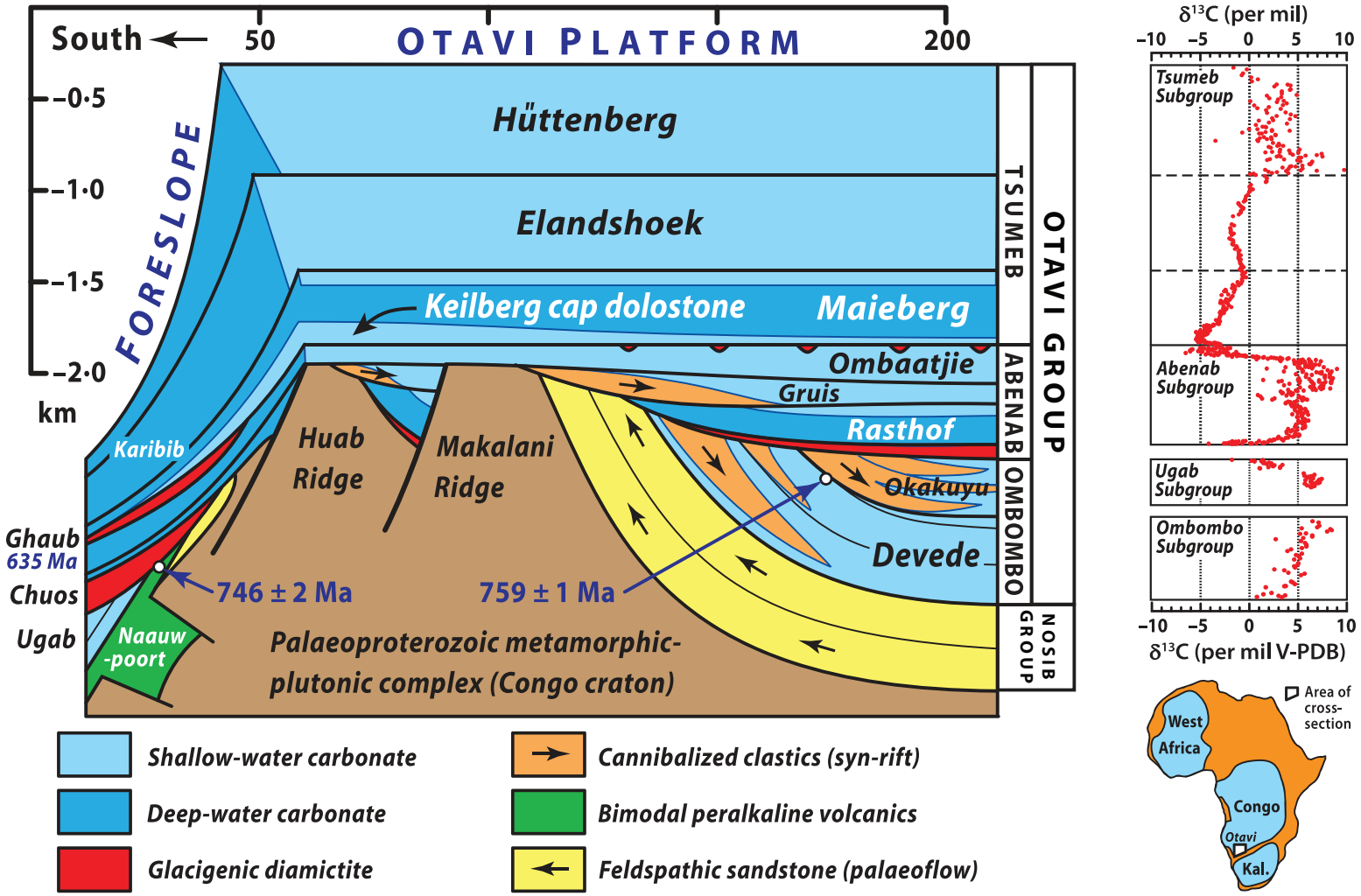


Figure 11: Generalised cross-section through the western part of the Otavi carbonate platform, illustrating the main lithostratigraphic subdivision, depositional ages and platform geometry. On the right side the carbon isotopic trend is plotted. Note the two negative excursions of approximately -5‰ during the two Snowball Earth glaciations. Modified after (Hoffman, 2011).

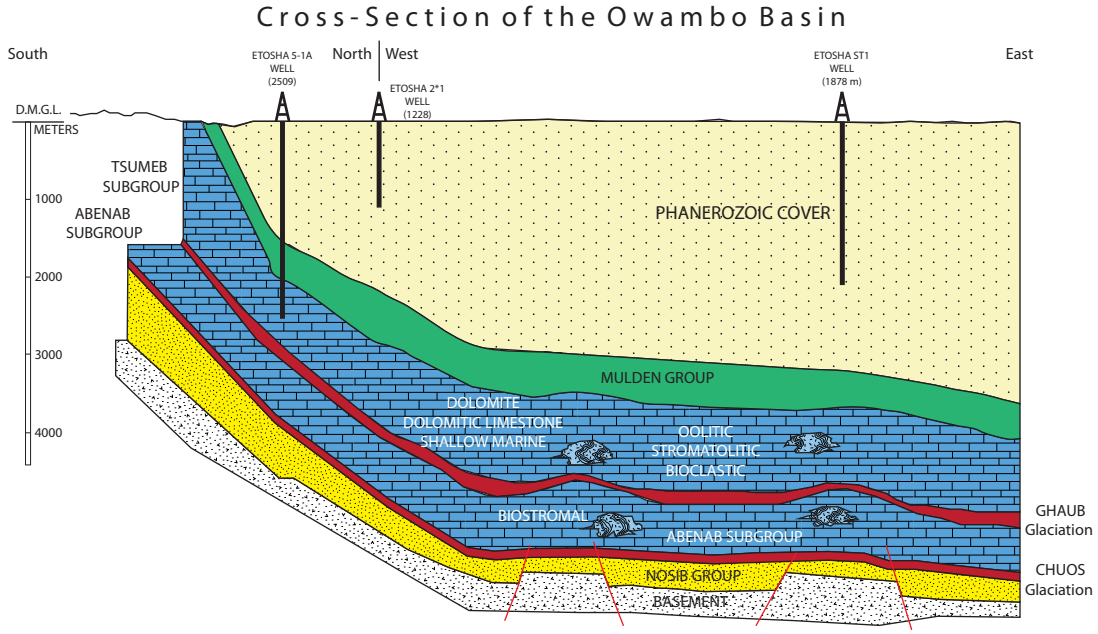


Figure 12: Schematic cross-section through the Owambo Basin. Note that only Etosha 5-1A penetrated the Otavi group. Location of cross-section is indicated in Figure 10. Modified after (Miller, 1997).

## 2.3 Field work in North Namibia

### 2.3.1 Field work strategy

Field work targeted strata exposed along the southern edge of the Owambo Basin on the Otavi carbonate platform. Field work was conducted from 7$^{th}$ of July until 28$^{th}$ of July, 2011 in collaboration with Erwan Le Ber.

The principle strategy was to obtain multiple transects through the potential source rock horizons of the Otavi Group. As described earlier, organic enrichment of sediments can be expected in post-glacial Snowball horizons and therefore, the main focus of the field work was on post-glacial sequences of the Otavi carbonate platform. Two intervals were investigated: (1), the Rasthof Formation at its type locality north of the Kamanjab Inlier (see Figure 10) and (2), the Maieberg Formation, studied at a road cut exposure north of Tsumeb (see Figure 10). The incentive to target the latter horizon was previously published evidence that this interval represents a potential economically viable source rock in the Keilberg Member, approximately 30 km to the south of Tsumeb (Bechstädt *et al.*, 2009). The principle strategy by picking this location was to the test if the Keilberg source rock horizon is laterally extensive and continuous over the platform.

In addition to the postglacial successions, two other sites were chosen: (1) Halali Waterhole and (2) a roughly 2.5 m horizon within the Tsumeb copper mine (see Figure 10). The decision to target these sequences was based on personal communication between the author and staff of NAMCOR, who reported elevated TOC values from these locations. However, the original documentation of the TOC analyses, dated from the mid-seventies of the last century was lost during the turmoil of the Namibian independence in early 1990. The investigated horizon in the Tsumeb copper mine is part of the upper Elandshoek Formation. The stratigraphic position of the exposed strata at the Halali Waterhole is not yet clear but shows similarities to the Maieberg Formation or upper Hüttenberg Formation. The overall aim of the four transects was to tie the observations to the existing seismic lines in the Owambo Basin and compare the observed and analysed horizons with cores and well logs of Etosha 5-1A and Etosha ST1 (see Figure 10).

Field work was carried out by means of traditional field work techniques, including stratigraphic logging of the target horizon and detailed sedimentological descriptions, and sampling with a geological hammer. Challenges during field work arose due to partly inaccessible areas at the Kamanjab area. Furthermore, the Halali Waterhole location lies within the Etosha National park and sampling could only be carried out in a confined and fenced area. Sampling outside the rest camp was not possible due to restrictions from the park authorities and potentially dangerous wildlife.

### 2.3.2 Rasthof cap carbonate sequence

The location of the outcrop lies north of the Kamanjab inlier (see Figure 10). At this location the entire Otavi group is exposed as a relatively thin sequence, dipping steeply north into the Owambo Basin (see Figure 13). This outcrop location was chosen for potential TOC analyses because both the Chuos and Rasthof formations are exposed. Furthermore, Miller *et al.* (2008) reported the occurrence of kerogen from the Rasthof Formation. The outcrop is located on the Rasthof Farm at which Hedberg (1979) completed the first description. In this project, the Rasthof type-section was investigated jointly with Erwan Le Ber. A joint publication of the sedimentological characteristics of the Rasthof type-section, focussing on the

microbial carbonate sedimentology and implications for post-Snowball recovery (Le Ber *et al.*, 2013), is appended to this thesis (APPENDIX I).

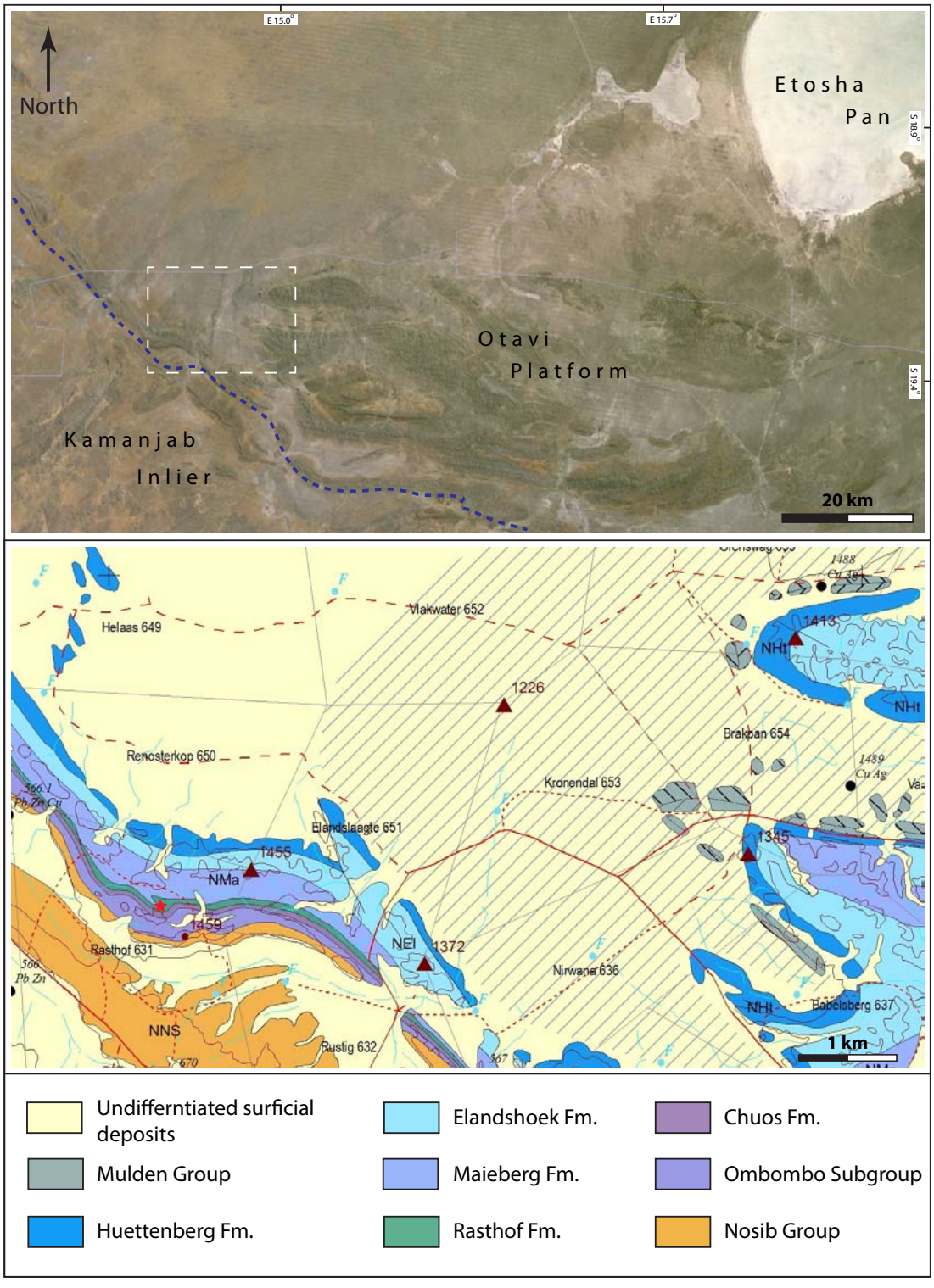


Figure 13: Location of the visited Rasthof cap carbonate sequence southwest of the Etosha Pan, directly north of the Kamanjab Inlier. The upper image is a Google Earth satellite image illustrating the position of the geological map. The blue dotted line indicates extent of the Otavi platform. The geological map is part of the 1:200 000 geological Kamanjab map. Red star indicates location of the visited outcrop at Rasthof Farm. White dashed rectangle in the satellite image indicates location of the geological map.

The study section at Rasthof Farm has a thickness of ca. 120 m (see Figure 14). Diamictites of the Chuos Formation are exposed at the base, overlain by the Rasthof cap carbonate sequence. This latter unit is subdivided into a 10-12 m thick cap dolostone interval, followed by 110 m of microbial carbonates. The microbialites are represented by a 55 m thick, thickly-laminated microbial member (MM1), which is overlain by an equally thick interval of finely laminated microbial mats, punctuated by individual stromatolite growth forms (domes and branching varieties). The following is a detailed description of the cab dolostones, which were analysed for total organic carbon content. Descriptions and interpretations of the overlying microbial carbonates are given in Le Ber *et al.* (2013).

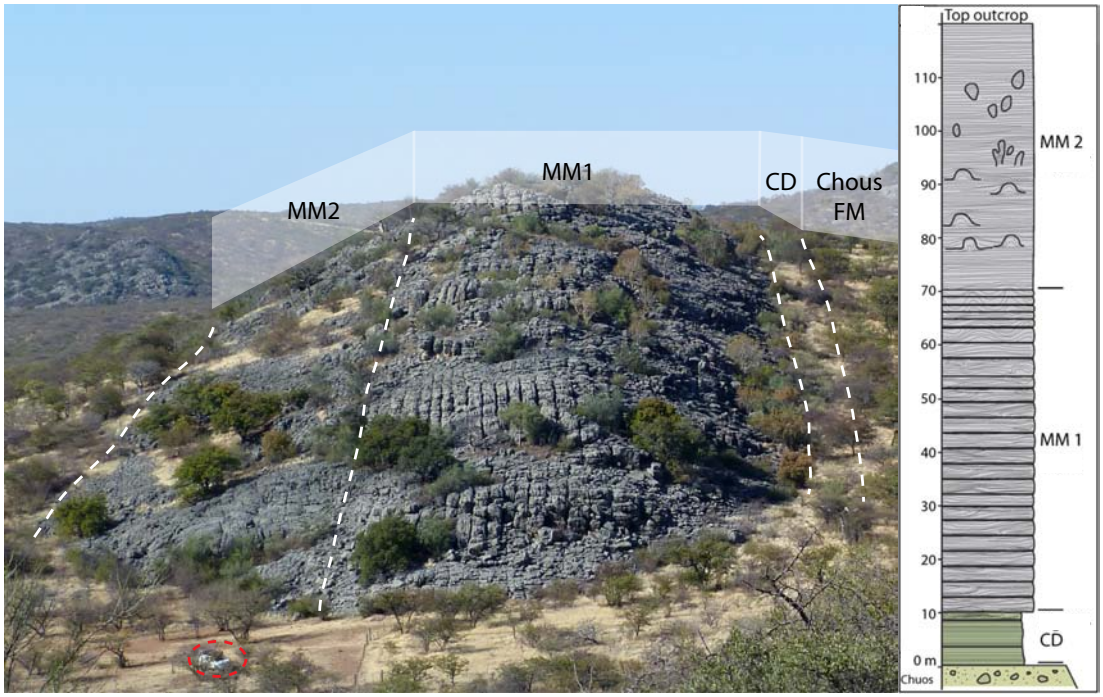


Figure 14: Outcrop overview of the Rasthof cap carbonate sequence and generalised stratigraphic log modified after (Le Ber *et al.*, 2013). CD=cap dolostones: MM1=Microbial Member 1, MM2=Microbial Member 2. Red, dotted ellipses indicates car for scale.

A total of three sections were logged of the cap dolostones along strike, approximately 140 metres apart (see Figure 15). The contact to the diamictites was only exposed at one location. Diamictites are represented by a brown to reddish fine-grained matrix and abundant pebble-size clasts. No internal layering or grading is apparent. The diamictites are followed by a 20 cm-thick interval of tan carbonate, which is finely layered (mm-scale) and has abundant mm-cm sized quartz nodules. The next 30 cm are marked by a reddish carbonate with abundant microbial clasts,

without internal grading. The clasts are several centimetres in diameter, light to dark grey and show a finely laminated, stromatolitic texture. This interval is in turn overlain by a 10 cm thick layer of red to dark red carbonate. The internal texture is represented by a fine lamination. The transition to the overlying blue-grey dolostones is gradational.

This blue-grey laminated dolostone represents the thickest interval at all three logged sections (see Figure 16.A). Lower levels of these strata are intensely fractured (see Figure 15, **Log I 2.0 – 2.95 m**). Intervals with mm-thick undulating, wavy laminae are additionally present in the lower part of the cap dolostone interval. The majority of laminae, however, are horizontal to sub-horizontal, parallel and do not show any wrinkles or crinkly textures. The dolostones are punctuated twice by approximately 10 cm-thick, fine-grained, non-laminated beds, which can be traced as marker beds over the entire sections (see Figure 15). Towards the top of the cap carbonate section, intrabed deformation structures appear such as cm- to dm-scale fault bend folds (see Figure 16.B). The uppermost part of the cap dolostones is marked by hummocky cross-stratified intervals (see Figure 16.C), characterised by low angle, concave and convex bounding surfaces. Laminae within the bedforms are parallel to the bounding surfaces. The transition to the overlying microbial carbonates is knife sharp. The microbialites directly start to grow on top of the cap dolostones, in general parallel to the contact surface but also vertically upward, relative to the contact surface (see Figure 16.C). The microbial carbonates are characterised by wavy, undulating sets of mm-thick laminae.

The logged and described cap dolostones at Rasthof Farm show comparable characteristics to other supra-Chuos cap dolostones in Namibia (Hoffman and Halverson, 2008; Pruss *et al.*, 2010). Tojo *et al.* (2007) and Hoffman & Halverson (2008) described non-laminated, fine-grained beds from the cap dolostones in the Warmquelle-Omutirapo and interpreted them as allodapic beds. The two identified marker beds in Rasthof might be comparable to these allodapic beds, although this awaits confirmation by additional regional mapping. The intrabed context of the deformational structures is interpreted to indicate soft sediment deformation. Additionally, syn-sedimentary deformation of the Rasthof Formation has been reported by Hoffman & Halverson (2008). Seismic shocks, potentially triggered by post-glacial rebound after ice melting might be responsible for the formation of these structures (Le Ber *et al.,* 2013). An intriguing characteristic at Rasthof Farm is the

transition from diamictites to the cap dolostones. In the literature the contact is generally described as knife-sharp, which is not the case at the type-location (Bosak *et al.*, 2011; Hoffman and Halverson, 2008). To the contrary, a transitional contact is observed, commencing with reddish to tan carbonates, with a 25 cm-thick layer of reworked microbialites. The intense colour was interpreted as hematite staining, due to mobilised fluids from the underlying diamictites and reworked material at the base of cap carbonates is rare but has been reported from other locations (Hoffman & Halverson, 2008)

A key observation is the occurrence of hummocky cross-stratification, indicating relatively high-energy conditions and a shallow water setting at the top of the cap dolostones, indicating a shallowing upwards sequence. The overall depositional setting for the cap dolostones at Rasthof Farm is interpreted as a deep-water environment with a shallowing upward trend (Le Ber *et al.,* 2013). This is in agreement with interpretations of the Rasthof Formation from other locations at the Otavi carbonate platform (Hoffman and Halverson, 2008; Pruss *et al.*, 2010). A total of 16 samples were taken from all three logged sections for subsequent total organic carbon analyses (see Figure 15).

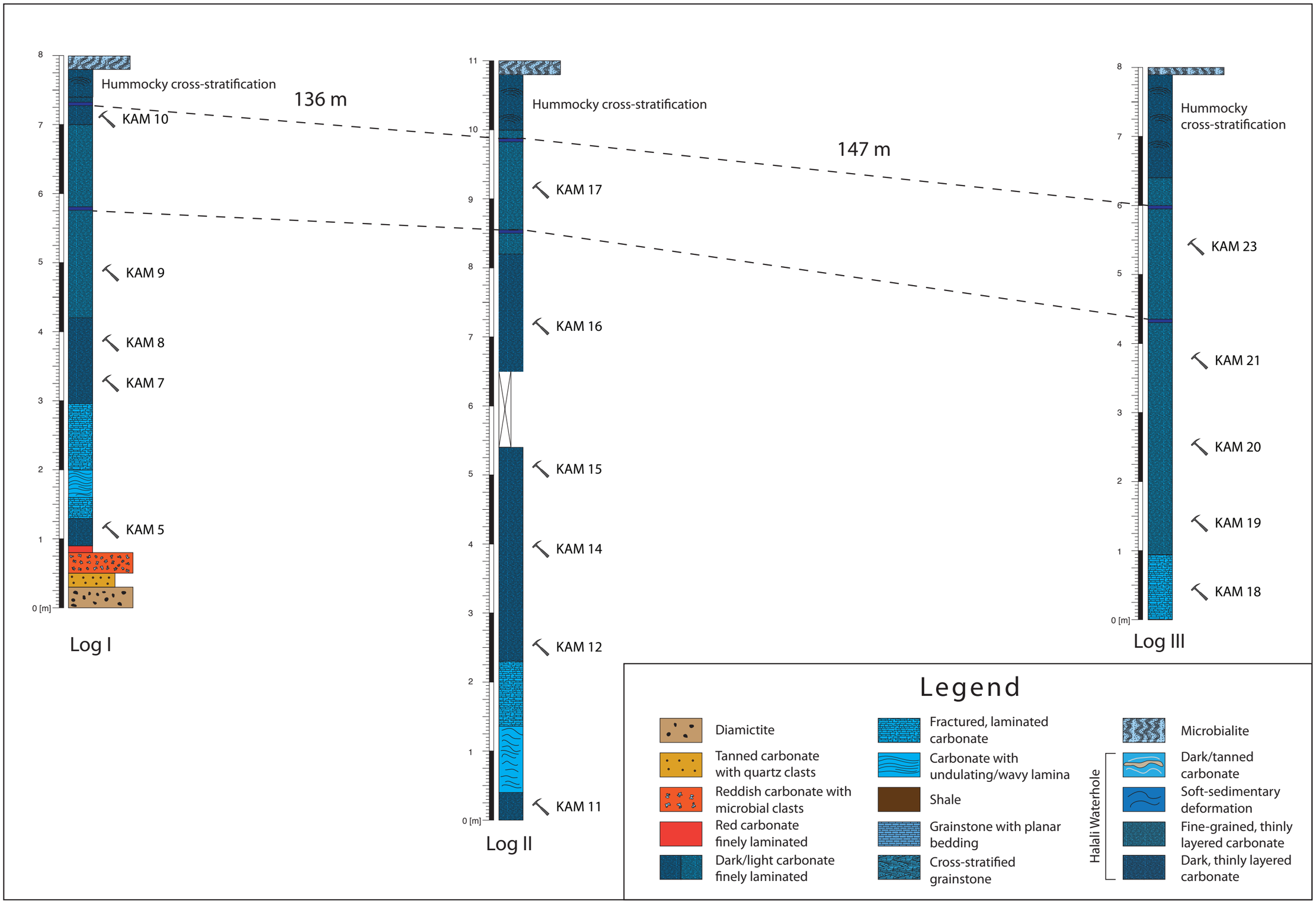


Figure 15: Stratigraphic logs of the cap dolostones at Rasthof Farm. Geological hammer icon indicates sample location and name.

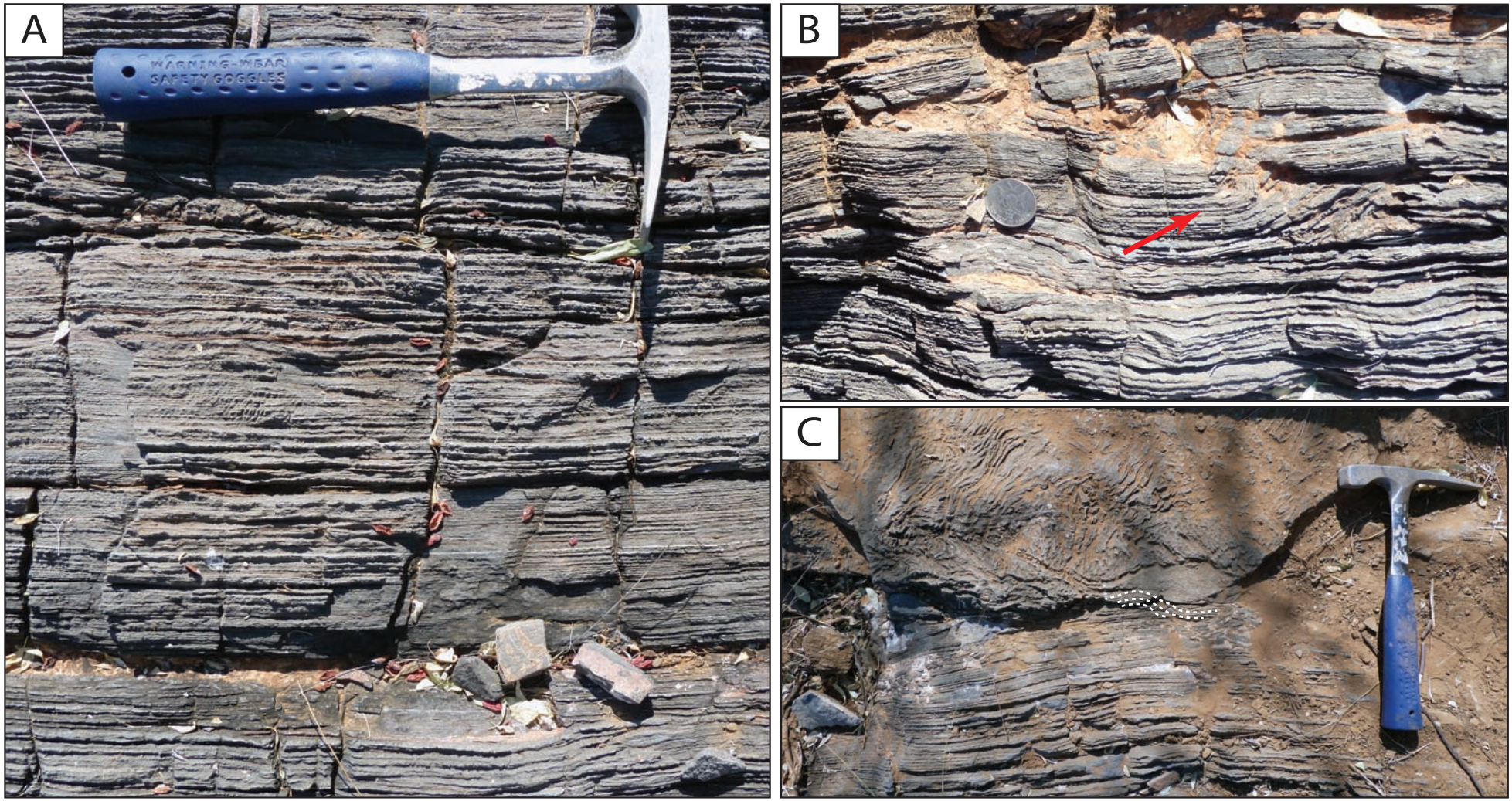


Figure 16: Cap dolostones of the Rasthof Formation. (A) Finely laminated dark dolostone. (B) Small-scaled fold (red arrow) in the upper part of the cap dolostone sequence. Not the fold is restricted to a set of beds and under- and overlying beds are undeformed, indicating soft-sediment deformation. (C) Transition of cap dolostones and microbial member 1. Note the hummocky cross-stratification at the top of the sequence (white dotted line). Microbialites appear abruptly and at this section grow almost vertically relative to the base.

### 2.3.3 Halali Waterhole

The field work location lies within the Halali rest camp area in the Etosha National Park, south of the Etosha pan (see Figure 17.A&B). The visited outcrop is an approximately 15 m high hill within the peneplain of the Etosha pan. As stated in the paragraph 2.3.1 above, this location was chosen for sampling and subsequent source rock analyses due to reported elevated TOC contents by members of NAMCOR. Although the original samples and analyses were lost, geologists from NAMCOR remembered that the samples with the highest TOC were taken from the upper third of the sequence. In order to test the entire succession a detailed sedimentological log of the exposed lithologies was produced and 14 samples for TOC analyses were taken.

The measured section at the Rest camp is 13.5 m thick and starts directly at the waterhole. However, the first 1.5 metres and very base of the section are not exposed and could not be logged. The base of the section is marked by a grey to light grey, fine-grained and thinly laminated carbonate. The laminae are dark grey and 1-2 mm-thick (Figure 18.A). These contain silica nodules up to 1.5 cm in diameter. The nodules are black to dark brown and commonly concentrated in individual layers (Figure 18, **0-0.95m**). The overlying interval (Figure 18, **0.9-4.15m**) is represented by a black to dark brown fine-grained carbonate, with abundant coarser grained, dark carbonate interbeds. The fine-grained layers are characterised by planar bedding and occasional mm-scale brown to reddish laminae (Figure 18.B). Millimetre-sized pyrite crystals are frequent. Fresh, unweathered specimens, taken with the geological hammer, exhibit an intense foul odour of rotten eggs. The coarse-grained interbeds exhibit frequent cross-laminated layers with sand-size grains and few larger clasts (a few mm in diameter). A few cm-sized quartz nodules are common within the coarse-grained horizons. The contacts between the underlying fine-grained and overlying coarse-grained beds are typically irregular. A 5 cm-thick dark grey to black dolo-mudstone bed punctuates this interval at **2.6 m**. The next 4 m of the section (Figure 18, **4.15-8.0m**) are characterised by an alteration of cm-thick grey-tan and black carbonate beds. Within the tan interbeds, brown to reddish laminae are common. This interval contains several dm- scale recumbent folds and convolute bedding (Figure 18.C). Brittle deformation structures also occur, marked by beds broken into a “brick-like” fabric, and the occurrence of sedimentary dykes. Towards the top of

the interval soft-sediment deformation gradually passes into a carbonate breccia, of coarse-grained clasts (mm- to cm-size) in a tan fine-grained matrix.


Figure 17: Location of the visited outcrop at Halali Waterhole rest camp within the Etosha National park. (A) Google Earth satellite image of the Etosha pan. Yellow pin indicates the rest camp and white dotted rectangle the location of the geological map in B. (B) Section of the 1:100 000 geological map of the Etosha national park.

The breccia is followed by a ~ 1 m-thick interval of an alternating sequence of dark and tan carbonate layers, without any soft-sediment deformation structures (Figure 18, **8.0-9.05 m**). Quartz nodules are present but are less common than in the underlying sections. In this interval, stylolites with mm- and occasional cm-high amplitudes occur, crosscutting several layers. Where stylolites extend into black beds, the area below the stylolite as additionally tan (Figure 18.D). The next 2.5 m (Figure 18, **9.05-11.55 m**) is similar to the interval at the base of the section (see Figure 18, **0.9-4.15m**) with coarse and fine-grained alternating carbonate beds, quartz nodules and pyrite crystals. The top of the section is again represented by an alternating sequence of tan and black layers without soft-sediment deformation (Figure 18, **11.55-13.30m**).

The sequences of laminated, fine-grained carbonates and coarse-grained carbonates, bounded by erosional surfaces with an overall coarsening-upward trend indicate deposition as gravitational mass flows. The recumbent fold and convolute bedding are interpreted as gravitationally-induced soft sediment deformation structures and indicate deposition on a slope. In concert with this, the breccias intervals are interpreted as debrites. These interpretations are in line with the interpretation of Miller, (2008). The overall characteristics of the section are indicative for gravitational mass transport of sediments towards deeper parts of the basin, in a slope setting. The observed abundance of pyrite crystals might indicate anoxic intervals during deposition. Pyrite is commonly present in sedimentary rocks, which are enriched in organic matter because it forms due to sulphate reduction, coupled with degradation of organic matter in an anoxic setting (Raiswell and Berner, 1985). Additionally the smell of rotten eggs, commonly derived from sulphur dioxide, indicates enrichment in sulphur and therefore potentially in organic matter. The sampling for TOC analyses was focused on the intervals without deformational structures and the occurrence of pyrite, since these potentially represent higher TOC value intervals.

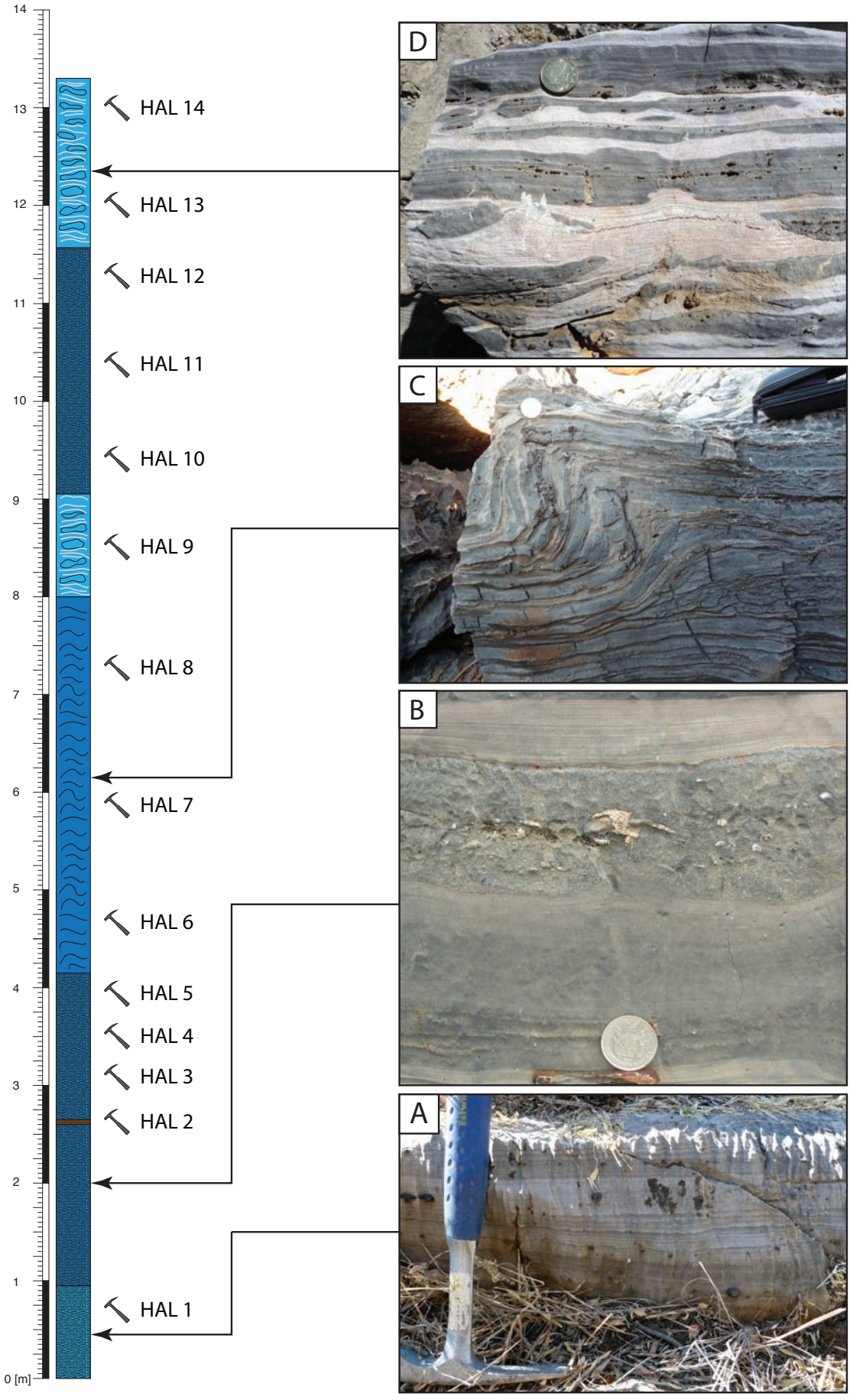


Figure 18: Logged section at the Halali Waterhole. Geological hammer icon indicates sample name and location. See Figure 15 for legend. (A) Finely laminated light grey dolostone with quartz nodules. (B) Sequence of fine to medium-grained carbonate with planar bedding and coarse-grained interbed. (C) Slumping structure in the middle of the logged section. (D) Sequence of tanned and dark grey carbonates.

### 2.3.4 Otavi Mountainland

#### 2.3.4.1 Maieberg road cut

This outcrop is situated approximately 8 km to the north of Tsumeb (see Figure 19). Recent road construction work exposed an entire section through the post Ghaub glacial cap carbonate sequence at a road cut of the M75 (Figure 20.A). Field work could only be conducted at the road cut because on the farm area at either side of the road the local community spotted several black mambas. The bite of the black mamba is lethal within 15-30 min. Although a hospital, which has the antidote stored, is close in Tsumeb, the risk of investigating the surrounding outcrops was too high.

Of special interest at this section is the dolostone sequence of the Keilberg Member, which represents the lateral equivalent of the potential source rock section investigated by Bechstädt *et al.* (2009), south of Tsumeb. The entire section is carbonate-dominated, represented by dolomites exhibiting various colours. The underlying Ghaub diamictite is not exposed at the road cut. The first 5 m of the logged section is marked by a sequence of brownish to tan dolostone with 10 cm-thick intercalations of gypsum beds (Figure 20, **1.0-5.0 m**). The dolostone is characterised by a massive appearance. The gypsum layers are brownish weathered and can be easily removed with the geological hammer to reveal white layers in fresh section (Figure 20.B). This interval is then followed by an approximately 5 m thick sequence of dark grey to black dolostone, also with interbedded gypsum layers (see Figure 20, **5.0-9.8 m**). The dolostone shows fine, dark grey, mm-thick internal layering. Blackish layers reach up to several cm (Figure 20.C-D). Millimetre-sized pyrite crystals are common. This dark interval is capped by a 4 m thick brownish, tan dolostone bed (see log Figure 20, **9.8-14.40 m**), which is then followed by a dark grey to black dolostone interval with abundant pyrite crystals at the base (see log Figure 20, **14.60-19.20 m**). The following log interval is characterised by the appearance of brownish to pink dolostone, interbeded with dark grey, black dolostone and gypsum beds (see log Figure 20, **19.20-29.00 m**). Towards the top of the sequence, the dolostone becomes increasingly pink to reddish but is devoid of internal texture and sedimentary structures. This pink dolostone layer is typical for the Keilberg Member and has been reported from several other locations (Hoffman

and Halverson, 2008; Miller *et al.*, 2009a). The upper 25 m of the logged section are represented by a sequence of m-scaled grey to black and pink to reddish dolostone (Figure 20, **29.00-53.40 m**). In the top part of the black dolostone, extensive pyrite crystals appear again. The overall frequency of the gypsum beds decrease towards the top of the section, and only one bed is recognised in the upper 30 m.

Samples for TOC analyses were taken from the dark grey to black, pyritiferous dolostones. These sections were assumed to have greater potential for organic enrichment owing to their dark colour and presence of pyrite, indicating a potential reducing and anoxic setting.

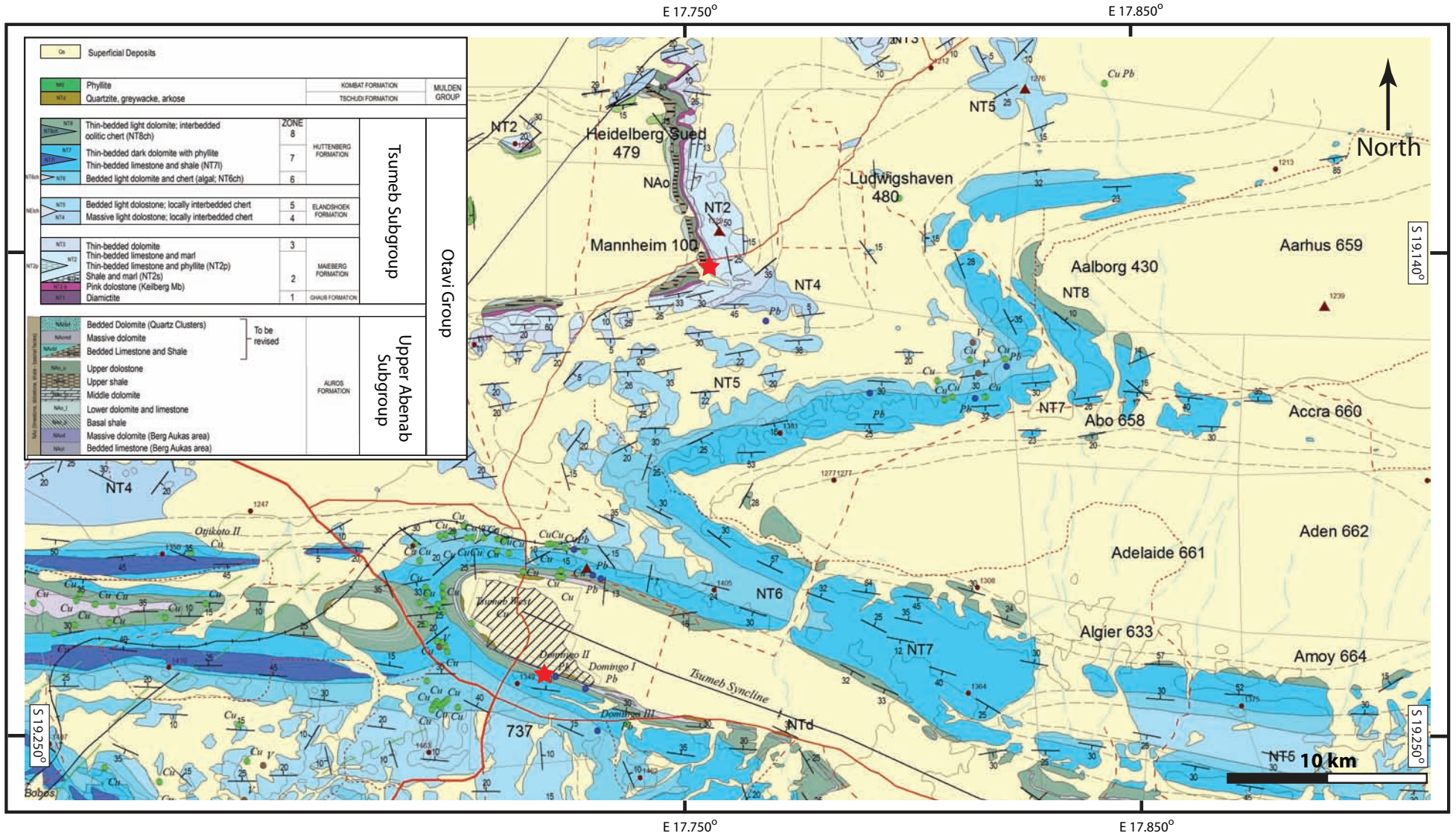


Figure 19: Section of the 1:125 000 geological map of the Otavi Mountainland. Red stars indicate the Maieberg road cut section (northern star) and outcrop location within the Tsumeb copper mine area (southern star). Source: 1:125 000 geological map of the Otavi Mountainland. Geological Survey of Namibia.

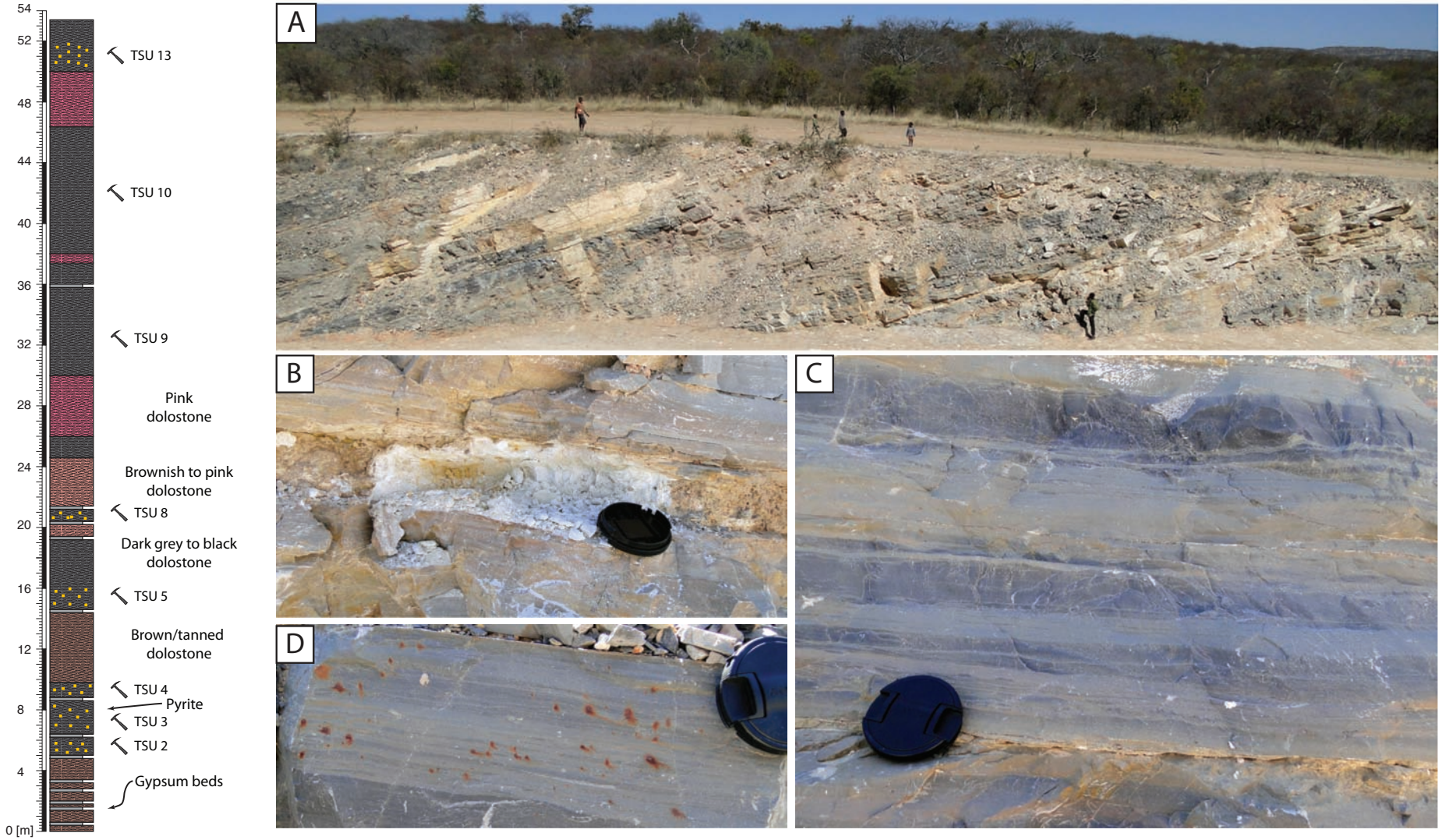


Figure 20: Maieberg road-cut section with stratigraphic log. Geological hammer icon represents TOC sample location and name. (A) Outcrop overview. The strata shows a gentle dipping of 30° towards the northwest. (B) Gypsum bed. (C) Sequence of dark grey to blackish and light grey layers. (D) Grey, recrystallized carbonate with abundant pyrite crystals.

#### 2.3.4.2 Tsumeb copper mine

The visited section in the Tsumeb open pit copper mine is the second location suggested by NAMCOR, which is assumed to be suitable for source rock sampling and analyses (see Figure 19). In common with NAMCOR's pre-1990 data for Halali Waterhole, the old results from Tsumeb were lost in the turmoil of independence. However, geologists from NAMCOR remembered the sample location within the mine. Only a limited section of the entire exposed outcrop was investigated and sampled because of restrictions from the mine authorities.

The exposed strata at the quarry are part of the upper Elandshoek Formation (Kamona and Gunzel, 2007; Schneider *et al.*, 2008). The entire sequence in the quarry is carbonate dominated and within this sequence a 2.65 m interval has been logged (see Figure 21.A) and sampled for subsequent source rock analyses. The base of the logged section is marked by a 35 cm-thick light-grey mudstone bed, which is followed by a 10 cm-thick grey grainstone bed. The grainstone bed exhibits planar stratification. Individual grains are still visible but the entire bed is affected by intense recrystallization and dolomitisation (see Figure 21.A). This basal package is then followed by a 50 cm-thick interval of microbial carbonates, interbedded with coarse-grained grainstone. The microbialites form mm-thick highly undulating mats of light grey to blackish colour. The mats are separated by up to several cm-thick grey mudstone beds and dark blue to black coarse-grained pack- to grainstones (see Figure 21.B). Mudstone interbeds dominate the base of the microbialites but grainstone beds become increasingly dominant towards the top, indicating an overall coarsening upward trend of the microbial sequence. Erosional surfaces between the underlying mudstones and grainstones are common. Decimetre-sized quartz nodules are frequent within the coarse grained interval. The microbial sequence is intercalated with a 10 cm-thick coarse-grained grainstone bed, which exhibits cross-stratification, indicative for a high-energy environment (see log Figure 21.A, **0.45-0.95 m**). A 10 cm-thick fine-grained, light grey grainstone bed with planar-stratification follows the microbial interval. A 35 cm-thick dark brown to black shale bed marks the onset of the second metre of the logged section. The shale beds are interbedded with cm-thick dark grey dolo-mudstone beds. The shale shows a planar layering and mm-scale pyrite crystals are frequent. In the middle of the shale interval, a dark blue to black mudstone bed occurs (see Figure 21.A, **1.00-1.35 m**).

The shale-dominated interval is then followed by 20 cm of microbial carbonates, which exhibit the same characteristics as the microbialites from 0.45 m to 0.95 m. The top of the logged section is marked by a 1.10 m thick interval of dark grey, coarse-grained grainstone bed, exhibiting cross-stratification. The transition from the microbialites is gradual and at the base of the grainstones microbial mats are still visible (see Figure 21.C). However, the microbialites quickly disappear with the increase of sedimentation, which terminates the microbial activity.

The depositional setting of the logged section is interpreted to be a medium to high-energy environment close to fair weather wave base. This is clearly demonstrated by the occurrence of cross-bedded grainstones and erosional surfaces. Shale and mudstone indicated times of quiescence whereas the microbialites represent a depositional setting where sediment supply was high enough in order to develop microbial mats, but not too high in order to keep up with the sediment input.

Two samples for total organic carbon analyses were taken, one from the lower shale bed at 1.10 m and one from the intercalated mudstone bed at 1.20 m. These two intervals were chosen because they were indicated by the geologists of NAMCOR and secondly because they represent the most promising sections in terms of potential organic matter enrichment, on the basis of their dark colouration and presence of pyrite crystals indicating a potential reducing environment.

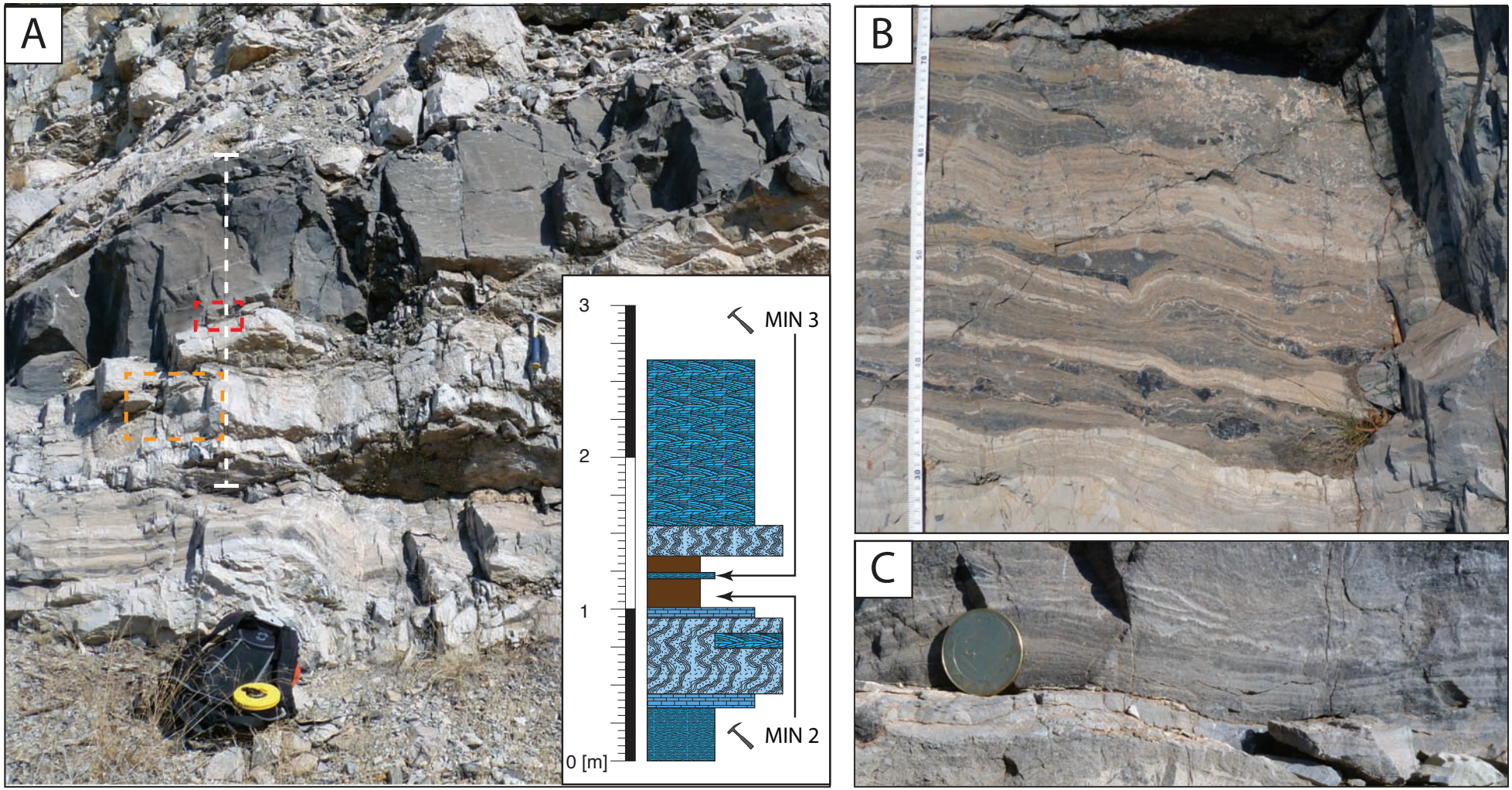


Figure 21: Visited outcrop at the Tsumeb copper mine. (A) Outcrop overview of logged section and logged interval. White dotted line indicates positions of sedimentological log. Orange, dotted rectangle shows position of outcrop photo in (B) and red, dotted rectangle shows location of outcrop photo in (C). Backpack for scale. (B) Microbial mats, interbedded with pack- to grainstones and mudstones. Note the highly undulating appearance of the microbialites. Measuring tape for scale. (C) Transition from the microbialites to the overlying grainstone interval. Note that the microbial carbonates quickly disappear towards the top of the photo with the increase of sediment supply. Coin for scale.

## 2.4 Source Rock Analyses

### 2.4.1 Leco elemental analyses: Method

The source rock analyses were carried out at the department for Applied Geosciences at the University of Leoben, Austria in collaboration with Stefan Neumeister, who specialises in upper Jurassic and Cretaceous source rock analyses in central and southeast Europe. A total of 40 samples were analysed in order to determine the organic enrichment and source rock potential by means of a Leco total organic carbon analyses (Matejovic, 1993).

Prior to the analyses, samples have to be washed to ensure no contamination and dried using a drying oven. Subsequently, samples were powderised using a common porcelain mortar. Determination of the organic content of the samples was carried out with a Leco 300 CSTM analyser (see Figure 22.A). The Leco analyses measures total carbon (TC), sulphur content (SC) and total organic content (TOC).

A Leco elemental analysis works on the basis that samples are combusted in a pure oxygen atmosphere at 1500 C°. At this temperature the chemical bonds of carbon and sulphur start to crack. Thus, molecules containing a carbon (C) or sulphur (S) bond, for example H-C bonds in organic matter or in carbonates ($CaCO_3$) break up. The free C and S ions consequently react with oxygen in the burning chamber, forming carbon dioxide ($CO_2$) and sulphur dioxide ($SO_2$), respectively. Subsequently, the oxidised combustion gases flow through infrared detection cells, using infrared absorption spectroscopy to measure the concentration of $CO_2$ and $SO_2$, which represents the carbon and sulphur content of the sample.

The Leco analyser requires about 80 mg of powdered sample in order to determine the chemical composition. Therefore, for each sample four ceramic crucible, containing between 75 and 85 mg of powdered material was prepared (see Figure 22.B). The degree of precision of the sample weight has to be at two decimal places (e.g.: 79.22mg) to calculate accurate elemental distribution from the $CO_2$ and $SO_2$ ratios. Each sample is measured twice to ensure that no error of measurement occurs. Hence four crucible are needed; two for TC and two for TOC analyses. The sulphur content is measured at every measurement run. After every tenth

measurement, the analyser has to be calibrated with carbon (501-937) and sulphur (502-449) standards with known carbon and sulphur contents.

The total carbon content is measured with untreated sample material. Therefore the measured carbon content represents bulk composition and carbon is derived from both, inorganic and organic material. The TC is used to calculate the inorganic carbon content (TIC) by simply subtracting the TOC from TC. The TIC is then used to calculate the calcite equivalent percentages ($Cc_{eq}$ = TIC x 8.333), which represents the amount of carbonate in the sample (either as limestone or dolomite). Leco TOC measurements need pre-treated sample material by means of dissolving all inorganic carbon. This step is critical in the TOC analysing process and has to be carried out with uttermost care. The inorganic carbon is dissolved by adding hydrochloric acid (HCl) into the crucible, which reacts with the carbonate but not with organic matter, hence separating inorganic from organic carbon. Dissolving pure limestone is a relatively straightforward process, since $CaCO_3$ reacts fast with HCl after following reaction:

Equation 1: $$\boldsymbol{CaCO_3(s) + 2HCl(l) \rightarrow CaCl_2(aq) + CO_2(g) + H_20(l)}$$

The $CO_2$ in the gas phase, derived from carbonate is consequently removed from the sample through gas discharge. Difficulties however arise when samples exhibit dolomite. Dolomite also reacts with hydrochloric acid, however the rate of reaction is significantly slower than compared with limestone. Dolomite ($CaMg(CO_3)_2$) reacts after following reaction:

Equation 2: $$\boldsymbol{CaMg\ (CO_3)_2(s) + 4HCl(l) \rightarrow CaCl_2(aq) + MgCl_2(aq) + CO_2(g) + H_20(l)}$$

Since the reaction speed is slow and twice as much HCl is needed, the process of dissolving dolomite has to be repeated several times until no visible reaction (no visible gas discharge on the surface) is recognised. The reaction speed is, as mentioned above, slow and the gas bubbles are not always clearly visible. Therefore, the samples were treated at least 15 times with HCl over 24 hrs to ensure that all dolomite is dissolved. If the process would be stopped to early, the remaining, undissolved dolomite would be combusted and detected as total organic carbon content. Hence, unrealistically high TOC values would be the consequence.

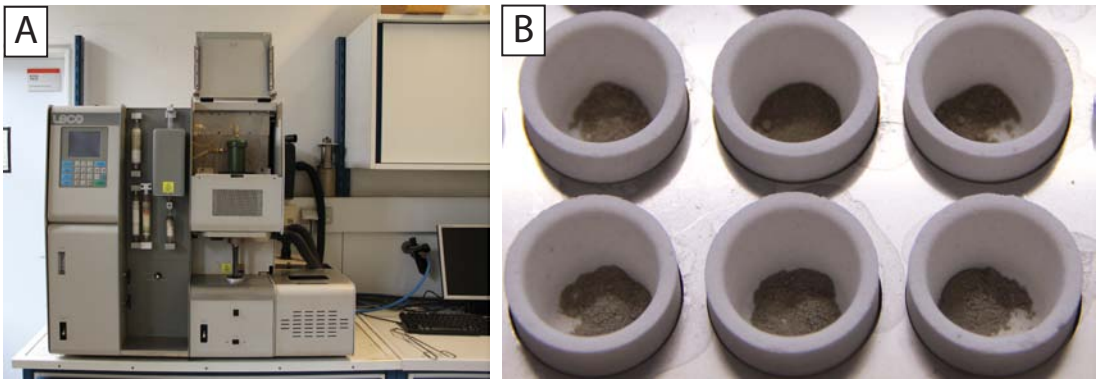


Figure 22: (A) Leco 300 CSTM analyser used for elemental analyses of carbon and sulphur. (B) Ceramic crucible with powderised sample material.

### 2.4.2 Leco elemental analyses: Results

The data sheets of the Leco elemental analyses, containing all results of total carbon content, total sulphur content, total organic carbon content and sample weight are attached in APPENDIX II. The following is a resume of the key results from each visit outcrop section.

A total of 14 samples from the outcrop at Halali Rest Camp in the Etosha National park were analysed. The majority of the samples (12 analyses) show $Cc_{eq}$ values higher than 90%, identifying them as almost pure carbonates. One sample, HAL 14 has a value of 86%. Only one sample has less than 20% carbonate (HAL 2), which was sampled from the mudstone/shale bed at the base of the logged section (see Figure 18). The bulk carbonate percentage is 89.96%. The bulk TOC value of the entire section is 0.15%. Only two samples showed slightly elevated values (HAL1 & HAL2) with an average TOC value of 0.25% and 0.28%, respectively. The average sulphur contents are low and generally under 0.05% with an average of 0.03%.

The two samples from the Tsumeb copper mine have an average TOC value of 0.10%. The sample MIN2, taken from the shale interval shows only 1% carbonate and low sulphur contents (0.02%) and very low TOC values (<0.1%). MIN3, taken from the mudstone interbed in the shale horizon is pure carbonate with 98% calcite equivalent percentage. TOC values are also low with an average of 0.075%.

The samples from the Maieberg cap carbonate sequence, north of Tsumeb have the lowest bulk TOC values of the entire measurement series with 0.09%. Only one sample showed slightly elevated values with 0.17% (TSU 8) from the middle of the logged section. The overall sulphur content is low with 0.05% and the bulk carbonate content is 70.50%. In 6 cases no second TOC measurements were carried

out because difficulties with the Leco system occurred. Second measurements are required to confirm high TOC values and to exclude the possibility of contamination through inorganic carbon. However, the first analyses show no elevated TOC signals and therefore second measurements could not have detected higher values.

The 16 samples from the Rasthof cap carbonates type section are all pure carbonates with calcite equivalent percentages of nearly 100%. In the field they were identified as dolomites and also during TOC sample preparation and treatment with HCL it was confirmed that the Rasthof cap carbonates are dolomites due to the very slow dissolving process. The samples had to be treated for more than 15 times adding HCL to the crucible over 24 hrs to ensure that all dolomite is dissolved. The bulk TOC value of the entire section is 0.64% with individual high TOC values between 1.5-2.0%. However, second measurements of the high TOC samples produced negligible results of less than 0.01%. For instance sample KAM 14 showed 1.72% TOC in the first measurement series but only 0.07% in the second series. Although the samples have been treated carefully with HCL over an extended period it is possible that small amounts of dolomite were not dissolved and therefore detected as TOC. TC are accurate for each sample and for both measurement series, however the total inorganic carbon contents and therefore calcite equivalent percentage values differ significantly and frequently exceed 100% between the two series, which is indicative for sample contamination. It is therefore argued that the high apparent TOC values do not represent organic enrichment but most likely represent sample contamination due to difficulties of dissolving all dolomite content.

## 2.5 Discussion of analyses results

In order to classify a sedimentary rock, enriched with organic matter as fair to good hydrocarbon source rock, TOC values have to be around 1% and this classification has also been applied to Neoproterozoic source rocks (Craig *et al.,* 2013). The lower threshold for siliclastics is 0.5% and for carbonates, 0.3% is sufficient to be regarded as fair source rock (Littke and Welte, 1992; Tissot and Welte, 1978a). None of the analysed samples shows more than 0.3% TOC. The high values from the Kamanjab area are the results of sample contamination and by excluding these analyses, the bulk TOC value of the cap carbonate sequence is <0.15%. Therefore, no analysed sample can be classified as potential source rock. However, two samples show

elevated TOC values from the base of the Halali Waterhole section. HAL 1 has an average value of 0.25% and is pure carbonate and therefore slightly below the threshold for a potential source rock. HAL 2 has a higher TOC bulk value of 0.28%, however the sample is derived from a shale bed and therefore would need at least 0.5% total organic carbon content to be classified as source rock. Nevertheless, the lower section of Halali Waterhole consists of sediments, enriched with organic matter of Neoproterozoic age. As Bechstädt (2009) pointed out, potential Neoproterozoic source rocks are challenging to describe due to their age and the possibility that they already produced hydrocarbons. Neoproterozoic rocks potentially underwent an enormous amount of time being exposed to weathering and long lasting degradation of organic material. Additionally, the analysed organic material in their study is inertinite, i.e. the residual component that remains once hydrocarbons are already expelled. It constitutes the remaining organic material after petroleum has been generated and is regarded as 'dead carbon' (Tissot and Welte, 1978b). Taking these two circumstances into account, low TOC values in Neoproterozoic rocks might be the result of already produced and/or intensely weathered samples. Thus, the Halali Waterhole samples might have exhibited significantly higher TOC values. Especially sample HAL 1, as almost pure carbonate with 0.25% TOC has the potential to have acted as source rock. The complexity of the situation lies in the nature of the organic material of HAL1, which has not been analysed in this research project. If subsequent studies indeed confirm that the organic matter is inertinite, than this horizon might have had the potential to produce hydrocarbons.

The discrepancy between the TOC values obtained during this research and the reported values from NAMCOR are considerable. The rocks at Halali Waterhole were supposed to have around 2% and the Tsumeb copper mine section up to 2.5%. Both value ranges could not be confirmed. For the Tsumeb mine, a potential explanation is that sampled horizons were slightly different. Although members of NAMCOR claimed to know the exact location, it cannot be ruled out that the wrong section was selected since the original documents have been lost. The situation at Halali is different since the entire section was logged and the outcrop location could not have been confused, since this is the only accessible outcrop in the entire national park. A possible explanation for the deviating results might be contamination of the sample material with dolomite during the analyses in the

1970's since the Halali carbonates are dolomites. However, this is speculative and cannot be confirmed, since the original sample material is not available and the used analysis methodologies are not known.

## 2.6 Conclusions

The search for potential Neoproterozoic source rocks within the Otavi carbonate platform included detailed sedimentological descriptions of 4 visited sections along the southern rim of the Owambo Basin and total organic carbon elemental analyses of 40 samples. Sampling was both strategic (regarding the cap carbonate sequences), and guided by NAMCOR (for outcrops belonging to the upper part of the Otavi Group). None of the samples are regarded as potential source rocks due to low to very low TOC values. This does not exclude the possibility, however, that these strata have expelled hydrocarbons previously.

However, samples from Halali Waterhole showed elevated TOC values and were slightly below the source rock classification threshold of 0.3% for carbonates. A key problem at this section is the unclear stratigraphic setting. The difficulty of the situation is that the Neoproterozoic carbonates at the rest camp are enriched in organic carbon and can almost be classified as source rocks, however additional studies are hampered because of the unknown stratigraphic setting. Miller (2008) regards the outcrop as upper Elandshoek whereas geologists of NAMCOR interpret the section as Marinoan post-glacial sequence (Maieberg Fm.). The interpreted mass flow deposits show similarities with both formations. Prave (1996) described gravitational mass flow deposits from the Maieberg Formation from the Kaokoveld in NW Namibia with similar characteristics. Furthermore, the Maieberg Fm. at Keilberg Farm has also been deposited by turbidites and debris flows in a slope setting with comparable characteristics (Bechstädt *et al.*, 2009). However, the upper Elandshoek Fm. at the Tsumeb mine shows also the same characteristics as at Halali Waterhole (personal observations). It was however outside the scope of this research project to define the stratigraphic position of the Halali Waterhole sequence because this would have needed much more extensive regional mapping.

The investigated post-glacial sequences (Maieberg road cut and Rasthof Formation) do not show organic enrichment at the visited section. A key observation is the absence of potential source rocks in the Keilberg Member at the road cut, north

of Tsumeb, although the lateral equivalent section 30 km south of Tsumeb shows up to 2.9% TOC (Bechstädt *et al.*, 2009). This demonstrates that the Keilberg Member is not a platform wide source rock horizon. The Otavi carbonate platform developed on an active fold and thrust belt, strongly influenced by tectonic activity, leading to complex platform geometry and tectonically controlled relief, with palaeohighs and sub-basins (see 2.2) Source rock deposition during post-glacial flooding can be expected in these sub basins with restricted circulation and therefore anoxic conditions. This scenario can explain the absence of organic matter in the carbonates of the Keilberg Member at the road cut, since they have been potentially deposited in a palaeohigh setting. Resemblances to the Maieberg post-glacial sequences and source rocks show the North African early Silurian-Ordovician source rock system (Le Heron *et al.*, 2009; Lüning *et al.*, 1999; Lüning *et al.*, 2000). Organic enriched sediments were preferentially deposited in tectonically controlled sub-basins and depressions of the glacial palaeorelief with restricted water circulation during post-glacial transgression. Source rocks are, however, absent in palaeohighs with active water circulation, which explains the areal discontinuous nature of the 'hot shales' in North Africa. A similar situation might be applicable for the Otavi carbonate platform: source rock deposition in tectonically controlled sub-basins and glacial palaeoreliefs across the platform. However, this has to be confirmed by additional regional mapping and investigation of the depositional settings of the Maieberg Formation in the Tsumeb area and along strike the platform.

The analysed section of the upper Elandshoek Formation in the Tsumeb mine can also not be regarded as potential source rock horizon. It has to be highlighted that only two samples from a 2.5 m section were analysed. The Elandshoek Formation has a maximum thickness of 1500 m (Miller, 2008) and therefore the implications of the results regarding source rock potential are limited. Thus, at this point it cannot be ruled out that the Elandshoek Formation does contain organic enriched sediments elsewhere.

## 2.7 Summary

- A total of four sections within the more than 4 km thick and 700 km wide Otavi carbonate platform were investigated and 40 samples were analysed

for source rock potential. None of the samples can be classified as potential source rock.

- Carbonates from the Halali Waterhole show elevated TOC contents and can almost be classified as source rocks. Initial TOC values might have been considerably higher because the carbonates were subject to long lasting weathering and degradation of organic matter. This has to be confirmed by additional analyses of equivalent sections and analyses of the kerogen type. However, this is hampered by the unclear stratigraphic position of the Halali carbonates.
- The Keilberg Member does not show source rock potential north of Tsumeb. This indicates that the Marinoan post-glacial source rock horizon is not continuous throughout the platform. In the light of these results it seems likely that organic-enriched sediments were deposited during post-glacial flooding in tectonically controlled sub-basins with restricted circulation throughout the platform. A potential analogue system is the early Silurian-Ordovician post-glacial source rock system of North Africa.
- This research effort is one of the first attempts to analyse the Otavi carbonate platform from a source rock point of view. Although no source rock could be identified the author wants to highlight that further regional mapping and organic carbon elemental analyses have a potential to find source rocks. Organic-enriched sediments have already been confirmed within the Keilberg Member of the Otavi platform, which might have acted as source rocks (Bechstädt *et al.,* 2009). Furthermore, the occurrence of organic matter has been reported throughout the platform. Thus, future studies have the potential to identify additional source rock horizons within the carbonate platform. The main challenge for future research is to establish a robust sequence stratigraphy and geodynamic evolution of the Otavi carbonate platform. This is crucial in order to identify potential source rock horizons and locations.

# 3 The Geology of the Nama Basin

## 3.1 Introduction and study location

The aim of this chapter is to give an overview of the general geology and sedimentology of the Nama Basin in south Namibia. Particular attention will be given to the Kuibis carbonate ramp system where the study location is situated. The first part of this chapter summarises previous work done on this terminal Proterozoic to lower Cambrian succession, with specific focus on the work of John Grotzinger and colleagues. In the second part of the chapter, the sedimentological results of the field work and interpretations are presented with special focus on hydrocarbon reservoir characteristics. This section is approached from the perspective that the investigated sequences of the Kuibis carbonate ramp have value as an outcrop analogue for microbial carbonate reservoirs in the Owambo Basin and elsewhere. Thus, attention is given to reservoir architecture, geometry and potential reservoir properties.

The study area is located in the Zebra River Canyon system at the NW edge of the Nama Basin, in south-central Namibia (Figure 23). The location of the Nama outcrops within the southern part of the Namib Desert, in concert with gentle regional structural dips of a few degrees, makes them ideal for studying both sedimentology and structure. Superbly exposed outcrops of the Nama Group occur in the Zebra River Canyon, owing to desert climate and absence of vegetation. Stratigraphic sequences can be studied in detail and facies belts traced over tens of kilometres (Figure 24.A). The canyon lands, some following regional faults and others forming more locally developed fracture sets, have been excavated by flash-flood processes, and hence a deeply dissected topography characterises the Zebra River area (Figure 24.B). The network of canyons yields exposures in excess of 100 m high, allowing sedimentology and structural phenomena to be studied in 3 dimensions.

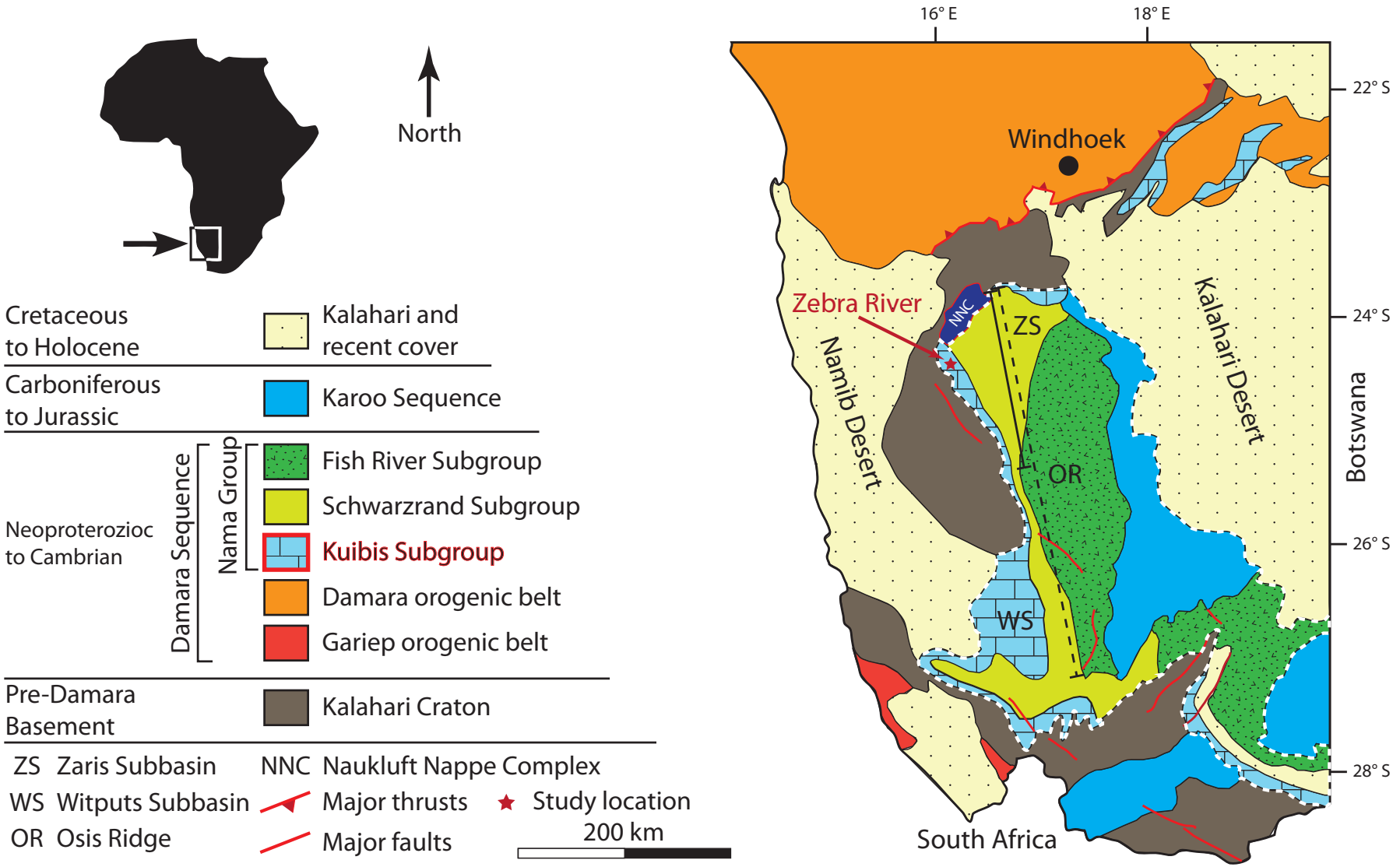


Figure 23: Geological map of southwest Namibia. The Nama Basin is outlined with withe-black dotted line. Black dotted line indicates location of the Nama Basin stratigraphic cross-section in Figure 26. Continuous black line indicates location of the Zaris sub-basin cross-section in Figure 29. Modified after Adams et al., (2005)

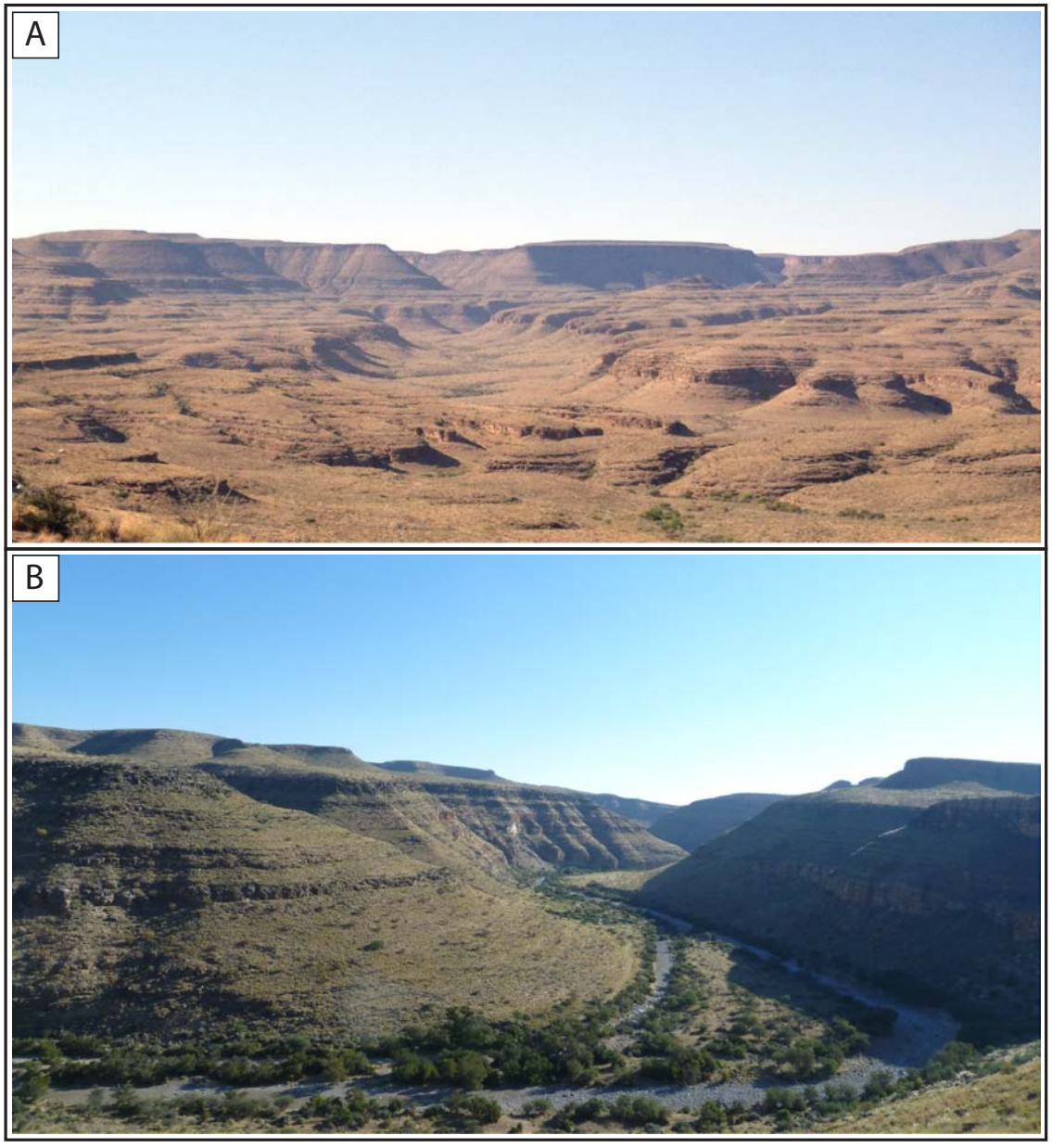


Figure 24: Outcrop overview images of the study area in the Zebra River Canyon system. (A) Overview image of the Kuibis carbonate ramp system. In the desert like environment and absence of vegetation, strata of the carbonate ramp system are almost 100% exposed. Note the almost horizontal bedding. Individual stratigraphic horizons can be traced over 10's of kilometres to analyse lateral facies changes and the entire evolution of the carbonate ramp system can be studied in detail in a sequence stratigraphic context. (B) Overview photograph of the Zebra River Canyon. The canyon system crosscuts the entire ramp sequence allowing field observations in all three dimensions.

## 3.2 Geodynamic framework

The terminal Neoproterozoic – early Cambrian Nama Basin has been interpreted as a foreland basin fill, which formed during the final stages of the Pan African Damara and Gariep orogenic events (Germs, 1974). The Damara and Gariep orogenies are the final collisional events between the Congo, including the Angola block, Kalahari and Rio de la Plata cratons. This Pan African mega-cycle is characterised by more than 200 Ma of continental spreading, the formation of oceanic basins and the subsequent closure of these basins. The Nama Group was deposited in the latest stages of the orogenic mega-cycle (compare paragraph 1.5). The advancing nappe fronts of the Damara and Gariep belts submerged the north-western part of the Kalahari Craton, which initiated the deposition of the mixed carbonate-siliclastic Nama sediment succession on the Kalahari Craton at around 550 Ma (Grotzinger and Miller, 2008). A schematic geodynamic evolution of the Damara belt and the formation of the Nama Basin are illustrated in Figure 25.

The age of the sediment succession is constrained by several dated ash beds in addition to Ediacaran body fossils *Namacalathus* and *Cloudina* (Grotzinger *et al.*, 2000; Wood, 2011; Wood *et al.*, 2002). The Cambrian boundary in the Nama Basin is situated in the Nomtsas Formation of the upper Schwarzrand Subgroup, constrained between two dated ash beds with U-Pb zircon ages of 543.3±1 and 539.4±1 (Grotzinger *et al.*, 1995). The geodynamic evolution of the Pan African system in SW Gondwana has been the subject of extensive research over the last two decades (e.g. Alkmim *et al.*, 2006; De Wit *et al.*, 2008; Frimmel *et al.*, 2010; Frimmel *et al.*, 2002; Li *et al.*, 2008; Pedrosa-Soares *et al.*, 2008; Scotese, 2009)

A prominent structural feature at the north-western part of the Nama Basin is the Naukluft Nappe Complex (NNC). This allochthonous unit was emplaced on top of the Nama Group due to gravity gliding after continental collision and exhumation of the Damara orogeny around 495 Ma (Korn and Martin, 1959; Miller *et al.*, 2008). The NNC consists of seven nappes, which correlate to the southern margin zone of the Damara belt, emplaced during 4 tectonic events. A parautochthonous nappe of Nama rocks forms the basal part of the NNC. A minimum translation distance was estimated to be more than 78 km (Martin *et al.*, 1983).

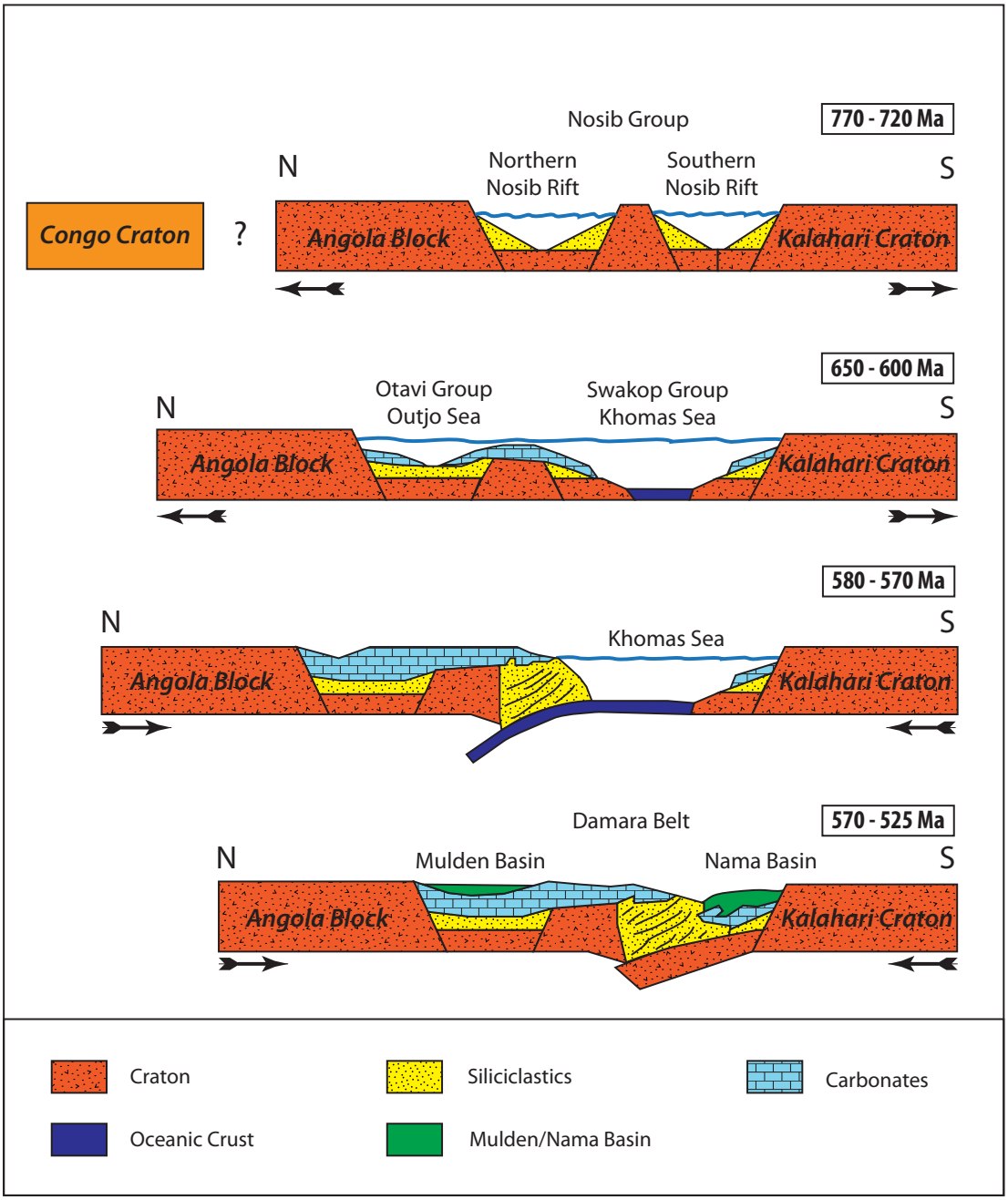


Figure 25: Generalised geodynamic evolution of the Damara belt and the deposition of the Nama Group. The orogenic mega cycle spans over more than 200 Ma years, starting around 770 Ma ago until the lower Cambrian at around 525 Ma. Continental drifting started with the break-up of Rodinia (compare paragraph 1.5) and the evolution of two basins between Congo-Angola and the Kalahari cratons. Subsequent closure of these basins at ca. 580 Ma and the formation of a subduction zone at the northern edge of the underlying Kalahari plate let to the formation of a foreland basin and the deposition of the Nama Group at the end of the Ediacaran and lower Cambrian. Modified after Frimmel *et al.,* (2010).

## 3.3 Stratigraphic framework

The general architecture and stratigraphy of the Nama foreland basin fill has been outlined in a series of papers by Germs and colleagues (Germs, 1972; Germs, 1974; Germs, 1995; Gresse and Germs, 1993). The Nama Basin in Namibia is subdivided into two sub-basins, namely the Zaris sub-basin in the north and Witputs sub-basin in the south. The two sub-basins are separated by the Osis ridge, which is interpreted as a peripheral forebulge in the foreland basin. The sediment successions thicken from the Osis ridge (1 km thickness) towards the deeper parts of the sub-basins (3 km thickness): to the north in the Zaris Sub-basin and to the south in the Witputs sub-basin, respectively. A detailed stratigraphic cross-section through the Nama Basin is illustrated in Figure 26.

The Nama Group is divided into three subgroups. In ascending stratigraphic order, these are the Kuibis, Schwarzrand and Fish River subgroups (Figure 27). The general trend of the subgroups characterises a typical foreland basin fill, represented by an overall decrease in sediment maturity up-section. The lowermost Kuibis Subgroup is characterised by a shallow marine, mixed carbonate clastic succession. The first deepening of the basin resulted in the deposition of fluvial to shallow marine clastic sediments, which exhibit a cratonic interior provenance. Palaeocurrent analyses from these deposits suggest an eastern source area from the Kalahari Craton (Blanco *et al.*, 2011).

Following this first transgressive event, extensive carbonate platforms developed in both sub-basins: the Kuibis platform in the Zaris sub-basin (Adams *et al.*, 2005; Adams *et al.*, 2004; Dibenedetto and Grotzinger, 2005) and the Huns platform in the Witputs sub-basin (Saylor, 2003; Saylor *et al.*, 1995) (see Figure 28.A-B). With the ongoing deepening of the Nama Basin and an increased input of siliciclastic material, carbonate production came to a halt, at first in the Zaris sub-basin and subsequently followed in a later stage in the Witputs sub-basin (Grotzinger and Miller, 2008) (see Figure 28.C). This succession is summarised in the Schwarzrand Subgroup, represented by flysch sediments derived from the advancing orogenic fronts of the Damara and Gariep belts. The first molasse sediments are found at the uppermost part of the Schwarzrand subgroup representing continental collision at around 542 Ma (Blanco *et al.*, 2009). The youngest Nama subgroup, the Fish River Subgroup, represents the final filling of the basin, characterised by more proximal molasse type sediments, originating from the un-roofing of the Damara and Gariep orogens (Blanco *et al.*, 2011) (see Figure 28.D)

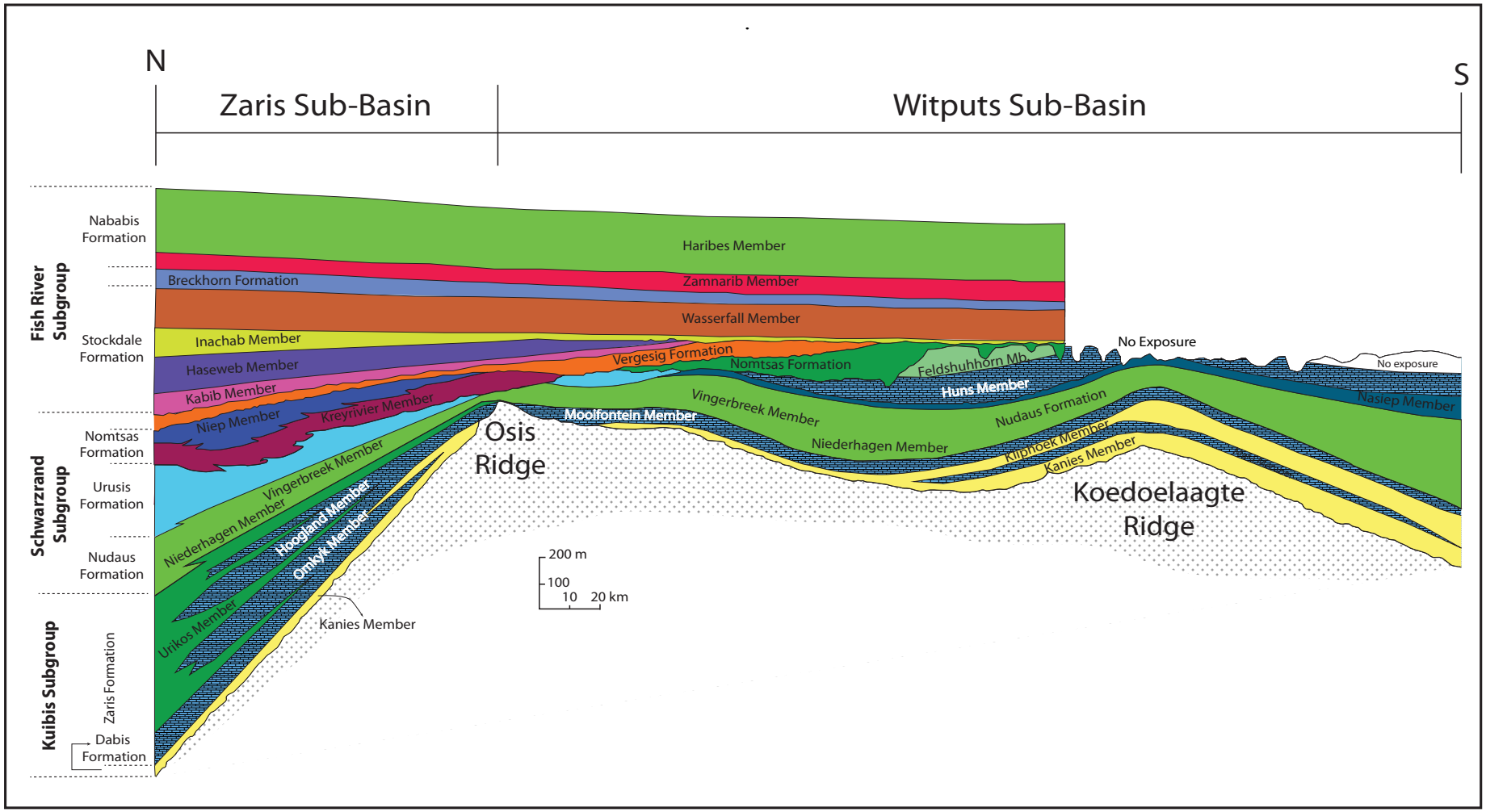


Figure 26: Stratigraphic cross-section through the Nama Basin in Namibia. The Cambrian boundary is situated in the lower Nomtsas Formation. See Figure 27 for location of data ash-beds. Modified after Gresse and Germs (1993)

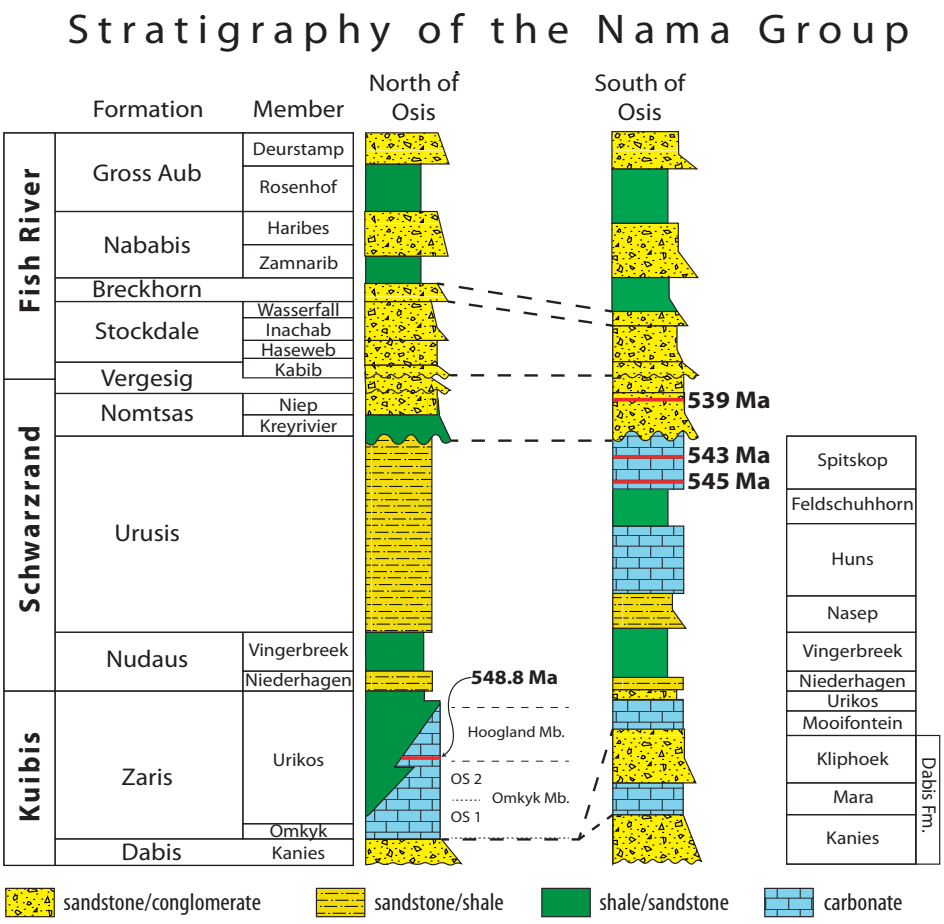


Figure 27: Stratigraphy of the Nama Basin, north and south of the Osis peripheral forebulge. Note the overall decrease of sediment maturity in both sub-basins indicating a typical foreland basin fill. Red line in the lower Hoogland Member, Urusis and Nomtsas Formations indicate dated ash-beds with an U-Pb zircon age date of 548.8 ± 1 Ma, 545 ± 1 Ma, 543 ± 1 Ma and 539 ± 1 Ma. The Cambrian boundary is situated in the Nomtsas Formation (Grotzinger *et al.*, 1995). Modified after Blanco *et al.,* (2011)

The Kuibis Subgroup of the Zaris subbasin comprises four depositional sequences (S1-S4, see Figure 29.A) (Grotzinger and Miller, 2008; Saylor, 2003; Saylor *et al.*, 1995). The S1 sequence includes the initial transgressive sandstones of the Kanies Member and the basal part of the Omkyk Member, characterised by fine to medium-grained grainstones. The base of the S2 sequence comprises mud-dominated facies in the lower Omkyk Member represented by heterolithic interbeds and mudstones. The S2/S3 sequence boundary is situated at the base of the biostrome, capping the Omkyk Member. This biostrome developed in an initial transgressive systems tract and is laterally extensive in the study area but breaks up into bioherms down-dips. The more than 500 metre-thick Driedoornvlakte pinnacle reef is the lateral equivalent section (Adams *et al.*, 2004; Grotzinger *et al.*, 2005). Note that the sequence boundary does not coincide with the lithostratigraphic sub-division of Omkyk and Hoogland Member. The development of the biostrome is terminated by an abrupt increase in water depth and the deposition of mid- to outer ramp

mudstones and shale. The S3 sequence subsequently coarsens upwards and forms extensive inner ramp grainstones in the middle of the Hoogland Member. The S4 sequence is characterised by transgressive basinal to mid ramp mud-dominated facies which grades upwards into inner ramp coarse-grained grainstones at the top of the Hoogland Member in the south of the Zaris sub-basin. A potential 5$^{th}$ sequence boundary (S5) in the middle of the Schwarzrand Subgroup needs yet to be confirmed with additional regional mapping.

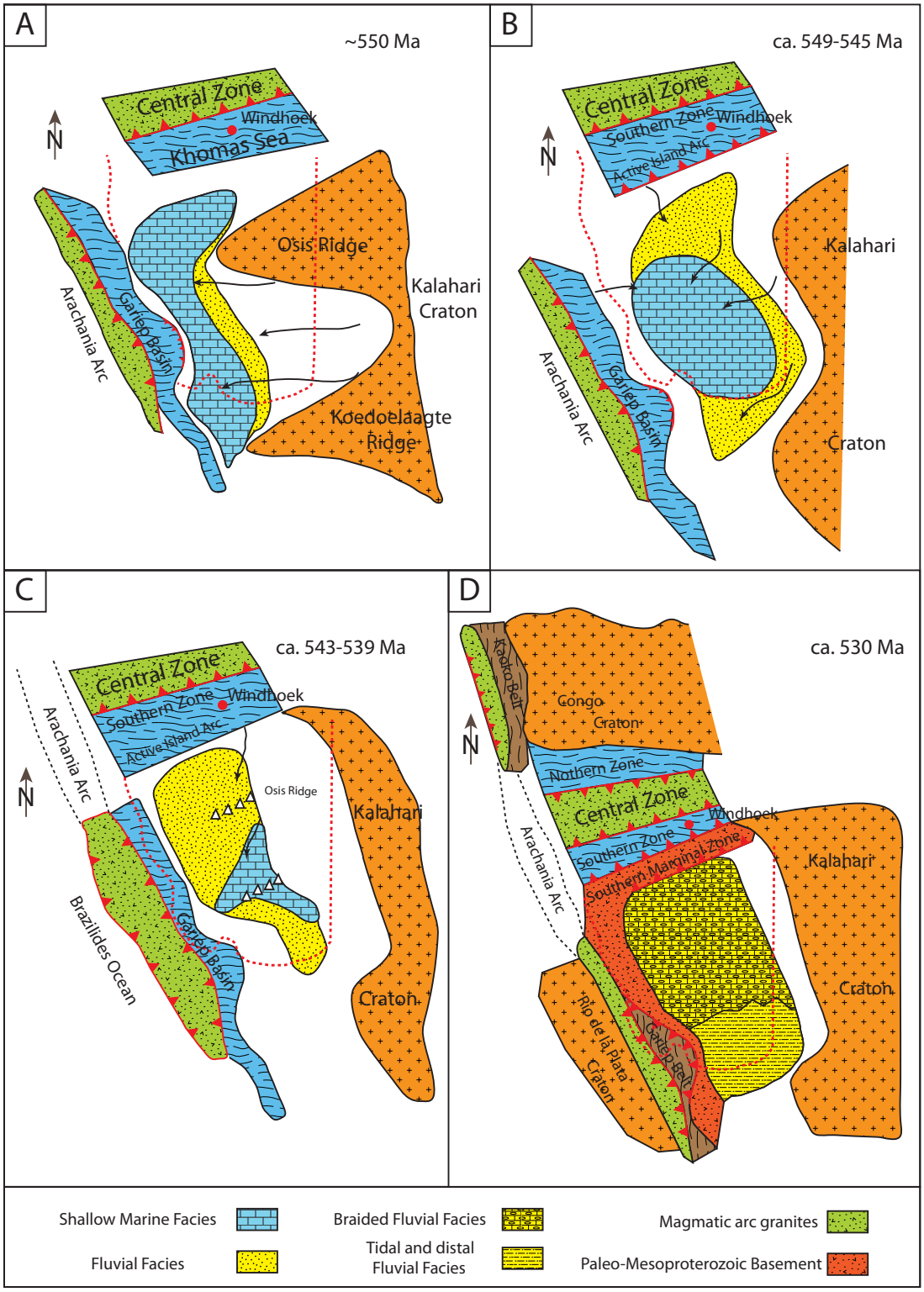


Figure 28: Cartoon illustrating a palaeogeographic reconstruction of the deposition in the Nama Basin. Red line indicate outline of Namibia. (A) Paleogeography during Kuibis Subgroup deposition at around 550 Ma. Black arrows indicate direction of sediment transport. (B) Depositional system during lower Schwarzrand Subgroup sedimentation. Note the advancing nappe fronts of Damara and Gariep belts resulting in an increase of siliciclastic input between 549 - 445 Ma. (C) The increased sediment input terminated carbonate production in the Zaris sub-basin but carbonates were still deposited in the Witputs sub-basin during times of the upper Schwarzrand Subgroup (543-539 Ma). (D) The final stages of the Nama Basin are characterised by the deposition of the molasse sediments of the Fish River Subgroup. Modified after Blanco *et al.,* (2011).

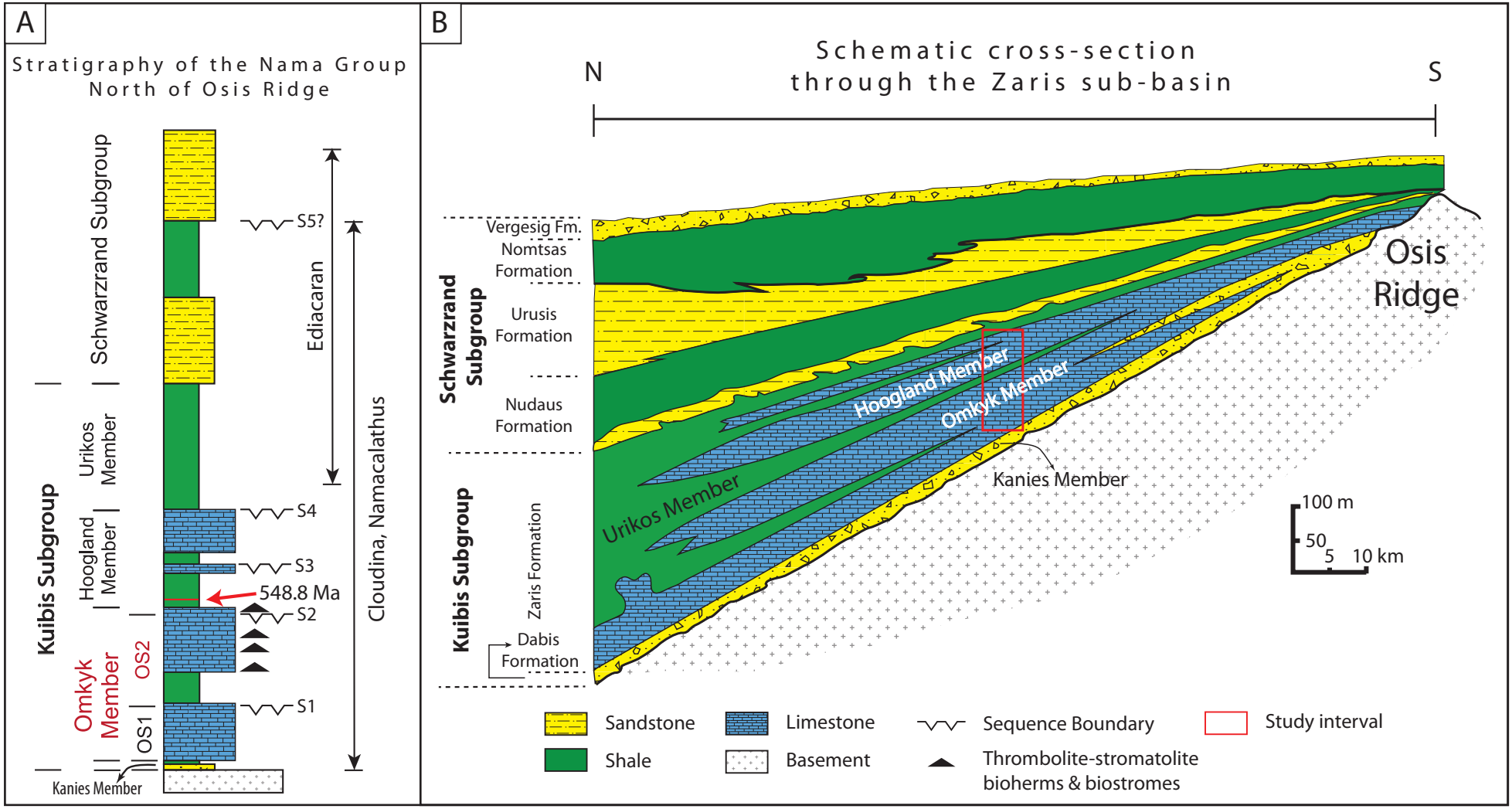


Figure 29: (A) Stratigraphy in the Zaris sub-basin with sequence-stratigraphic boundaries. Red line indicates dated ash-beds in the lower Hoogland Member with an U-Pb zircon age date of 548.8 ± 1 Ma (Grotzinger et al., 1995). (B) Schematic cross-section of the Zaris sub-basin. Red rectangle indicates the location of the study area in the Zebra River Canyon system. Modified after Adams et al., (2005).

## 3.4 The Kuibis Subgroup of the Zaris Subbasin

The study interval is situated in the lower parts of the Kuibis Subgroup in the Zaris sub-basin (see Figure 29.B). Excellent exposures of the Kuibis carbonate platform are present in the Zebra River Canyon system of the Zaris Mountains of south-central Namibia. The superb quality of the outcrops in the dendritic canyon systems provides an exceptional opportunity to study the Omkyk and Hoogland members of the Kuibis carbonate platform (Figure 30).

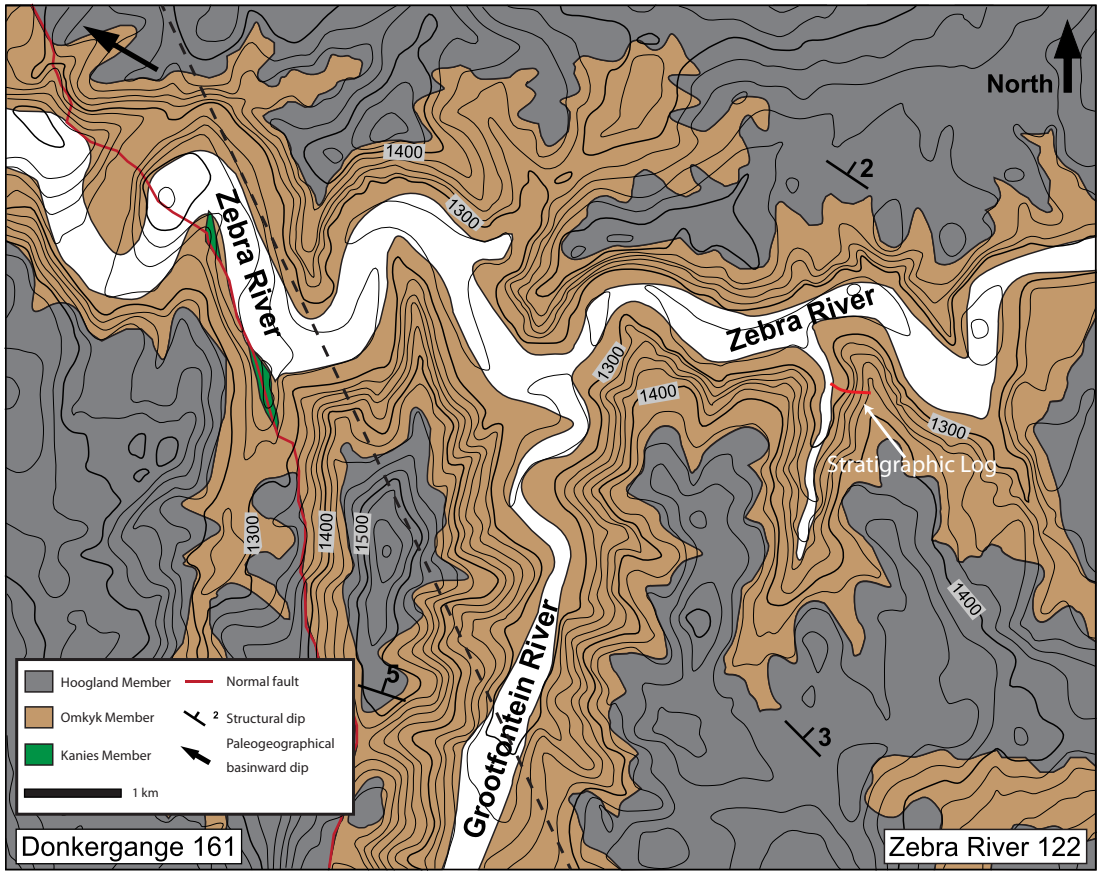


Figure 30: Geological map of the study area in the Zebra River canyon system. Black dotted line indicates border between the farms Donkergange 161 and Zebra River 122. Modified after Adams *et al.,* (2005).

The subgroup is divisible into the Dabis and overlying Zaris formations. The overall character of the Kuibis Subgroup reflects the increase in accommodation space on the Kalahari Craton, defined by shallow marine clastics at the base, followed by the development of the extensive Kuibis carbonate ramp. The ramp

eventually drowns due to the increasing subsidence and the deposition of basinal shale. The whole succession reflects a typical foreland basin fill.

The basal unit of the Kuibis succession, the Dabis Formation, unconformably overlies pre Nama basement strata and is represented in the study area by the Kanies Member. The Kanies Member has been interpreted as the first flooding event on the Kalahari Craton in the Nama Basin and is characterized by brown to greenish immature sandstones, which reach a maximum thickness of 1-3 m. These are interpreted as braided fluvial deposits (Germs, 1983). With the ongoing deepening of the basin, this succession grades upward into the Zaris Formation, which encompasses three members: Urikos, Omkyk and Hoogland members. The latter two formations have been interpreted as a carbonate ramp system (sensu Burchette and Wright, 1992) with a palaeogeographic dip towards the NW (Germs, 1983; Grotzinger *et al.*, 2000; Saylor *et al.*, 1995). The age of the Kuibis platform is directly constrained by a U-Pb zircon date of 548.8 ± 1 Ma in the lowermost part of the Hoogland Member (see Figure 29.A) (Grotzinger *et al.*, 1995).

The carbonate strata downlaps onto the siliciclastic strata of the Urikos Member towards the NW. The Urikos Member represents distal facies and is characterised by basinal shales and outer- to mid-ramp mudstones. Up-dip, the Urikos Member interfingers with the proximal carbonate dominated successions of the Omkyk and Hoogland members. These latter two members comprise the Kuibis carbonate platform of the Zaris sub-basin. The platform has a thickness of approximately 150 m near the Osis ridge and thickens to more than 500 m northward to the Naukluft Mountains (Germs, 1983; Grotzinger *et al.*, 2005). The Kuibis carbonate platform exhibits a ramp geometry: it has been interpreted as a storm and wave dominated carbonate ramp, subdivided into inner-, mid- and outer ramp facies (Dibenedetto and Grotzinger, 2005). Inner ramp facies were deposited above fair-weather wave base and represents the shallowest facies. These consist of sand bars, thrombolitic and stromatolitic biostromes and bioherms associated with medium to coarse-grained packstones and grainstones, regarded as inter-bioherm facies. Back-barrier and peritidal deposits of the inner ramp include mudstones, calcisiltite and minor shale. Sand bars are characterised by high-energy calcarenite and grainstones, exhibiting a variety of sedimentary structures (e.g.: planar stratification, cross-bedding, etc.). These sand shoals occur seawards of the lagoonal deposits and are forming extensive shoaling upwards sequences in the upper Omkyk and Hoogland Member.

Mid-ramp facies, deposited between storm- and fair-weather wave-base is characterised by mudstones, calcilutite and minor shale. Graded storm beds with hummocky-cross stratification are common.

The outer-ramp succession, deposited below storm-wave base marks the transition zone to the basinal shale of the Urikos Member and consists mainly of greenish shale and minor mudstones, interbedded with a few storm deposits. Microbial carbonates are found throughout the entire Zaris Formation but are best developed in the upper half of the Omkyk Member.

## 3.5 Omkyk Member

The Omkyk Member was examined in some detail in the early part of this century (Adams *et al.*, 2005; Adams *et al.*, 2004; Dibenedetto and Grotzinger, 2005; Grotzinger *et al.*, 2005; Grotzinger *et al.*, 2000). Ramp carbonates of the Omkyk Member form two coarsening-upward shoaling sequences, Omkyk Sequence 1 (OS1) and Omkyk Sequence 2 (OS2) (See Figure 29.A). The lower part of Omkyk Sequence 1 is characterized by mid-shoreface hummocky cross-bedded grainstones, intercalated with storm-generated shale and mudstone beds. It overlies fluvial sandstones of the Dabis Formation and represents the first occurrence of carbonates in the Zaris Sub-basin. OS1 grades upward into wave influenced, shoreface grainstones, which are typically coarse-grained and cross-bedded. The second shoaling upward sequence is Omkyk Sequence 2, which is split into five further sequence-stratigraphic units; OS Units 1-5 (Adams *et al.*, 2005). Each of these units is in turn divided into a transgressive systems tract and a highstand systems tract. Three facies associations represent each of these five units of OS2: (1) mud-dominated facies, (2) grain-dominated facies and (3) thrombolite-stromatolite facies (see Figure 31). The mud-dominated facies consists of siliciclastic shale, lime mudstone, intraclast breccias and irregular laminate. The grain-dominated facies is represented by coarse-grained grainstones, minor fine- to medium-grained grainstones and sandstones. Thrombolite-stromatolite facies thus represents the microbial carbonates, developed as bioherms and biostromes, respectively.

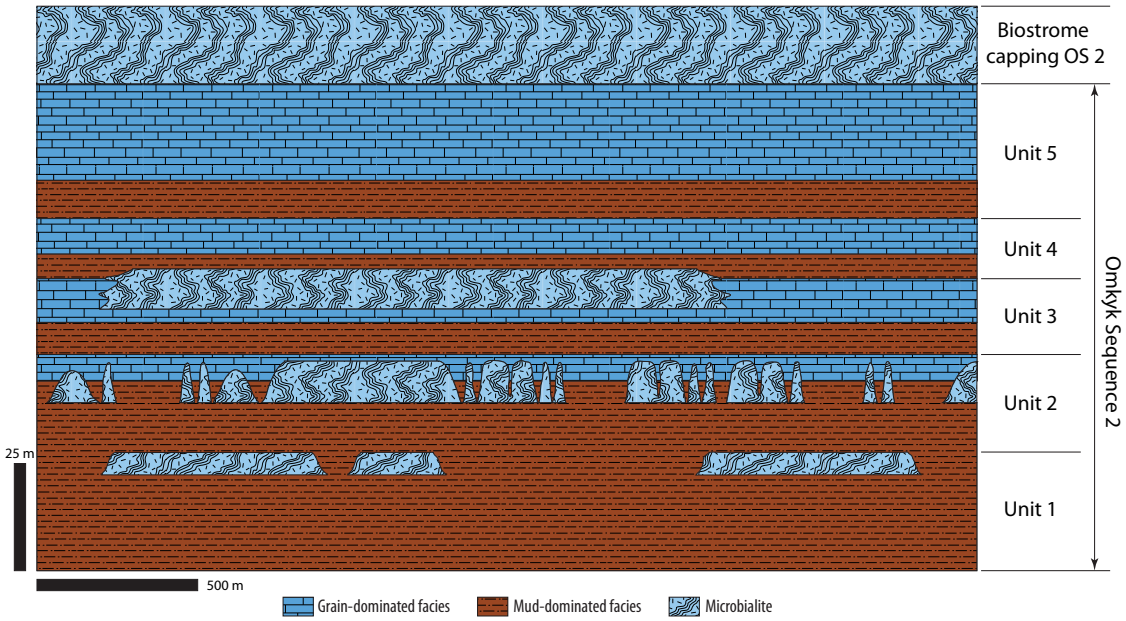


Figure 31: Schematic illustration of the ramp architecture of Omkyk Sequence 2 with the 3 facies association. Modified after Adams *et al.,* (2005)

## 3.5.1 Sedimentary facies and field observations

### 3.5.1.1 Mud-dominated facies association

#### *3.5.1.1.1 Irregular laminite facies*

This facies is characterised by microbial beds, named irregular laminites, which are interbedded with mudstones fine- grained grainstones and minor intraclast breccias. Figure 32.A shows a typical sequence of irregular laminite facies and characteristic undulating microbial bedding surfaces. A recurring pattern within this facies is up to m-scale coarsening upwards sequences with grainstone-dominated tops (see Figure 32.B) and mud-dominated facies at the base (see Figure 32.C). Microbial mats are well defined at the bottom of the coarsening-upward sequences but become increasingly diffuse within the grainstone caps. Mudstone rip-up clasts are abundant within the upper part of the shoaling sequences, indicating the presence of storm and wave activity. Common features are dm-scale thrombolite columns, which start to develop at the base of the shoaling sequences and terminate with increased input of grainstones at the top of the coarsening sequences.

The depositional setting of the irregular laminate facies has been interpreted to represent the shallowest setting of the mid-ramp (Adams *et al.*, 2005). The

intermittent grainstone beds and shoaling tops indicate that deposition occurred close to the fair-weather wave base.

#### 3.5.1.1.2 Intraclast breccia facies

The intraclast breccia facies is represented by dm to m-scaled beds of chaotic intraclasts in a fine-grained matrix. The clasts are poorly sorted and show no grading (see Figure 32.D). Intraclasts are generally angular and consist of grainstones, mudstones and irregular laminites. The breccia beds are associated with fine to medium-grained grainstone beds, which exhibit hummocky cross-stratification.

The observed sedimentary structures and the autochthonous origin of the intraclasts indicate that this facies was generated by occasional storm events. Deposition has been interpreted to have occurred in a storm-dominated mid-ramp setting (Adams *et al.*, 2005).

#### 3.5.1.1.3 Heterolithic facies

The heterolithic facies contains mostly siliciclastic shale and is interbedded with thin mudstone beds. Shales exhibit a variety of colours, from light grey to beige where they are associated with mudstone beds, or purple to black when associated with thrombolite columns. Fine-grained grainstone beds occur occasionally within this facies. Sedimentary structures within the grainstone beds are planar-stratification and small-scale hummocky cross-stratification. Furthermore, irregular laminite and intraclast breccias occur intermittently.

The depositional setting has been interpreted as typical for an outer-ramp setting (Adams *et al.*, 2005). The presence of grainstone beds and the deposition of storm-generated intraclast breccias suggest that deposition was close to the storm-wave base.

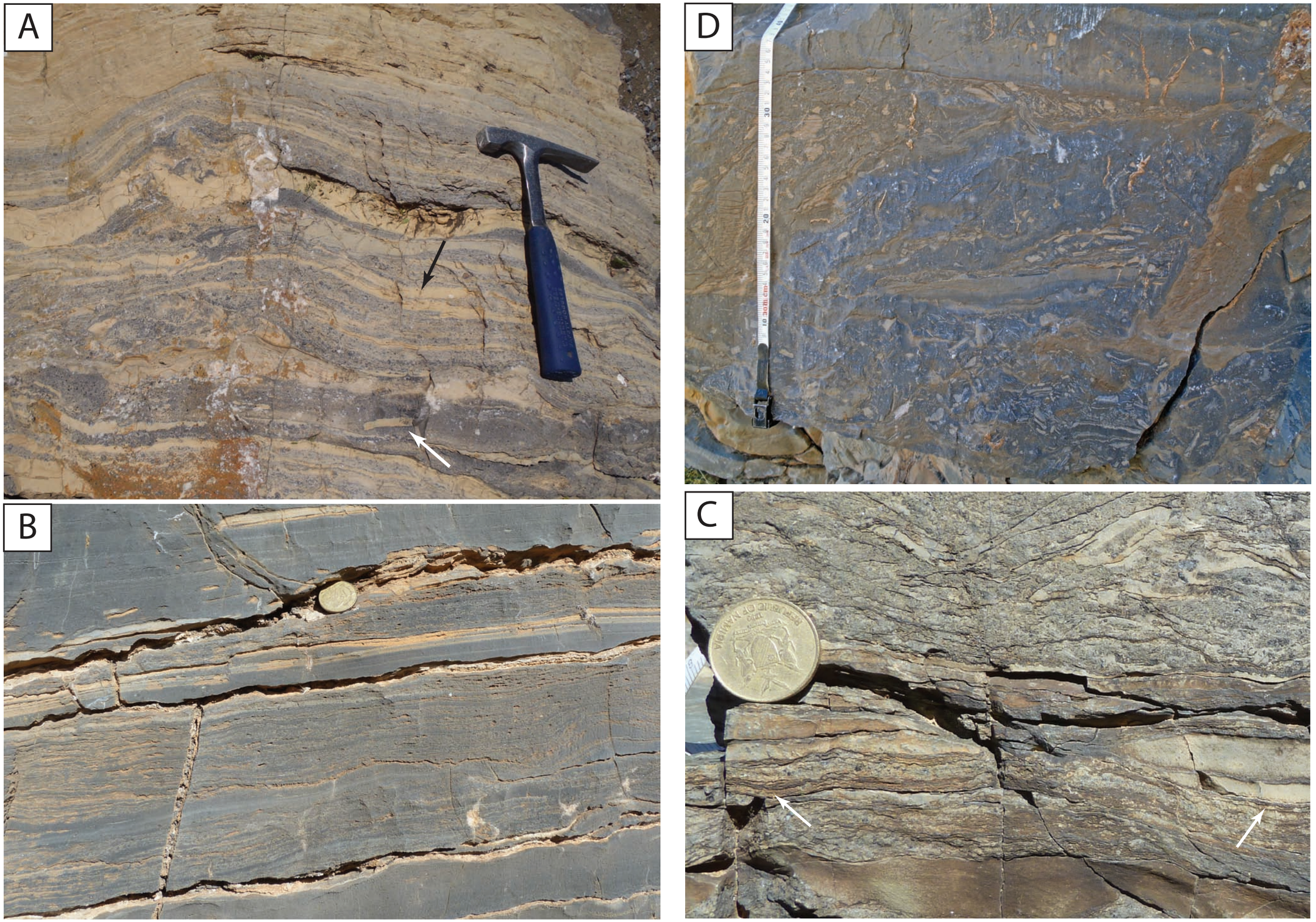


Figure 32: (A) Irregular laminites in the lower part of OS 2, Unit 2. Note the sequence of grainstone beds with rip-up clasts (white arrow) and mud-dominated beds (black arrows). Microbial mats are best visible at the top of the sequence (top of the geological hammer). (B) Photograph showing the top of an irregular laminites coarsening upwards sequence. Note the abundance of planar stratified grainstones with minor rip-up clasts. (C) Photograph showing the base of an irregular laminite coarsening sequence with microbial mats intercalated with mudstone beds. Microbialites are well preserved forming undulating mats (white arrow). (D) Intraclast breccia. Note the chaotic association of angular mudstone and irregular laminite clast in a fine-grained matrix.

### 3.5.1.2 Grain-dominated facies association

#### *3.5.1.2.1 Sandstone facies*

The sandstone facies is only present in the western most part of the study area (see Figure 30) where it has a thickness of only 2-3 metres (Figure 33.A). The facies is characterised by fine- to coarse-grained, well-sorted sandstones. The sandstones are inter-bedded with siltstones and minor siliciclastic mudstones. Rip-up clasts are present at the base of this facies. Sedimentary structures range from planar cross-stratification, trough cross-bedding to symmetrical ripples (Figure 33.B).

Prominent features within the coarse-grained sandstones are mm-thick microbial mats (Figure 33.C). The mats form wrinkle structures (Hagadorn and Bottjer, 1997), which are restricted to bedding planes of well sorted, quartz rich sandstones. Microbial mat preservation has been reported from siliciclastic successions in the Neoproterozoic part of the Nama Group, but they occur further up in the succession, in the Naudus Formation (Bouougri and Porada, 2007; Noffke *et al.*, 2002). They have been interpreted to record hydrodynamic conditions that inhibited the deposition of mud, yet too weak to erode the sandstone substrate. The palaeoenvironment for these structures has been interpreted as shallow marine to tidal.

The upper part of the sandstone facies is marked by a transition zone between the carbonate-dominated succession, characterised by a dm-thick polymict breccia bed (Figure 33.D). Clasts are angular and reach up several centimetres in size and consist of fine-grained grainstone and sandstone clasts in a muddy matrix.

The observed sedimentary structures in combination with the preserved microbial mats are indicative for a shallow-marine to tidal depositional system, which reflects the first flooding of the Kalahari Craton and deposition in an inner-ramp setting. The top of the facies marks the onset of carbonate production in Zaris sub-basin.

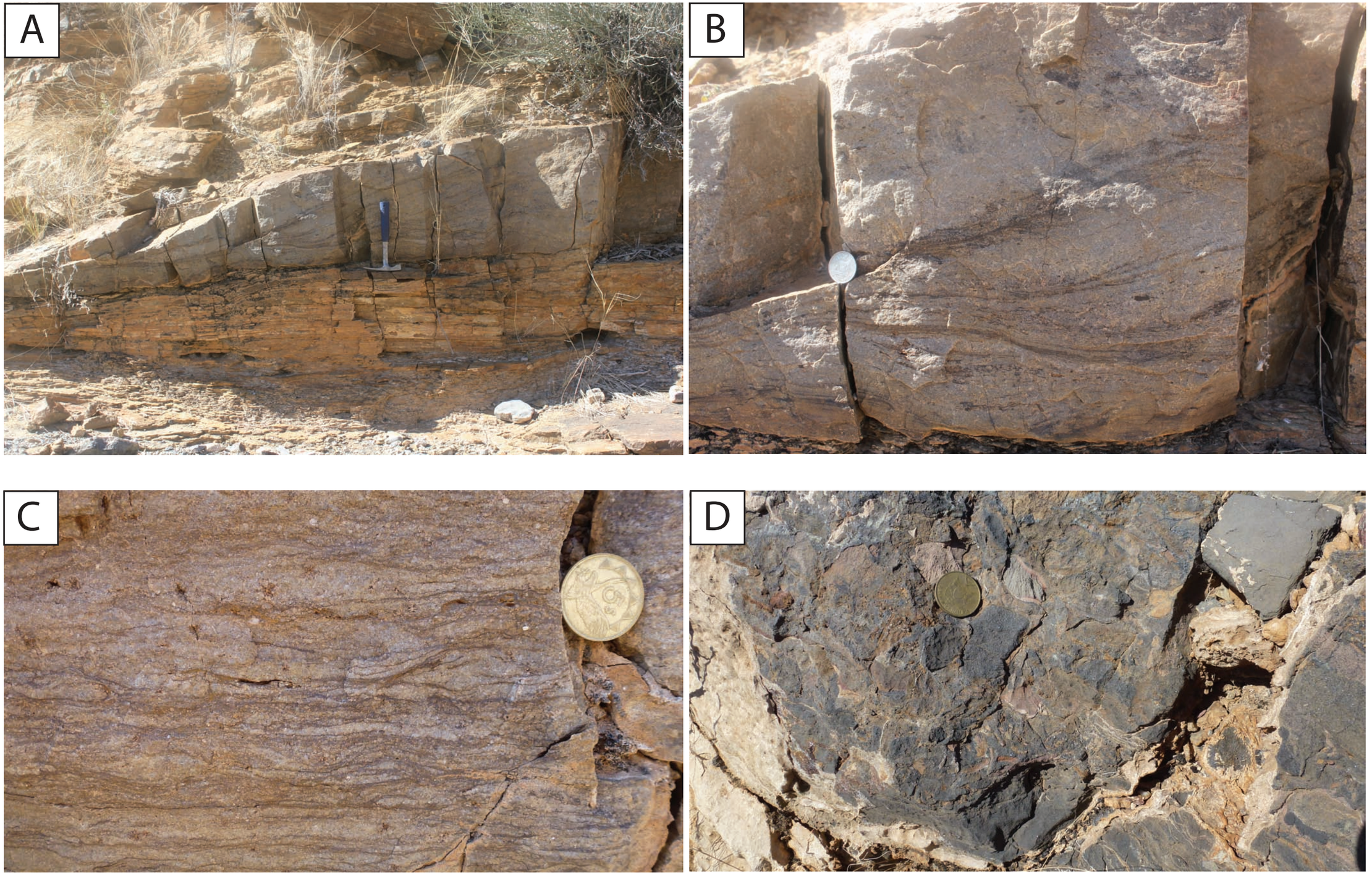


Figure 33: (A) Well sorted sandstone bed showing trough cross-bedding. (B) Close-up photograph of the trough cross-bedding. (C) Preserved microbial mats in the well sorted, quartz rich sandstones forming wrinkle structures. (D) Polymict breccia at the top of the sandstone facies, marking the transition to carbonate sedimentation. Note the grainstone and brownish-reddish sandstone clasts.

#### 3.5.1.2.2 Grainstone facies

Two types of grainstones can be identified in this facies association within the study area; coarse-grained and fine-to-medium grained grainstones. The coarse-grained grainstone horizons are ample in the high stand systems tracts of the Omkyk Sequence 2 units. The grainstones form several m-thick beds. They are characterised by large-scale hummocky, trough cross-stratification and planar-stratification (Figure 34.A-B) and are lateral continuous bodies. The grainstones are well sorted and rip-up clasts are seldom.

Based on the observed sedimentary structures and textures these grainstone horizons have been interpreted as grainstone shoals and bars, deposited in a high energy environment, strongly influenced by wave agitation and currents (Adams *et al.*, 2005). The depositional setting of the coarse-grained grainstones was interpreted as typical for a high-energy shore face in an inner ramp setting (Adams *et al.*, 2005; Grotzinger *et al.*, 2000).

The fine- to medium-grained grainstones form dm-scale beds and are inter-bedded with mudstones, siliciclastic shale, and irregular laminite. Abundant rip-up clasts, wave ripples and deformation structures are commonly present (Figure 34.C-D). Sedimentary structures range from planar, hummocky, to trough cross-stratification and symmetrical ripples (Figure 34.E).

They are interpreted to have been deposited under moderate energy conditions (Grotzinger *et al.*, 2000). The presence of ample rip-up clasts suggests the occasional influence by storms and strong currents. The inter-bedded lime mudstones, shales and irregular laminites, by contrast indicate times of low energy conditions. Deposition is interpreted to have occurred in the lee of grainstone shoals and bars in an inner-ramp setting (Adams *et al.*, 2005; Grotzinger *et al.*, 2000). Furthermore the fine- to medium-grained grainstone facies with inter-bedded mud-dominated facies is typical in the inter-bioherm facies, where they were deposited in the lee of bioherm structures.

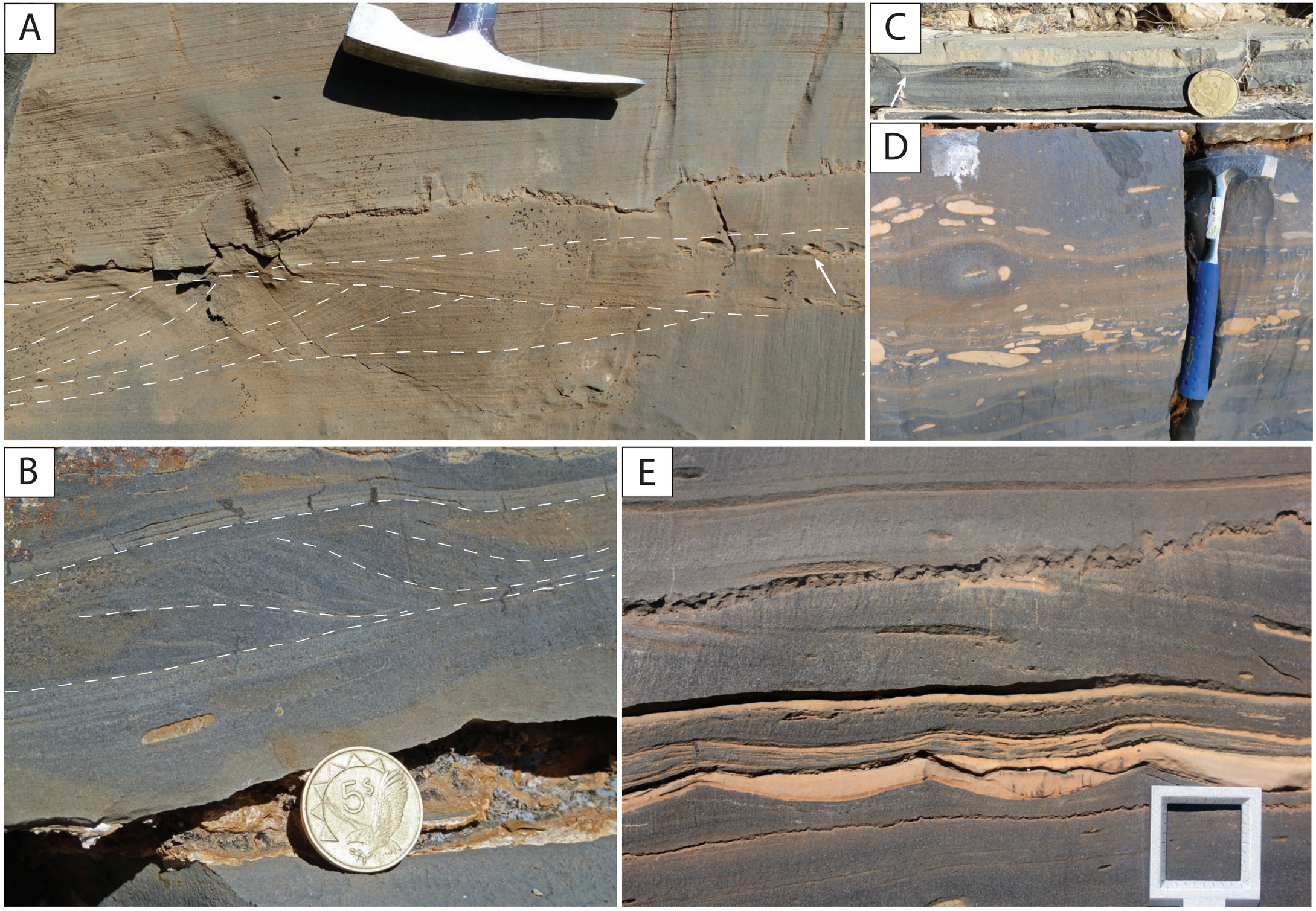


Figure 34: (A) Partly dolomitised coarse-grained grainstone (beige colour) with redrawn cross-stratification and rip-up clasts (white arrow) (B) Coarse-grained Grainstone with redrawn trough cross-stratification. (C) Fine-grained grainstone with planar bedding in the lower part and symmetrical wave ripples, capped by a mudstone layer. White arrow indicates microbial mats intercalated with thin mudstone layers. (D) Fine-grained grainstone with ample mudstone rip-up clasts.
(E) Medium- to fine-grained grainstone at the base with symmetrical wave ripples, capped by mudstone beds. This is followed by a cross-bedded coarse-grained grainstone bed.

#### 3.5.1.3 Thrombolite-stromatolite facies

The thrombolite-stromatolite facies is represented by microbial carbonates, which exhibit a variety of microbial geometries. The microbialites are characterised by columnar (Figure 35.A), goblet-shaped to domal geometries (Figure 35.B-C). Between these end-members a range of different microbial shapes and forms is present, defined by coalesced and merging domal structures and branching fine-scaled columns (Figure 35.D-E). In plan view the microbialites are round to highly elliptic. The diameters of the round microbialites are between a few cm (Figure 35.A-B) but can reach up to several dm. The short axes of the elliptic varieties are generally a few dm whereas the long axes can reach several metres. The height of the individual microbial structures can reach a few metres. Throughout the study area the elongated columns are consistently aligned at 275º-310º. The individual microbial structures are separated by inter-column fill. This fill is variable according to the stratigraphic position. It may comprise sequences of inter-bedded shale, mudstone and pack- to grainstone. Sedimentary structures within the inter-column fill range from planar-stratification to cross-stratification (Figure 36.C). Furthermore, layers of grainstones with rip up clasts are frequent, indicating occasional high-energy conditions (Figure 36.D-E). The size of the inter-column fills range from a few cm to dm. A common feature is the association of microbialites with fossil rich grainstone beds (Figure 37.A) and fossiliferous inter-column fills (Figure 37.B). Microfossils are represented by the tube-like microfossil *Cloudina* (Figure 37.C) and goblet-shaped *Namacalathus* (Figure 37.D), which frequently exhibit geopetal structures (Figure 37.E).

Throughout the study area the microbialites of the Zebra River Canyon show stromatolitic and thrombolitic microbial textures (Kennard and James, 1986; Shapiro, 2000). Stromatolitic fabrics are characterised by a laminated to thinly layered texture. Microbial clots separated by interstitial sediment represent thrombolitic fabrics. Clots are highly irregular but can be elongated and form branching varieties (see Figure 38.A). Microbial textures are variable according to the background sedimentation. When microbialites are associated with mud-dominated sediments the resulting textures are finely laminated stromatolites. Thrombolites exhibit a fine-grained matrix and equidimensional clots. These textures are indicative of microbial growth during mud-dominated times.

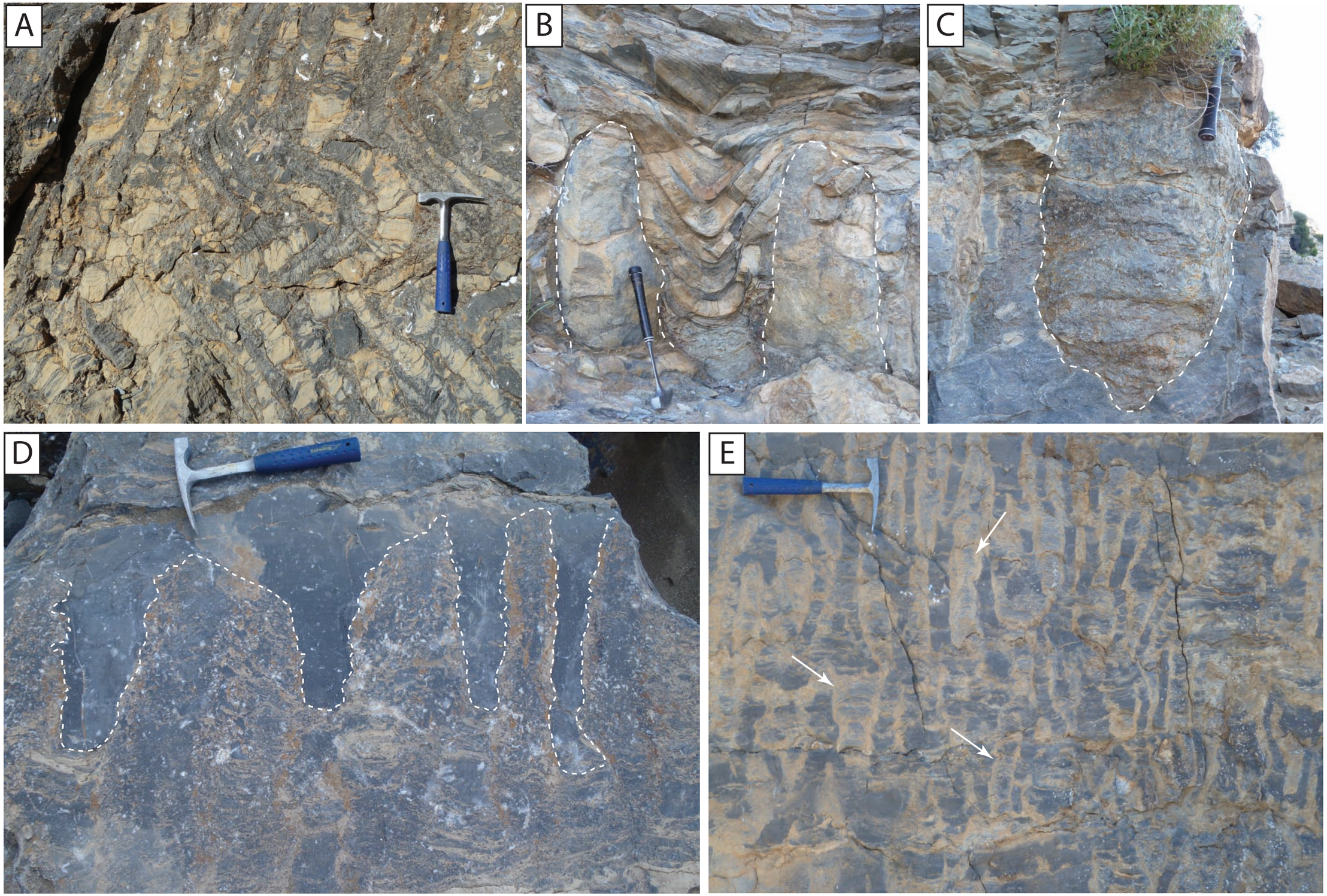


Figure 35: (A) Isolated and rotated, stromatolitic thrombolite columns separated by inter-column fill. Geological hammer for scale. (B) Massive domal to goblet shaped thrombolites. Geological hammer for scale. (C) Massive goblet shaped thrombolite. (D) Coalesced thrombolite columns at the bottom of the image, which break up into individual small-scaled columns at the top. Inter-column fill consists of fine-grained grainstone. Geological hammer for scale. (E) Fine-scale, branching stromatolitic-thrombolite columns form a dendritic network. White arrows indicate microbial columns. Geological hammer for scale.

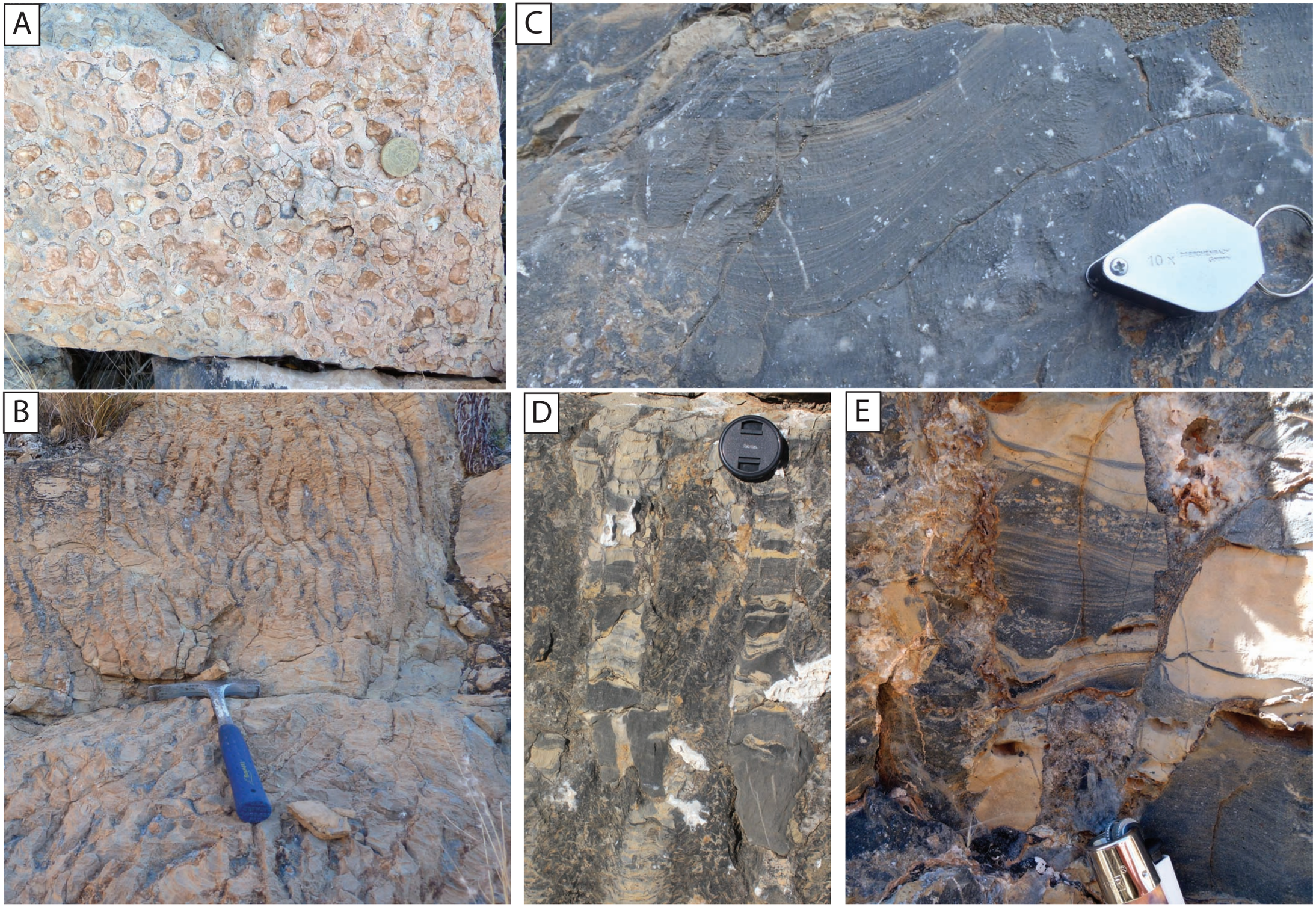


Figure 36: (A) Plan view of fine-scale thrombolite columns. Coin for scale with a diameter of 2.1 cm. (B) The corresponding cross-section view to figure (A), showing a dendritic network of the fine-scale, branching columns. (C) Cross-bedded grainstone inter-column fill. Hand lens for scale. (D) Stromatolitic-thrombolite columns separated by inter-column fill, which shows an alternating sequence of mud-dominated sediments (beige layers) and grainstone layers. (E) Cross-bedded grainstone in inter-column area, capped by a coarse-grained grainstone with abundant mudstone clasts indicating periodically high-energy conditions. Lighter for scale.

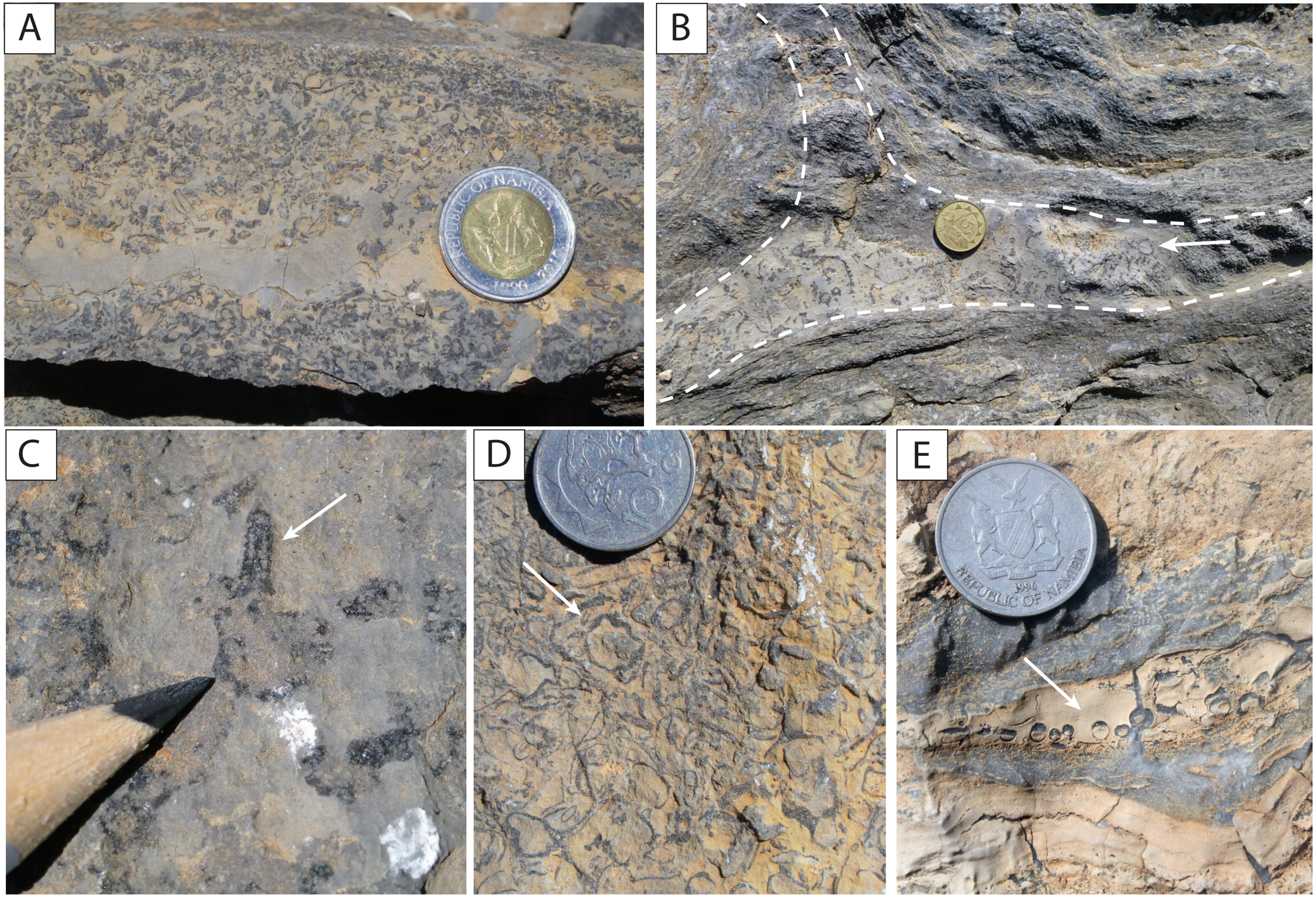


Figure 37: (A) Grainstone bed in the inter-bioherm area with abundant fossils of Namacalathus and Cloudina fragments. (B) Fossil fragments closely associated with the microbial carbonates and enriched in inter-column fills, leading to the interpretation that the sessile Namacalathus and Cloudina grew on the thrombolites (Wood, 2002; Wood, 2011). (C) Close-up of a Cloudina fragment (white arrow). Characteristic for this microfossil is the shape like an elongated bell. (D) Transversal section through the goblet shaped Namacalathus. (E) Geopetal structures within Namacalathus are frequent throughout the Zebra River area.

Coarse, agglutinated stromatolitic textures are the result of increased coarse-grained sediment input, where larger sediment grains are incorporated into the microbial structure. These textures indicate that the microbialites formed due to a combination of grain trapping and microbial carbonate precipitation (Figure 38.B), which is generally the case in a medium to high energy environment (Feldmann and MacKenzie, 1998; Riding, 2011). Typically, the cores of individual microbial structures tend to be thrombolitic but progressively become stromatolitic towards the margins of the structures (Figure 39.A-C).

Figure 40.A-C show two slabbed sections of a goblet shaped microbial structure where both microbial textures are clearly visible. Figure 40.B shows a transverse cut of two closely spaced microbialites. Note the incorporation of intraclasts into the microbial structure. Furthermore, clasts with microbial overgrowth are present in the inter-column fill, indicating occasional high-energy conditions. In times of quiescence, the microbialites also start to develop in the inter-column area, but growth becomes arrested with the input of sediment (Figure 40.C).

The bridging of microbialites over inter-column fill indicates that the synoptic relief of microbialites was tentatively small (cm-scale). Microbialites need a substrate in order to grow and thus cannot develop between exposed columns. Additionally, if the thrombolite columns and domes stand out well above the sediment surface (e.g.: several dm), microbialites would lack a supply of sediment grains. This is, however, essential for microbialites in order develop through trapping and binding of sediments. This interpretation is inline with the observation of modern thrombolites of the Bahamas where thrombolite columns are only a few centimetres above the sediment surface (Feldmann and MacKenzie, 1998).

The consistent column elongation, trough cross-laminated inter-column fills and microbial carbonate texture indicate high-energy conditions in the thrombolite-stromatolite facies (Adams *et al.*, 2005; Grotzinger *et al.*, 2005; Grotzinger *et al.*, 2000). The growth of the microbial carbonates is interpreted to have occurred in a mid to inner ramp setting (Adams *et al.*, 2005) within transgressive systems tract and early high stand systems tract settings, during times of increased accommodation space (Grotzinger *et al.*, 2005; Grotzinger *et al.*, 2000).

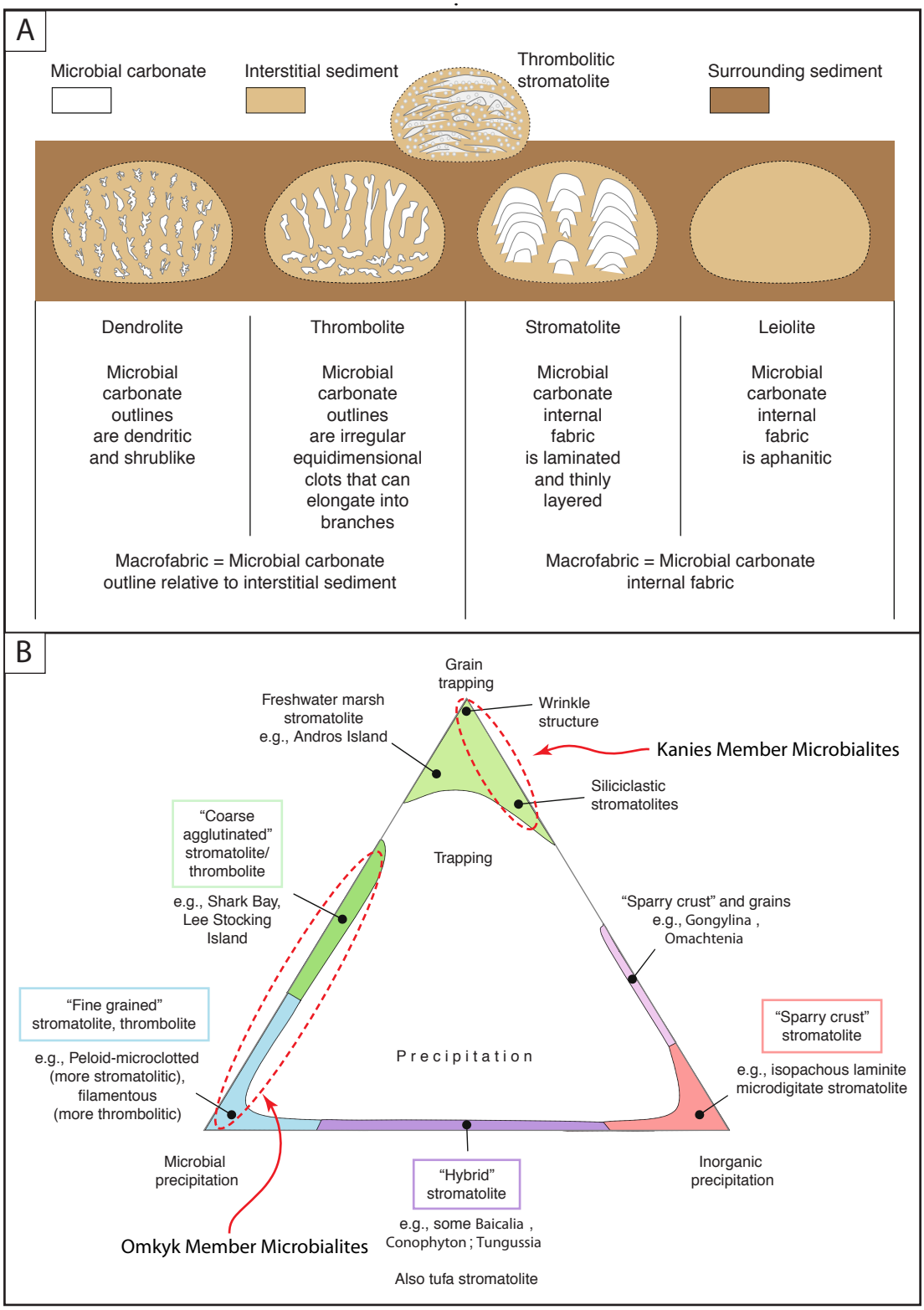


Figure 38: (A) Classification of microbial textures. (B) Cartoon illustrating the mechanisms involved in the formation of microbialites. It involves a combination of inorganic/microbial precipitation and grain trapping. The microbial carbonates in the Omkyk Sequence 2 are plotting on the left side of the diagram, formed by microbial precipitation and grain-tapping. The observed wrinkle structures in the sandstone facies plot on top of the diagram, indicating that these structures formed primarily through grain-trapping. Modified after Riding (2011).

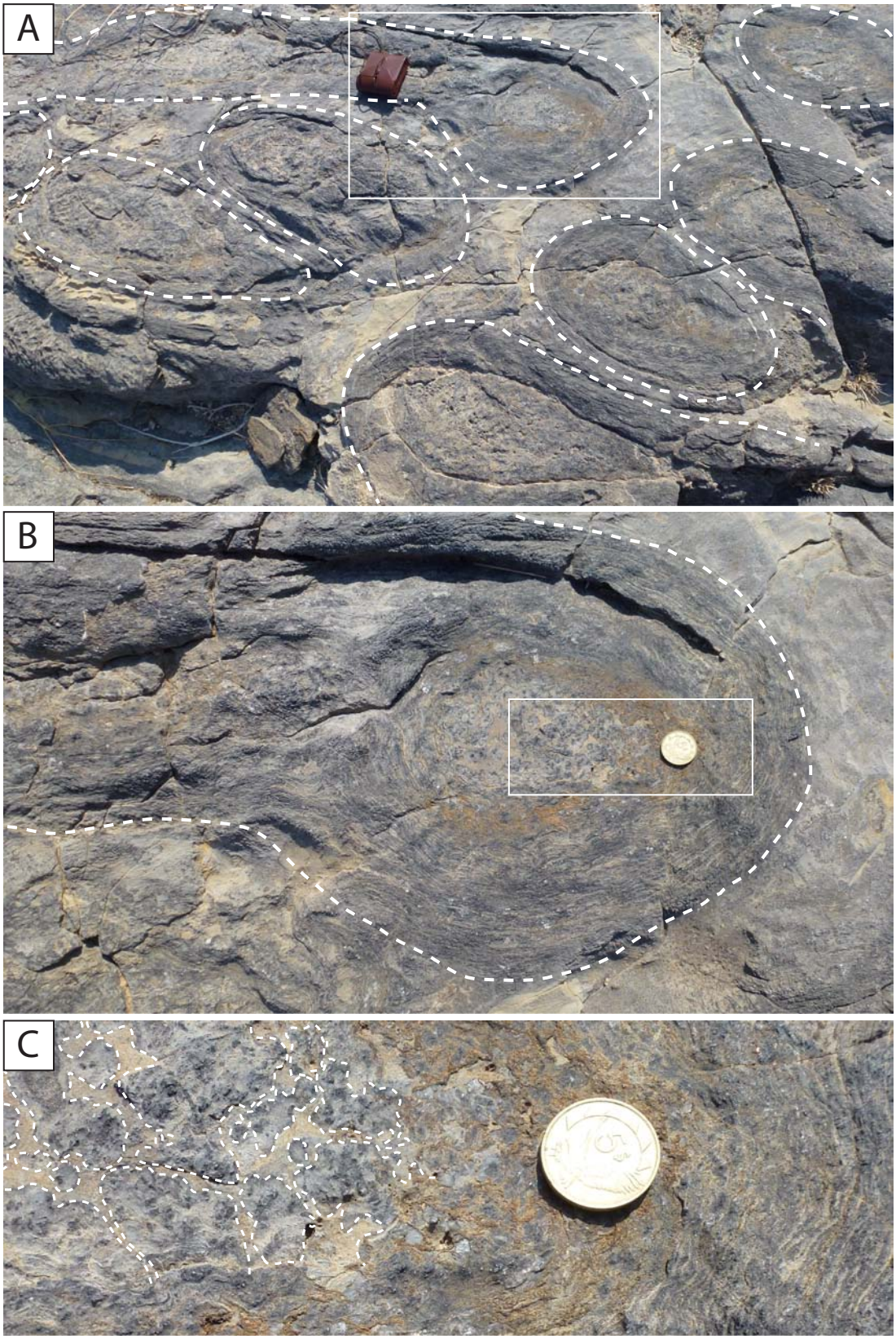


Figure 39: (A) Elongated massive stromatolitic-thrombolite columns showing both, stromatolitic and thrombolitic textures. Compass case for scale with diameter of 11 cm. (B) Close-up picture showing that the core of columns are generally thrombolitic and became progressively stromatolitic towards the margin. (C) Close-up picture of figure (B) showing the irregular microbial clots, characteristic for a thrombolitic texture (white dotted outlines) and the thinly layered structures of the stromatolitic texture.

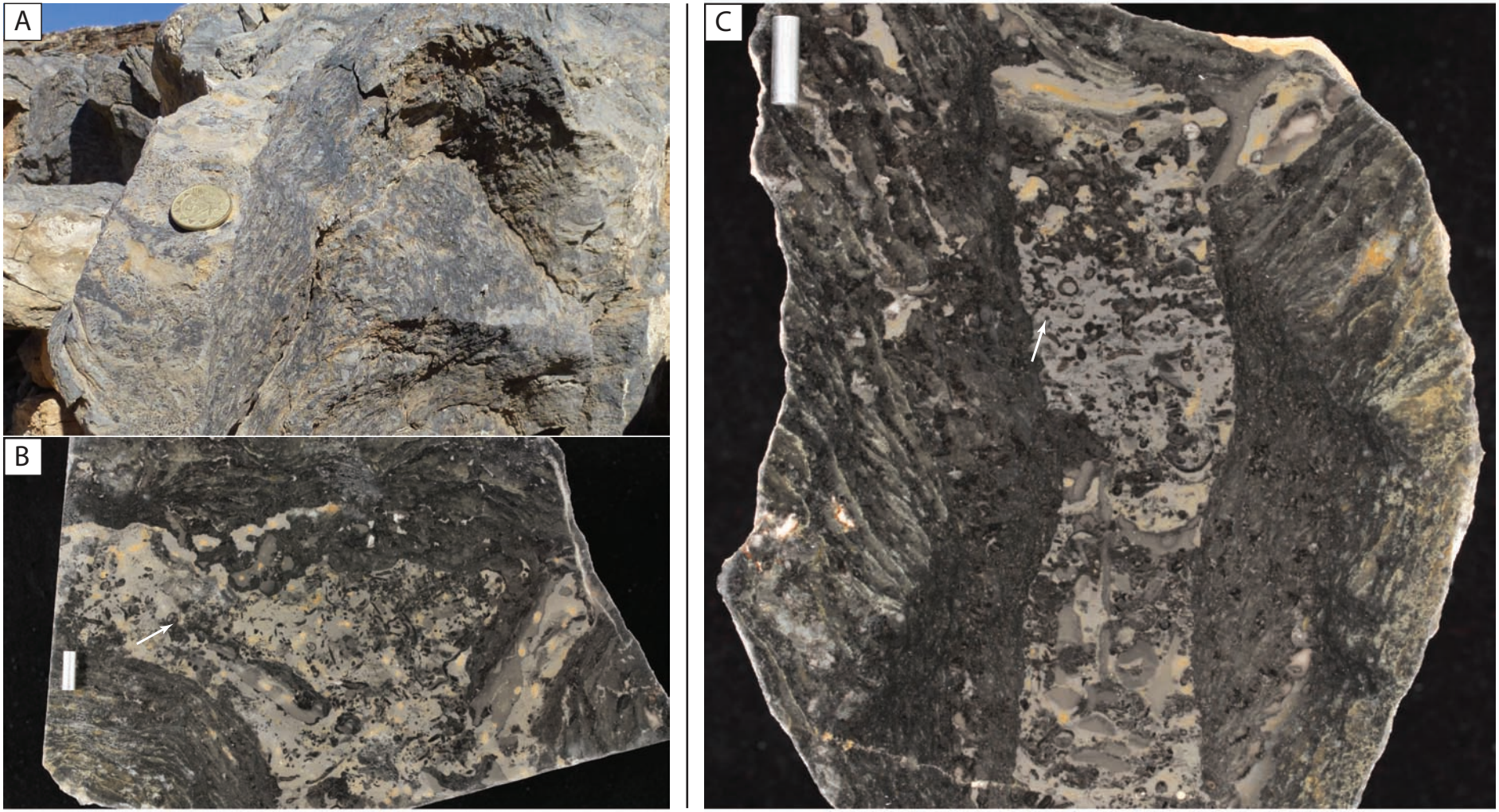


Figure 40: (A) Thrombolite dome with fossiliferous inter-column fill, which was subsequently cut in the lab. Photographs of the slabbed sections are shown in figure B-C. Note the thrombolitic texture in the core, which gradually passes into a more stromatolitic texture. (B) Transversal section through dome. Note the abundant microfossils in a mud-dominated matrix. White arrows indicate mudstone clasts with microbial overgrowth and clasts, which get incorporated into the dome structure. (C) Cross-section through the inter-column fill and adjacent domes. Note at the top the microbial branching over peloids and fossil fragments. Microbial growth in the inter-column fill gets terminated with the input of mud-dominated sediments. Scale in figure B&C is 5 cm.

## 3.6 Thin-section analyses and reservoir properties

A total of 46 thin-sections of selected samples have been prepared in order to analyse the microfacies of the facies association. An additional aim was to describe the porosity characteristics of each facies in order to define analogue reservoir and non-reservoir units for subsequent geocellular reservoir modelling and fluid flow simulation. However, pervasive recrystallization and selective dolomitisation of the rocks made it difficult to obtain accurate data from the poorly preserved specimens. The following descriptions are a summary of key-observations from the thin-section analyses from the best-preserved samples.

### 3.6.1 Thrombolite and inter-column fill

Figure 41.A-B show two thin-section photomicrographs of a thrombolite sample obtained from a bioherm in Unit 2. The general appearance of the microbialite is characterised by a grey to brownish, fine-grained, micritic matrix, which represents the microbial mesoclot. An internal texture, indicating microbial activity is not visible. The cavities between the clots are filled with dark brown to black geopetal sediment. Clearly visible are drusy, void-filling calcite cements, characterised by subhedral crystals, which grow from the clot-margin normal towards the centre of the void (Figure 41.B).

Figure 41.C shows a thin-section image of an inter-column fill. Abundant *Namacalathus* and *Cloudina* fossils in a fine-grained matrix are characteristic for the inter-column fill. Transversal sections through the goblet shaped *Namacalathus* have the appearance of shell-like structures. Note the tube-like microfossil fragment with completely recrystallized interior at the top of the thin section, which is typical for *Cloudina*.

Primary porosity of the thrombolites is best described as growth framework porosity, generated by the microbial growth activity. The initial porosity of the thrombolite might have been fair to good, based on the abundant voids and cavities in the thrombolite structure. However, framework porosity tends to become quickly reduced due to the infill of sediment and the precipitation of cements as seen in the thin sections. This might be especially the case for the microbial carbonates in the Zebra River sections, where inter-column fill and inter-bioherm facies changes

according to the stratigraphic position. For instance, primary porosity is most likely being reduced in the microbialites where the laterally corresponding facies consists of fine-grained material, which subsequently plugs the pores and cavities. The initial primary porosity of the fossiliferous floatstone in the inter-column areas was most likely poor due to the fine-grained, micritic matrix.

Based on the thin-section analyses and field observations the overall porosity characteristics of the microbialites are likely to be highly variable and heterogeneous. Fair to good primary porosity can be expected in areas where the inter-bioherm and inter-column fills consist of grain-dominated sediments. Reduced porosity values, due to the infill of mud-dominated material into the growth framework porosity, are expected to be in mud-dominated stratigraphic positions. Thus, an entire bioherm structure might exhibit highly variable porosity values and heterogeneities corresponding to the background sedimentation and stratigraphy.

### 3.6.2 Grainstone

All thin-sections of grainstones are highly recrystallized and therefore microfacies analyses results are limited. However, the remnants of intraclasts, peloids and *Cloudina* fragments have been identified. Figure 41.D shows the thin-section appearance of a typical coarse-grained grainstone from the study area. Note the elliptical structure in the lower left of the thin-section image with a clearly visible rim. On the upper part, multiple encrustation rims are still recognisable. This structure is interpreted to represent a recrystallized, coated ooid indicating high-energy conditions.

Primary porosity estimations solely based on thin section analyses is not possible due to limited data. However, based on the facies interpretation as high energy environment and the presence of intraclasts and ooids suggest that primary interparticle porosity of the grainstones was good.

### 3.6.3 Irregular laminite

Figure 42.A-B show the thin-sections photomicrographs of irregular laminites. Irregular laminites appear as alternating sequence of microbial mats and fine-grained grainstones in thin section. This can be seen in both thin-section micrographs. Note at the base of Figure 42.A a thin layer of coarse-grained material followed by a microbial, brownish, micritic layer. At the top of the image the start of the next

coarsening cycle is visible. Figure 42.B shows an enlarged area in order to better visualise the microbialites. The white arrows indicate arrays of calcite particles. Cells of bacteria and calcimicrobes are typically organised within threads, forming filamentous grid-like structures (Flügel, 2004). Therefore, the observed array structures are interpreted as remnants of microbial activity. The initial overall porosity was most likely poor but might have reached higher values within the coarse-grained layers.

### 3.6.4 Mudstone and intraclast breccia

The photomicrograph in Figure 42.C shows a thin section of a recrystallized and dolomitised mudstone. Note the large well preserved dolomite rhomb at the upper right side of the image. Dolomite crystals are euhedral to sub-hedral, but generally poorly preserved. The crystals are enclosed in a fine-grained, brownish matrix. The texture is best described as inequigranular and porphyrotropic.

Figure 42.D shows the matrix of an intraclast breccia. It is characterised by a brownish, fine-grained matrix, representing a recrystallized mudstone. Initial porosity values for both, mudstones and the matrix of the intraclast breccias were low.

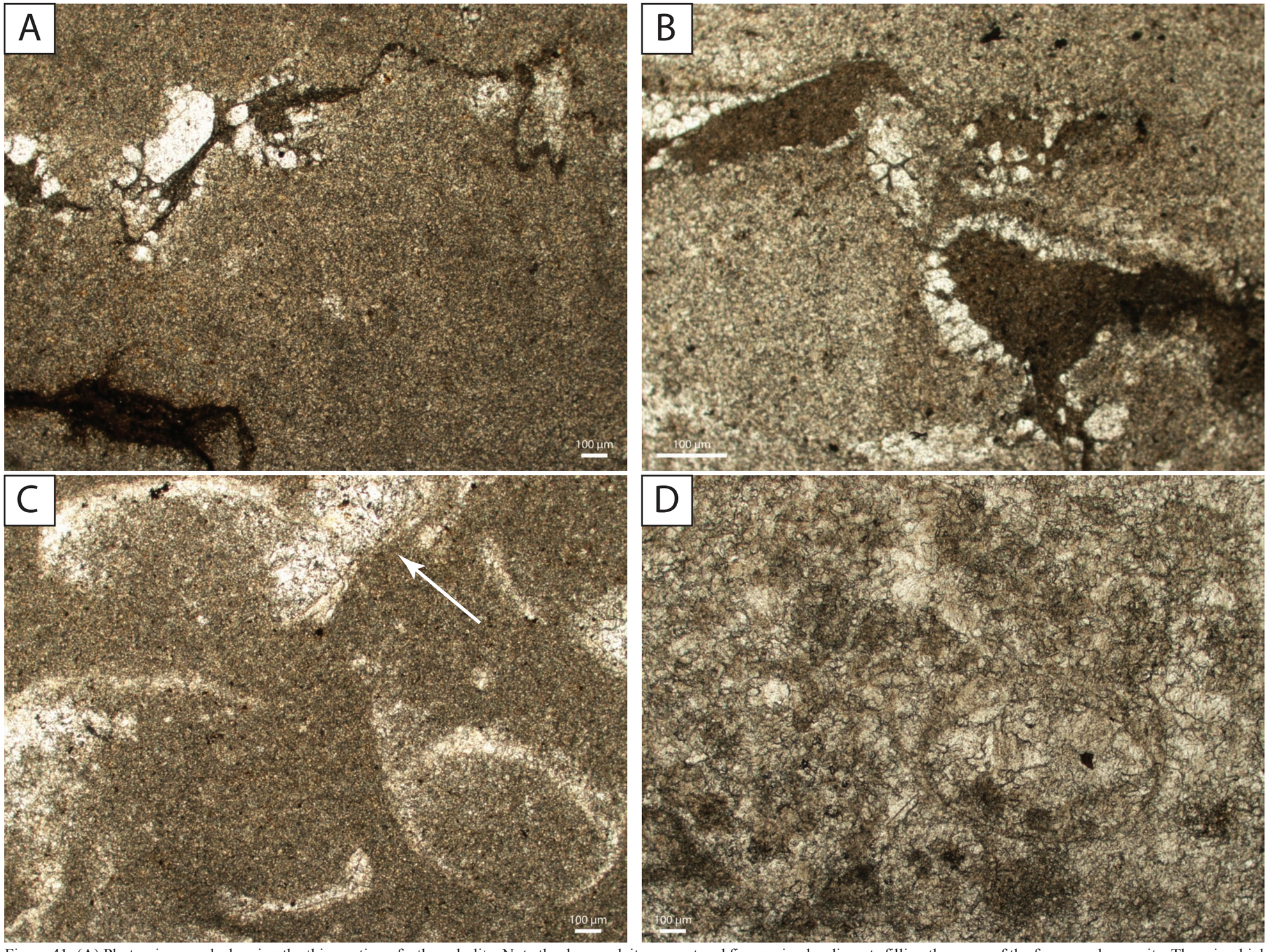


Figure 41: (A) Photomicrograph showing the thin-section of a thrombolite. Note the drusy calcite cement and fine-grained sediments filling the pores of the framework porosity. The microbial clots are characterised by a fine-grained carbonate matrix. (B) Close-up of a thrombolite. Note the calcite cement, which grows from the rim of the thrombolite cavity into the pore space. (C) Photomicrograph showing the thin-section appearance of Namacalathus (shell-like structures) and Cloudina (white arrows) in an inter-column floatstone. (D) Completely recrystallized grainstone. Note the rounded structure in the lower right of the photomicrograph, interpreted as the remnants of an ooid.

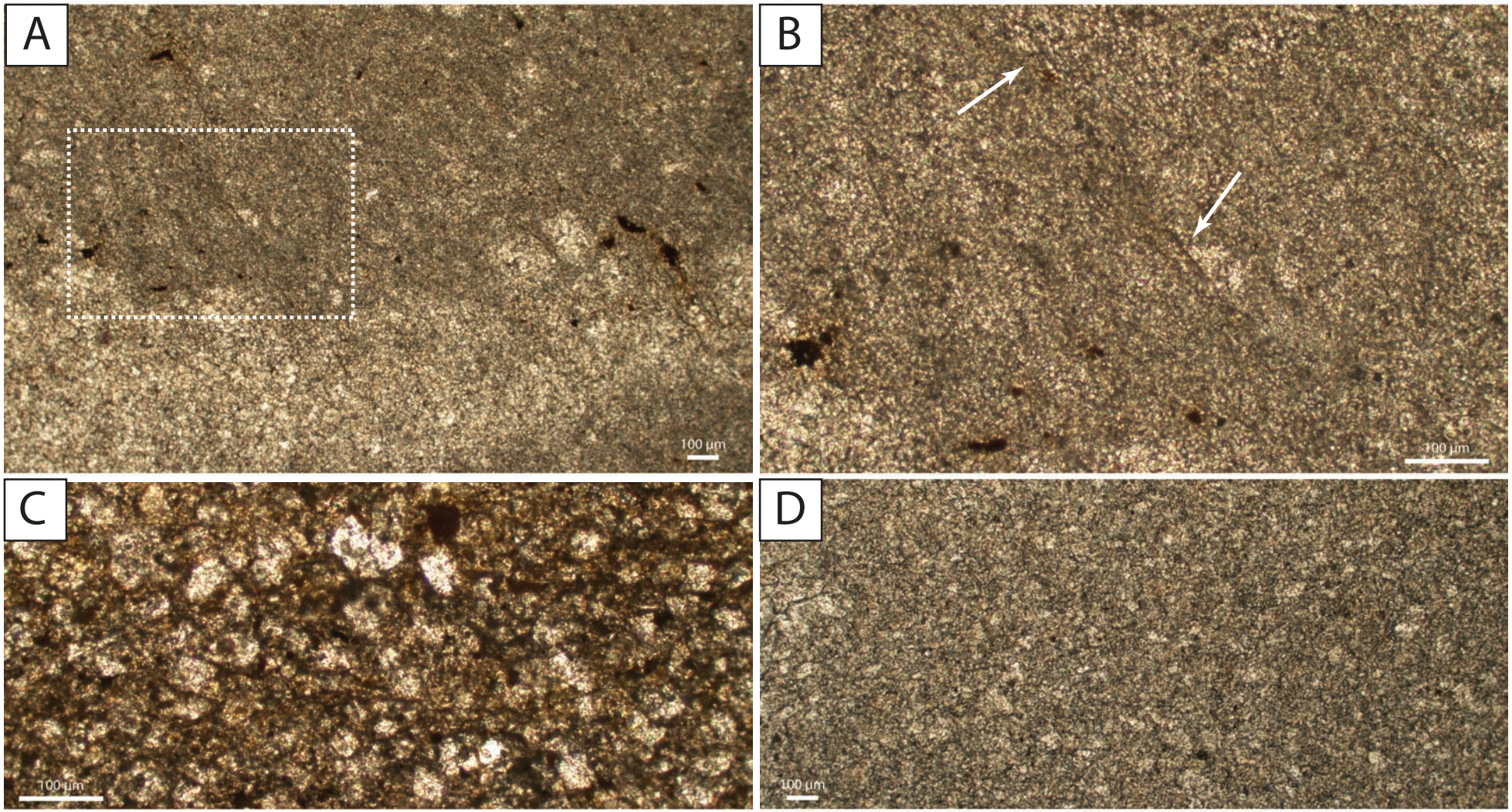


Figure 42: (A) Thin-section photomicrograph of an irregular laminite. Note at the bottom of the image a coarse-grained packstone layer, followed by dark micritic layer. Within the micritic layer, one can see a preferred orientation of elongated features towards the upper left side of the image. White doted rectangle indicates position of figure B. (B) Enlarged area of picture A, showing a close-up of elongated features, which consist of an array of carbonate crystals. This pattern is indicative for microbial activity (Flügel, 2004). (C) Recrystallized mudstone, characterised by dolomite crystals in a brownish, micritic matrix. (D) Fine-grained micritic matrix of an intraclast breccia.

## 3.7 Origin of sand-sized grains

The dominant facies of the Kuibis carbonate platform are lime mudstones and silt- to sand-sized clastic carbonates (Dibenedetto and Grotzinger, 2005; Grotzinger *et al.*, 2005). Clastic carbonates exhibit grainstone textures and abundant evidence of current- and wave-produced cross-, hummocky-, and planar-stratification (see paragraph 3.5.1.2.2). The Kuibis carbonate ramp developed before the advent of higher organised animal life and in absence of skeletal metazoan. Nevertheless, *Cloudina* and *Namacalathus* show evidence of biomineralisation and the formation of carbonate exoskeletons (Wood, 2011). Fossils are locally abundant in the vicinity of microbialites and occur in inter-column and inter-bioherm facies. Field observations and thin-section analyses, however, indicate that fossil shells do not constitute a main source of carbonate grains in the grainstone horizons. The problem then is to generate a large volume of essentially silt- to sand-sized grains without the availability of skeletal grains.

Thin-section analysis of the grainstones provided only limited information about the origin and types of grains due to intense recrystallization. Remnants of peloids, intraclasts and minor ooids were, however, identified (see paragraph 3.6.2). The origin of the peloids could not be determined in thin-section because of intense recrystallization. However, it is important to establish the source of peloids because they constitute the main part of the grainstones.

Flügel (2004) differentiates 9 types of peloids according to their origin. The majority of these peloid classes are related to the interaction with metazoan life, such as fecal pellets or bioerosional peloids. Thus, these types of peloids can be discarded for the Neoproterozoic carbonates of the Kuibis shelf. The remaining types of peloids that might have formed despite the absence of higher organised animal life are: (1) algal peloids, (2) mud peloids and (3) microbial/precipitated peloids.

Algal peloids originate from the disintegration and gradational abrasion of calcified microbes. Mud peloids are genetically intraclasts and form by erosion and reworking of carbonate mud and aggradation of micrite and subsequent redeposition on the platform The last types of peloids for Neoproterozoic carbonates, based on the classification of Flügel (2004), are microbial and precipitated peloids. Microbial peloids develop in situ in microbial mats (Leinfelder and Hartkopf-Fröder, 1990;

Pickard, 1992). These are commonly rounded, micritic grains formed by biochemical precipitation, triggered by microbial activity. Precipitated peloids also form in situ are, however, products of inorganically induced carbonate precipitation (Shinn, 1969).

All above described processes could explain the origin of peloids in the Kuibis carbonate ramp, where microbialites dominate the carbonate factory. The carbonate ramp was wave- and storm-dominated and microbialites occur in inner and mid ramp settings. Strong wave and current activity may have had the potential to torn off fragments of calcified microbes to form algal peloids over a wide range of ramp settings. This process seems to be particularly common in Cambrian shelf carbonates (Coniglio and James, 1985; Wolf, 1965) and might have also played an important role for the Kuibis carbonate ramp. Furthermore, through occasional storms and constant wave agitation, sediments were continuously reworked, transported and resedimented, potentially forming mud peloids. Additionally, microbial and precipitated peloids may have developed across the platform through organically and inorganically induced precipitation. This scenario for the development of peloids does, however, not explain to occurrence of abundant sand-sized particles in the Kuibis ramp since peloids are typically silt-sized. A potential explanation for the abundant occurrence of sand-sized grains might be the formation of aggregate grains, consisting of peloids.

Aggregate grains are composite grains, composed of smaller particles such as peloids, and their size ranges typically from 0.5 mm up to several millimetres but are commonly around 1 mm (Flügel, 2004). These composite grains are subdivided into grapestones and lumps. Grapestones are irregular-shaped aggregates of spherical grains and resemble clusters of grapes whereas lumps are characterised by a smoother outline. A schematic model illustrating the formation of aggregate grains is shown in Figure 43. In the binding stage particles are bound together by microbial filaments and organic biofilms. Through subsequent calcification of the microbiota the particles form grapestones (grapestone stage, see Figure 43). Occasional reworking and cementation eventually leads to the formation of rounded grains (lump and mature lump stage, see Figure 43).

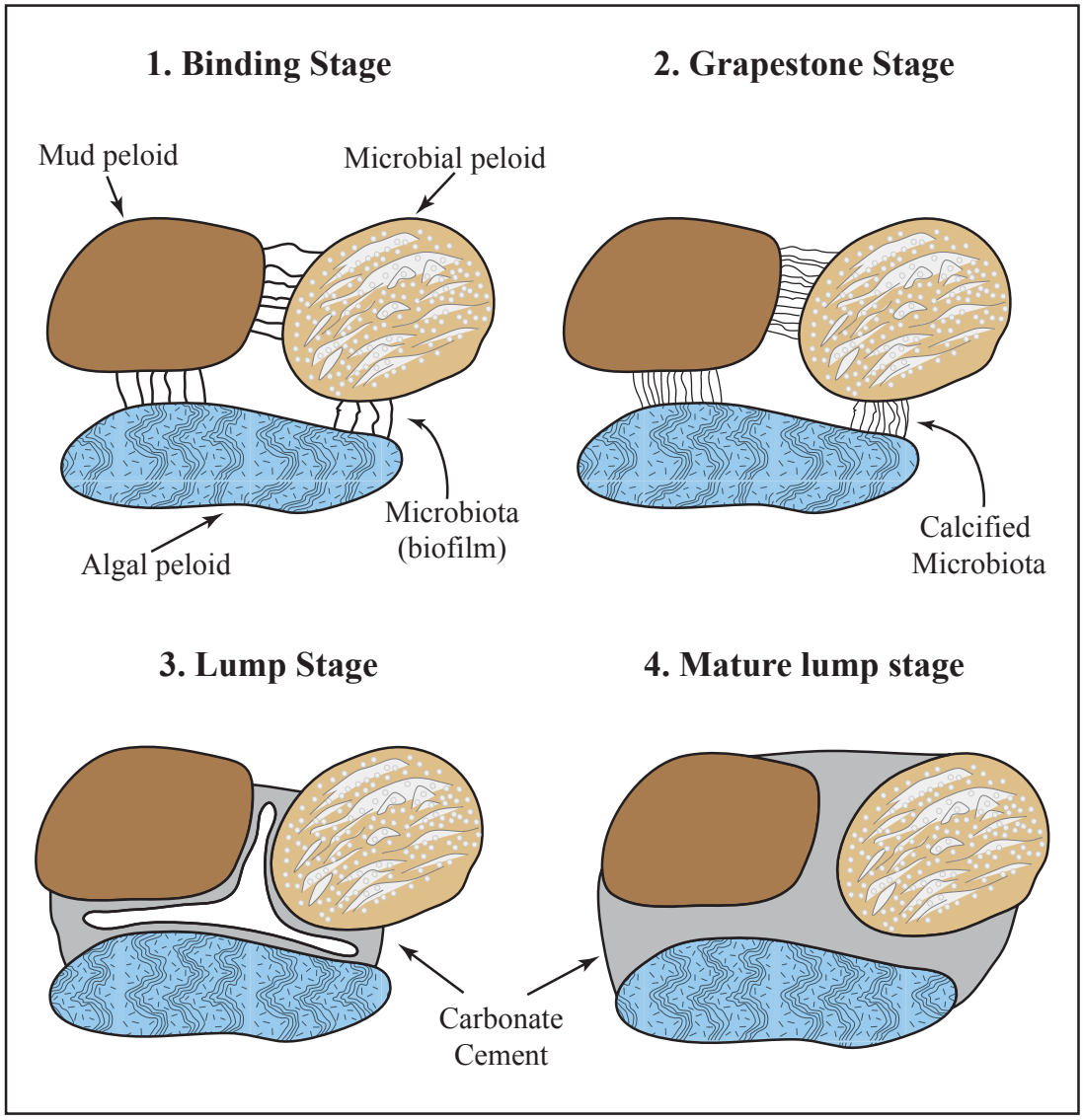


Figure 43: Schematic illustration showing the formation of aggregate grains. Modified after Tucker and Wright (1990).

Combining this model with the formation of peloids leads to following scenario for the formation of sand-sized grains in the Kuibis carbonate ramp: Peloids are formed due to a combination of erosion and abrasion of microbialites (algal peloids), communition of intraclasts (mud peloids) and in situ precipitation of microbial and precipitated peloids. This occurred over a wide range of settings within the ramp. Storm- and wave-generated currents acted as efficient transport mechanism, transporting silt-sized material across the ramp into shallower parts (e.g.: from mid ramp towards the inner ramp). Following deposition of the particles during times of quiescence, peloids were bound together by microbita and subsequent microbial calcification and cementation formed aggregate grains. Repetition of transport, sediment settling and cementation progressively produced larger grains (e.g.: lumps). Furthermore, constant wave agitation might have been an efficient size-sorting

process, forming well-sorted coarse-grained grainstones and sandbars and fine-grained grainstones in the inter-bioherm areas.

The occurrence of extensive grapestone-composed grainstones in the Urikos Member of the Witputs sub-basin of the Nama Basin has been reported by Saylor (2003). Additionally, aggregate grains compose the majority of grains in highstand systems tract grainstones of the terminal Neoproterozoic Buah Formation in Oman (Cozzi *et al.*, 2004), interpreted as inner ramp deposit of a storm-dominated carbonate ramp. These observations substantiate that extensive aggregate-grain grainstones occur in terminal Proterozoic ramp carbonates. Thus, the presented model for the formation of large volumes of sand-sized particles can certainly explain the origin of grains of the grainstones in the Kuibis carbonate ramp. However, further detailed studies of the microfacies of the Omkyk grainstones have to be carried out to validate the presented hypothetical model.

From a petroleum point of view, aggregate-grain grainstones constitute good to very good reservoir facies. They are generally well-sorted and comprise high interparticle and intraparticle porosity (Roberts and Moore, 1971; Winland and Matthews, 1974).

## 3.8 Sequence Stratigraphic evolution of OS2

Adams *et al.* (2005) published a detailed sedimentological and sequence stratigraphic log (resolution of 1 m) of the Omkyk Member approximately 1 km to the west of the study area. In the present study, a detailed stratigraphic log was measured (resolution of 10 cm) within the southwestern part of the study area (Figure 30). The following is a resume of the key sedimentological and stratigraphic aspects of this succession. Whilst the observations are the author's own, it is recognised that inevitably several of these features overlap with those described in Adams *et al.* (2005) along strike.

Thrombolite-stromatolite carbonates are found at several stratigraphic levels within Omkyk Sequence 2 (Adams *et al.*, 2005; Adams *et al.*, 2004; Grotzinger *et al.*, 2000). A laterally extensive thrombolitic biostrome directly caps the OS 2 in an initial transgressive systems tract. A second level of microbial carbonates is found in the middle Omkyk Sequence 2 and comprises both, bioherms and biostromes within the Zebra River Farm. Bioherms are laterally discontinuous microbial geobodies

with a mound-like geometry and separated by inter-bioherm facies. Laterally extensive microbial carbonates, characterised by a tabular morphology, are better described as a biostrome.

The first unit of OS2 is composed of grain-dominated facies at base in an early transgressive systems tract. Grainstones are forming massive beds at the base and are characterised by planar- and cross-stratification (Figure 44**, 0.0-8.0 m**). These grainstone beds are interbedded with decimetre-scaled irregular laminites, intraclast breccias and minor mudstones and shale. With the ongoing deepening during the transgression this succession grades upwards into mud-dominated facies. The transition zone is represented by the occurrence of hummocky cross-stratified grainstones, several decimetres thick irregular laminites and intraclast breccias, indicating an increase in water depth (Figure 44**, 8.0-16.5 m**). The top of the unit TST is marked by a 2 metre-thick interval of shale, intercalated with irregular laminites (Figure 44**, 16.5-21.0 m**).

In the HST of Unit 1, the first thrombolite-stromatolite bioherms (**Bioherm 1**) developed, which are the most restricted microbial carbonates of the Omkyk Sequence 2. Outcrop conditions did not allow to accurately map the inter-bioherm facies on a centimetre scale. However, the general trend of the inter-bioherm facies of Bioherm 1 is represented by grain-dominated facies. Furthermore, these bioherms feature the enigmatic "Leaning Towers of Stromiza" - columnar thrombolites and stromatolites that are systematically inclined to the southeast. The origin of the systematic inclination is, however, not understood at the moment.

The base of Unit 2 is represented by shale, which is occasionally inter-bedded with microbial carbonates and irregular laminites (Figure 44**, 27.5-36.5 m**). The microbialites are characterised by small-scale thrombolitic domes, surrounded by mud-dominated facies (see Figure 35.B). Up-section within the unit TST, thrombolite-stromatolite bioherms (**Bioherm 2**) started to develop. Bioherm growth terminated at the top of the unit HST (Figure 44**, 37.5-52.0 m**). The internal structure of Bioherm 2 is characterised by massive domal and columnar stromatolitic thrombolites at the base. Towards the top of the bioherms the predominant growth form changes into small-scale, branching columns. Inter-bioherm facies are represented by mud-dominated facies, interbedded with decimetre-thick microbialites at the base. This succession gradually coarsens upward into grain-dominated facies, with planar and cross-stratified grainstones. Within the planar

stratified grainstones wave ripple marks are common (see Figure 45). A massive, 1.5 m thick grainstone layer marks the top of the unit HST, coinciding with the top of Bioherm 2 (Figure 44**, 52.0 m**).

The lower part of Unit 3 is characterised by the abundant occurrence of intraclast breccias, grainstones and minor mud-dominated facies. Metre-thick intraclast breccias, interbedded with dm-thick fine-grained grainstones, mudstones and shale represent the onset of the of Unit 3 transgressive systems tract (Figure 44**, 52.0-62.0 m**). The latest stage of Unit 3 TST is marked by fine-grained, hummocky cross-stratified grainstones, irregular laminites, mudstones and shale. A massive 2 m-thick grainstone layer marks the onset of the HST. This layer is followed by the evolution of the laterally extensive **Biostrome 1** (Figure 44**, 64.0-72.0 m**). Small-scaled coalesced and branching stromatolitic thrombolite columns represent the internal architecture of the biostrome. Fluvial channels, several metres in width, with coarse-grained cross-stratified grainstones, dissecting the biostrome are frequent. At the location of the stratigraphic log, the biostrome is inter-fingering with massive, cross-stratified grainstones (**Grainstone 1**), eventually pinching out altogether.

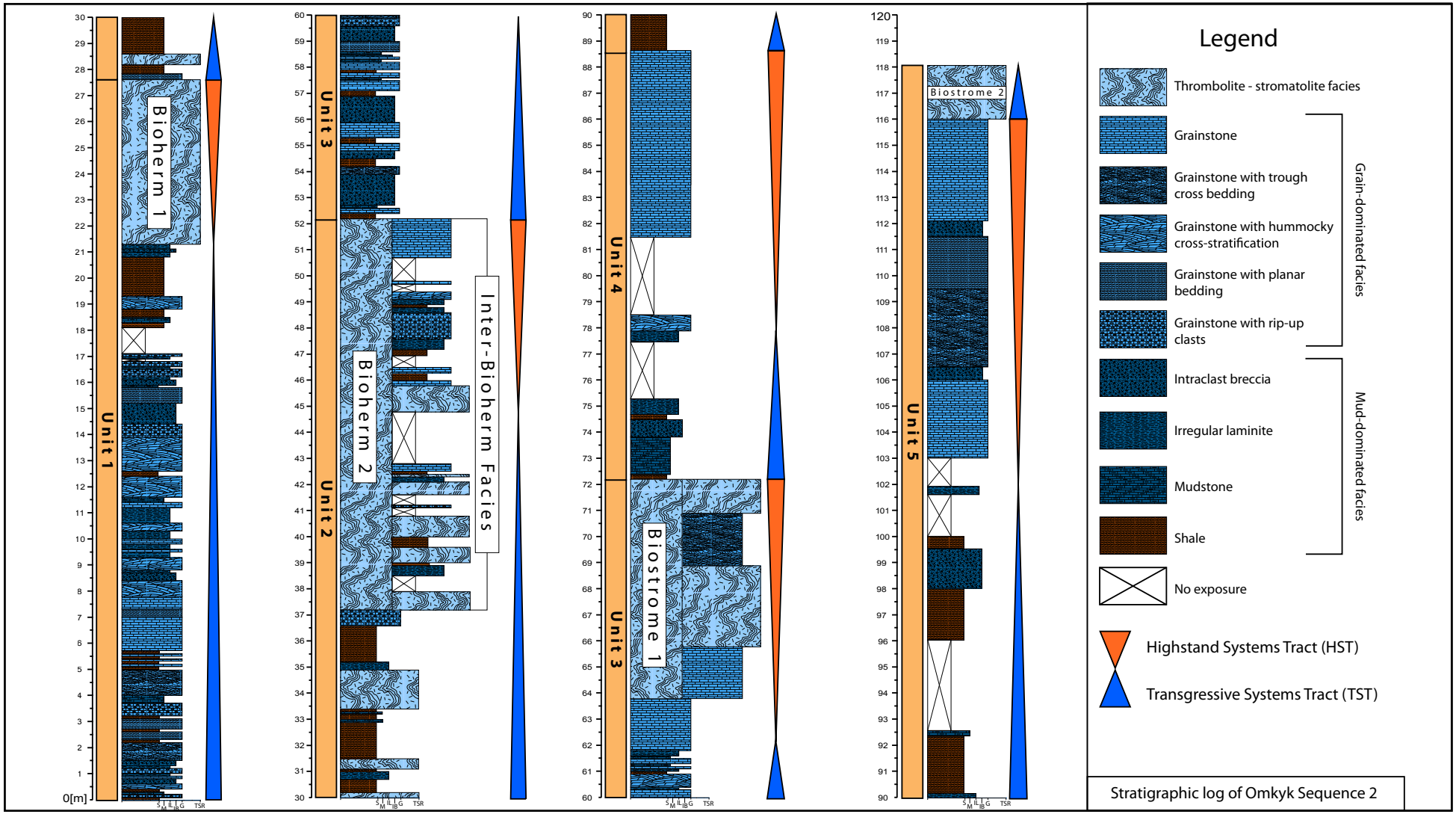


Figure 44: Stratigraphic log of the Omkyky Sequence 2. See Figure 30 for location.

The microbial growth in Unit 3 is terminated with the input of mud-dominated facies at the onset of the Unit 4 transgressive systems tract, which is characterised by mudstones, irregular laminites, intraclast breccias and shale (Figure 44**, 72.0-78.0 m**). A 0.5 m thick layer of hummocky cross-stratified grainstone marks the transition from transgressive to highstand systems tract. The unit HST is represented by a 7 m-thick, laterally extensive interval of massive, coarse-grained grainstones (**Grainstone 2**) (Figure 44**, 81.5-88.5 m**).

The transgressive systems tract of Unit 5 is characterized by abundant mud-dominated facies, represented by m-thick shale layers, inter-bedded with mudstones, several dm-thick intraclast breccias and irregular laminites (Figure 44**, 88.5-102.0 m**). This sequence subsequently grades upwards into a thick interval (13 m) of grain-dominated facies towards the HST of Unit 5 (**Grainstone 3**). This uppermost grainstone horizon is characterized by hummocky and trough cross-stratified coarse-grained grainstones, interbedded with dm-thick intraclast breccias (Figure 44**, 102.0-116.0 m**).

The top of the Omkyk Sequence 2 is marked by the onset of the evolution of the laterally extensive **Biostrome 2** (Figure 44**, 116.0-118.0 m**). The deposition of this top biostrome has been interpreted to have occurred in an initial transgressive systems tract (Grotzinger *et al.*, 2000).

Within the canyon system, the grain- and mud-dominated intervals tend to be uniform in thickness and are laterally extensive. Figure 46.A-D shows two representative outcrop overviews with interpreted microbial and grainstone horizons.

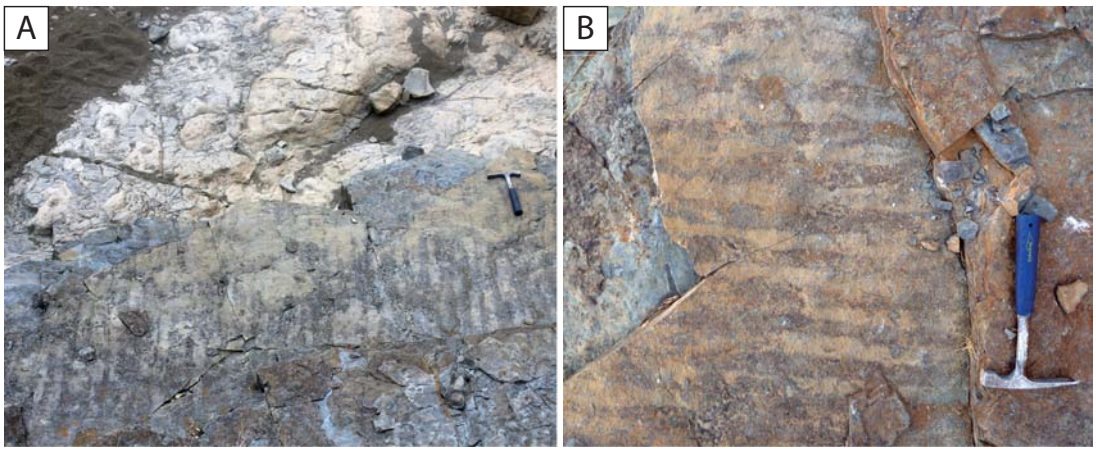


Figure 45: (A) Symmetrical wave ripples in a fine-grained grainstone in the inter-bioherm facies, indicating medium to high-energy conditions at the top of bioherm evolution. (B) Close-up of wave ripple marks.

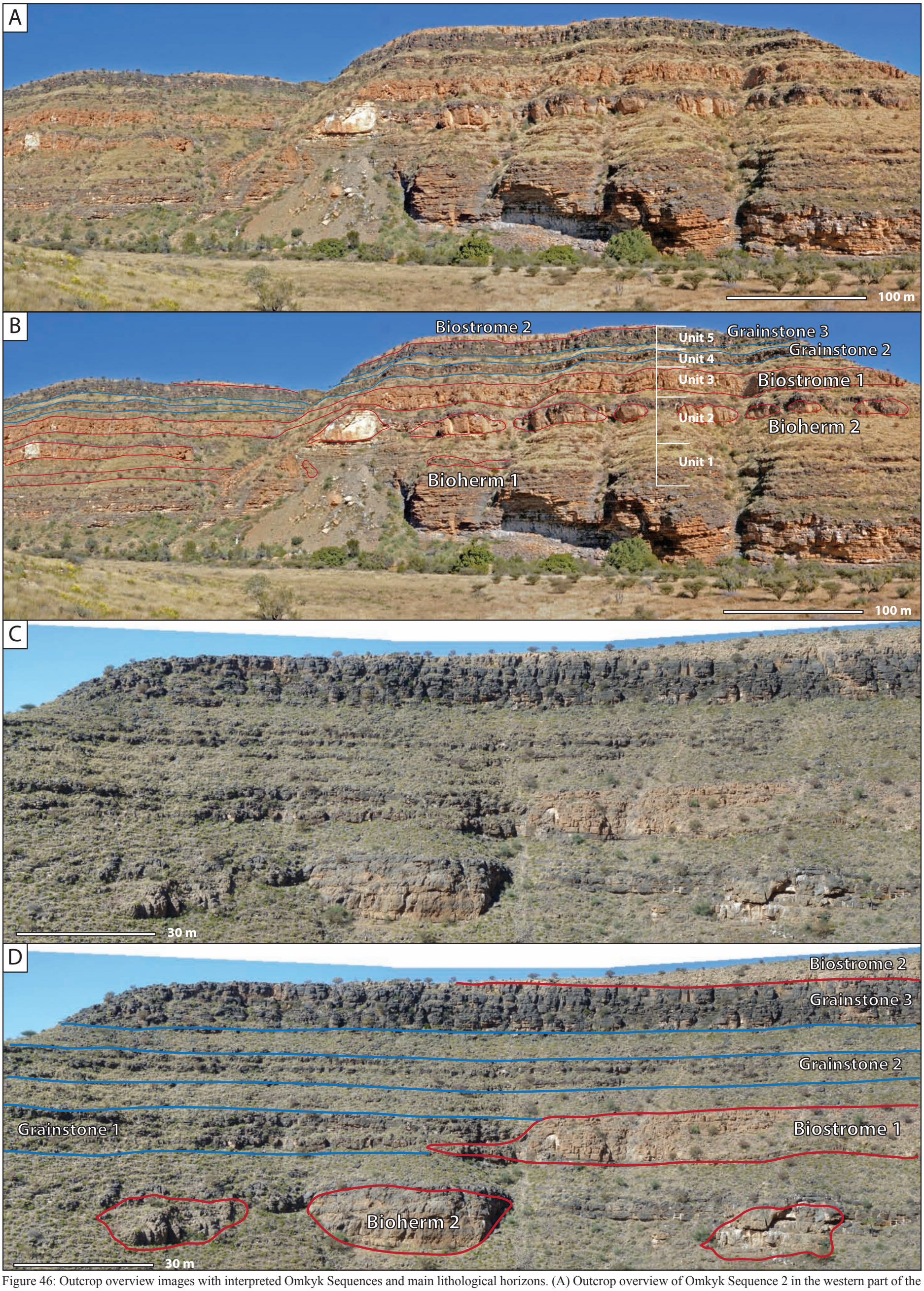


Figure 46: Outcrop overview images with interpreted Omkyk Sequences and main lithological horizons. (A) Outcrop overview of Omkyk Sequence 2 in the western part of the study area. (B) Photomosaic interpretation showing the mapped OS2 units. Note the laterally discontinuous bioherm structures, separated by inter-bioherm facies. Grainstone 1 is not visible at this section because Biostrome 1 is laterally continuous at this location. The overall geometry of OS2 is characterised by a simple layer cake architecture. (C) Outcrop overview of Omkyk Sequence 2 in the south-eastern part of the study area. (D) Photomosaic interpretation showing the pinching out of Biostrome 1, which laterally passes into Unit 3 HST grainstones (Grainstone 1).

### 3.8.1 Evidence of sub aerial exposure

The sequence stratigraphic interpretation of the Omkyk Sequence 2 in this thesis followed the subdivision of Adams et al (2005) and Grotzinger et al. (2005). It was outside the scope of this research project to conduct detailed sequence stratigraphic work because of time constraints and also additional regional mapping outside the Zebra River Canyon system would have been required to identify regional unconformities.

However, during the logging of the above-presented sedimentary log, evidence for sub-aerial exposure was recognised. At the top of the Unit 3 TST and directly at the base of the grainstone package underlying **Biostrome 1**, desiccation cracks in a mudstone bed were identified. They are characterised by a polygonal pattern of 1-2 mm to up to 1 cm wide, wedge shaped cracks (see Figure 47.A&B). The polygonal pattern clearly identifies the fractures as desiccation cracks rather than syneresis cracks. Syneresis cracks form through under water shrinkage of mudstones and shale and are marked by simple, straight fractures. In contrast to that, desiccation cracks form under sub-aerial exposure and complete drying-out of clayey sediments in a polygonal pattern (e.g. Astin and Rogers, 1991). The identification of this exposure surface stands in clear contrast with the current sequence stratigraphic interpretation. This section is interpreted as the change from TST to HST in Unit 3 of the Omkyk Member. Grotzinger et al. (2005) actually places the maximum flooding surface at exactly the location of the desiccation cracks and interprets the mudstones and shale as outer ramp deposits. However, this cannot be the case because of the newly identified exposure surface, which requires an inner ramp, probably tidal to subtidal environment. As a consequence, the interpretation that **Biostrome 1** developed during the latest stages of the unit HST has to be revised. In the light of this new evidence it seems more likely that **Biostrome 1** started to grow in an initial TST, similar to **Biostrome 2.** This, however, requires that the top grainstones of the unit 3 TST represent in fact a high stand systems tract. These grainstones show similarities to the fine-grained grainstones, deposited for instance in the lee of sandbars (compare facies description) in an inner ramp setting, rather than being interpreted as mid ramp deposits, associated with intraclast breccias and storm deposits. This interpretation is however speculative and additional mapping of the exposure surface and under- and overlying strata is needed to confirm this analysis. Future research

will show if the entire sequence stratigraphic subdivision of Omkyk Sequence 2 needs to be revised.

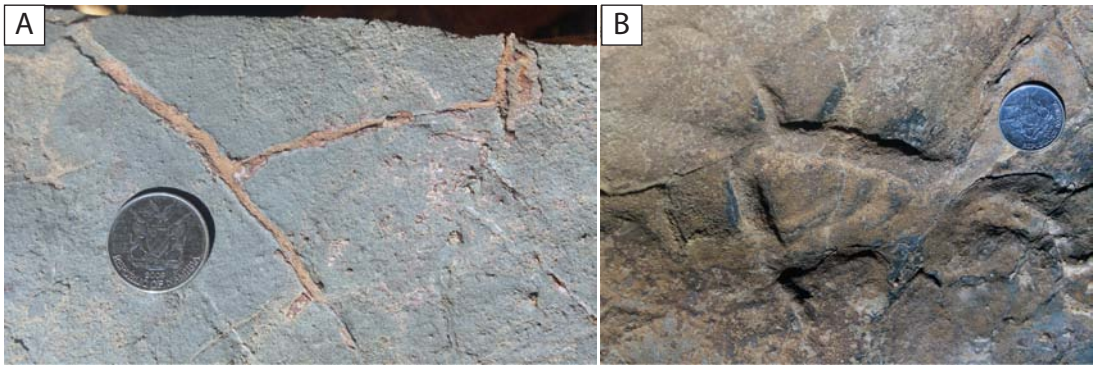


Figure 47: Photographs showing desiccation cracks, represented by mm- to cm-wide, wedge-shaped fractures. Note the polygonal pattern of the fractures, identifying them as desiccation cracks.

## 3.9 Microbial carbonates in the Omkyk Member

### 3.9.1 Bioherms

Due to limited outcrop of bioherms in Unit 1, the following descriptions derive mainly from observations and photomosaic interpretations of bioherms in Unit 2 of the Omkyk Sequence 2. Bioherms exhibit a mound-like geometry in cross-section view and are laterally discontinuous. The cross-section geometry of the bioherms is characterised by steep flanks and flat tops. The bioherms range from ca. 1-20 m in height, and several meters to hundreds of meters in width. The individual mounds are separated by inter-bioherm facies and the plan view shape of the bioherms has been interpreted to be circular (Adams *et al.*, 2005).

Previous authors interpreted shutdown of bioherm growth in Unit 1 at the latest stages of the unit highstand systems tract (Adams *et al.*, 2005). Thus, bioherms have been interpreted to be restricted to each unit. However, several bioherms have been observed, which kept up with the increasing sediment input during Unit 1 highstand systems tract and early Unit 2 transgressive systems tract (see Figure 48.A-B). These remaining mound structures form topographic highs and subsequently served as preferential growth location for bioherms during the onset of microbial growth in Unit 2. The higher topographies provided ideal growth locations for the microbialites in the initial transgressive systems tract of Unit 2. The increase of mud-dominated sediments during the transgression did not allow microbial activity in topographic

lows. However, the elevated positions allowed the microbial carbonates to keep up with the increase in water depth and sedimentation of fine-grained material. This in turn leads to the formation of stacked bioherms where one mound grows over rigid topographies of the remaining underlying mounds.

During the onset of the bioherm evolution in Unit 2, the microbialites were associated with mud-dominated facies and bioherms only aggraded: they did not branch or merge together. Thus, the nucleation of the bioherms was interpreted to have occurred during times of maximum accommodation space and reduced background sedimentation in a mid-ramp setting (Adams *et al.*, 2005; Grotzinger *et al.*, 2005). At that stage, microbial carbonates are best described as microbial patches (Figure 49.A). These small-scaled mounds are characterised by an association of massive columns, domes and goblet shaped thrombolitic structures (Figure 49.B). These pinnacle-like structures are isolated over the carbonate ramp. Inter-column widths attain several decimetre, and distances between the mounds ranges from <10 m to >100 m. The microbial texture in that stage is represented by fine-grained thrombolites, indicating preferred microbial precipitation due to the absence of coarse-grained sediments. Thus, microbial growth was restricted to aggradation in order to keep up with the increase of water depth.

The first input of grain-dominated material enabled the microbialites to spread out laterally over the inter-column fills as well as over entire inter-bioherm areas. The lateral spreading was favoured by the increase of grain-dominated material and the formation of coarse agglutinated thrombolites, which formed due to a combination of grain trapping and microbial precipitation. This allowed the microbialites to form rigid frameworks and to grow over inter-column and inter-bioherm areas. In the case of closely spaced microbial patches, the lateral spreading zones merged together (Figure 50). These ‘merging zones’ are defined by offlap and onlap geometries. An alternation between mud-dominated and grain-dominated background sedimentation is common in the lower half of Unit 2.

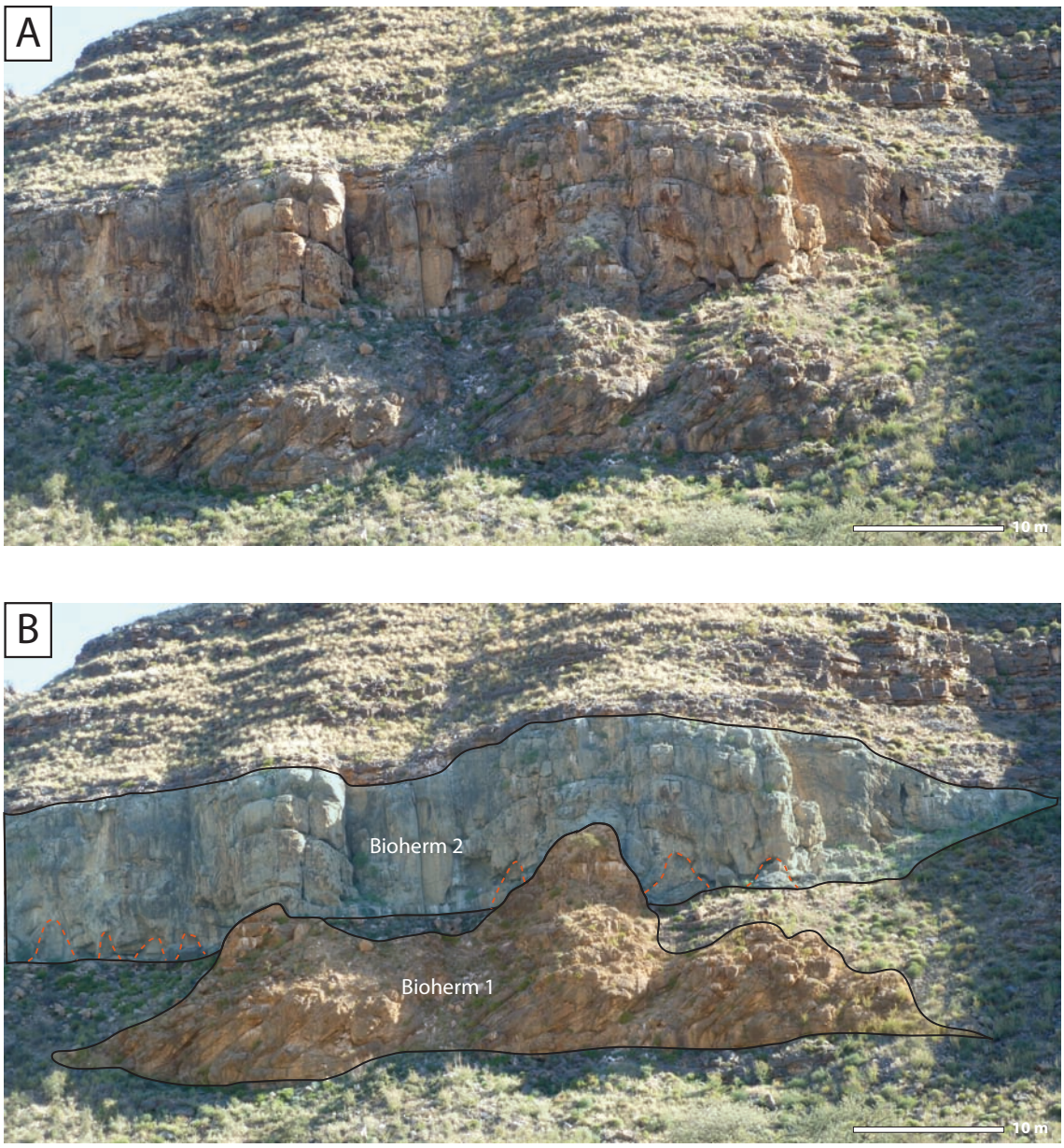


Figure 48: Interpreted photomosaic interpretation of bioherm structures in OS Unit 1&2. (A) Outcrop overview and (B) interpreted structures. Note that Bioherm 1 evolution was not terminated at the unit HST. The remaining structures served as preferential growth location of Bioherm 2. Orange dotted lines indicate incipient, pinnacle-like microbialites. See Figure 49.

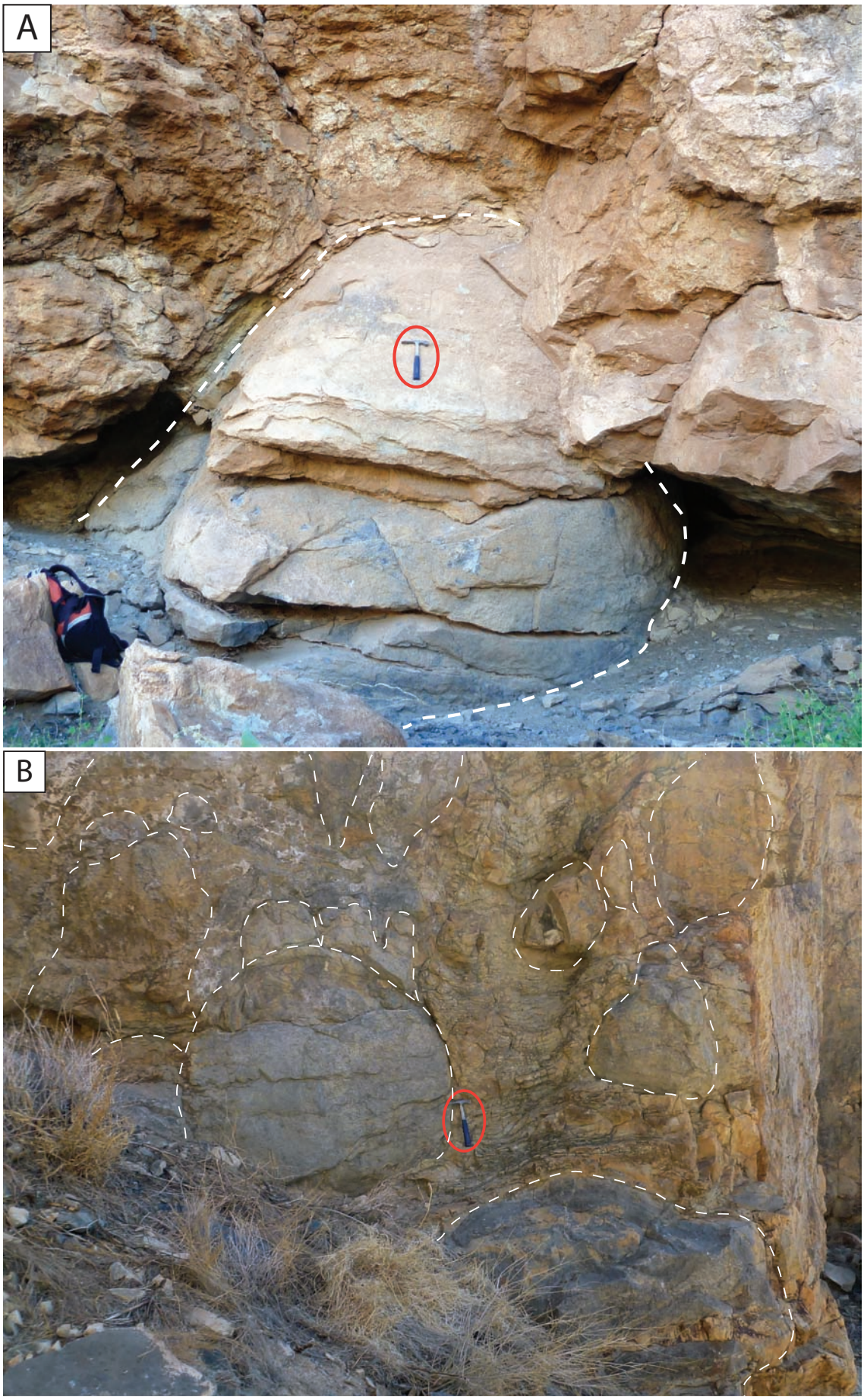


Figure 49: (A) Massive microbial pinnacle, in the lower half of the Bioherm 2 evolution. Geological hammer for scale. (B) The incipient small-scaled microbial mounds are characterised by an association of massive thrombolite domes and goblets. Geological hammer for scale.

During times of coarse-grained carbonate sedimentation microbialites tended to spread out laterally and merge together. In contrast to that, shale and mud deposition forced microbialites to aggrade and prohibited lateral spreading. Shale and mud beds can be traced over entire bioherm bodies but preferentially occur in local topographic lows, such as the merging zones. The input of mud-dominated sediments locally terminates microbial activity and growth is restricted to topographic highs (e.g. bioherm cores). The microbial structural framework evolution is thus directly related to background sedimentation and can be subdivided into aggradational phases during mud-dominated sedimentation, and lateral spreading phases during grain-dominated sedimentation.

Given sufficient time, these processes eventually led to amalgamation of the individual microbial structures to bioherms, and on a larger scale, to composite bioherms. The lateral spreading, bioherm-amalgamation and growth termination is repeated up to 3 times resulting in a complex bioherm and composite bioherm internal stacking pattern in the lower half of Unit 2.

During the highstand systems tracts (i.e. times of decreasing accommodation), the bioherms became progressively more associated with grain-dominated facies. The upper half of Unit 2 is characterised by grain-dominated background sedimentation and the growth-form of the microbialites is changing to smaller-scale columns. The columns have diameters of 1-2 dm in the middle of Unit 2 HST but get continuously smaller (1-5 cm) when reaching the top of the sequence. This growth form tends to branch laterally and forms continuous coalesced bodies within the mounds and composite bioherms (Figure 50.A-B). Sediment pockets, filled with packstones and grainstones, are common. The increasing sediment input at the latest stages of Unit 2 terminated the microbial growth and grainstones covered the bioherms. A schematic illustration of a composite-bioherm is given in Figure 51.

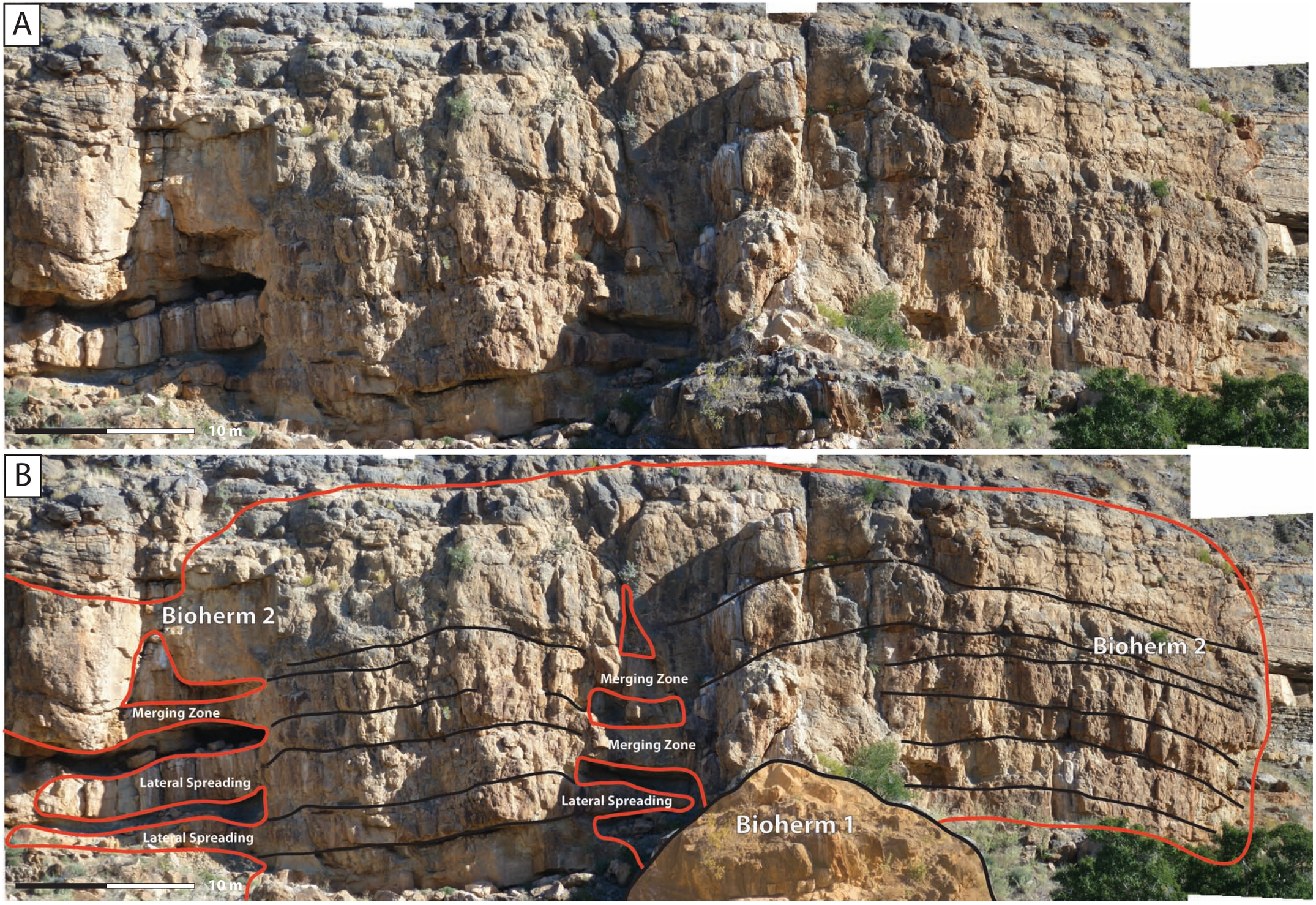


Figure 50: (A) Outcrop photomosaic and (B) interpretation of a composite bioherm in OS2 Unit 2. Red lines indicate the outline of the microbial structure. Note in the lower half of the composite bioherm structure the reoccurring lateral spreading and subsequent merging of the microbialites. Black lines indicate cm-thick mudstone beds.

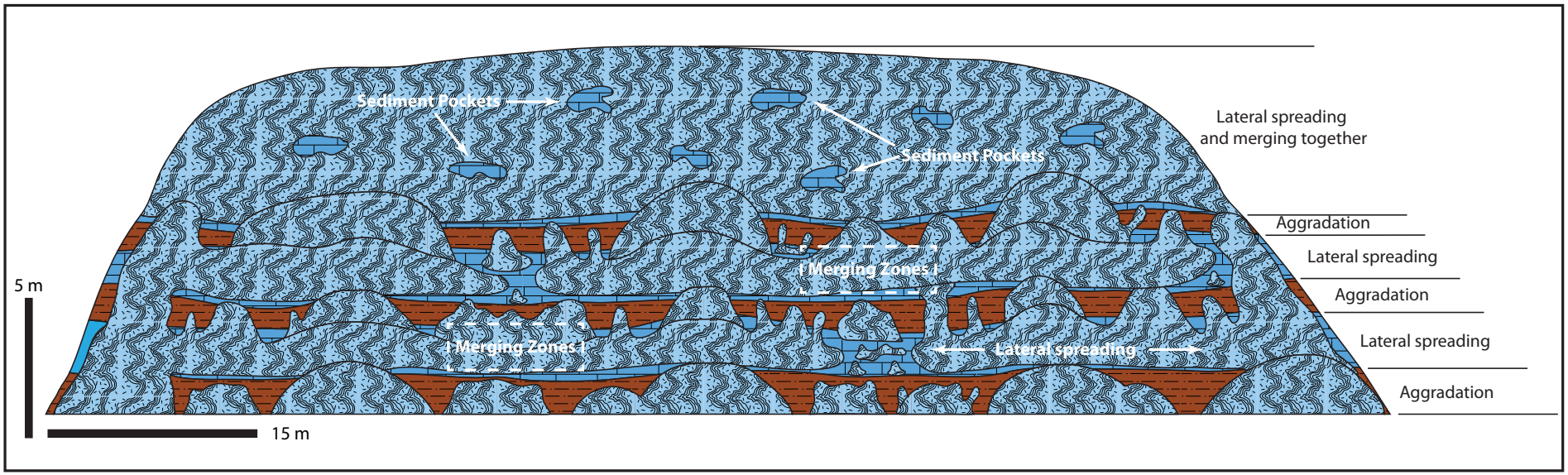


Figure 51: Schematic model of a composite bioherm structure. See text for discussion.

### 3.9.2 Biostromes

Biostromes are characterised by a tabular, sheet-like geometry and are laterally continuous geobodies (up to several kilometres). Their thickness in the Zebra River area is about 11-13 m. The microbialites forming the lateral continuous biostromes are in general more homogenous than the microbial carbonates of Unit 2. Biostrome 1 is associated with grainstones throughout the entire HST sequence of Unit 3 and the dominant growth forms are fine-scaled branching columns (cm to a few dm). Biostrome 2, which is capping the Omkyk Sequence 2 started to develop in the latest stages of Unit 5 HST. In that stage the biostrome is defined by branching thrombolite columns. This changes with increased mud-dominated sediment influx to domal and goblet shaped thrombolites at the top of the biostrome and the onset of the first transgression in the Hoogland Member.

Both biostromes in the study area are associated with grain-dominated facies, indicating shallow water depths and high-energy conditions. Furthermore, the observed frequent grainstone channels demonstrate a shallow marine, high-energy environment. Therefore, the evolution of the biostromes was interpreted to have occurred during times of reduced accommodation space and high sediment input such as the unit highstand systems tract of Biostrome 1 or the initial stages of transgressive systems tract for Biostrome 2 (Adams *et al.*, 2005).

The microbial carbonates in OS2 show no evidence of karstification. Biostromes and bioherms are both affected by intense selective dolomitisation. Most of the succession comprises limestone, and are only partly dolomitised in the vicinity of the microbial carbonates.

## 3.10 Bioherm evolution

Adams *et al.,* (2005) interpreted the bioherms to be simple, hemispheroidal constructions. This assumption was necessary by those authors who required such approximations to develop a geocellular reservoir model. However, the author wishes to emphasize some caution with this approach. In this study, based on the field observations and photomosaic interpretations of the microbialites in cross section, the author tentatively proposes a simple three-stage model.

Incipient bioherms were an initial loose association of dome and goblet-shaped thrombolites at the onset of the bioherm evolution in the latest stages of transgressive systems tract. During progradation of the carbonate ramp, the incipient bioherms began to branch, merge and expand laterally. Given sufficient time, lateral amalgamation of these incipient forms produced merged and on a larger scale, composite bioherms. This preliminary model has important implications. The composite architecture of the bioherms suggests that these constructions are unlikely to exhibit a simple circular or elliptical map expression as a general rule, even if such morphologies can be mapped out in limited exposures. Whether predictable bioherm geometries do occur remains to be tested. In addition to the consequences for the mound geometry this model has implications for the bioherm internal architecture. Merged bioherms and composite bioherms are the result of recurrent phases of aggradation and lateral microbial spreading, eventually leading to the development of complex microbial, rigid frameworks (Figure 51). This system is prone to instability due to internal weaknesses (compare structural **chapter 5** for implications).

Johnson & Grotzinger (2006) studied the response of microbial growth morphology regarding changing background sedimentation in the Zebra River area. The authors showed that the microbial communities tended to form individual separated domes and large columns during shale sedimentation. Carbonate sedimentation instead favoured the development of smaller-scale columns, which tend to branch and form a dendritic, coalesced network. Incorporating these observations into our model, results in thrombolite dome development during aggradational phases and coalesced columns during spreading phases.

### 3.10.1 Plan-view geometries and spatial distribution of bioherms

Based on the above-presented model for the evolution of merged and composite bioherms it is unlikely that the microbial mounds exhibit simple circular or elliptical plan-view geometries. However, it was not possible to analyse the plan-view geometries of the bioherms in the Zebra River canyon system, since they are only exposed as 2D cross-sections. Thus, a satellite image was used to analyse their plan-view shapes and spatial distributions.

Figure 52 shows a satellite image of a modern day erosional surface of the bioherm horizon, approximately 1 km to the west of the Zebra River study area.

Clearly visible are the outlines of 19 bioherms. The enlarged section in Figure 52 shows the interpreted bioherm structures. 11 bioherms have diameters < 10 m and show approximately circular to elliptical plan-view geometries. 8 microbial mounds have diameters > 10 m (up to 60 m for the long axes of elongated structures). Plan-view shapes are characterised by elliptical to highly irregular geometries. The distances between the mounds are generally between several meters up to a few 10's of metres. However, also very closely spaced bioherms (~ 1 m distance) occur.

This satellite interpretation of the bedding-plane view of the bioherm horizon shows that individual mounds and merged bioherms with diameters less than 10 m can be approximated by circular plan-view geometries. Larger structures and composite bioherms are, however, defined by highly irregular shapes, as proposed by the bioherm evolution model. Furthermore, the occurrence of very closely spaced bioherms (see Figure 52, enlarged section) demonstrates that bioherms developed in close vicinity to each other and had the potential to merge together over inter-bioherm facies, forming composite bioherms. A limitation of the remote sensing analysis is that the exact position of the erosional surface within Unit 2 cannot be resolved. Therefore, it is unclear if this 'time-slice' of Unit 2 represents the initial or latest stages of bioherm evolution. It was, however, not possible to visit the location of the satellite image because the outcrop lies within Donkergange Farm and access to the farm could not be obtained.

Nevertheless, the satellite interpretation shows that the approximation of bioherms as hemispheroidal structures is too simplistic to describe mound geometries. Therefore, the assumption of circular plan-view shapes as a general rule for bioherm geometries in the Omkyk Sequence, as input for modelling purposes, might lead to non-realistic bioherm facies models in subsequent reservoir modelling. Thus, new methodologies in order to construct a realistic facies model, honouring the complex shapes and distribution of the microbial mounds, had to be developed. This is presented and discussed in paragraph 6.7.

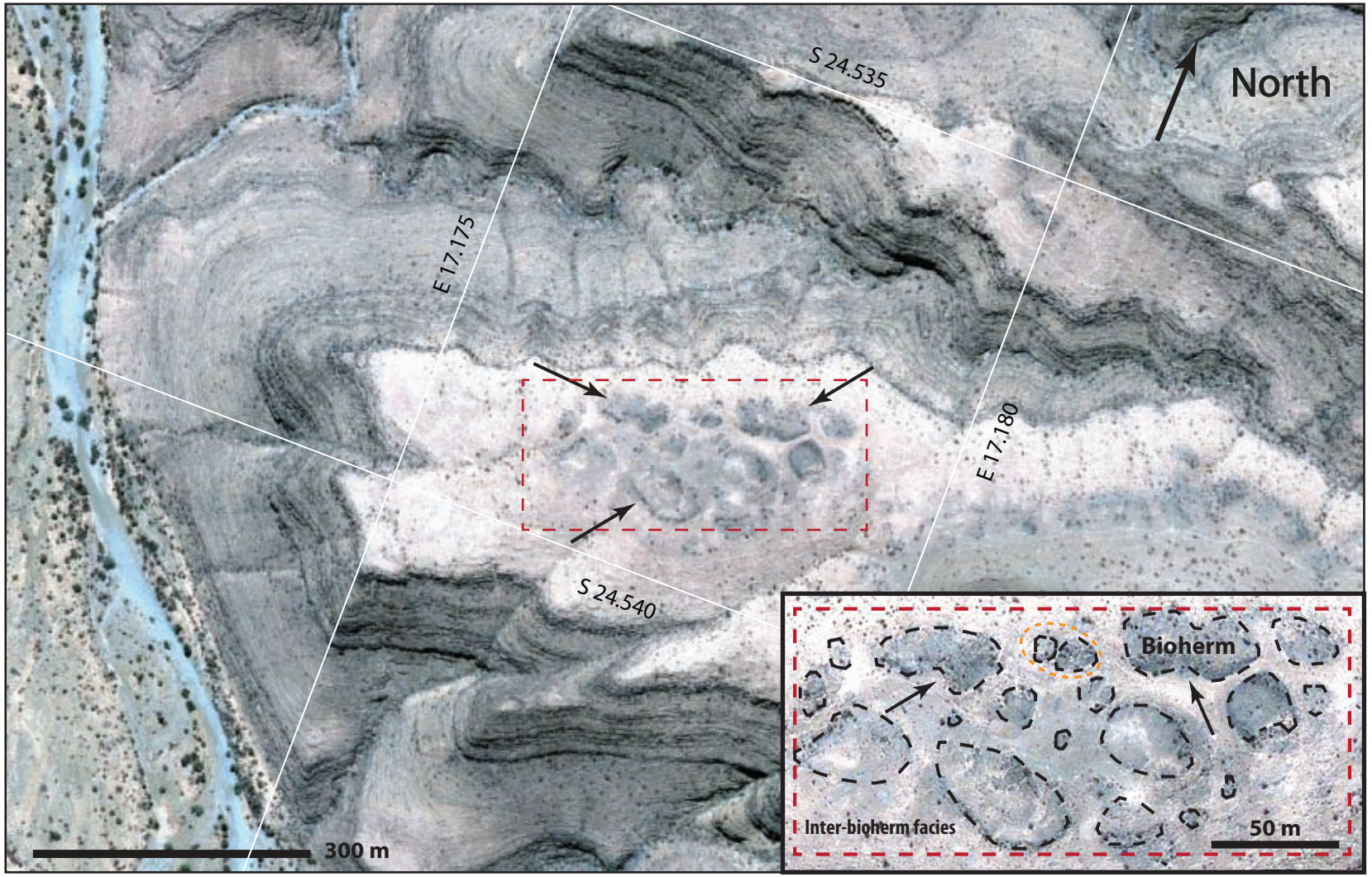


Figure 52: Google Earth satellite image showing a modern day erosional surface of the bioherm horizon of Omkyk Sequence 2. Clearly visible are the outlines bioherms (black arrows), showing the plan-view shape and distribution of the microbial mounds. Location of the outcrop is approximately 1 km to the west of the Zebra River canyon. Enlarged section in the lower right shows interpreted bioherm structures. Orange-dashed circle indicates closely spaced bioherms. Red dashed rectangle indicates location.

## 3.11 Regional facies model

In order to place the observed and interpreted facies into a palaeogeographic context, a regional facies model of the Omkyk Sequence 2 was created (Figure 53). As noted earlier, the Kuibis carbonate platform is interpreted as a carbonate ramp system, developed in a foreland basin setting, which was strongly influenced by wave, currents and storm events. These types of carbonate platforms accumulate on distal margins of the foreland basins in response to flexural loading of orogenic wedges on the proximal side and are defined by gentle slopes, generally dipping less than 1º (Burchette and Wright, 1992). Facies belts are laterally extensive and can reach several tens to hundreds of kilometres along strike. The width of the ramp systems depends on basin geometry, tectonic history and eustatic sea level changes but is generally less than 100 km (Bosence, 2005).

Based on the authors' observation a model is proposed (see Figure 53) that differentiates inner-, mid- and outer ramp deposits. The inner ramp facies belt extends from the shore-face until the fair-weather wave base and experiences agitation by waves and occasional storms. Proximal deposits are represented by sandstone facies, deposited in a tidal flat setting. This gradually passes into the fine- to medium- and coarse-grained grainstones of the more distal inner ramp (see Figure 34). The coarse-grained grainstones were deposited as sandbars and shoals, which interfinger with microbial biostromes (e.g. Biostrome 1 interfingering with the HST grainstones of Unit 3: see Figure 46). The biostromes show variable aerial sizes and shapes. Close to fair-weather wave base of the inner ramp, biostromes break-up into bioherm structures. The majority of microbial bioherms are situated in deeper parts of the inner ramp and mid ramp. The mid ramp setting is constrained by fair-weather wave base (upper boundary) and storm wave base (lower boundary). Composite bioherms (see Figure 48), associated with coarse-grained grainstones are situated in the lower parts of the inner ramp. In contrast to that, incipient bioherms and individual microbial domes (see Figure 49.A&B) are below fair-weather wave base, in association with mud-dominated facies such as irregular laminites. Mud and shale inter-bioherm sedimentation becomes increasingly dominant towards storm wave base. Storm deposits are frequent in the mid-ramp facies belt, expressed by abundant intraclast breccias and storm-generated grainstone beds. Sedimentation below storm-wave base in an outer ramp environment is marked by deposition of shale and

mudstones of the heterolithic facies, with occasional storm generated intraclast breccias and fine-grained grainstones in the transition zone. This gradually passes into the basinal shale of the Urikos Member.

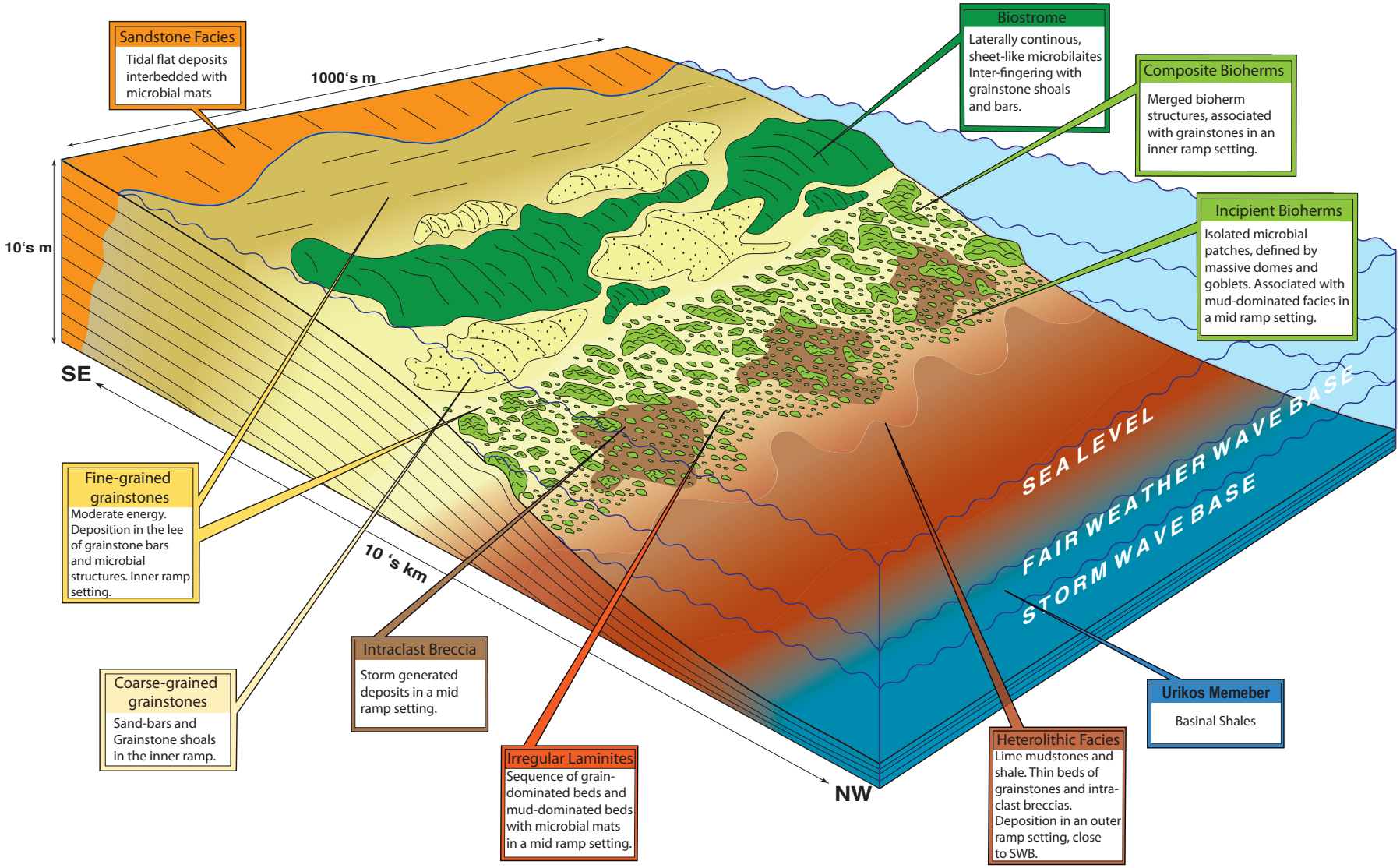


Figure 53: Developed regional facies model of the Omkyk Sequence 2 of the Kuibis carbonate ramp system. See facies descriptions for the depositional setting of the individual facies.

## 3.12 Reservoir analogue architecture

Field work and thin-section analyses were used to better understand the Omkyk Member ramp carbonates from a hydrocarbon reservoir characterisation point of view. The main purpose was to better understand the carbonate ramp architecture and geometries for subsequent geocellular reservoir analogue modelling. In particular the reservoir characteristics of the microbial carbonates in terms of heterogeneities, connectivity and geometry were the main focus. Based on the presented observation and results, an analogue reservoir classification of the Omkyk Sequence 2 into reservoir and non-reservoir units is presented.

The overall geometry of the Omkyk Sequence 2 in the study area exhibits a simple layer cake architecture. It comprises a sequence of grain-dominated and thrombolite-stromatolite facies layers in the highstand systems tracts, separated by mud-dominated units in the transgressive systems tract.

In general the HST's of OS2, represented by grain-dominated and thrombolite-stromatolite facies association can be regarded as potential reservoir units. The grainstone horizons are uniformly thick and exhibit minimal facies variations. Primary interparticle porosity is expected to be good to very good and homogenous throughout the grainstone horizon. Thus, the grainstone horizons of Unit 4 and 5 are considered as reservoir and flow units, respectively.

In addition to the grainstone layers, microbial biostromes are also regarded as potential reservoir units. The biostromes form laterally extensive and continuous geobodies. Thin-section analyses indicate that initial framework porosity of the microbialites was fair to good. Biostrome 2 is regarded as one reservoir and flow unit. The Unit 3 highstand systems tract, represented by Biostrome 1, inter-fingering with the Unit HST grainstones is also regarded as one potential reservoir unit. However, different porosity values are expected between the microbial carbonates and grainstones.

The complexity of the system lies, however, in the lateral heterogeneous bioherm horizons in OS Unit 1 and 2. Limited outcrop exposures of bioherms in Unit 1 do not allow to define the HST of this unit as a reservoir analogue unit because the geometry of the microbialites could not be resolved. The bioherms in Unit 2 are however interpreted as reservoir analogue units. The bioherms are laterally

discontinuous reservoir bodies surrounded by inter-bioherm facies. Previous authors defined the inter-bioherm areas as non-reservoir units (Adams *et al.,* 2005). However, detailed stratigraphic logging revealed that metre-scaled grainstone and microbial layers are present in the inter-bioherm facies. Thus, the inter-bioherm sequence is approximated by an alteration of reservoir and non-reservoir units.

The initial growth-framework porosity of the bioherms was fair to good. However, vertical porosity heterogeneities are expected due to early sediment infilling and cementation of the growth-framework. Reduced porosity zones are estimated in bioherm areas where the lateral corresponding inter-bioherm facies consist of mud-dominated facies.

Mud-dominated horizons in the transgressive systems tracts are regarded as non-reservoir analogue units due to the low estimated porosity values of mudstones, shales, intraclast breccias and irregular laminites. Furthermore, they are regarded as no-flow unit and therefore may act as flow barriers between the analogue reservoir units. The general reservoir architecture and definition into reservoir and non-reservoir units of the Omkyk Sequence 2 in the study area is illustrated in Figure 54**.**

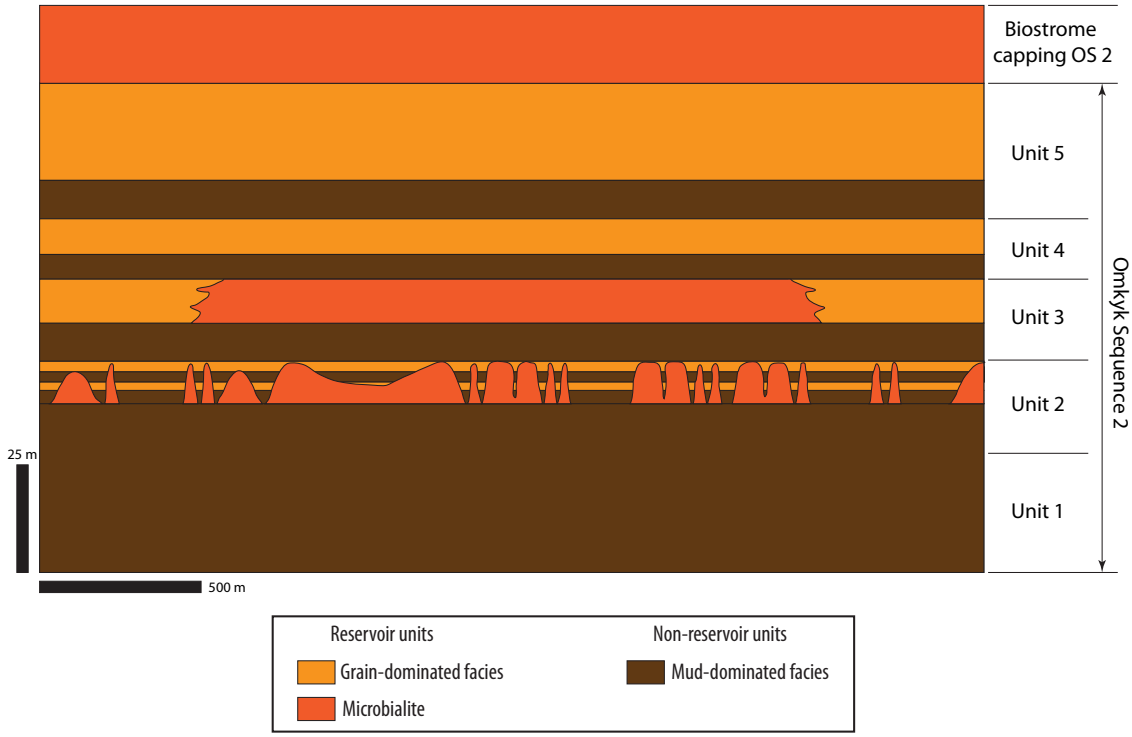


Figure 54: Cartoon illustrating the schematic hydrocarbon reservoir analogue architecture of OS2. See text for discussion. Modified after Adams et al. (2005).

## 3.13 A source rock in the Nama Basin?

The Zebra River section of the Nama Basin was chosen for the investigation of the reservoir characteristics of microbial dominated carbonates in order to better understand expected microbial reservoirs in the subsurface of the Owambo Basin of North Namibia and South Angola. The study of potential source rocks targets exposed strata along the southern rim of the Owambo Basin (compare **chapter 2**). Nevertheless, during field work in the Zebra River Canyon system, several sections were recognised which showed several indicators for a potential source rock such as fine-grained, dark mudstones and shale with abundant pyrite crystals indicating organic enrichment. Thus, two samples were taken for total organic carbon analyses to test source rock potential.

One sample analysed for organic carbon enrichment with the Leco system showed 0.5% TOC content. The sample was taken from a shale bed in the lower part of Unit 2. Based on the classification of Tissot & Welte (1978a), which requires 0.5% TOC for a siliclastic sediment to be classified as potential source rock, the shale bed can be regarded as a potential source rock. The shale bed constitutes inter-bioherm facies of the incipient bioherm structures. At this stratigraphic position, **Bioherm 2** is associated with mud-dominated facies in an initial transgressive system in a deeper mid-ramp setting. This is an interesting finding because deposition of the organic-enriched sediments occurred contemporaneously with and in close vicinity to the reservoir facies. A potential explanation for the source of the organic matter might constitute microbial communities within the mud-dominated sequences. However, their recognition in shaly deposits is in general a challenging task due to lack of preserved microbial mats (Schieber, 1998) and could not be proven in the field. Nevertheless, the recognition of microbial communities in the sandstones of the Kanies Member clearly shows that microbial activity in the Kuibis Subgroup is not exclusively restricted to carbonates. Thus, microbial growth might also have been present within the shale-dominated sequences. The depositional setting is characterised by a low-energy environment and fine-grained sediments were deposited in topographic lows between incipient bioherms and individual columns and domes, sheltered from wave and current activity. This system of restricted water circulation could have induced reduced oxygen availability and thus suitable conditions in the sediment layer to preserve organic matter of microbial

mats. Additionally the sheltered positions prohibited physical disturbance through waves and currents, thus preventing oxygenation of the sediment layer. This hypothetical scenario shows close similarities to the Neoproterozoic petroleum system of Oman, where organic-enriched sediments were deposited contemporaneously with microbial carbonate reservoir facies (Schröder *et al.*, 2005). Although, the authors showed that hydrocarbon expulsion from these sediments occurred, and probably also influenced reservoir quality through organogenic dolomitisation, they do not constitute an economically viable source rock in the Oman situation. The main source rock in the South Oman Salt basin is situated in deeper parts of the basin (Schoenherr *et al.*, 2007).

Based on these observations it is unlikely that the organic-enriched sediments form a basin wide economically viable source rock. Nevertheless, the findings show that organic-enriched sediments with source rock potential were deposited in the Nama Basin. Future research might show that sections in deeper parts of the basin might have source rock potential.

## 3.14 Chapter summary

This chapter summarised the sedimentological and analogue hydrocarbon reservoir characteristics of the Kuibis ramp carbonates of the Omkyk Member in the Zebra River Canyon of the Nama Basin, Namibia. The main contribution of the field work and interpretation to better understand this microbial dominated system from a petroleum geology point of view is as follows:

- Well-preserved microbial mats, characterised by winkle structures have been observed in the sandstones of the Kanies Member. This illustrates that microbialites are not restricted to the carbonate-dominated sequences of the Kuibis Subgroup in the study area as assumed previously.
- The recognition of a subaerial exposure surface in the middle of Omkyk Sequence 2 is in contrast with the present sequence stratigraphic interpretation. However, it was outside the scope of this research project to reinterpret the sequence stratigraphic evolution of the upper Omkyk Member due to time constraints. Therefore the current subdivision was used in this research project.

- Microbial carbonates of the Nama Basin comprise a variety of bioherm, biostrome and inter-mound facies. The former comprise a suite of stromatolitic-thrombolite mounds, whilst the latter include allodapic grainstone-packstones produced from crestal collapse, wave rippled and cross-bedded strata. Understanding the vertical and lateral evolution of the bioherms is essential because this influences the reservoir heterogeneity and connectivity. A simple three-stage model describing bioherm evolution comprising microbial aggradation, lateral spreading and final merging is presented. This model has important implications for reservoir architecture because bioherms are unlikely to exhibit simple hemispherical geometries and have the potential to merge together. Thus, incorporating this model, a more precise reservoir characterisation in terms of lateral connectivity of the bioherms can be developed.
- A new nomenclature for bioherms in the Omkyk Sequence 2 has been established. Incipient bioherms are a loose association of massive thrombolite domes, goblets and columns, which subsequently amalgamate forming merged bioherm structures at the onset of the bioherm evolution. During platform progradation this merged bioherms have the potential to form composite bioherm structures, which are unlikely to exhibit a circular plan view. Furthermore, stacked-bioherm structures are introduced. These structures are characterised by topographic highs, which are formed by bioherm structures of the underlying horizons. These 'sheltered islands' served as preferential growth location for microbialites in the next parasequences. This observation has important implications for microbial reservoir analogue modelling because the distribution of the bioherms can be used as conditioning data in stacked microbial horizons.
- The occurrence of organic-enriched mud-dominated sediments with 0.5% TOC content within the transgressive systems tract of Unit 2 of the Omkyk Member indicates the presence of a potential source rock in the Nama Basin. However, based on field observations and comparison with the South Oman Salt basin it is unlikely that these sediments represent an economically viable, basin-wide source rock horizon. Nevertheless, the recognition of

organic-enriched Neoproterozoic sediments gives incentive to further investigate successions of the Nama Basin for source rock studies.

# 4 Terrestrial laser scanning (lidar)

## 4.1 Introduction

The previous chapter presented and discussed in detail the sedimentological characteristics and geometries of the Omkyk Sequence 2 ramp carbonates, with special focus on the microbial carbonates. The overall aim of this research project is the development of a geocellular analogue model for potential microbial reservoirs in the subsurface of the Owambo Basin and elsewhere. The construction of such needs accurate geometries and dimensions of the microbial system in order to model the general reservoir architecture and the microbial facies distributions. Traditional field work techniques, such as mapping and stratigraphic logging are not sufficient enough for this purpose because they cannot provide accurate geometries and measurements over the entire canyon system. In particular, the dimensions of the bioherm structures needed to be captured with high precision to model the laterally discontinuous mound structures in terms of heights, widths and spatial arrangement. Furthermore, the canyon walls in the Zebra River Canyon form steep cliffs and are often inaccessible. Thus, it was concluded to use terrestrial laser scanning (lidar) to capture the ramp architecture and the spatial dimensions of the microbialites. The acquired lidar data consequently served as main input data for the development of the geocellular analogue model.

The aim of this chapter is to give a detailed overview of lidar-based field work and the workflows for acquiring and processing of lidar point-cloud data. The first part covers the specifications of the terrestrial laser scanning measurement system and provides an in depth description of how to plan and conduct a lidar-based field season in remote field areas. The second part outlines techniques involved in the post-processing of the lidar data. Particular attention is given to visualisation of data and to the construction of the digital outcrop model (DOM) and digital elevation model (DEM). Furthermore, methodologies for the interpretation of the virtual outcrop model will be discussed. This includes the digital mapping of stratigraphic contacts, faults, fractures and three-dimensional objects (e.g.: mapping of bioherm structures). The chapter concludes with a summary of the advantages but also of the limitations of this digital data acquisition methodology in geoscience research.

## 4.2 Lidar in geoscience research

Light detection and ranging (lidar) or laser scanning, is a technique that has come to the forefront of digital surveying in the last decade. This laser-based measurement system allows the rapid acquisition of detailed point data describing the topography of an outcrop in 3D (Bellian *et al.*, 2005; McCaffrey *et al.*, 2005). It can be applied from both, aerial and terrestrial platforms (Buckley *et al.*, 2008a; Buckley *et al.*, 2008b; Rittersbacher *et al.*, 2013) and is used for a variety of purposes, ranging from architecture, urban and regional planning, archaeology to geology.

Lidar has become an important technique in Earth sciences for the development of 3D digital outcrop models (DOM) in recent years. These virtual outcrop models are highly valued datasets in geoscience research because they facilitate detailed analysis and visualisation of outcrops using a workstation. Special impetus has come from the petroleum industry. A comprehensive review of laser scanning and the use of digital outcrop geology in petroleum research is given in Hodgetts (2013).

Lidar-based field work is increasingly common in petroleum geology research and hydrocarbon reservoir characterization (e.g. Jones *et al.*, 2011; Kurtzman *et al.*, 2009; Verwer *et al.*, 2009). In conjunction with traditional mapping methods, 3D photorealistic DOMs can be used as a basis for the development of static and dynamic reservoir models (e.g. Enge *et al.*, 2007; Fabuel-Perez *et al.*, 2009; Fabuel-Perez *et al.*, 2010; Wilson *et al.*, 2011a). The advantage of lidar is that large and probably otherwise inaccessible areas can be captured in a short amount of time to high precision (a few cm resolution).

The lidar scanner, like sonar or radar scanners, is an “active” device. Lidar uses laser light to measure distances with high precision. The instruments are capable to measure $>10^5$ points (3D coordinates *x,y,z*) every second and the results are often several multi-gigabyte data sets acquired within a few hours. For the development of a photorealistic virtual outcrop model a digital camera is placed on the sensor head and overlapping outcrop pictures are then shot for every section of the outcrop. Subsequently, the digital outcrop model can be constructed through merging the digital images onto the point-cloud data and the end-result is a photorealistic outcrop model with a maximum resolution of a few millimetres to centimetres.

The use of outcrop analogue models and studies in the hydrocarbon industry and research is a common practice and are of particular importance in subsurface

reservoir characterisation and modelling (e.g. Adams *et al.*, 2011; Adams and Hasler, 2010; Enge and Howell, 2010). The petroleum industry relies heavily on geophysical methods such as seismic interpretations (resolution of >15-20m) and wireline logging (penetration depth of a few cm to dm) to indirectly map the subsurface. Hard data, such as core descriptions and their interpretations of reservoir facies and petrophysical properties assist during the evaluation of the reservoir geology. However, challenges arise during the integration of these datasets with different resolutions. Furthermore, core descriptions comprise point information of the hydrocarbon reservoir and well correlation is a challenging task (e.g. Borgomano *et al.*, 2008). Virtual outcrop geology has some potential to fill this gap and suitable outcrop analogues can be used to validate and improve subsurface reservoir interpretation and modelling (Bryant *et al.*, 2000; Fabuel-Perez *et al.*, 2009; Fabuel-Perez *et al.*, 2010).

Figure 55.A shows the spatial range of terrestrial and airborne lidar and other digital measurement systems used in geoscience research in comparison with scales of geological and geophysical features. In this research project only terrestrial lidar has been used and the following descriptions are tailored accordingly. The dimensions, which can be captured with lidar ranges from the sub outcrop scale (cm-dm scale: bedding planes, fractures) up to scales of sequence boundaries and fault zones (hundreds of m to several km). This range of scales is thus able to encapsulate a range of reservoir-scale heterogeneities with high precision.

Figure 55.B shows the spatial range of a typical virtual outcrop model, developed with a terrestrial lidar laser scanning system. The extent of a DOM can reach up to several km in the horizontal direction and from a few cm to hundreds of m in the vertical extent. The cartoon furthermore illustrates the spatial dimensions of typical geological features (e.g.: sedimentary beds, faults), which can be captured with lidar and the resolution of datasets used is subsurface reservoir modelling (e.g.: wireline logs, seismic data). The resolution and dimension of the DOM covers the majority of these features. It can therefore be used to assist during the integration of datasets with different resolution in subsurface reservoir modelling processes. The virtual outcrop can be regarded as a bridge, which potentially fills the gap between core descriptions, wireline logs and seismic data interpretation in reservoir modelling.

Virtual outcrop analogue models are increasingly used to improve the understanding of fractured carbonate reservoirs (Kurtzman *et al.*, 2009; Larsen *et al.*,

2010a; Larsen *et al.*, 2010b; Olariu *et al.*, 2008; Rotevatn *et al.*, 2009; Wilson *et al.*, 2011a). Fracture network characterisation in the subsurface is challenging since fractures are commonly beyond seismic resolution and difficult to accurately predict with core and wireline logs. A key advantage of outcrop analogues and virtual outcrop models is that fracture characteristics (e.g.: fracture length, spacing etc.) can be accurately measured in a short amount of time. Subsequently stochastic discrete fracture models can be developed for input in flow simulations to study and predict reservoir performance (Wilson *et al.*, 2011b).

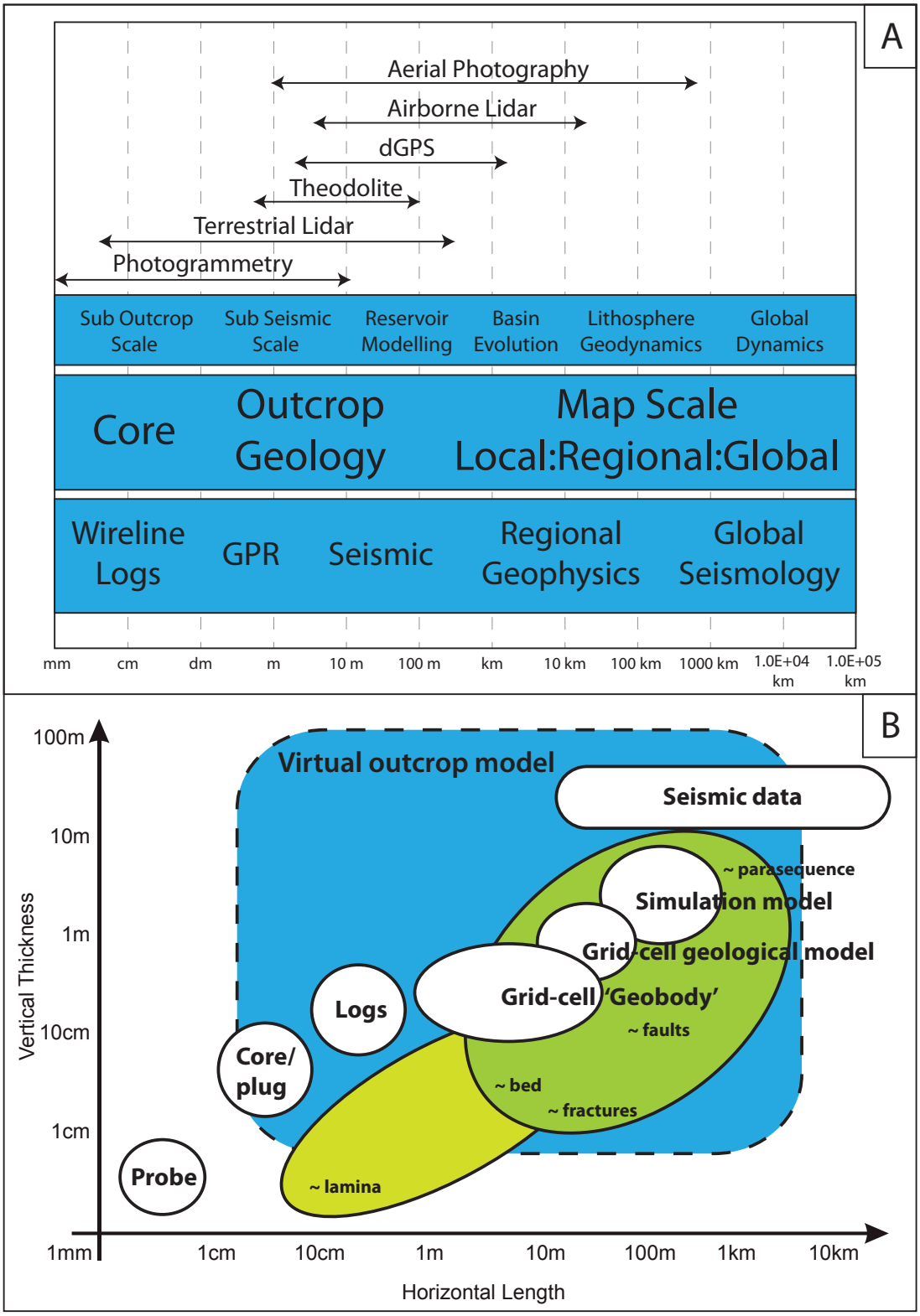


Figure 55: (A) Cartoon illustrating the spatial range of digital measurement systems used in geoscience research in comparison with geological scales, geological features and investigation methods used in petroleum geoscience. Note that terrestrial lidar operates in the typical range of reservoir modelling, ranging from sub outcrop to seismic scale. Modified after Hodgetts (2013) (B) Cartoon illustrating the spatial dimension of a typical virtual outcrop model (blue dashed rectangle) in comparison with geological features (green ellipses). White circles indicate the resolution of subsurface investigation methods and the dimensions of grid-cells in geocellular reservoir modelling. The sketch highlights that terrestrial laser scanning has the potential to encapsulate the majority of in subsurface reservoir modelling important heterogeneities. Modified after Enge *et al.* (2007).

## 4.3 Lidar-based field work

### 4.3.1 The Riegl terrestrial laser scanning system

The lidar survey in the Zebra River canyon system was carried out by using a ZMS-Z420i terrestrial laser scanning system from the company Riegl GmbH (Figure 56.A). Lidar is an active measurement system and the instrument generates an eye-safe laser pulse on its own. The laser beam is diverted by internal mirrors and reflected to the outcrop surface. The laser is subsequently backscattered at the outcrop surface and detected by the laser system. The majority of commercially available instruments use the principal of "time of flight" to calculate distances on the basis of the average speed of light in air. The time, which the emitted laser pulse needs from the scanner head to the target and back is recorded, divided in half and multiplied by the speed of light to calculate the distance from the laser head.

Equation 3: $$(\boldsymbol{x = \frac{t}{2} * c});$$

$$\boldsymbol{x = distance, t = time, c = speed\ of\ light};$$

The measurement varies with air density, however these perturbations are negligible for distances less than several kilometres because of the enormous speed of light.

The relative distance of a scanned point to the scanner head is insufficient to define a point in 3D space. Therefore, the scanner system uses the internal mirror angles, rotation and angle of the scanner head to calculate the horizontal and vertical components. Consequently, every single point can be described with *x,y,z* coordinates. In addition to the spatial coordinates the scanner also detects the loss of intensity (*I*) of the backscattered laser pulse. This is variable according to the material and relative distance of the target surfaces and the wavelength of the laser pulse. The intensity loss can be used to obtain further information about the scanned material (e.g.: lithology) because different rock types have different reflectivity values (Bellian *et al.*, 2007; Burton *et al.*, 2011). The scanning range is directly related to the reflectivity of the target surface (Figure 56.B). White limestone cliffs with a high reflectivity can be scanned up to a distance of 1000 m. Sandstone outcrops with a lower reflectivity limit the maximum range to 850 meters. It is advisable, however, to keep the scanning distance below 600 m to ensure optimal results.

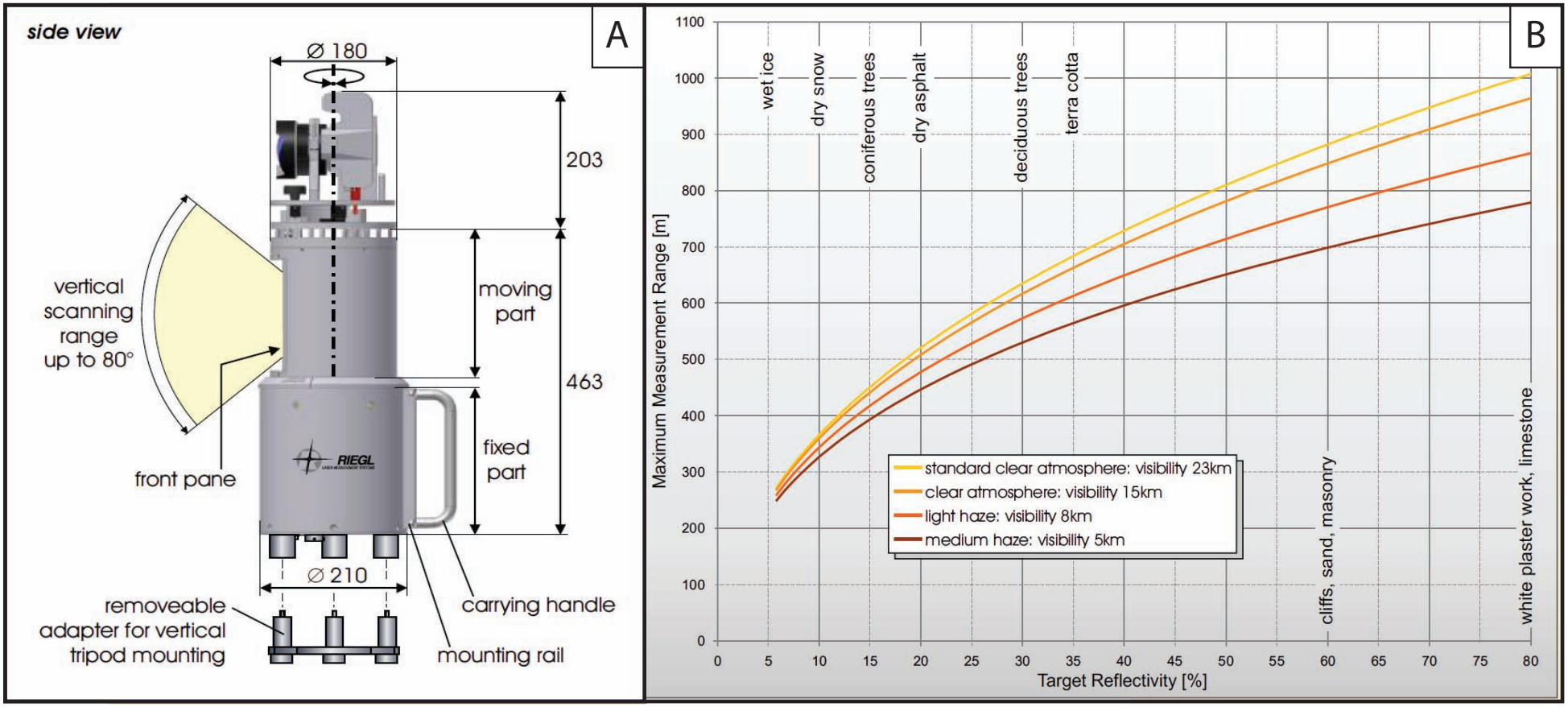


Figure 56: (A) Technical specification of the ZMS-Z420i terrestrial laser scanning system from the company Riegl GmbH. The maximum vertical scanning range is up to 80º. A complete 360º horizontal view is achieved through to rotation of the moving part of the scanner. (B) Diagram illustrating the maximum measurement range of the ZMS-Z420i depending on the target surface reflectivity and weather conditions. Source: Riegl ZMS-Z420i user manual.

The Riegl LMS-Z420i has a maximum measurement rate of 11000 points/sec and a maximum field of view of 80° in the vertical direction and 360° horizontally. The complete horizontal view is achieved through the automatic rotation of the scanner head. Figure 57 shows the LMS-Z420i set up in the field. The weight of the entire scanning system is approximately 80 kg and two persons are needed to carry and handle the equipment in the field. External batteries (two 12V batteries) provide the power supply for the scanner, which is sufficient for about 4 hours of scanning. Additionally, a laptop is required to operate the scanning system. On top of the scanner head a digital SLR camera (Nikon D200 with a wide angle lens) is attached, which takes 8 photos per scan-position in 45° intervals in order to cover the entire 360° of the scanned area.

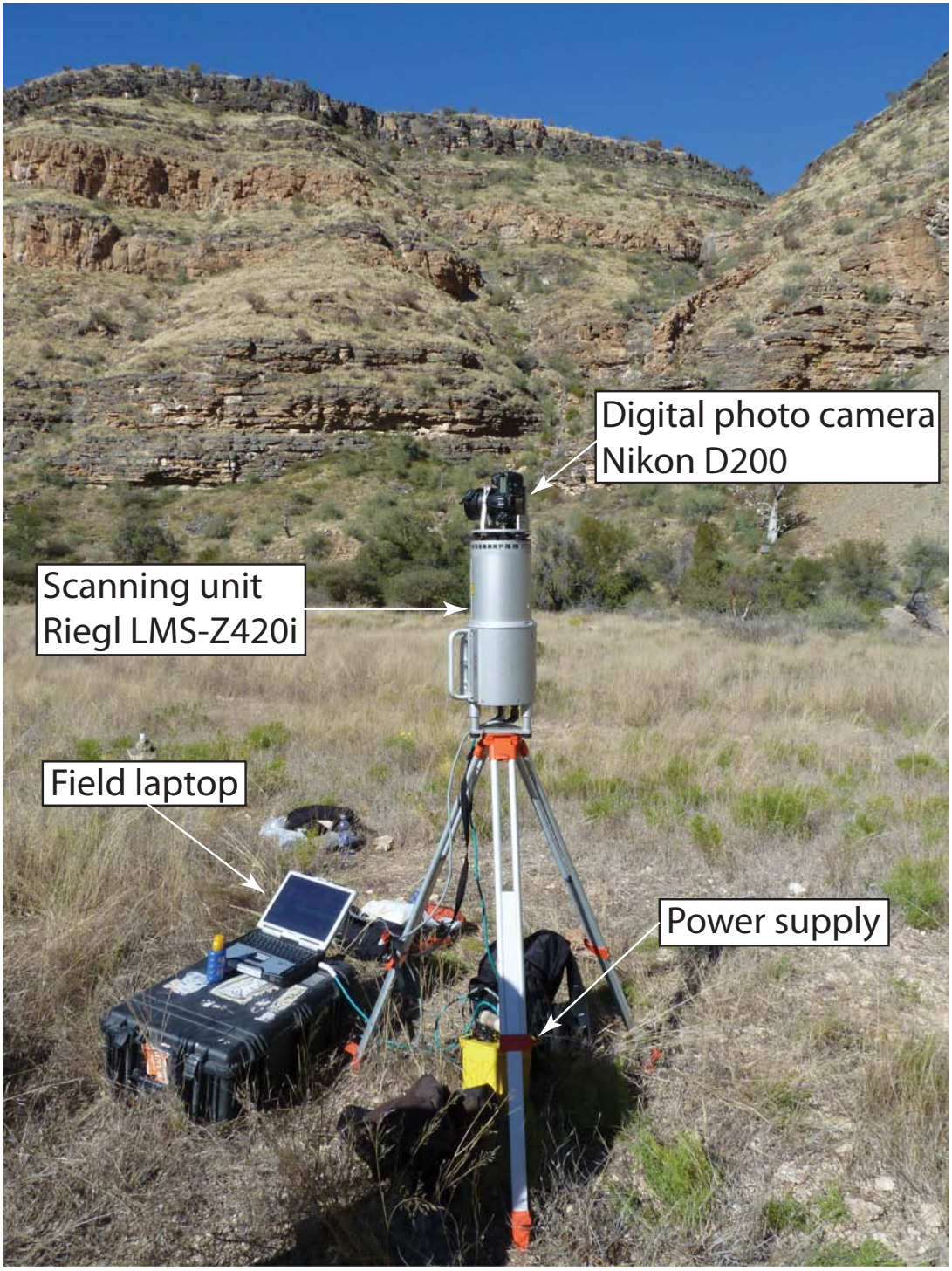


Figure 57: The ZMS-Z420i terrestrial laser scanner and equipment set up in the Zebra River Canyon. The scanner needs an external power supply and a laptop to operate the scanner system. The digital photo camera attached to the scanner head takes eight digital images in 45º intervals.

### 4.3.2 Field work planning

Prior to a lidar-based field season, thorough planning starts with the selection of appropriate outcrops. The decision about the optimal outcrop for laser scanning should be driven by the geological problem to be addressed, rather than selection on an ease-of-scanning basis. The selected outcrop should furthermore fulfil 5 criteria (modified after Enge *et al.*, 2007):

1. Suitable to the addressed question
2. High level of three dimensionality
3. Outcrop quality
4. Accessibility
5. Lighting conditions at the outcrop

The overall objective in this research project was the development of a geocellular reservoir analogue model of a microbial carbonate system. The main challenge in characterising and modelling these types of reservoirs is their complex internal structure and high level of heterogeneity. In particular, the size and spatial distribution of the microbial bioherms, which have an important impact on reservoir quality, connectivity and performance poses challenges in the modelling process. Thus, the accurate geometries of bioherms and their spatial arrangement needed to be captured.

Therefore, the chosen outcrop needed to be of: **(1)** sufficient lateral extent to encapsulate the geometries and spatial distribution of bioherms and **(2)** contain sufficiently high quality outcrops of the microbial carbonates and inter-bioherm facies for fault and fracture characterisation.

The exceptionally good quality of the outcrops in the Zebra River canyon satisfies these requirements. The dendritic canyon system of the Zebra River area provides furthermore a high level of 'three dimensionality'. In order to be able to accurately capture spatial heterogeneities the selected outcrop should be able to be scanned from various positions, which reveal three-dimensional geometries. The rationale behind determining the location of lidar transects in some ways compares to the procedure used in acquiring of a 2D seismic survey. 2D seismic lines represent cross-section of earth crust and three-dimensional interpretations are limited. Thus, 2D seismic lines are generally arranged in a grid-geometry where several lines are perpendicular orientated to each other in order to capture 3D geometries. A similar

approach should be used with the lidar system. The scanning of a suitable outcrop should be possible from different angles and directions in order to scan multiple cross-sections of 3D geological features in various directions. Scanning from different angles additionally fills data-shadows (data-gaps behind obstacles) and improves the quality of the virtual model.

Optimal results are attained when scanning in a dendritic canyon system such as the Zebra River area. The entire area is dissected by an N-S and E-W canyon system allowing the scanning from different positions and angles (see Figure 58).

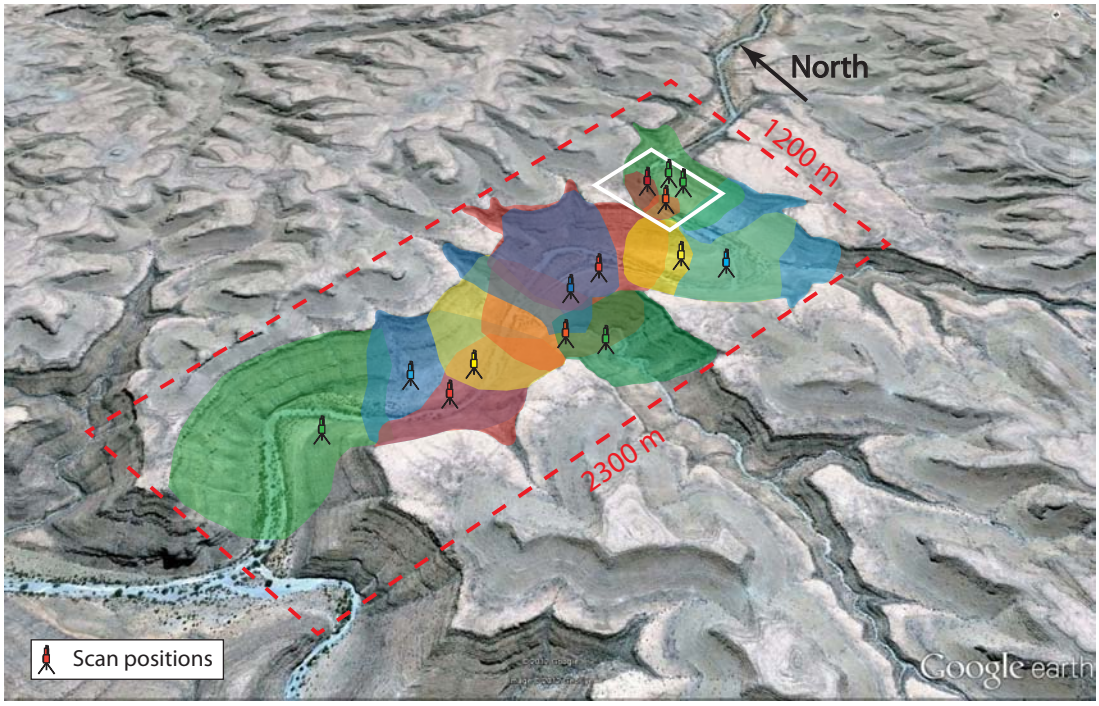


Figure 58: Oblique view of the scanned section in the Zebra River Canyon system. A total of thirteen scan positions were needed in order cover the entire section. The coloured areas represent the scanned areas from each position. Note the interference colours, which represent overlapping of individual scans. This ensures an accurate matching of individual scans to one virtual outcrop model. White rectangle indicates location of Figure 60. Source of imagery: Google Earth.

The outcrop quality, as the third criterion refers as implied to the overall condition of the scanned sections. The lidar system works on a 'line of sight' basis and as a non-invasive surveying system, extensive vegetation or talus should be avoided. Most outcrops however will exhibit some sort of vegetation. In general larger objects, like for instance trees are easier to handle during the post-processing. These obstacles can be deleted in the DOM and blank areas can be interpolated. Smaller-scale vegetation, like bushes or grass vegetation is more difficult to process. Grass, partly covering an outcrop represents a challenge in the post-processing. It is time consuming and almost impossible to delete the grass vegetation since each blade of grass has to be deleted manually. Subsequently these small obstacles constitute

problems during the triangulation process (construction of triangulated surfaces, see below) and visualisation of the virtual outcrop model. The Zebra River area is a desert environment and vegetation is sparse, however occasional rains favour the growth of grass. Prior to the lidar-based field season in South Namibia, intensive rainfall occurred and grass flourished, which resulted in difficulties in the post-processing.

The accessibility of the outcrop is the last criterion introduced by Enge *et al.* (2007). Terrestrial laser scanners were originally designed for the construction industry and architecture. Thus, they are not necessarily optimised for remote field areas. The used ZMS-Z420i scanner and equipment has a weight of about 80 kg and therefore it was necessary to avoid long walking distances. The maximum distance, which could be covered in one working day, was 4 km on the canyon bottom. This was due to heat, sun and impassable terrain. Carrying the equipment up the canyon slopes proved to be impractical, which further reduced the effective working/scanning area. Accessibility of the outcrop also implies a regular access to electricity. The power supply for the scanner and the laptop is next to the weight of the equipment the main constraint when working with lidar in remote areas. After a maximum of 3 scans the batteries of the scanner have to be recharged. Therefore it is necessary to incorporate daily access to electric power supply in the lidar-based field work planning to avoid data loses due to dying batteries.

An important element, which has not been presented by Enge *et al.* (2007) is the weather or more precisely the effect of the seasons on the lighting conditions at the outcrop. The development of a photorealistic virtual outcrop model requires digital photographs, shot during the laser scanning. These images are subsequently merged onto the lidar point-cloud data for the construction of the DOM. The quality of the textured virtual model consequently depends on the quality of the digital imagery.

Problems arise when scanning in the direction of the sun (e.g.: scanning N-S trending section from a relative westerly position during sunrise). This results in lens reflection and probably in a complete loss of the digital image and subsequent data loss. The opposite would be scanning an outcrop when it is under shade. This leads to dark virtual outcrops and possibly to black areas (completely in shade). No visual information can be gathered from these areas. Therefore, each scan-position has to be planned according to the seasonal lighting conditions to ensure optimal picture quality.

The lidar survey in the Zebra River Canyon was carried out in late June and early July, which is the winter season in Namibia. The altitude of the sun was, thus relatively low and a thorough planning of where and when to scan was important to avoid lens reflection due to dazzling sunlight in the morning or afternoon, respectively. In addition it was necessary to avoid scanning shaded cliff faces.

### 4.3.3 Field work planning with Google Earth

A powerful tool during lidar field work preparation and planning is Google Earth. This software package is a virtual map and geographical information system, which is available for free on the internet (http://www.google.co.uk/earth). Potential field areas can be studied in high detail on satellite images and a first glance of the terrain can be obtained. In addition to the satellite imagery, Google Earth provides a digital elevation model (DEM) with a spatial resolution of 30 metres. The virtual globe can be rotated and looked at from different positions and angles, thus allowing the geologist to simulate the planned scanning from each position. This enables the user to accurately plan scan positions because potential obstacles (e.g.: trees in line of sight) can be detected and scan positions can be planned accordingly. Furthermore, visible access roads on the satellite images can be selected and time-optimised scanning routes can be planed.

Figure 58 shows the lidar survey section of the Zebra River Canyon within Google Earth, illustrating the planned scan-positions. An important factor, which has to be considered in the planning procedure, is that the individual scans should overlap each other. The overlapping of scans is necessary in the subsequent data-processing and positioning of the scans to ensure accurate matching relative to each other. Furthermore, the perspective view of the Google Earth DEM enables one to plan the scan position accurately in order to avoid data shadows.

Google Earth additionally offers a function to simulate the position of the sun for any given time per day of the year. This is very useful while planning a scanning day since the user can determine which part of an outcrop will be illuminated at a given time during a day. Figure 59 shows the plan view of the Zebra River canyon with lighting conditions at the beginning of July 2011 in the morning and evening, respectively. The image with the morning lighting conditions indicated that the best scan-positions during early hours field work is to scan eastward facing sections from an eastward position relative to the outcrop. In the late afternoon it is opposite:

westward-facing sections from a relative westward position. Thus, the simulation of the lightning conditions assists the planning of the lidar survey in order to avoid dwell times, extra costs and data losses. The lidar scanning campaign in the Zebra River Canyon was planned according to the above-described considerations, which significantly facilitated the scanning work, due to minimising walking distances and dwell-times.

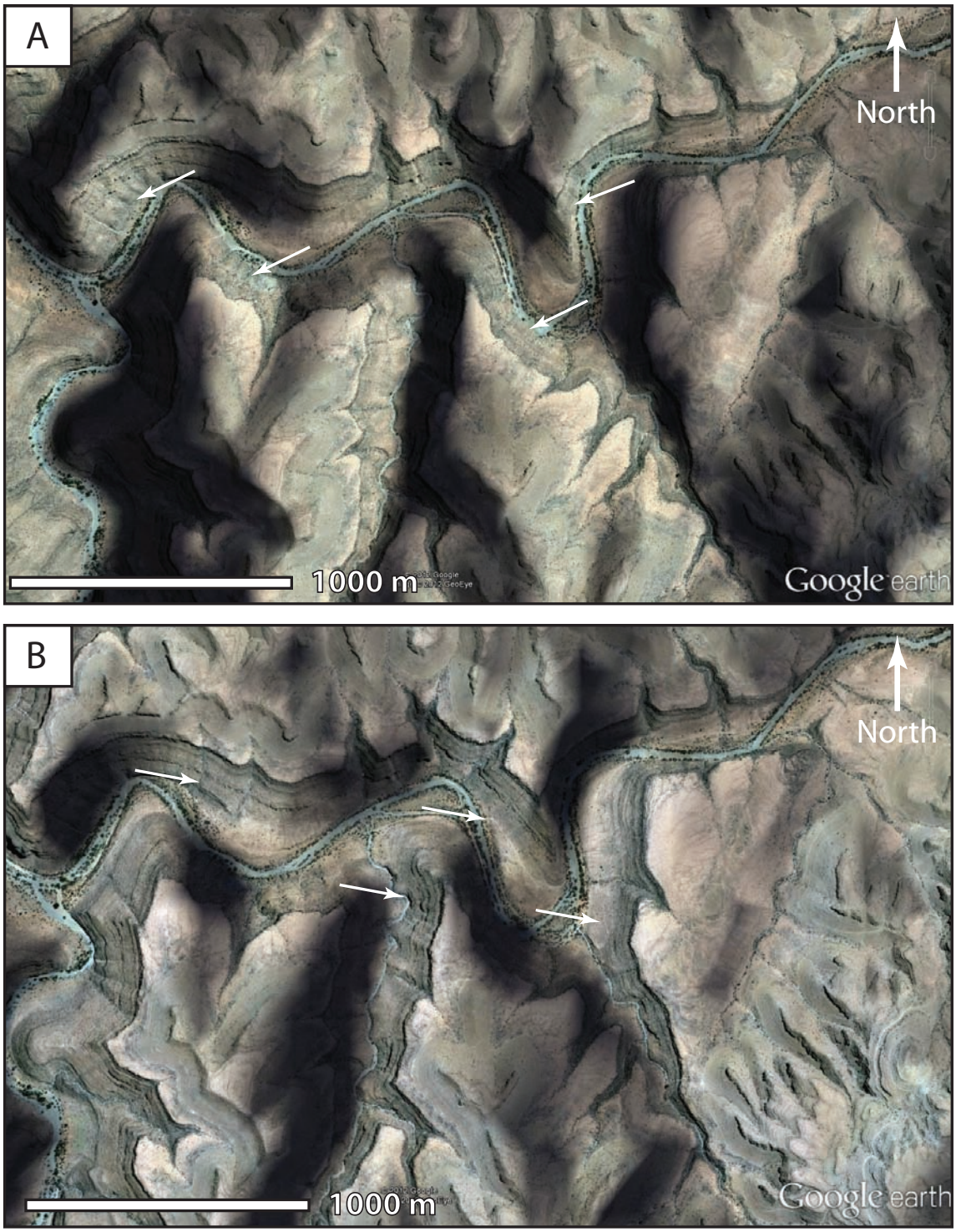


Figure 59: Plan view of the Zebra River Canyon section in Google Earth with simulated lighting conditions on the 3 of July 2011 in the morning at 9am (A) and in the late afternoon at 4pm (B), respectively. Optimal results are obtained when scanning eastward facing cliff sections in the morning and westward facing cliff sections in the late afternoon (see white arrows). Source of imagery: Google Earth.

### 4.3.4 Laser scanning in the field

Once the scanner is set up at the planned scan position, reflectors have to be positioned in the field prior to the start of the scanning. The Riegl lidar system measures 3D coordinates in its internal coordinate system. In order to georeference the scans during the post-processing it is necessary to define fix-points or tie-points in the real world coordinate system. Reflectors are objects (generally tubes a few dm in height), which are covered with a high reflectivity surface. These reflectors are then positioned at elevated locations and their real world coordinates are measured with a handheld GPS device. A Garmin 62st GPS receiver was used to measure the coordinates of the reflectors with a relative accuracy of approximately 8-10 m horizontally and 10 m vertically. The high reflectivity surfaces are easily recognised in the individual scans and their real world coordinates can be assigned. Subsequently each point in the dataset can be triangulated using the reflectors as georeferenced fix-points.

The Riegl measurement system needs at least three reflectors for the triangulation of the scan-position in order to transfer the data to real world coordinates. However, four to five reflectors are recommended due to the increasing accuracy during triangulation. The locations of the reflectors should be ideally concentric relative to the scan position and should comprise good visibility. Furthermore, three of the tie-points have to be used at the next scan position to ensure the matching of the individual scans (see Figure 60). Therefore, the locations of the reflectors have to be carefully chosen in the field in terms of visibility from each position.

Once the reflectors are set up, the next step is to perform a panorama scan. This scan takes about 15 minutes of time and it is a 360° scan of the entire area. It gives a first glance of the scanned section and has a density of about $1*10^6$-$2*10^6$ data points and a resolution of about 10 cm. It is necessary to do the panorama scan in order to locate and define the reflector positions. Once this has been done, detailed scans of areas of interest can be performed. These scans take about 15-30 minutes depending on the extend of the chosen area and have a data density of $2*10^6$-$9*10^6$ points with a point-spacing of up to 2 cm. The last step in the workflow is to take the digital photographs, which needs about five minutes.

After finishing the scans at one position, the scanner is moved to the next position. Typically all sections are scanned from different angles to avoid the above

mentioned data shadows in the data sets. For instance, when scanning a section from northeast, areas or planes, which are striking parallel, cannot be captured. Therefore the next scan position should be in a northwestwardly position. Furthermore, moving the scanner closer to the outcrop section increases the resolution of the areas of interest (see Figure 60).

After scan-completion of one section, which is normally done during one field work day, the next section can be scanned. Similar to the procedure for each outcrop, with overlapping individual scans, also the neighbouring sections should have overlapping scans to ensure the accurate merging of the individual sections.

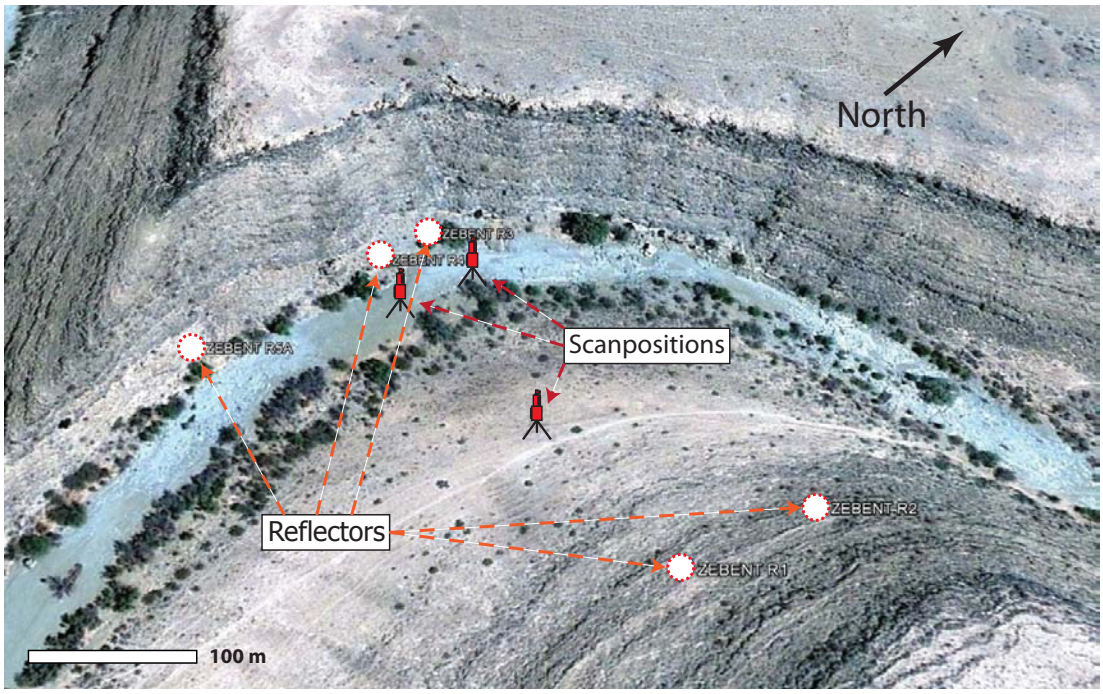


Figure 60: Oblique Google Earth view with scan and reflector positions of a scanned cliff section (see Figure 58 for location). Note that five reflectors are placed concentric relative to the scan positions on the slope and that at least four reflectors are visible from each scan position in the river bed. This is necessary in order to ensure accurate georeferencing and merging of individual scans to one section. Source of imagery: Google Earth.

## 4.4 Terrestrial laser scanning in the Zebra River Canyon

The lidar-survey in the Zebra River Canyon system was carried out from 28.6.2011 until 03.07.2011 in collaboration with Ken McCaffrey from the University of Durham. An area of approximately 2.4 km$^2$ comprising of 14 scan-positions and 37 individual scans was scanned within 5 working days. The principle idea in the Zebra River Canyon was to work in an open traverse line through the canyon, comprising of individual, overlapping scans and sections (see Figure 58). A total of three lidar sections were needed to cover the area of interest in the canyon system, which are

named east-section, at the canyon entrance, linking-section in the centre of the canyon and west-section at the westerly end of the scanned area (see Figure 61). The canyon can be accessed by car until the beginning of the east section and from this point onwards the lidar system had to be carried. This limited the scanning area in the west because from the canyon entrance until scan position 3 of the west-section the distance is more than 2.5 km. This proved to be the maximum distance, which could be covered during one day.

A total of 14 panorama scans were performed and 23 detailed scans of sections of interest. Panorama scans have generally less than 2 million points with an average resolution of 10 cm point spacing. Detailed scans range from around 2 million up to 9.9 million scan points with a maximum resolution of 2 cm point spacing. A detailed list of all scans containing data density, reflector positions and post-processing steps is provided in the APPENDIX III.

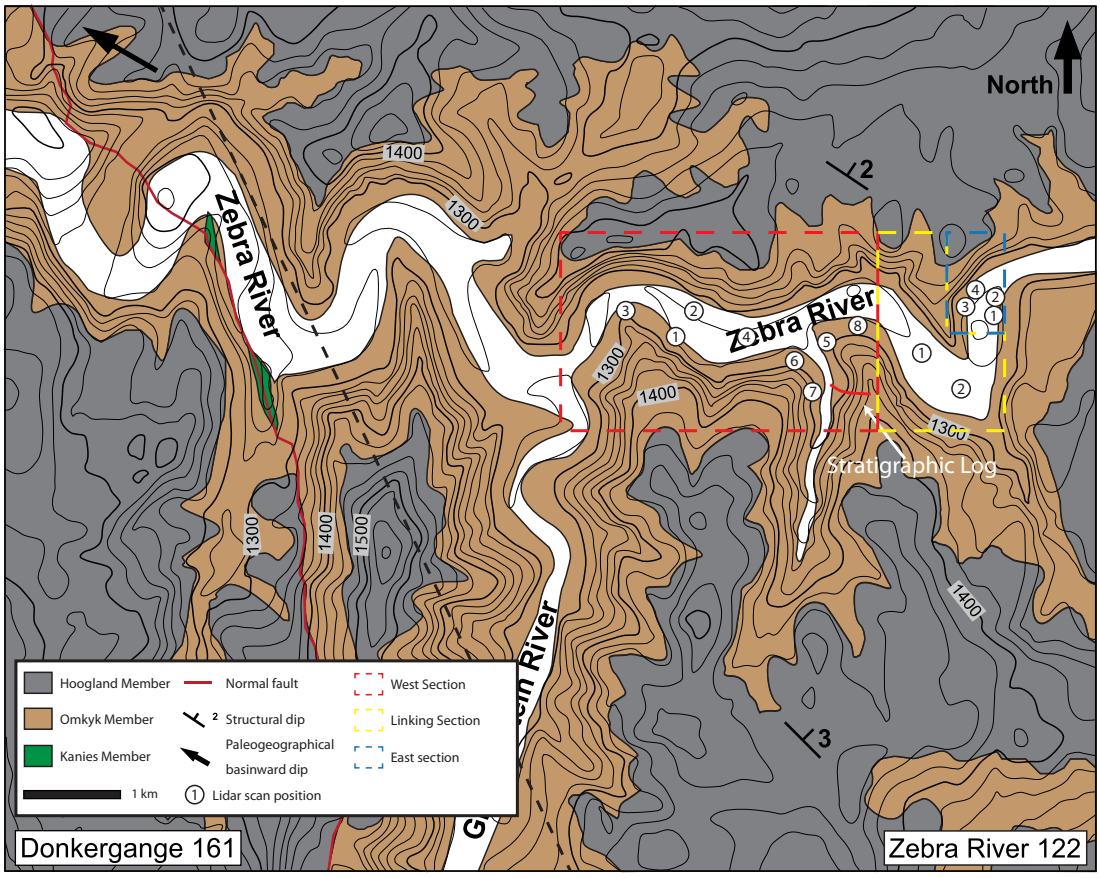


Figure 61: Geological map of the Zebra River Canyon showing lidar scan positions and sections.

## 4.5 Lidar data processing

### 4.5.1 Data cleaning and texturing

The collected lidar raw data has to be processed and cleaned before the final virtual outcrop model can be developed. The lidar data-set is a matrix of *x,y,z* coordinates plus the associated attributes, like RGB colour (red-green-blue channels) and intensity loss for each point. It is an ASCII file (American Standard Code for Information Interchange) organised by columns and rows. Each row comprises one data point and each column the corresponding attribute (see Figure 62). The raw data is a list of all scanned points in a randomly distributed order, by means that there is no internal data structure of the point matrix. This kind of data set is called point-cloud data and every scan represents one point-cloud.

| X [m] | Y [m] | Z [m] | R | G | B |
|---|---|---|---|---|---|
| -1077.092 | 367.304 | 289.945 | 0.931 | 0.963 | 1.000 |
| -1076.664 | 367.415 | 289.930 | 0.929 | 0.943 | 0.978 |
| -1078.666 | 366.910 | 289.142 | 0.941 | 0.945 | 0.969 |
| -1078.646 | 366.915 | 289.110 | 0.925 | 0.924 | 0.933 |
| -1078.583 | 366.932 | 289.093 | 0.912 | 0.912 | 0.912 |
| -1078.582 | 366.932 | 289.053 | 0.894 | 0.869 | 0.837 |
| -1078.195 | 367.031 | 289.153 | 0.912 | 0.861 | 0.792 |
| -1077.828 | 367.125 | 289.244 | 0.904 | 0.863 | 0.798 |
| -1078.085 | 367.061 | 289.111 | 0.918 | 0.875 | 0.802 |
| -1078.368 | 366.990 | 288.970 | 0.943 | 0.892 | 0.820 |
| -1078.485 | 366.961 | 288.889 | 0.951 | 0.898 | 0.786 |
| -1078.549 | 366.945 | 288.827 | 0.935 | 0.884 | 0.792 |
| -1078.001 | 367.084 | 288.977 | 0.814 | 0.790 | 0.767 |
| -1077.979 | 367.090 | 288.944 | 0.873 | 0.827 | 0.722 |
| -1076.952 | 367.351 | 289.255 | 0.839 | 0.786 | 0.671 |
| -1077.795 | 367.138 | 288.925 | 0.896 | 0.847 | 0.733 |
| -1076.906 | 367.364 | 289.184 | 0.829 | 0.792 | 0.725 |
| -1076.928 | 367.359 | 289.133 | 0.871 | 0.865 | 0.867 |
| -1077.523 | 367.209 | 288.892 | 0.853 | 0.814 | 0.751 |
| -1077.601 | 367.189 | 288.825 | 0.865 | 0.865 | 0.845 |
| -1077.650 | 367.177 | 288.767 | 0.814 | 0.767 | 0.645 |
| -1076.959 | 367.353 | 288.951 | 0.863 | 0.831 | 0.712 |
| -1077.580 | 367.196 | 288.708 | 0.859 | 0.810 | 0.727 |
| -1076.832 | 367.386 | 288.906 | 0.869 | 0.798 | 0.704 |
| -1077.680 | 367.172 | 288.593 | 0.871 | 0.853 | 0.835 |
| -1076.900 | 367.370 | 288.799 | 0.786 | 0.741 | 0.622 |
| -1076.512 | 367.469 | 288.877 | 0.898 | 0.839 | 0.710 |
| -1077.129 | 367.314 | 288.642 | 0.841 | 0.776 | 0.684 |
| -1077.072 | 367.329 | 288.617 | 0.953 | 0.914 | 0.851 |
| -1077.069 | 367.330 | 288.576 | 0.871 | 0.812 | 0.727 |
| -1077.366 | 367.255 | 288.444 | 0.902 | 0.841 | 0.735 |
| -1077.380 | 367.252 | 288.398 | 0.906 | 0.835 | 0.733 |

Figure 62: Format of the lidar point-cloud data. The data format is an ASCII file. In each row of the files the coordinates (*x,y,z* here in the scanner internal coordinate system) and associated attributes (Red/Green/Blue – RGB colours) are stored.

The majority of data processing and cleaning can be done with RiscanPro from the company Riegl GmbH. This is a specially designed software package for the Riegl laser-scanning system. The first step in the data processing is to georeference all individual scans with the reflector coordinates in order to define the scan-positions in real world coordinates. This step enables the merging of individual scans to one continuous section in a later stage. After that has been finished, the next step is to merge the digital imagery onto the point-cloud data. Before merging the digital

images onto the point-cloud, the images should be edited with photo-editing software to maximise the recoverable information. This can be done with standard digital photo editing software (e.g.: Adobe Photoshop was used for this purpose during the course of this research project) to modify the contrast and gamma values of the images. Additionally, it is possible to highlight dark areas and to reduce the brightness of overexposed areas. The photo editing significantly improves the quality of the images and therefore the photorealistic outcrop model. The final merging of the images onto the point-cloud is an automated process within RiscanPro, where the exact position of each pixel of the digital photo is calculated to the corresponding data point in the point-cloud data.

After texturing the point-cloud the first photorealistic model is constructed and additional data cleaning can be performed. The first step is to delete areas of no interest in order to increase the processing speed of the DOM. In particular the scanned area directly adjacent to scanner can be deleted (e.g.: talus in the river bed at the scan position). These areas have high data densities due to the proximity to the scanner and therefore file-size but generally do not contribute any geological information to the DOM. Deleting this data significantly reduces the processing time of the DOM. Furthermore, data points at the far end of the scanned sections, which also do not contribute any significant information, should be erased. Once the data cleaning is finished the individual scans can be merged together and the end-result is a cleaned photorealistic three-dimensional virtual outcrop model (see Figure 63.A). It was necessary to produce three virtual models for the entire Zebra River canyon section because otherwise the file-size of one combined model would have been too big to handle with the workstation. A schematic workflow, illustrating the individual steps from field work planning until the development of the photorealistic outcrop model is provided in the APPENDIX IV.

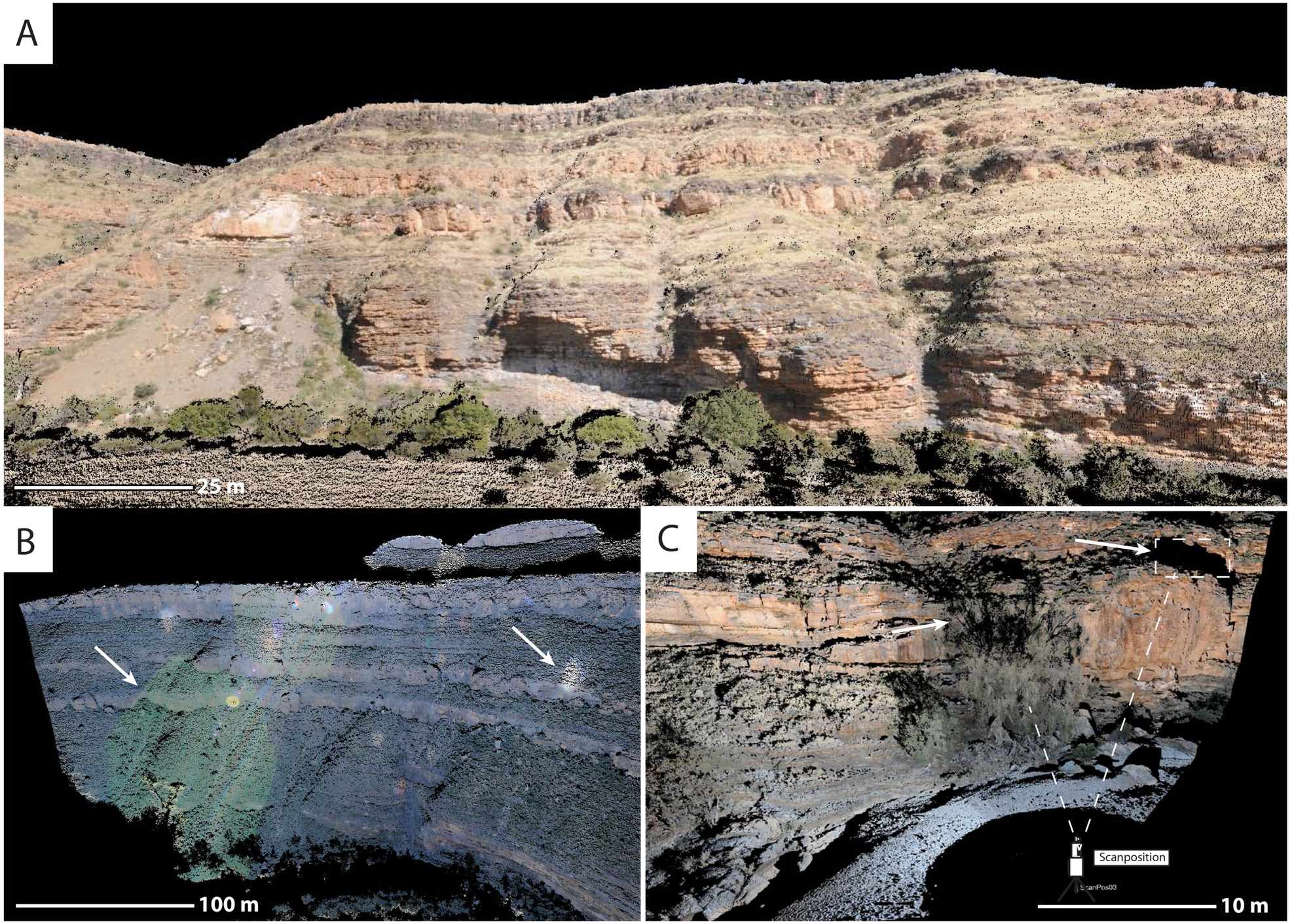


Figure 63: (A) Extract of the final photorealistic Zebra River virtual outcrop model. The resolution of the DOM is 10 cm spacing between the points in the point-cloud. (B) Virtual outcrop with distorted colours due to lens reflections in the digital imagery (white arrows). Lens reflections cannot be removed with photo editing software and subsequently the interference colours are merged onto the point-cloud. It is not a complete data loss, however, interpretations are hampered due to the false colours of the outcrop surface. (C) Virtual outcrop with data-shadows (black areas). The outcrop area behind the tree is not visible from the scan position and therefore no data can be collected (obstacle in the line of sight). White rectangle indicates an area, which is also not visible from the scan position due to the topography of the outcrop. These no-data areas are usually compensated by scanning the outcrop from a different position and angle

### 4.5.2 Quality control of the digital outcrop model

Following the construction of the preliminary virtual outcrop model a quality control of the DOM should be performed. Despite all field work planning, data cleaning and image post-processing as described earlier, the DOM will most likely show data shadows and or obstacles in the point-cloud. Figure 63.B&C show two of the most common problems with ground-based lidar. Figure 63.B illustrates the effect of lens reflections in the digital imagery. The reflections could not be removed with image editing software and subsequently the interference colours are visible on the digital outcrop. It is not a complete data loss but the interpretation of the DOM became more complicated due to the distorted colour of the outcrop. Figure 63.C shows data-shadows due to two reasons: (1) data loss due to an obstacle in the line of sight and (2) data loss because of the relative scanning angle of scanner and outcrop. In the first case a tree blocks the sight of the outcrop and no data of the outcrop behind the tree could be collected. The second case illustrates that the area on top of the outcrop is not visible from the scan position and therefore no data can be obtained. The first case proved to be problematic because also through moving the scanner to a different scan position the outcrop area behind the tree was not visible. Thus, the only solution was to interpolate this no data area during the triangulation process (see below) and compare and contrast the results with field work photos to ensure a maximum accuracy of the interpolated area. The data shadow in the second case could be filled by moving the scanner to an elevated position from which this section was visible.

### 4.5.3 Further processing of the DOM

After the initial data cleaning and preparation, further processing steps are necessary according to the subsequent usage of the digital outcrop model. For the purpose of this research project three different models were used and developed: (1) an unaltered model, (2) a triangulated meshed model and (3) an octree filtered model.

The unaltered DOM was primarily used for high detail interpretation. It can be analysed either with photorealistic colours (see Figure 63.A) or as simple colour (black&white) variation. Figure 64.A shows a part of the constructed virtual outcrop model. In this model all data points are coloured white. Black areas represent no-data areas. The advantage of such a model is the reduced file size (no RGB colours) and therefore increased processing performance during interpretation. Additionally, it is

visually easier to detect structural elements (e.g.: fracture planes) in a single colour model due to the increased contrasts. Figure 64.B shows an enlarged part of the unaltered DOM and illustrates how the outcrop topography is represented by the point-cloud data. This unaltered DOM was used for fracture and stratigraphic contact mapping (see description below).

The second digital outcrop model used during interpretation is a triangulated DOM. In order to create a continuous surface, each point in the point-cloud has to be connected with triangles. Such a surface is shown in Figure 64.C and is called a triangulated irregular network (TIN) (Buckley *et al.*, 2008b). Rendering large point-clouds can be problematic due to the required computing capacity and depending on the workstation the triangulation can take up to several hours. A common and fast method to create triangulated meshes is the Delaunay triangulation, which minimises the amount of long or sliver triangles (Delaunay, 1934). With the triangulation, however, the file size increases significantly and large triangulated surfaces are difficult to visualise and to work with. The reason for the big file size is because triangles consist of 3 points and each point of the point-cloud belongs on average to six triangles in the mesh. The amount of triangles created from a point-cloud with n amount of points is 2n-2-k (k is the number of points at the margin of the point-cloud). A point-cloud with 1,000,000 point could theoretically produce a TIN with 1,999,998 triangles (Hodgetts, 2013). The triangulated virtual outcrop models are easier to interpret in terms of for instance sedimentological interpretations because they are visually easier to work with. Additionally, a higher resolution can be obtained when merging the digital imagery onto the mesh. The process of merging images onto the meshed surface is more complex than the calculation of the RGB values of the point-cloud data. The software uses the camera internal information (focal length, lens distortion etc.), camera position and orientation to merge the photos onto the triangulated surfaces. The resulting textured digital outcrops have a higher resolution than the point-cloud DOM since the images are used to fill the gaps between the points. This approach enables the user to map for instance bedding surfaces with a thickness of less than one cm. The disadvantage of the triangulated DOMs is however the large file size and potential difficulties in the construction of such.

The virtual outcrop model of the Zebra River Canyon proved to be less suitable for creating triangulated surfaces because of the partly dense grass vegetation. Grass

vegetation is time consuming to delete manually from the point-cloud data and often impossible. During the triangulation process the grass stems are taken into account as data points, resulting in surfaces which are highly irregular and do not represent the outcrop surface. Therefore only selected parts of the canyon cliffs, without grass vegetation and overall good outcrop quality were chosen for triangulation (see Figure 64.C).

Triangulated surfaces can be used to quickly analyse triangle orientations in the data set. Figure 64.D&E show the meshed surface of a fracture plane at scan position three in the east section of the lidar survey after a triangle orientation analysis has been performed. Dip and dip-azimuth of each triangle are calculated, which highlight predominant orientations in the dataset. The calculated strike directions and dip angles can be subsequently plotted in stereonets to analyse the main orientations of geological features such as fracture planes. A common dip direction, which is detected with this semi-automated orientation analysis is between 35º-45º, which represents the repose of sediment. This generally represents talus and therefore no data areas and has to be considered in the analysis. A curvature analysis of the data set can enhance the results of the orientation analysis. Figure 64.F shows the same surface after the curvature analyses and enables the user to only analyse planar surfaces (e.g.: fracture planes). The accuracy of this semi-automated approach depends, however, on the quality of the TIN. Wilson *et al.* (2011b) used this approach for automatic fracture extraction out of a point-cloud but only detected three out of 7 in the field identified fracture sets. Thus this method should only be used as a preliminary mapping option and manual control is needed to ensure the quality of the analysis.

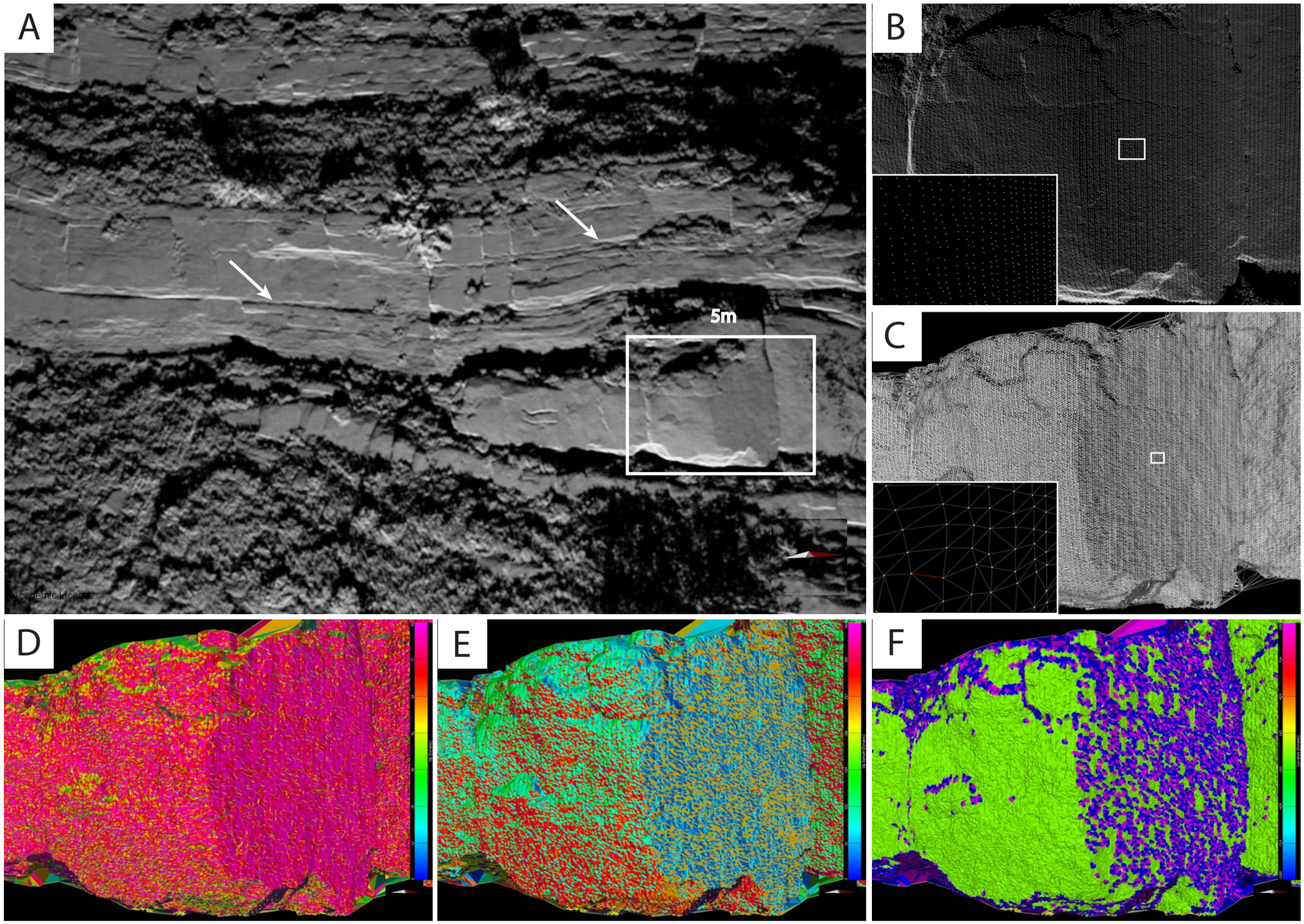


Figure 64: (A) Virtual outcrop in simple colours (black&white). The stark contrast between black (no-data) and white (data-points) makes it visually easier to map changes of the outcrop topography. The white arrows indicate a shale layer between two packstone packages which is deeper weathered than the carbonates and is represented by a lower point density (weathered features are not entirely visible) and therefore has a lower contrast. White rectangle indicates location of figure 9.B-F. (B) Detailed view of a fractures plane in the unaltered single colour DOM. Enlarged image shows a detailed view of the point-cloud. Average point spacing is 3cm for this section. (C) Delaunay triangulated surface. The enlarged picture shows a close-up of the irregular triangulated network (TIN). Red triangle edge has a length of 4 cm. Note that each point is the corner of on average 6 triangles which increases the file size significantly. (D-F) The images show the triangulated mesh after surface analyses for each triangle in the mesh. (D) Dip analysis with pink colour representing 90ºdip. The fracture plane has a dip of 88º (average of all triangles in the fracture plane). (E) Dip-azimuth analysis. The average dip-azimuth is 60º (light blue). The orange colours indicate triangles with a dip azimuth of around 240º which is due to the high dip angle. (F) Gaussian curvature analysis. Purple colours indicate the smooth and planar surface of the fracture plane.

The third DOM, which was used during the interpretation, is an octree-filtered model. The octree-filter significantly reduces the file-size and therefore increases the processing and visualisation speed. This filter uses an octree structure, which is a tree data structure commonly used in 3D graphics (Figure 65.A). The structure is based on a cube, which is internally divided into eight equally sized octants. These eight cubes are again divided into eight octants, until a minimum octant base length is reached. The algorithm calculates one point for each cube, which represents the centre of gravity or centre of subdivision. After the filtering process each octant contains only one point, representing in general a larger number of points within the volume of the octant. Reducing the file size in this way is of particular advantage for large-scale interpretations where the entire model needs to be loaded (e.g.: stratigraphic horizon mapping). Through the octree filtering the necessary resolution of the DOM for mapping is preserved and it is possible to reduce the file-size enough so that the entire model can be loaded. Once these three different virtual outcrop models are constructed, one can start with the data interpretation.

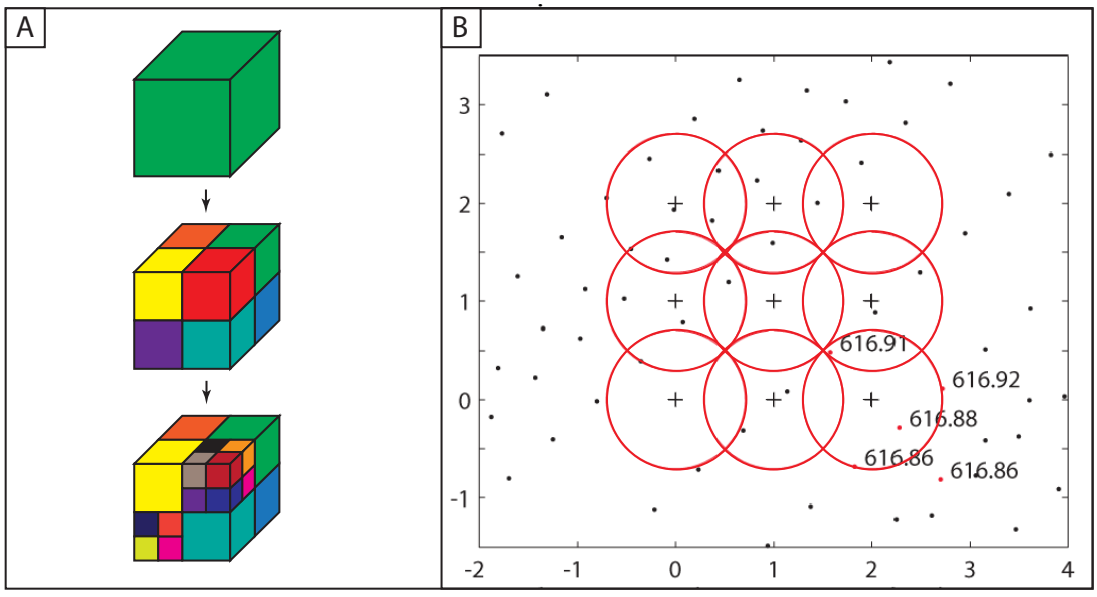


Figure 65: (A) Illustration of the octree data structure. A cube is divided into 8 equally sized octants and each octant is again divided into 8 octants. This is repeated until a minimum cube edge length (defined by the user) is reached. Subsequently for each octant the centre of gravity is calculated, which represents in general a larger number of data points within the volume of an octant. Filtering the point-cloud data in this way significantly reduces the data density. (B) Illustration of the gridding algorithm used to construct the digital elevation model. Black points represent the point-cloud. A regular grid (in this case 1m spacing) is draped over the point-cloud (black crosses represent DEM data nodes). Red circles indicate search radii for the subsequent elevation calculation for the DEM data node. Numbers indicate elevation values of the lidar point. See text for explanation.

### 4.5.4 Development of a digital elevation model (DEM)

The terrestrial laser scanning survey in the Zebra River Canyon system was carried out for the purpose of the development of a lidar-based geocellular reservoir analogue model. However, reservoir modelling software packages (e.g.: JewelSuite, Petrel) are designed to handle and process subsurface data, like seismic and borehole data with a lateral extend of tens of km or point information data (e.g.: wireline logs), respectively. They are not designed to process surface data and especially not high-resolution lidar point-cloud data with a resolution of up to a few cm over several km. This high density and resolution data format exceeds at the moment the capability of reservoir modelling software packages. Thus, data manipulations have to be performed before a reservoir model, based on a virtual outcrop model, can be developed

The first step in the reservoir modelling workflow is the construction of a digital elevation model (DEM) based on the lidar point-cloud data. A DEM is a representation of a given topography as a regular spaced point-cloud with *x, y, z* coordinates, where *x, y* are the horizontal coordinates and *z* the elevation. The difference between a DEM and a DOM is that for one given *x, y* coordinate pair only one elevation value can be assigned in the DEM. Hence, overhangs for instance cannot be represented in a digital elevation model. Furthermore, DEMs are commonly regular spaced (raster files) with a lower resolution (m to tens of m) in order to be able to cover large areas. The process of constructing a DEM is known as gridding and the resulting elevation model is the basic framework for the geocellular model. Gridding is similar to octree-filtering, it reduces significantly the point density and it brings a structure into the point-cloud data (Liu and Zhang, 2008). Both data manipulations are necessary in order to reduce the needed computing power. As described earlier the point-cloud data is a matrix of data points, which are randomly distributed over the entire scanned section. A DEM with a grid resolution of three metres was constructed, which served subsequently as basic framework during geocellular reservoir modelling.

Points2Grid was used for the construction of the DEM, which is available for free on the internet (http://lidar.asu.edu/points2grid.html). The algorithm works on the basis that a horizontal 3-m grid is draped over the point-cloud. This defines the DEM in 2D-space and each grid node represents one data point in the projected DEM.

Subsequently for each grid node the elevation has to be calculated. For each DEM data point a search radius is defined according to the grid resolution, which is given by:

Equation 4: $$\boldsymbol{r = \frac{\sqrt{2}}{2} * x;\ r = search\ radius, x = grid\ resolution}$$

The search radius is for a 3-m grid 2.12132034 m. The algorithm searches for all points in the data-matrix, which are located in the defined radius. In this process step, only the *x,y* coordinates of the points are considered after following equation:

Equation 5: $$\boldsymbol{d_{j,k} \leq \sqrt{\left(x_i - X_{j,k}\right)^2 + \left(y_i - Y_{j,k}\right)^2}}$$

The algorithm step computes the distance $d_{j,k}$ for the points relative to the node point $X_{j,k}$, $Y_{j,k}$. If $d_{j,k}$ is smaller than the defined search radius, the point will be considered in the following $Z_{j,k}$ calculations. Figure 65.B shows an example of an unordered lidar data matrix and the principle of the gridding algorithm. The next increment is the calculation of the $Z_{j,k}$ value (elevation) for the centre of the search radius (DEM data point). Four different calculation methods are available to assign a *Z* value to the centre node:

Equation 6: $$\boldsymbol{Z_{min} = \mathbf{min}(Z_l)}$$

Equation 7: $$\boldsymbol{Z_{max} = \mathbf{max}(Z_l)}$$

Equation 8: $$\boldsymbol{Z_{mean} = \mathbf{mean}(Z_l)}$$

Equation 9: $$\boldsymbol{Z_{IDW} = \frac{\sum_{l=1}^{n} \frac{z_l}{d_l^p}}{\sum_{l=1}^{n} \frac{1}{d_l^p}}}$$

Each method results in a significantly different digital elevation model. $Z_{min,\ max,\ mean}$ are assigning a *z* value to the grid node by emphasizing the minimum, maximum and mean elevation values of the prior identified points in the search radius. $Z_{IDW}$ is similar to the mean value method, however, it uses the Inverse Distance Weighted mean values to calculate the elevation at the grid node and takes the distance of the points to the grid node into account. It therefore emphasis more weight to data points closer to the DEM node.

The DEM after $Z_{min}$ is for reservoir modelling purposes the most suitable. The resulting surface of this elevation model provides the minimum elevated grid surface. It acts as pseudo vegetation filter because this method does not assign elevated values of, for instance bushes or loose boulders and thus reduces the noise. Furthermore, the resulting DEM grid is smoother than the raster surfaces constructed

with the three other methods. This significantly facilitates the triangulation of the digital elevation model. Figure 66.A shows the developed DEM of the Zebra River canyon after $Z_{min}$. This DEM was subsequently used as the basic framework for geocellular modelling. The digital elevation model, based on the lidar data is constrained to the scanned canyon surfaces and shows data gaps due to no data areas. In order to fill these data gaps a regional digital elevation model was developed.

Digital elevation models for most parts of the world are commercially free available through the SRTM (Shuttle Radar Topography Mission, http://www2.jpl.nasa.gov/srtm/) database, provided by NASA. These DEMs have a grid spacing of 30 meters outside of the United States, and are provided as raster data sets. The raster data set of the north-western part of the Nama Basin was used to develop a regional triangulated DEM (Figure 66.B). Additionally, Google Earth satellite imagery was used to texture the regional DEM (see Figure 66.C). The satellite imagery of the Zebra River Canyon is derived from the GeoEye-1 satellite, which provides panchromatic imagery with a resolution of 41 cm. The resultant high-resolution photorealistic digital elevation model was used to assist during the interpretation of the virtual outcrop model (e.g.: mapping of stratigraphic contacts outside of the lidar point-cloud data) and during the reservoir modelling process.

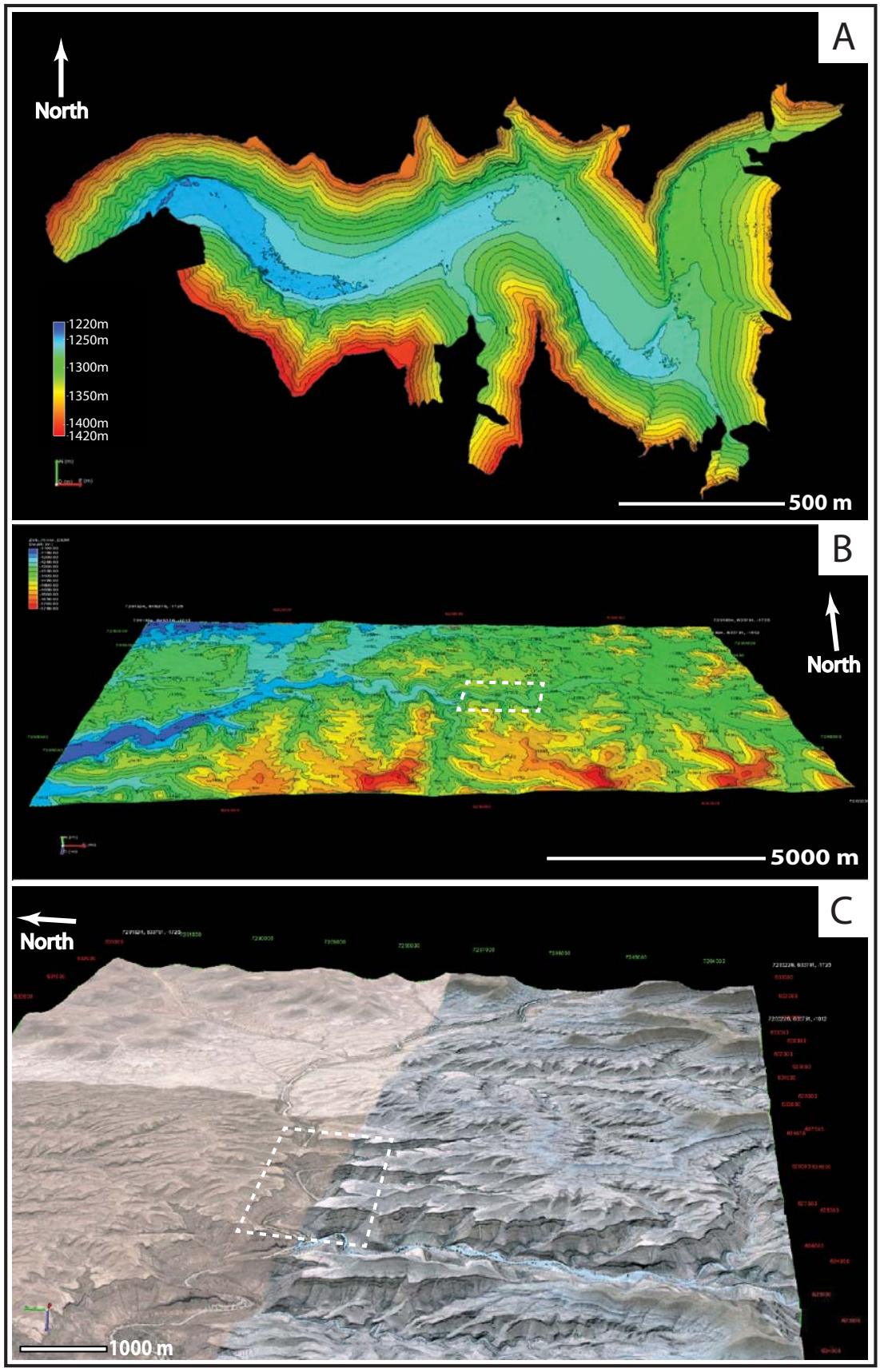


Figure 66: (A) Digital elevation model of the scanned Zebra River Canyon section based on the lidar data. Grid resolution is 3m. (B) Digital elevation model of the north western part of the Nama Basin. Grid resolution is 30m. Based on SRTM data. (C) Google Earth satellite imagery merged onto the SRTM DEM. White rectangles in (B&C) indicate the section of the Zebra River Canyon where the lidar survey was carried out.

## 4.6 Interpretation of the virtual outcrop model

The aim of the lidar-based field work was to capture the heterogeneities of the microbial carbonate system for the development of a static geocellular reservoir model. The main emphasis was on the sedimentological characteristics (e.g.: bioherm dimensions, shape and spatial distributions) and structural characteristics (fault and fracture patterns). In both cases it was necessary to accurately measure the spatial dimensions of these geological features. The advantage of the terrestrial laser scanning over traditional field mapping techniques becomes particularly obvious in the fracture characterisation. It is not a trivial task to acquire accurate and quantitative fracture data in the field. The main input parameters for fracture modelling are fracture length, orientation and spacing, which are challenging to measure in the field. For that purpose lidar is a powerful tool because large areas can be digitised in a short amount of time and in high detail. The DOM allows the geologist to precisely map fractures traces, faults and horizons in three-dimensional space over large areas. Furthermore, all data and interpretations are already in digital format, georeferenced and therefore easy to process in subsequent structural and subsurface modelling software packages.

### 4.6.1 Mapping of geological features (stratigraphic contacts & faults)

During the course of this research project only manual methods were used to carry out the interpretations. As mentioned earlier, research is underway to develop automated approaches in order to extract data from a virtual outcrop model (Gigli and Casagli, 2011; Olariu *et al.*, 2008; Wilson *et al.*, 2011b). However, at the moment they are still in at an infant stage and further research has to be done to improve the quality of the extracted data. Therefore, the author chose the manual method to analyse and interpret the virtual outcrop model. This is time consuming but ensures optimal data quality.

The simplest way to map geological features, like stratigraphic contacts and faults is to trace their outlines with 3D-polylines on the virtual outcrop. A 3D-polyline is a line in 3D space, which is defined by individual, connected data nodes. The nodes are the points of the point-cloud data, which represent the outline of the geological feature (e.g.: fracture trace). The user defines these nodes by selecting manually each point along the trace and subsequently a 3D polyline can be constructed. Figure

67.A&B show mapped stratigraphic contacts in the inter-bioherm area at scan position four of the east section (see Figure 61). In the case of Figure 67.A&B the mapping was carried out on the raw, simple colour (black & white) point-cloud because it is visually easier to recognise the outlines due to the high contrast of the data (points) and no data areas. The so created polylines can be subsequently exported into the modelling software and stratigraphic horizon and fault surfaces can be triangulated (see paragraph 6.3 for detailed description).

### 4.6.2 Fracture mapping

For the mapping of small-scaled features (e.g.: fracture traces) it is useful to perform preliminary mapping on the digital imagery of the lidar survey. Figure 67.C shows an outcrop picture taken from the lidar scan position number 2 east section, with interpreted fracture traces. The image is then again merged onto the virtual outcrop model and the prior mapped features appear as highlighted traces in the DOM (Figure 67.D). This procedure significantly facilitates the mapping process since the fracture traces appear as red outlines on the point-cloud and the user merely needs to select data nodes on the highlighted traces for the mapping with 3D polylines.

The mapping of fracture traces in this way is, however, not without difficulties. For instance when two traces intersect each other with an obtuse angle, they are easily mistaken as one single fracture, which would lead to an inaccurate modelling result. On the other hand, two fracture traces, intersecting with an acute angle are not necessarily two separate fractures and might just represent one fracture plane. It depends on the relationship of fracture plane orientation and outcrop shape (e.g.: if a vertical plane cross-cuts an entirely exposed sediment layer the vertical and also the horizontal outlines are visible). Given these difficulties when mapping fractures on the virtual outcrop model, it is advisable to rotate the model after a few selected polyline nodes, to validate that it is still one fracture trace. The fracture traces can be subsequently used to analyse fracture spacing and intensity for each part of the virtual outcrop.

In some cases 3D surfaces of fractures can be directly constructed out of the lidar point data. This can be done when the fracture plane is visible on the outcrop. The procedure works on the basis of the earlier described Delaunay triangulation. The interpreter selects the area of the point-cloud, representing the surface and a plane can be triangulated (Figure 67.D). It can then be directly used for dip and azimuth

measurement. These with this method constructed surfaces however do not represent the accurate geometry of the fracture plane because they only represent the at the outcrop visible part. The parts of the fracture surfaces, which extend for instance into the outcrop, are hidden. The exact shape of fractures has to be modelled manually. Fracture planes are assumed to exhibit a rectangular shape with a short to long axis ratio between 1:2 to 1:3 (Pollard and Fletcher, 2005). The height of the fractures (short axis) can be measured in the DOM, which is represented by fracture trace. Subsequently an accurate fracture plane can be constructed and merged onto the prior triangulated fracture patch (Figure 67.E). This method is, however, time consuming since each fracture has to be modelled separately but it does generate an accurate fracture network model of the selected outcrop.

One disadvantage in the fracture mapping process on the virtual outcrop is the varying resolutions in the vertical extent of the outcrop. Figure 68 shows the south-western part of the scanned Zebra River canyon at scan-position 1, in the west section. The distance from the scanner to the lower part of the cliff is 150 m and to the uppermost part of the section more than twice, 335 m. The laser beam diverts with increasing distance from the scanner head and therefore two different DOM resolutions are obtained. The density for the mapable fractures in the lower part of the section is about 0.5 m whereas at the top of the canyon it is approximately 2 m. If this circumstance is not taken into account during the interpretation a wrong fracture model would be developed. Higher fracture spacing and density would occur in the lower parts of the section compared to the upper section. This fact leads to two alternative fracture-mapping strategies: (1) the fracture spacing of the area with the lowest resolution defines the spacing for the entire section (e.g.: for scan-position 1 only fractures with a spacing of 2 m or more are mapped) or (2) only parts of the DOM, with areas of special interest and highest resolution are selected for fracture mapping.

Given the fact that the DOM was subsequently used for static reservoir modelling the second described procedure is more efficient because one does not loose information due to the varying resolutions and the interpretation results from the high resolution areas can be extrapolated to areas with lower resolution in the modelling software.

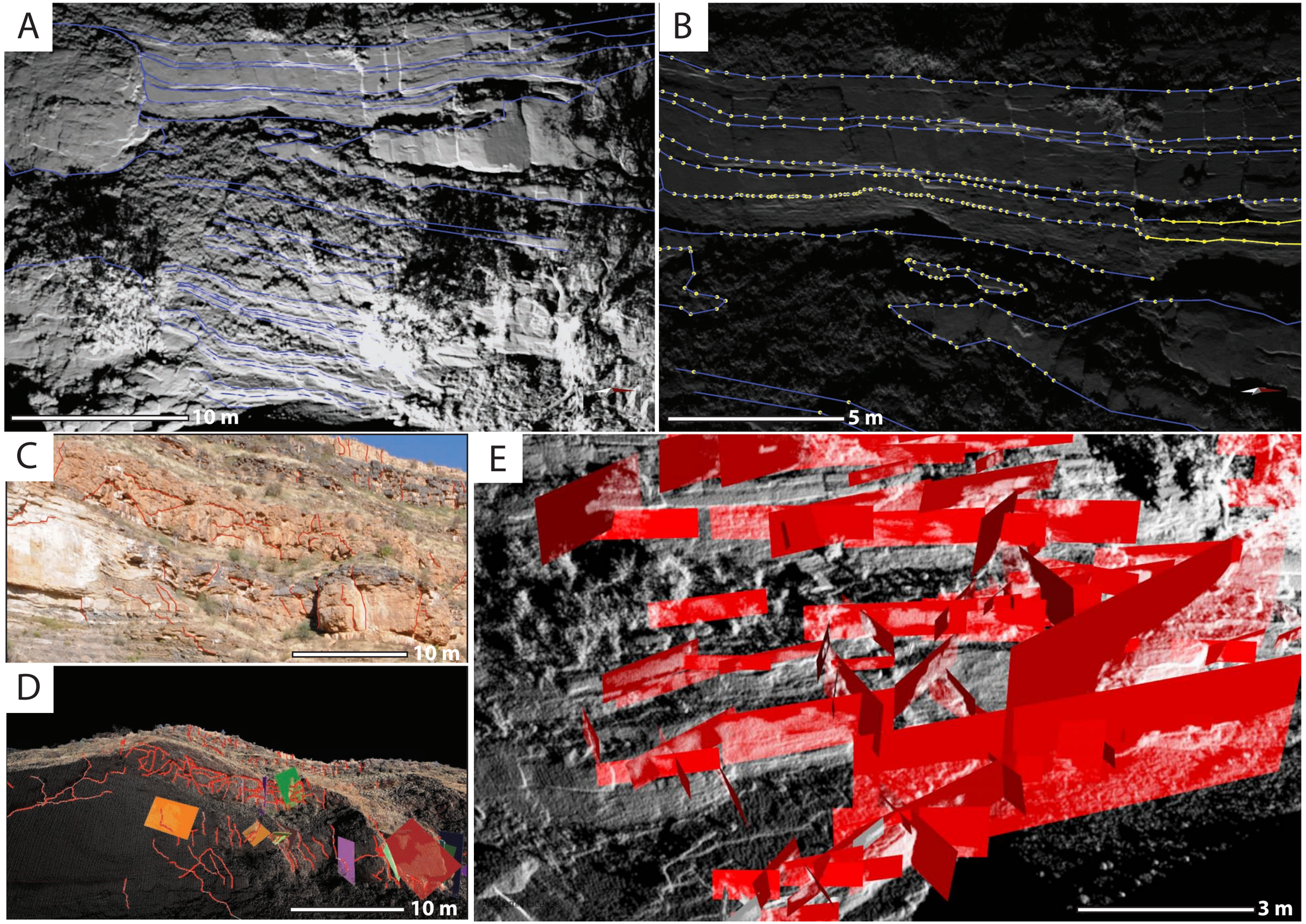


Figure 67: (A) Digitally mapped inter-bioherm area on the simple coloured raw point-cloud data. Blue lines indicate mapped contacts with 3D polylines. Location: Scan position 3, east section. (B) Detailed view of (A) with highlighted data nodes (yellow points). Data notes are manually defined by the user. (C) Mapped fracture traces on an outcrop image taken at scan position 2, centre section. The interpreted image is subsequently merged onto the point-cloud data where the fractures appear as highlighted traces (D), which makes it visually easier to map. Coloured rectangles are directly mapped fracture planes. (E) Constructed fracture planes (rectangles with 1:3 short to long axes ratio) based on fracture traces. Location: Scan position 3, east section. See topographic map for scan position.

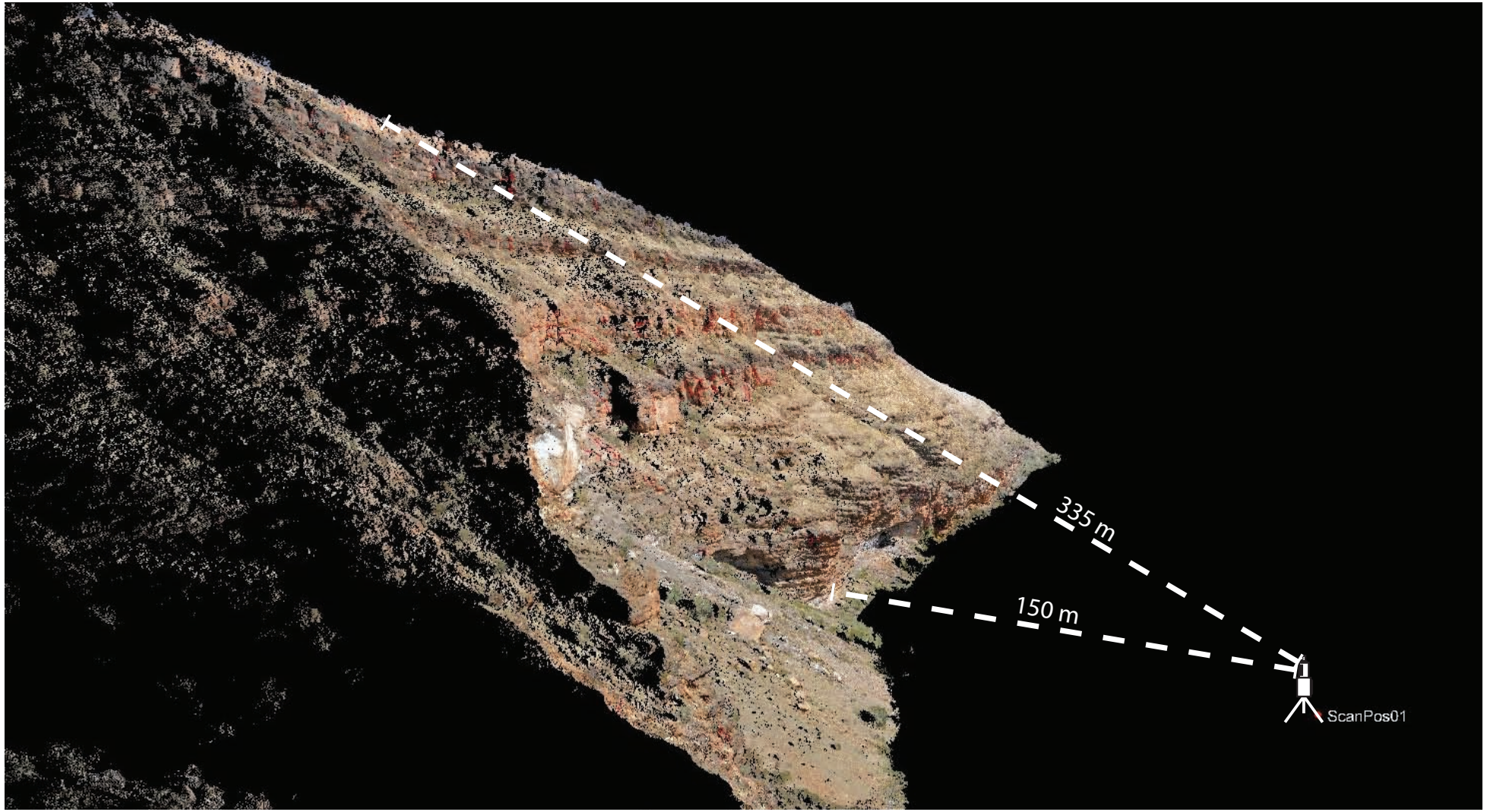


Figure 68: Due to the diverting of the laser beam the resolution of the virtual outcrop model varies with the distance to scanner head. The lower part of the cliff section is 150 m away from the scan position and the higher resolution in this part allows a more accurate fracture mapping than in the upper cliff section (335 m distance to the scanner and therefore lower resolution).

### 4.6.3 Mapping of three-dimensional objects

The measurement of the dimensions of three-dimensional objects (e.g.: bioherm widths and heights) on the virtual outcrop model is not a straight forward process. Although the mapped objects are in 3D or more precisely the mapped features are represented by a three-dimensional topography, it only constitutes a 2D cross-section through a 3D object. The appearance of 3D objects depends on the geometry of the cliff faces and on the geometry and orientation of the object itself. Therefore direct measurements of the objects will result in the measurement of apparent widths and heights.

An approach to measure the true widths and heights of 3D objects is to project the mapped polylines onto a projection plane, where the dimensions can be accurately mapped on cross-sections. Fabuel-Perez *et al.* (2009) used this technique to map the sizes of channel widths and heights in the Oukaimeden Sandstone of Morocco. The authors mapped the outlines of the channel shapes and projected the shapes in flow direction of the channel onto perpendicular cross-sections and could consequently measure the exact 2D channel dimensions. Figure 69.A shows the adapted method for mapping bioherm structures on the virtual outcrop of the Zebra River canyon. The projection plane is oriented parallel to the cliff face and the mapped polylines, representing the outlines of microbial carbonates are projected (normal to the projection plane) onto the cross-section. Subsequently the true widths and heights of the bioherm structures in cross-section can then be measured (Figure 69.B).

## 4.7 Limitations of lidar

Despite the enormous potential of lidar in geoscience research there are also several limitations. A major limitation is the costs associated with a lidar survey. The scanners cost up to several 100.000£ and are thus rather expensive compared to other digital measurement systems. Additionally, it is expensive to bring the equipment into remote field areas. As mentioned earlier the entire system weighs more than 80 kg and shipping costs can potentially be high.

Limitations in the field arise due to the weight of the scanners. It is hard work to handle and carry 80 kg of equipment in impassable remote areas. Thus, the field geologist is dependent on easy access to the field area and long walking distances

have to be avoided. Furthermore, lidar is dependent on power supply and the batteries of the scanner and laptop have to be recharged every day. Both cases, easy access to the field area and power supply are challenges in remote areas and limit the application of lidar.

Next to the cost and limitations of the laser measurements system in the field, the currently available software packages for processing lidar data are the main constraints. At the moment there is no geological software package available on the market, which is designed for the processing of lidar point-cloud data from a geological point of view. Therefore, the geologist has to rely on multiple software packages, which are not developed for the processing of lidar point-data. This can be tedious and impractical due to different file formats and compatibilities of the various products. The lidar point-clouds, acquired during the course of the lidar survey in the Zebra River Canyon are very large datasets with up to 9 million points. This proved to be very difficult to handle with a common modern workstation due to the limit of processing capacities. Challenges occurred during the triangulation of the point-cloud data, such as hours of processing time and frequent computer crashes. Furthermore, the outcrops in the Zebra River Canyon are partly covered with dense shrub-size vegetation, which made it impossible to develop continuous triangulated surfaces. This impeded detailed interpretations of bioherm internal structures due to the loss of image resolution. Alternative digital mapping techniques such as photogrammetry might be more suitable for high detail studies of the microbial geometries. Furthermore, mapping of geological features and the interpretation of the virtual outcrop model is time consuming. Research is undertaken to facilitate the interpretation with automated methodologies to extract information from lidar data (e.g.: Olariu *et al.*, 2008; Wilson *et al.*, 2011b). However, these approaches are at an infant stage. Therefore, the time consuming manual method (e.g.: mapping with user defined 3D polylines) is at the moment the only reliable method to extract high quality geological information. Additionally, virtual outcrop geology and the usage of the DOM need experience and training. This is particular the case during the post-processing, where the interpreting geologist is faced with the difficult task to use several software packages with different file-formats and in-built functionalities. Therefore, for each interpretation, methodologies have to be developed according to the functionality of the software.

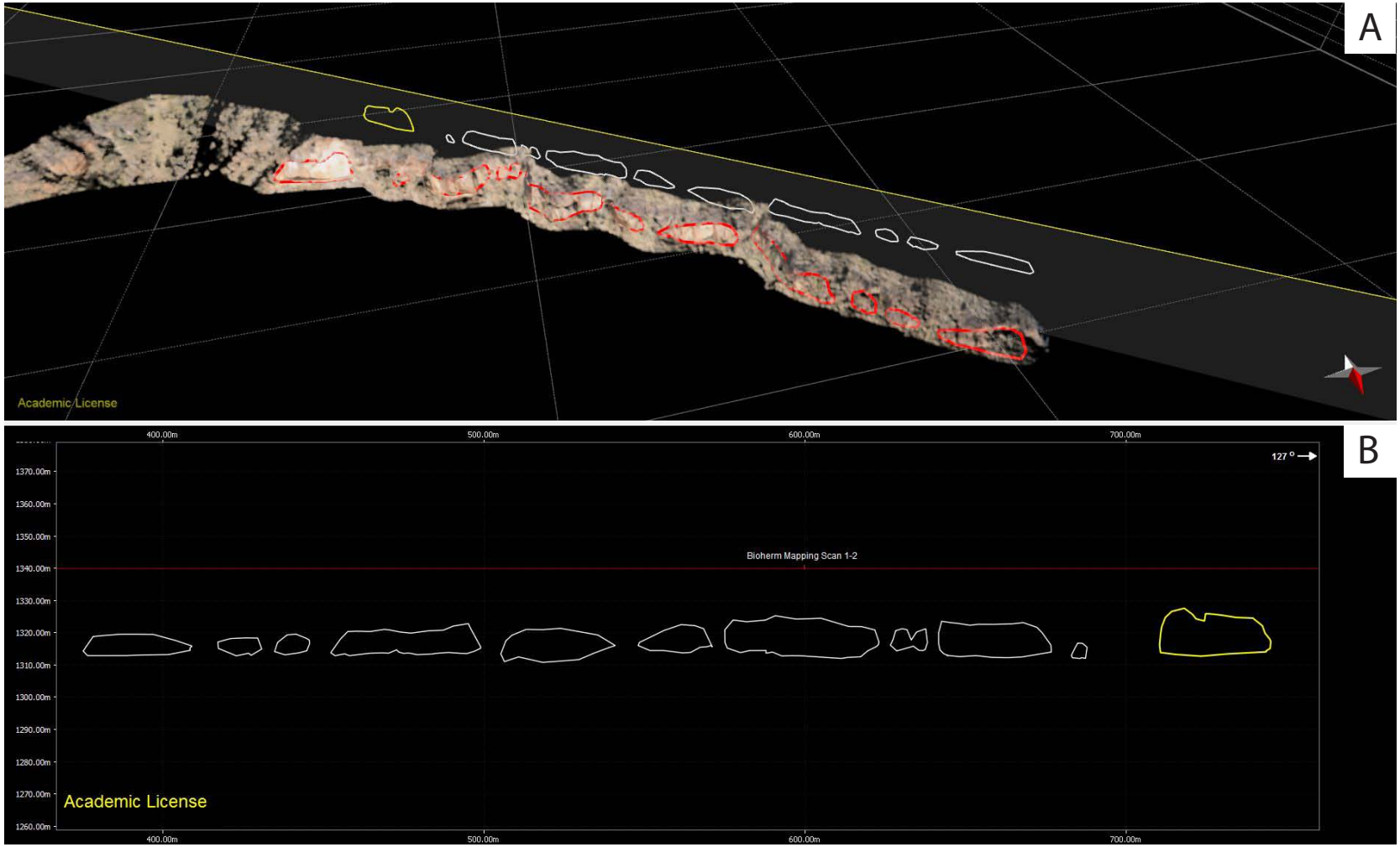


Figure 69: (A) Mapped bioherm structures in the bioherm horizon (red 3D polylines). The polylines are in three dimensions and the widths and heights cannot be measured. Therefore the polylines are project (perpendicular to the cliff section) onto a cliff-parallel cross section. In cross section view (B) the widths and heights of the bioherms can be accurately measured.

## 4.8 Chapter summary

This chapter presented the procedures and methodologies used in terrestrial laser scanning and discussed the workflows for the interpretation of the Zebra River virtual outcrop model. A detailed description of the Riegl laser scanning system, used for the lidar acquisition in the Zebra River Canyon has been provided. This includes technical specifications of the laser scanner and how to operate the system in the field. Subsequently, the necessity of lidar-based field work planning has been discussed, emphasising the use of virtual geographical software (Google Earth) during the planning stage. A detailed description of the conducted lidar survey in the Zebra River Canyon system has been given and the lidar meta data of 14 scan-positions plus associated individual scans is provided in the APPENDIX III.

In the second part the post-processing, visualisation and methodologies for virtual outcrop interpretations have been presented. Special focus was on point-cloud data manipulation for subsequent usage in reservoir modelling (e.g.: development of the digital elevation model). Furthermore, virtual mapping techniques have been discussed such as horizon and fracture mapping with 3D polylines, which subsequently are used for input in geological modelling software packages. The chapter concludes with the current limitations of lidar in geoscience research.

# 5 Structural Characterisation of the Omkyk Member

## 5.1 Introduction

The Nama Basin and in particular the Zebra River sections have been subject to extensive sequence stratigraphic and sedimentological research over the past two decades (compare paragraph 3.4). Research targeting the structural characteristics of the Nama Basin is sparse and no structural research has been published concerning the Kuibis ramp carbonates. The published geocellular reservoir analogue model of Adams *et al.* (2005) of the Zebra River sections is a high-resolution sedimentological model without incorporating structural features. Thus, in order to improve our understanding of microbial hydrocarbon reservoirs, the response of microbialites to structural stress and deformation was studied in detail.

The aim of this chapter is to present the structural data collected from remote sensing analyses, field work, photomosaic interpretations, terrestrial laser scanning and subsequent interpretations. In the first part the collected remote sensing data of the north-western edge of the Nama Basin is presented in order to establish the main regional trend of liniments, faults and fractures. Subsequently, the measured field data in the Zebra River canyon is placed into the regional framework.

The second part of the chapter describes in detail the response of microbial carbonates to stress, the resultant structural behaviour and deformational geometries. Consequently, the results are discussed from a petroleum geology point of view and implications for microbial hydrocarbon reservoir characterisation are given.

## 5.2 Structural History

The Nama Basin has been investigated in some detail regarding sedimentology, sequence stratigraphic basin development and the evolution of higher organised life in the Ediacaran (compare chapter 3 and references therein). Very little work has been published on the structural characteristics of the Nama Basin and Zaris sub-basin. A recently published study by Viola *et al.* (2012) represents the first attempt to reveal the long-lived structural history of the southern Nama Basin in the

Namaqualand. Realising that the study area of the authors is more than 450 km to the south and in a different sub-basin, it does present an opportunity to tie observations into the regional context. However, the linking to the regional context must be done with caution and interpretations are at a preliminary stage.

Viola *et al.* (2012) recognised a series of deformational events since the latest Neoproterozoic, which affected the Nama Group (Figure 70). The authors identified a total of twelve deformational events, beginning from the Pan African orogenic cycle until present day. Pan-African events are represented by four compressional episodes, each defined by strike slip faulting: an initial NW-SW event (D1) is followed by a clockwise rotation of the stress field (D2 and D3, to the NNW-SSE and N-S, respectively). The latest compressional event in the Precambrian has a main compressional direction to ESE-WSW. These first four events have been linked to development of the Damara orogen to the north, and the Gariep Belt to the west, respectively. Phanerozoic extensional events relate to opening of the South Atlantic (see Figure 70): the main extensional direction was NE-NW and E-W, and this was associated with subsequent margin uplift, marked by regional uplift and normal faulting Viola *et al.* (2012).

The study area is situated on the north-western edge of the Zaris sub-basin (see Figure 23). In this area some detailed structural work has been done in the Naukluft Mountains, approximately 70 km north of the Zebra River canyon. Korn & Martin (1959) described syn-sedimentary NW-striking reverse faulting and fracturing from the sandstones of the lower Dabis Formation (lowermost Kuibis sub-group). Ahrendt *et al.* (1978) reported from folding of the Kuibis Group south of the Naukluft Nappe Complex (NNC) and extensive cleavage for a distance of up to 30 km south of the Naukluft Mountains. The authors interpreted these structures to predate the emplacement of the Naukluft onto the Nama Basin. The main focus of the research in this area was however on the characteristics of the gravity induced emplacement of the Naukluft Nappe Complex onto the Nama sediments (Behr *et al.*, 1981; Martin *et al.*, 1983; Miller *et al.*, 2008; Viola *et al.*, 2006). The basal part of the NNC is a para-autochthonous nappe of the lower-most Kuibis Sub-group, which was thrust onto the Schwarzrand Subgroup. This is accompanied by intense faulting and folding along the basal thrust front at the southern edge of the NNC.

Miller (2008) summarised the features described above as the result of two separated events: (1) features predating the emplacement of the NNC are related to the peak of Damara metamorphism in that area around 535 Ma and consequently (2) all later features are related to the sliding of the NNC onto the Nama sediments at around 495Ma.

Note that the syn-sedimentary faulting must predate 535 Ma, because the approximate depositional age for the lower Kuibis group (Kanies and Omkyk Member) is around 550 Ma (compare chapter 3 for age constraints of the Kuibis Subgroup). Thus, deformation must have happened 15 Ma earlier, probably related to the onset of the basin evolution. One explanation might be tectonic pulses during the closure of the Khomas Sea. This interpretation however has to be confirmed by regional mapping.

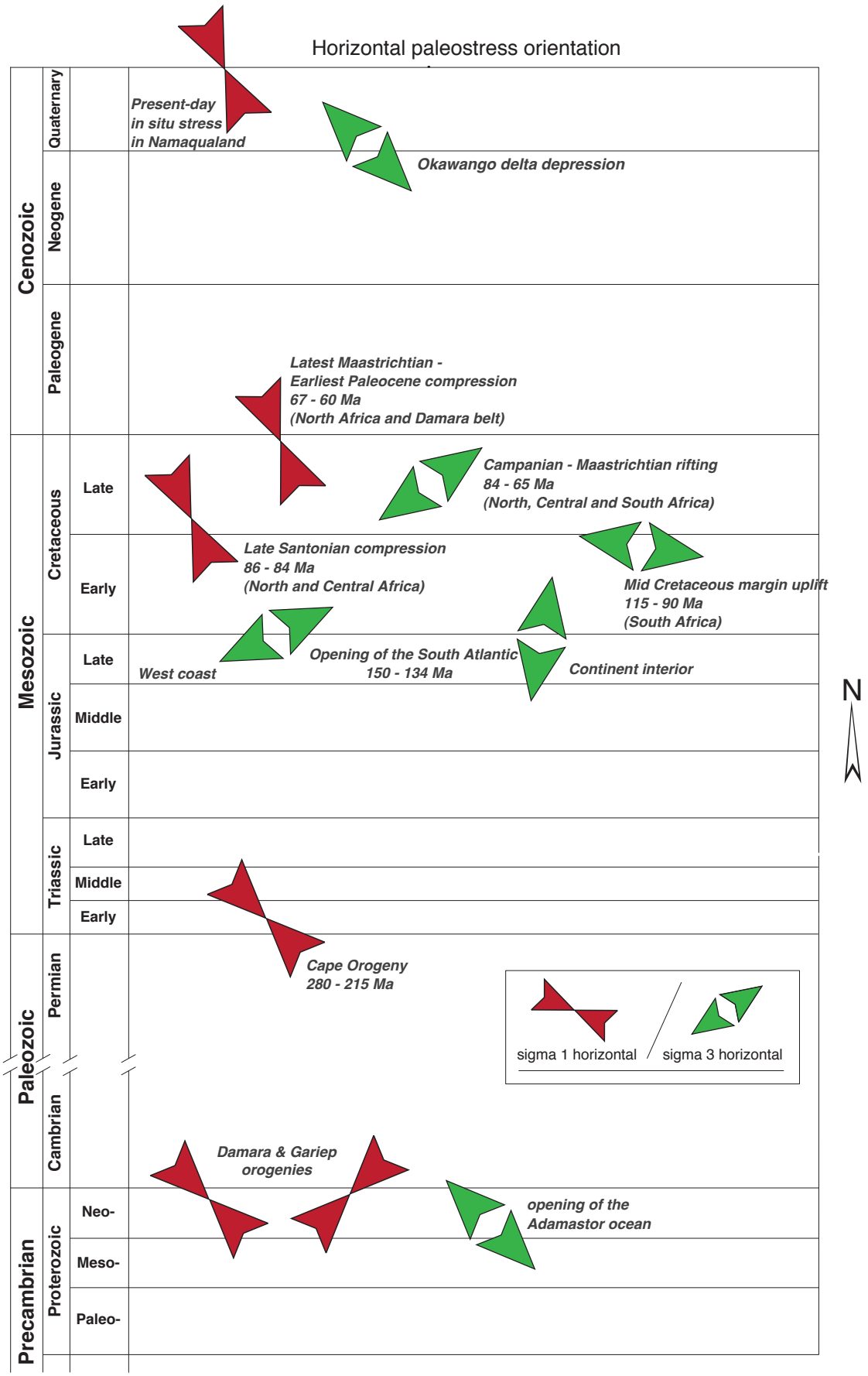


Figure 70: Diagram showing the structural history of the south-western part of the Nama Basin approximately 450 km to the south of the study area in the Zebra River Canyon. Red arrows indicate compressional settings whereas green arrows represent extensional tectonic regimes. Modified after Viola *et al.* (2012).

## 5.3 Methods

### 5.3.1 Remote sensing

The Zebra River Canyon system was placed into its structural regional context by means of a basic remote sensing study using Google Earth imagery and digitising lineaments and fracture data from the 1:250 000 geological map of Mariental (Schalk and Germs, 1980). Lineaments on the virtual globe of Google Earth were mapped onscreen without applying a minimum length rule. The excellent high resolution of the Google Earth images and absence of vegetation in the Zaris Mountains made it possible to trace faults (Figure 71) and as well fractures (Figure 72). A total of 278 fractures and 108 lineaments from the Mariental sheet were integrated with data collected from satellite imagery mapping (1169 fractures and 106 faults). The digitised structural features were then imported into Midland Valleys Move software in order to analyse their spatial orientation. Move is a structural modelling software, which offers a wide range of orientations analysis for surfaces and lineaments. The digitised features from the geological map were grouped according to their geological affiliation by means of placing all faults and fractures, belonging to one lithostratigraphic member in separate groups (e.g.: two groups for Hoogland member faults and fractures, respectively). All mapped Google Earth faults were put into one group. The mapped fractures of the virtual globe were summarised into 3 separate groups according to their locations. Rose diagrams for each of these groups were plotted and are attached in APPENDIX V.

It should be noted that this is a preliminary structural analysis of the area, and there was no attempt to analyse the structural history of the results of the remote sensing. The purpose of the remote sensing was to define the regional trend of faults and fractures.

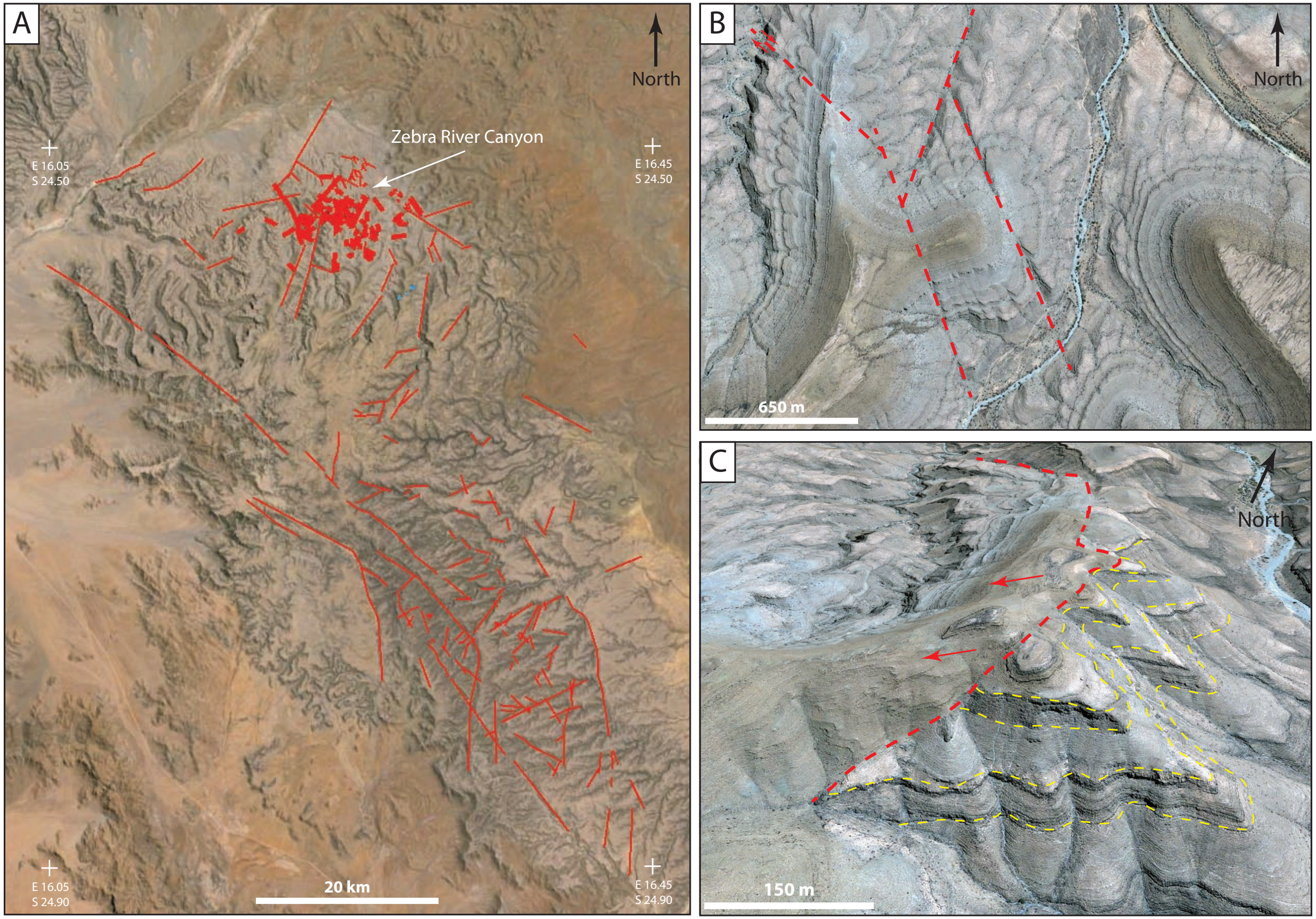


Figure 71: Google Earth images showing mapped faults. (A) A total of 106 faults were mapped on the virtual globe of Google Earth. Red lines indicate mapped faults. Note a higher density of interpreted faults in the Zebra River section. (B) The excellent quality of the Google Earth imagery and absence of vegetation made it possible to accurately map fault structures. Most of the mapped faults represent steep strike-slip faults, determined on the visible horizontal offset and absence of vertical offset. Note the dextral displacement of the upper left fault. (C) Mapped normal fault in the west of the study area. Rotating the virtual globe provides an oblique view of the Google Earth DEM and vertical fault offsets can be studied. The yellow lines indicate the upper grain-dominated intervals of OS1&2 of the Omkyk Member which are juxtaposed against the overlying Hoogland Member (western part of the fault). Horizontal offset is approximately 120 m.

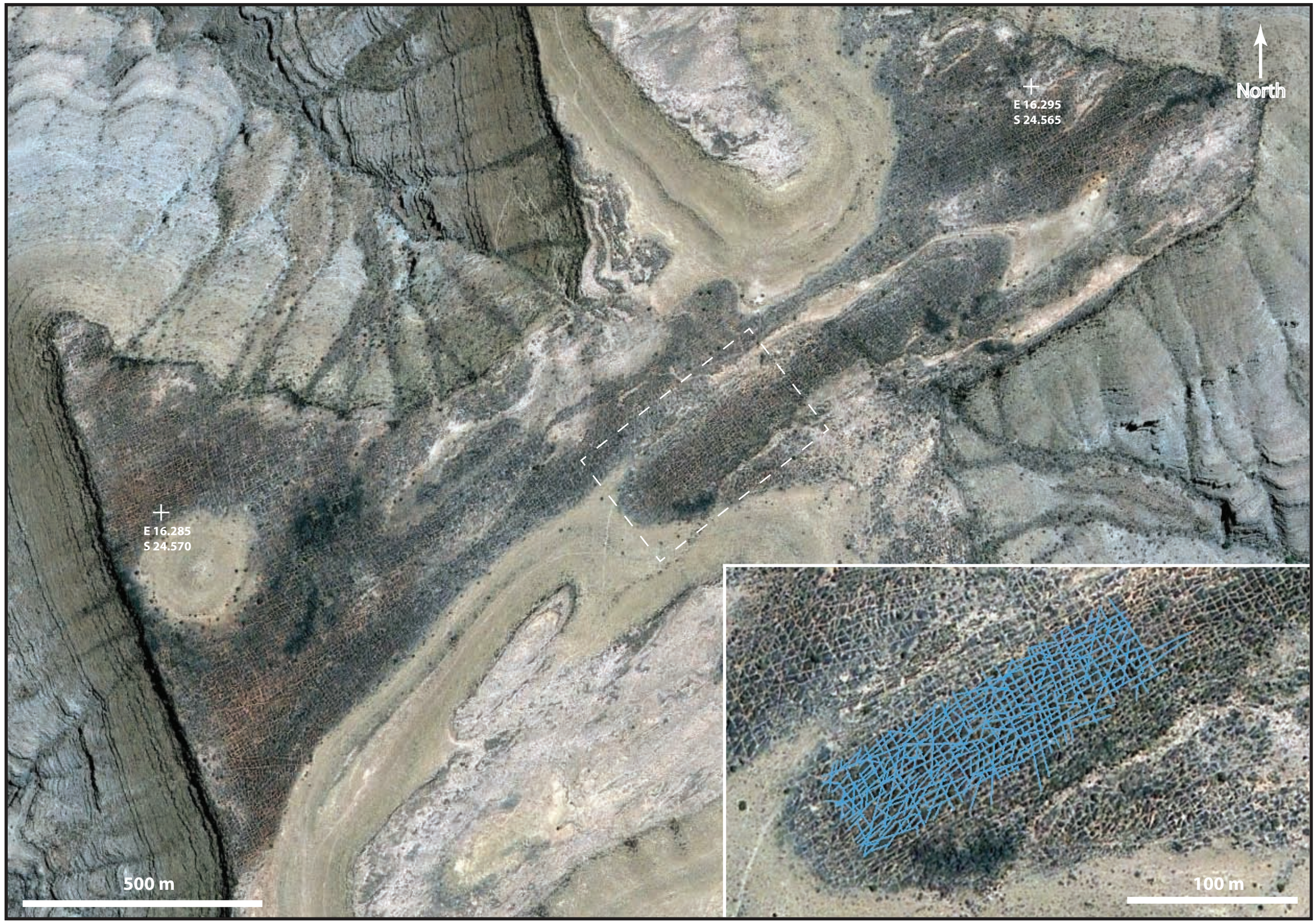


Figure 72: Google Earth image showing a present day erosional surface, exposing the OS2 Unit 5 grainstone unit. Clearly visible is the intense fracturing of the grainstones, which has been subsequently mapped onscreen. The enlarged area shows one of the mapped sections. Blue lines indicate mapped fracture traces.

### 5.3.2 Field work

At outcrop, field work focussed on the description of the fault and fracture network characteristics of the Kuibis ramp carbonates of the Omkyk Sequence 2 in the Zebra River Canyon system. The geometry, morphology and internal structure of the microbial carbonates are critical, from a structural geology perspective. Work included detailed descriptions of brittle and ductile deformation of microbialites and inter-bioherm facies. Thus, a detailed investigation of the microbial framework development and associated deformational structures was carried out. In addition to these combined structural and sedimentological observations of the microbialites, a comprehensive analysis of the structural characteristics of the carbonate system in the Zebra River Canyon was conducted. More than 500 strike and dip measurements were collected, focussed on the inter-bioherm areas and grainstone horizons. The microbial carbonates form steep almost vertical cliffs and only a few reliable field measurements could be obtained. All fault and fracture data were then plotted on stereonets. One stereoplot has been produced for each field work location within the study area. Fracture and fault planes are represented by great circles at each location. The relatively high number of visualisations was intended in order to analyse potential orientation variations with the canyon system. If not otherwise stated on the stereoplot legend, data are derived from grainstone horizons and inter-bioherm facies, respectively. A rose diagram and contour plot of the entire data-set was produced to subsequently link the observed and measured structural features to the regional trend. All stereoplots and field work locations are attached in the APPENDIX V.

### 5.3.3 Lidar survey

In order to obtain accurate fracture data from the microbialites fracture mapping was carried out on the developed virtual outcrop model of the Zebra River Canyon. Additionally, fractures in the inter-bioherm areas and grainstone horizons were mapped to complement field work data. Compare chapter 4 for scanner specification, lidar data processing and fracture mapping workflows. A total of four sections were digitally mapped: (1) inter-bioherm area (182 fractures), (2) grainstone horizon (74 fractures), (3) bioherms of Unit 2 (210 fractures) and (4) part of the biostrome in

Unit 3 (75 fractures). The contour plots of all four sections and locations are attached in the APPENDIX V.

### 5.3.4 Photomosaic interpretation

High-resolution photos were taken of selected bioherms and biostromes. The individual photographs were then merged into one photomosaic image with Adobe Photoshop. Fracture interpretation was carried out onscreen the panorama photomosaic images within Adobe Illustrator using 2D polylines. The resulting 2D fracture trace map was then imported into Move software were it was ground-truthed with the lidar datasets to obtain accurate geometries. A total of 628 fracture traces were mapped on the photomosaic. These were subsequently grouped and their cross-cutting relationships and fracture termination analysed. A simple linear fracture-density analysis (number of fractures per unit length) was conducted by applying a horizontal scanline (length 101 m) on the spatially referenced fracture traces.

## 5.4 Results

### 5.4.1 Remote sensing

Two main lineament trends were identified from the Mariental sheet, which are to the NNE-SSW and SSE-NNW. Two sub-sets have an orientation to NE-SW and SW-NW. The satellite image interpretations yield the same four main orientations. The absence of vegetation and the near horizontal bedding of the Nama Group in the study area, allowed the majority of the mapped lineaments to be identified as strike-slip faults (no visible vertical offset on the satellite images, (see Figure 71.A)) A few normal faults could be identified based on the visible vertical offset of the sub-horizontal bedding in the area. The normal fault in the west of the study area shows an offset of about 120 m of the Hoogland Member against the Omkyk Member and can easily be recognised on the satellite imagery (Figure 71.C). The analysis of the fracture traces from the satellite image interpretation show that the main fracture sets are orthogonal, and strike NE-SW and NW-SE, with subordinate sets trending N-S and SSE-NNW (Figure 72). Digitised fractures of the Hoogland Member from the geological map show a predominant direction to SSE-NNW and N-S.

### 5.4.2 Field work data

#### 5.4.2.1 Faults

In the study area, two types of faults have been identified: (1) steep dipping (80º-90º) strike-slip faults, which constitute the majority of the observed faults and (2) one normal fault in the west of the study area. Strike slip-faults are characterised by sub-vertical to vertical dips, without any vertical offset. The horizontal translation distances could not be measured owing to the near horizontal bedding of the Kuibis ramp carbonates. The core zones of faults show intense deformation, represented by fault breccia and fault gouge. Later cement typically sealed the fault cores (Figure 73.A). Common features near to the faults in mud and shale beds are striated surfaces (Figure 73.B) In the damage zones to either side of the fault cores, in the vicinity of the faults (up to about 4-5 m) intensive small-scaled fracturing, vein development and subsequent cement occurs (Figure 73.C)

#### 5.4.2.2 Field work fracture data

The field analyses revealed two categories of fractures - primary and secondary - defined by their cross-cutting relationships. Primary fractures are only found in the microbial carbonates and crosscut entire bioherms and biostromes, as well as shale and mud-horizons within the microbialites. The fractures are typically open (cm-dm), filled with brecciated inter-column material, cataclastic material and cement. They show no consistent orientation and the dip is primarily steep to vertical. In areas above topographic highs (e.g.: stacked bioherms) primary fractures are inclined towards the antecedent topography, resulting in medium to high dip-angles (60º-85º). Centimetre to decimetre horizontal offset of fractures can be observed where fractures cross cut mud and shale horizons (Figure 74). Decimetre wide vugs and dissolution cavities are common where primary fractures crosscut shale and mud beds (Figure 75). Prominent examples of primary fractures were observed in stacked bioherm complexes and in biostrome areas overlying inter-bioherm facies. In these cases, the fractures are inclined towards the underlying bioherm and inter-bioherm facies zones and crosscut the entire microbial carbonates.

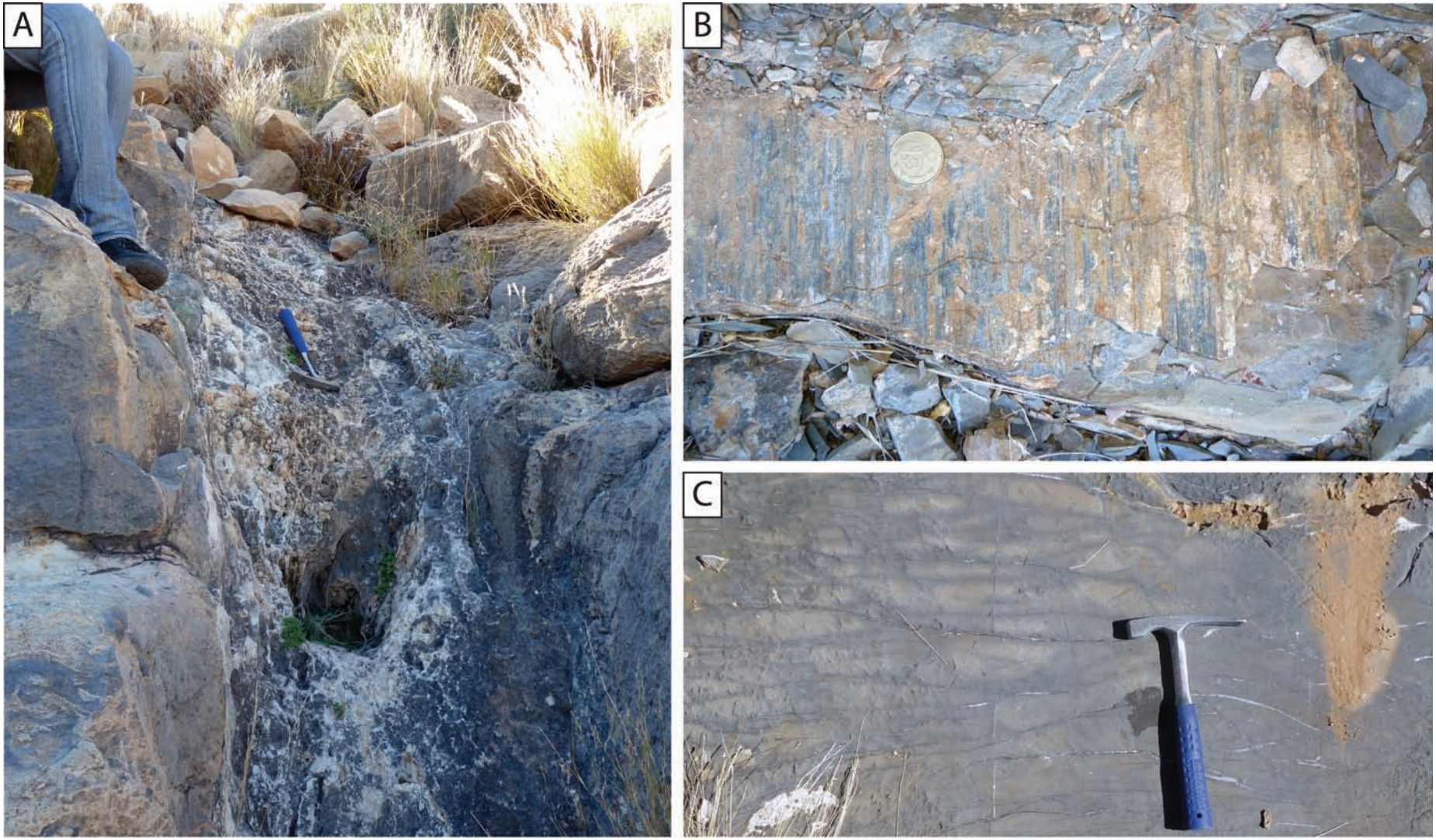


Figure 73: (A) Photograph showing the core of a strike-slip fault. Note the intense cementation. (B) Striated surface near the fault. (C) Grainstone bed showing intense fracturing and veining in the close vicinity of strike-slip faults.

A total of nine secondary fracture sets could be identified which are grouped according to four main directions: (1) north-south; (2) northeast-southwest; (3) east-west and (4) southeast-northwest. All fractures are vertical to sub-vertical with dip of 80°-90° (Table 1). Plumose structures could be identified on several fracture surfaces indicating that these fractures are open-mode joints (Figure 76.A). The majority of the fractures are however shear fractures. On several occasion, both dextral and sinistral relative displacement directions were observed. The amount of displacement is typically a few centimetres. Common features of shear fractures are horsetail and splay structures at fracture terminations (Figure 76.B). No dependency between the nature of the fracture as joint or shear fracture and the four main directions has been observed. On the contrary, shear as well open-mode joints were observed in the same fracture-set, indicating reactivation of pre-existing weaknesses.

The age and *relative* age of the individual secondary fracture sets is problematic owing to numerous tectonic events and likely intervals of reactivation throughout the Phanerozoic (Viola *et al.*, 2012). Furthermore, a detailed analysis and interpretation of the structural history, solely based on fracture data from a relatively small area compared to the size of the Zaris sub-basin is not possible. Additional regional structural mapping has to be carried out to establish a robust structural evolution. This was, however, outside the scope of this research project.

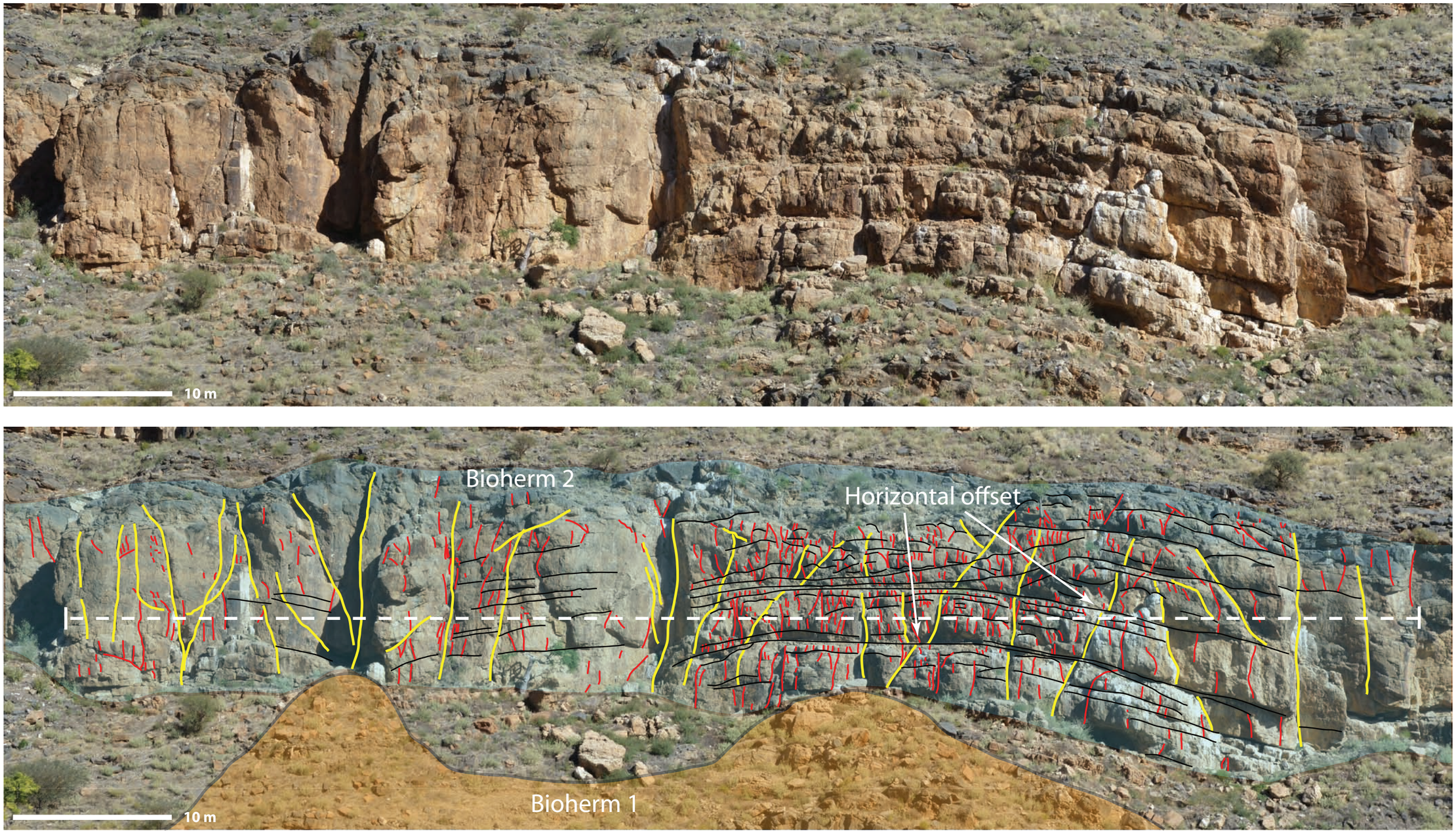


Figure 74: Photomosaic of a composite bioherm (upper image) in OS2 Unit 2 and with interpretations (lower image). Note the stacked bioherm geometry. Yellow lines indicate primary fractures, red are secondary fractures and black horizontal lines are mapped mud and shale beds. Note that primary fractures crosscut the entire bioherm structure and show a vertical offset at shale and mud beds. White dotted line represents location of the scanline.


Figure 75: Outcrop photomosaic (upper image) and interpretation (lower image) of a stacked bioherm complex in OS2 Unit 2. See description of Figure 74 for legend. Note the primary fracture development directly above the underlying bioherm structure of unit 1 and within the merging zones.

Nevertheless, two categories of secondary fracture sets could be identified: (1) through-going fractures (5-20 m in height), which crosscut several bedding planes and (2) strata-bound fractures, which terminate at bedding planes and at fracture surfaces of category one (see Table 1 and Figure 76**.**C). It is therefore argued that fractures of category (1) are the older, since fracture planes of category two fractures abut at fracture surfaces of category one.

| **Fracture Set** | **Orientation (strike)** | **Category** |
|---|---|---|
| Fracture Set 1 | ~ 5° | 1 |
| Fracture Set 2 | ~ 30° | 2 |
| Fracture Set 3 | ~ 45°-50° | 1 |
| Fracture Set 4 | ~ 75° | 2 |
| Fracture Set 5 | ~ 90° | 2 |
| Fracture Set 6 | ~ 110° | 2 |
| Fracture Set 7 | ~ 135° | 1 |
| Fracture Set 8 | ~ 155° | 1 |
| Fracture Set 9 | ~ 165°-170° | 2 |

Table 1: Identified fracture sets with average strike direction and grouping

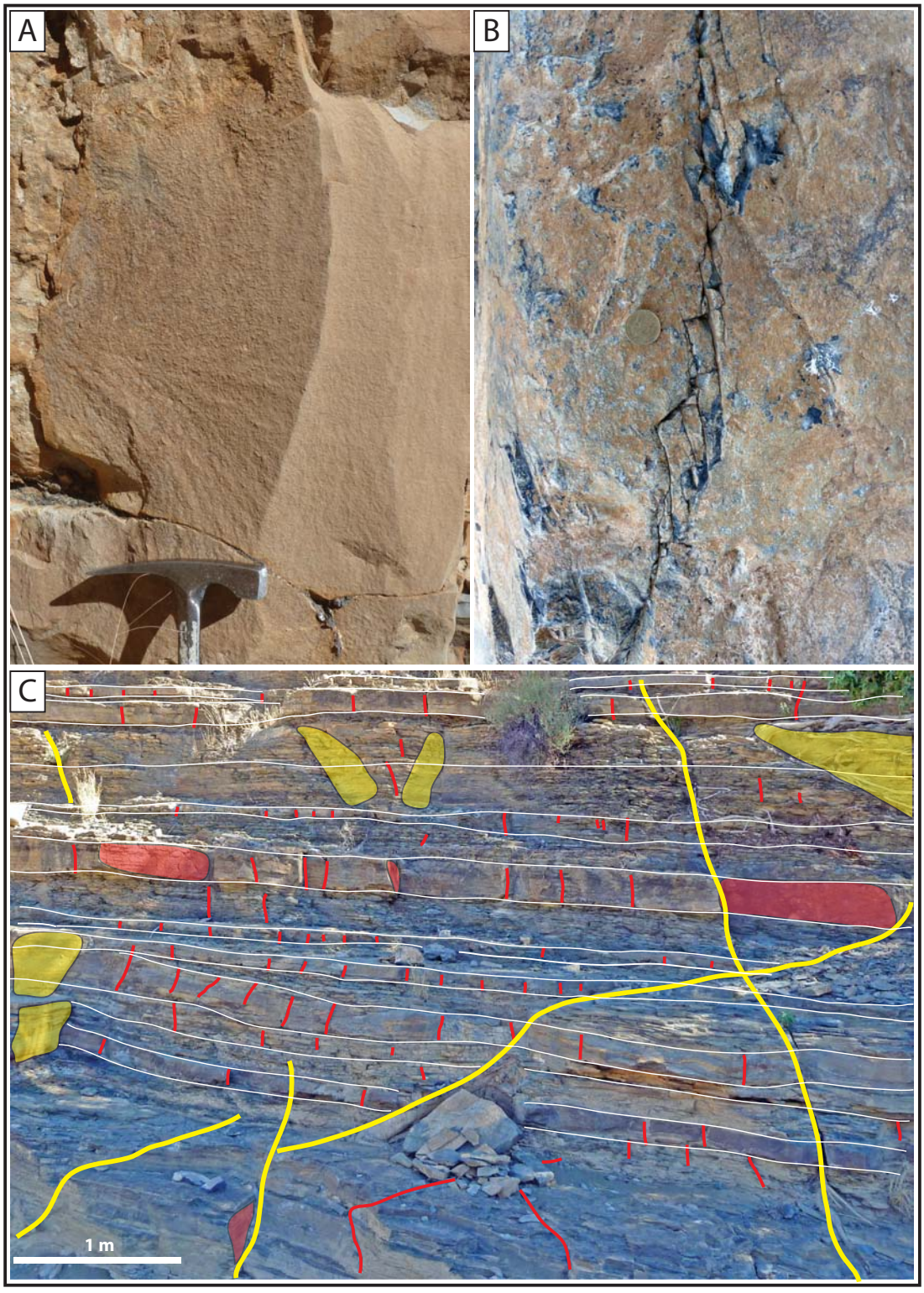


Figure 76: (A) Photograph showing a joint with plumose structure in a dolomitised grainstone. (B) Photograph of horsetailing at the end of a shear fracture. Photograph of an inter-bioherm area with interpreted secondary fractures. Yellow fracture traces correspond to category 1 and red traces to category 2 fracture sets. Note that the category 2 fractures are stratabound, whereas category 1 fractures cross-cut several bedding planes.

#### 5.4.2.3 Lidar fracture data

Lidar fracture mapping has been carried out at two lidar scan positions and fractures were mapped in the inter-bioherm facies, bioherm and biostrome horizon and in the grainstone horizon of Unit 4-5. All nine fracture sets from the field observation were identified with the lidar interpretation in the inter-bioherm area at locations C and D (see map in the APPENDIX V). At locations E, F, G only five of the fracture sets could be identified. The reason for that is most likely the lower resolution (10 cm point cloud spacing to 2 cm spacing in the inter-bioherm area of digital outcrop model) of the virtual outcrop model. Primary fractures were detected in the bioherm and biostrome horizon (note the lower dip angles in the contour plots of the bioherm and biostrome in the APPENDIX V). No consistent orientation of primary fractures in the microbial carbonates is apparent.

### 5.4.3 Photomosaic interpretation

Primary and secondary fractures have been identified on the photomosaic interpretation (Figure 74). A distinct variation in secondary fracture abundance occurs: a higher density of secondary fractures is noted (1) in stacked bioherm complexes and (2) where several mud and shale beds are present within the mound structure (Figure 74). In the case of the latter, secondary fracture termination occurs at shale horizons. In order to quantify relative fracture abundance, fractures were ground-truthed with the virtual outcrop model and a scanline analysis was carried out (see Figure 74 for scanline location). The total fracture density of the entire composite bioherm is 0.664 fractures/m whereas the density in the stacked bioherm interval with abundant shale and mud beds is almost double with 1.155 fractures/m.

### 5.4.4 Competency of microbial carbonates

From a structural perspective, an understanding of the external morphology and internal structure of thrombolite-stromatolite bioherms and biostromes is crucial as a means of understanding brittle and ductile deformation and the development of complex fracture patterns within the microbialites.

The structural behaviour of the microbialites is predominately affected by the geometry of the microbial framework. Bioherms and biostromes are internally heterogeneous and the microbial framework is prone to early deformation due to internal weakness. Furthermore, the stacking patterns of the microbialites affect the

early deformation. This is documented in two situations: (1) where a biostrome overlies bioherms and (2) in stacked bioherm complexes. In the first case prominent features within the biostrome are sinkhole-like structures (Figure 77). The underlying mounds are less compressible than the inter-bioherm sediments during compaction resulting in deformed zones in the biostrome over inter-bioherm facies. These areas are characterised by increased primary fracturing, orientated towards the depression, and rotated thrombolite blocks and columns (Figure 77).

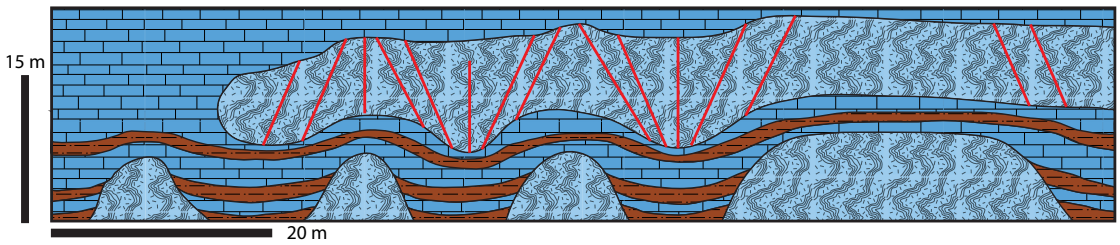


Figure 77: Cartoon illustrating primary fracture development in a biostrome overlying bioherm. See text for explanation.

In the second case of stacked bioherms, an increased primary fracturing and deformation is apparent in the overgrowing bioherm (Figure 78.A-B). Dissecting open-mode fractures are orientated towards the top of the underlying antecedent topographic highs. The contact zones between the mounds show intense deformation, such as fracturing and folding (Figure 78.A). An additional zone of deformation occurs on the flanks of the stacked mounds where they overly inter-bioherm facies, represented by vertical to sub-vertical primary fractures in the bioherms (Figure 78.B-C) and folding around small-scaled thrombolite columns in the inter-bioherm facies.

Brittle and ductile deformation structures characterise the internal disintegration of the microbial framework. There is a distinct difference in the competency of the various microbial growth forms. Isolated, massive thrombolite columns and domes associated with mud-dominated facies are competent whereas fine-scaled columns tend to have an incompetent behaviour (Figure 79.A-D).

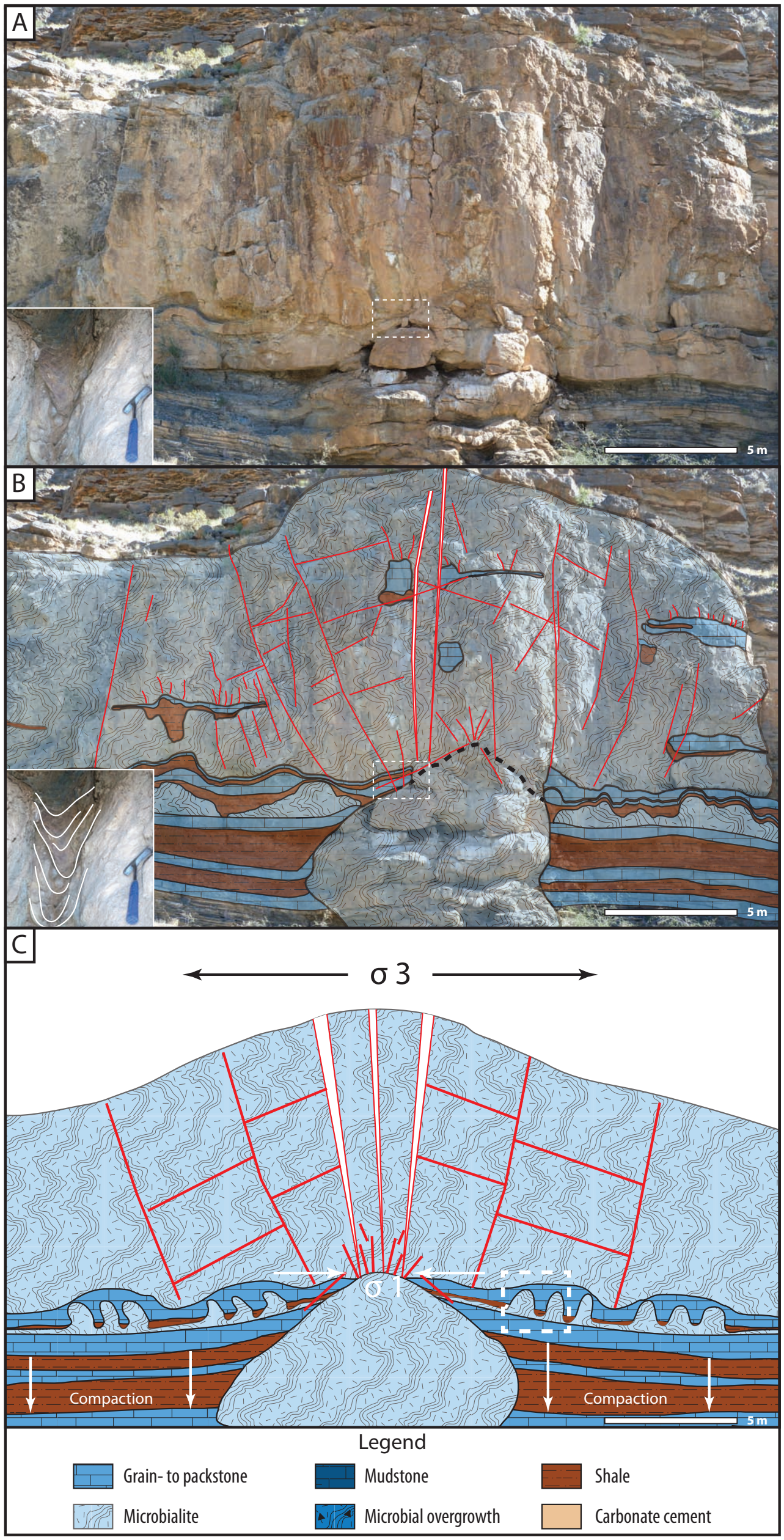


Figure 78: (A) Outcrop photo and interpretation (B) of a stacked bioherm structure in Unit 1 and 2: Note the mapped sediment pockets within the mound structure. The black dotted line indicates the upper margin of the mound structure originated in Unit 1. Note the first lateral spreading of the microbialites near the top of the underlying mound structure, which gets terminated by shale input. Red lines are mapped fractures. Enlarged picture shows folding of fine-grained sediments at the contact zone within the stacked bioherm (white dotted rectangle indicates location). (C) Conceptual cartoon showing syn-depositional fracture development due to differential compaction and the formation of antecedent topographic highs. White rectangle indicates the location of Figure 79.C. See text for discussion. Legend for figures 77, 79 and 82.

Differentiation between isolated massive domes and inter-column sediments reveals that the latter typically drape the thrombolite dome topography, thicken laterally into it, and onlap the dome margins (Figure 79.C-D). Many of the thrombolites exhibit column structures oriented sub-normal to bedding, which show evidence of brittle deformation. Figure 79.A and B show broken and rotated thrombolite columns within a bioherm, forming thrombolite column fold structures. A consistent inclination or trend of these folds has not been observed. To the contrary, photomosaic interpretation of a bioherm in Unit 2 shows that different fold directions occur within one mound and are preferentially found above shale and mud beds (Figure 80).

The thicknesses of shale and mud beds can reach up to several cm and are the lateral equivalents of mud-dominated inter-bioherm sediments. They are characterised by stylolites with several cm of amplitude. Small-scale fold structures are common within the shale and mud beds, indicating displacement along these gliding horizons (Figure 81). Primary open-mode fractures crosscut these shale beds whereas secondary fractures terminate. A sub-horizontal offset of primary fractures, ranging from several cm to a few dm, at these beds occurs. This demonstrates that gliding along the shale beds, indicated by the fold structures, happened after primary fracture development.

Sedimentary dykes or open-mode fractures are common throughout the microbial carbonates (Figure 82). The dykes are filled with brecciated material of inter-bioherm sediments and marine cements. At several locations microbial overgrowths around and between clasts in the dykes were observed. The overgrowth occurs as laminated microbial fabric, characterised by a thin-layered stromatolitic to thrombolitic texture around clasts, growing into the cavities of the dyke (Figure 82.A-D). Note the white arrows in Figure 82.C and the white lines in Figure 82.D indicating the microbialites**.** This indicates that the sedimentary dykes were injected in an actively depositing carbonate platform. In addition at least three generations of sedimentary dykes can be differentiated. Figure 82.E shows an inter-column fill area with a sequence of early fracture development. Furthermore, the presence of stylolites, cross-cutting the open-mode joints indicate that fracture development occurred during earliest stages and before burial of the carbonate strata. The overgrowth is followed by a thin layer of dark dolomitic rim cement and blocky marine calcite cement, filling up the remaining cavities.

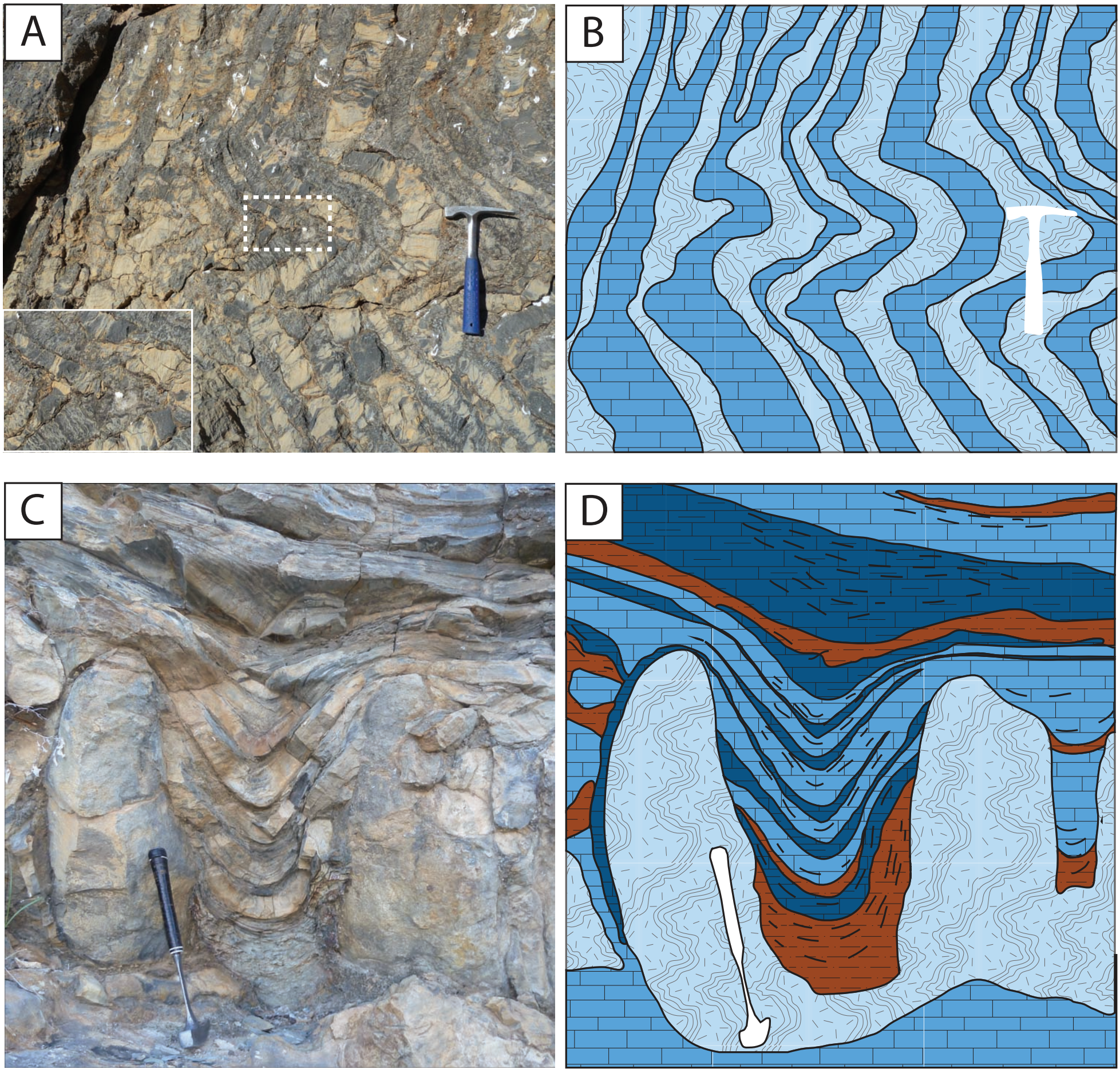


Figure 79: (A) Outcrop photo showing brittle deformation of microbial carbonates. Note broken and rotated small-scale thrombolitic columns. Enlarged section of outcrop photo shows detailed view of the brittle deformation. White dotted rectangle shows size and location of enlarged section. Geological hammer for scale. (B) Redrawn structures of outcrop photo. Geological hammer for scale. (C) Outcrop photo of syn-depositional deformation around massive thrombolite columns. Note the ‘wrapping around’ of inter-column sediment layers forming inter-column folds. (D) Redrawn structures of outcrop photo. Geological hammer for scale.


Figure 80: Outcrop photomosaic of a bioherm in Unit 2 with photo interpretation. White lines indicate centre of thrombolite and stromatolite columns. Note different orientation of column-folds at the top of the mound. Black lines are shale and mud beds, yellow lines are primary fractures and red lines are secondary fractures.


Figure 81: Outcrop photograph with redrawn small-scale fold within a mud and shale bed, crosscutting a bioherm.

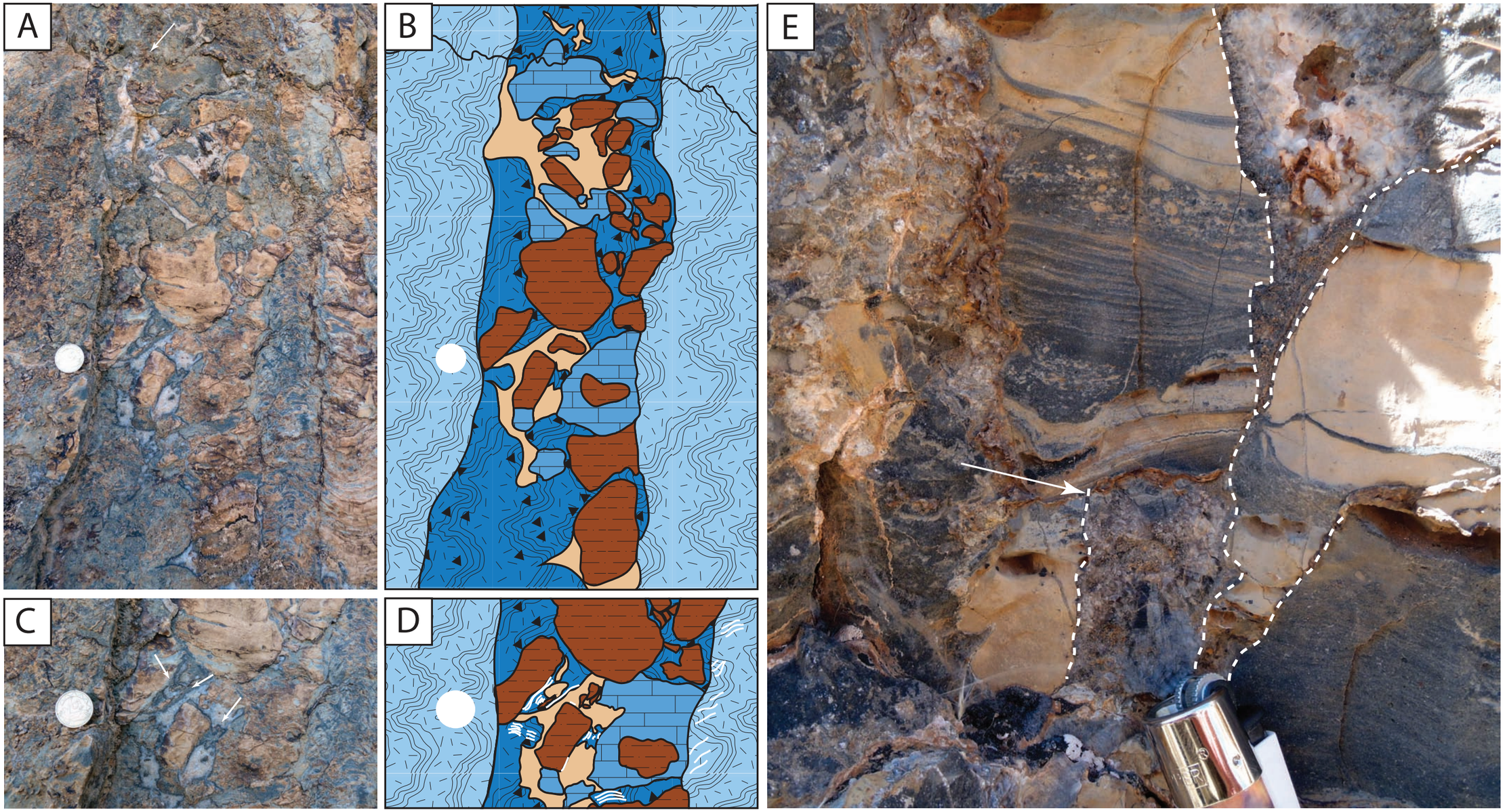


Figure 82: Sedimentary dykes observed in the microbial carbonates. (A) Outcrop photo of an open mode fracture in Bioherm 2 and (B) redrawn structures. The sedimentary dyke is filled with mudstone and grain- to packstone clasts with microbial over-growth, surrounded by a thin dark layer of dolomite cement and blocky white calcite cement. Note the stylolite at the top of the image, crosscutting the entire dyke. Coin for scale. (C&D): Zoomed in section of figure A. Note the microbial overgrowth indicated by arrows in (C) and white lines in (D). (E) Outcrop photo of a sequence of syn-sedimentary dykes in Bioherm 2. The sedimentary dykes are outlined by white dotted lines. Note the inter-column sediments capping the lower dyke (white arrow) showcasing that fracture development occurred syn-depositional. Lighter for scale.

## 5.5 Discussion

### 5.5.1 Regional trend

Two main orientations of structural features have been identified from the combined results of remote sensing analyses and field work. The predominant orientations in the north-western part of the Zaris sub-basin are to the NE-SW and NW-SE. The majority of the mapped lineaments are steep, sub-vertical strike-slip faults. Only a few normal faults could be identified from the remote sensing analyses and one during field work. All secondary fracture sets are sub-vertical and show the same main orientations with subsets to N-S and E-W, respectively.

The recent study by Viola *et al.* (2012), focussing on the tectonic brittle evolution of the Namaqualand metamorphic complex at the south-western edge of the Nama Basin, is the only available reference in order to tie the observation into the regional framework. Recognising that the Zebra River study area is approximately 450 km to the north of the Namaqualand, the study of Viola *et al.* (2012) provides evidence that the north-western edge of the Nama Basin is most likely to have undergone a similar long lived structural history. However it is not possible at the moment to link individual faults or fracture sets in the Zebra River area to individual tectonic events in SW-Africa. The purpose of the remote study and fracture analyses was not to unravel the structural history of the Zaris sub-basin, but rather to provide a basis for the differentiation of primary and secondary fractures. Nevertheless, as the results show, all sub-vertical secondary fracture sets with their consistent orientations and dip angles can be tentatively linked to more regionally recognisable deformational events in SW-Africa. The few normal faults that are recognised are most likely linked to the opening of the South-Atlantic and/or regional uplift.

By clear contrast, primary fractures with their lower dip angles, random orientations and restriction to microbialites cannot be linked to the regional structural events. A key observation is the recognition of microbial overgrowth in open mode fractures, which illustrates early development of primary fractures during deposition. Furthermore, the observation of at least three generations of sedimentary dykes, separated by inter-column sediments clearly suggests that fracture development occurred during platform evolution. Additionally, primary fractures crosscut and are offset at shale and mud beds within the microbialites. This indicates that primary

fracture development predates: (1) the bedding plane gliding between the beds and (2) the evolution of mechanical boundaries within the bioherm where secondary fractures abut. Evidence of syn-depositional deformation in the microbialites of the Omkyk Member has been reported by the occurrence of the sponge like metazoan *Namapoikia rietoogenesis,* which preferentially grew in the protection of open-mode fractures (Wood *et al.*, 2002). Furthermore, evidence of early brittle deformation of thrombolite columns and block rotation in the Zebra River area was reported by Johnson & Grotzinger (2006). Korn & Martin (1959) reported syn-sedimentary faulting and fracturing from the Kanies Member in the north-western part of the Nama Basin. These reports substantiate the observations presented herein and it is therefore argued that primary fractures are syn-depositional and are consequently the oldest structural features observed in the Zebra River area.

### 5.5.2 Syn-depositional fracturing in microbialites

Syn-depositional deformation and fracture development in carbonates is increasingly recognised as an important process (Berra and Carminati, 2012; Boro *et al.*, 2012; Cozzi, 2000; Frost and Kerans, 2009; Frost and Kerans, 2010; Hunt *et al.*, 2003; Kosa and Hunt, 2005; Kosa and Hunt, 2006; McNeill and Eberli, 2012; Underwood *et al.*, 2003). Syn-depositional fracture development in carbonates has been categorised into 3 groups: (1) gravitationally controlled fractures, (2) antecedent topography controlled fractures and (3) tectonically controlled fractures (Frost, 2007; Guidry *et al.*, 2007). Mechanisms for gravitationally controlled fractures include: overstepping of platform margins and related instabilities, basin ward tilting due to compaction of basinal sediments and sliding along dipping bedding planes. Antecedent topography-related fractures originate through differential compaction of slope and basinal sediments. The resulting deformational features have been described where early-cemented strata are deformed over rigid topographic highs such as platform escarpments, bioherm complexes, drowned reef spines and crystalline basement highs. Tectonically-controlled syn-depositional fractures are related to local faulting and folding processes and are genetically related to the local stress field. An important difference between these three subgroups is that the main driver for gravitational and antecedent topography related fractures is of *intrinsic* nature. This means that fractures in response to the particular architecture and

geometry of the carbonates whereas tectonically related fractures need an *extrinsic* force in order to develop.

A significant factor for all three syn-depositional fracture groups is early cementation and lithification of carbonate sediments, which enables the brittle deformation of carbonates from early stages onward. Microbial carbonates form by definition through trapping and binding of sediment grains and through the precipitation of calcium carbonate (Dupraz *et al.*, 2009; Dupraz and Visscher, 2005; Fairchild, 1991; Nose *et al.*, 2006; Riding, 2000; Riding, 2008; Russo *et al.*, 2006). The precipitation strengthens the microbial deposit by providing a rigid structure that allows the microbial community to keep up with the surrounding sedimentation. Lithification occurs *instantly* in microbial carbonates, and hence typically before that in surrounding sediments. Thus, an early-lithified, rigid microbial framework is established. From the outcrop-scale to the micro-scale, this becomes prone to internal weaknesses and failure owing to later compaction of inter-bioherm sediments, along with sediments trapped inside bioherms within sediment pockets.

As described in chapter 3, bioherms from the Zebra River area have previously been described as simple hemispheres (Adams *et al.*, 2005). However, the present author's results and photomosaic interpretations suggest that this is an over-simplification. In particular, syn-depositional fracturing, which develops in two cases due to intrinsic body forces, an extra "layer" of geometrical complexity is revealed. Therefore the complex geometries of merged and composite bioherms have a direct effect on syn-depositional fracture development in the microbialites. The internal architecture of the mounds is characterised by a change of the microbial growth form in a sequence stratigraphic context. Thus, a single bioherm is built up by a sequence of changing microbial structures, which in turn exhibit different mechanical behaviours.

Therefore, within merged bioherms and composite bioherms, both ductile and brittle deformation occurs. Folds of mud-dominated sediments around domes and goblet-shaped thrombolites demonstrate ductile deformation. The 'wrapping' of shale and mud layers around microbial build-ups has been reported and interpreted as a syn-depositional feature (Goldhammer et al., 1985). The differential compaction and syn-depositional deformation of the aggradational microbial system affects in turn the coalesced microbial bodies. The thrombolite domes form topographic highs within the mounds during compaction, which causes instability and fracturing in the

flanks of the overgrowing coalesced microbialites due to differential compaction. Sediment pockets within the coalesced column bodies are a further source of internal instability resulting in increased fracture zones and rotated columns in the overlying strata. Figure 83 schematically illustrates the breakdown of a composite bioherm structure due syn-depositional deformation.

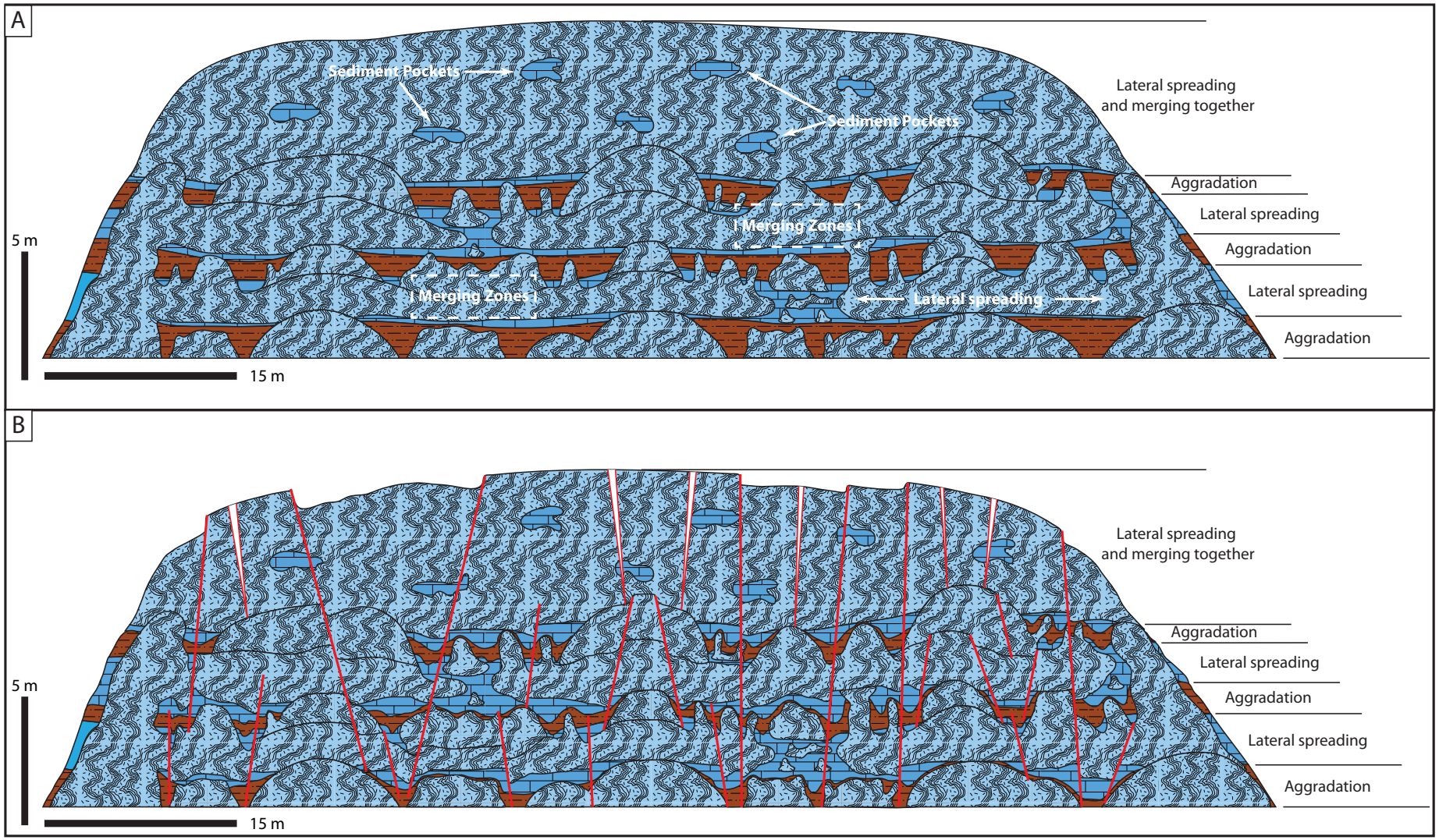


Figure 83: Cartoon illustrating the syn-depositional deformation of a composite bioherm. (A) Initial bioherm geometry. (B) Syn-depositional deformation. White filled fractures indicate open-mode fractures over rigid, antecedent topographies. See text for discussion.

On the larger scale, antecedent topography-related syn-depositional fractures can be observed at two different situations in the sequence: (1) within bioherms of Unit 2 which started to grow over bioherms from Unit 1 (stacked bioherms) and (2) in biostromes in Unit 3 where the biostrome is overlying bioherm structures. In the first case of stacked bioherms, differential compaction of surrounding and underlying sediments leads to syn-depositional deformation (Figure 78.B). Johnson & Grotzinger (2006) measured in detail the inter-bioherm sediments and the contemporaneous bioherm layers at the location of Figure 78. A total compaction rate of more than 40% was calculated for the inter-bioherm sediments and only ~10% in the bioherm itself. In consequence of this differential compaction, the mound is affected by a horizontal σ3 at the upper part of the structure and a compressional deformation (local σ1) at the contact zone. Cross-cutting, syn-depositional opening-mode fractures develop due to this flexural stress pattern and are inclined towards the underlying bioherm-top (Figure 78.A-B). The same process can also be seen in composite bioherms where only a part of these amalgamated structures are above bioherms (see Figure 74). In addition to that, mud and shale beds within composite bioherms act as gliding horizons as indicated by the small-scaled folds. The gliding follows the local topography as indicated by the lack of trend of the folds of the deformed and broken microbial columns. This eventually leads to the gravitational breakdown of entire composite-bioherm bodies during compaction. In the case of biostromes overlying bioherms, primary fracture development and block rotation is observed in sinkhole-like structures (Figure 77). Since the inter-bioherm facies compacts more than the rigid microbial mounds, the bioherms form antecedent highs.

The features described above are clearly related to gravitationally induced deformation for two reasons: (1) a gravitational driven breakdown of the rigid early-cemented microbial framework and (2) breakdown of bioherms through the development of gliding horizons in the mud and shale beds. This also explains why there is no consistent orientation of primary fractures because primary fracture development follows internal architecture and local topographic morphology. Both features are intrinsic to the microbial system and therefore randomly orientated. However, it should be noted here that there is no clear separation between the gravitational and antecedent topographic-high controlled fractures since they influence and condition each other. For instance, the differential compaction in a

stacked bioherm causes space in the inter-bioherm facies, which in turn enables the bedding plane gliding at the shale horizons. It can be regarded as a feedback loop where one event causes the other and vice versa.

The temporal evolution of mechanical layering in carbonates is also important (Frost and Kerans, 2010). A mechanical layer is generally defined as unit with same mechanical properties (for instance rigidity) and do not necessarily correlate with lithological boundaries or bedding planes. These mechanical boundaries develop over time and fractures generally terminate at these boundaries. During early lithification and burial in particular, boundaries can shift (see Figure 84). This temporal evolution of mechanical layering is apparent in Bioherm 2. Early syn-depositional fractures crosscut entire mounds in various directions and secondary post-depositional fractures terminate at the shale and mud beds within the mounds (Figure 74 & Figure 75). The shale beds therefore influence the mechanical layer. This implies that the bioherms acted as one mechanical layer during early lithification and primary fracture development. The development of multiple mechanical layers in the mounds, bounded by shale and mud beds, evolved at a later stage.

Vugs occur preferentially at the intersections of primary fractures and are here interpreted as dissolution features. The importance of syn-depositional fracture networks, contributing to an early fluid flow system is increasingly recognised (Frost *et al.*, 2012; Guidry *et al.*, 2007; Ortega *et al.*, 2010) and in particular for carbonate reservoirs (Carpenter *et al.*, 2006; Collins *et al.*, 2006; Narr *et al.*, 2004). Furthermore, it has been shown that this type of network can act as a long-lived conduit for diagenetic fluids and is likely to be reactivated during regional tectonic events (Budd *et al.*, 2013). This observation has important implications for the sub-surface flow behaviour of microbial carbonates. Microbial carbonate systems are likely to be affected by intense early fracture network development and therefore this network can potentially significantly enhance or undermine fluid flow.

It is intriguing that only the microbialites and the carbonates in close vicinity of the microbialites in the study area are affected by selective dolomitisation. The syn-depositional fractures might have provided an early pathway for dolomitising fluids within the microbial carbonates. Thus, only bioherms, biostromes and surrounding strata show dolomitisation but not the inter-bioherm and grainstone facies. However, this hypothesis requires confirmation by detailed diagenetic studies of the Omkyk

Member. Currently, therefore, microbial dolomitisation cannot be discounted (Vasconcelos *et al.*, 2006).

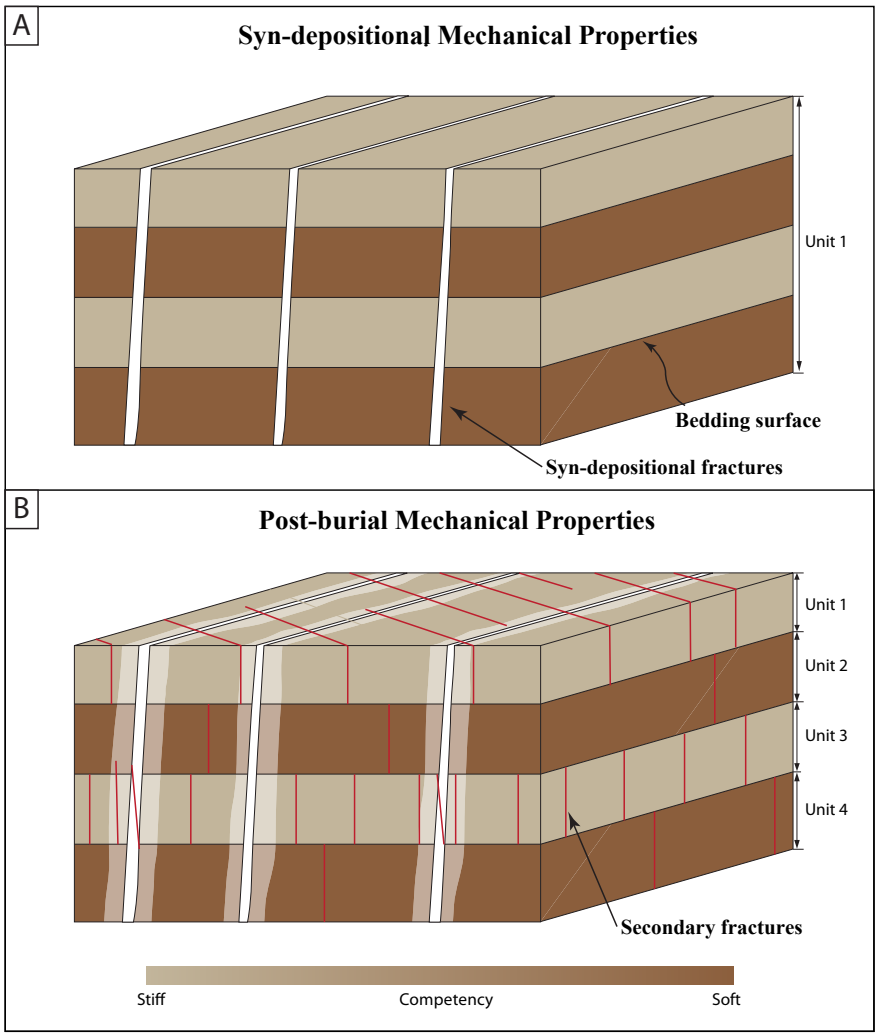


Figure 84: Evolution of mechanical layering. (A) Fracture development during deposition. Note that syn-depositional fractures crosscut multiple bedding planes. The whole system is acting as one mechanical layer. (B) After burial and the evolution of additional mechanical layers, fracture termination preferentially occurs at the mechanical boundaries. Modified after Frost (2009).

## 5.6 Chapter summary

This chapter presented new data and interpretation of the structural characteristics of the Kuibis ramp carbonates at the north-western edge of the Nama Basin, Namibia. Findings are based on detailed field observation and measurements of the Omkyk carbonate sequence in the Zebra River Canyon, dovetailed with an extensive remote-sensing dataset. Whilst an attempt was made to analyse the structural history of the area, it is emphasised that the paucity of published data, precludes putting the results into a regional tectonic context. Nevertheless, the research presented in this chapter

has progressed our understanding of microbial carbonate systems from a structural point of view. The main outcomes are as follows:

- An important syn-depositional phase of structure development is recognised. A primary fracture system developed during the early stages of lithification, as a result of differential compaction and formation of antecedent topographic highs. The primary fractures are confined to the microbialites and immediately adjacent and supra-adjacent packages. Large dissolution vugs at intersections of primary fractures and extensive cementation demonstrate that this fracture network acted as an early fluid flow system. Primary fractures formed due to intrinsic body forces and internal weakness and geometries of the microbial system. Thus, no external driver is needed.
- These observations have implications for reservoir characterisation in microbial carbonates because primary, open-mode fractures have the potential to significantly enhance reservoir performance through providing preferred fluid flow pathways. Furthermore, the syn-depositional fractures are most likely to be reactivated during later deformation. Additionally, the syn-depositional fracture network develops separately from the regional tectonic history and can be overlooked or underestimated in areas with minor or no expected fracturing. Therefore a careful characterisation of this early syn-depositional fracture system is needed in order to accurate predict fluid flow in microbial carbonate reservoirs.
- Nine sub-vertical secondary fracture sets developed during the long-lived structural evolution of the Nama Basin of more than 500 Ma. The overprint of primary and secondary fractures resulted in a complex fracture network system in the bioherms and biostromes. However, the relative age of the individual fracture sets could not be established due to the lack of published data. Future structural geology research in the north-western part of the Nama Basin should focus on establishing a robust structural history in order to stimulate further research.

# 6 Static Geocellular Reservoir Modelling

## 6.1 Introduction

This chapter summarises the methodologies and workflows used by the author to develop a geocellular analogue model based on the collected lidar data from the Zebra River sections. The overall geometry of the Omkyk Member in the Zebra River area is defined by a simple layer-cake architecture with minimal lateral and horizontal facies variations, except those shown in the bioherm horizon. Thus, the main goal and focus of the reservoir modelling part was to develop a realistic, stochastic facies model of the laterally discontinuous bioherms, with special emphasis on their shape, connectivity and spatial distribution.

The first part of this chapter deals with the development of the reservoir framework, including surface construction and subsequent reservoir gridding of the main lithological horizons. The second part focuses on the stochastic modelling of the microbial bioherms. Two different modelling approaches, numerical object-based modelling and multiple-point statics are presented and their advantages and disadvantages are discussed.

The geocellular reservoir modelling and lidar point-cloud data manipulations were carried out in collaboration with the development team of Baker Hughes JewelSuite in Delft, Netherlands. In particular, support and help to integrate lidar outcrop data into the JewelSuite platform has been provided by Erik Scheele, who is senior software developer and has more than 25 years of experience in reservoir modelling.

## 6.2 Introduction to reservoir modelling

Geocellular reservoir modelling, as a discipline in petroleum research and industry, aims to develop three-dimensional numerical models. The approach is applied either to potential hydrocarbon reservoirs in the subsurface (Mancini *et al.*, 2008; Pöppelreiter *et al.*, 2008; Seifert and Jensen, 2000) or on outcrop analogues (Adams *et al.*, 2011; Barnaby and Ward, 2007; Howell *et al.*, 2014; Lapponi *et al.*, 2011;

Lipinski *et al.*, 2013; Phelps and Kerans, 2007; Tomás *et al.*, 2009). Numerical reservoir modelling relies heavily on the concepts of geostatistics in order to calculate rock properties at un-sampled locations (Clayton, 2002) and a geocellular model is not a fully accurate representation of the geology in the subsurface.. The ultimate goal of a reservoir model is to accurately predict future flow performance under different boundary conditions.

The incentives for constructing a numerical reservoir model are numerous. Key aspects for the development are summarised by Clayton (2002). These are:

- To estimate the volume of hydrocarbons in place. Reservoir models form the basis for assessing the economic viability of a given, potential or producing reservoir through volumetric calculations of potential hydrocarbons in the subsurface.
- To define and simulate well locations and trajectories. Optimising well planning has the potential to reduce costs for reservoir development and production and therefore increase the economic value of the reservoir.
- To test reservoir behaviour through fluid flow simulation in order to predict reservoir performance under different production scenarios in order to estimate the recoverable amount of hydrocarbons during primary and secondary production.

The numerical geocellular model forms the basis for exploration, development and production plan decisions throughout the lifetime of a hydrocarbon reservoir in the subsurface. Despite these economical and technical tangible considerations there are profound intangible considerations incentivising the development of a numerical reservoir model. A reservoir model is essentially the end result of pulling together all available and necessary data and interpretations of geological, petrophysical and reservoir engineering data. It is therefore a database of all data from varies disciplines in one model. Additionally, hard data (core descriptions) and soft data (wireline logs, seismic surveys) are brought together to one platform and their different scales are normalised to the reservoir scale (Gilbert *et al.*, 2004). Core description and wireline logs (cm-scale) have to be up-scaled and seismic data has to be down-scaled to the grid resolution. This process of data integration facilitates the interpretation of all data sets in the same time at one platform. The end-result, the

numerical geocellular reservoir model, is a tool to focus attention to the essential unknowns and uncertainties.

Reservoir models are subdivided into two groups: *static* and *dynamic* numerical models. Static models aim to capture the reservoir architecture such as stratigraphic layering and fault networks. These framework models are then populated with geological properties such as facies distribution in order to develop accurate facies models. The final step in static reservoir modelling is the development of petrophysical models, which are constructed by using the facies models as conditioning templates, and each facies and reservoir layer is populated with *static* properties.

The term *static* properties refers to reservoir variables, which generally do not change over the lifetime of a reservoir. The two main static characteristics of interest are porosity and permeability, which have the main influence on reservoir fluid flow (Lucia, 2007a). Static models form the basis for dynamic modelling and the static models have to be adapted to the specification of dynamic models. The purpose of dynamic models is to simulate and forecast reservoir performance during production and it therefore tests the dynamic behaviour of the reservoir. Fluid flow is simulated, taking account of dynamic properties. *Dynamic* properties are those that change over time and during production, e.g. fluid saturations, reservoir pressure and temperature. Fluid flow simulation requires powerful computational capacities, and cannot typically be performed at the resolution of static models. Thus, the resolution of static models has to be reduced and the transformation from static to dynamic models is known as *up-scaling*. Fluid flow simulation is performed in every grid cell and thus has a need for high processing power of the workstations. Up-scaling essentially involves the coarsening of the grid of the static model in order to reduce the grid cell number and reducing the required computational capacities.

### 6.2.1 Reservoir analogue modelling

The modelling of subsurface reservoirs essentially relies on the available input data of hard data (core description) and soft data (wireline logs and seismic surveys). Based on these datasets a numerical model is developed with the help of geostatistical methods. These methods allow the geomodeller and geologist to predict the geological characteristics and rock properties at un-sampled locations in the subsurface. However, every statistical method involves some level of uncertainty

(Matheron, 1989) and there is hardly ever enough data available to develop a robust and reliable geostatistical reservoir model solely based on subsurface data (Borgomano *et al.*, 2008). Difficulties arise especially when modelling heterogeneities with scales between core description (cm-dm) and seismic survey (>10m) like fractures or in the case of microbial carbonates, bioherm structures.

In order to improve high-uncertainty models, the use of outcrop analogues has become a more common practice in petroleum geoscience (Barnaby and Ward, 2007; Borgomano *et al.*, 2013; Lapponi *et al.*, 2011). With the advance of digital survey methods, allowing the rapid acquisition of high-resolution outcrop data, analogue models are standard practice. In particular lidar-based models are increasingly used in petroleum industry and research (Bellian *et al.*, 2005; Bryant *et al.*, 2000; Buckley *et al.*, 2008b; Fabuel-Perez *et al.*, 2010; Janson and Madriz, 2012; Pringle *et al.*, 2006). As described in chapter 4, the lidar system is capable of capturing large areas with high precision in a short amount of time. The collected data is in 3D, georeferenced and relatively easy to import into reservoir modelling software packages. Lidar-based reservoir models are being developed for a range of different purposes. They are developed to better understand the stratigraphic architecture and sedimentological characteristics (e.g.: Adams *et al.*, 2011; Bellian, 2005). Virtual outcrop models are increasingly developed to better understand structural characteristics such as fault geometries and fracture networks (Kurtzman *et al.*, 2009; Larsen *et al.*, 2010b; Pearce *et al.*, 2011). These models form subsequently the basis for fluid flow simulation in order to forecast dynamic reservoir performance (Enge *et al.*, 2007; Enge and Howell, 2010; Wilson *et al.*, 2011a; Wilson *et al.*, 2011b).

The recent advance in lidar-based reservoir modelling has led to a series of publications about lidar-based reservoir modelling workflows (Buckley *et al.*, 2008b; Hodgetts, 2013; McCaffrey *et al.*, 2005). As discussed in the chapter 4, one of the main challenges in lidar data manipulation is the lack of suitable software packages. Similar difficulties arise with the integration of lidar data into reservoir modelling software packages. Each platform has different functionalities and data compatibilities. However, a general workflow is the same throughout all platforms and is illustrated in Figure 85.

The workflow involves the digital mapping of the main geological features with 3D polylines on the virtual outcrop model. The polylines are then imported into the

reservoir modelling software and serve as input data for stratigraphic and fault surface construction. Subsequently a basic geocellular model can be constructed and populated with geological properties such as facies distribution. A detailed description of the workflow is given below.

## 6.3 Development of the reservoir model framework

The basic framework of a geocellular reservoir model consists of surfaces. These may represent lithological contacts or faults. Such surfaces are the boundary conditions for the subsequent reservoir gridding process, which populates the model with geological (e.g.: a facies model) and petrophysical properties. JewelSuite Subsurface Modelling software from Baker Hughes was used for the development of the reservoir analogue model. This is a reservoir modelling software package which offers all required workflows ranging from structural framework building, reservoir gridding to facies modelling for the development of geocellular models. JewelSuite was provided for free from Baker Hughes for the purpose of the development of the analogue model. An additional reason to use JewelSuite instead of more traditional reservoir modelling packages (e.g.: Petrel) was to enable the possibility to collaborate with the JewelSuite development team in order to get assistance with the integration of lidar outcrop data into subsurface modelling software.

The main lithostratigraphic contacts in the Omkyk Sequence 2 were mapped on the virtual outcrop model with 3D polylines. The mapping followed the field interpretations and the subdivision of OS2 into reservoir and non-reservoir units established by Adams *et al.* (2005). Each of the 5 mapable units in OS2 (compare paragraph 3.7) is subdivided into a highstand systems tract and a lowstand systems tract. The TSTs, generally consisting of shale and lime mudstones are interpreted as non-reservoir units, whereas the HSTs, consisting of grain-/packstones and microbial carbonates, are proposed analogue reservoir units (compare paragraph 3.12 for reservoir analogue architecture). Therefore, the lithostratigraphic contacts of each unit, consisting of basal and upper contacts and the change from TST to HST were mapped (Figure 86.A-D). The change in lithology from LST to HST was visually easily recognisable, due to the change in the outcrop topography. Shale and mudstone horizons are intensely weathered and recessive and exhibit slope angles of 35º-45º whereas the grain-dominated and microbialites are forming steep cliffs with

70º-90º dip (Figure 87). A total of 10 contacts were mapped on the virtual outcrop (Figure 86.A). The top surface of the biostrome 2 horizon could, however, not be mapped continuously because it was not always visible at the outcrop due to modern day erosion. The mapped 3D polylines representing the stratigraphic contacts were then imported into JewelSuite and grouped according to their position (e.g.: every polyline of the basal surface representing the bioherm horizon was placed into one group).

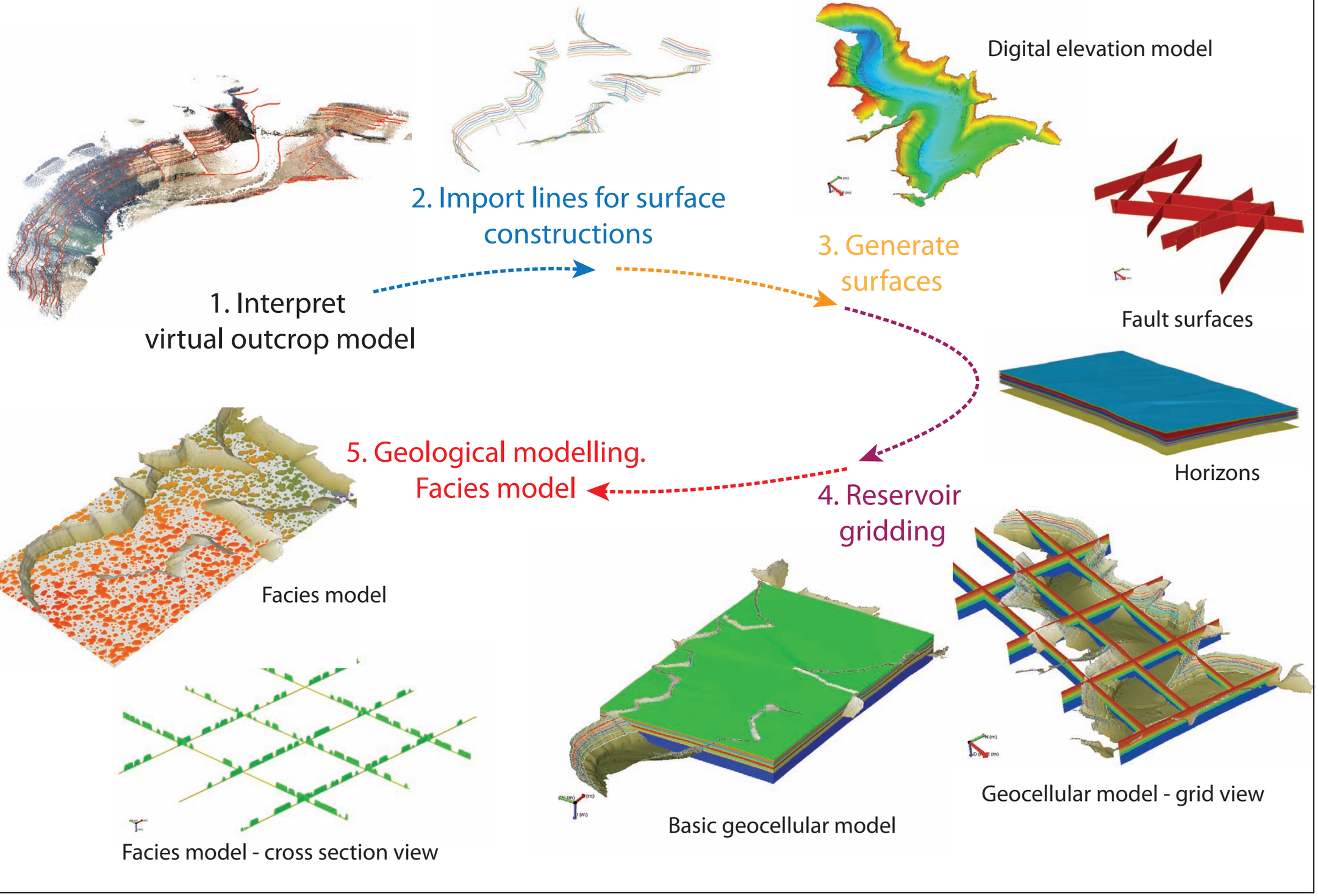


Figure 85: Sketch illustrating the development of a geocellular reservoir analogue model based on terrestrial laser scanning. The workflow involves 5 steps: (1) Digital mapping of geological features on the virtual outcrop model, (2) import of 3D polylines and surfaces into the reservoir modelling software and subsequent surfaces construction (3). Consequently a basic geocellular model can be developed (4) and populated with geological properties (facies model) in the last step (5). See text for detailed explanation. Modified after Enge & Howell (2010).

For each group of polylines a surface was then triangulated where the polylines represent the boundary of the surface and the area between the polylines was interpolated. After the surface interpolation for each polyline group, the horizons between the cliff faces were constructed (see Figure 86.B). However, these horizons are highly irregular and constrained by the boundary polylines, representing the intersections with the canyon cliff faces.

In order to define the size of the final geocellular model, a model area grid was constructed. This is a 3D grid with a cuboid geometry and dimensions of 2360 m * 1080 m * 180 m (*x,y,z*) in order to encapsulate the entire scanned Zebra River Canyon section. The triangulated stratigraphic horizons between the canyon walls were then extended through interpolation until they intersected the model area grid (Figure 86.C). The settings for the surface interpolation were based on a pre-performed curvature analysis of the initially triangulated surfaces. The structural dip of the carbonate ramp is only a few degrees (3º-5º) towards the northeast and the horizons are uniform in thickness. Interpolation distances were generally short (<200m) and therefore the interpolation generally produced acceptable surface representation (Figure 86.D). However, the further surfaces are interpolated away from fixed points (mapped polylines), the lower the accuracy, and hence manual adjustment of the surfaces had to be done. The intersections of the surfaces with the photorealistic digital elevation model were visually checked in areas where no lidar data was available. In only 4 cases manual adjustments of the surfaces were necessary.

As described earlier, the top surface of biostrome 2 could not be mapped continuously because of outcrop conditions. However, all mapped horizons in the Zebra River canyon are uniformly thick over large distances, which is also the case for biostrome 2 as observed outside the lidar scan area during field work. The thickness of biostrome 2 was obtained by measuring visible contacts in the virtual outcrop model, which shows an average of roughly 11 m. Thus, the top surface was created by duplicating the basal contact and translating it 11 m vertically upwards.

### 6.3.1 Fault and fracture network model

The development of the fault system presented difficulties because for each fault only one 3D polyline could be mapped on the virtual outcrop model. The mapped polylines represent the intersection of the fault and outcrop surfaces. In some cases it was possible to identify polylines, which belong to the same fault (e.g.: a strike slip

fault intersecting the entire canyon, which is visible at several cliff faces). However, in most of the cases this was not possible and fault surfaces had to be fitted onto the polylines.

The first step in the fault surface construction is to extrapolate a surface by using the 3D polylines as boundaries such that each node of the polyline has to be represented by the constructed plane. Since 3D polylines can be regarded as functions of *x,y,z* coordinates in 3D space, it is possible to develop a surface based on differential geometry by using an in-build functionality in JewelSuite. These constructed surfaces are, however, restricted to areas in the vicinity of the fault polylines. The reason for that is that the extrapolation algorithm becomes increasingly inaccurate with increasing distance from the polyline nodes. Therefore, a best-fit planar surface, which is averaged through the extrapolated surface, was fitted onto the fault plane. These planar surfaces were then extended by interpolation until they intersected the model area grid, resulting in a fault network model. However, in almost every case, a manual adjustment of the interpolated fault surfaces had to be done. This was done by importing the surfaces into the virtual outcrop model to manually adjust dip angle and dip-azimuth by means of visually best fit the surfaces onto the DOM. The corrected fault surfaces were then again imported into JewelSuite for the second step of corrections. This was done on the photorealistic digital elevation model of the Zebra River Canyon. Additionally, the remote-sensing analysis of the fault structures was imported as DEM overlay to best fit the interpolated surfaces with the regional fault structures. A total of 43 faults were constructed in this way. All surfaces created in the model area are steep (80º-90º) strike-slip faults trending NW-SE, N-S and ENE-WSW (Figure 88.A). These strike directions are in line with the satellite image interpretation (compare chapter 5). The definition as strike-slip faults is based on field observation and on the interpretation of the virtual outcrop model. Each fault intersection has been visually checked within the virtual outcrop model and no vertical offsets have been detected, which confirmed the strike-slip nature of the faults. The fault network was created on the basis that the faults, which could be traced over the entire canyon constitute the main lineaments. Smaller faults, where the surface intersections could only be identified at one canyon wall, were extended until the segments intersected one of the main lineaments. All small faults intersected the main lineaments with acute angles between 25º-35º indicating that these are linking faults between the main

strike slip faults. The end result is a complex fault network model, comprising 8 main strike slip faults and 36 linking strike slip segments (Figure 88.B).

One of the initial objectives of the structural characterisation of the microbial carbonates in the Zebra River canyon was to include fracture data into the reservoir analogue model. Thus, significant effort has been devoted on the development of a Discrete Fracture Network (DFN) model (not presented in this thesis) of the bioherm and inter-bioherm facies, based on the structural characterisation presented in **chapter 5**. The main input parameters for DFN-models are fracture size, orientation, spacing and aperture. Fracture orientation and spacing within the bioherms could be measured within the virtual outcrop model. The modelling of the fracture sizes was, however, not successful. This was due to a combination of outcrop quality and inadequate resolution of the virtual outcrop model. The measured fracture sizes exhibited high error margins and therefore the developed DFN-models showed highly variable properties in terms of fracture connectivity and permeability. Furthermore, the syn-depositional fracture system, intrinsic to the microbial carbonates, does not show any evidence of preferred fracture orientation or size distribution. Thus, it was not possible to develop a realistic, stochastic DFN-model. Whether predictable syn-depositional fracture patterns (e.g.: parallel to the strike direction of the Kuibis carbonate ramp) do occur remains to be tested in subsequent studies. Thus, it was deemed that the DFN-models are not accurate enough to merit incorporation into the reservoir characterisation and subsequent fluid flow modelling.

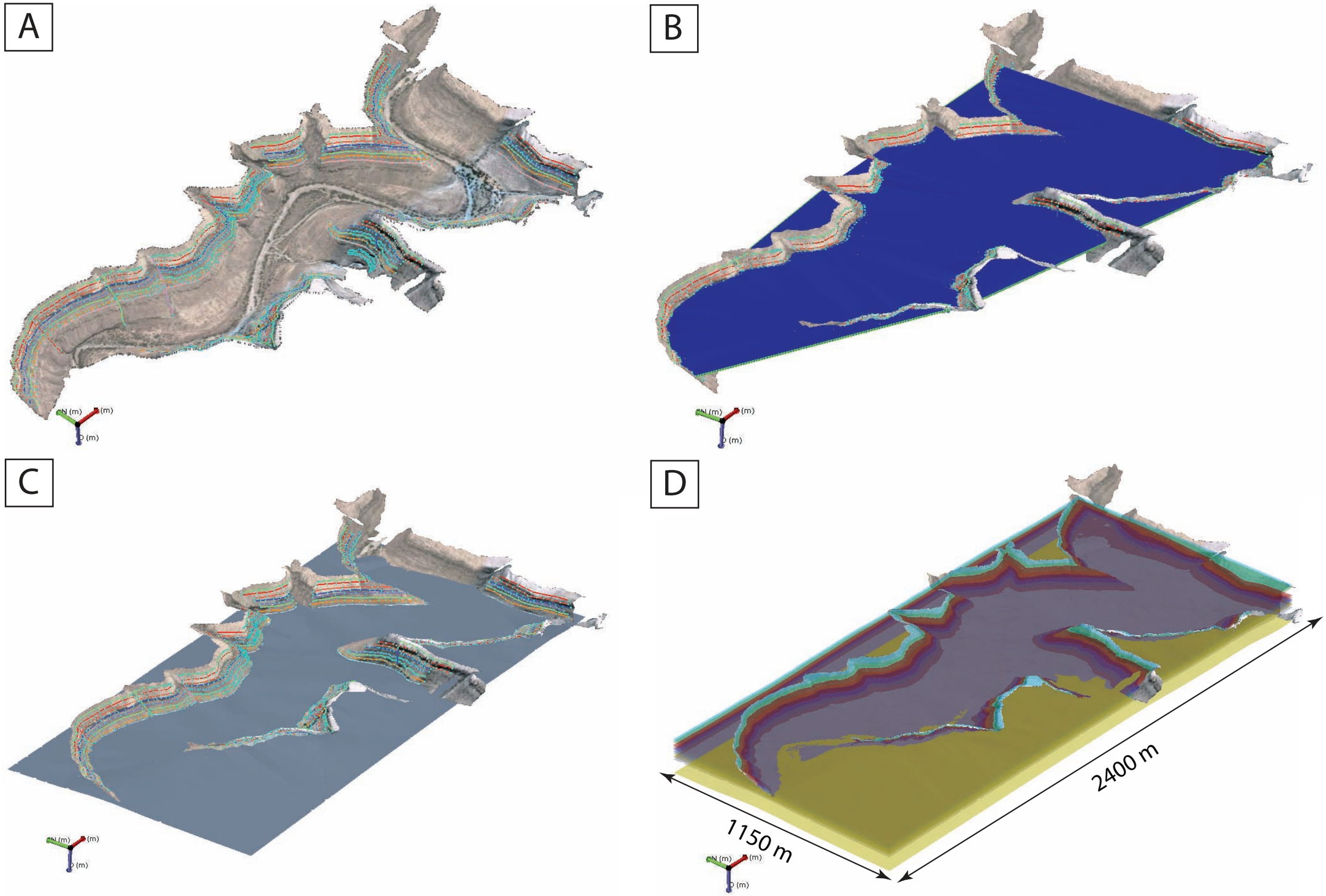


Figure 86: (A) Lidar photorealistic digital elevation model and mapped stratigraphic contexts and main fault lineaments represented by 3D polylines. (B) Interpolated horizon surface between canyon cliffs. (C) Extended horizon surface by interpolation until the model area grid was intersected. (D) Final surface model of the horizons in the Zebra River Canyon system consisting of 10 surfaces representing the major lithological contacts. Note the layer cake architecture of the entire system.

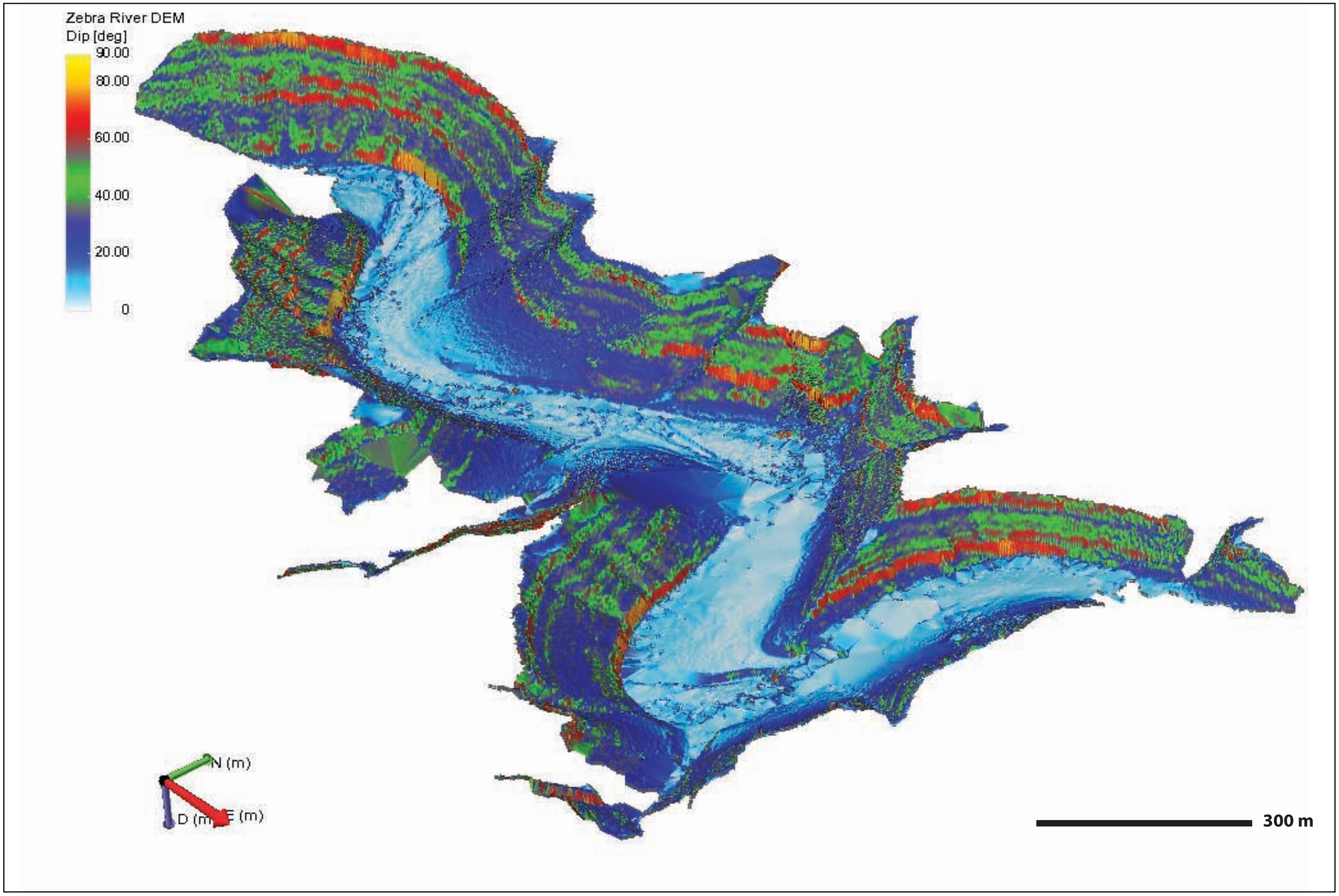


Figure 87: Image showing the triangulated lidar Zebra River DEM after an orientation surface analysis. The analysis shows the dip angle of the triangles constituting the meshed surface. Clearly visible are the steep cliff areas of bioherms and grainstone horizons in red to yellow colours with dips between 70º and 90º degrees. Green colours represent weathered outcrop section whereas blue areas (<25º degrees) represent talus and no data areas. The surfaces analysis quickly highlights the layer-cake architecture of the Kuibis carbonate ramp and assisted in the validation of the interpolated horizon surfaces.

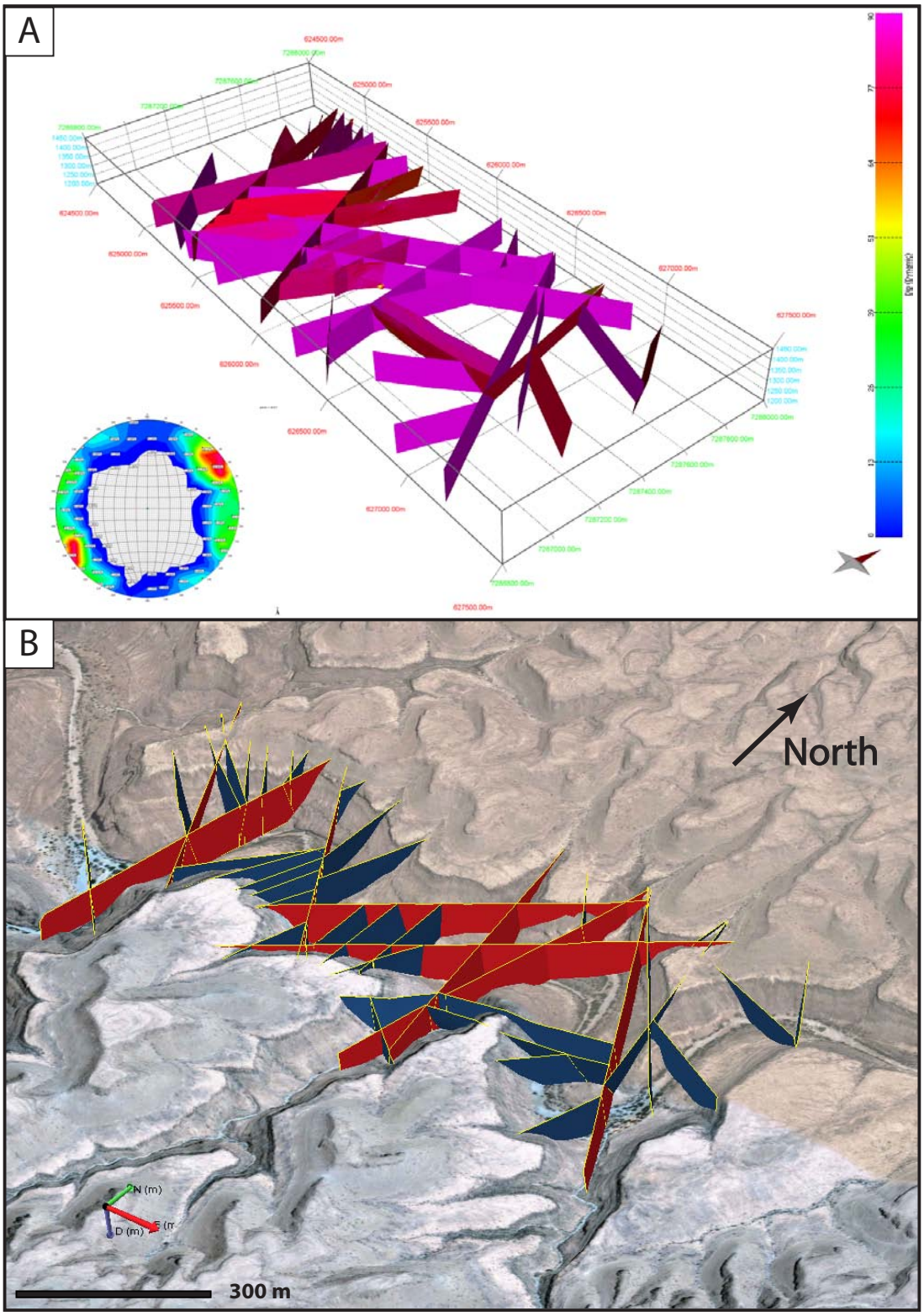


Figure 88: (A) Developed fault network model in the Zebra River Canyon section. The legend on the right hand side of the image shows the dip surface analyses of the individual faults. All modelled faults are steep with dipping between 80º and 90º degrees. The lower left of the image shows a stereo plot of surface poles. The main direction of the faults is NW-SE, N-S and NNE to SSW. (B) Fault network within the photorealistic digital elevation model. The virtual globe of Google Earth was used to validate the constructed fault network. Red fault surfaces correspond to main lineaments, which could be mapped on 2 or more cliff faces. Dark blue fault surfaces are linking segments, which end at the main lineaments or at the model area grid, respectively. Linking segments were only visible at one outcrop surface.

## 6.4 Geocellular model building

### 6.4.1 Reservoir gridding

The developed reservoir framework, consisting of stratigraphic horizons and faults, forms the basis for the construction of the geocellular analogue model. A geocellular model consists of grid cells with a rectangular plan view shape and of varying vertical extent (Figure 89.A). The cells can be regarded as the "building blocks" of the model and each geological feature is defined by these grid cells (Figure 89.B). Once the basic geocellular model is developed, the cells are then populated with geological data (e.g. facies distribution) and petrophysical data such as porosity and permeability and the values are stored an each grid cell.

The construction of a geocellular model is known as reservoir gridding. During the gridding process the model framework is filled with grid cells. Pre-defined surfaces such as the mapped and interpolated stratigraphic contacts and faults serve as boundary conditions. For example, the space between two stratigraphic contacts is one basic grid layer and is filled with among each other connected grid cells (see Figure 89.A). This process is called gridding reservoir layers, and is an automated function within JewelSuite. This step defines the main reservoir architecture. The basic reservoir architecture of the Zebra River model is illustrated in Figure 89.C. Subsequently the grid is populated with the first geological information by means of subdividing the model in analogue reservoir and non-reservoir layers, therefore defining the reservoir definition, which is shown in Figure 89.D. The Zebra River model consists of 9 main grid layers, which are constrained and separated by the stratigraphic contacts, constructed from the mapping results of the virtual outcrop model. The classification into reservoir units and non-reservoir units of the Omkyk Sequence 2 is based on field observations and is in alignment with the interpretation of Adams *et al.* (2005).

The first grid layer comprises unit 1 of OS2 and the uppermost sections of Omkyk Sequence 1. The basal grid surface is the canyon bottom at the west section of the lidar survey. Although numerous grainstone and microbial carbonate beds were mapped within this unit, poor outcrop quality made it impractical to include Unit 1 as reservoir unit. As discussed in the chapter 3 and in Adams *et al.* (2005) the outcrop conditions did not allow a robust characterisation of this unit. Thus, the base

Unit 1 grid layer was defined as non-reservoir unit without any further subdivision. In addition, the limited vertical resolution of the Zebra River model was a reason for defining Unit 1 as non-reservoir unit (see below for explanation). The overlying unit contains the microbial bioherms within the TSTs and HSTs of Unit 2. This grid layer is defined as one grid layer and is sub divided into for sub layers, which have proportional thickness and are conform to the base surfaces. The quality of the outcrops and the resolution of the virtual outcrop model did not allow to accurately map the inter-bioherm contacts. Thus, the four internal layers approximate the inter-bioherm bedding (see Figure 89.C and Figure 54).

The next 3 units are always defined by a couplet of TSTs (e.g. heterolithic facies) as non-reservoir units and HSTs as reservoir units. The HSTs are represented either by grainstone horizons or microbial biostromes. The top grid layer of the reservoir model is the laterally extensive biostrome 2, which is also defined as a reservoir unit.

The mean thickness of the grid layers is shown in Figure 90. All horizons show a thickness between 9 and 12 m and minimal horizontal variation (see Figure 91). Every horizon is represented by one column-chart showing the thickness distribution of the horizon grid blocks. One exception to this is the grid layer of Unit 1, which exhibits a mean thickness of 61 m. This is because the base of the unit coincides with the base of the lidar data and canyon floor, which is located at the upper part of Omkyk Sequence 1. Additionally, there is no subdivision of Unit 1 into TST or HST units.

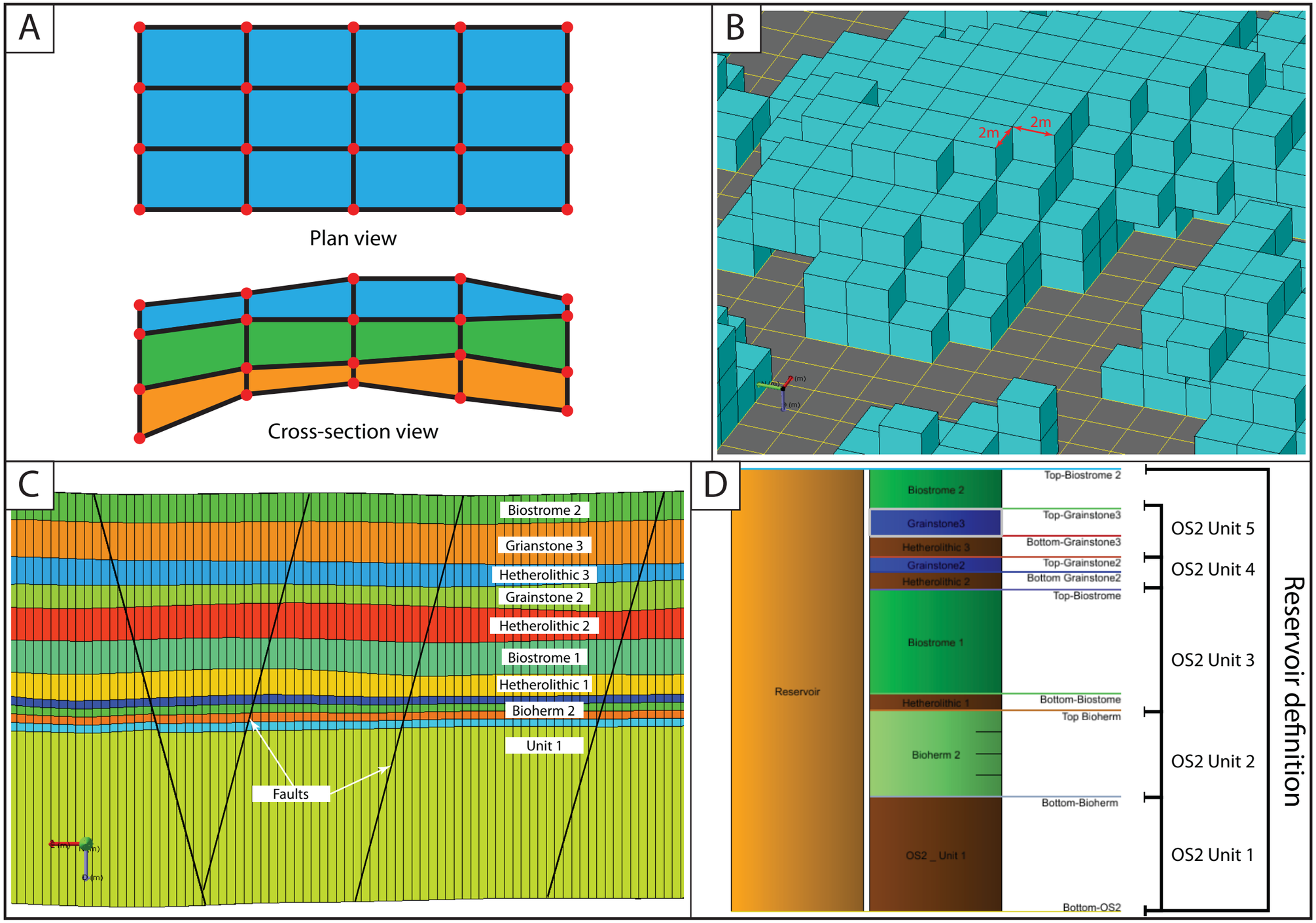


Figure 89: (A) Cartoon illustrating the nature of a reservoir grid used in geocellular modelling. The grid consists of among each other connected grid cells, which exhibit a regular geometry in plan view (square or rectangular plan view shape). The vertical dimensions are defined by surfaces, representing for instance stratigraphic or depositional surfaces. Therefore the vertical extends of the grid cells vary according to the grid layer thickness. The cross-section view illustrates 3 grid layers and their grid cell architecture. Modified after Clayton (2002). (B) Each geological shape, facies and petrophysical model is build up by grid cells. The image showcases a hypothetical facies realisation constructed with a regular quadratic 2x2 m grid in three dimensions. (C) Cross-section through the Zebra River Canyon analogue model illustrating the main reservoir architecture. The model consists of 9 major grid layers separated by the constructed stratigraphic horizons. Note that only the bioherm horizon has internal layering. See text for explanation. (D) Illustration showing the Zebra River reservoir analogue definition. The model consists of 9 grid layers constrained by the constructed stratigraphic horizon surfaces. Note that only the bioherm grid layer has 4 internal layers and the subdivision of the reservoir model into Omkyk Member Units. Grid layer thickness is not at scale.

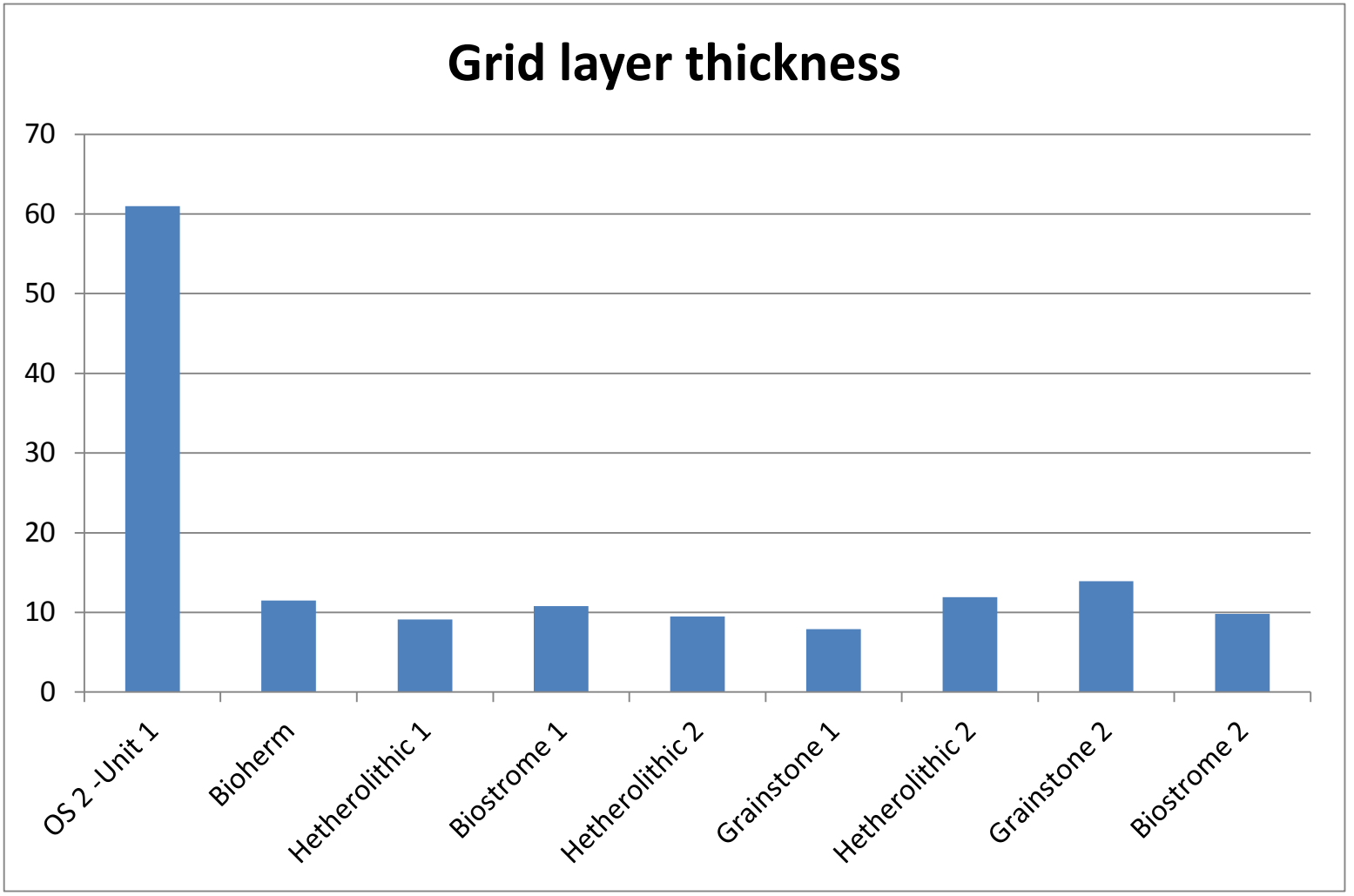


Figure 90: Column chart showing the mean thickness in m of the reservoir grid layers. Except OS2-Unit one all grid layers show a mean thickness between 8 and 11.5 meters.

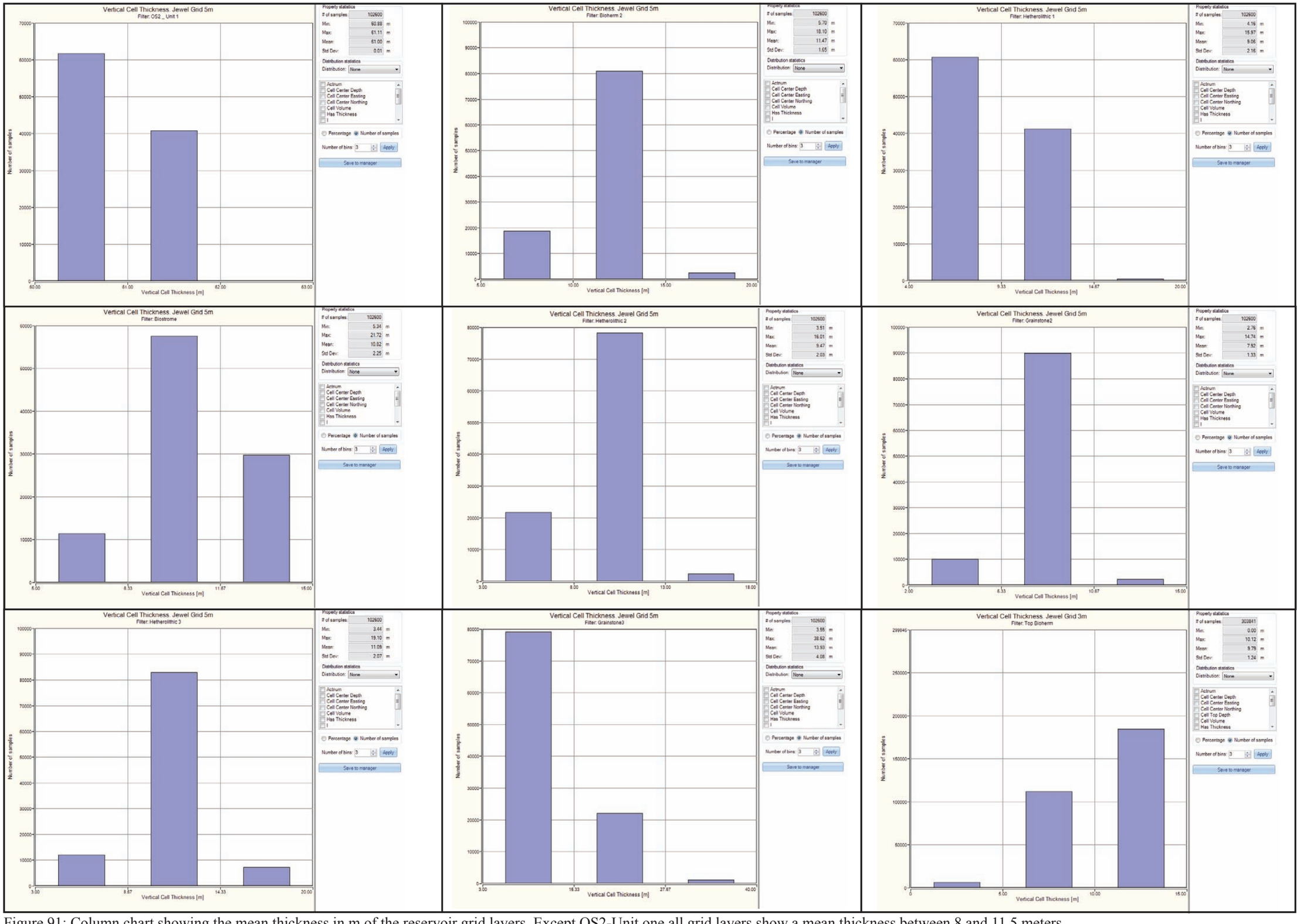


Figure 91: Column chart showing the mean thickness in m of the reservoir grid layers. Except OS2-Unit one all grid layers show a mean thickness between 8 and 11.5 meters.

### 6.4.2 Modelling scale

Following the development of the basic grid network and geological subdivision the appropriate modelling resolution has to be defined. The modelling scale defines the size of the grid cells. A number of important issues must be considered. Foremost of these is the technical specification of the workstation used for the modelling. Static reservoir models in the petroleum industry can reach up to 100 million grid cells but these models need high-end computers to be processed and can hardly be visualised with common workstations.

The workstation used during the course of this research project has 2 Intel Core 2.8 GHz processors, 12Gb physical memory and a Nvidia Quadro 4000 graphics card. After a series of trial gridding runs the maximum number of grid cells which can be handled with that workstation was set to be 4 million to ensure optimal performance.

Besides the technical limitations of software and hardware, the resolution of the model has to be carefully chosen from a geological point of view. The challenging task is to find the appropriate scale which honours all available data and their different scales (Gilbert *et al.*, 2004; Liu *et al.*, 2004). In the case of a lidar-based reservoir model it is neither possible nor feasible to model at the lidar resolution. This would result in a cm-scaled grid cells and the hypothetical final model would have billions of grid cells. Too coarse a resolution, on the other hand, might result in important geological heterogeneities being ignored.

The main consideration for the Zebra River model was to accurately model and visualise the laterally discontinuous bioherms. Therefore, the horizontal grid dimensions (i,j directions) had to be small enough in order to represent the bioherms. A model with 20 x 20 m grid cells would, for instance, not be able to define bioherms of < 20 m diameter. Consequently, facies modelling of the microbial carbonates was carried out on a grid with 2x2 m horizontal grid resolution. The facies modelling was performed only in the bioherm grid layer with four internal layers and the bioherm horizon model has more than 2.5 million cells. This high-resolution model was used to visualise the microbial bioherms and to accurately assess the results of the facies modelling.

The entire model of the Zebra River Canyon has a horizontal grid resolution of 5x5 m, which results in a model with 1.22 million cells. The vertical thickness of the

grid cells is constrained by the stratigraphic surfaces. This resolution proved to be sufficient to visualise the bioherms. An additional important consideration was that the model was built with the intention to perform streamline flow simulation and for that the model had to be less than 1.5 million cells (compare chapter 7). The results of the 2 m grid facies modelling were subsequently transferred to the 5 m grid by a JewelSuite in-built property-mapping algorithm. The grid-to-grid mapping tool works on the basis that grid cells from the source grid are averaged according to the resolution of the target grid and consequently the values are transferred to the target grid. It is essentially a grid up-scaling based on the arithmetic average.

In general reservoir models tend to have large grid cells with respect to the horizontal extent (tens to hundreds of m) and small vertical thicknesses (dm-m scale). This is because it is assumed that the main heterogeneities affecting fluid flow are in the vertical direction. Additionally, the main input data in subsurface reservoir modelling is derived from vertical wells. Therefore, the vertical resolution of hard data (core descriptions) is high, compared to the limited horizontal information and geocellular models are created accordingly. This is especially practiced for carbonate ramp reservoir where facies belts are laterally extensive and homogenous but exhibit only small vertical thicknesses (Wilkinson and Drummond, 2004; Williams *et al.*, 2010).

However, this small-scaled vertical resolution was not realistic to achieve for the Zebra River model because of the high horizontal resolution of 2x2 m and 5x5 m, respectively. An additional cm or m-scale sub-layering would have exceeded the maximum number of grid cells. Thus, with the exception of the bioherm layer, no reservoir grid layers have internal layering. For reservoir modelling purposes this is a reasonable assumption because the facies association show minimum lateral variation and can be treated as one flow or non-flow unit. The final basic geocellular model, constructed by using these specifications is shown in Figure 92.A-B.

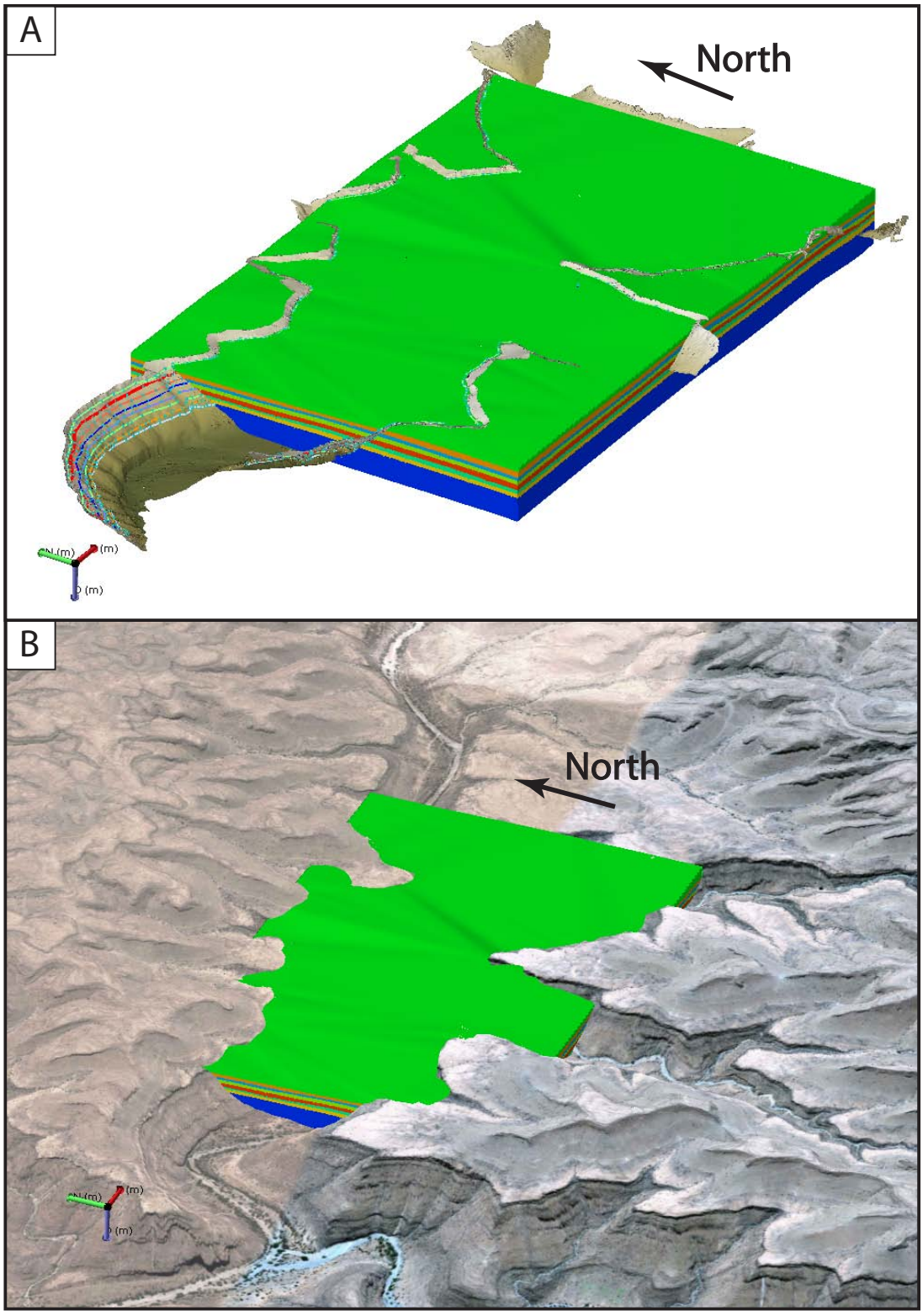


Figure 92: (A) Final basic geocellular model of the Omkyk Sequence 2 in the Zebra River Canyon area. Only 3/4 of the model were visualised in order to show the mapped 3D polylines on the digital elevation model which separate the grid layers. (B) Reservoir analogue model visualised within the photorealistic DEM of the Zebra River area. The dimensions of the model are the same as in figure A.

## 6.5 Previous reservoir model constructed in Zebra River Canyon

Adams *et al,* (2005) developed a static reservoir model of the Omkyk Sequence 2 in the Zebra River Canyon. Their focus was on the construction of a high-resolution 3D stratigraphic and sedimentological model of the Omkyk Sequence 2 and in particular of the microbial bioherms. The main part of the here presented research project was to develop a static geocellular reservoir model in the same location and therefore a detailed discussion of the model of Adams *et al.* (2005) is necessary. Such a discussion necessarily involves comparing and contrasting the modelling approaches taken by the author during the course of this research project with those of Adams *et al.* (2005). The developed upper bioherm surface and final geocellular model of Adams *et al.* (2005) is illustrated in Figure 93.A-B.

Adams *et al.* (2005) used digital field techniques to acquire quantitative data of the geometry of the carbonate ramp sequence in the Zebra River area and of the bioherm dimension for input into the modelling process. The authors used real time kinematic global positioning system (RTK-GPS) receivers and a total ground station. With the total station the authors measured the visible contacts of stratigraphic horizons and bioherm outlines from the canyon bottom. Handheld GPS devices were used by the researchers to measure additional data points by physically walking along sedimentological contacts. Data points were generally collected every 2 m and information about lithology, type of contact and facies association was recorded. A total of more than 60,000 data points were collected, which were then used in combination with a digital elevation model to develop a static geocellular model. Next to the development of the basic 3D model of the OS2 sequence, the main focus was on the modelling and visualisation of the bioherms.

The main challenge in modelling the bioherm geometries is their shape, dimensions and their spatial distribution over the carbonate ramp. The approach chosen by Adams *et al.* (2005) is based on the measurement of the bioherms in cross-section (along the canyon surface) and subsequent transformation into 3D space. For that, the authors compiled a list of all measured bioherm data points and computed statistics regarding bioherm dimensions (width and height of each bioherm) and probability-density functions of width and height distribution in 3D

space. In order to visualise the microbial carbonates an object based modelling approach was used to generate the upper boundary surface of the bioherm unit. This means that the surface encapsulating all bioherms was mathematically described using numerous mathematical functions and equations.

Several assumptions by Adams *et al.* (2005) regarding bioherm shape, dimensions, distribution and abundance had to be made in order to calculate the upper surface. The authors assumed that the growth location of the bioherms is randomly distributed over a horizontal grid, which represents the carbonate ramp surface. In other words, they assumed no spatial trend in the distribution of the bioherms. The density, with which the bioherms cover the base plane, was assumed to be roughly 45%. The shape of the bioherms was approximated to be circular in plan view and that any measured width of the mounds can be paired with any height in the data set (no correlation of width and height).

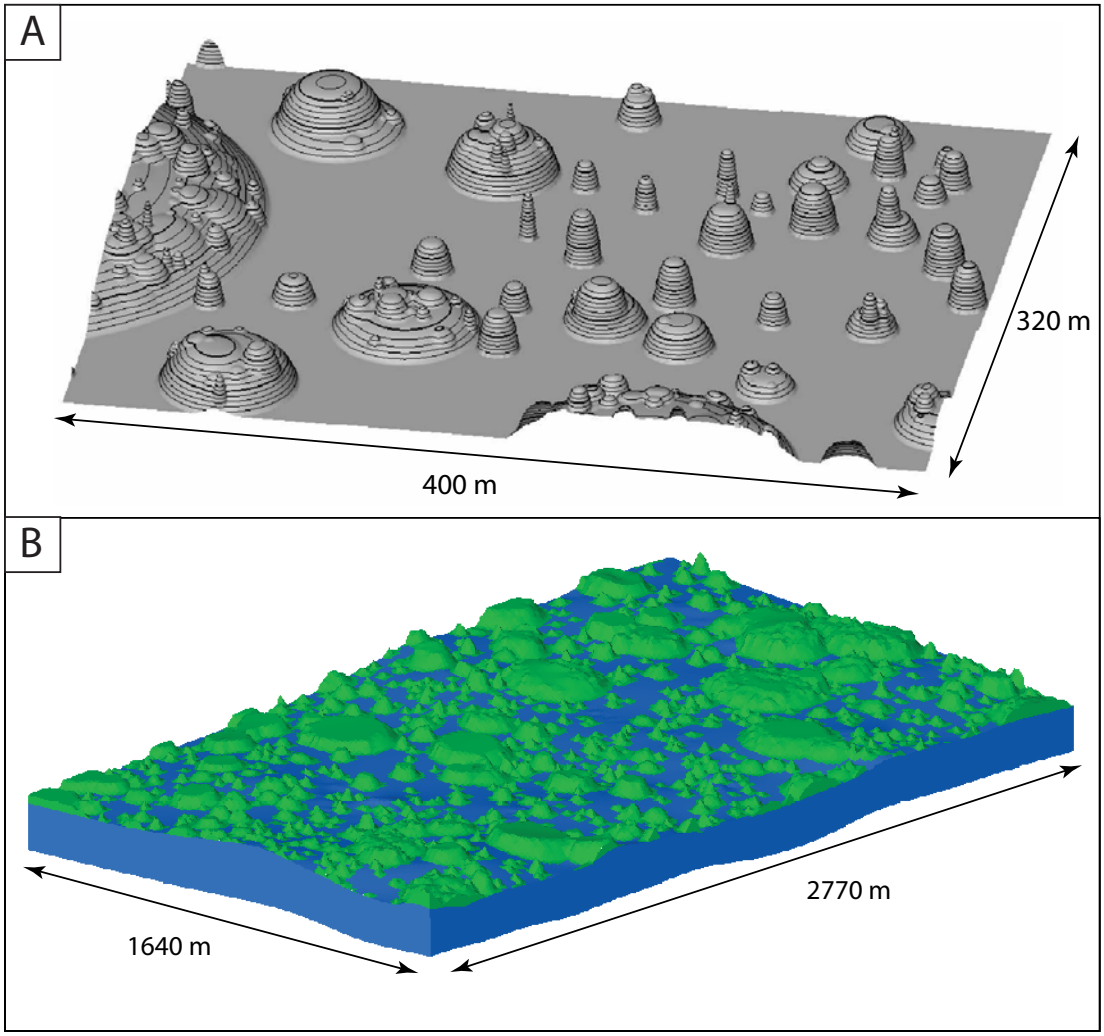


Figure 93: Published 3D models of the Kuibis ramp carbonates in the Zebra River Canyon by Adams *et al.* (2005). (A) Upper bioherm surface used as boundary condition for reservoir gridding. (B) Final static geocellular model, showing the bioherm horizon. Horizontal grid resolution is 10 by 10 m. Modified after Adams *et al.* (2005).

An important factor in their modelling code was that the authors explicitly prevented the possibility of overlapping bioherm structures and therefore excluded the development of composite bioherms. The end result of Adams *et al.* (2005) is a high-resolution bioherm facies model of individual isolated mound structures, randomly distributed over the carbonate ramp.

The two latter assumptions and code specifications regarding bioherm shape and excluding the formation of composite bioherms, are the main differences in the numerical model developed during this research project. The second facies model, the multiple-point statistics facies model additionally incorporates a trend of the spatial distribution of the bioherms.

## 6.6 Bioherm dimensions

In order to develop a robust facies model of the bioherm horizon the dimensions of the mound structures had to be accurately assessed. This was done by digitally mapping the bioherm outlines on the virtual outcrop model. A total of 66 individual mound structures were mapped onscreen with 3D polylines. The 3D polylines were then projected onto cliff-parallel cross-sections (compare chapter 4, paragraph 4.6.3 for methodology). For that a total of 14 cross sections were needed. On the cross-sections the widths and heights were measured and compiled in one file. Figure 94.A shows a scatter plot of the mapping results. The majority of the bioherms plot in the lower left of the diagram and exhibit heights between 3-13 m and widths are between 2-75 m (group 1 bioherms). Bigger mound structures (group 2 bioherms) range from 75 m up to 300 m in width with heights up 21 m.

The results are in line with the published data from Adams *et al.* (2005) (see Figure 94.B). There is no correlation between bioherm width and height for bioherms and Adams *et al.* (2005) concluded that each given bioherm width can be paired with any height, which plots between two boundary conditions (see Figure 94.B). The boundary conditions are given by following equations:

Equation 10: $\boldsymbol{h = 0.0335w + 1}$ $(\boldsymbol{lower\ boundary})$; $\boldsymbol{h = 0.0335w + 13}$ $(\boldsymbol{upper\ boundary})$;

$$\boldsymbol{h = height, w = width}$$

The author of this thesis is following this assumption for bioherms in group 1 because they constitute individual mounds and simple geometries can be approximated (e.g.: circular in plan view). The dimensions of group 1 bioherms were

used as input data for the numerical modelling. Bioherms of group 2 with widths > 75 m are not individual bioherms but they constitute composite mound structures. This interpretation is based on field observations, photomosaic and virtual outcrop interpretations. A total of 11 composite mounds are present in the data set and the largest is > 300 m in width and 15 m high (see Figure 74). The average width of the mapped composite bioherms is roughly 150 m. Bioherm dimensions of group 2 have not been used as input parameters in the modelling process but were used to validate the geometry of the modelled composite bioherms.

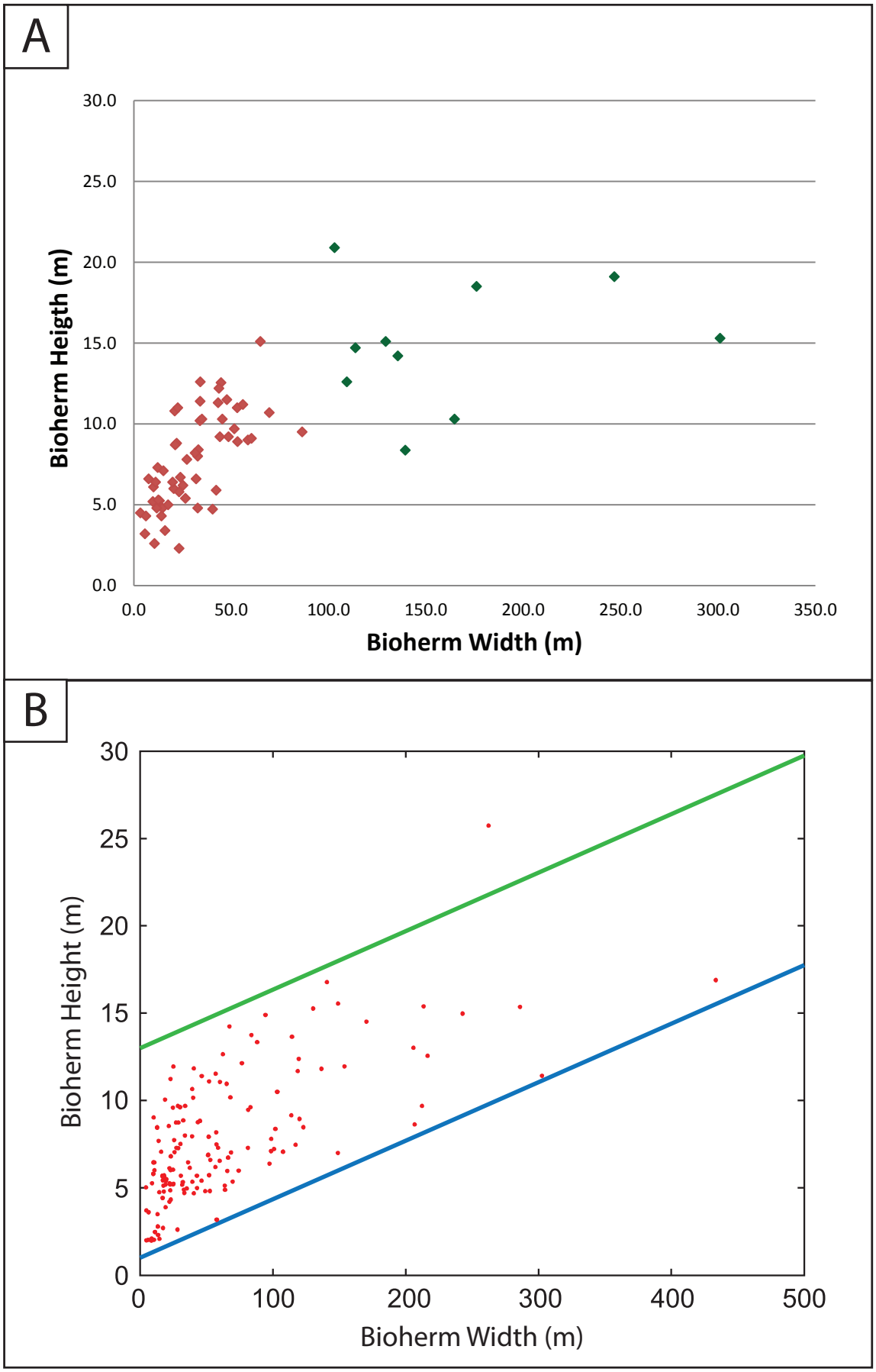


Figure 94: (A) Scatter plot of measured bioherm width versus height on the virtual outcrop model. The dataset consists of 66 individual bioherm measurements. Data points in red correspond to bioherms of group one whereas red data-points correspond to measurements of group two. (B) Published bioherm dimensions from the Zebra River Canyon. Blue line corresponds to lower and green line to upper boundary. See text for description. Modified after Adams et al. (2005).

## 6.7 Bioherm facies modelling

Challenges in modelling the microbial carbonate horizon lie in the complex shape of its bioherms (e.g. possible plan view shape, height and width dimensions) and the spatial distribution of these over the carbonate ramp. In both cases the information is not directly obtainable from the outcrops in the Zebra River Canyon. Although the lidar data and the virtual outcrop model are in 3D the measured dimensions and spatial arrangements describe the 2D cross-sections of the bioherms. Therefore the main challenges in the modelling process of the microbial bioherms were:

1. Shape: A simple approximation of the bioherms as circular in plan view does not produce a sufficiently realistic model to describe the cross section views as observed in the outcrop. Thus, a new approach to model the geometries of bioherms and composite bioherms had to be established.
2. The second challenge was to find a way to model the spatial arrangement of the bioherms on the carbonate ramp with only limited conditioning data such as the relative abundance of bioherms versus inter-bioherm facies in cross-section view. The lateral arrangement of the bioherms has a major influence on reservoir connectivity and therefore on performance.

Two modelling approaches were chosen to model the microbial facies: (1) object based facies modelling and (2) Multiple-Point Statistics (MPS facies modelling). The former approach is based on a numerical source code, developed during the course of this research project. The input data is derived from bioherm measurements from the virtual outcrop model (compare paragraph 6.6). MPS facies modelling, which is based on a conceptual geological model was used in order to incorporate all available data such as field work interpretations and remote sensing analyses.

### 6.7.1 Object-based facies modelling approach

The first approach used to model the laterally discontinuous microbial carbonates during this research project is similar to the one used by Adams *et al.* (2005): the development of an upper surface encapsulating the bioherms. This surface represents the boundary condition for the subsequent facies modelling and filling the model

with geological properties (reservoir-gridding). This approach is known as object-based modelling where each geological object is modelled individually (e.g.: Pyrcz *et al.*, 2005; Seifert and Jensen, 2000). Object-based or more precisely surface-based models are visually more attractive than other modelling approaches (e.g.: pixel-based modelling) because the facies realisations aim to capture accurate geometries as interpreted at outcrops and reservoir analogues. Objects are created in high detail and facies can be assigned to well-defined geological shapes and complex geometries can be modelled with this approach. The challenge in the object-based modelling approach is however the realisation of the boundary conditions or geological shapes. Accurate input parameters are needed in order to generate a realistic model. The key questions in the object-based approach are: (1) what is the shape and parameter distribution of the geological objects, (2) how to distribute the objects throughout the geological grid and (3) what is the relevant data to constrain the resulting realisation (Clayton, 2002).

The incentive of the object-based modelling was to simulate the formation of composite bioherms. The assumptions of the object based modelling are that the bioherms are circular in plan view and randomly distributed over a base plane and exhibit a basal coverage of roughly 45-50%. The overlap of individual bioherms is not excluded. Therefore, the formation of composite bioherms is enabled in contrast to the model of Adams *et al.* (2005).

In order to generate the upper bioherm surface, a matlab code was developed. Matlab is a numerical computing environment and programming language widely used in academia and industry (http://www.mathworks.co.uk/).

### 6.7.2 The numerical matlab bioherm source code

The numerical code was developed to simulate the shapes of the bioherm structures and their distribution in 3D. The following paragraphs are detailed descriptions of the code structure and how the code operates in order to define the upper encapsulating bioherm surface. The code is divided into six main code sections and each section has one specific function (see Figure 95).

The first section, called ‘input’ is dedicated to the input of user-defined modelling parameters. A total of 10 parameters have to be specified in order to generate the upper bioherm surface. The first parameters are the dimensions of the 3D grid of the 3D volume (as length (l), width (w) and height (h) in metres). This defines the spatial

extents of the volume in which the bioherms will be positioned during simulation. Throughout the various modelling realisations the geometry of the grid was kept constant with 1080m*2360m*60m (l, w, h), which represents the horizontal extent of the bioherm horizon in the Zebra River reservoir model.

The next parameter to define is the number of bioherms to be simulated. The code does not check the density with which the bioherms cover the base plane. After several model runs and calculations of the base density (trial and error runs) it showed that approximately 2000 bioherms result in roughly 45-50% base coverage. The base density was calculated by projecting the points onto the base plane and subsequent calculation of the bioherm and inter-bioherm facies area.

The last 4 parameters to define, specify the dimension of the bioherms itself and their relative positioning to each other. The underlying assumption regarding the shape of the bioherms in the code is that the plan view shape is circular and therefore the mounds were modelled as hemispheres, which is the geometrically easiest form to describe the mounds. The widths and heights are therefore a function of the input radii: bioherm width is defined by the diameter of the sphere (2r) and the height is the radius. In order to simulate the entire range of measured widths and heights distribution a minimum and maximum radius have to be defined. These input minimum and maximum radii are the thresholds and in between these thresholds the radius for each of the 2000 bioherms is assigned randomly. The range value of the radii in the code is derived from the group 1 bioherm measurements with a minimum radius of 2 m and a maximum of 37 m (see Figure 94.A).

In order to prevent that bioherms, positioned randomly over the base plane, are placed at the same location a minimum distance to each starting point must be defined. To simulate composite bioherms the minimum distance between the individual mound structures was always kept by 2/3 of the maximum radius.

The matlab code does not generate a meshed surface but calculates a point cloud, which represents the upper bioherm surface. The alpha and beta values in the input section define to point density of the cloud. The alpha value from 0-360º specifies that each bioherm is circular in plan view and that in every 10º interval one point is calculated. The beta value specifies the vertical extend from 0-90º also in 10º intervals. The last parameter, which the user has to define is the filename under which the results are stored. The file format is an ASCII file consisting of rows and

columns, which stores each point as *x,y,z* coordinates. It is the same format as a lidar point-cloud matrix.

The second section of the code ('main') is dedicated to the calculation of the bioherm structures. The hemispheres are modelled after following equation:

Equation 11: $$\boldsymbol{f}_{(x,y)} = \sqrt{(\boldsymbol{x} - \boldsymbol{x_o})^2 + (\boldsymbol{y} - \boldsymbol{y_o})^2}$$

The process of calculating and placing the bioherms onto the base plane is embedded in a for-loop. A for-loop is a programming statement, which is defined by a starting and an end argument. The arguments in this for-loop are the number of bioherms, which starts with 1 (starting argument) and the end statement is the user defined maximum number of bioherms. The for-loop is repeatedly executed until it reaches the maximum amount of bioherms and every iteration calculates and positions one bioherm onto the simulation grid.

The next section of the code ('check intersections') has the purpose of checking the point-cloud for overlapping bioherms. In order to create a meshed surface, the point-cloud has to be triangulated in the post processing. Data points within the overlapping areas (within the composite bioherms itself) would constitute difficulties in the triangulation process because these points would be taken into account by the triangulation algorithm and thus would lead to surfaces, which would extend into the bioherms. Consequently, these points have to be removed. The checking of these data points is executed in another for-loop and all identified points are stored. The identified points are then removed in the next section of the code, 'clear intersections'. The last part of the code ('plot' and 'save') is designed to visualise the point-cloud either as to 2D plan view map or as 3D visualisation and to save the file.

The entire matlab source-code is attached in APPENDIX VI.

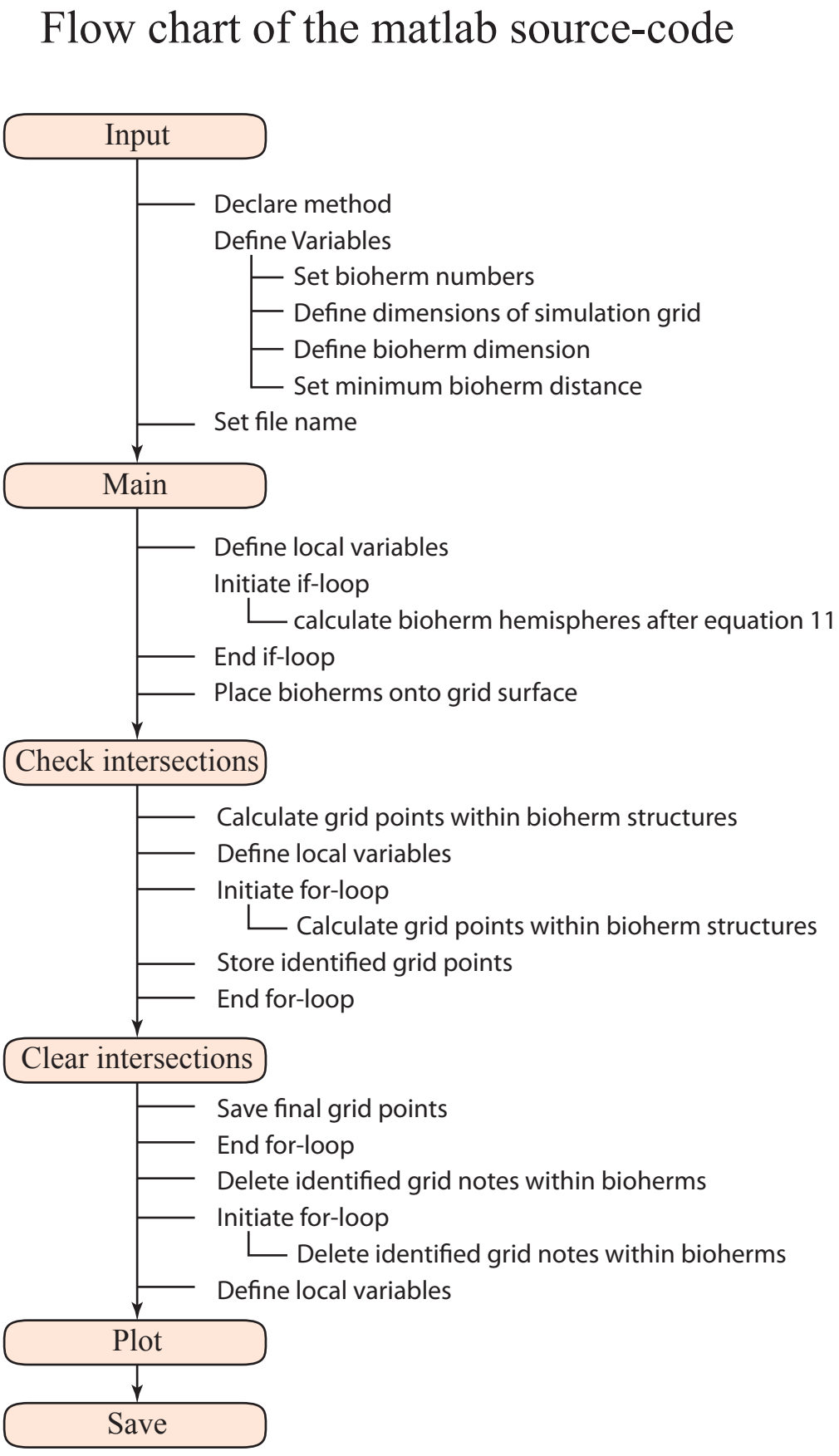


Figure 95: Flow-chart illustrating the matlab source-code.

### 6.7.3 Post-processing of the code

The matlab ASCII file was subsequently imported into Midland Valley's Move software to generate the surface. The triangulation and construction of the irregular triangulated surface was done by using the Delaunay triangulation algorithm (Delaunay, 1934). Once the surface was created, it was imported into JewelSuite for the development of a 3D geocellular model.

In JewelSuite the bioherm surface was defined as the upper boundary surface of the reservoir layer. A lower horizontal plane was constructed to simulate the base plane and an upper horizontal surface to simulate the top of the bioherm horizon. The internal layering was set to be four, conformable to the base plane. Since the radii of the bioherms can reach up to 37 m, the heights reach up to 37 m. The internal layering allowed the removal of the upper parts, which extended outside of the bioherm horizon. Additionally, with the removal of the upper 2 internal layers the oblate geometry of large bioherms (radius is bigger than horizon thickness) and of composite bioherms was achieved. The simulation grid of the matlab code is a horizontal base plane and therefore does not represent the structural dip of the Zebra River area. In order to dip-correct the modelling results the facies model was mapped onto the corresponding bioherm grid layers of the Zebra River model by using a JewelSuite in-build property mapping workflow. The end result of the post processing is a dip and height corrected geocellular facies model of the bioherm horizon (Figure 96).

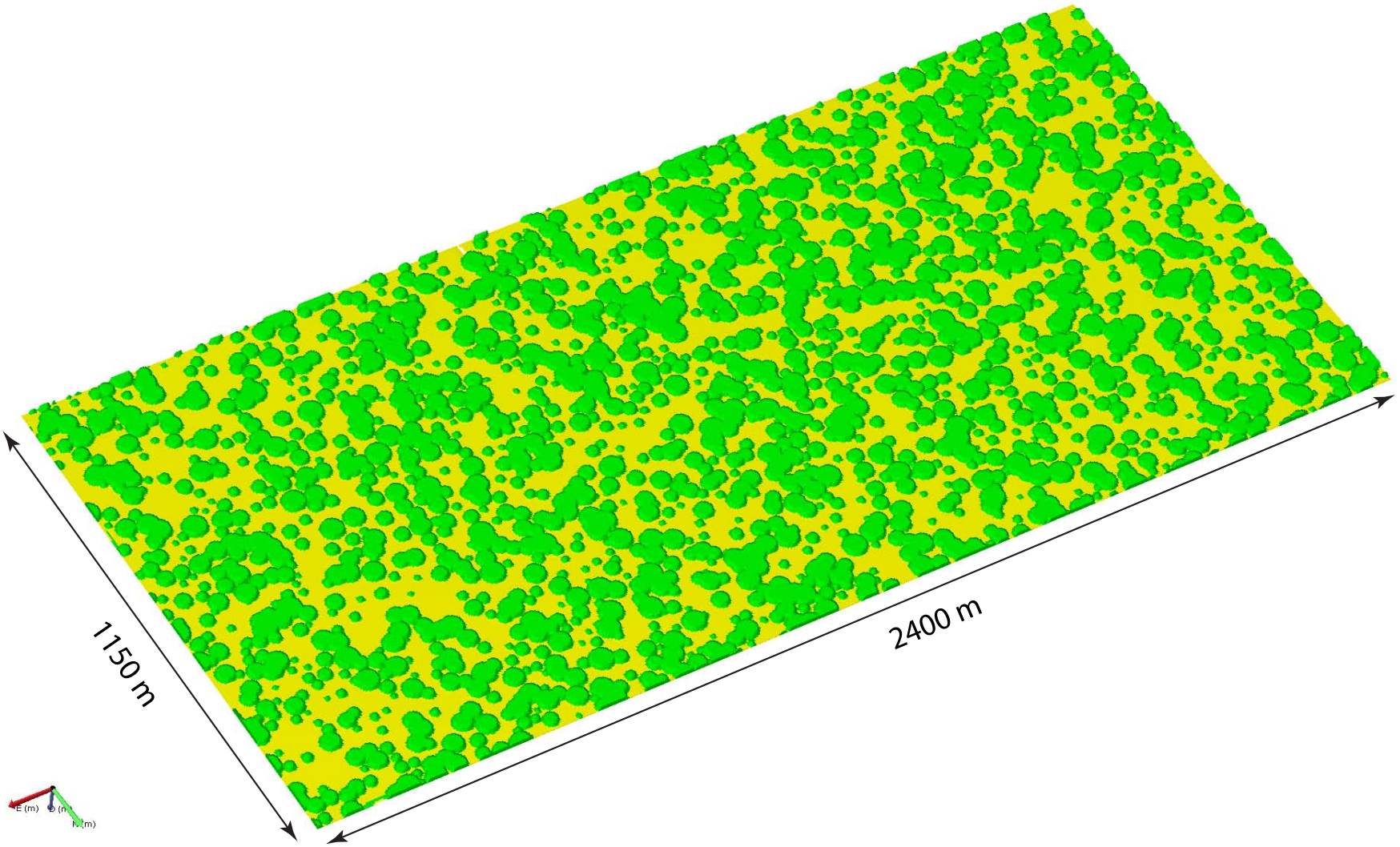


Figure 96: Final height and dip corrected geocellular model of the object-based numerical facies modelling. Green colours represent bioherms and yellow the grid base surface.

### 6.7.4 Results of the numerical bioherm modelling

The visualisation of the basic matlab point-cloud shows that the code reproduces the formation of bioherms and composite bioherms (Figure 97.A-B). In order to test the matlab code, 30 point-cloud realisations with the above-described input parameters were performed. Six of the realisations are illustrated in Figure 97.C-H. Each of the simulation runs produced similar results. Interestingly, in each realisation two end-members of composite bioherms were reproduced. They appeared either as network-like structures, where individual bioherms form chain like arrays or as clusters (Figure 98.A-B). The clusters are characterised by a dense accumulation of numerous individual bioherms and exhibit highly irregular plan view shapes. Clusters have dimensions from less than 100 meters up to approximately 200 meters in diameter. The upper surface of the clusters is not homogenous since they constitute amalgamated bioherms with varying diameters and therefore have an undulating upper surface.

The bioherm arrays form highly irregular chains with length up to 300 meters and are characterised by overlapping, connected large mounds. Individual smaller bioherms with a thickness smaller than the bioherm layer are circular in plan view as defined by the code. Each bioherm structure has steep flanks as observed in the outcrop. During the gridding process the hemispheres were approximated by grid-cells, which resulted in steep flanks of the mounds. Figure 98.C shows the 3D visualisation of the facies model within the canyon system and shows the spatial distribution of the laterally discontinuous bioherms between the canyon cliffs. Figure 98.D shows a 3D visualisation of bioherms intersecting with the canyon cliff surface.

In order to compare the facies model with the outcrop data, cross-sections through the model were computed, which are illustrated in Figure 99.A-B. Figure 99.A shows a cross-section grid, simulating possible outcrop configurations and illustrates the spatial distribution and geometry of the bioherm facies. It highlights that significantly different geometries are obtained depending on the position of the cross-section. Figure 99.B is a detailed view of the calculated 2D cross-section representations of microbial mounds. Smaller mounds exhibit a half elliptic geometry whereas the bigger mounds are oblate with steep flanks. The sizes range from $< 10$ m to $> 70$ m. These cross-sections also demonstrate that complex geometries such as composite bioherms are represented by simple geometries in 2D space.

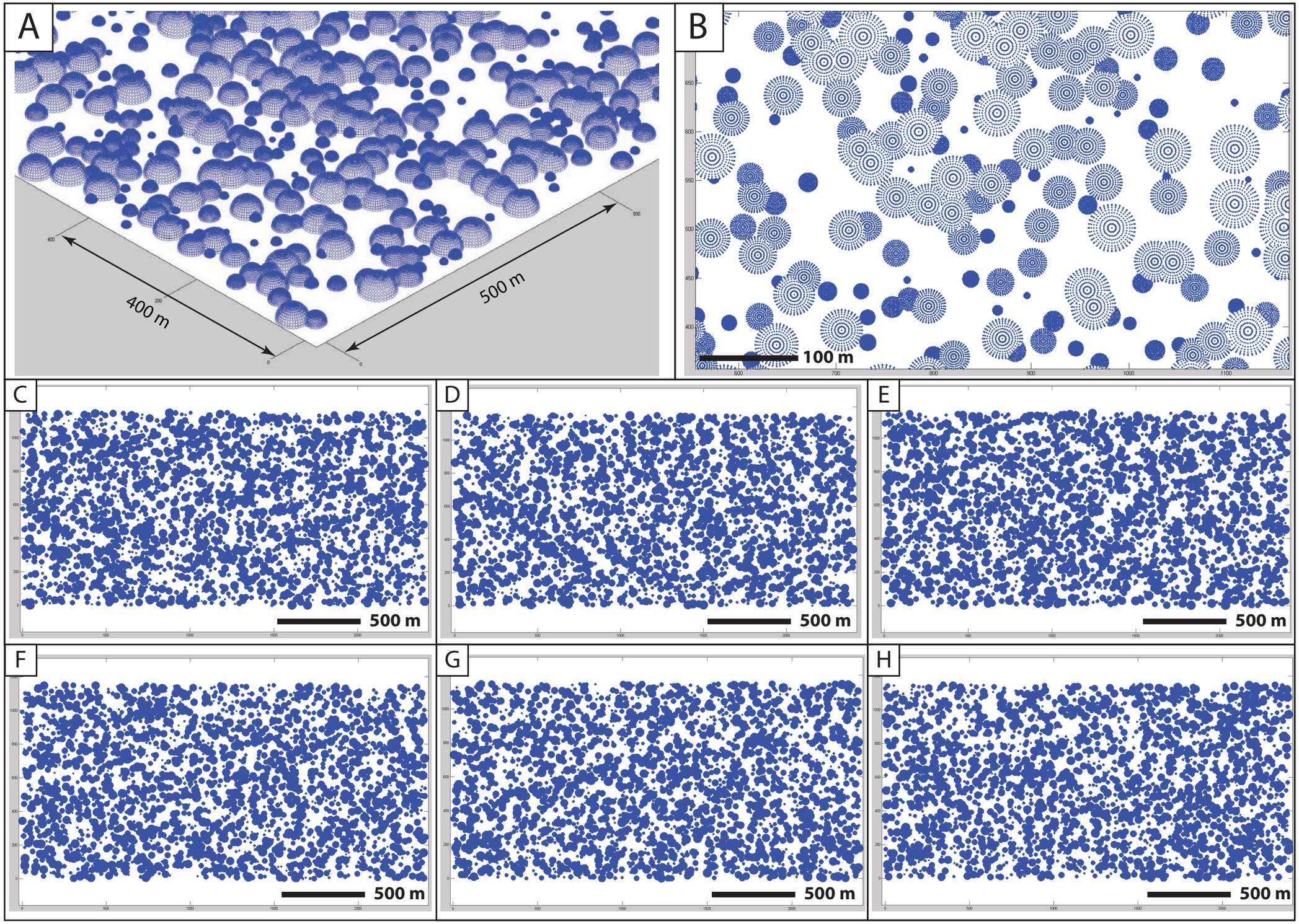


Figure 97: Visualisation of the matlab point-clouds. (A) 3D oblique view of the simulation grid with calculated bioherm structures. Note the formation of composite bioherm. (B) Enlarged section of the simulation grid with detailed plan view of the bioherm realisation. Note the merging of the bioherms and the resulting irregular shapes of the microbialites. (C-H) Plan view of the simulation grids, which show six realisations of the matlab facies modelling.

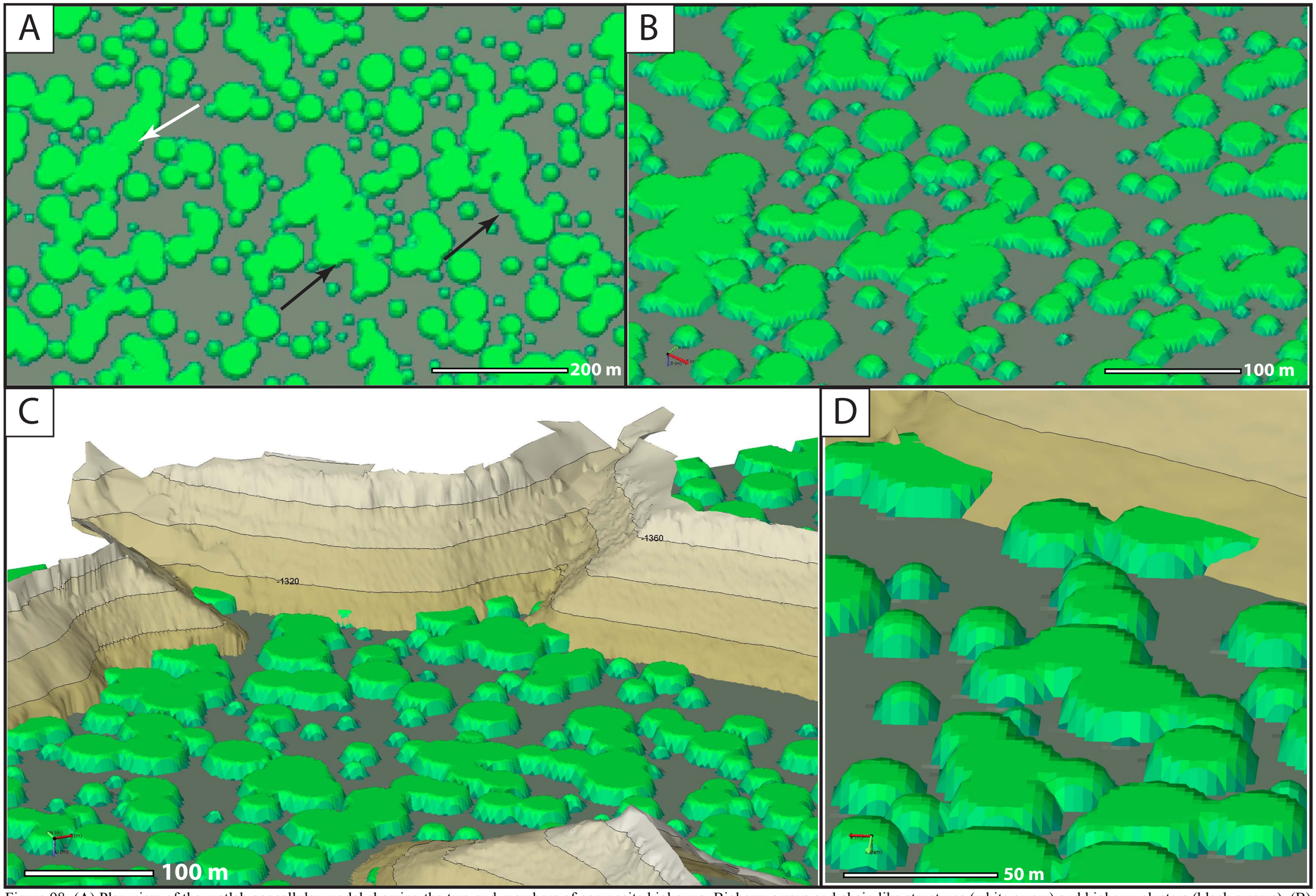


Figure 98: (A) Plan view of the matlab geocellular model showing the two end-members of composite bioherms: Bioherm arrays and chain like structures (white arrow) and bioherm clusters (black arrows). (B) Oblique view of composite cluster bioherms from figure A. (C) Oblique view of matlab bioherm facies model showing the spatial distribution of bioherms in the Zebra River Canyon. (D) Detailed oblique view of bioherms intersecting the canyon wall.

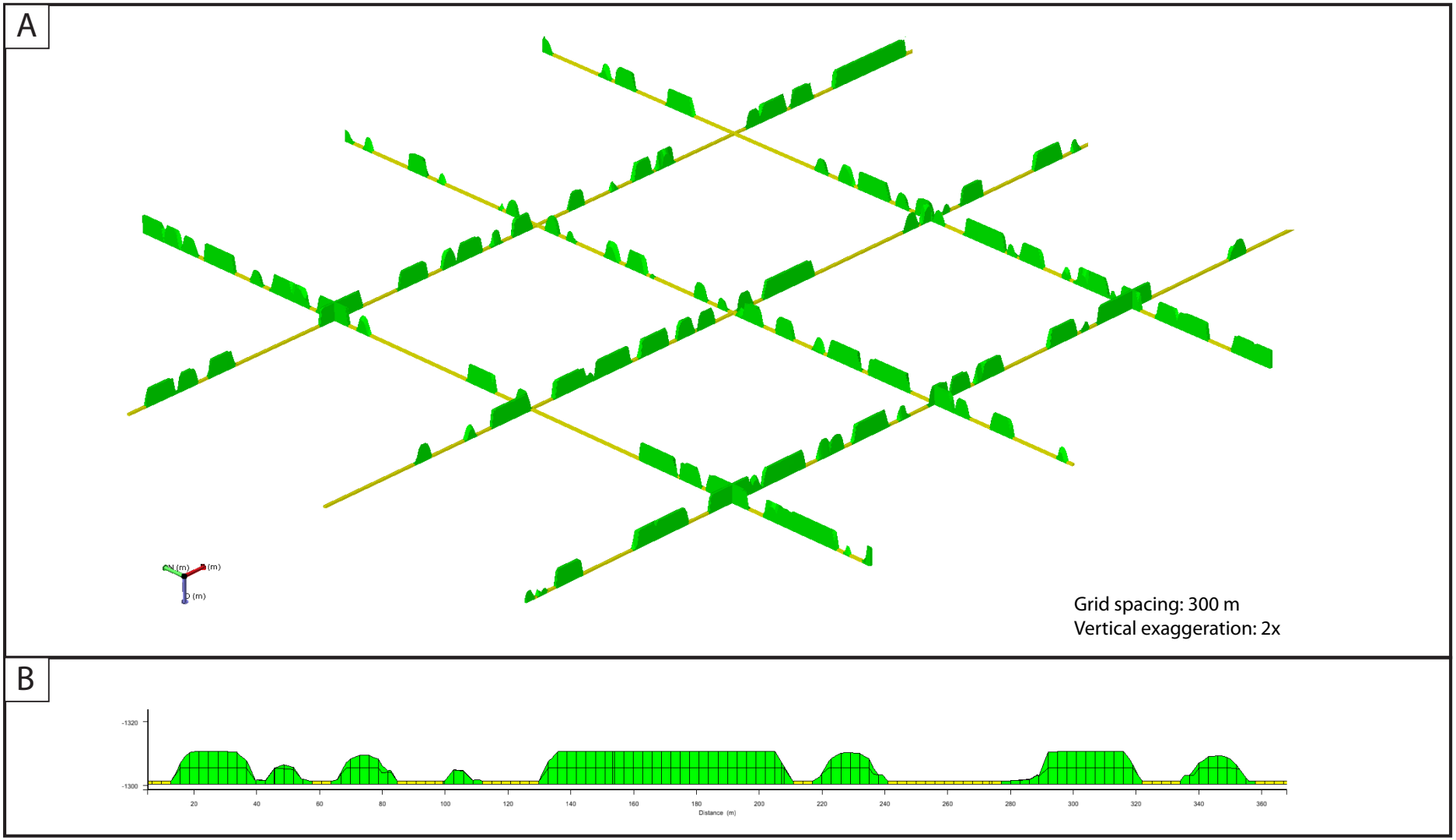


Figure 99: (A) Fence cross-sections through the matlab bioherm facies model illustrating possible outcrop geometry configuration. Grid spacing is 300m and structures are two times vertical exaggerated. (B) Detailed cross-section of the matlab microbial mounds.

The object-based approach proves to be effective in producing a realistic facies model for the microbial carbonates. The limitation of this approach is the random distribution of the bioherms over the base plane (carbonate ramp) and the random selection of the radii for the bioherms. The first case of randomly placing the bioherms over the base plane does not allow the prediction and simulation of any trend within the bioherms. This is due to the lack of available data from the outcrop and virtual outcrop model and also because of the limitation of the programming code. The second limitation is that bioherm radii are picked randomly out of a user-defined radius range. Adams et al. (2005) calculated probability-density functions for bioherm widths and heights and showed that higher frequency occur for bioherms with width under 10 m. The matlab code does not incorporate this data and therefore larger structures might be over represented. However, the modelling of small-scale structures was excluded because those of < 5 m diameter are below the resolution of a reservoir model with a 5 m grid size. An additional limitation of the code is that the base bioherm density is not calculated automatically and has to be done manually in the post-processing, which is not an elegant way.

## 6.8 Multiple-point statistics facies modelling

As discussed, the matlab-based object modelling reproduces a bioherm facies model with sufficient accuracy. However, in order to develop and execute the code several parameters regarding bioherm geometry and spatial distribution had to be assumed. This leads to a certain degree of uncertainty in the model. To overcome these limitations of the numerical matlab modelling, a facies model, which is based on more sophisticated geostatistical tools was created during the course of this research project, namely a multiple-point facies model.

### 6.8.1 Introduction to multiple-point statistics

In numerical reservoir modelling the basic geostatistical tool to model spatial variability of a given reservoir property is the variogram (Clayton, 2002). A variogram is calculated on the basis of a pool of data and aims to describe and predict the dissimilarity of a property at two locations. It is therefore a two-point geostatistical tool and describes the variance of a stochastic process and is based merely on sample values (Cressie and Hawkins, 1980). Variogram-based

geostatistics has its origin in the mining industry where it is successfully applied for the prediction of local recoverable grades of ore (David, 2012). The initial situation in mining industry is, however, different to the one in petroleum geology. In mining exploration, an abundant amount of core data and sample analyses is typically available whereas hydrocarbon reservoir models are mostly based on a few wells and hence lack of information. Therefore, the implementation of variogram-based geostatistics into reservoir characterisation, with its need of high input data, has its limitations. A major disadvantage is that two-point correlation modelling methods are not capable of reproducing curvilinear geometries accurately. In order to predict and model such features as fluvial channels, multiple point data has to be considered simultaneously (Strebelle, 2002; Strebelle and Levy, 2008).

A relatively new methodology in reservoir modelling, which aims to overcome the limitations of variogram-based algorithms, is multiple-point statistics (MPS) facies modelling (Caers and Zhang, 2004; Liu *et al.*, 2004; Strebelle, 2002). This method is capable of incorporating multiple point information to predict the value of a given reservoir property at un-sampled locations. Furthermore, multiple-point facies modelling enables the geomodeller to reproduce complex non-linear geological structures on the basis of robust geostatistics (Dovera *et al.*, 2006; Falivene *et al.*, 2006; Playton *et al.*, 2010; Zhang *et al.*, 2006).

MPS modelling relies on training images as input data. A training image is a conceptual visual representation of the geological heterogeneity (Hu *et al.*, 2013; Jung *et al.*, 2013; Strebelle, 2002). It is developed either as 2D pattern map or as three-dimensional geocellular models (Arpat and Caers, 2007). The training image is essentially a representation of geological patterns and can be developed on the basis of simple field sketches, photographs, satellite images or any representation of the geological structure. The training image is purely a reproduction of geological patterns and does not need to be conditioned to any subsurface data or to exhibit local accuracy. An advantage of the MPS modelling workflow is that it is intuitive and based on a prior geological concept. Thus, it is generally easier for geologists to develop a training image rather than calculate a complex variogram.

Especially for reservoir modelling, based on outcrop analogues, MPS facies simulation has an enormous potential (Caers and Zhang, 2004; Janson and Madriz, 2012; Jung and Aigner, 2012). Outcrop analogues and in particular virtual outcrop models provide an abundance of data, which cannot easily be extracted for reservoir

modelling purposes. Traditionally, outcrop analogue data has to be transformed to be suitable for variogram calculation and the resulting facies models are often poorly representation of the observed heterogeneities due to the limitations of two-point geostatistics. The development of training images based on analogue data significantly eases the extraction of data (Jung and Aigner, 2012).

### 6.8.2 Bioherm training image development

The incentive of the author to employ the use of multiple-point geostatistics was to improve the quality of the existing matlab-based facies model. The main uncertainties in the matlab code were the spatial distribution of the bioherms and their shapes. The distribution was set to be random, with roughly 45% base coverage and the plan view shape to be circular. In order to overcome these limitations a training image was created which reproduces these bioherm specific parameters more realistically. For the purpose of the creation of a training image neither the virtual outcrop model, neither outcrop interpretations nor the photomosaic interpretation were suitable on its own because they only represent cross-sections through the bioherms. Thus, the satellite image showing the plan-view shapes and distribution of bioherms (see Figure 52) to the west of the study area was used as primary data input for the training image development.

The image was subsequently used as a base map and the outline of the mound structures were digitally mapped with 3D polylines and georeferenced (Figure 100.A-B). Consequently by using the geometrical properties of the bioherm cross-sections of the virtual outcrop model and in conjunction with field observations, 3D mesh surfaces were constructed to represent the bioherms (Figure 100.C). The heights of the bioherms were assumed to be half the length of the bioherm long axes. Figure 100.D shows a cross-section view of the constructed, three-dimensional visualisation of the bioherms. It shows a close resemblance to the geometries observed at outcrop.

The surface model was then used to construct a geocellular training image with 2x2 m horizontal grid resolution. An upper, planar horizon, which coincides with the highest bioherm, was constructed to represent the upper boundary surface of the bioherm layer. The internal layering was set to be four, proportional (four equally thick layers) and conformable to the base plane. The final bioherm training image is shown in Figure 101.A.

### 6.8.3 Quality control of the training image

Figure 101.B shows two cross-sections through the geocellular training image. Both cross-section views show a similar pattern of bioherm and inter-bioherm facies as observed in outcrop. Besides the purely visual quality control of the training image and of the realisation of the geological patterns, the training image also has to be stationary in order to get realistic results with JewelSuite. Although non-stationary training images can be used with other MPS modelling algorithms, JewelSuite does not yet provide this feature.

Stationarity is a decision in geostatistics, which implies that the statistics of an unknown variable is independent of the spatial location of the sampled and un-sampled values (Carle and Fogg, 1996). This is a standard concept in geostatistical modelling and is also required in two-point statistics and variogram calculation. The stationary quality control of MPS training images is however not a straight-forward process because of the lack of suitable methodologies. Recent work on this problem has been done by Mirowski *et al.* (2008). The authors developed a methodology to assess whether training images show stationary or not. However, this methodology is constrained to 2D training images and 3D images cannot be tested at the moment. An informal rule of thumb to evaluate the stationarity of training images, proposed among geomodellers, is that a training image can be considered stationary if every portion of the image 'looks like' every other portion of the image. More precisely, that the geological structures form a repeating pattern and the whole image looks approximately homogenous. The author wants to highlight that this is a very vague method to validate the stationarity of a given 3D training image, however it does present the only method at the current stage of research. Clearly, future research has to focus on establishing a robust methodology of the training image quality control process.

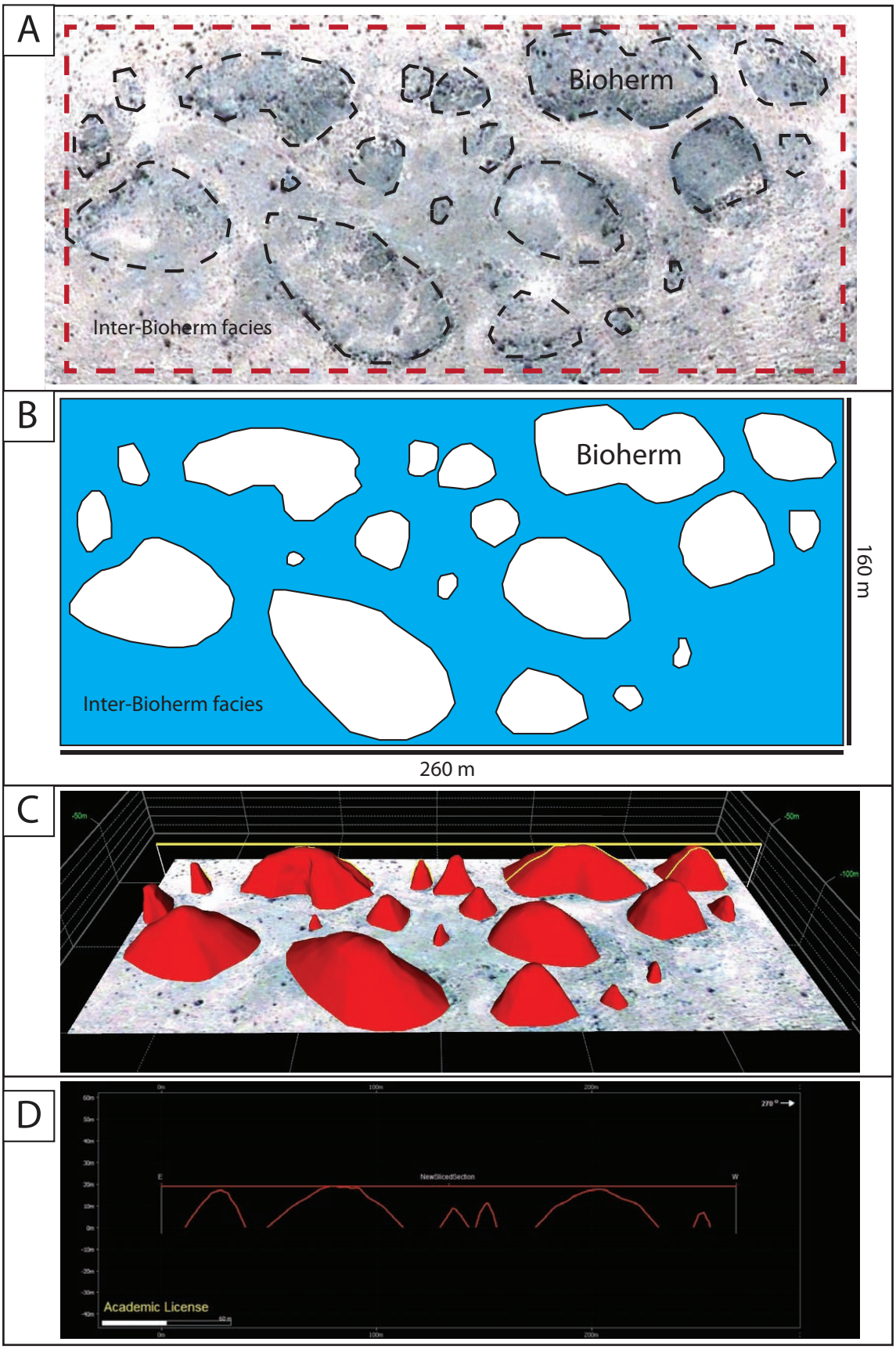


Figure 100: (A) Enlarged area of the bioherm satellite image with digitally mapped bioherm outlines (black dotted lines). (B) Constructed base map of bioherms (white areas) and inter-bioherm facies (blue areas). The base map shows the exact geometries, dimensions and spatial distribution of bioherms in the Omkyk Sequence 2. (C) The base map was subsequently used to develop a 3D visualisation of the mound structures. (D) Cross-section view of the constructed 3D meshed surfaces. The cross-section representations closely resample the observed mound geometries at the outcrop and in the virtual outcrop model. Location of cross-section: Yellow line in image C.

Nevertheless, the Zebra River bioherm training image does not show any trend, like for instance a predominant distribution of larger bioherms at one side of the image. Furthermore, mounds are homogenously distributed by means of widths and heights distribution. The overall image looks approximately homogenous and therefore it is concluded that the bioherm training image is stationary.

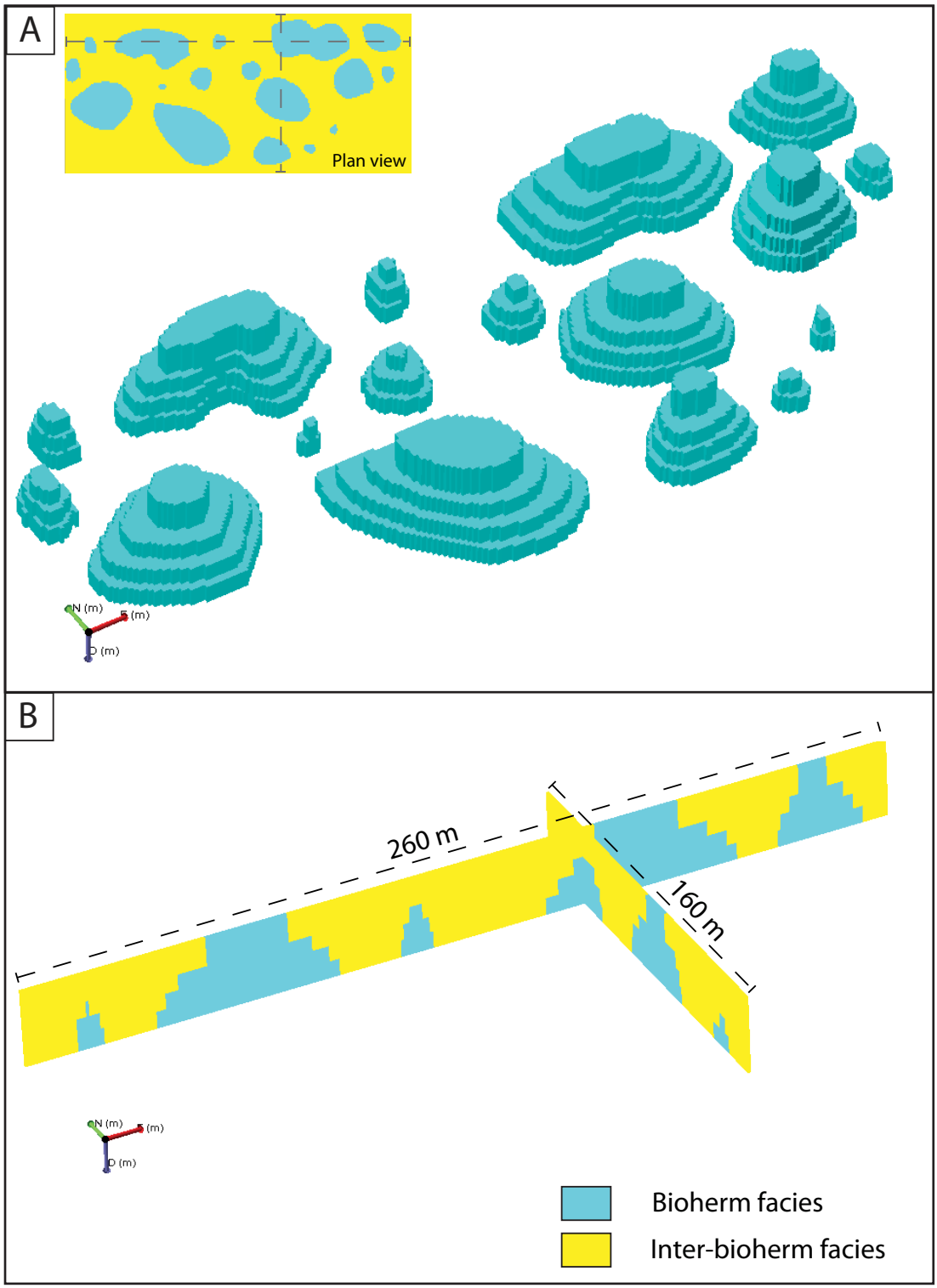


Figure 101: (A) Oblique view of constructed bioherm geocellular training image. Note that only the bioherm facies is visible showing the geocellular representation of the microbial mounds. In the upper right a base map of the lowest grid layer is plotted. (B) Cross-section through the training image with full facies association. Blue represents bioherm facies and yellow inter-bioherm facies. See image (A) base map for cross-section location.

### 6.8.4 MPS facies modelling parameters and results

The multiple-point facies modelling was performed with JewelSuite in-built MPS modelling workflow. The advantage is that the simulation is directly performed in the Zebra River model and within the bioherm horizon. Therefore, the results do not have to be height or dip corrected and no further post-processing is required. The modelling parameters were set to have no scaling of the training image to reproduce the same geometries and patterns of the bioherm in the simulation grid as defined in the training image. A trend parameter in the modelling workflow was not used since an expected trend across the simulation grid (e.g. change of bioherm dimension and distribution from up-dip to down-dip) was not expected. The shapes (facies patterns) of the training image were specified to be isotropic and irregular. The MPS-simulation algorithm populates the simulation grid by visiting cells following a certain path and this path was set to be random. No conditioning data were used (e.g. bioherm distribution at the outcrop surface constrained by pseudo-wells) because the objective of the modelling was to compare the modelling results with the outcrop distribution. If the training image would have been tied to the outcrop facies distribution, the exact facies patterns would have been reproduced. Therefore, no outcrop comparison would have been possible.

#### 6.8.4.1 Results

A total of 30 facies realisations were produced and each facies run produced similar results. Figure 102.A-C shows three plan view examples of the MPS facies model of the entire simulation grid. The MPS modelling workflow successfully reproduced the laterally discontinuous bioherms. Smaller individual bioherms exhibit circular to elliptical plan view shapes (Figure 102.D-E). A distinct feature of the MPS-realisation is the reproduction of composite bioherms. These larger mound structures show highly irregular shapes of merged bioherms. Additionally, composite bioherms in turn are observed to merge together, forming large interconnected microbialite bodies (Figure 102.D-E). The internal structure of the composite bioherms is not homogenous and pockets of inter-mound facies occur. Although the shapes and distribution of the bioherms might seem to be random, a trend of bioherm alignment towards the NW-SE can be deduced in Figure 102.A-C. In order to validate this apparent trend the MPS simulation was repeated on a simulation grid four times larger (Figure 102.F) which clearly shows that the microbialites form elongate,

array-like structures, striking roughly towards NW-SE, perpendicular to the strike of the Kuibis carbonate ramp.

Figure 103 and Figure 104 show the multiple-point facies model in 3D within the lidar digital elevation model and the photorealistic DEM from the Zebra River area, respectively. Both images show the modelled, three-dimensional architecture of the microbial carbonates within the Zebra River Canyon. Figure 105.A shows an enlarged area of the 3D facies model and bioherms show steep flanks with oblate tops. Figure 105.B shows an enlarged area with abundant composite bioherms. The 3D geometry of the bioherms is complex and is characterised by merging areas connecting individual bioherms. In Figure 106 a close up of the bioherms, intersecting the lidar DEM, is illustrated, showing the three-dimensional realisation of the microbialites at outcrop scale.

In order to compare the MPS facies model with the geometries observed in the virtual outcrop model, several cross-sections were computed. Figure 107 shows fence cross-sections through the entire simulation grid illustrating potential cross-section realisations. In the enlarged section, the simulated 2D spatial distribution of small-scaled bioherms and large composite bioherms is visible. Figure 108 shows an E-W canyon cliff parallel section and a detailed cross-section view of more than 500 metres. The cross-section shows that the MPS facies model resamples closely the 2D geometry in the Zebra River canyon system. Bioherms appear domelike with flattened top-layers.

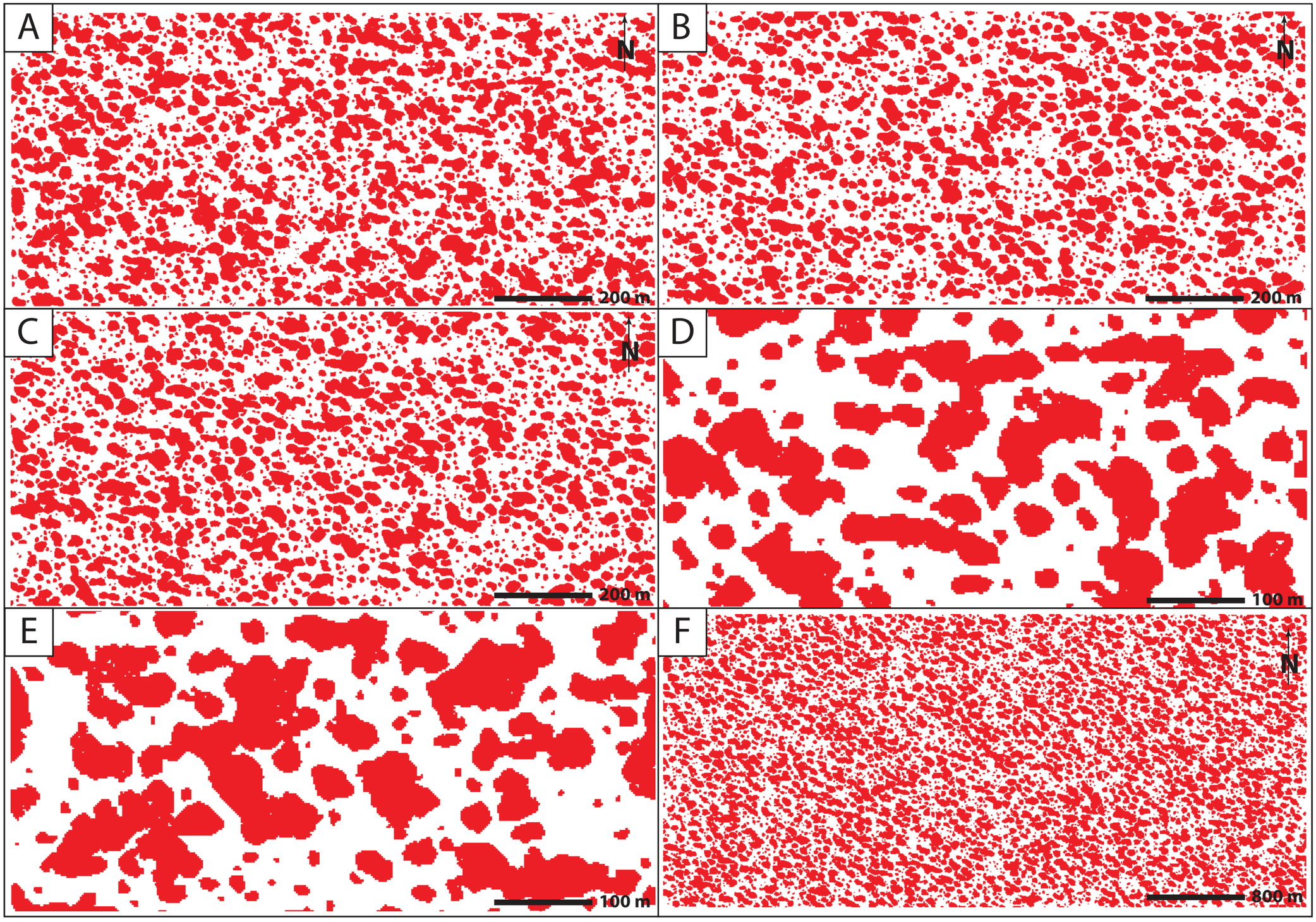


Figure 102: (A-C) Plan views of the MPS facies models over the entire simulation grid. (D-E) Enlarged simulation grid areas of the MPS realisations, illustrating the plan view shapes of simulated bioherm structures. Smaller bioherms (<50 m in diameter) exhibit circular to elliptic geometries, whereas composite mounds show a highly irregular geometry. (F) In order to proof the spatial trend of bioherm alignment a MPS simulation was carried out on a 4 times bigger simulation grid. Clearly visible is that the mound structures are orientated towards the NW-SE, perpendicular to the strike direction of the Kuibis carbonate ramp succession.

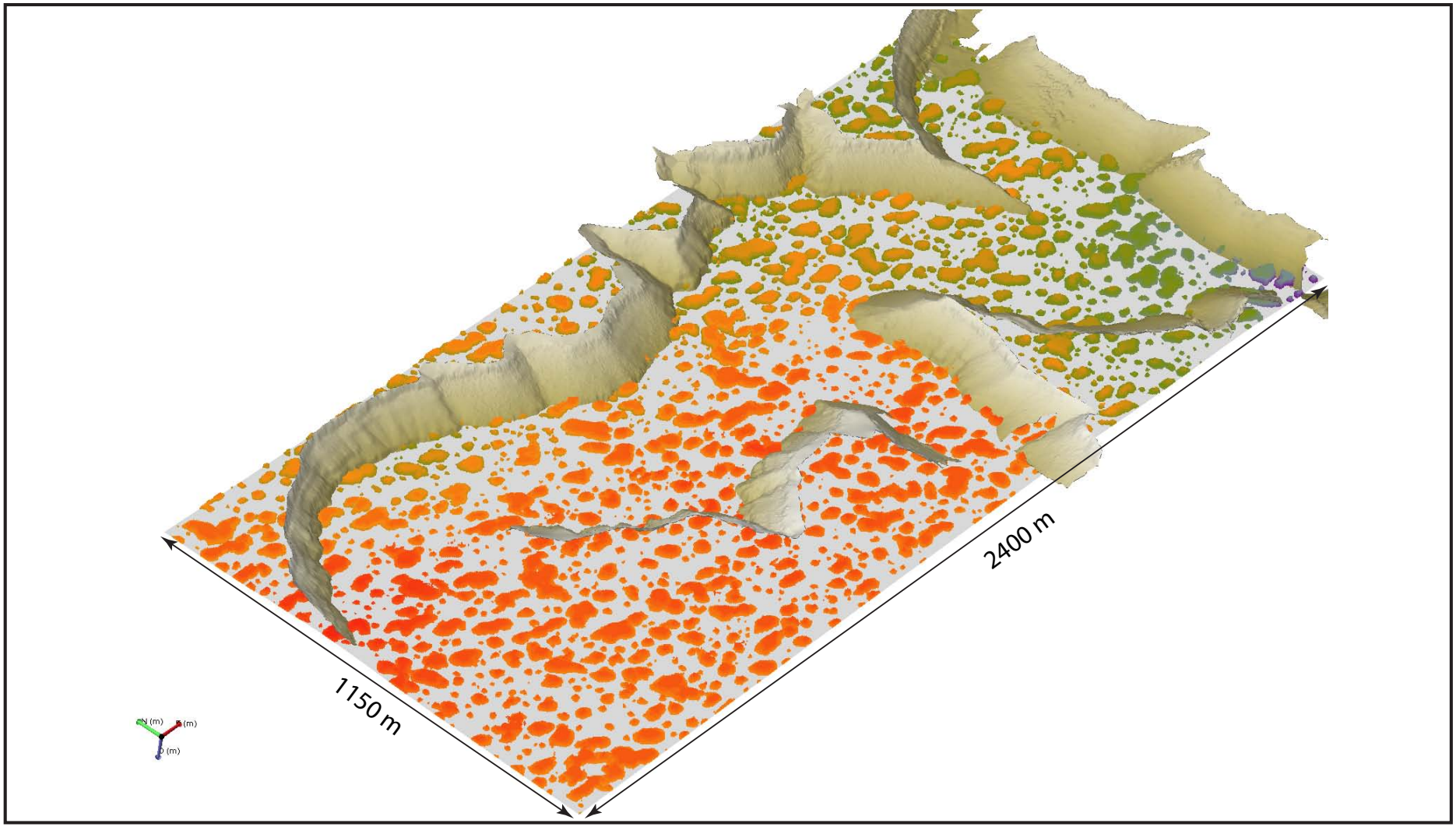


Figure 103: Entire multiple-point facies model plotted within the lidar digital elevation model showing the spatial arrangement of the simulated microbial mounds. Oblique view from the southwest. The colouring of the bioherms corresponds to grid-cell centre depth. The colouring was chosen to better visualise the mounds in three dimensions and shows the gentle dipping (structural dip) of the model towards NE. Red to orange colours indicate higher elevation whereas green to blue colours indicate lower cell centre depth and elevation.

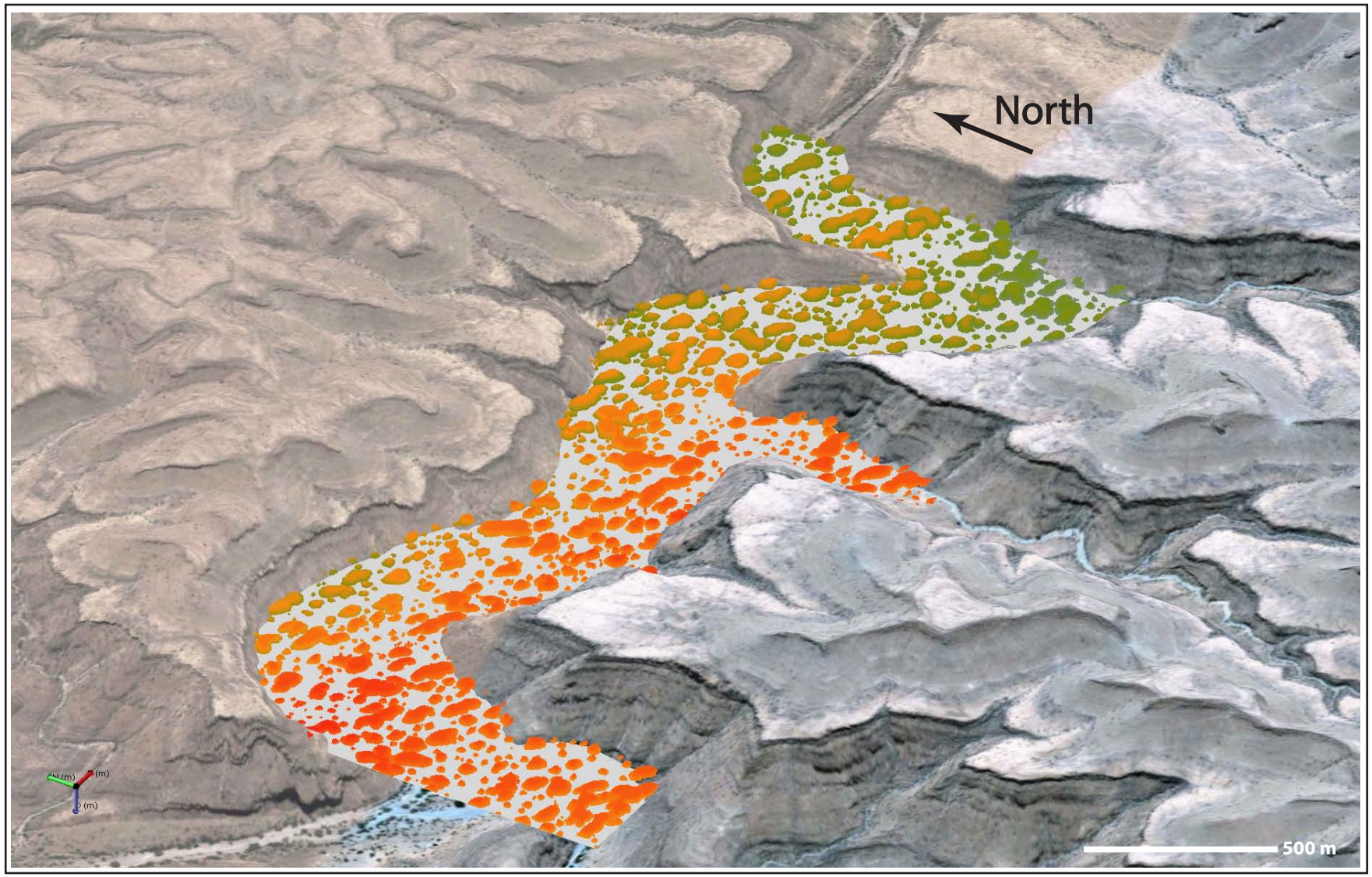


Figure 104: Multiple-point facies model visualised within the photorealistic Zebra River digital elevation model. Colour coding is the same as in Figure 103.

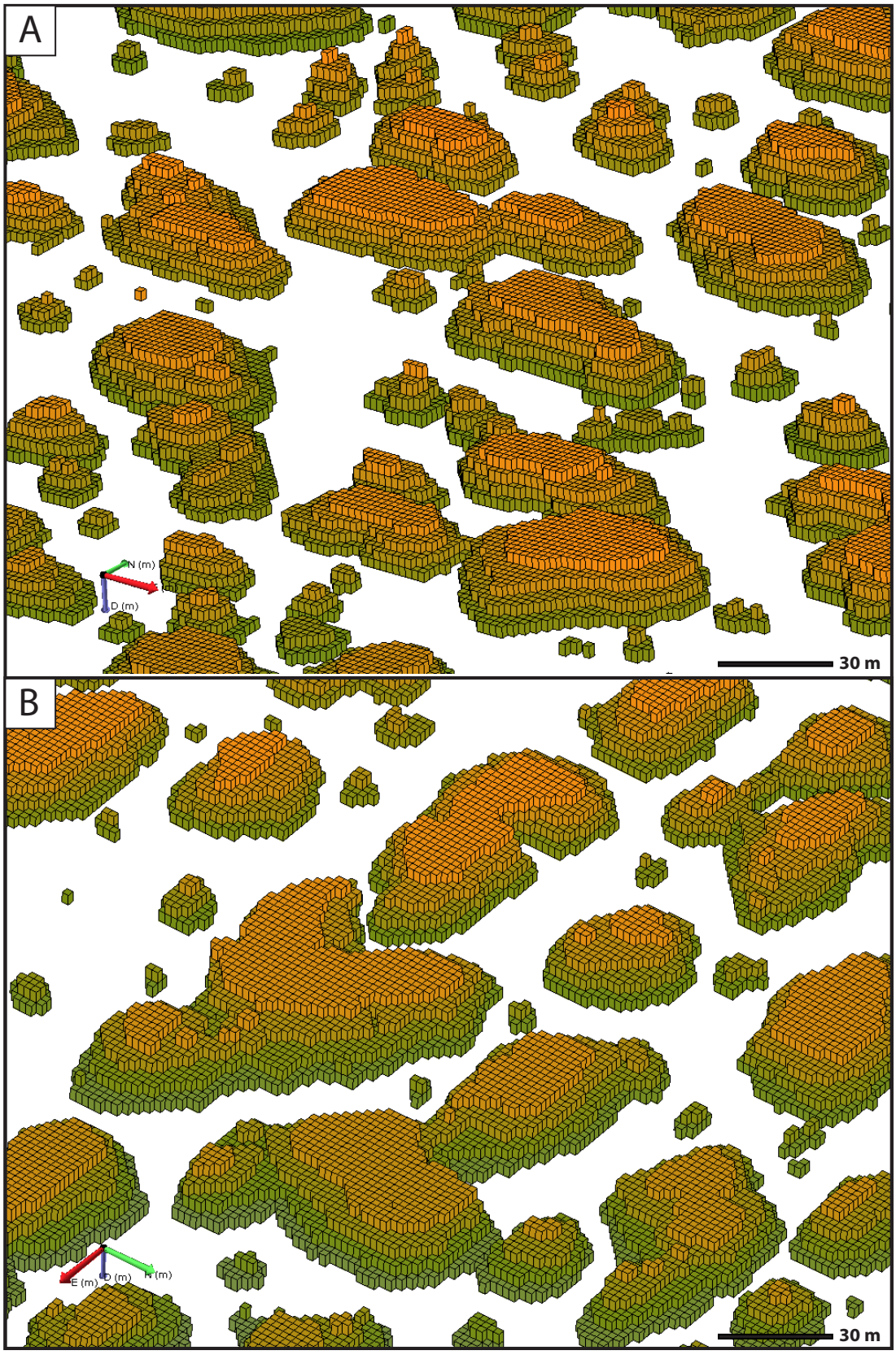


Figure 105: (A-B) 3D visualisations of MPS bioherms. See text for discussion. Same bioherm colour coding as in Figure 103.

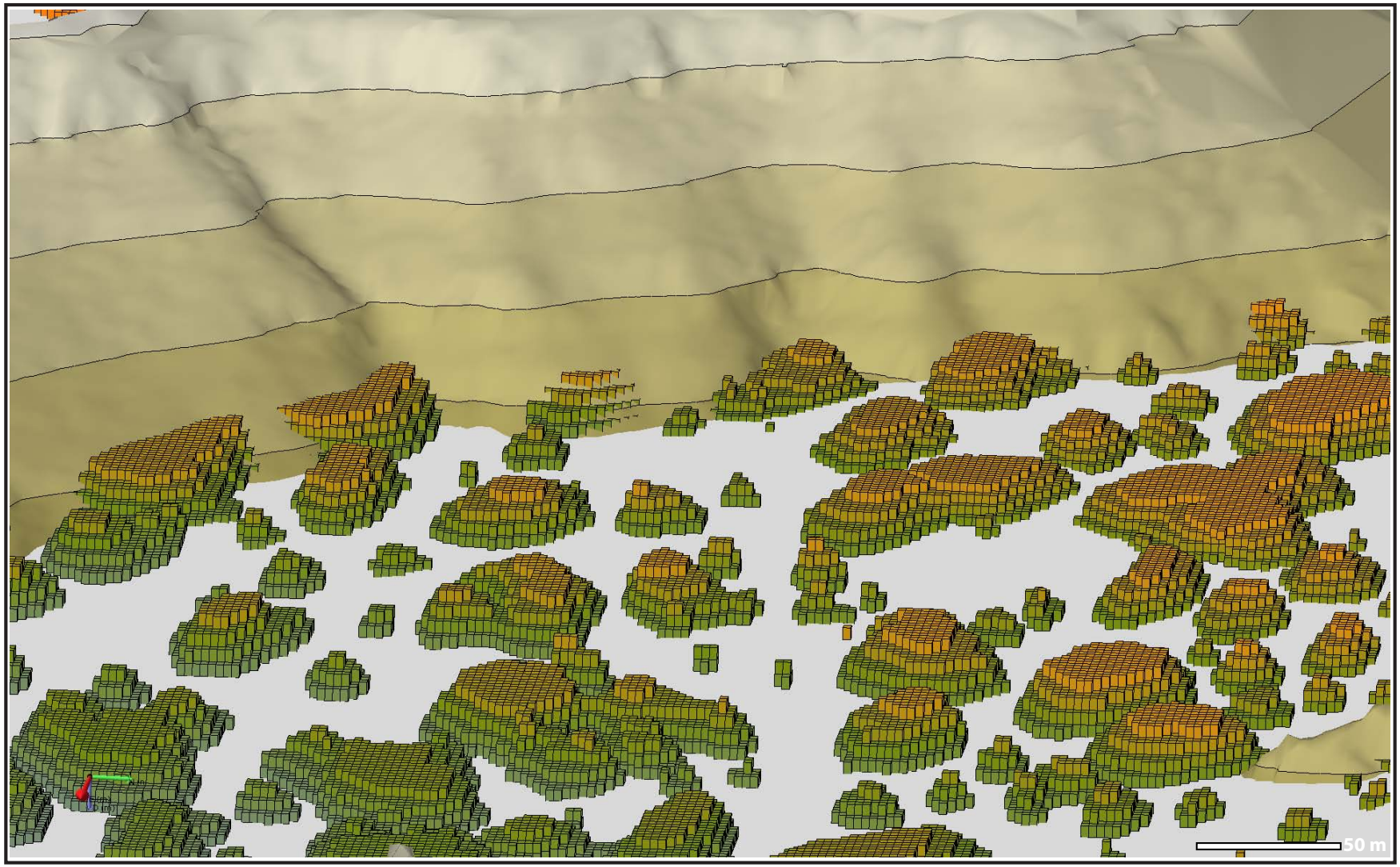


Figure 106: 3D visualisation of MPS bioherms intersecting the Zebra River DEM canyon wall. Same bioherm colour coding as in Figure 103.

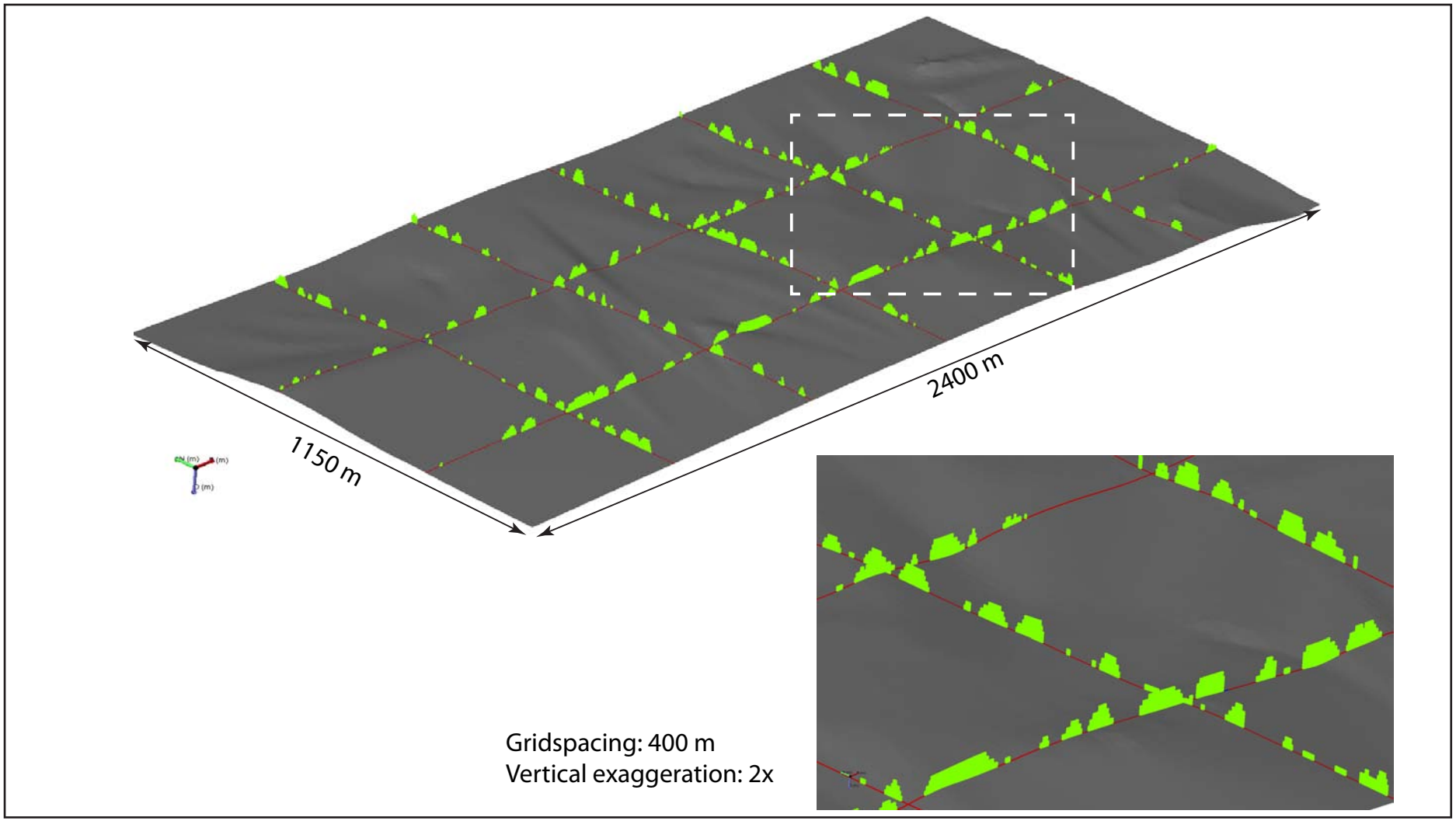


Figure 107: Fence cross-sections through the entire MPS facies model illustrating possible outcrop configurations of bioherm geometries (green mound structures). For better visualisation an enlarged area is plotted in the lower right of the image. White rectangle indicates location. The images are 2 times exaggerated vertically and the grid spacing is 400 metres.

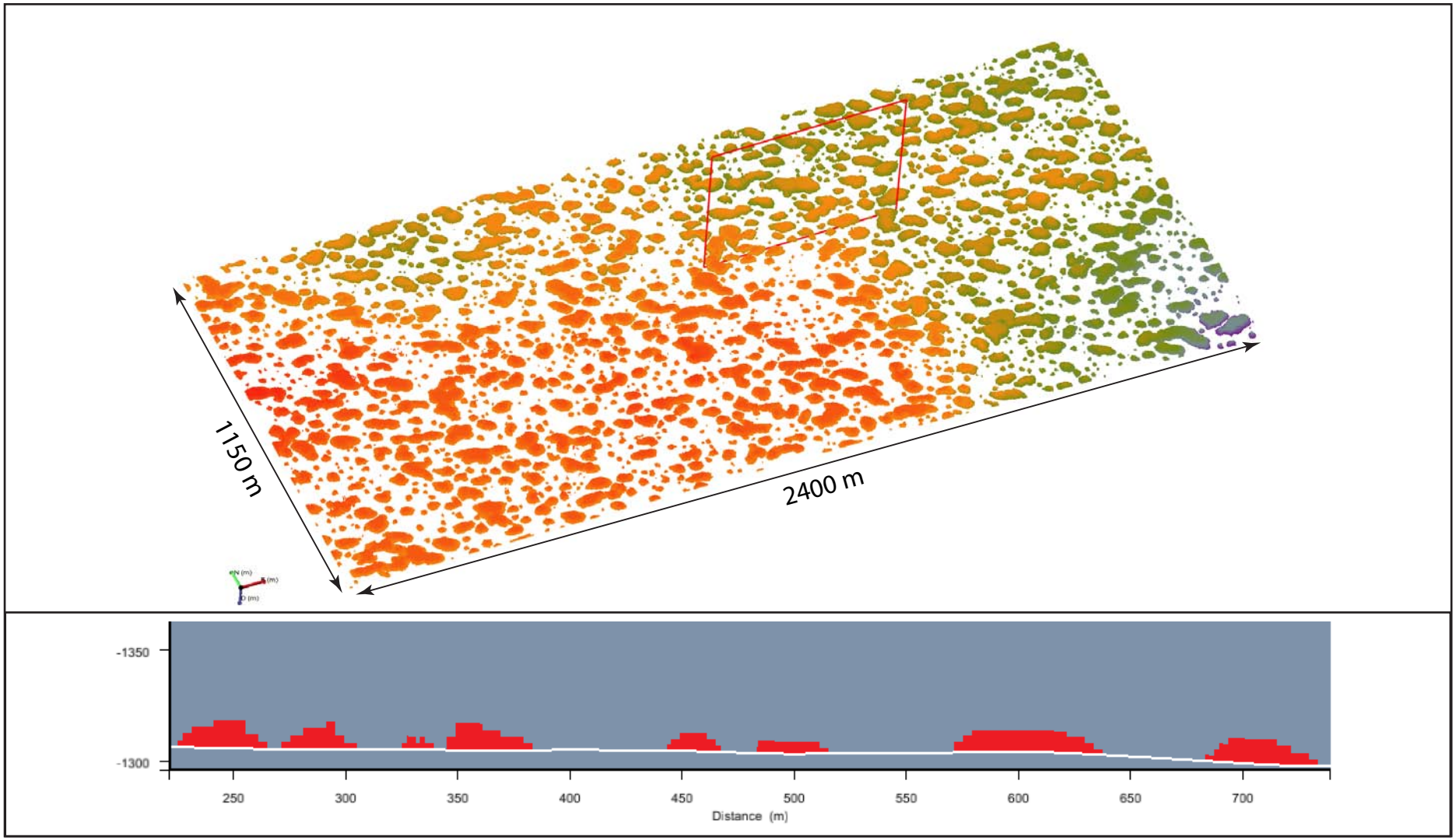


Figure 108: Entire MPS facies model with associated E-W, canyon parallel cross-section. Red rectangle indicates cross-section plane. See text for discussion. Same bioherm colour coding as in Figure 103.

## 6.9 Discussion

### 6.9.1 Outcrop comparison of facies models

In order to test the validity of the matlab and multiple-point statistics facies model, the two models were visually compared with the outcrop. Figure 109.A shows a snapshot of the lidar virtual outcrop model and the equivalent cross-sections through the matlab (Figure 109.B) and MPS facies model (Figure 109.C), respectively. In both modelling approaches, the locations and dimensions of the bioherms were not conditioned to the data from the virtual outcrop model. This was necessary in order to test the results with canyon-wall-parallel sections. Therefore, the modelled bioherms do not accurately represent the exact patterns and locations of the bioherms. However, the same basic distribution and geometry (spacing and size of bioherms) has been reproduced in both facies modelling approaches. The section in the virtual outcrop comprises 11 bioherms and the same number of bioherms was reproduced with the matlab code whereas 13 bioherms were generated with multiple-point statistics. Their over-representation in the MPS can be explained by statistical variance. In both modelling realisations, the shapes of the bioherms resemble the actual bioherms in the field with steep flanks and oblate tops. Additionally, the same distribution of larger bioherms and potential composite bioherms was reproduced. Therefore, both modelling approaches simulated statistically acceptable facies realisations.

### 6.9.2 Comparison of modelling approaches

Both modelling approaches resulted in bioherm facies models which reproduced the observed microbial geometries and spatial arrangement with high precision. Additionally, with both approaches the formation of composite bioherms could be realised. However the numerical object-based modelling requires substantial post-processing (gridding, height and dip correction). Furthermore, the code is limited by random distribution of the bioherms and therefore fails to predict a trend within the microbial sequence. An advantage is that the input parameters can be quickly changed and numerous sensitivity runs with varying bioherm specification can be

performed, which makes the code flexible. The construction of the code however needs profound knowledge in source code development and takes time to develop.

In contrast to that, MPS facies modelling and the development of the training image is intuitive for geologist since it is based on a conceptual geological model and relatively fast. It additionally incorporates all available data, which was not possible with the numerical modelling. A success in the MPS approach was the modelling of a spatial trend; the alignment of the bioherm structures towards NW-SE. This direction is roughly parallel to the palaeo-dip of the Kuibis carbonate ramp. Elongation of microbialite domes and columns is a known feature of Neoproterozoic microbial carbonates (Riding, 2002; Sami and James, 1993) and has been reported from the Kuibis platform (Adams *et al.*, 2004; Grotzinger *et al.*, 2005). Adams *et al.* (2005) recognised the preferred orientation of the internal architecture but could not observe the general alignment in outcrop. This is due to the limitation of the cross-section geometries in the canyon system and the numerical surface modelling. The alignment of microbialites has been interpreted as a response to incoming wave activity and the microbial structures try to minimise their exposure to wave energy (De Boever *et al.*, 2006; Moore and Burne, 1994). This simulated trend has major implications for subsurface well planning. In order to optimise horizontal wells, the preferred well trajectories should be along the strike of the carbonate ramp. By choosing such a trajectory a maximum number of bioherms would be penetrated.

However, the weak point of the MPS approach is that the entire model is based on one satellite image. The image represents one time-slice in the bioherm evolution and one possible spatial bioherm configuration. Satellite images, derived from other locations might result in significantly different facies models. Future research should aim to develop a training image catalogue for the microbialites in order to improve the facies realisations.

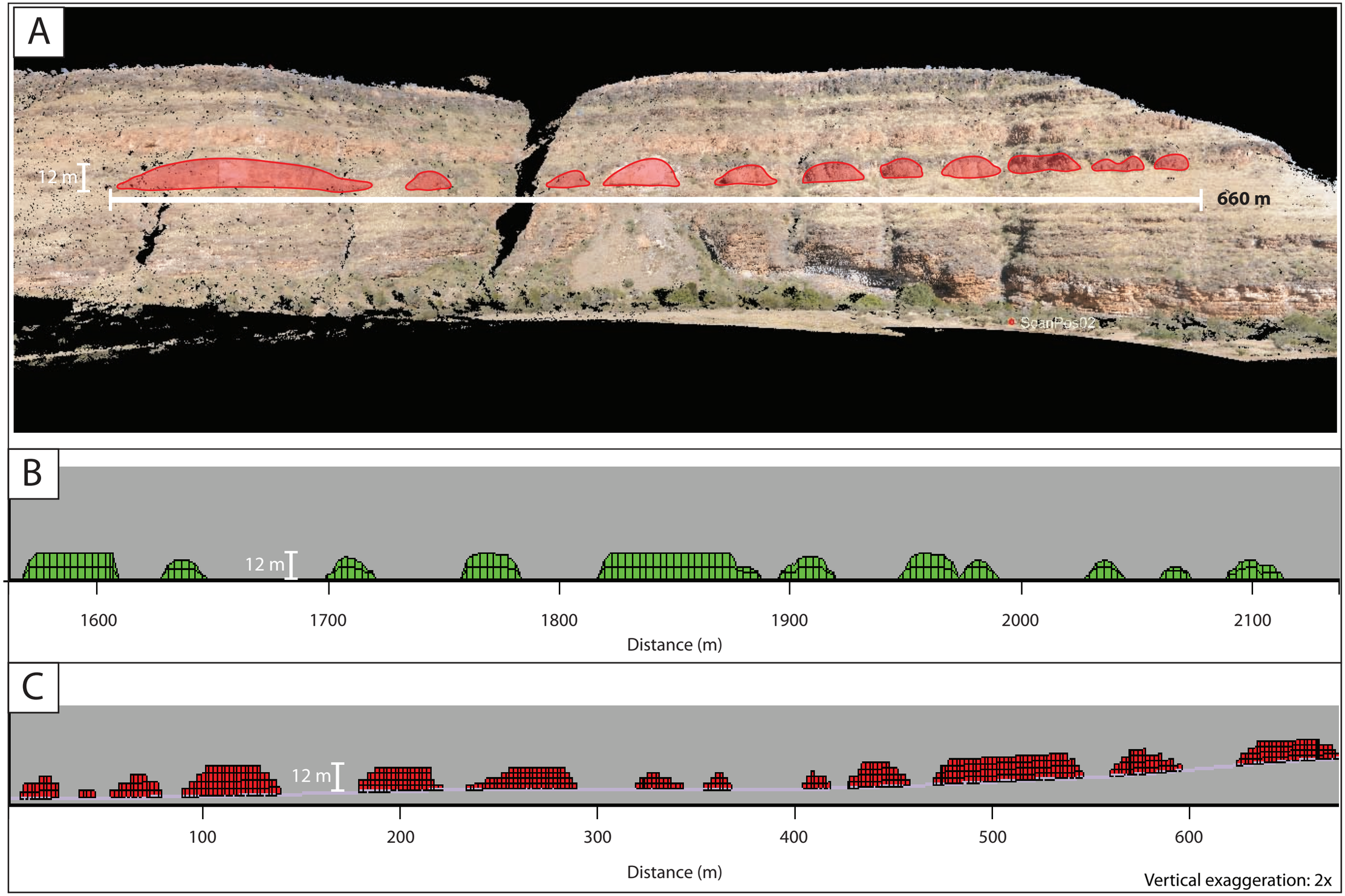


Figure 109: Comparison of the bioherm geometries observed in the virtual outcrop model with computed section equivalent cross-sections of matlab and MPS-facies model. (A) Snapshot of virtual outcrop model with mapped bioherm structures (red, transparent areas). (B) Equivalent matlab facies model cross-section (not dip corrected). Cross-section length is 600 m. (C) Equivalent MPS facies model cross-section. For better visualisation the cross-section is 2 times vertical exaggerated. Cross-section length is 660 m.

### 6.9.3 Comparison to the existing Zebra River model

The constructed geocellular model of the Omkyk Sequence 2 in the Zebra River Canyon, developed during this research project shows the same simple layer cake architecture as the model presented in Adams *et al.* (2005). However, the main difference between the models is the interpretation and modelling of the bioherm horizon. Although, both bioherm facies models look similar (see Figure 93), distinct differences in the bioherm geometries occur. Adams *et al.* (2005) excluded the possibility of merged and composite bioherms and assumed that bioherms are simple hemispheres. This is in stark contrast to the here presented facies models, where highly irregular bioherms and composite bioherms were reproduced. The results show that the facies models accurately represent the observed geometries in the outcrop. Adams *et al.,* (2005) did not compare the facies model with the outcrop sections and therefore detailed visual comparisons between the models cannot be made. A key observation of the author's modelling approach is the realisation of the spatial trend within the multiple-point facies model. Although this trend was recognised by Adams *et al.,* (2005), it could not be implemented into their reservoir model. This was successfully achieved during this research project.

The author wants to highlight that there is inconsistency in the modelling process of Adams *et al.* (2005). The authors especially focussed on the visualisation of bioherms with widths of approximately 5 m, however the horizontal resolution of the geocellular model was set to be 10 m in the horizontal extend. Consequently, the majority of bioherms could not have been reproduced in the geocellular model because they are well below grid-resolution. However, this is not discussed in Adams *et al.* (2005) and limited accurate comparison between the models. The comparison of the volumetric calculations is discussed in chapter 7, were detailed volumetric calculations for the bioherm facies models are presented.

## 6.10 Conclusion

This chapter presented the methodologies and workflows required and used to develop the static geocellular analogue model of the Omkyk Sequence 2 in the Zebra River Canyon section, based on the terrestrial laser scanning survey. The observed and in the field interpreted geometries were digitally mapped on the virtual outcrop

model, which then served as main input data for the geocellular model construction. The basic geocellular model has a simple layer cake architecture with nine grid layers. The base grid layer has a thickness of more than 60 m. This is due to the incorporation of all available data from the virtual outcrop model, which extends outside of Omkyk Sequence 2. The following 8 grid layers are equally thick (8-11 m) and show minimal lateral variation.

The main focus of the reservoir modelling was on the visualisation of the bioherms and newly interpreted composite bioherms. For that, two different approaches were used by the author: (1) a numerical object based modelling approach and (2) a multiple-point statistics approach. The object modelling is based on a matlab code developed by the author, which incorporates the measured dimensions of the bioherms from the virtual outcrop model. This approach is limited by the possibility to incorporate all available data but reproduces an acceptable facies model, based on outcrop comparison. The MPS modelling workflow used a training image, which incorporates all available data in one conceptual geological model. The MPS realisation produced a stochastic realistic model with high precision and additionally realised a spatial trend, which is compatible with the palaeogeography of the Kuibis carbonate ramp succession.

# 7 Fluid flow analysis of the microbial carbonate system

## 7.1 Introduction

The analysis of the dynamic behaviour of the microbial carbonate system constitutes the last step of reservoir characterisation performed during this research project. Dynamic reservoir studies test fluid flow characteristics of flow units to predict optimal well placements and well trajectories in order to maximise recoverable oil and gas reserves. Furthermore, through analysing fluid flow pathways, the main flow and baffle units within the reservoir can be recognised. Thus, a dynamic reservoir study constitutes a predictive tool, used to focus on critical variables affecting fluid flow and therefore production rates. In the petroleum industry a vast amount of dynamic data are generally available for accurate fluid flow behaviour studies. This typically includes historical well production rates, dynamic data of the hydrocarbon reservoir, such as the temporal evolution of pressure and temperature. In addition, physical and chemical studies of the produced hydrocarbons are considered to predict flow characteristics at a given pressure and temperature field. The combined dataset subsequently forms the basis for history matching analyses and the study of past fluid flow, which is consequently used to predict future flow performance.

The developed geocellular model in this research project is an outcrop based analogue model for potential hydrocarbon reservoirs in microbial carbonates in the subsurface of the Owambo Basin and elsewhere. Consequently, no production took place and thus no dynamic data are available. Therefore, the only available tool to investigate flow performance of this microbial system is dynamic forecasting analysis (Baker, 2001). This technique allows the prediction of the temporal evolution of flow performance on the basis of estimated flow relevant properties. Thus, it provides a first approximation of the dynamic behaviour of the reservoir.

The developed multiple-point facies model of the Zebra River canyon system served as a basis in order to test two reservoir architecture scenarios, with different reservoir geometries, porosity and permeability distribution. A total of 5 petrophysical models for input in the flow simulator were developed. The aim of using 5 models with different architectures and petrophysical characteristics was to

test a range of possible scenarios in order to investigate the critical variables affecting fluid flow in the microbial system. The development and specification of these 5 models is covered in the first part of this chapter. The main part of the chapter covers the streamline fluid flow analyses by means of detailed description of the methodology and flow results. The chapter concludes with an in depth discussion and interpretation of the simulated flow performance.

The streamline fluid flow analysis was carried out in collaboration with Sandhu Kerry, senior reservoir engineer of Baker Hughes at Chiswick Park office, London. Sandhu Kerry has extensive knowledge of Streamsim and streamline fluid flow modelling and gave advice regarding simulation settings (e.g.: incompressible mode, flow scenarios) and well configurations.

## 7.2 Petrophysical reservoir properties

In order to test the dynamic behaviour of the microbial reservoir analogue, the model had to be populated with petrophysical properties. The two main properties controlling fluid flow are porosity and permeability (Ahr, 2008; Flügel, 2004; Lucia, 2007a). Porosity (**Φ**) is the measure of the pore space in a rock and it is the fraction of the pore volumes over the total rock volume. Porosity is typically expressed in percentage (0-100%) but can also be stated as ratio between 0 and 1. It is an important rock property because it is an estimator for the maximum storage volume for hydrocarbons in the reservoir facies. In geocellular modelling the *effective* porosity is of main interest, which represents the porosity, which contributes to fluid flow. The *total* porosity includes the pore volumes, which generally cannot be accessed through practical recovery methods. Porosity is specific to the rock type and is measured by visual methods and laboratory measurements. Indirect measurements of reservoir porosity are carried out through wireline log interpretations, such as for instance a neutron log but can be also estimated through seismic data on a reservoir scale. Visual methods, based on thin section analyses of core samples are broadly used for carbonate reservoir characterisation. Analysing the reservoir rock on micro scale allows detailed analyses of the pore spaces in terms of type, geometry and how the pore space is connected.

Permeability ($K$) is a property that defines the ability of the reservoir rock to allow fluids to pass through. It is commonly expressed in millidarcy and 0.1 mD is

considered to be the minimum for oil production in carbonates (Lucia, 2007b). Typical permeability values are between 100-250 mD for carbonate reservoirs. In contrast to porosity, permeability is not *intrinsic* to the reservoir rock, but depends on the nature of fluid (e.g.: viscosity) passing through the rock and on the reservoir boundary conditions, such as reservoir pressure and temperature. Permeability is measured in the laboratory and subsequently corrected to the reservoir boundary conditions. However, permeability depends on the volume of the sample and different sampling scales often show significantly different values (e.g. Jennings and Ward, 2000). In order to obtain an accurate measure of the effective reservoir permeability the only way is often to perform production tests using pressure built-up analyses in wellbores. Permeability is not an isotropic property, by means that it varies in different directions. Therefore it is expressed in horizontal ($K_x$,$K_y$) and vertical ($K_z$) permeability, respectively. Vertical permeability is commonly less than horizontal.

Porosity is modelled in each reservoir layer and for each facies. It is typically a 'well-behaved' property since it shows small variability within each facies and averages according to a simple arithmetic average. Wellbore porosity values are up-scaled to grid resolution and subsequently modelled. Porosity modelling is based on standard variogram-based techniques, such as Sequential Gaussian Simulation (SGS) to create stochastic porosity models. The porosity model is then used as template for porosity/permeability transformation to distribute permeability values throughout the individual facies.

### 7.2.1 Petrophysical reservoir analogue data

The initial plan at the start of the field work in the Zebra River Canyon was to obtain samples from the analogue reservoir flow units (e.g.: grainstone and thrombolite-stromatolite facies) for porosity-permeability measurements. However, during ongoing field work it became increasingly obvious that such analogue data would not represent initial reservoir conditions due to intense recrystallization of the Zebra River sections. In particular permeability measurements of the microbialites would have had only limited informative value. As noted above, permeability measurements and estimates strongly depend on the sample strategy (sampling density and sample sizes). This is a challenging task for the highly heterogeneous

microbial structures, which are built-up by microbial domes and columns and separated by inter-column fill. Extensive sampling at different scales would have been necessary to establish a robust permeability distribution of the microbial carbonate structures. This was however outside the scope of this research project, because of time constraints. Additional constraints arose from a logistical point of view in terms of obtaining samples in the remote Zebra River Canyon and cost expensive shipping of large quantities of sample material.

The second approach to obtain porosity and permeability data was to use analogue core data from the AC4 stringer of the South Oman Salt basin provided by Baker Hughes. The South Oman Salt reservoirs are terminal Neoproterozoic petroleum reservoirs, developed in a carbonate ramp setting and reservoir facies is represented by microbial carbonates (Schoenherr *et al.*, 2009; Schröder *et al.*, 2005). The Kuibis carbonate ramp shows similarities to these reservoirs and the existing Zebra River analogue model of Adams *et al*. (2005) was partly intended to better understand reservoir heterogeneities of the South Oman Salt basin. However, data release could not be obtained by the end of this research project and therefore the petrophysical reservoir properties and constructed geocellular models cannot be presented. However, the used methodology and learned lessons of using analogue core data can be discussed.

In order to populate the facies model with petrophysical properties a series of pseudo-wells were used, which is a common practice in geocellular reservoir modelling (Ayeni *et al.*, 2008; Xu *et al.*, 2003). Pseudo-wells are hypothetical wells within the geocellular model and by implementing theoretical well logs, such as porosity and permeability logs along the well trajectory, exploration scenarios can be simulated. Every single sediment bed or layer, which the wellbore theoretically penetrates, can be populated with petrophysical properties and subsequently be up-scaled to grid resolution. Using multiple pseudo wells throughout the geocellular model therefore allows the lateral distribution of petrophysical variables, constrained by each facies. Subsequently, variogram analyses can then be carried out to describe the lateral variabilities and be used for input in stochastic modelling approaches. The author wishes to highlight that this approach has to be used with caution. A range of porosity and permeability values were available for each facies and each sediment bed was populated with an arbitrary value out of the facies specific range. Therefore, within one facies the entire spectrum of possible facies specific porosity and

permeability is present. By using these values as input for modelling, highly complex petrophysical patterns were produced. The aim for the development of the petrophysical models was to simulate the dynamic behaviour of the bioherm horizon. Main focus was on connectivity analyses of the laterally discontinuous microbial bioherm structures in order to test if fluid flow occurs under production conditions between the reservoir facies. The generated petrophysical realisations added a level of complexity to the model, which is geological reliable but might have masked first-order flow effects due to emphasising small scaled heterogeneities, based on a hypothetical distribution of variables.

Since the Oman analogue data are not in the public domain, simple petrophysical models based on published data were developed. For each facies, one porosity and permeability value, constant throughout the geocellular model was assigned. This approximation is based on the considerations described above. Furthermore, lateral petrophysical variations within each facies of the layer cake architecture are expected to be minor. The latter is a valid assumption for an analogue model representing a small part of a carbonate ramp system, were individual facies belts shows widths exceeding several kilometres (compare chapter 3). An additional factor to test fluid flow behaviour on single porosity-permeability models was the limitation of the model itself. The geocellular model has a 5x5 m horizontal grid resolution and the vertical thickness of each grid layer is constrained by the stratigraphic context. Horizontal heterogeneities were modelled in high detailed at the expense of losing vertical resolution (compare chapter 6, paragraph 6.4.2). However, the main porosity-permeability heterogeneities in a carbonate ramp setting are typically in the vertical direction because individual sediment beds are laterally extensive but typically show small thicknesses. This is also the case for the Zebra River sections, where individual beds are typically less than 1 m in thickness (compare chapter 3). However, incorporating these small-scale vertical sediment beds would have exceeded the maximum grid cell number. Therefore, sediment packages were summarised as flow and non-flow units (compare chapter 3, paragraph 3.12) and subsequently populated with the same petrophysical properties.

The most common porosity type in carbonate reservoirs is interparticle porosity, where pores are located between individual sediment grains. This type of porosity is common for instance in grainstone horizons. Next to the interparticle pore space there are several other porosity types in carbonate reservoirs, such as for instance

intraparticle, growth-framework, vuggy or fracture porosity. A detailed overview about their recognition and characteristics is given by Flügel (2004).

The thin section analyses of the Zebra River carbonates established that 2 types of initial porosity for the flow units can be expected: interparticle porosity for grainstones and growth-framework porosity for microbialites (compare sedimentology 3, paragraph 3.6). There is a vast amount of published data available for grainstone porosity-permeability cross-plots and Lucia (2007b) provides an extensive summary of published data. In order to approximate porosity and permeability values for the grainstones a comparison plot for non-vuggy limestone was used. The porosity in each model was set to be constant with 25%, however permeability varies in each model with a range from 100-400 mD (see Table 2). These assumed values represent grainstones and grain-dominated packstones (see Figure 110). This is a geological reliable assumption based firstly on the presented sedimentological characteristics of the Omkyk Member and secondly on thin section analyses of the grainstones in the study area.

Published petrophysical data for microbial carbonates is sparse and only a few publications with porosity-permeability data are available (e.g. Koralegadara and Parcell, 2008; Lipinski *et al.*, 2013; Mancini and Parcell, 2001). The general difficulty in describing and measure porosity and permeability is the high level of heterogeneity of microbial carbonates. The reason for that is the nature of porosity in thrombolites, which often includes several types of porosities within one microbial mound (e.g.: growth-framework and superimposed vuggy porosity) (Shinn *et al.*, 1983). Therefore, porosity-permeability analyses often show high variabilities although samples were taken in close proximity to each other. For instance Lipinski *et al.* (2013) reported average permeability values of 50 mD to up to 4200 mD for Jurassic thrombolites in southwest Spain. Individual measurements showed permeabilities as low as 0.01 mD and more than 10000 mD. Although the authors analysed numerous thrombolite samples a robust porosity-permeability best-fit curve for petreophysical modelling could not established. Parcell (2002) described upper Jurassic thrombolites of the Smackover Formation from the eastern Gulf Coast of the USA. This paper provides reservoir characterisation and analyses of petrophysical properties from several types of thrombolite growth forms. Parcell's type 3 thrombolite facies is represented by a dendritic texture and a strong vertical growth component, resulting in the development of individual columns, separated by inter-

column fill. The microbialites are interpreted to be deposited during late TST to early HST under moderate water energies and reservoir quality of theses microbialites is described to be good. The Zebra River thrombolites show close similarities to the Smackover type 3 microbialites in terms of texture, growth form and sequence stratigraphic setting. Thus, it was concluded to use this published petrophysical data as analogue data for the microbial facies during this research project.

The used porosity-permeability cross-plot is given in Figure 111. Porosity was kept constant for all 5 models with 17%, which compares to the average porosity for Smackover type 3 thrombolites. Permeability was altered between each model ranging from 1 mD up to 400 mD (see Table 2). The aim of this wide range was to establish several permeability contrasts between grainstones and microbialites to test various possible scenarios.

The net-to-gross ratio describes the net rock fraction of a reservoir rock within each grid cell. This was kept 1 for all reservoir facies and 0 for non-flow units. Therefore, a microbial grid block is for instance composed of 100% microbial carbonates. Furthermore, all volumetric calculations are based on this net-to-gross ratio. All non-flow units were approximated with 5 % porosity and 0.001 mD permeability, thus well below the required 0.1 mD for oil production and prohibiting fluid flow. This was kept constant throughout all 5 models.

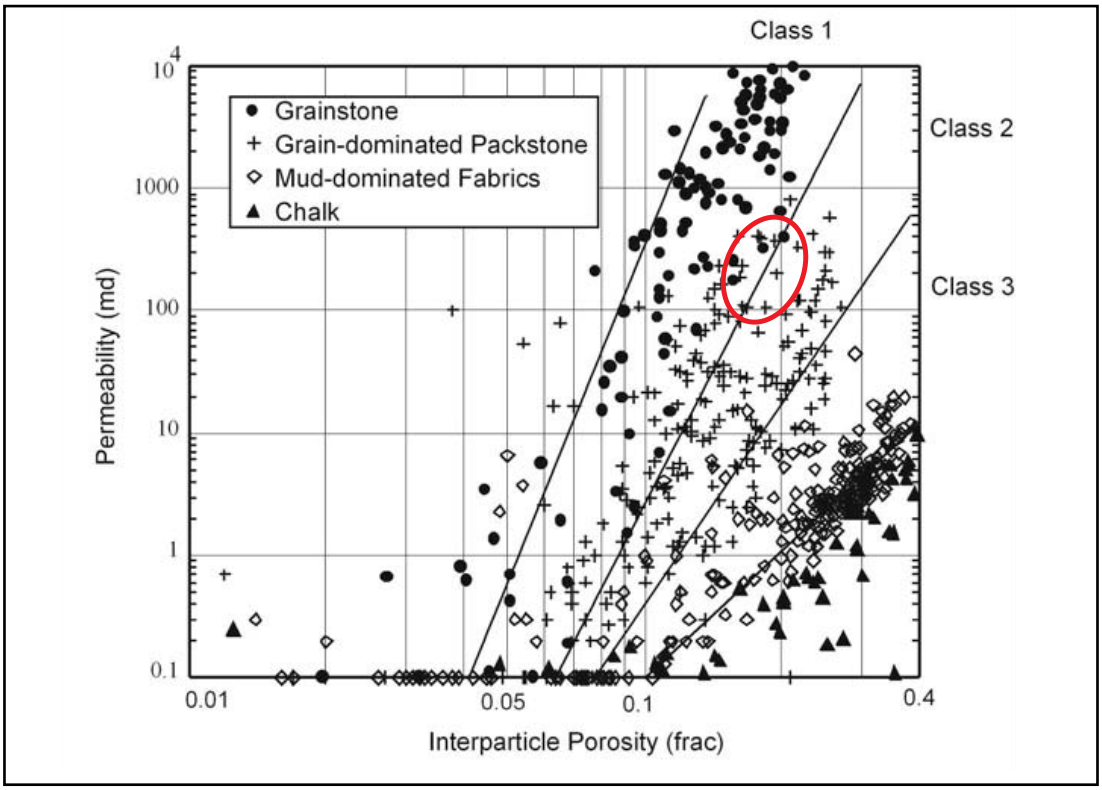


Figure 110: Interparticle porosity-permeability cross-plot for non-vuggy limestone. A red ellipsis indicates range of used porosity and permeability couplets for dynamic modelling. This represents grainstones and grain-dominated packstones. Modified after Lucia (2007b).

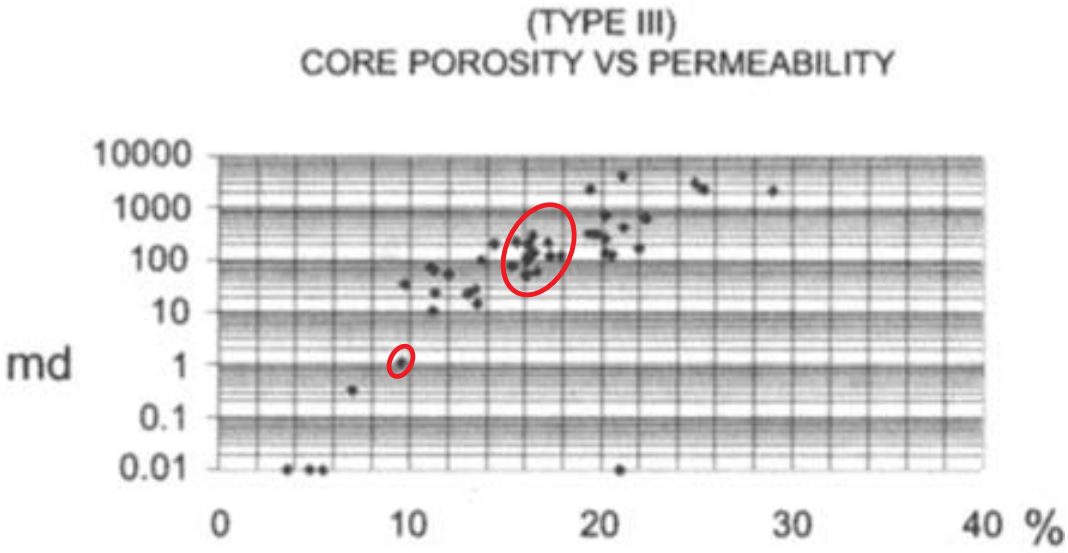


Figure 111: Porosity-permeability cross-plot for type 3 thrombolites of the upper Jurassic Smackover Formation. Red ellipses indicate used permeability ranges. Modified after Parcell (2002).

## 7.3 Streamline fluid flow analyses

### 7.3.1 Introduction and background

Streamline analyses have become increasingly used in petroleum geoscience over the last 2 decades. (Aarnes *et al.*, 2005; Blunt *et al.*, 1996; Klise *et al.*, 2009; Samier *et al.*, 2002; Taware *et al.*, 2012; Thiele *et al.*, 2010) and it finds especially application in geologically complex and heterogeneous systems (Brandsäter *et al.*, 2001; Burton and Wood, 2011; Huang *et al.*, 2004; Jung *et al.*, 2013; Pranter *et al.*, 2007). Streamline simulations are a powerful alternative and complimentary tool to more traditional dynamic modelling approaches such as finite differences because this method is particularly effective in solving field wide fluid flow problems where fluid flow is predominately governed by well positions and rates, rock properties such as permeability and porosity, reservoir facies architecture and gravity (Batycky *et al.*, 1996; Qassab *et al.*, 2003). One of the key advantages of streamline simulation is primarily the computational efficiency allowing large-scale and high-resolution models to be analysed without the necessity of upscaling static geocellular models. Additionally, the visualisation of streamlines is a powerful tool to immediately assess the flow field in order to identify how wells, reservoir geometry and heterogeneities interact and influence flow performance.

The principle mathematical formulation, underlying streamline analysis was developed by Pollock (1988). Key to Pollock's method is the formulation of streamlines in terms of time-of-flight (TOF). The simulator algorithm calculates the total flux for each grid cell, based on Darcy's Law. Once the total flux is known the velocity, depended on the pressure field, with which the fluids are passing through each grid cell is calculated (see Figure 112.A). Consequently, the velocities can be integrated to determine the time need by a given volume of fluid to pass each grid cell. These calculations are executed in all three possible directions (*x, y* and *z*-directions). Given an arbitrary streamline entry point at a grid cell, the shortest travel time through the grid cell can be calculated, which defines the exit point. Subsequently, the exit point forms the next entry point of the neighbouring cell and the algorithm repeats the calculation. Using this mathematical approach field wide, allows the calculation of the shortest travel time form a source block (grid block) to a sink area (e.g.: producer well) (see Figure 112.B).

A more visual explanation is to consider streamlines as the centreline of streamtubes (see Figure 112.C). The volume of the tube is known, which equals the total flux of a given grid cell multiplied by the travel time needed to cross a given grid block. However the boundaries are not known because grid blocks are rarely strictly orthogonal. Consequently, a given volume injected in such a streamtube is equivalent as moving along the streamline with a given time-of-flight. Thus, streamlines with low TOFs are equivalent to streamtubes with small volumes, which implies fast flow regimes. On the other hand, high TOFs indicate streamtubes with larger volumes and therefore slower flow regimes. The fluid transport problem is merely reformulated using TOF properties rather than fluid volumes. This makes streamline analyses so efficient because through using TOF, velocities and therefore distances (e.g.: shortest way to the wellbore) can be calculated.

Streamsim 3DSl streamline simulator was used for the dynamic analyses of the microbial system (www.streamsim.com). This is a standard streamline simulator based on the above-described principles. Due to the lack of actual production data and fluid analyses of potential stored hydrocarbons the simulations were performed under incompressible and immiscible parameters. The latter defines that there is no mixing of fluids and each fluid is only present as one phase during the simulation. The incompressible setting defines that there is no expanse of fluids with change of

pressure and temperature. In actual hydrocarbon reservoirs this is however not the case because oil will expand with pressure drop during production (e.g.: volume increase through degasing). This, however, strongly depends on the composition of the hydrocarbons in combination with the pressure and temperature boundary conditions. None of which is available for the outcrop based analogue model. Therefore, it was concluded to run the simulations in incompressible mode. This simulation parameter requires that each given volume has to be replaced by the same volume of the replacing fluid, because fluid volume increase does not take place. Therefore fluid has to be injected at source areas in order to be produced at sink areas (producer wells).

### 7.3.2 Fluid flow scenarios

The fluid flow simulations were only carried out within the bioherm horizon and the multiple-point facies model (see figure 106). The MPS bioherm model has an average thickness of 11.5 m and a horizontal extent of 1150 m * 2400 m. The same workstation which was used for the development of the static geocellular model, was used for the streamline fluid flow analyses (see paragraph 6.4.2 for specification).

The main focuses of the fluid flow analyses were to test the dynamic behaviour of the bioherm structures and to get insights for potential well trajectories. Furthermore, with the exception of the bioherm horizon the rest of the Omkyk Sequence 2 shows a simple layer cake architecture, were flow units do not exhibit significant lateral variabilities. Therefore, homogenous flow regimes can be assumed for the grainstone horizons and do not have to be modelled. Additionally, hardware constraints made it unpractical to run streamline simulations on the entire reservoir model. A full field streamline analysis exceeded the computational power of the workstation.

The streamline simulations were carried out on an un-faulted grid. The modelled strike-slip faults are specific to the Zebra River Canyon system. However, the Zebra River analogue model was developed to better understand potential microbial reservoirs in the Owambo basin and elsewhere. The main goal of the dynamic simulations was to test fluid flow dynamics governed by the microbial architecture. Thus, fluid flow simulation, carried out on a locally specific faulted grid would have added a level of complexity to the model that may mask the influence of the microbial architecture on fluid flow. Furthermore, fractures were not included in the

simulation because the 3DSL simulator does not support dual porosity/permeability flow simulations.

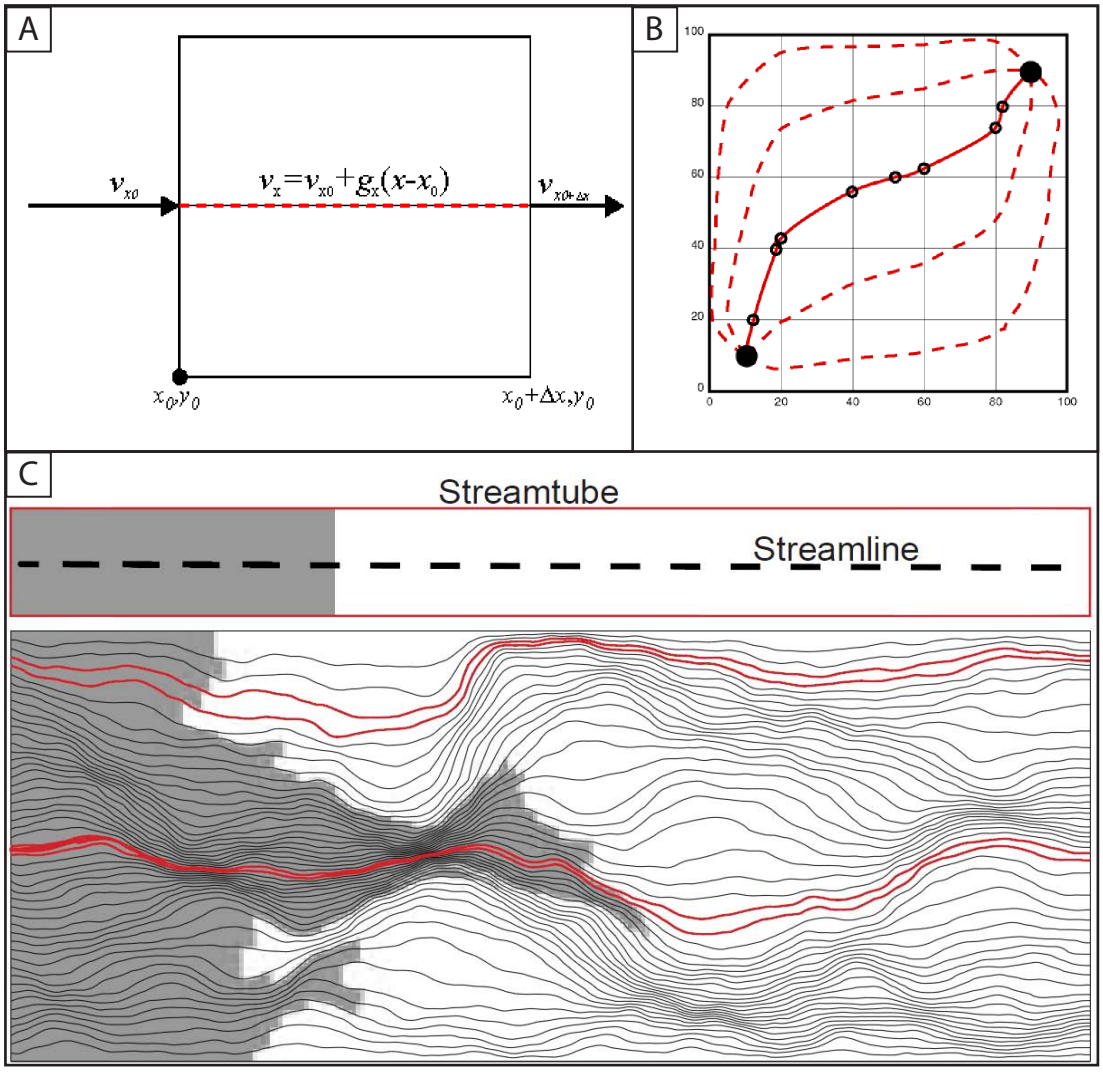


Figure 112: (A) The total flux of each grid cell is known by applying Darcy's Law and consequently fluid velocity through each cell can be calculated. (B) Repeating the algorithm for each cell allows the calculation of the shortest travel time from a source area (lower left) to a sink area (upper right). (C) Streamlines can be visualised as centre lines of streamtubes. Injecting a given volume into a streamtube is equivalent to moving along the streamline to a given time-of-flight. Modified after Thiele et al. (1996).

The streamline simulations were carried out under a reservoir pressure of 8000 kPa (80 bars). This pressure regime simulates a hypothetical reservoir depth of 800 m. This relative shallow depth was chosen because high reservoir pressures, in for instance 3-4 km depth (30 000 – 40 000 kPa), would lead to high flow regimes and early water breakthrough within a few years. Thus, in order to extend the length of the observable oil displacement a shallow reservoir setting was chosen to increase data resolution during each simulation step. In both scenarios two producer wells were situated in the centre of the model and 1000 m apart from each other. This well scenario was chosen due to two reason: firstly because the bioherm reservoir model

is relatively small with respect to the horizontal dimensions and secondly because of computational limitations. The bioherm facies model has the extent of typical inter-well spacing. Therefore, more conventional production scenarios, like 5-spot well patterns, were not feasible because resulting inter-well distances would have been very small (e.g.: producer and injector wells in adjacent bioherm structures). This would have simulated an unrealistic production scenario and fluid flow across several bioherms could not have been analysed. Computational limitations made it necessary to define both wells as producers, rather than simulate a producer-injector scenario. The 3DSL streamline simulator does not allow simulating injector wells in an incompressible mode with open boundaries. Simulations of injector wells with closed boundaries in an incompressible scenario, however, lead to highly unrealistic flow patterns. Every injected volume of fluid at the source area (injector), represented by one streamline, has to find a way to the only possible sink area (producer). This results in a flow pattern where the majority of the injected volumes move along the closed model boundaries until streamlines reach the sink area. A more visual explanation is that the closed reservoir model acts as one tank and streamlines start to rotate around the producer well until they reach the well bore. Therefore, it was not possible to simulate a producer-injector scenario in an incompressible mode with close boundaries. Thus, it was decide to use two producer wells with open boundaries to analyse the fluid flow characteristics of the microbial carbonates.

As mentioned above, the simulations were run in incompressible mode and therefore fluid had to be injected in order to generate fluid flow. In all simulations the reservoir boundaries were defined as source areas and water entered the boundary reservoir grid blocks with 8000 kPa, leading to a scenario that the entire pore volume was flushed with water. Thus, the water flood front was the main force driving the petroleum towards the wellbores. The two producer wells were kept open the entire simulations runs with a fixed bottom hole pressure of 1000 kPa. The fixed bottom hole pressure was necessary to provide a pressure differential to ensure fluid flow. The simulations were run until water breakthrough occurred and a watercut of more than 65% was reached. The maximum simulation length was set to 20 time steps, regardless of the water breakthrough. One time step represents 365 days and therefore the maximum simulation time was 20 years. Relative permeability for given water and oil saturations values were calculated after Honarpour *et al.* (1986)

for limestone reservoirs in a water wet system. An initial oil saturation of 70 % was assumed and 30 % interstitial water. After water flooding the remaining oil saturation was set to be 30 % and 70 % water, respectively (see Figure 113).

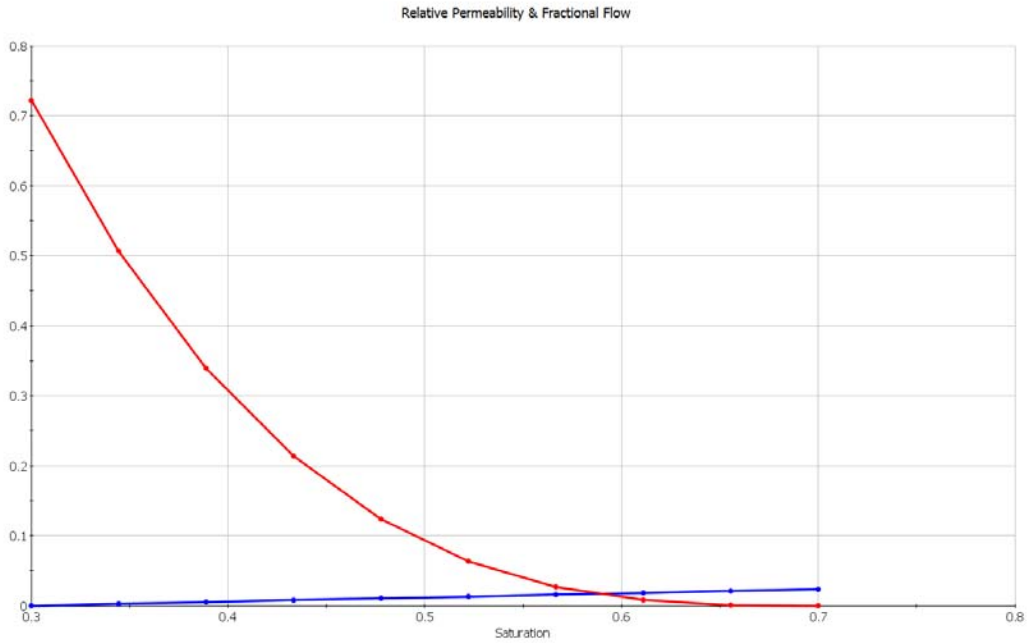


Figure 113: Relative permeability curves for oil and water saturations for limestone reservoirs after Honarpour *et al.* (1986).

#### 7.3.2.1 Reservoir architecture scenarios

Two scenarios of varying bioherm horizon architecture were simulated during the analysis. In both cases the same multiple point microbial facies model was used, however inter-bioherm facies was altered between the models. The first model has one continuous grainstone horizon as top reservoir grid layer, therefore connecting all bioherms with heights reaching to the top of the bioherm horizon. This model reflects the initial interpretation of the bioherm horizon reservoir architecture after Adams *et al.* (2005) in the sense that the only connectivity between individual bioherm structures is provided by a top grainstone flow unit (see Figure 31).

An additional grainstone layer was added in the second model, therefore following the interpretations and reservoir architecture obtained during this research project. The second flow unit is situated in the middle of the inter-bioherm sequence (see Figure 54).

The aim of the first scenario was to test if bioherms are produced when the top grainstone layer provides the only connectivity between the mounds. For that purpose two models (model 1.1 and model 1.2) with the same geometry but different

facies specific permeabilities were constructed. The permeability was assumed to be isotropic for both simulation runs. The porosity for each facies was kept the same in both models. The reason for that was to have the same amount of initial oil in place before production start, in order accurately compare and contrast production rates. Model 1.1 has a permeability contrast of 1:2 by means of 100 mD for microbialites and 200 mD for grainstones. Model 1.2 simulates a high permeability contrast of 1:400, with 1 mD for the bioherms and 400 mD for grainstones. The petrophysical data for both simulated models in scenario 1 is given in Table 2.

The focus of the second scenario was to analyse the effect of an additional flow unit in the middle of the reservoir layer, therefore connecting all bioherm with a second grainstone layer. In this scenario, 3 petrophysical models (model 2.1-2.3) were developed with the same reservoir architecture but different permeability values. As in scenario 1, the porosities for each facies were kept constant. Model 2.1 has the same petrophysical properties as model 1.1 with the additional middle grainstone layer. In model 2.2 the permeability of bioherm areas was reduced to 1 mD, where the lateral corresponding inter-bioherm facies is composed of non-flow units (e.g.: inter-bioherm beds are mud-dominated). This approximates a layer cake architecture. The incentive for this petrophysical realisation was the recognition of vertical permeability contrasts within the bioherm complexes (compare chapter 3, paragraph 3.6.1). The last model tested the effects of high permeable microbialites with 400 mD and 100 mD in the grainstone units. The petrophysical data for all three models of scenario 2 is given in Table 2. The porosity and permeability values for non-flow inter-bioherm facies was constant in all scenario models in order to simulate the same non-flow unit in each simulation run.

Additionally for each scenario model simple volumetric calculations were performed. This was done by calculating the bulk cell volume for the entire model and for each facies, respectively. Subsequently, pore volumes for each reservoir facies were calculated by simply multiplying the bulk volume with the porosity values. The pore volumes represent the maximum fluid storage volume and are given in standard cubic metres ($sm^3$) and million barrels (Mbbl).

| | Grainstone | | Microbialites | | |
|---|---|---|---|---|---|
| | Porosity | Permeability (kx,ky,kz) | Porosity | Permeability (kx,ky,kz) | Net-to-gross |
| **Scenario 1** | | | | | |
| Model 1.1 | 25% | 200 mD | 17% | 100 mD | 1 |
| Model 1.2 | 25% | 400 mD | 17% | 1 mD | 1 |
| **Scenario2** | | | | | |
| Model2.1 | 25% | 200 mD | 17% | 100 mD | 1 |
| Model2.2 | 25% | 200 mD | 17% | 100/1 mD | 1 |
| Model2.3 | 25% | 100 mD | 17% | 400 mD | 1 |
| **Volumetric calculations** | | | | | |
| | | **Bulk volume ($m^3$)** | **Bulk volume %** | **Pore volume ($m^3$)** | **Mbbl** |
| | **Entire model** | 29588756 | 100 | | |
| Scenario 1 | **Inter-bioherm facies** | 15910966 | 53.77 | | |
| | **Grainstone** | 6692565 | 22.62 | 1673141.25 | 1.0524E+07 |
| | **Microbialites** | 6985225 | 23.61 | 1187488.25 | 7.4691E+06 |
| | **Total** | | | **2860629.5** | **1.7993E+07** |
| | | | | | |
| Scenario 2 | **Inter-bioherm facies** | 10642653 | 35.97 | | |
| | **Grainstone** | 11960878 | 40.42 | 2990219.5 | **1.8808E+07** |
| | **Microbialites** | 6985225 | 23.61 | 1187488.25 | **7.4691E+06** |
| | **Total** | | | **4177707.75** | **2.6277E+07** |

Table 2: Petrophysical grid properties used in streamline simulations and volumetric calculations.

#### 7.3.2.2 Fluid flow results scenario 1

##### *7.3.2.2.1 Results model 1.1*

The evolution of the pressure distribution within the microbial reservoir layer is illustrated in a series of screenshots in Figure 114. The initial reservoir pressure before production start is heterogeneous throughout the grid layers and shows variability between 8007 and 8372 kPa. Relative low pressure (around 8000 kPa) is located at the western part of the grid layers, in a structural up-dip position and additionally in the centre of the model. The highest pressure regime occurs at the south-eastern part of the model with 8372 kPa (Figure 114.A). This coincides with the lowest elevation of the grid layer in a structural down-dip position. In general, pressure increases from the west to the east within the reservoir layers. After the first time step and production start, pressure drops to under 3000 kPa near the wellbores but keeps constant at 8000 kPa near the model boundaries (Figure 114.B). The westerly well, Well-P3 shows a bigger pressure drop radius than Well-P4 (Figure 114.C). The low-pressure regime subsequently spreads out over the following years further away from the well bores. Simultaneously the high-pressure fronts from the

boundaries develop further into the grid layers (Figure 114.D-E). The overall behaviour of the pressure field during production is that the high boundary pressure fronts move radial towards the well pair after the initial pressure drop at production start. After 20 time steps the pressure differentials between boundaries and well bores form an elliptic pattern around the well pairs (Figure 114.F).

The temporal evolution of the oil saturation in the top grainstone layer is illustrated in 6 time steps in Figure 115. The initial situation before production start is that the grainstone layer, including the bioherm areas shows a homogenous oil saturation of 70 %. Figure 115.A shows the saturation distribution after 365 days of water influx from the grid boundaries. Dark blue to violet colours indicate complete water flooding and replacement of oil, whereas red colours show high oil saturations. Water flooding occurs at the model boundaries where water enters the reservoir model and replaces oil. Note that water floods are not homogenous fronts but are highly undulating. In addition, in already flooded areas, patches of oil remains (Figure 115.A&B). These patches coincide with bioherm structures connected to the top grainstone layer. However, these volumes get increasingly depleted over time. See Figure 115.C&D where bioherm structures at the grid margins are already flooded. Water breakthrough in both wells occurs after 10 years of production, originated from the southern boundary. Oil saturation continues to decrease over the next 10 years. The overall depletion pattern shows close similarities with the pressure field evolution in terms of radial flooding towards the well pair. Bioherm areas with low oil saturations (between 0.4-0.55%) still remain after 20 years of production (Figure 115.E&F). They are located close to the water fronts and along axes between wellbores and grid layer edges.

The change of oil saturation in the bottom grid layer is illustrated in 3 time steps in Figure 116.A-C. In all three images a grid display mask was applied to only show the bioherm structures and not the inter-bioherm facies where no fluid flow occurred. The bioherm depletion pattern is the same as in the top grainstone horizon, originating from the grid boundaries. Individual bioherms get first flooded in the centre of the bioherms and oil saturations are still high at the transition to the inter-bioherm facies (see enlarged area in Figure 116.A). Nevertheless, also these regions get depleted with increasing time and by the end of the simulation run after 20 years, the majority of the oil in the bioherms is replaced (Figure 116.C). However, no water flooding occurs in the abundant small-scale bioherms (see Figure 116.D-E). These

small bioherm structures are not connected to the top grainstone layer and are not being produced. A total of 617 not connected bioherms are present throughout the grid, which represents 2.98 % of the total microbial carbonate volume (grid block volume). In addition to these isolated structures, several bioherms were identified where the oil remains behind, although they are connected to the overall flow zone. This occurs in two situations: (1) in merged bioherms and (2) in bioherms which are only connected to the top layer through on grid block. In the first situation, smaller mounds within merged bioherm complexes are not connected to the top grainstone but are connected through 1 block with larger bioherm structures (see Figure 116.F). The bigger mounds are completely depleted but oil remains in the un-connected smaller bioherms and no fluid flow occurs. In the second situation, fluid flow occurs in the connected top grid block but does not extend in the underlying mound structure. These connected but not drained bioherms constitute 4.80% of the total grid block volume of microbial carbonates within the reservoir model. In combination with the isolated bioherms this sums up to a total of 7.78% not produced microbial reservoir facies throughout the entire reservoir model.

The field and well production rates are plotted in Figure 117. The cumulative oil production from both wells after the end of the simulation is 763200 $sm^3$ (standard cubic metre), which equals to 4.8004 Mbbl (million barrels oil) (Figure 117.A). The production curve is steep at the beginning but flattens out towards the end of the simulation run, indicating higher production rates within the first 3 years of production. This is confirmed in Figure 117.B, illustrating the entire daily field production rate. After the initial flow built-up in the first simulation step a maximum of 330 $sm^3$ is reached. This high rate drops rapidly within the first 1000 days and reaches a value 200 $sm^3$. From that point on the production rate steadily drops until it reaches a minimum 45 $sm^3$ at the end of the simulation. A small negative spike in production occurs at around 3700 days, which coincides with the breakthrough of the water flood at Well-P3. Form this point onwards the watercut curve steeply increase until it reaches a maximum of 24% at the end of the simulation. Comparing the wells shows that Well-P3 has a higher production rate with a maximum of 185 $sm^3$ than Well-4P with 145 $sm^3$ (Figure 117.C&D). At both wells water breakthrough takes place during the same simulation step after 10 years of production. However, Well-P3 reaches a maximum watercut of 19% whereas Well-P3 shows a final watercut of more than 30%.

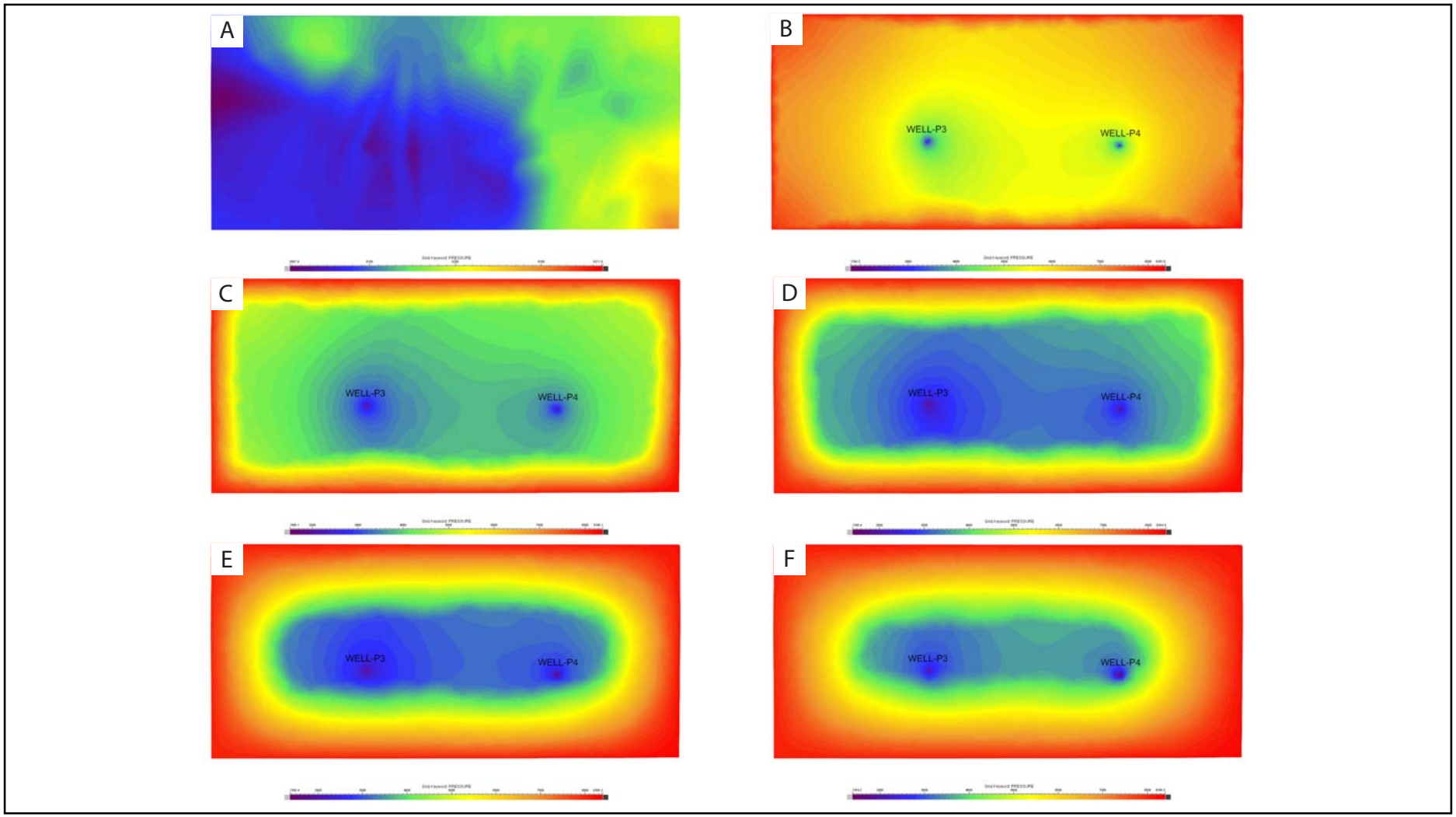


Figure 114: Evolution of the pressure field in model 1.1. (A) Initial pressure distribution. Note that the highest pressure is located in the south-eastern part in a down-dip position. (B) Pressure field after 2 years, (C) 5 years, (D) 10 years, (E) 15 years and (F) after 20 years of production.

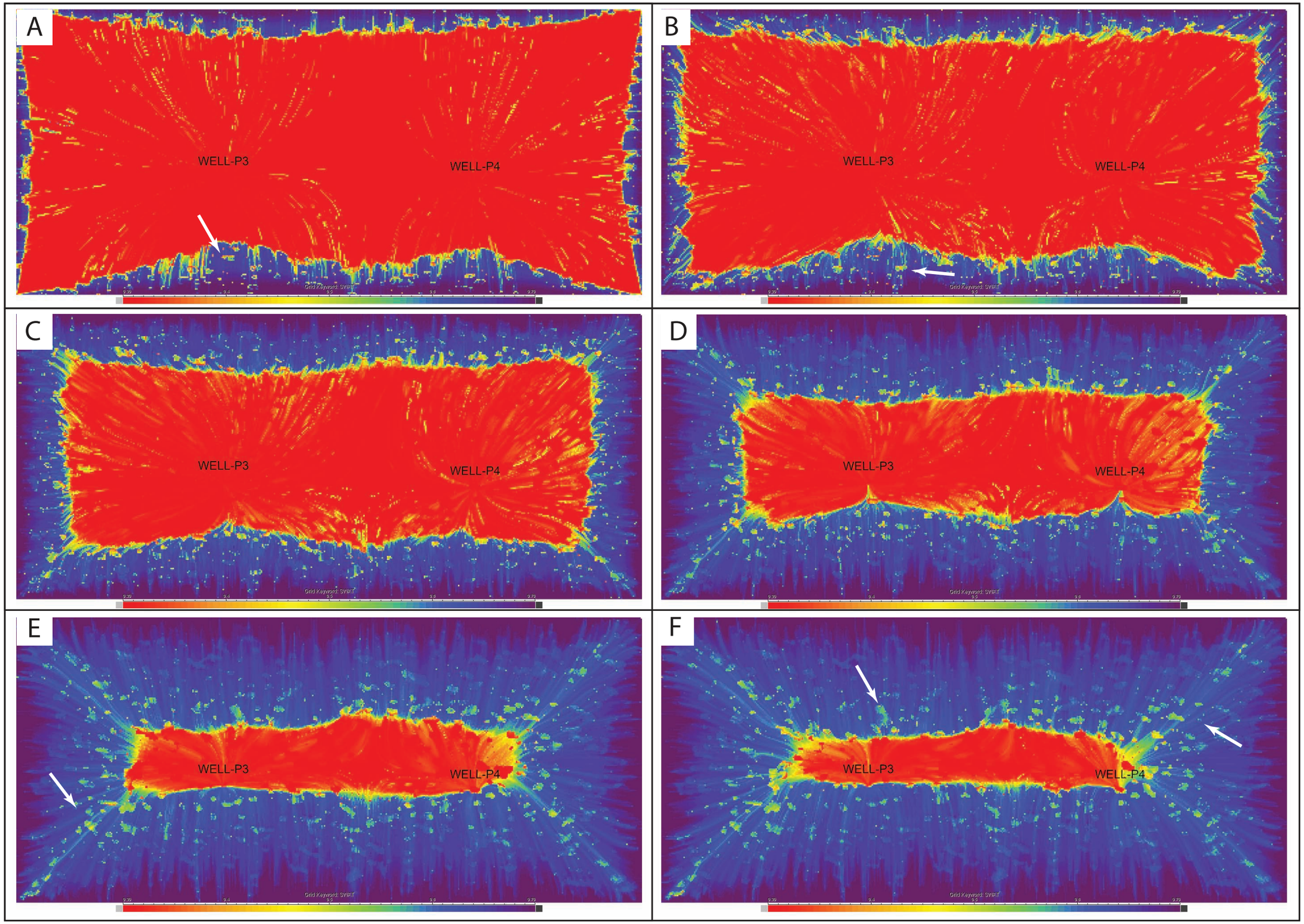


Figure 115: Temporal evolution of oil saturation in the top grainstone layer. Red colours indicate 70 % oil saturation whereas purple colours indicate water saturation of 70 %. A-B illustrates oil saturations after 1 and 2 years of production, respectively. B-F are snapshots after 5, 10, 15 and 20 years. White arrows indicate residual oil in bioherm areas near water flood fronts and along axes between wellbores and grid corners.

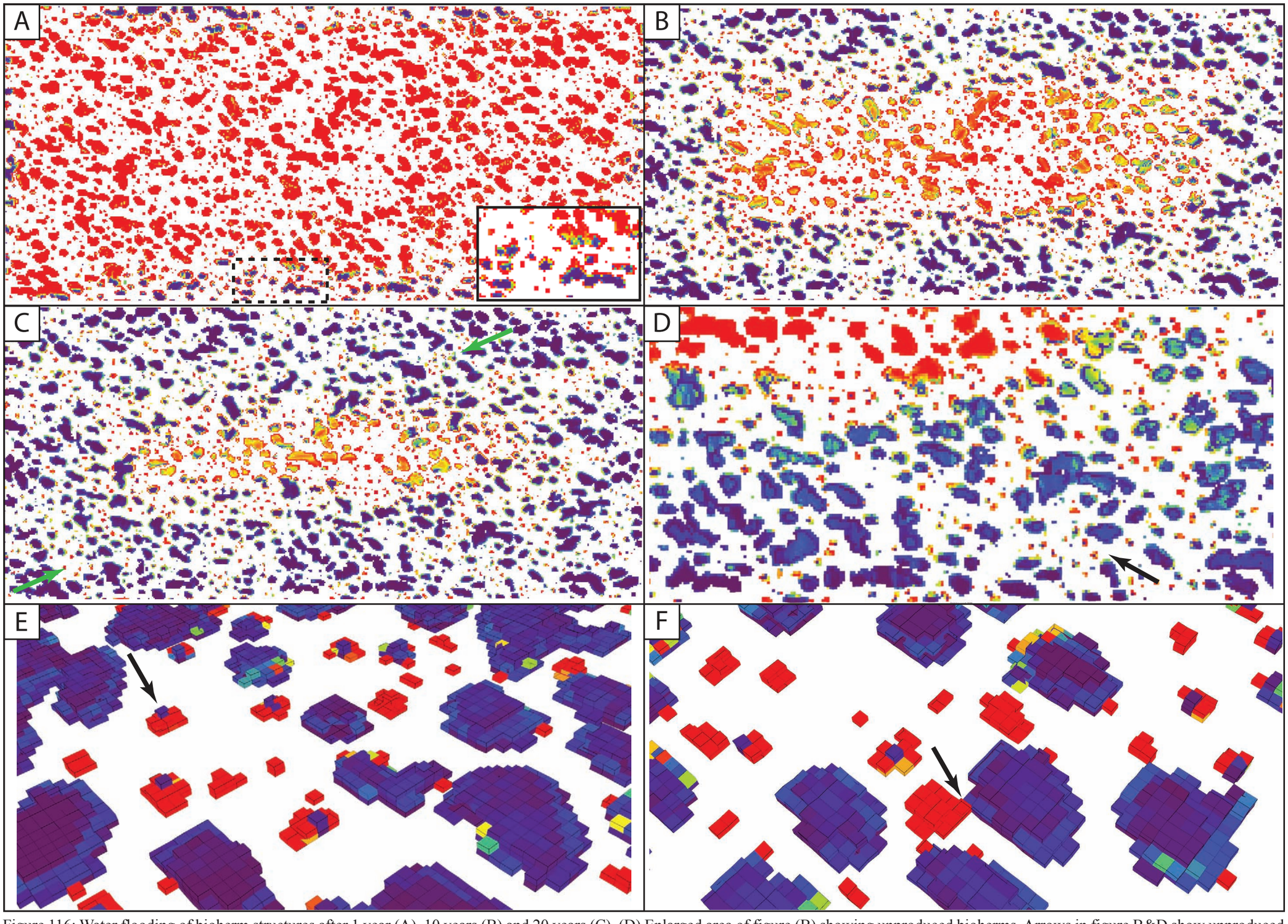


Figure 116: Water flooding of bioherm structures after 1 year (A), 10 years (B) and 20 years (C). (D) Enlarged area of figure (B) showing unproduced bioherms. Arrows in figure B&D show unproduced bioherms whereas surrounding bioherms are already depleted. (E) Arrow indicates a bioherm which is only connected through one grid block with the top flow unit and does not get produced. (F) Unproduced merged bioherm where the connection to the drained bioherm is only one grid block (black arrow). Same colour coding in all pictures as in Figure 114.

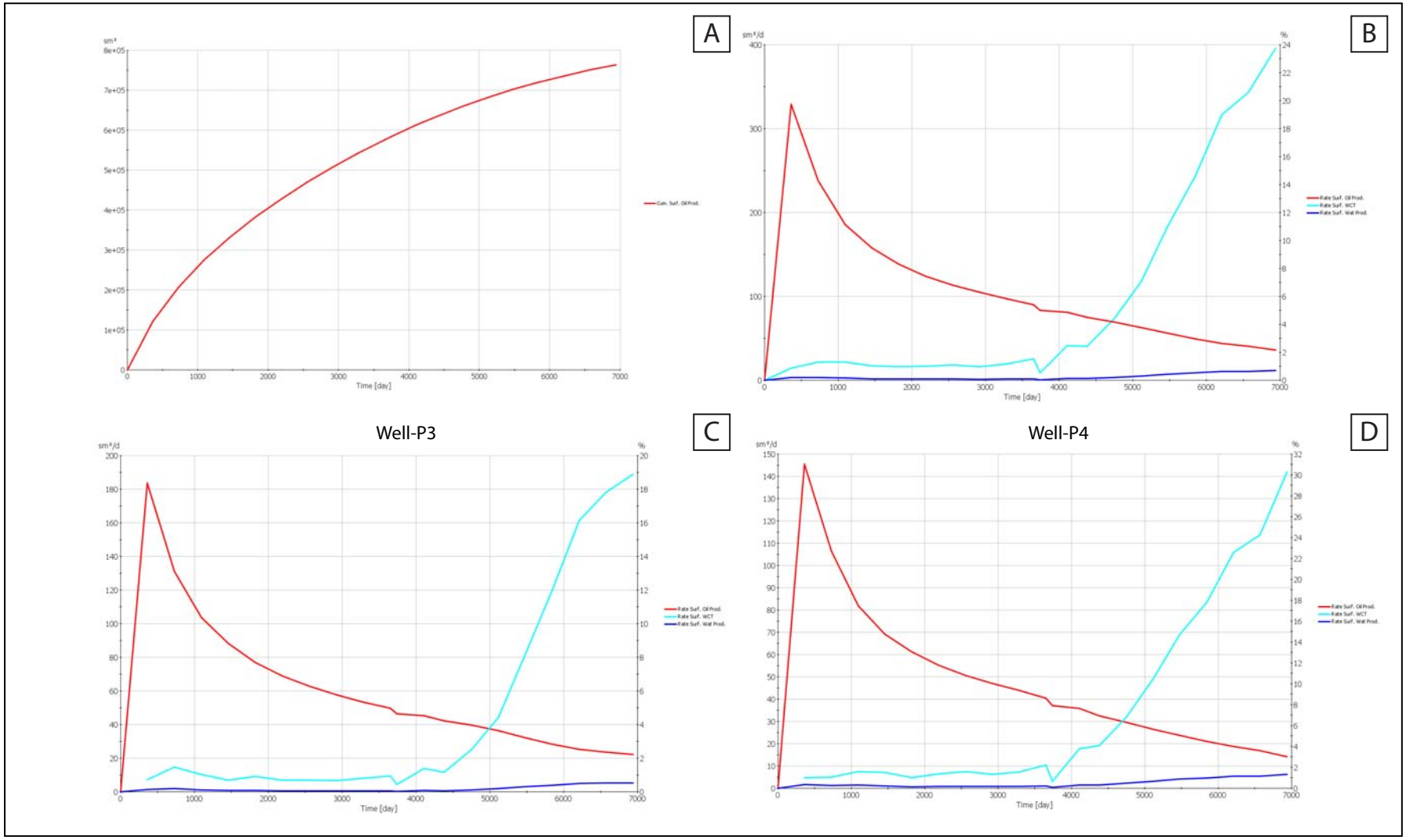


Figure 117: Production cross-plots of model 1.1: (A) Cumulative production, (B) field wide daily production rates and daily production rates for Well-P3 (C) and Well-P4 (D).

The visualisation of the streamlines in Figure 118 shows the fluid flow pathways and well allocations. Figure 118.A shows all streamlines entering the reservoir modelling from the grid boundaries, coloured according to boundary and producer well. For instance the yellow streamlines represent the flow from the southern boundary to Well-P3. In Figure 118.B these yellow streamlines are coloured after time-of-flight property. Blue to greenish streamline indicate low TOFs and hence faster flow regimes whereas red colours indicate higher TOFs and slower flow rates. The TOF cutoff for this property colour coding was set to 3650 days and therefore the image illustrates streamlines, which reach the well within 10 years. Dark grey streamlines are above the cutoff and hence need longer than 10 years to reach the wellbore. The picture also illustrates that the fastest flow regime is directly to the south of the well (note the green to blue colours of the streamlines in the centre). Furthermore, the picture shows vortexes where streamlines crosscut bioherm structures. This is clearly visible in Figure 118.C, which shows a close-up of the above described streamline section with the underlying bioherm grid. Where blue and fast streamline fronts enter bioherm structures the flow regime is reduced whereas neighbouring streamlines in grainstone do not show this effect. Higher TOFs in the lee of bioherms indicate reduced flow rates. Recoloring the streamlines with oil saturation shows the water flooding of the yellow streamline section after 365 days in Figure 119.A. Clearly visible are red streamlines (high oil saturation) originating from bioherm structures, whereas streamlines to the side of the bioherms are continuously blue (high water saturation). This shows that oil is still drained from bioherms when the surrounding grainstones are already completely depleted. In cross-section view this vortex effect is more visible because also the vertical flow directions can be observed. Figure 119.B shows a grid block cross-section of bioherm structures and connecting top grainstone layer. Additional bioherm outlines are indicated by streamline vortexes. The streamlines are coloured according to oil saturation and this clearly shows that blue, water saturated streamlines enter bioherm structures via the top grainstone layer. Once within the bioherms, the streamline pathways migrate towards the bottom and ascend at the lee side of the mound structure. In addition to the streamline diversion, a change in property colour occurs, from water saturated blue at the entry point over greenish colours (0.5% water and oil saturation) at the bottom to oil saturated red at the exit grid block.

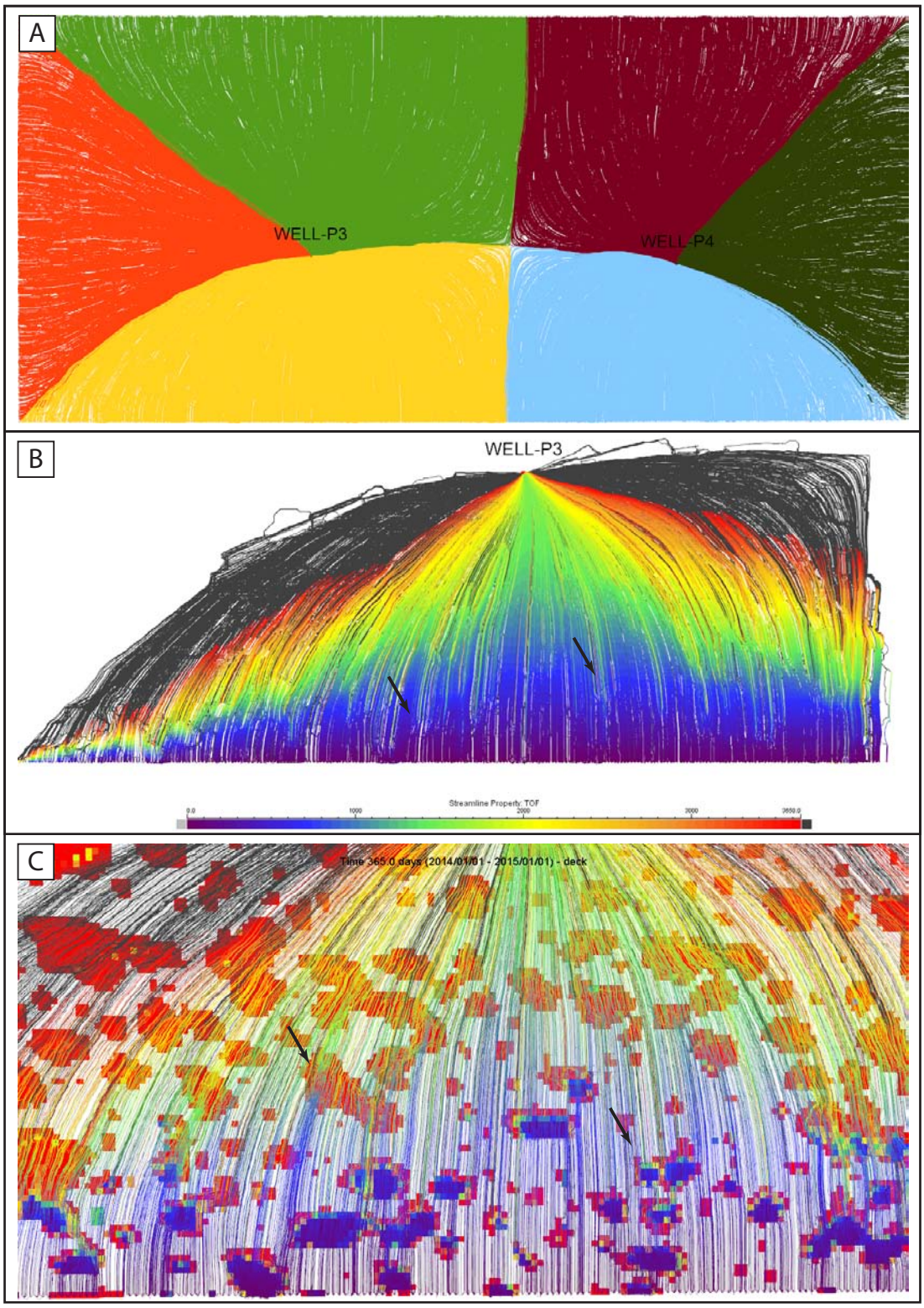


Figure 118: Streamline fluid pathways of the microbial system. (A) Entire fluid flow pathways originating from the borders of the reservoir model towards the producer wells coloured after injected boundary and producer well. (B) Enlarged yellow streamlines from figure A with TOF colour coding. Arrows indicate higher TOF's and therefore lower drainage in the lee of bioherms. (C) Enlarged area of B with bioherm grid display mask showing the slowing down affect in the lee bioherms. TOF colour coding for streamlines.

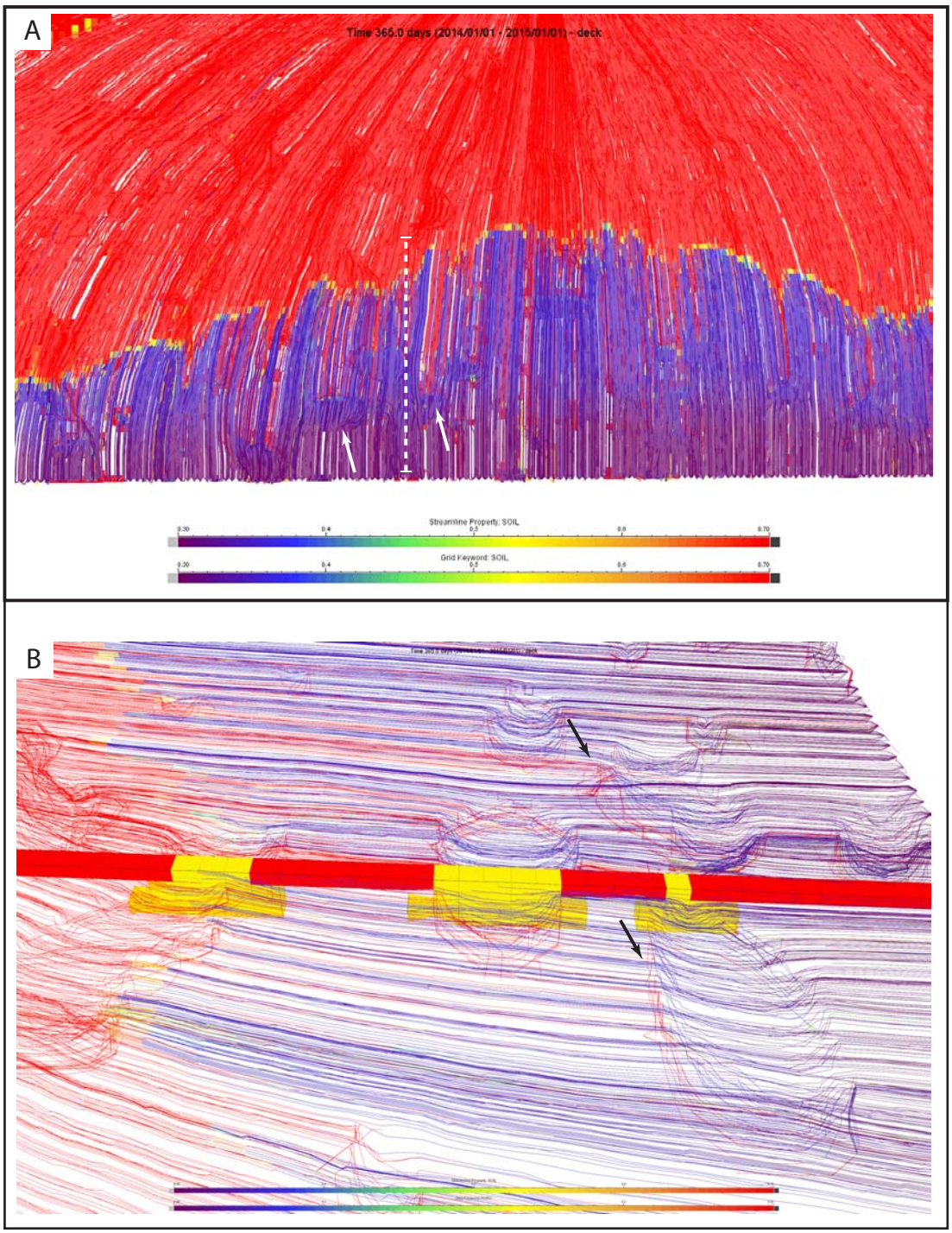


Figure 119: (A) Same enlarged streamline section of Figure 118.C with oil saturation colour coding of streamlines. White arrows indicate bioherm structures and the drainage of oil in bioherms. (B) Grid cross-section view of bioherms and connecting top grainstone layer illustratingthe descending fluids upon entering bioherms and ascending oil saturated fluids at the lee side of the structures (black arrows). Location of the cross section is given by dotted line in figure A. Fluid flow in the image is from the right to the left.

A series of images in Figure 120 shows the bioherm internal fluid flow behaviour. Figure 120.A shows a merged bioherm structure at the south-western end of the reservoir model, chosen to better visualise the mound specific fluid flow. Note the connection of the bioherms via 3 gird blocks. Figure 120.B shows superimposed streamlines onto the mound structures with oil saturation property colouring. The water-flood front is situated in the middle of the bigger mound structure as indicated by blue to red colour change. By plotting only the streamlines without the bioherm grid, the mound internal flow patterns are visible in Figure 120.C. The streamline flow pattern illustrates that the descending streamlines in the smaller mound exit through the bottle neck connection to the bigger bioherm. Additionally, high oil saturation occurs in this connecting pathway. Recoloring the streamlines with time-of-flight properties shows that particularly streamlines, which pass through the bottle neck, have high TOFs indicating slower flow regimes (Figure 120.D).

Besides the vertical streamline path diversion there occurs also a horizontal diversion of streamlines. Figure 121.A shows that streamlines get focused in the top layer in bioherm zones. This occurs when the water flood is passing through and is replacing the oil in place. Two grid cross-sections in *k* and *j* directions are plotted in Figure 121.B, with pressure grid property colour coding. Surprisingly low-pressure areas are located in the bioherm top layer whereas high-pressure zones are located in the inter-bioherm grainstones. Clearly visible is the pressure distribution in Figure 121.C by only visualising the top flow layer with associated pressure field. Note the green low-pressure areas coinciding with the top of the bioherms showing that the pressure field is a heterogeneous front. However, after the water flood front passes the streamlines resume on a straight line towards the wellbore and no horizontal deviation is obvious (see Figure 121.D). Additionally, the pressure distribution of the grid is homogenous again. There is a general increase of pressure from the left to the right but this coincides with the general elliptic pressure field described earlier. Furthermore, small-scale pressure variations as compared to the passing of the water flood are absent.

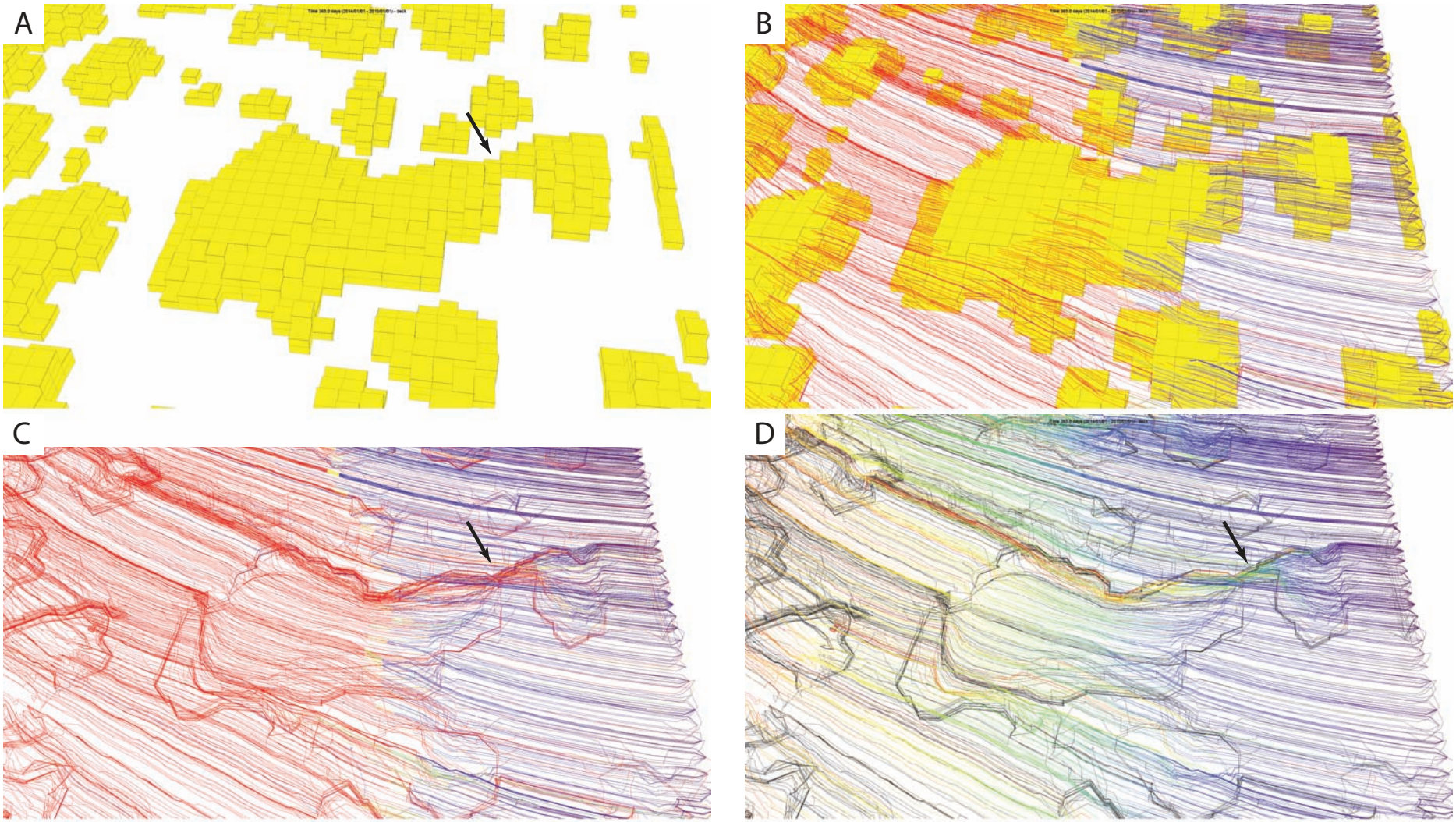


Figure 120: Series of images showing the internal fluid flow in composite bioherms of model 1.1. (A) Composite bioherm connected via several grid blocks (black arrow). (B) Superimposed streamlines with oil saturation colour coding. (C) Highly oil saturated fluids are channelled through the bottle neck connection within the composite bioherm. Recoloring streamlines with TOF property (D) shows that the channelled streamlines have a higher TOF and therefore longer drainage times. Flow direction from the right to the left of the image.

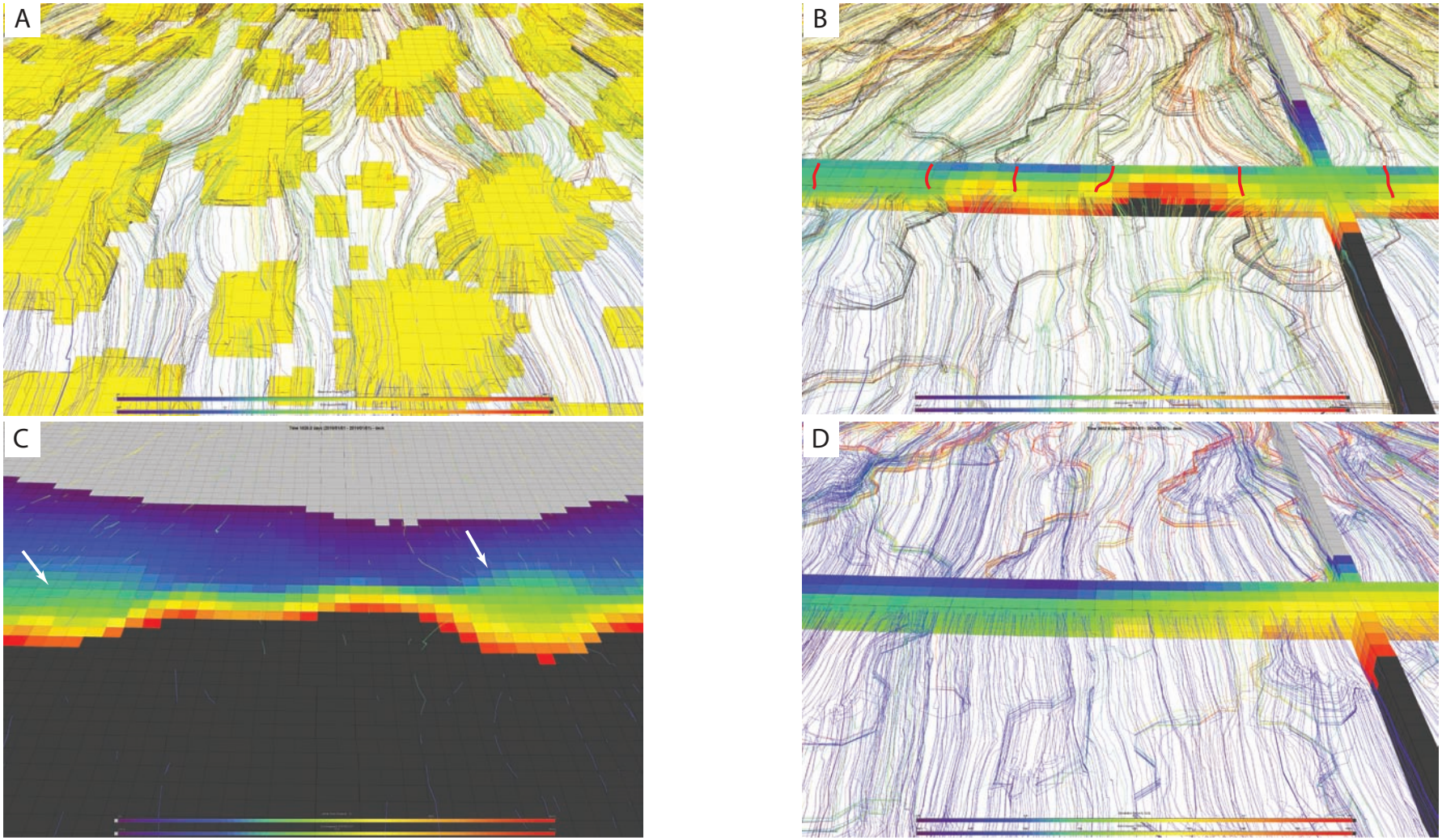


Figure 121: Sequence of images showing horizontally channelled streamlines and local pressure distribution of model 1.1. Flow direction from the bottom to the top of the image. (A) Channelled streamlines with TOF property colouring through bioherms. (B) Grid cross-section view colour coded with pressure property. Red colours indicate high pressure and green to blue lower pressures. Red lines indicate outline of bioherms. Note the relative lower pressures within the bioherms as compared to the inter bioherm facies. (C) Low pressure zones are clearly visible in the top layer coinciding with bioherm areas (white arrows). Same colour coding as in figure C. (D) Straight fluid flow after the water front has passed and the pressure field is equalised again.

#### 7.3.2.2.2 Results model 1.2

The temporal variations of the oil saturation in the top grainstone layer of scenario model 1.2 are illustrated in 6 time steps in Figure 122. Water breakthrough at Well-3P occurs within the first 365 days, originated from the southern margin of the reservoir model (Figure 122.A). The main difference to the evolution to model 1.1 is that oil stays behind in the bioherm areas and is only drained at very low rates. The latter is indicated by oil-saturated fronts in the lee of bioherm structures whereas the surrounding grainstones are already completely drained of oil (Figure 122.B&C). This general depletion pattern remains the same over the entire simulation length. Similar to model 1.1, high oil saturated zones are aligned on axes between the well bores and the reservoir model edges (Figure 122.D&E). By the end of the simulation the majority of the oil in the grainstone layer has been drained, however the area between the wells has not been produced (Figure 122.F). Furthermore, the majority of the oil stored in the connected top bioherm areas stays in place. Figure 123 shows the evolution of the oil depletion in the microbial carbonates. In the first two years of production (Figure 123.A&B) the bulk of oil remains in the mound structures and only minor drainage occurs at the very borders of the model. After 5 and 10 years respectively (Figure 123.C&D) some of the larger mound structures become drained. This pattern resumes throughout the last 10 years of production Figure 123.E&F). By the end of the simulation only a few, larger bioherm structures have been partly drained. The most part of the stored oil in the microbial carbonates remains in place.

The production rates of the flow simulations are plotted in Figure 124. Similar to model 1.1 the cumulative production curve is steep at the beginning of the production period but flattens out towards the end (Figure 124.A). After simulation end a total of 679245 $sm^3$ oil was produced, which is the equivalent 4.2727 Mbbl. The total field wide daily production rate has a maximum of 415 $sm^3$ after one year of production (Figure 124.B). However, this high production rate drops to 100 $sm^3$ within the first 2500 days of simulation. The final daily oil production rate is 15 $sm^3$. The rapid increase in watercut occurs early in the simulation and starts after 2100 days and reaches a maximum of 56% after 20 time steps. Therefore at the end of the simulation more water than oil is produced. Plotting the individual well productions shows that Well-P3 has a higher maximum flow rate of 245 $sm^3$ as Well-P4 with 170

$sm^3$ (Figure 124.C&D). However, for both wells this flow rate drops under 100 $sm^3$ during the first 3 years. Well-P3 shows a short increase of production between 730 and 1096 days, which coincides with the start of the partly drainage of bioherms after water breakthrough at the wellbore P3. The watercut curve for both wells starts to increase early during simulation after 2000 days and reaches 52% for Well-P3 and 61% for Well-P4 at simulation end, respectively. Both wells produce more water than oil at the end of the simulation.

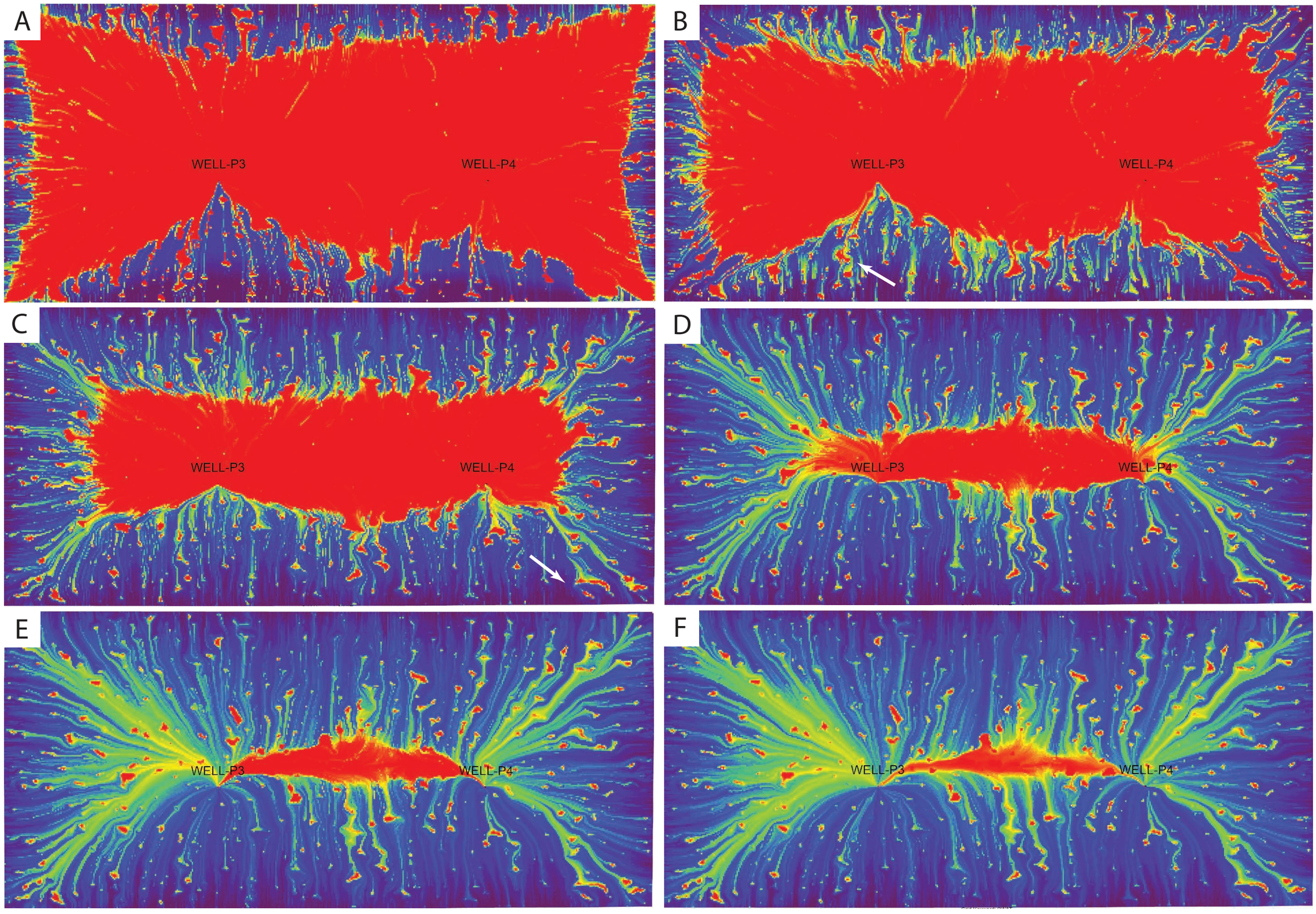


Figure 122: Temporal evolution of oil saturation in the top grainstone layer. Same colour coding as in Figure 115. A-B illustrates oil saturations after 1 and 2 years of production, respectively. B-F are snapshots after 5, 10, 15 and 20 years. White arrows in B and C indicate oils saturated fronts in the lee of bioherm structures.

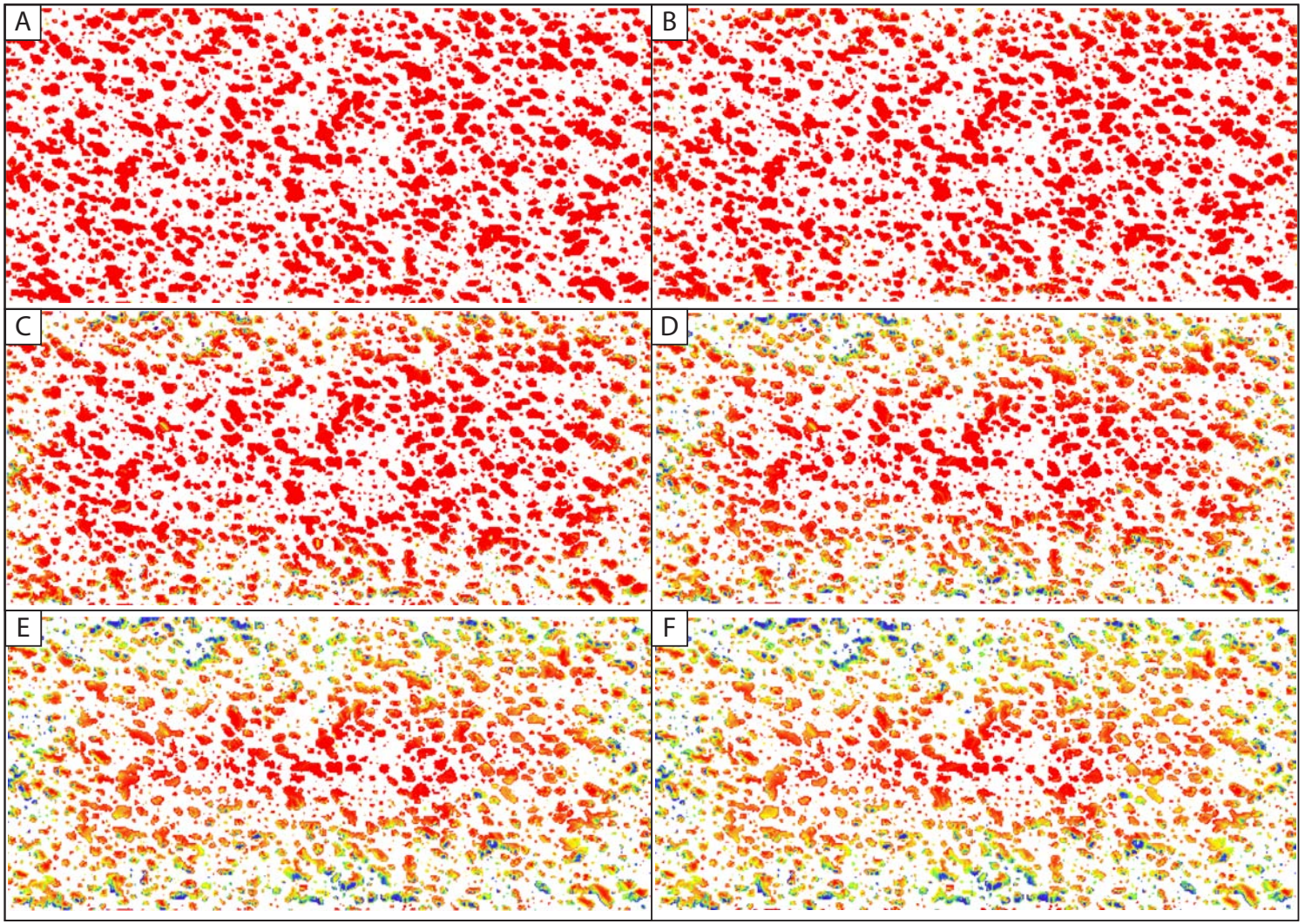

Figure 123: Change of oil saturation of bioherm structures after 1 year (A), 2 years (B), 5 years (C), 10 years (D), 15 years (E) and 20 years (F)

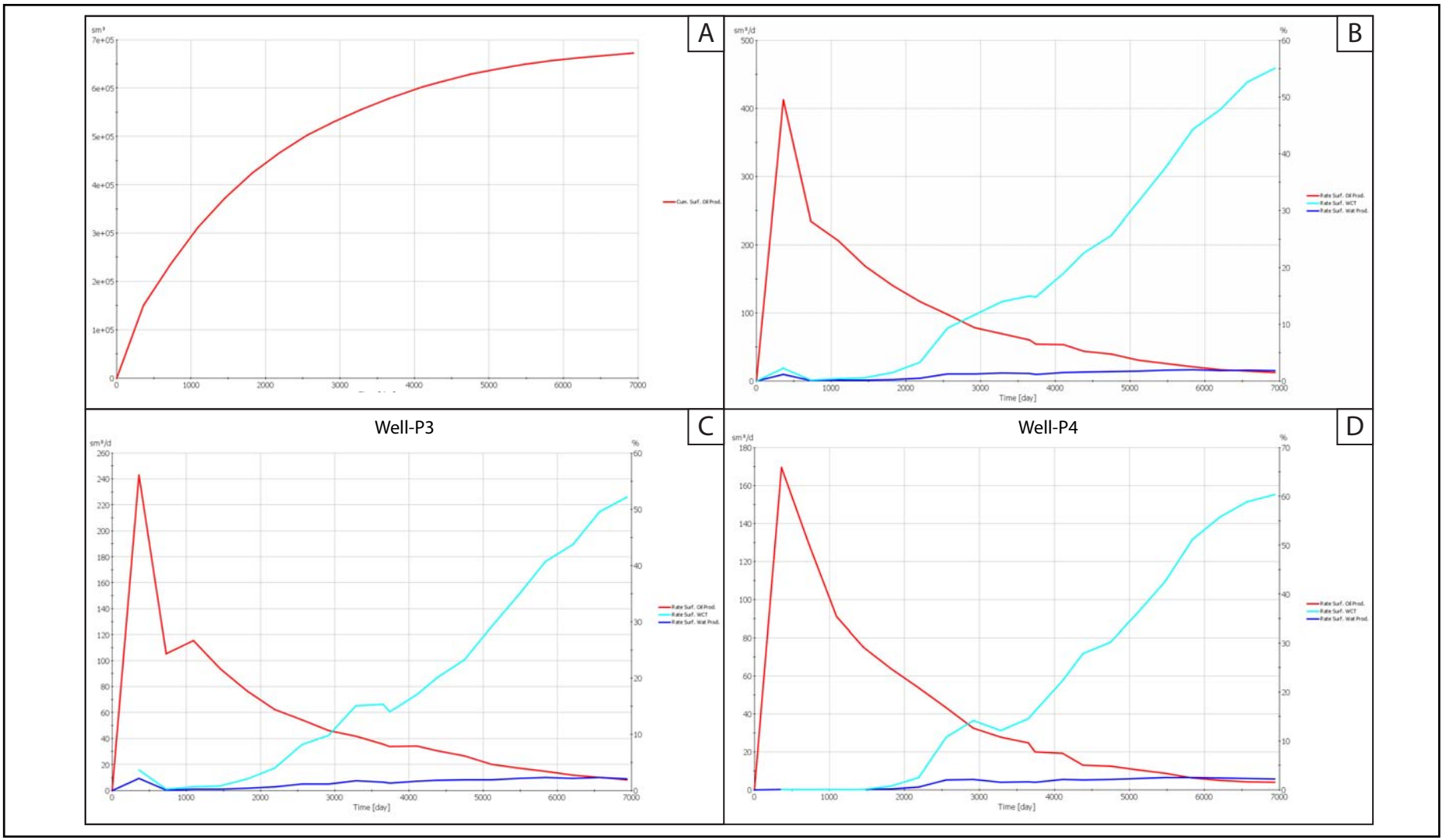


Figure 124: Production cross-plots of model 1.2: (A) Cumulative production, (B) field wide daily production rates and daily production rates for Well-P3 (C) and Well-P4 (D)

The streamline visualisation in Figure 125.A shows the field wide fluid flow pattern and clearly illustrates that streamlines deviate around bioherm structures. This is clearly visible in Figure 125.B, illustrating that streamlines are channelled through the inter-bioherm areas. In this illustration streamlines are colour coded according to water saturation by means of red colours indicate water saturated and purple colours oil saturated streamlines. Red streamlines are channelled in the inter-bioherm areas and represent already depleted grainstone volumes. Purple streamlines are located within and behind bioherms and represent the active drainage of the bioherms as seen by the oil fronts in the lee of bioherms.

Through analysing the drainage time (DRT) of streamlines the exact fluid flow pattern and catchment areas for each well can be analysed. Figure 126 shows a series of screenshots of DRT's coloured streamlines for both wells. The DRT cutoff is set to 3650 days and therefore the streamlines show the radius of depletion achieved after 10 years of production. Figure 126.A shows the entire model with streamline DRT radii. Clearly visible is that streamlines are channelled around the bioherm structures. Smoother streamline pathways towards the wellbores occur from a north-western and south-eastern direction, respectively. This coincides with the general alignment of bioherms towards the NW-SE. However, this smoothing effect only occurs along NW-SE axes in the line of sight of the wellbore. Streamlines become deviated at bioherms and have to flow around the structures and hence cover longer distances and need higher DRT's (Figure 126.B). Large streamline vortexes develop around merged bioherms to the south and north of the wellbores, respectively. At these locations the maximum surface of the NW-SE aligned bioherms is exposed to the streamline fluid path (Figure 126.A&C). In general, grainstone areas behind bioherms relative to the wellbores get drained slower than areas without mound structures in the line of sight to the wellbores. However, these small streamline vortexes do not affect the overall drainage areas. Both well catchment areas are concentrically aligned towards to boreholes.

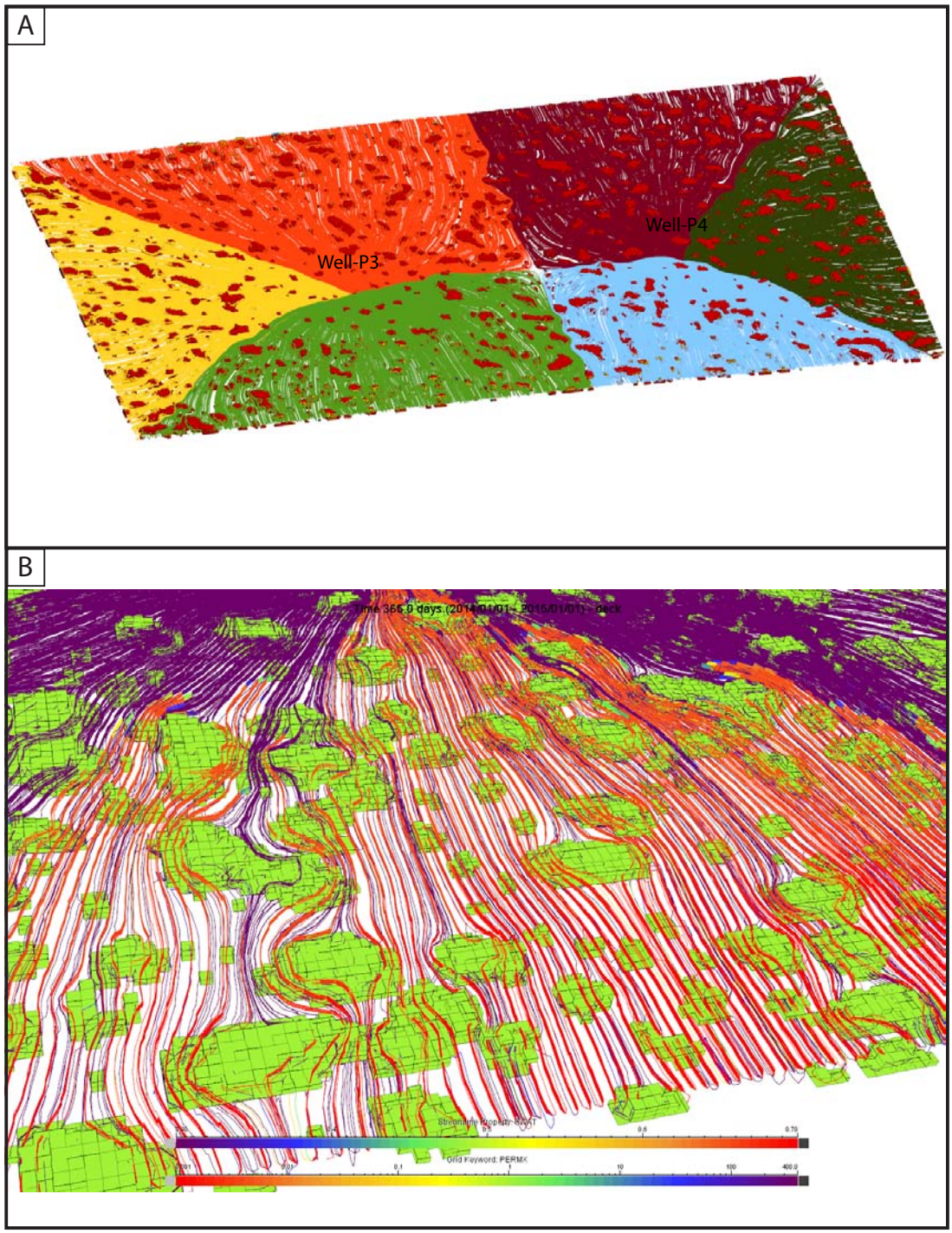


Figure 125: Field wide visualisation of streamlines. Coloured after injected boundary and producer well. Note that red bioherms are clearly visible indicating fluid flow around bioherms. (B) Enlarged area of yellow streamlines in figure A with water colour coding (red colours indicate water whereas purple colours indicate oil saturated streamlines). Note the channelling of the streamlines in the inter-bioherm areas. Fluid flow towards the top of the image.

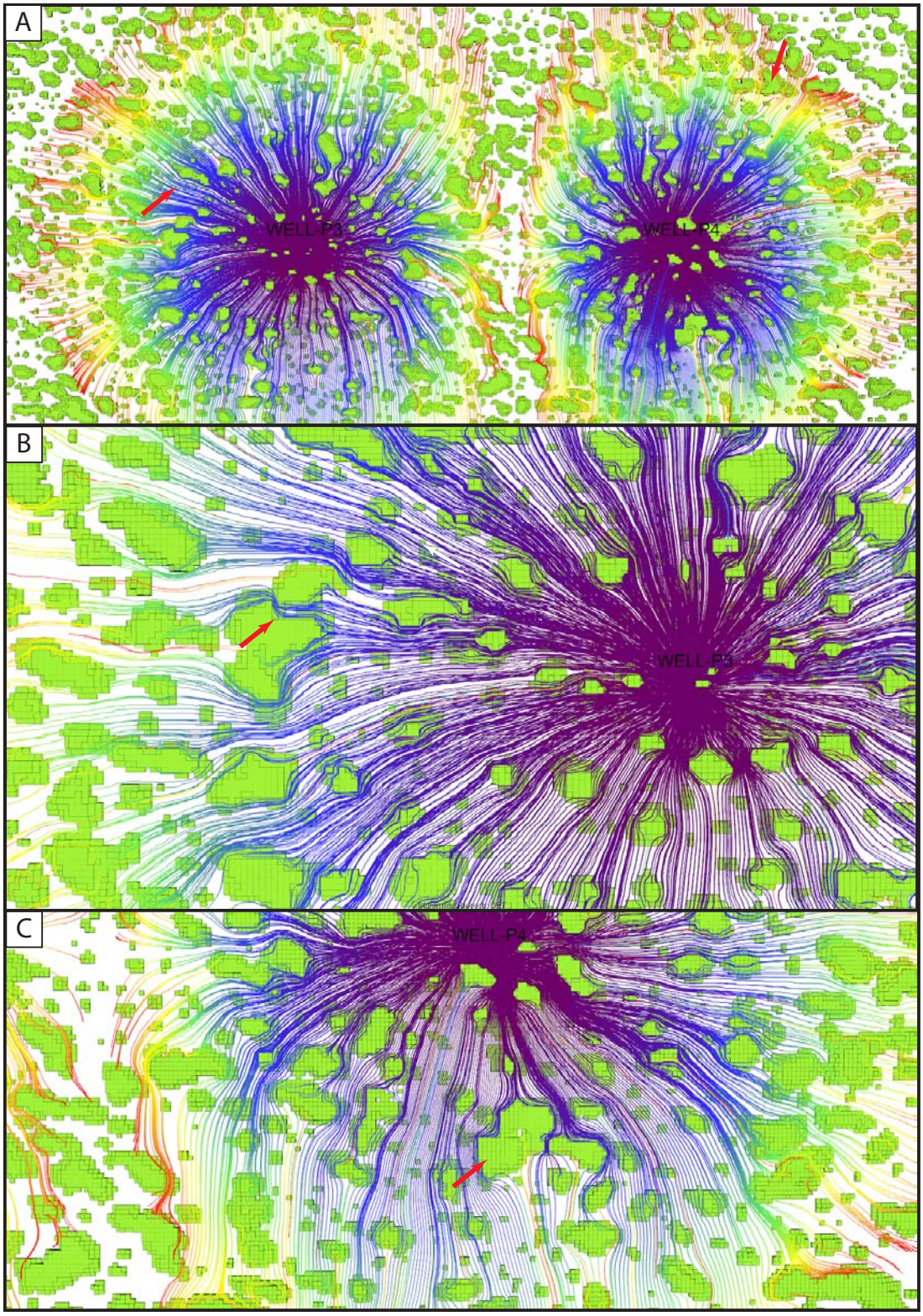


Figure 126: Series of images showing the drainage radii for Well-P3 and Well-P4. (A) Drainage areas shown for both wells. DRT cutoff of 3650 days. Note the channelling around the elongated bioherm structures (red arrow). (B) Enlarged area showing that streamlines are focussed in the inter bioherm areas. (C) Directly to the south of the wells the exposed bioherm surface relative to the wellbore reaches a maximum, which leads to abundant flow vortex developments (red arrow).

#### 7.3.2.3 Fluid flow results scenario 2 models

Fluid flow characteristics of the scenario 1 microbial reservoir analogue layer have been presented in detail in the previous paragraphs. The flow results of reservoir architecture scenario 2 models are essentially the same, in terms of pressure evolution, overall fluid patterns and drainage behaviour. The subsequent description of the dynamic behaviour of the microbial system will thus focus on the flow differences due to an additional fluid flow unit in the middle of the geocellular model.

The temporal evolution of the top grainstone flow unit of all three models is illustrated in Figure 127. For each model the oil saturation distribution after 10 and 20 years is plotted, which show the same radial depletion patterns as scenario 1 models in accordance with the evolution of the pressure field (see Figure 114). Subtle differences between the individual petrophysical realisations can be noted in the water-flushed grainstones and in terms of residual oil saturation in the microbialites. Bioherms in model 2.1 (Figure 127.A&B) have slightly higher oil saturations than the surrounding grainstones whereas the top layer of model 2.2 gets homogenously depleted over the production period (Figure 127.C&D). No oil saturation gradients are visible. Saturation contrasts between microbialites and grainstones shows model 2.3 (Figure 127.E&F). Here both situations occur of completely flushed bioherms and higher saturations in surrounding grainstones and vice versa. The first situation occurs at the border of the reservoir model. The latter situation is found near to the water flood front. An additional difference of model 2.3 is the irregular, undulating shape of the water frond compared to model 2.1 and 2.2. The visualisations of the middle grainstone layer show the same flow patterns as the top flow unit (Figure 128.A-F). However, one change is visible in the relative oil saturations. In both models with connected bioherms (model 2.1 and model 2.3) the microbialites show higher oil depletion than the surrounding grainstones as indicated by dark purple colours. This is the opposite in the oil-saturated zones, clearly visible by the dark red microbial areas in the oil zones. The middle flow unit of model 2.2 is again depleted homogenously without visible saturation differences.

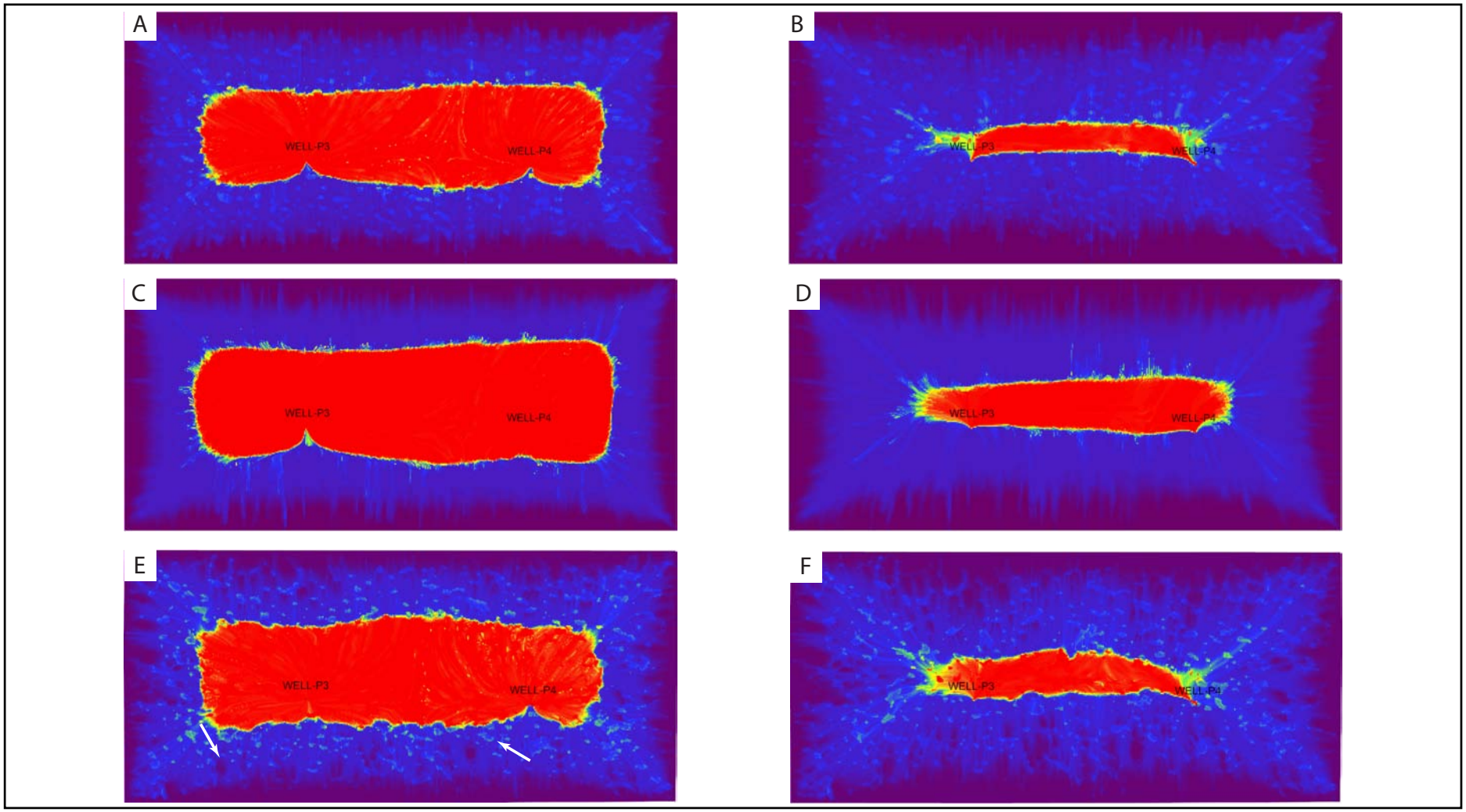


Figure 127: Temporal evolution of oil saturation in top grainstone flow unit after 10 and 20 years, respectively. A-B for model 2.1, C-D for model 2.1 and E-F for model 2.3. White arrows in figure E indicate completely and partly flushed bioherms. Same colour coding as in Figure 115.

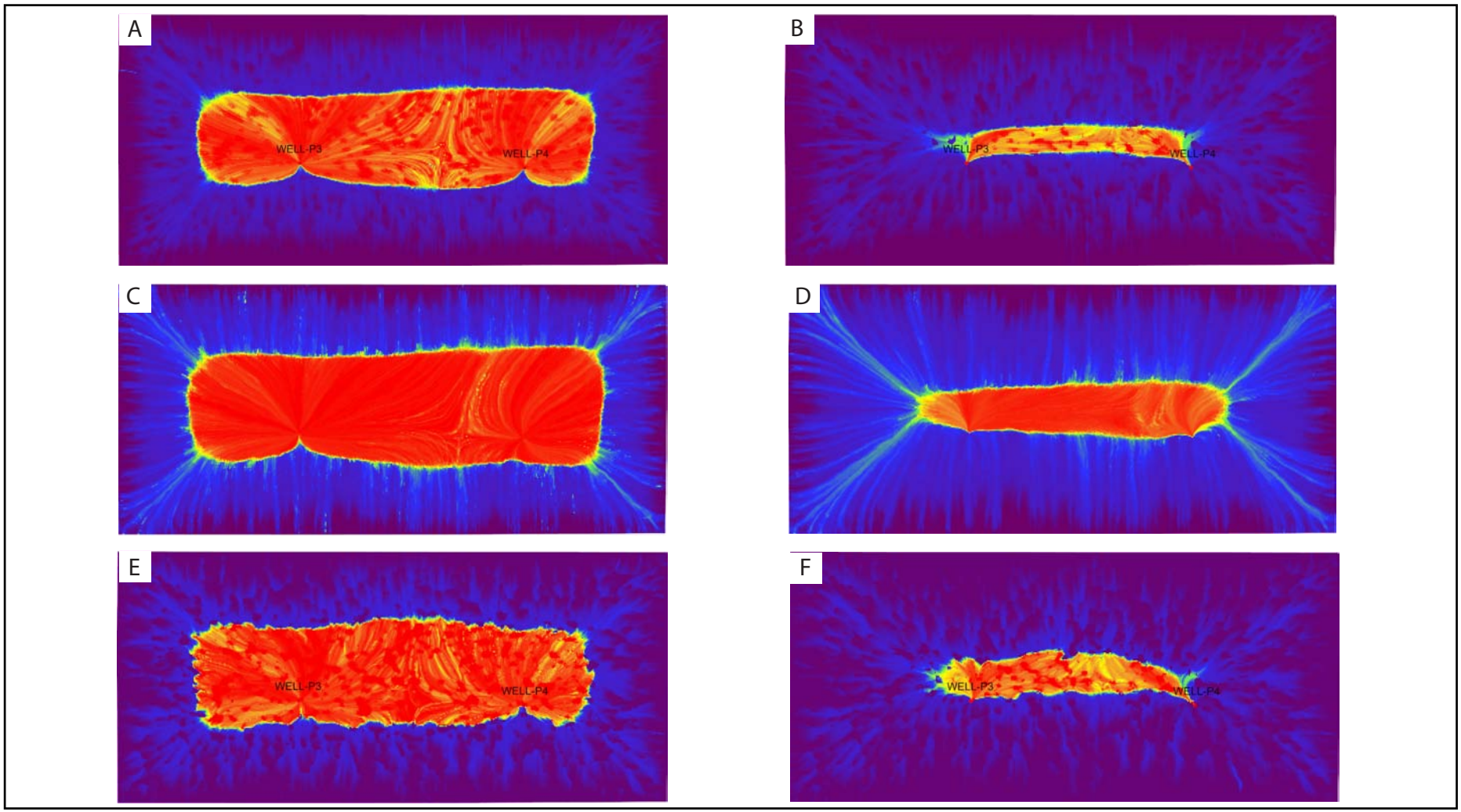


Figure 128: Temporal evolution of oil saturation in middle grainstone flow unit after 10 and 20 years, respectively. A-B for model 2.1, C-D for model 2.1 and E-F for model 2.3. Same colour coding as in Figure 115.

The dynamic evolution of the oil saturation within the bioherms is illustrated in Figure 129.A-F. Clearly visible is the same radial flushing pattern as in the grainstone layers. Note that all bioherm structures within the flooding zones in model 2.1 and 2.3 are completely drained after simulation end. This however differs in model 2.2 where several bioherms of all scales are only partly flushed (Figure 129.C&D). In all three models 8 bioherms show the initial oil saturation after simulation end. These are mounds at the bottom layer, which are only represented by one grid cell (e.g.: bioherm with an horizontal extent of maximum 5 m). The visualisation of the streamline pathways of model 2.1 shows that the fluids are moving along straight lines and as one homogenous front towards the wellbore

Figure 130.A). There is no visible deviation of streamlines in the horizontal directions near the microbial mounds.

Figure 130.B illustrates the cross-section view and a vertical deviation of streamlines is visible. Similar as in model 1.1 and 1.2, streamlines descend once they enter bioherm areas. However, the pathways only sink for one layer and continue on a straight line until they ascend at the lee side of the mounds again. In model 2.2 fluids also advance along a homogenous front towards the producer well (Figure 131.A). A slight channelling of streamlines around bioherms is visible. Furthermore, this shows that oil is still only partly displaced from microbialites although the waterfront already passed through. The analysis of the grid saturation properties of the microbial mounds show that bioherm areas connected to the flow units are entirely flushed, whilst oil is still in place in the low permeability zones (Figure 131.B). The cross-section view of model 2.2 shows that there is only negligible vertical flow movement and the majority of the streamlines are aligned horizontal and parallel towards the wellbore.

In stark contrast to the homogenous flow behaviour of model 2.1 and model 2.2 are the fluid pathways of model 2.3 (Figure 132). The streamlines are highly channelled through the high permeability microbialites and the overall pattern is characterised by this channel development (Figure 132.A). This effect also takes place after the water front has passed through (Figure 132.B). This focusing of fluids is, as described earlier, also visible by the undulating flood front. In cross-section view a vertical flow movement is clearly visible when oil is displaced through the water flood (Figure 132.C).

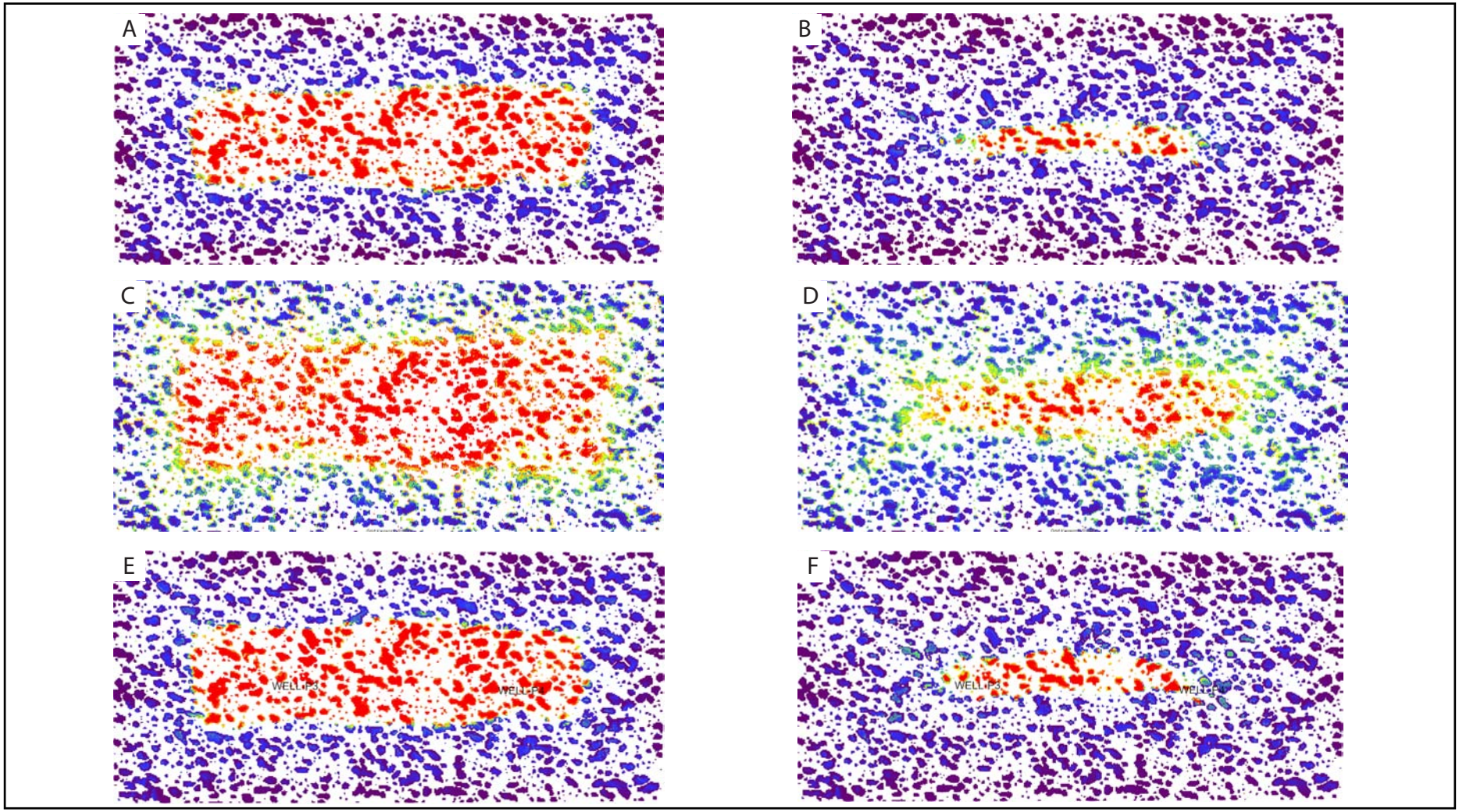


Figure 129: Temporal evolution of oil saturation in microbialites after 10 and 20 years, respectively. A-B for model 2.1, C-D for model 2.1 and E-F for model 2.3.
Same colour coding as in Figure 115.

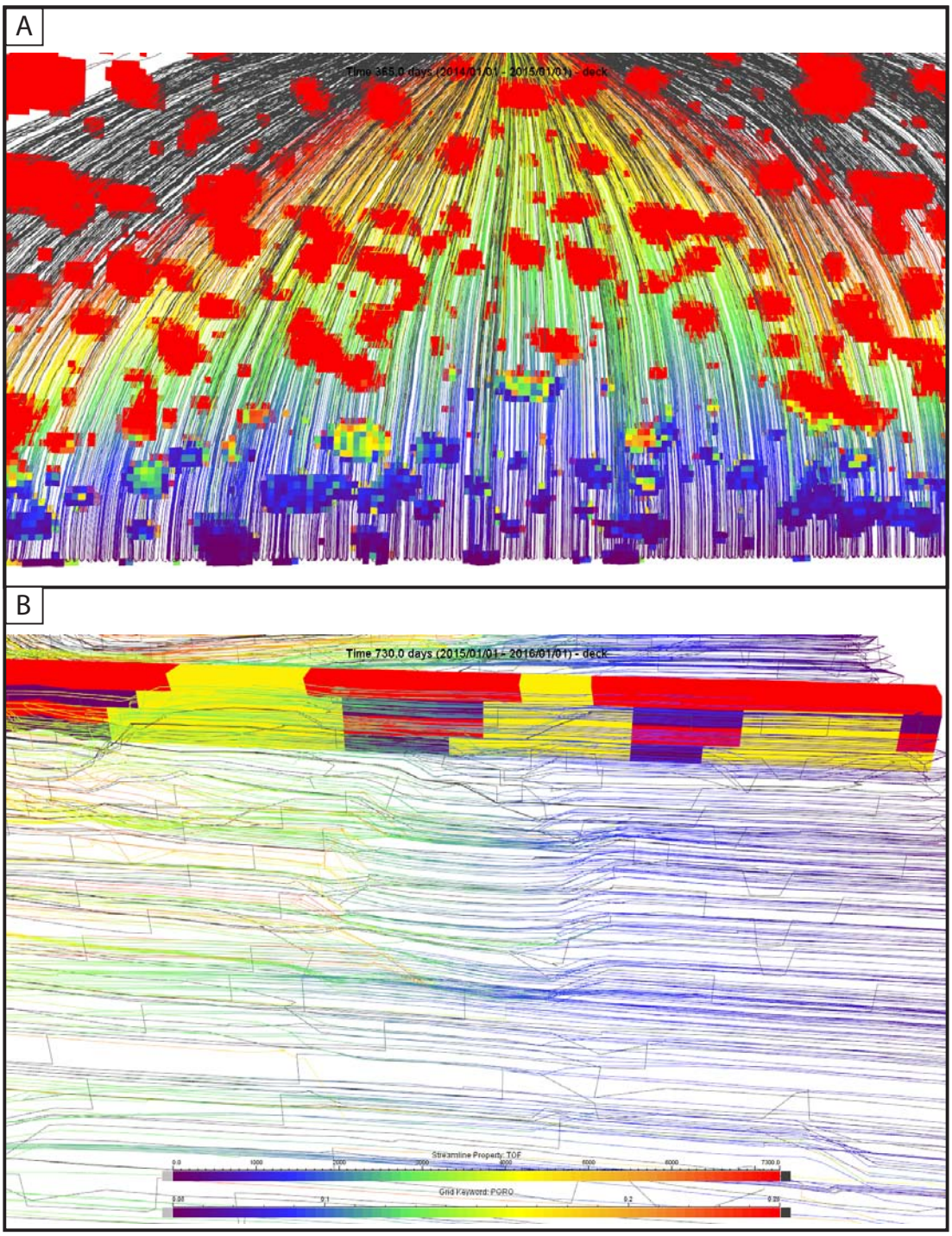


Figure 130: Visualisation of streamlines for model 2.1. Fluids are moving along streamlines without vortex developments near bioherms. TOF colour coding with blue streamline colours indicating higher and red slower flow regimes. (B) Grid cross-section view with superimposed streamlines showing that descending water does not reach the bottom of bioherms and no horizontal deviation takes place.

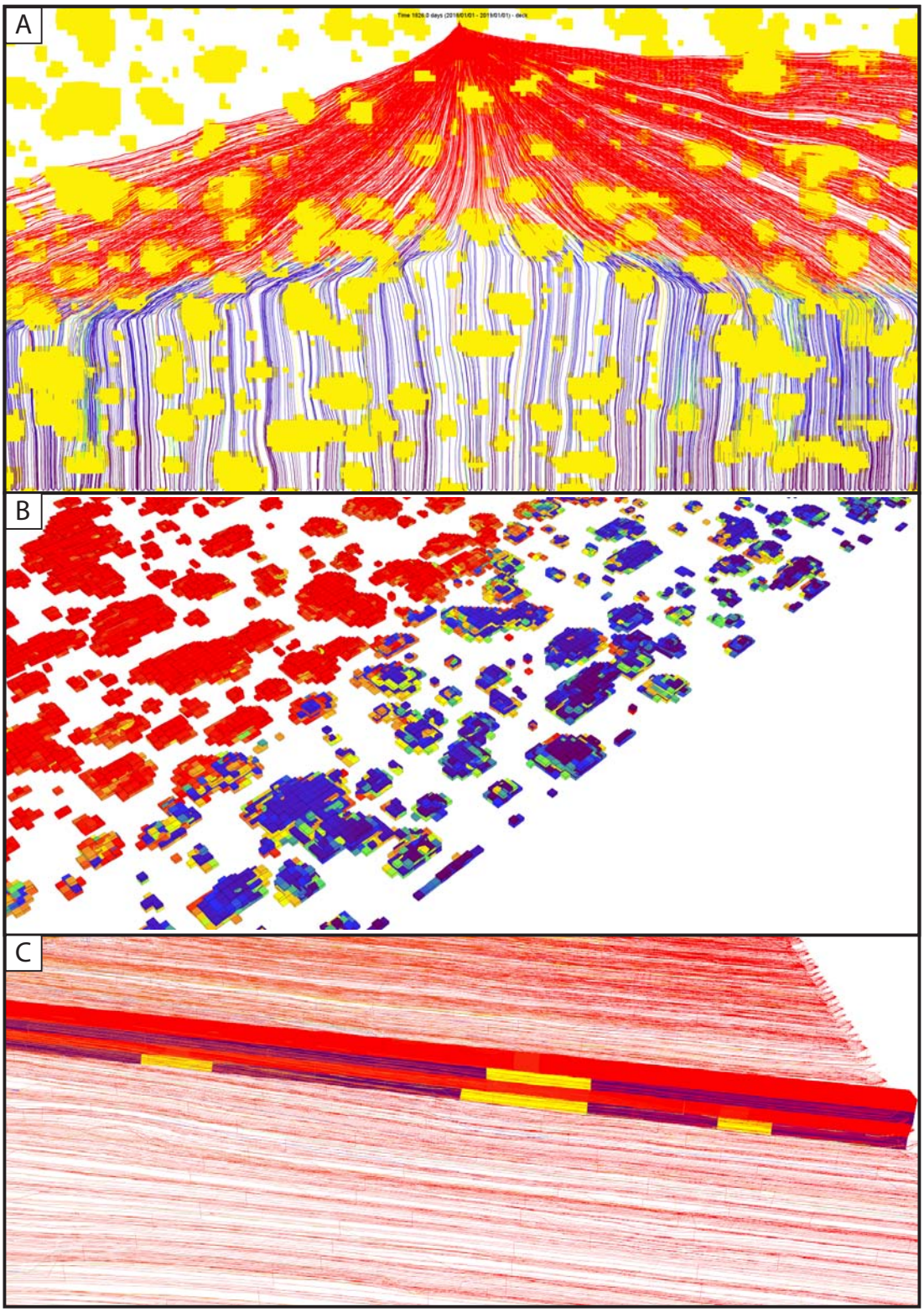


Figure 131: Visualisation of streamlines for model 2.2. (A) Fluids are moving along straight pathways towards the well bore (top of the image). Only minor horizontal around bioherms is visible. (B) Bioherm facies model with oil saturation. Blue colours represent flushed grid cells whereas red colours indicate initial oil saturation. Note that the middle layer and bottom layer of bioherms are only partly drained. Wellbore to the upper right of the image. (C) Grid cross-section with superimposed streamlines showing that streamlines are moving along straight lines towards the producer wells. No vertical fluid flow takes place and model 2.2 acts as a simple layer cake model.

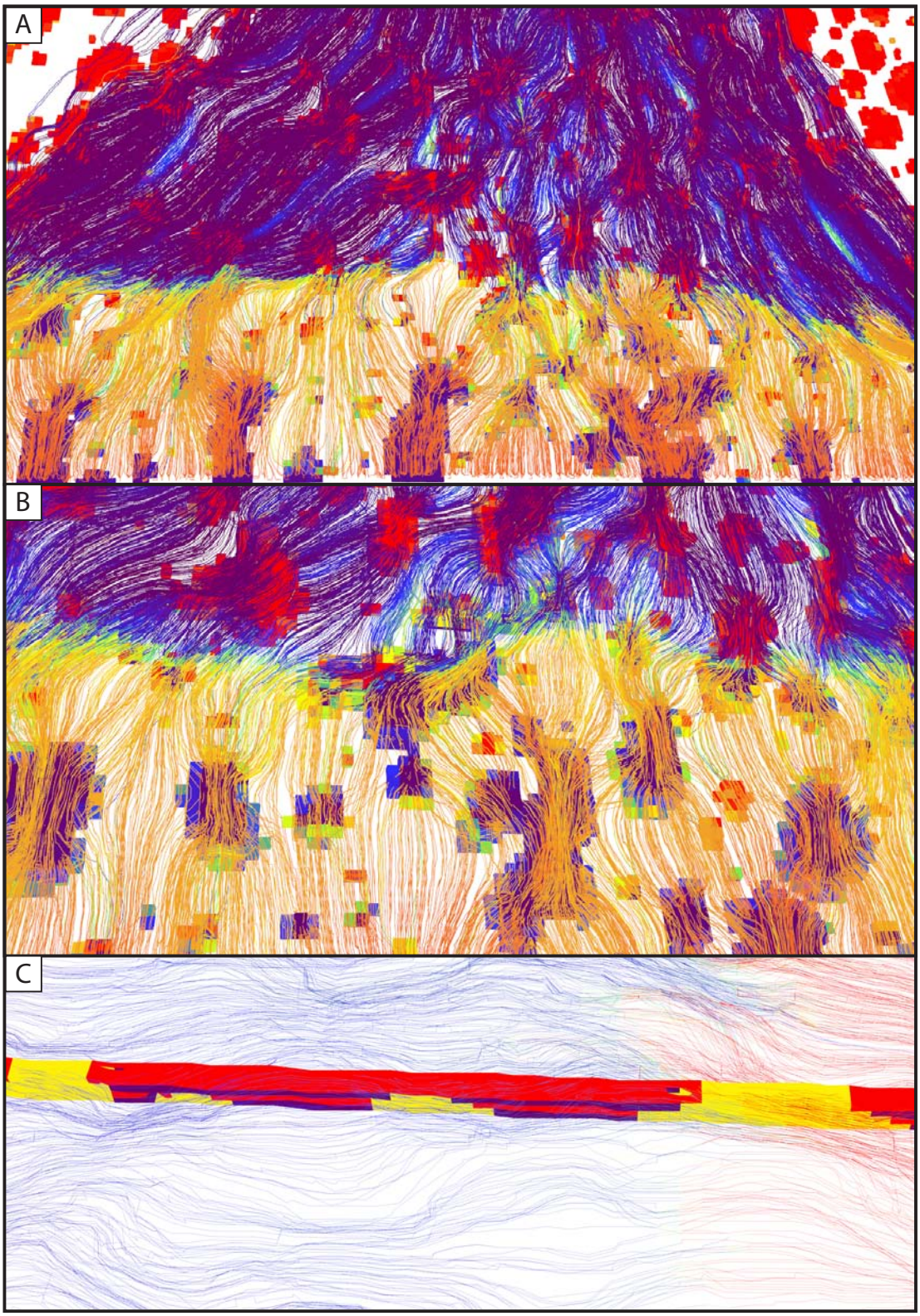


Figure 132: Visualisation of streamlines for model 2.3. (A) Highly heterogeneous fluid flow and streamlines are channelled through bioherms. (B) Enlarged area of figure A illustrating the highly diverted fluid flow pathways. Fluid flow in both images towards the top of the image. Colour coding represents water saturation with orange colours for water and purple for oil saturation. (C) Grid cross-section view with superimposed streamlines illustrating that channelling of fluids occurs in vertical but also in horizontal directions.

Comparative production cross plots of all three models are illustrated in Figure 133. The model 2.3 initial daily production rate is the highest of almost 600 $sm^3$ per day after one year, followed by model 2.1 (475 $sm^3$/day) and model 2.2 of 355 $sm^3$/day (Figure 133.A). These initially high values drop rapidly within the first 2000 days to approximately 355 $sm^3$/day and from this point on the productions are similar and continuously drop down to 50 $sm^3$/day at the end of the simulation run. In all three models the watercut happens late around 3700 days but then rapidly climbs to 37% for model 2.1. The lowest watercut has model 2.2 with 17% after a drop of 4% in the last simulation year (Figure 133.B). The cumulative production rates are similar for all the three models, however the production wells of model 2.1 extract most of the oil in place, of more than 1.1+E*06 $sm^3$ oil, followed by model 2.3 and 2.2 (Figure 133.C). This ranking is also recorded in the oil-in-place plots (Figure 133.D), where model 2.2 shows the least recovery rate (1.27+E*06 $sm^3$) and subsequently higher oil-in-place volumes. The results for model 2.1 and 2.3 are similar with approximately 1.15+E*06 $sm^3$ remaining oil in the reservoir.

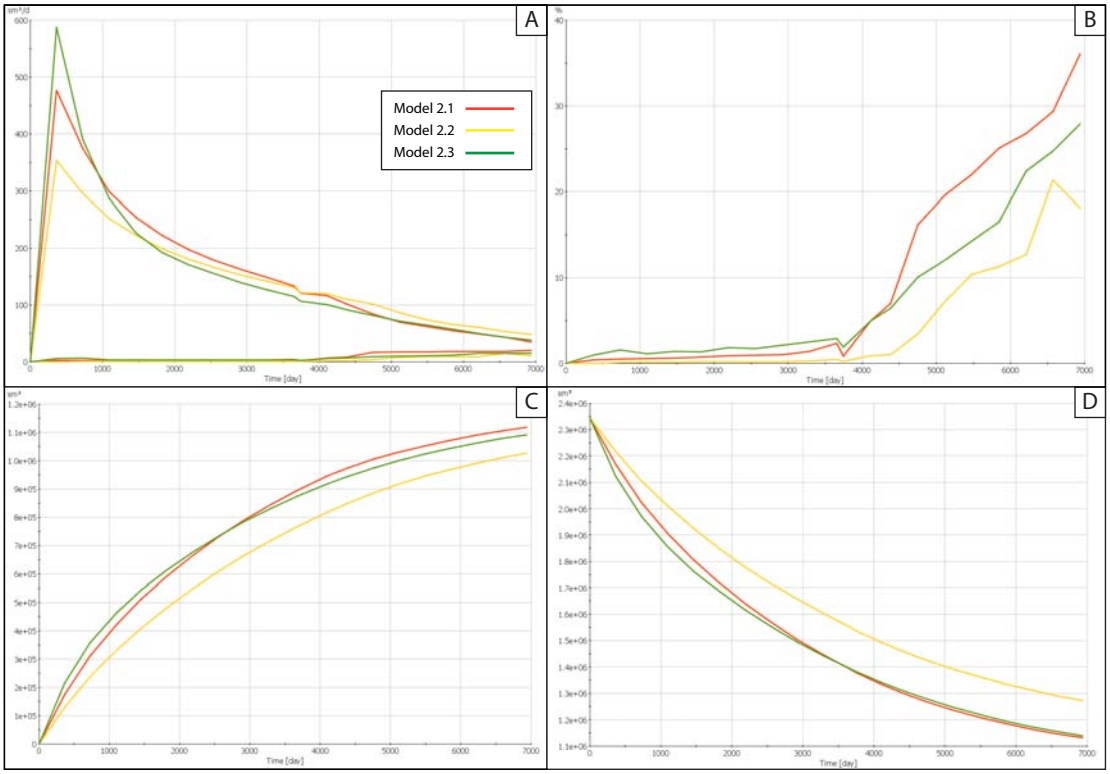


Figure 133: Production cross-plots of model 2.1-3: (A) field wide daily production rates, (B) watercut, (C) cumulative production rates and (D) oil in place volumes.

### 7.3.3 Discussion of streamline flow results

#### 7.3.3.1 Scenario 1

The aim of the fluid flow analyses of reservoir architecture scenario 1 was to test the dynamic behaviour of the bioherm system, where bioherms are only connected through one fluid flow unit at the top (grainstone layer). The main question addressed was: does oil get drained from the microbial carbonates or do oil/water fronts bypass the mound structures and oil stays behind in the microbialites. The majority of the bioherms in model 1.1 got drained during production. In this model realisation the permeability ratio was 1:2 (100 mD microbialites and 200 mD grainstones). Not produced bioherm complexes are either completely isolated in the sense that there is no connection to the flow unit (embedded in non-flow inter-bioherm facies) or are only connected through a maximum of 1 grid block to the flow unit.

The first case shows that no bioherms are produced, which have less than 2/3 of the reservoir height. The average thickness of the reservoir model is roughly 12 m and the base of the grainstone layer is at 9 m height. Therefore, bioherms which have heights less than 9 m will not be drained because there is no connection to the grainstones. Although 617 microbial mounds have these characteristics within the reservoir analogue model, this only represents less than 3% of the microbial reservoir facies. The connected but unproduced bioherms constitute 4.8% of the bioherm volume. In that cases fluid flow is hampered because of the narrow and small connections with the overall flow unit. In the case of bioherm tops connected with only one grid block to the grainstones the water fronts are bypassing and the oil stays behind in the bioherm. The explanation for this is relatively straight-forward. Fluid flow in every grid block is only allowed in one direction and no cross-fluid flow can happen. Since the bioherms are closed systems, in the sense that the inter-bioherm facies does not allow fluid flow, fluid circulation has to occur in the top layer. However since only one grid block is available for that in the top layer no fluid flow can take place because the connecting grid block cannot accommodate a fluid flow system in two directions – entry and exit flow. The same fluid flow restrictions are also applicable to the merged bioherm complexes. Although, they are connected to the general flow unit (produced bioherms) the connection is only via one grid block. Also because these constricted segments have heights < 9 m they are not

connected to the top grainstone flow unit. Therefore, entering fluid has no way to exit these compartments. However, the author wants to highlight that these results have to be regarded with caution because of two reasons. Firstly the simulation was carried out in incompressible mode, assuming that there is no expansion of fluids while being produced. These assumptions require a displacement of fluids by other fluids, which is water in the here presented simulation runs. However, in reality oil is most likely to expand during reservoir pressure drop and therefore fluid flow might take place without the necessity of a replacing fluid. Secondly, the grid block representing the bottle neck has a dimension of 5x5 m in the horizontal directions. This represents an actual area of 25 $m^2$ in reality, where fluid exchange and flow can potentially happen. A higher grid resolution, for instance 2x2 m, is most likely to produce results where oil is drained since more grid blocks are available for cross fluid flow. Thus it is concluded that les than 3% of the bioherm facies cannot be produced because there is no connection to the flow unit. Computational limitations and assumptions in the streamline simulation parameters are most likely to be responsible for the additional unproduced 4.8% microbial reservoir facies. These bioherms are most likely to be produced under real conditions.

Nevertheless, more than 92% of the microbial carbonates in the simulation run of model 1.1 were drained during production. The visualisation of the streamlines and flow pathways helps to better understand the oil voidage replacement dynamics by the advancing water fronts. As illustrated in Figure 119.B streamlines descend once they enter the bioherm structures. On the way to the bottom of the mounds the water front actively pushes the oil out of the bioherms. The fluids ascend once the reach the lee side of the bioherm (Figure 119.B). Next to the pushing effect residual oil at the edges of the mounds is picked up by water until the entire bioherm is flushed. This water flooding occurs first in the centre of the mounds. The explanation for that is that bioherms are getting narrow towards the top (dome to pyramid shaped). Therefore water flushing happens in the cores and progressively spreads out towards the sides. If the connections between merged bioherm structures are sufficient big enough, cross-bioherm fluid flow takes place and the entire oil in the microbial complexes is replaced by water (see Figure 120). The question is however why do streamlines descend to the bottom? An initial hypothesis of the author was that the water front would bypass the bioherms and the oil in the microbial carbonates stays

behind. However, in the model 1.1 simulation run, the permeability differential between microbialites and grainstones was too low to prevent water entering bioherms. But why does the water flush the bioherm and is not flowing on the shortest streamline towards the wellbore? The cause for this is interpreted to be gravity driven.

In the initial simulation settings water has a specific density of 1050 kg/m$^3$ (brine) whereas the density of oil was assumed to be 850 kg/m$^3$ (API gravity of 35$^o$). This was kept constant throughout the simulation run. Once the water flood front is entering the bioherms a fluid layering occurs by means of a relative lighter fluid (oil) is overlain by denser and therefore heavier fluid (water). This density contrast initiates subsequently vertical fluid flow and bottom oil is replaced by water. This system closely resamples the characteristics of a convection cell. This phenomenon in fluid dynamics describes fluid movement in a liquid or gas body when density differences are present. The driving force for the fluid flow is solemnly due to buoyancy differentials between the fluids or gases in the stratified body. Consequently, buoyancy differentials imply a pressure gradient within the bioherms. This is confirmed by the observation of the temporal evolution and shift of the pressure field in the bioherms during the passing of the water front (see Figure 121.B). While the water flood passes through, low-pressure areas are located within the bioherms and high-pressure fields in the inter-bioherm facies. Streamline pathways are diverted towards and channelled through the mounds (see Figure 121.A). This is interpreted as response to the down-welling of water in the bioherms. The down-welling effect, due to pressure differentials, creates lower pressures in the bioherms because fluid is also moved vertically. Thus, streamlines entering the bioherm grid blocks have two potential exit directions: downwards into the bioherms or continue on a straight path towards the wellbore. Consequently, a higher fluid volume can be channelled through the bioherm complexes as compared with the inter-bioherm facies where only the horizontal directions are possible. This is also confirmed by lower TOFs in the bioherm complexes, indicating higher fluid flow rates and therefore drainage rates. A schematic illustration of a bioherm convection is given Figure 134.

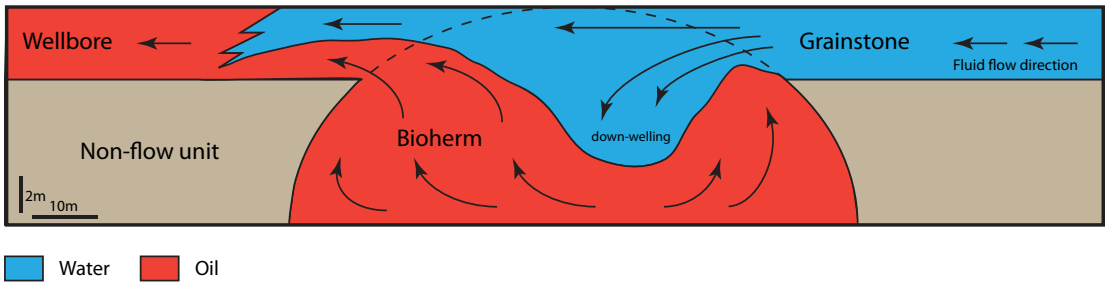


Figure 134: Cartoon illustrating the convection cell dynamics within microbial bioherms. See text for explanation.

A key observation is the disappearance of the convection cells within the bioherms after the water flood passes and the oil in the bioherms has been displaced (see Figure 121.D). After the flushing of the bioherms, streamlines resume on a straight line towards the wellbore and no streamline channelling occurs. Furthermore, the pressure field is equalised again. This clearly shows that the driving force of the down-welling effect is due to buoyancy differentials and thus gravity induced. After flushing, the two phase, two density system is replaced by water and therefore no density differentials occur within the bioherm body. Thus, vertical fluid flow does not take place.

This is an important conclusion because of two reasons: Firstly, these findings imply that oil stored in the bioherms is not drained during primary production due to the absence of water induced gravity differentials. This could not be confirmed with the streamlines analysis, because bioherms cannot be source areas in an incompressible simulation run. Therefore, streamlines cannot originate from the microbial carbonates and flow behaviour in primary production could not be analysed. However, the above findings show that no fluid flow in the bioherms will happen in a single-phase system during incompressible simulation.

Secondly the results show that during secondary recovery the injected phases have to have a sufficient high enough density difference relative to the oil phase in place. If the density differences are too low, the oil in the microbial carbonates cannot be recovered. For instance gas injection would simply bypass and overflow the mounds without creating a convection cell effect.

Results of the model 1.2 simulation run show the dynamic behaviour of the microbial carbonate system with high permeability contrast between microbialites

and grainstones. The simulated permeability ratio was 1:400 with 1 mD for the bioherm structures and a high value of 400 mD for the grainstones. The results show that under these conditions the majority of bioherms will not be produced. Only top layers of the mounds get partly drained over 20 years of production. Due to the high flow rates, the grainstone layer gets almost completely drained within the first 10 years. This is also reflected by the initial high production rate and the early water breakthrough within the first 365 days of simulation.

The visualisation of the streamlines shows that fluid flow is diverted around bioherm structures and channelled through the high permeability inter-bioherm zones. An interesting observation is the smoothing effect of streamlines in NW-SE directions towards the wellbores. The opposite, streamline vortexes, occurs in NE-SW direction. This pattern is interpreted as the flow response to the alignment of the bioherms towards the NW-SW. The longer axes of the bioherms are orientated normal to the Kuibis ramp strike direction (compare chapter 6) and therefore the minimum surface of the asymmetric mounds is exposed to the flow direction. This implies that streamlines can easily flow around the elongated mounds. The exact opposite occurs in a NE-SW direction relative to the boreholes where the maximum mound surfaces are exposed. Thus, fluids have to flow around large bioherm areas and are channelled through bottle necks in merged mounds, which create fluid vortexes. This effect did in fact not affect the drainage areas because fluids were flowing radial towards the well. Therefore, only streamlines along NW-SE and NE-SW axes, aligned with the wellbores showed this effect. However, in the case of a production scenario with 2 or more injector and 2 or more producer wells, streamlines will flow on parallel lines towards the boreholes. Thus, it is favourable to flush the system from a relative NW or SE direction relative to the wellbores in order to minimise vortex development and hence optimise production rates through higher fluid flow rates.

In both simulated models, Well-P3 has a higher production rate than Well-P4 and also a larger drainage area. Well-P3 is located up-dip in respect to Well-P4, and therefore in a lower pressure field. This can be seen in the initial reservoir pressure plot of Figure 114.A. Therefore, the relative pressure gradient at Well-P3 is higher and thus more fluid volume gets drained through this well. An additional pattern in both simulation runs are remaining oil saturations aligned on axes between wellbores and reservoir edges. This coincides with the collision zones of the water fronts (see

Figure 118.A), for instance the southern front mixes with the western flood front. In these areas reduced drainage occurs due to the vortex development. However, this takes place due to simulation parameters and due to the rectangular shape of the reservoir analogue model. Thus, this will not take place under real conditions.

A series of production plots are illustrated in Figure 135, comparing both model production rates. The initial cumulative oil drainage is higher in model 1.2 but after approximately 3600 days the cumulative production of model 1.1 becomes higher (Figure 135.A). This coincides with the complete drainage of the top grainstone layer of model 1.2. Since the oil stays behind in the model 1.2 simulation, the cumulative oil rate flattens out from this point on towards to end of the simulation. However, oil is still produced in model 1.1 because bioherms are still actively drained. In both models, the initial oil in place is 1606000 $sm^3$ (10,101 Mbbl). 54.4 % of the oil stays in place in model 1.1 whereas 64.5% of the oil stays back in model 1.2 (Figure 135.B). Therefore, the drainage of the bioherms adds approximately **10 %** to the cumulative oil production. The comparison of the daily well production rates shows that in both model simulations the initial high peak production rapidly decreases (Figure 135.C&D). This is interpreted to be the response of the fast drainage of the grainstone horizon. The field wide production rates show that after approximately 2000 days the daily production rates of model 1.1 exceed production rates of model 1.2 (Figure 135.E). This is interpreted as the additional drainage of the bioherms in model 1.1, which contributes to the daily production rates.

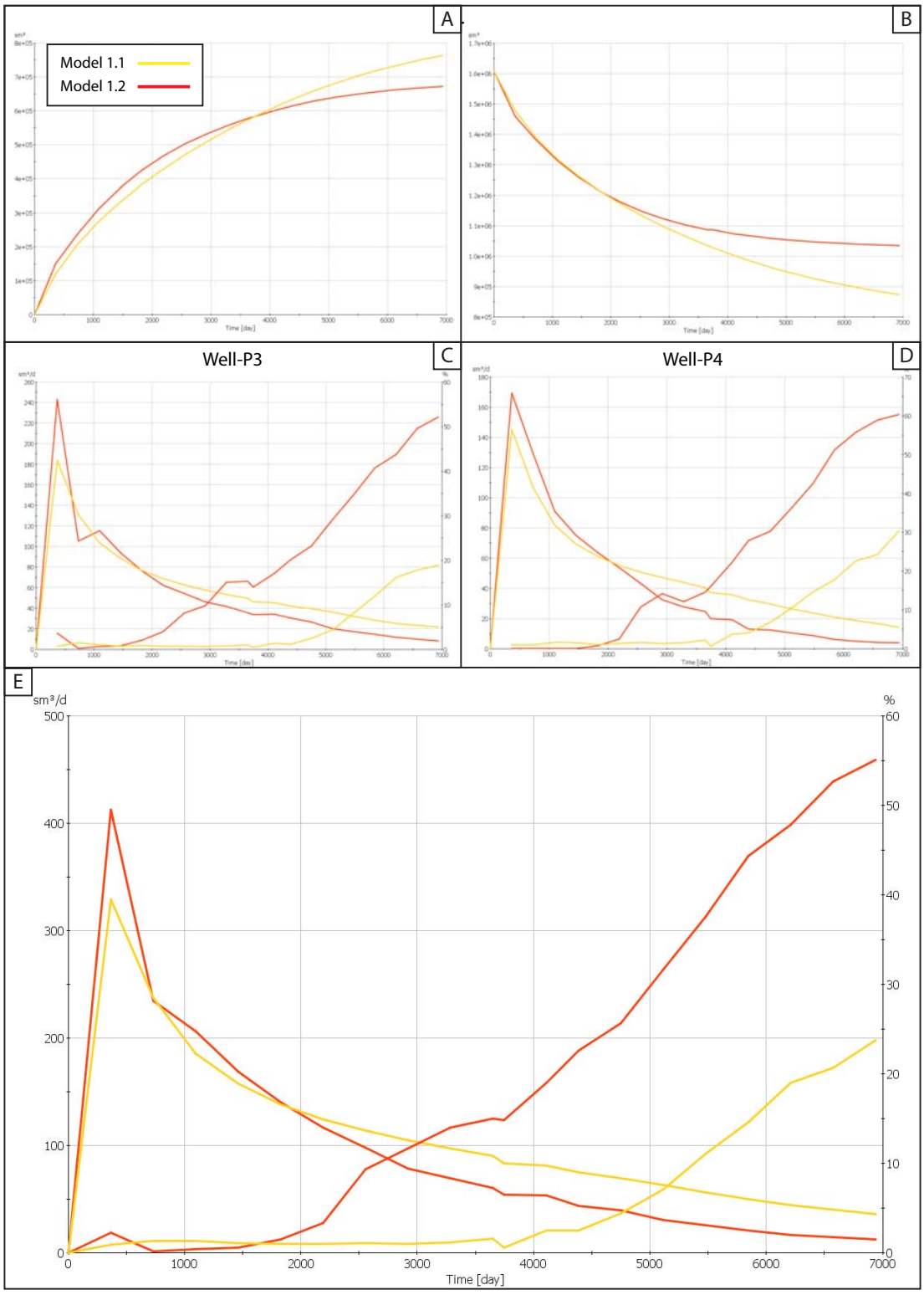


Figure 135: Comparative production cross-plots for scenario 1 models. (A) Cumulative production, (B) Oil in place, (C) Daily production rates for Well-P3 and (D) Well-P4 and field production rates (E).

#### 7.3.3.2 Scenario 2

The scenario 2 models were especially designed to analyse the influence of an additional flow unit in the middle of the reservoir layer. The key observation of model 2.1 is that all bioherms are produced in the entire reservoir model throughout the simulation in contrast to the scenario 1 models. The interpretation for that is straight forward: all bioherms in the model area are connected at least through one flow unit and thus in all bioherms fluid flow exchange can take place. Throughout the model area only 8 single cell bioherm structures could not be produced. The reason for that is as described above; the limitation of the streamline simulator, in terms of one grid cell surface can only serve either as entry or exit point. Therefore, the single cell bioherms, surrounded by no flow units cannot be produced. The water flooding of the microbialites in model 2.1 shows the same convection cell characteristics as in model 1.1. However, the top water floods do not descend towards the bottom of the bioherms but get diverted at the top of the middle grainstone layer. In the simulation, the water floods in both grainstone units advance with the same speed towards the wellbore. Thus, descending water from the top layer in bioherms hits cross-flowing water flood in the middle layer. Subsequently, no pressure differentials due to different fluid densities occur because only water is present. This also explains the absence of vortexes of streamlines around and within bioherms because oil in the microbialites gets replaced layer by layer. This only requires vertical displacement within the grid blocks in contrast to the oil drainage in scenario 1 models where highly irregular isolated ‘pockets’ had to be flushed which requires horizontal flow.

Model 2.2 aimed to simulate a layer cake permeability architecture. The incentive for this was the recognition of vertical porosity and permeability heterogeneities within the bioherms. By means of that mud and shale sediment input is plugging the pores of thrombolites when the lateral equivalent inter-bioherm facies is mud-dominated. The flow results show that in this situation the entire model acts as a simple layer cake model. Both grainstone horizons get homogenously drained and only minor channelling of fluids in the flow units is observable (see Figure 131.A). This is interpreted as the relative low permeability contrast between microbialites and grainstones in the flow units (100 mD:200 mD). The low permeability bioherm zones, forming the lateral equivalent of the non-flow inter-bioherm facies act as flow baffles between the grainstone horizons and prevent vertical fluid flow (see Figure

131.C). These zones get only partly drained during the simulation and the majority of the oil stays behind (see Figure 131.B). This is also reflected by the lowest cumulative production rate of the model 2.2 wells, because not all oil of the bioherms can be accessed.

The most heterogeneous flow regime in scenario 2 occurs in the simulation of model 2.3. In this petrophysical realisation, microbialites have a higher permeability (400 mD) than the grainstones (100 mD). The visualisation of the streamlines show that the majority of streamlines are channelled through the bioherm complexes. However, oil in both grainstone horizons also gets drained and does not stay behind. Although, channelling occurs through the mounds, they are not connected with each other. This requires that fluids have to pass on the shortest way between the bioherms through grainstones in order to reach the adjacent bioherms. Thus, also the grainstone flow units get drained by this fluid flow regime. Additionally, 100 mD of permeability is high enough to ensure fluid flow in the grainstones on its own. Several bioherms show higher oil saturations than the surrounding grainstones near the water flood front after the end of the simulation run (see Figure 129.E&F). This is however not interpreted as residual oil in the mounds. Since fluid flow is channelled through the microbialites the higher oil saturation values represent the additional drainage of oil stored in grainstone horizons, through the microbialites. Bioherms, further away from the water flood front are completely flushed and show that the entire microbialites can be produced. A key observation is that the channelling effect does not disappear after the water flood passes through as compared to model 1.1. This implies that the permeability contrast between grainstones and microbialites is high enough to generate this highly heterogeneous flow field in a single-phase system without the necessity of gravity induced vortex development. This is similar to model 1.2 were the opposite permeability contrast was tested and fluid flow gets channelled in the inter-bioherm facies.

Daily production rates for all three models are very similar except within the first 3 time steps (1095 days). Here the channelling through the bioherms in model 2.3 accounts for the highest initial production rates. Cumulative production rates are additionally very similar for model 2.1 and 2.3. Model 2.2 shows the lowest recovery rate, which is interpreted to reflect the residual oil in the not produced bioherm areas with low permeability zones.

### 7.3.4 Volumetric comparison

In scenario 1 models, microbialites constitute 23.61% of the reservoir facies. 22.62% of the bulk reservoir volume is represented by grainstones. The majority of the model volume (53.77%) is characterised by non-reservoir inter-bioherm facies. Although, grainstones have roughly 1 % less of total volume, they comprise the majority of the oil in place due to the higher porosity and therefore pore volume. The additional layer of grainstones in the middle of the bioherm horizon in scenario 2 models results in an increase of grainstone volume to 40.42% and a decrease of inter-bioherm facies to 35.97% of the bulk volume. Microbialites are the same with 23.61% of the bulk reservoir volume. Therefore, most of the oil in scenario 2 models is also stored in the grainstones.

The volumetric calculations for the bioherms compare well with the reported volumes of the microbialites of Adams *et al.* (2005). In their model the microbialites constitute roughly 20%, which is almost the same to the simulated microbial facies in this research project. However, Adams *et al.* (2005) modelled 55% grainstone reservoir facies, which is 15% more than in the scenario 2 models and 30% more than in scenario 1 models. The reason for the difference is not entirely clear. In Adams *et al.* (2005) final geocellular model, the inter-bioherm facies consist to 2/3 of grainstones, which is surprisingly because it does not reflect their presented conceptual model. It seems likely that a mistake during the reservoir model building process occurred, resulting in overrepresented grainstone facies. Therefore it is concluded that the here presented volumetric calculations are tentatively more accurate.

## 7.4 Discussion

The use of outcrop analogue models for fluid flow studies has become a well-established practice in recent years (e.g. Deveugle *et al.*, 2011; Jackson *et al.*, 2009; Labourdette *et al.*, 2008; Sech *et al.*, 2009). The advance of digital mapping methods, such as lidar or DGPS and the development of high-resolution digital outcrop models stimulated fluid flow analyses based on outcrop data (Agada *et al.*, 2014; Agar *et al.*, 2010; Belayneh *et al.*, 2006) and in particular for carbonate ramp systems with its need to capture small-scale heterogeneities in detail and with high precision (e.g. Adams *et al.*, 2011; Benson *et al.*, 2014; Shekhar *et al.*, 2014).

Outcrop-based simulation models tend to have dimensions typically in the range of inter-well spaces and therefore represent small-scale heterogeneities influencing fluid flow. This is, however, in stark contrast to common field-wide dynamic reservoir models, which are used to guide drilling strategies and ultimately try to predict flow performance throughout an entire production field. The construction of large dynamic models necessarily involves up-scaling of static models, due to the need of reducing the grid resolution (compare reservoir scale paragraph 6.4.2). This consequently leads to the reduction of geological information. Thus, outcrop-based fluid flow models can be used to identify critical variables effecting flow performance in order to optimise up-scaling processes.

This was the main goal of the performed streamline forecasting analyses to identify the critical variables effecting fluid flow within the microbial carbonate system. The streamline analysis tested the dynamic behaviour of the microbial-dominated reservoir layer of Unit 2, in the middle of Omkyk Sequence 2. This was done with 5 hypothetical reservoir analogue scenarios and the results proved to be unexpected because an early working hypothesis of the author was discarded. The initial assumption was that significant fluid flow might not occur within the bioherms under production because microbialites are laterally discontinuous, generally not connected and separated by inter-bioherm facies, which act as fluid flow baffles. The only connection is established via a top grainstone fluid flow layer and thus oil might stay behind in bioherms during production. The streamline analyses however refuted this hypothesis to a large extent.

In 4 tested models all bioherms are drained independently of the reservoir architecture, except in model 1.2 where a large number of small-scale bioherms are unproduced. However, non-recoverable oil in these microbialites is stored in less than 3% of the bulk microbialite volume and will only have a minor impact on potential feasibility studies. The main driving force for oil displacement in bioherms is gravity induced down-welling of water. During primary production, oil tentatively stays behind in the bioherms and needs consequently water flooding to be drained. In one model (model 1.2) bioherms were partly drained. The reason for that is the high permeability contrast between microbial carbonates and grainstones.

One of the main focuses of this research project was the development of a high-resolution geocellular model, representing the microbial facies in high detail in order to test the impact of reservoir architecture on reservoir performance. However, the

results show that this has only minor impact on the dynamic behaviour of the microbial system and even the most complex composite bioherms are produced. The critical variable in this system, under the assumed reservoir conditions in concert with simulation parameters is the permeability contrast between the flow units. The results of Model 2.2 dramatically show the impact of potential vertical permeability heterogeneities in bioherms. In this scenario the model acts as a simple layer cake and fluids move towards the wellbore without impact of the bioherm architecture.

To the authors knowledge no publications have hitherto presented results of fluid flow modelling in microbial carbonate reservoirs or outcrop analogues. However, Al Haddad & Mancini (2013) presented a detail reservoir characterisation and evaluation of the Upper Jurassic Smackover microbial carbonates of the Little Cedar Creek petroleum play of SW Alabama. Although, the authors did not present a dynamic case study, their interpretations and conclusions are partly based on an unpublished master thesis by Mostafa (2013), performing dynamic history matching of the producing wells in the Little Cedar Creel field. Furthermore, the authors incorporated an extensive database consisting of well data (112 wells with core descriptions and wireline logs) and well production rates into their reservoir evaluation. Thus, allowing them to develop detailed interpretations of the fluid flow influencing reservoir properties.

The Omkyk Sequence 2 analogue model shows striking similarities to the microbial dominated system of the Little Cedar Creek field. These Oxfordian carbonates were deposited in an inner- to mid-ramp setting (Benson *et al.*, 1996; Parcell, 2002; Parcell, 2003). The reservoir facies is characterised by grainstone beds and microbial carbonates. The latter are developed as thrombolite boundstones and laterally discontinuous thrombolite mounds with a thickness of up to 13 m. Bioherms are separated by inter-bioherm facies such as mudstones and wakestones (Koralegadara and Parcell, 2008; Mancini and Parcell, 2001; Mancini *et al.*, 2008). Interestingly, the Cedar Creek thrombolite bioherms also show a regional trend by means that the microbial structures are aligned towards the NE-SW on the carbonate ramp (Al Haddad and Mancini, 2013). The underlying reason is, however, not yet understood. The reservoir geometry is represented by a layer cake architecture. The upper reservoir zone is represented by grainstone-packstone reservoir facies. The lower reservoir unit comprises microbial carbonates, which is separated by an interval of heterolithic beds from the upper reservoir zone. The thrombolites exhibit

growth-framework porosity with superimposed vuggy porosity (Al Haddad and Mancini, 2013; Koralegadara and Parcell, 2008; Mancini *et al.*, 2008).

Al Haddad & Mancini (2013) showed that wells, completed in the microbial reservoir layer have higher hydrocarbon productivity compared to wells in the upper grainstone reservoir. The authors identified that the overall governing factor in the microbialites, influencing fluid flow and therefore productivity, is the distribution of porosity and permeability, in terms of porosity-permeability corridors of the aligned thrombolite bioherms. Thus, fluid flow gets channelled through the bioherm structures which compares well to the performed streamline analyses. Furthermore, bioherms have a high potential for secondary recovery operations due to their high porosity and permeability values and because individual bioherms are connected via thrombolite boundstones, therefore forming an interconnected fluid flow unit. This interpretation is also in line with the conclusion of Sloan (2003). The author compared more than 250 carbonate reservoirs worldwide and defined that bioherms have one of the highest recovery factors of more than 50%, which is fundamentally controlled by the size and petrophysical properties of the mounds.

The Omkyk Sequence 2 carbonates show ample similarities to the Cedar Creek microbial hydrocarbon reservoirs in terms of depositional setting, reservoir facies architecture and porosity types. Furthermore, the same conclusion regarding fluid flow can essentially be drawn from the performed streamline analysis. The permeability distribution and contrasts in concert with the spatial arrangement of bioherms is the overall crucial variable influencing fluid flow in the analogue microbial system of the Zebra River sections. Thus, potential exploration in the Owambo Basin and elsewhere should try to establish a robust porosity-permeability characterisation of microbialites and associated sediments in order to accurately predict fluid flow. Furthermore, spatial trends in the microbial facies should be considered to optimise well-planning strategies.

A second important factor, influencing fluid flow in the microbial carbonate system is the density differential of fluids, which is of special importance during secondary production. If the injected fluids are lighter and less dense than the oil in place, the development of buoyancy differentials will not take place. Thus, convection cell fluid flow will not be initiated and oil in bioherms will stay in place. In contrast to the permeability variations the density differentials are a necessity as required by the reservoir architecture. Bioherms are isolated ‘pockets’ from a fluid

flow mechanics point of view. Therefore, the stored fluids have to be pushed out of the microbial mounds. In an incompressible system oil will not be produced during primary production from the bioherms due to the lack of fluid convection induced by volume increase.

The author emphasises that all simulations were run in incompressible and immiscible mode. These simplifying assumptions were necessary in order to perform a forecasting streamline analysis because no actual production data was available. In an incompressible mode all replaced fluid voidage has to be replaced by the same volume of injected fluid (e.g.: water front). Hence, streamlines cannot start at any reservoir grid block. They have to start at injector grid blocks, such as injector wells or in the presented case at boundaries injecting fluids. Thus, primary production cannot be studied. In a compressible simulation, streamlines can however start at any grid block due to fluid expansion and volume increase, which would allow characterisation of primary depletion. Furthermore, the effects of PVT (pressure-volume-temperature) on fluids were not modelled. Nevertheless, in reality there are no real incompressible systems and compressible flow takes place to some extent. This includes for instance fluid expansion, which occurs when reservoir pressure drops at production start and therefore oil expands. In addition fluid flow characteristics will be affected by a change of reservoir temperature by means of temperature dependent change of fluid properties such as viscosity, density and hydrocarbon composition (e.g. Szilas, 2010). Additionally, all simulations were carried out assuming the same set of relative permeabilities for water and oil in a water wet system, therefore simulating one water/oil mobility ratio scenario. All this has to be taken into account in more sophisticated dynamic modelling approaches but this requires PVT analyses of hydrocarbons in place and has to be done on a case by case basis by petroleum engineers and chemists. The developed geocellular model and performed streamline analyses aimed to analyses the crucial uncertainties from a geological point of view in terms of reservoir architecture and petrophysical properties. It was outside the scope of this study to incorporate PVT property aspects.

However, a recent study by Fitch *et al.* (2014) investigated the effect of fluid properties on fluid flow performance in a carbonate ramp setting. They tested different relative permeability curves for water and oil and varying fluid parameters. Additionally, the authors investigated the effect of various production scenarios,

such is different well spacing and injector positions. The authors concluded that the modelled geology in terms of simulated heterogeneities such as fluid baffles and porosity-permeability contrasts is more important regarding fluid flow behaviour than the impact of fluid properties. Thus, it is concluded that the presented results of the streamline analysis, even though performed with simplified fluid properties, are valid and interpretations identified the crucial fluid flow significant variables of the Omkyk microbial system. Therefore, the analogue model can be used to incorporate PVT and relative permeability considerations and subsequently be calibrated to case specific subsurface conditions.

## 7.5 Conclusion

In summary, two factors govern the fluid flow behaviour and determine recoverable oil reserves in the microbial system based on the presented streamline analyses: (1) ***permeability contrast*** between grainstones and microbialites and (2) the ***density differential*** of injected fluid and oil in place during secondary production. Future research should target to define the permeability threshold upon which bioherms are bypassed or drained. The complexity of the situation however lies in the co-dependence of these two factors. Permeability is not an intrinsic rock property and depends on the viscosity of the fluid, passing through the rock. This implies that simulations with different fluid characteristics will result in different permeability thresholds. Both factors have to be investigated on a case by case study.

In summary the key observations and interpretations of the streamline forecast analyses are as follows:

- In 4 out of 5 tested petrophysical models with different reservoir architecture bioherms are produced during secondary production. These results discarded an initial hypothesis of the author, stating that only minor fluid flow will take place in bioherms during production.
- The overall governing factor, influencing fluid flow is the distribution of petrophysical properties. This is also the reason why bioherms in one model where only partly drained because of a high permeability contrast between grainstones and bioherms. Future research should target to establish a robust permeability characterisation of microbialites in order to identify the permeability threshold under which production takes place.

- Flow results show that the permeability contrast between microbialites and grainstones outweighs the spatial arrangement and architecture of bioherm structures. Even the most complex structures are drained during secondary production.
- The main driving force for oil voidage replacement during secondary production is gravity induced down-welling of water. This establishes a convection cell fluid flow regime, which flushes bioherms and pushes oil out of microbial carbonates. Injected fluids have to be denser than the oil in place in order to enhance secondary recovery.
- Results suggest that oil in bioherms will stay in place during primary production. This is, however, based on incompressible simulation runs and without modelling fluid changes due to PVT property changes. More sophisticated modelling approaches might come to a different conclusion.
- The microbial analogue model shows ample similarities to the late Jurassic Smackover microbial reservoir play. These hydrocarbon reservoirs are currently produced and a recent integrated reservoir characterisation and evaluation study showed that fluid flow is channelled through aligned bioherm structures. This compares well with the here presented results.
- The presented flow results have to be regarded as preliminary fluid flow characteristics. Pressure-volume-temperature dependent changes of the fluids in terms of hydrocarbon composition, volume increase, change in viscosity and density and resulting effects on their flow behaviour has not been modelled. Recent studies, however, indicate that PVT changes have minor impact on the identification of first-order flow heterogeneities. Nevertheless, future research should include these properties in order to fine-tune the model with case specific boundary conditions.
- The presented volumetric calculations for the microbial reservoir facies are in line with the data of Adams *et al.* (2005). Bioherms constitute roughly 23% of the bulk reservoir volume. The majority of the oil in place in both scenario models is, however, stored in the grainstone horizons.

# 8 Synthesis and conclusion

## 8.1 Introduction

Many aspects of Neoproterozoic petroleum geology have been investigated at different levels of depths during the course of this research project. The presented project is the result of a multidisciplinary research effort including extensive and detailed sedimentological and structural field observation in north and south Namibia, total organic carbon elemental analyses of potential source rocks, thin section evaluation of microbial carbonates, remote sensing analyses, virtual outcrop geology, geocellular reservoir modelling and dynamic reservoir performance studies. Each chapter contains a detailed discussion of the results and conclusion section. Therefore, this chapter synthesises the main outcomes of each chapter in order to provide an integrated perspective of the presented research project.

Neoproterozoic petroleum geology is still in its infancy, in spite of an increasing research effort over the last decade. Despite the existence of proven and producing fields worldwide, the petroleum industry has been slow to explore Neoproterozoic basins due to the significantly higher risks involved in exploring these 'old' systems. Moreover, the lack of even a basic understanding of Neoproterozoic systems in terms of potential source rocks, reservoir rocks, global and regional geodynamic evolution restrains exploration efforts. However, the steady global increase for the demand of oil and gas will force petroleum companies to consider Neoproterozoic systems in their exploration plans eventually. Furthermore, the discovery of huge oil reservoirs, in the pre-salt formations offshore Brazil (Beglinger *et al.*, 2012; Wright, 2012) provided an additional impetus to study in particular Neoproterozoic carbonates. These pre-salt reservoirs are located within microbial carbonates and a better understanding of microbial reservoirs is needed to optimise exploration and reservoir development strategies. The Precambrian carbonate factory was dominated by microbial communities, which constitute the main reef builders during this period. Primary sedimentary structures are preserved in detail due to the paucity of burrowing organisms, which appeared in the latest stages of the Ediacaran (Jensen *et al.*, 2006). Neoproterozoic microbial carbonates can therefore be investigated in

great detail, over a range of scales, with potential value in outcrop analogue studies that transcend their use in understanding Neoproterozoic petroleum systems.

## 8.2 Neoproterozoic geology and source rock evaluation

The search for potential hydrocarbon source rocks requires a deep understanding of global and regional geodynamic evolution in concert with palaeo-climatic considerations. Source rocks are globally preferentially deposited during greenhouse periods with sea level highstands and flooding of shelf areas. Regional investigation of the geodynamic evolution and geological history of a given exploration area allows subsequently the identification of potential source rock horizons. This general workflow is well established for the Phanerozoic, where global tectonics and climatic conditions are well understood. However, this is not the case for a good part of Precambrian successions. The configuration of Neoproterozoic supercontinents is still vigorously debated within the Precambrian research community (De Wit *et al.*, 2008; Hoffman, 1991; Li *et al.*, 2009; Li *et al.*, 2008; Piper, 2009) (compare paragraph 1.4). Challenges to constrain the Neoproterozoic tectonic history arise from lack of suitable outcrops worldwide and difficulties to obtain accurate age and palaeo-magnetic data. Attempts to determine the global climatic conditions face similar problems. The composition of Neoproterozoic atmosphere and ocean chemistry are yet not identified and the absence of higher organised forms of life hampers efforts to accurately constrain Precambrian climate.

Nevertheless, the increased research effort in Neoproterozoic geology over the last two decades resulted in the heavily discussed Snowball Earth hypothesis, which tries to explain some of the unique and enigmatic geological characteristics of Neoproterozoic strata (compare paragraph 1.3.1). This hypothesis proposes at least two global glaciations during super-icehouse conditions, where the entire planet was frozen over. The aftermath of these glaciations is marked by super-greenhouse periods, flooding of extensive shelf areas and the recovery of life. Thus, these horizons constitute ideal source rock depositional systems on a global scale.

Some of the fundamental research regarding the Snowball Earth hypothesis has been carried out in Namibia (e.g.: Domack and Hoffman, 2011; Halverson, 2002; Hoffman and Halverson, 2008; Hoffman, 2011; Kaufman *et al.*, 1991; Le Heron *et al.*, 2013b). Furthermore, Sonangol and NAMCOR, the funding bodies of this

research project, recognised the prospect of potential economically viable Neoproterozoic hydrocarbon reservoirs onshore SW-Africa. Thus, the first part of this research project was devoted to the evaluation of potential hydrocarbon source rocks in north Namibia in order to better understand Neoproterozoic petroleum geology in general and the possibility of a petroleum play in the Owambo Basin in particular.

### 8.2.1 Source rock evaluation in north Namibia

The investigation of potential source rock horizons targeted exposed Neoproterozoic strata along the southern rim of the Owambo Basin in north Namibia. A total of four transects of the Otavi carbonate platform where logged and samples were taken for subsequent total organic carbon analyses. The Otavi platform has a thickness of more than 4 km and extends for >700 km. Field locations were chosen according to two considerations: (1) post Snowball Earth horizons, deposited during super-greenhouse periods (Rasthof Formation at the type locality and Maieberg Formation north of Tsumeb) and (2) locations which were indicated by geologists from NAMCOR (Halali Waterhole and Tsumeb copper mine).

A total of 40 samples were collected and total organic carbon (TOC) was analysed by means of a Leco elemental analysis. None of the samples can be classified as potential source rock due to the low TOC values. Nevertheless, the carbonates of the Halali Waterhole in the Etosha National Park show elevated TOC values. The low values might be the result of long lasting weathering and degradation of organic matter and initial TOC values might have been considerably higher upon deposition. However, further investigation is impeded due to the unclear stratigraphic position with the platform sequence.

A key observation is the absence of an economically viable source rock north of Tsumeb in the Maieberg Formation. The laterally equivalent section, 30 km south of Tsumeb, contains organically enriched sediments of up to 2.9 % TOC (Bechstädt *et al.*, 2009). This shows that the Maieberg post-glacial horizon does not constitute a basin-wide source rock horizon. Based on this finding, and in combination with the understanding of the regional geodynamic evolution, it is concluded that potential source rock horizons were deposited in restricted sub-basins and glacial palaeoreliefs across the Otavi carbonate platform. Thus, post-glacial flooding of a tectonically controlled palaeorelief, which is overprinted by glacial processes, controls source

rock deposition. The Ordovician – early Silurian 'hot shales' of North Africa might constitute a suitable analogue system (Bechstädt *et al.*, 2009; Lüning *et al.*, 1999; Lüning *et al.*, 2000). This system is characterised by source rock deposition during post-glacial transgression. Glacial and tectonic processes formed the palaeorelief of the North African shelf, leading to sub-basins with anoxic conditions due to restricted water circulation. Freshwater influx from glacial melt back enhanced water stratification in the sub-basins. Additionally, the relatively low input of clastic sediments during transgression allowed the deposition of organic enriched shale and mudstones. A schematic illustration of the 'hot shales' depositional system is given in Figure 136. Future research on the post-glacial Maieberg Formation should, therefore, try to better understand lateral facies variations within the sequence in order to predict the source rock distribution over the platform. This requires extensive regional mapping and further TOC analyses of potential organic enriched horizons.

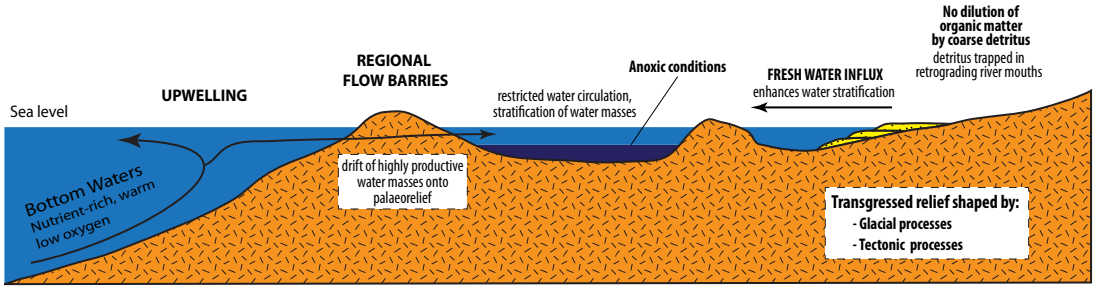


Figure 136: Depositional system of the Ordovician – early Silurian source rocks in North Africa. See text for explanation Modified after Lüning et al., (2000).

The samples from the Rasthof Formation showed the lowest TOC values of all 40 analysed samples. A potential explanation for this is proposed in common with similar strata from the Maieberg road cut, north of Tsumeb. Sediments at that locality were potentially deposited in a palaeogeographically elevated position and therefore no organic matter was preserved due to active water circulation. This is, however, speculative and has to be confirmed by additional regional mapping of lateral equivalent sections and subsequent TOC analyses.

In summary, no potential source rocks could be identified during the course of this research project. However, an important finding is the absence of organic-enriched sediments in the post-glacial sequence of the Maieberg Formation. This has implications for future research on source rocks in the Owambo Basin. Although

post-glacial sequences have the potential to serve as source rocks, they might not represent basin wide horizons. This emphasises the need of a better regional understanding of platform evolution and geometry of the Otavi carbonate platform in order to predict source rock depositional systems. Thus, future research should establish a robust geological history of the platform in terms of sequence stratigraphy, sedimentology and structural history.

## 8.3 Microbial analogue reservoir characterisation

The main part of this research project focused on hydrocarbon reservoir characterisation of a microbial carbonate system in the Nama Group of the Nama Basin in southwest Namibia. These Ediacaran ramp carbonates of the Kuibis carbonate platform were chosen for analogue studies to better understand potential hydrocarbon reservoirs in the subsurface of the Owambo Basin in north Namibia and elsewhere. The scale and quality of the carbonate outcrops form a world-class natural laboratory for carrying out research from micro to production scale. The Kuibis ramp system is exposed at an exploration scale over > 100 km and the high quality of the outcrops is due to a combination of the arid climate, regional uplift with relatively minor regional deformation and numerous canyons that cut-through and expose the system in 3D. Analogue reservoir characterisation was carried out in the Zebra River Canyon system covering an area of roughly 2.5 $km^2$. The ramp carbonates exhibit a layer cake architecture and approximately 120 m of the Omkyk Member is exposed in the Zebra River Canyon system. The Omkyk Sequence 2 (OS2) was chosen for reservoir analogue studies, because microbial carbonates are best exposed in this sequence. Analogue reservoir layers are generally 10 m in thickness, comprising grainstone, microbial and heterolithic horizons. The studied section represents typical inter-well spacing in hydrocarbon field production and the defined reservoir layers are generally below seismic resolution.

Burchette (2012) highlighted the challenges in subsurface reservoir characterisation and well correlation by calculating the available volume of hard data (cored wells) compared to the bulk reservoir volume of a typical Middle Eastern reservoir development scenario (Figure 137). A standard five-spot well development pattern in a 200 m thick reservoir interval, with a well spacing of 2 km encompasses 800 million $m^3$ bulk volume. 2 $m^3$ of reservoir rock can be potentially recovered per

well, assuming a core diameter of 10 cm and 100 % core recovery. Therefore, 10 $m^3$ sample material is available to interpret and model 800 million $m^3$ of reservoir volume. This represents 0.00000125% of the bulk reservoir volume. Wireline logs will sample a slightly bigger volume but at a lower resolution. This emphasises the lack of available data to analyse and predict sub-seismic reservoir characteristics at an inter-well scale. Thus, the objective of the analogue reservoir characterisation was to better understand the microbial carbonate system on a scale, which straddles the full range of typical seismic, well log and core description datasets. The ultimate goal was to provide insights for potential reservoir architecture, geometry and facies distributions that might help in influencing reservoir exploration and development strategies for microbial carbonate reservoirs.

The presented microbial reservoir characterisation is the result of a multidisciplinary research effort, from outcrop observations to dynamic reservoir performance studies. This included detailed sedimentological and structural field observations, which were subsequently used, in combination with terrestrial laser scanning and virtual outcrop geology, to develop a geocellular model. The static analogue model served then as basis for facies modelling in order to predict the spatial arrangement of microbial structures and overall reservoir architecture. The final step was fluid flow performance analyses by means of streamline forecasting to investigate the dynamic behaviour of the microbial analogue system. A schematic workflow, illustrating the main steps of the integrated reservoir characterisation is given in Figure 138.

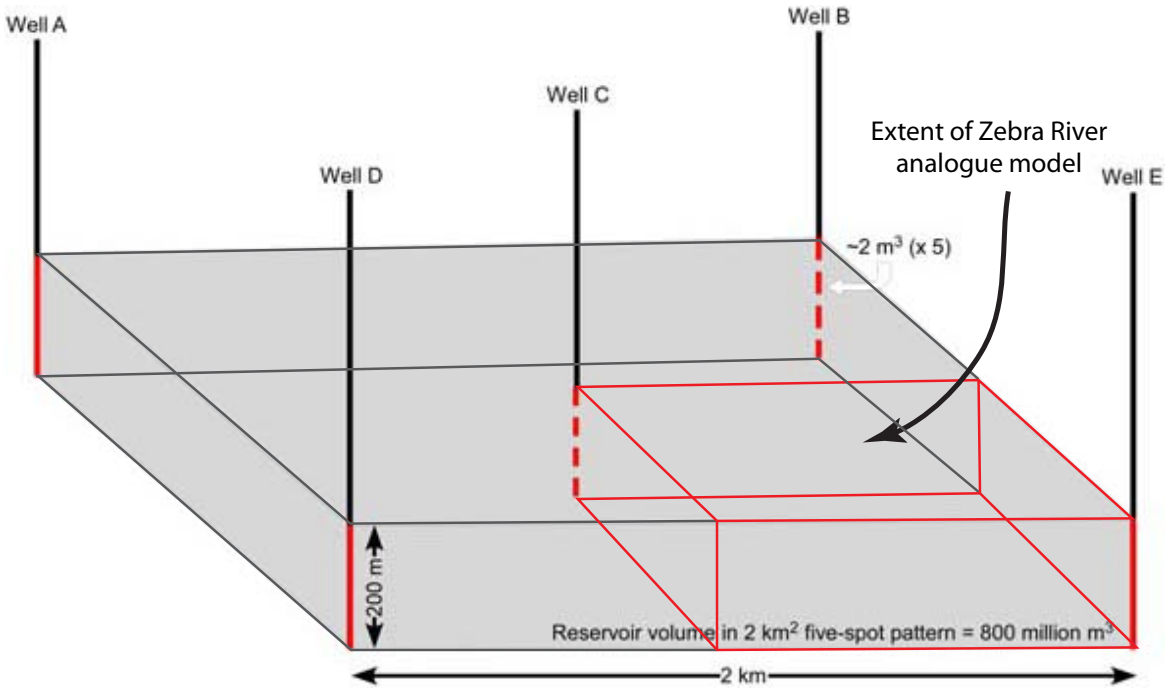


Figure 137: Typical dimensions of a five-spot development pattern in Middle Eastern reservoirs. Note the red cube, which indicates approximately the size of the Zebra River analogue model. Therefore, the analogue model represents typical dimensions of inter-well spacing in development scenarios. Modified after Burchette (2012).

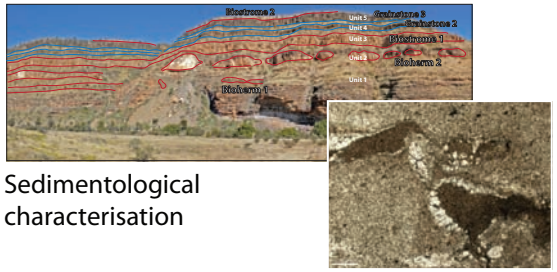

Sedimentological characterisation

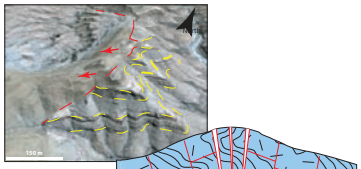

Structural characterisation

1. Field work characterisation, remote sensing & thin section analyses

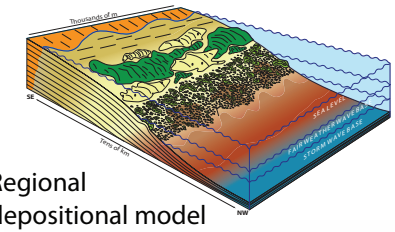

Regional depositional model

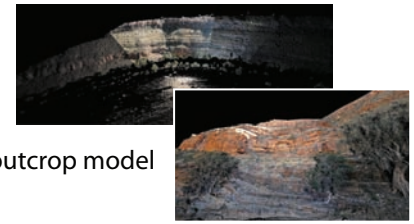

Virtual outcrop model

2. Depositional model and virtual outcrop geology

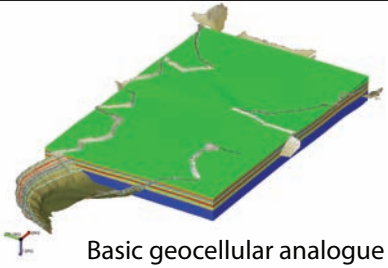

Basic geocellular analogue model

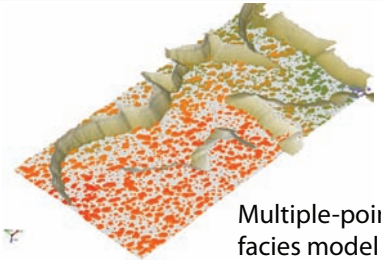

Multiple-point statistics facies model

3. Geocellular analogue modelling

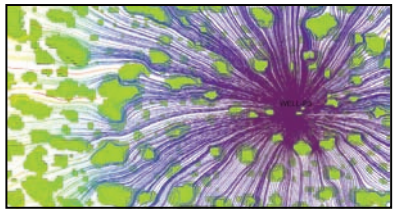

Streamline fluid flow forecasting analysis

4. Dynamic reservoir performance analysis



Figure 138: General workflow illustrating the main steps of the multidisciplinary microbial analogue reservoir characterisation: from outcrop observations to dynamic reservoir performance analysis.

### 8.3.1 Field interpretations

Detailed sedimentological characterisations of the microbial carbonates have been presented in **chapter 3**. The microbial carbonates of the Omkyk Sequence 2 of the Kuibis Subgroup comprise a variety of bioherm, biostrome and inter-mound facies. Bioherms are defined by stromatolitic thrombolite mounds, comprising a variety of growth-forms ranging from massive to small-scaled columns, domes and goblet shaped mounds. Inter-bioherm facies is characterised by cross-bedded grainstone-packstones, intercalated with heterolithic facies and intraclast breccias. A key outcome of the sedimentological characterisation is the detailed description of the bioherm evolution. A generic, simple three-stage model describing bioherm evolution has been developed. This comprises microbial aggradation, lateral spreading and final merging (see figure 50). The underlying factor for this sequence of changing growth pattern is a change of background sedimentation from mud-dominated during aggradational and grain-dominated during progradational phases. In order to classify these newly interpreted microbial structures a new nomenclature for bioherms in the Omkyk Sequence 2 has been established. Incipient bioherms are a loose association of massive thrombolite domes, goblets and columns which develop in a lower mid-ramp setting. These incipient mounds subsequently amalgamate forming merged bioherm structures at the onset of the bioherm evolution and reducing accommodation space. During platform progradation this merged bioherms have the potential to form composite bioherm structures during further decreasing accommodation space in a lower inner-ramp setting. Based on these observations a regional depositional model for the microbialites of OS2 has been developed (see figure 51).

The recognition of these characteristics has important implications for the microbial reservoir architecture and geometry because bioherms are unlikely to exhibit simple hemispherical geometries and have the potential to merge together. Thus, understanding the vertical and lateral evolution of the bioherms is essential because this influences the reservoir heterogeneity and connectivity. Incorporating these observations in the geocellular modelling process allowed the development of a precise microbial facies model in terms of lateral connectivity of the bioherms. The importance of these observations has been confirmed by the performed streamline

analyses. All merged and composite bioherm structures were produced during production due to fluid flow channelling through the merging zones.

An additional bioherm structure, stacked-bioherms has been introduced. The recognition of these structures has shown that bioherm growth and evolution is not restricted to one unit in the Omkyk Sequence. Stacked-bioherms are characterised by mounds, which develop on underlying bioherm structures of the lower units. The underlying bioherms were able to keep up with the increasing sediment input during the unit highstand systems tract and these topographic highs served consequently as preferential growth location for microbialites in the next parasequence. This demonstrates that microbial mounds are not randomly distributed over the platform. However, the reason for the growth location of unit 1 bioherms could not be established due to limited outcrop exposure. A second order trend of bioherm geometry has been identified in the field, which subsequently could be modelled with multiple-point statistics. Bioherms are preferentially aligned towards NW-SE, which is perpendicular to the palaeo-strike direction of the Kuibis carbonate ramp. Thus, the longer axes of bioherms are aligned towards the incoming waves in order to minimise the exposed surface towards the waves. Future research should try to analyse the underlying factors controlling bioherm nucleation and overall growth geometry. This could be achieved through palaeo-ecological studies of bioherm evolution, incorporating background sedimentation patterns, water depths and response of microbial communities to wave energy and currents. Additional focus should be devoted to large-scale patterns of bioherm distribution. Al Haddad & Mancini (2013) argued that the large scale distribution and alignment of microbial mounds in the upper Jurassic Little Cedar Creek field in southern USA might be connected to inherited depositional topography of the underlying fluvial clastics. The authors argued that large-scale topographic highs are located above fluvial sand bodies, therefore providing preferred growth locations for microbial communities. Consequently, leading to aligned porosity and permeability corridors within the Cedar Creek microbial reservoir horizon (see Figure 139.A) similar scenario could be present in the Kuibis Subgroup, where the palaeotopography of the transgressive fluvial clastic of the Kanies Member defines preferred large scale growth areas. This, however, has to be confirmed by detailed sedimentological investigations of the Kanies Member and the transition to the Kuibis carbonate ramp. Another possibility for the development of large-scale topographic highs could be the formation of

structural features (e.g.: anticlines or reverse thrust faults) due to the ongoing closure of the Khomas Sea and subduction of the Kalahari Craton under the Congo Craton. Gupta and Allen (2000) investigated the influence of inherited basement topography on ramp carbonate facies patterns of the Eocene distal Alpine foreland basin of southeast France. The authors showed that although plate flexure exerts first-order control on facies patterns, pre-existing foreland structural elements significantly impact smaller scale depositional pattern (see Figure 139.B). Future research on the Kuibis carbonate ramp should investigate the possibility of such inherited palaeotopographies. This has to be investigated through regional structural mapping of the basal unconformity. The identification of such constraining factors would significantly improve reservoir modelling due to the identification of porosity and permeability corridors.

Besides these large-scale characteristics and trends, an important factor on the micro-scale has been identified. The carbonates and analogue reservoir units of the Omkyk Sequence 2 are defined by two types of porosity: grainstones exhibit interparticle porosity whereas microbialites are predominantly defined by growth framework porosity. The porosity distribution of the grainstone is controlled by the depositional environment (e.g.: grain sorting), whereas the porosity in bioherms is predominantly the result of the microbial communities and their response to the depositional setting. The importance of this observation has major impact on the dynamic behaviour of the microbial system because bioherms are likely to comprise vertical porosity and therefore permeability heterogeneities. The implication of this regarding impact on fluid flow is presented in detail in the fluid flow paragraph 8.3.2.

The structural characterisation of the microbial carbonates, presented in **chapter 5**, revealed an important syn-depositional phase of structure development. A primary fracture system developed during the early stages of microbial lithification, as a result of differential compaction and formation of antecedent topographic highs. The syn-depositional fractures are confined to the microbialites and are affecting immediately adjacent and supradjacent sediment packages. A key observation is that these syn-depositional fractures form due to *intrinsic* body forces by means of internal weakness due to the geometries of the microbial system. Therefore, no external driver, such as regional tectonic events, is needed. This implies that the syn-depositional fracture network develops independently of regional tectonic events and

can be overlooked or underestimated in areas with minor or no expected fracturing. Additionally, the recognition of large dissolution vugs at intersections of primary fractures and extensive cementation demonstrate that this fracture network acted as an early fluid flow system. These observations have implications for reservoir characterisation in microbial carbonates because primary, open mode fractures have the potential to significantly enhance reservoir performance through providing preferred fluid flow pathways. Furthermore, the syn-depositional fractures are most likely to be reactivated during later deformation. Therefore, a careful characterisation of this early syn-depositional fracture system is needed in order to accurately predict fluid flow in microbial carbonate reservoirs.

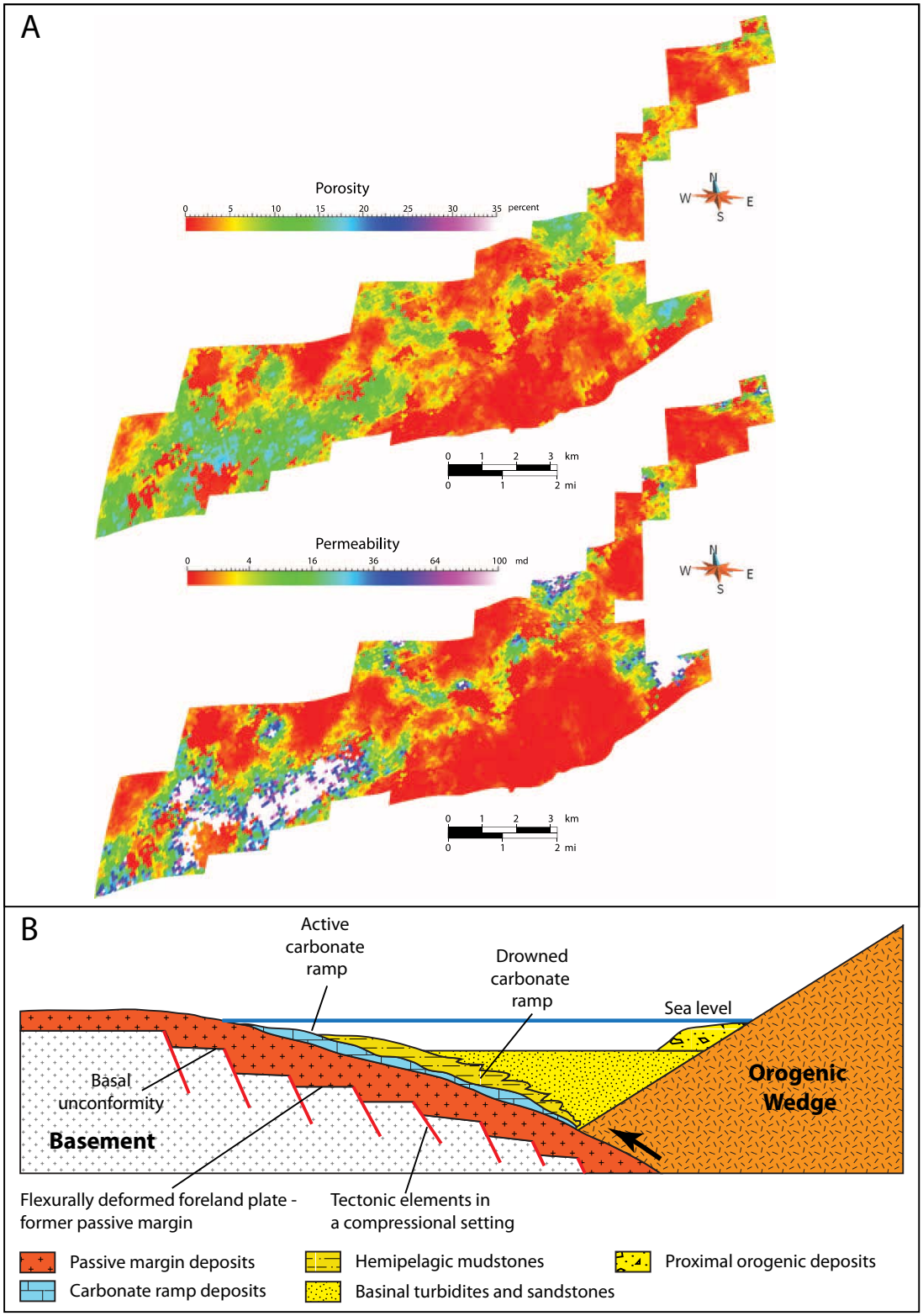


Figure 139: (A) Porosity and permeability models of the microbial reservoir layer of the Little Cedar Creek field in the southern USA. Note the porosity/permeability corridors aligned towards the NE-SW. See text for explanation. Modified after Al Haddad & Mancini (2013). (B) Schematic illustration showing the evolution of a carbonate ramp on a flexurally deformed foreland plate. Note the pre-existing foreland structural elements, influencing facies patterns of the ramp carbonates. Modified after Gupta and Allen (2000).

The combined sedimentological and structural characterisation of the microbial carbonate system show that two factors govern reservoir quality, which are the depositional system and the syn-depositional fracture development in the microbial carbonates. The crucial element of reservoir architecture is the spatial distribution of the pore systems (e.g.: Ahr and Hammel, 1999; Flügel, 2004; Lucia, 2007a), which essentially defines reservoir heterogeneities. Porosity not only defines the maximum storage capacity of a given reservoir facies, but has also important implications for fluid flow performance by means of pore geometry and pore-throat size distribution. Furthermore, pore-throat size has crucial influence on permeability, since it impacts the rate at which fluids can pass through the rock. In the case of the Zebra River ramp carbonates the porosity distribution is inherently connected to the evolution and spatial distribution of microbial bioherms. Therefore, mechanisms connected to depositional processes control the microbial reservoir heterogeneity. However, the syn-depositional fracture system has the potential to create additional porosity (e.g.: fracture porosity, vugs) and permeability corridors. According to the carbonate reservoir classification of Ahr (2008) this system corresponds to a hybrid 3 type reservoir (see Figure 140). This reservoir type is one where porosity is created by depositional mechanisms and affected by a fracture system, which is in turn influenced by the depositional character. Another type of reservoir classification applicable to fractured reservoirs, has been proposed by Nelson (2001). In this classification scheme the microbial system would tentatively correspond to a type III fractured reservoir. This type corresponds to a fractured body of rock wherein the fractures do not necessarily contribute to the overall porosity, although they provide permeability pathways. The syn-depositional fracture system is restricted to the microbialites and thus it is concluded that the additional generated porosity does not significantly contribute to the bulk porosity of the entire reservoir model. The reservoir subdivision after Ahr (2008) is a more holistic classification, incorporating depositional characteristics and fracture networks, therefore it is used in this research project. Consequently, based on the combined sedimentological and structural investigation the microbial carbonate analogue system of the Zebra River Canyon system is best described as hybrid 3 type carbonate reservoir.

In the course of the present author's research, the diagenetic development of the Omkyk Sequence 2 has not been studied. The selective dolomitisation of the Omkyk carbonates, constrained to the microbialites clearly show that diagenetic alteration

took place to some extent. This merits future research. An interesting approach would be to analyse the calcite cements within the syn-depositional fractures with clumped-isotope thermometry (Eiler, 2007; Huntington *et al.*, 2009). This relatively new technique allows the determination of the temperature of calcite formation independent from the water chemistry. It has been recently successfully applied to analyse in detail syn-depositional fracture cements of Permian carbonates exposed in the Guadalupe Mountains to identify fracture evolution, the impact on early fluid flow and diagenetic history (Budd *et al.*, 2013). A similar approach could be perused for the Zebra River carbonates to analyse the diagenetic history with special focus on the impact of the fluid flow network provided by the syn-depositional fracturing. Therefore, future research might refine or overturn the reservoir classification presented herein, if diagenetic features outweigh the depositional or fracture mechanism.

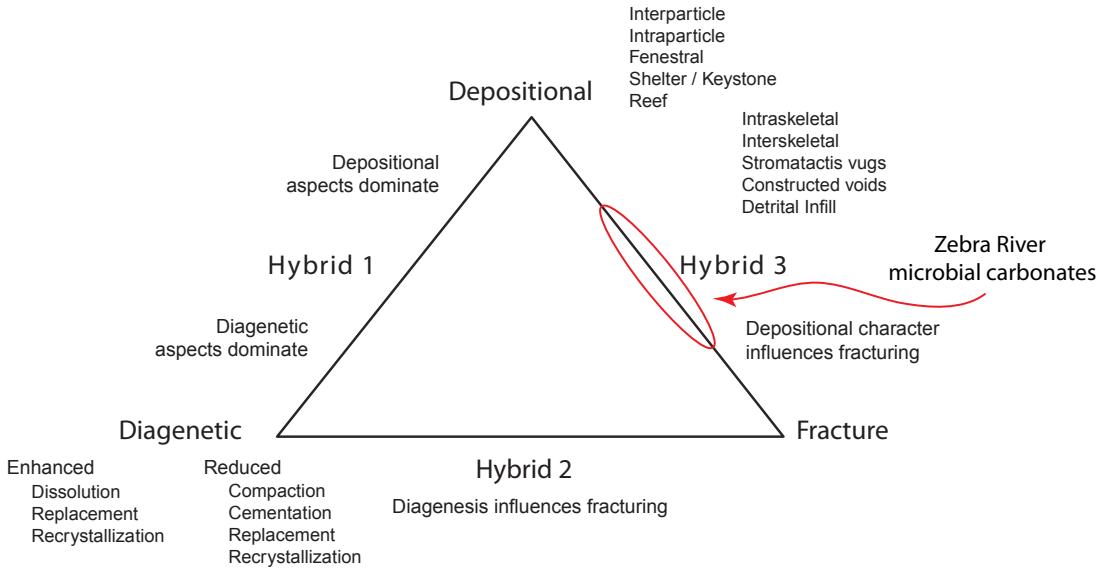


Figure 140: Carbonate reservoir classification based on porosity type. Modified after Ahr (2008)

### 8.3.2 From lidar to fluid flow modelling

In order to develop a geocellular analogue model of the ramp carbonates, terrestrial laser scanning (lidar) was used to acquire 3D digital outcrop data. The specification of the lidar system and workflows for acquiring and post-processing of lidar point-cloud data has been discussed in detail in **chapter 4**. The virtual outcrop model of the Zebra River Canyon system subsequently served as basis for the construction of the static reservoir model. As with all methods, lidar has advantages but also

disadvantages. Lidar proved to be the optimal digital acquisition method to capture the overall geometry and architecture of Omkyk Sequence 2, and within 4 working days the entire canyon system was scanned and digitised. The rugged terrain of the canyon system posed difficulties in handling and carrying the rather heavy equipment and limited the scanning area. However, this has to be expected in remote field areas without direct access to roads and might be the same with other digital mapping techniques. The development of the basic virtual outcrop model proved to be straightforward. This DOM was used for mapping of lithological and stratigraphic contacts, faults and bioherm outlines. Thus, the basic framework and architecture of the reservoir model was easily extracted in a short amount of time.

However, difficulties arose during detailed interpretations of the virtual outcrop model in terms of detailed mapping of the bioherm internal architecture and fracture mapping. The main reason for the problems was the difficulty during the triangulation of the point cloud. The outcrops in the Zebra River Canyon are partly covered with shrub-sized vegetation (small bushes, grass), which could not be deleted manually. Furthermore, the outcrop quality was not optimal for laser scanning due to partly intense weathering. Therefore, it was impossible to create meshed surfaces for the majority of the bioherm structures, which hampered the digital interpretations of the internal architecture of microbial carbonates due to lack of resolution of the virtual outcrop model. This meant that detailed interpretations had to be carried out on photomosaic panoramas. Future research, targeting the bioherm internal geometries should consider photogrammetry as an alternative method (e.g.: Haneberg, 2008). This would provide high-resolution images and virtual models of bioherms in order to accurately map and measure the internal geometry of bioherm complexes. Problems during fracture mapping occurred because of 2 reasons: (1) lack of suitable methodologies to extract quantitative fracture data of sufficient quality and (2) outcrop conditions. The former limitation of the virtual outcrop model has been discussed in detail in **chapter 4** (compare paragraph 4.6.2). Resent research is focussing on the development of automated workflows to obtain fracture data from lidar point cloud data, but these are at an infant stage and were not used during this research project. Significant effort has been devoted to the development of a Discrete Fracture Network (DFN) model of the inter-bioherm facies, which is not presented in this thesis. The main input parameters for DFN-models are fracture size, orientation, spacing and aperture. Fracture

orientation and spacing within the bioherms could be measured within the virtual outcrop model and has been presented in **chapter 5**. The modelling of the fracture sizes was, however, not successful. This was due to a combination of outcrop quality and inadequate resolution of the virtual outcrop model. The measured fracture sizes exhibited high error margins and therefore the developed DFN-models showed highly variable properties in terms of fracture connectivity and permeability. Additionally, the syn-depositional fracture system does not show any evidence of preferred fracture orientation or size distribution. Thus, it was not possible to develop a realistic, stochastic DFN-model. A possibility to incorporate the syn-depositional fracture system into the fluid flow modelling would have been to randomly distribute fractures within the bioherm fractures, in terms of orientation and fracture sizes. However, this would have introduced a level of complexity which might be geologically reliable, but would have potentially biased first order flow characteristics (e.g.: high fluid flow pathways within the bioherms). A better understanding of this fracture system is needed and whether predictable syn-depositional fracture patterns (e.g.: parallel to the strike direction of the Kuibis carbonate ramp) do occur remains to be tested in subsequent studies. Thus, it was concluded that the DFN-models are not accurate enough to merit incorporation into the reservoir characterisation and fluid flow modelling.

Nevertheless, the combined structural analyses comprising detailed field observations, photomosaic interpretations and fracture orientation analyses within the digital outcrop model led to the identification of the syn-depositional fracture network of the microbial carbonates. The importance of this fracture network for microbial reservoir characterisation has been discussed in detail in **chapter 5** and was published by Winterleitner *et al.,* (in press).

An additional limitation of the virtual outcrop model was the modelling of bioherm structures because only 2D geometries in cross-section view could be mapped. This is not a limitation *per se* of lidar but a general limitation of non-invasive digital mapping techniques. A possibility to accurately map bioherm structure would be three-dimensional ground-penetrating radar (3D GPR) (e.g.: Corbeanu *et al.*, 2001; Grasmueck *et al.*, 2004). This technique could be used to map a modern day erosional surfaces of the bioherm horizon in order to analyse the dimensions and spatial distributions of bioherms for input into reservoir modelling.

Lidar-based, analogue reservoir modelling is increasingly used in petroleum research and industry (e.g.: Agada *et al.*, 2014; Amour *et al.*, 2013; Fabuel-Perez *et al.*, 2009; Hodgetts, 2013; Jones *et al.*, 2011; Rarity *et al.*, 2013; Shekhar *et al.*, 2014; Verwer *et al.*, 2009; Wilson *et al.*, 2011b). A general workflow illustrating the individual interpretation and processing steps has been given in figure 83 and all required workflows have been discussed in detail in **chapter 6**. Although the workflow seems to be intuitive and simple, challenges arose resulting from different file formats and software packages. Thus, significant data and file manipulation had to be carried out in order to use lidar point-cloud data, virtual outcrop interpretations and triangulated surfaces within different software platforms. This was time-consuming and emphasised the need for the development of a geological software package, especially designed for lidar data interpretation and preparation for reservoir modelling software packages.

Once the workflow was established, development of the basic geocellular model was a comparatively simple process. The analogue model comprises 9 basic reservoir grid layers following the subdivision of reservoir and non-reservoir facies established during field work. The challenge of the reservoir modelling was the development of an accurate microbial facies model of the laterally discontinuous microbial mounds. For that purpose two different modelling approaches were used: (1) object based modelling and (2) multiple-point statistics facies modelling. Both approaches resulted in geologically viable facies model of the microbial bioherms in Unit 2, as the comparison with the virtual outcrop model and geocellular facies cross-section has shown (see figure 107). The object based modelling approach required the development of a matlab source code in order to simulate the bioherm structures and their spatial distribution. However, significant post-processing steps were necessary to develop the final geocellular facies model (e.g.: height and dip-correction). The MPS method was in this respect simpler to handle since all modelling could be performed directly within the geocellular model. Furthermore, the matlab code is to some extent inflexible because only hemispheres with varying dimensions could be simulated. Different principle bioherm geometries (e.g.: ellipses as plan view shape) would need extensive code rewriting.

A more intuitive way for geologists to model the bioherm horizon is the MPS approach, based on a training image as main input source. The training image, as a conceptual model of the facies association, combined all available data from lidar

data, field work interpretations and remote sensing. The development of the training image followed the methodology proposed by Strebelle and Levy (2008) by means of creating the conceptual model through unconditioned object based modelling and additionally combining a 2D satellite base map showing bioherm outlines. The end result is a highly complex bioherm facies model. Moreover, the spatial trend of aligned bioherm complexes could be simulated with MPS, which was impossible with the matlab code. The main problem with MPS, however, lies in assessing whether a given 3D training image is "stationary" or not. Stationarity is a decision in geostatistics, which implies that the statistics of an unknown variable is independent of the spatial location of the sampled and un-sampled values (Carle and Fogg, 1996). At the time of writing (September 2014), there are no reliable techniques available to test this. Thus, stationarity of the training image was checked by using an informal 'rule of thumb' approach, which states that a training image can be considered stationary if every portion of the image 'looks alike' every other portion of the image. This was the case for the Zebra River training image and thus it was concluded that the conceptual model fulfils the requirement of stationarity (compare paragraph 6.8.3.). Nevertheless, future research has to focus on establishing a robust methodology of the training image control processes to accurately assess training image quality.

The end result is a MPS facies model, which is geological reliable as the outcrop comparison has shown. The multiple-pint statistics proved to be a powerful method to model the microbial system. It combined all available data and additionally incorporated the personal knowledge and understanding of the microbial system in one conceptual geological model. The combination of lidar and MPS has ample potential in future outcrop based analogue reservoir studies. Future research in the Nama Basin should try to develop a catalogue of 3D training images of several microbial facies association to simulate various scenarios. Additionally, recent research has shown that MPS fracture modelling might be an appropriate alternative to the tedious process of developing a DFN model, emphasising the potential of multiple-point statistics (Jung *et al.,* 2013).

Volumetric calculations (compare paragraph 7.3.4) have demonstrated that, the developed facies models during this research project and the published model of Adams *et al.* (2005) have approximately the same microbial reservoir volume of

23%. Thus, both approaches resulted in the same approximation of microbial reservoir facies. A key difference between the final facies models is that Adams *et al.* (2005) explicitly excluded the formation of merged bioherm structures. The authors assumed, based on their field observations, that bioherm geometries can be approximated by simple circular plan view shapes. However, the newly interpreted composite and merged bioherms in this thesis suggest that this is an over-simplification and thus particular focus during the course of this research project has been devoted to simulating merged bioherms. The impact of this enhanced lateral connectivity was one of the main focuses of the streamline forecasting analyses.

The final step of analogue reservoir characterisation during this research project has been a dynamic performance study of the microbial carbonate system by means of a streamline forecasting analysis developed in **chapter 7**. Streamline simulation was chosen because it can be performed on high-resolution grids, thus avoiding the problem of up-scaling of the reservoir grid. Furthermore, streamline forecasting analyses can be carried out under simplified reservoir boundary conditions, such as incompressible mode and approximated PVT parameters. This was necessary due to lack of actual production data. The fluid flow results of the tested scenario models showed that the majority of the bioherm facies would be produced during production. Two factors govern the overall dynamic behaviour of the microbial system and consequently determine recoverable oil rates: (1) permeability contrast between grainstones and (2) density differential of injected fluids during secondary production. The first of these is of major importance. Permeability is not an *intrinsic* rock property but depends on the viscosity of fluids passing through the rock and on the pressure gradients. However, the type of porosity has a significant impact on permeability values by means of pore- and pore-throat geometry. Thus, it is crucial to understand and essentially predict the porosity distribution of the microbial system. This has been clearly shown with the results of scenario 2.2 model. The entire system acts as a simple layer cake model due to the presence of vertical porosity heterogeneities in the microbial mounds (see Figure 131). Therefore, the type of and distribution of porosity within the microbialites has a profound impact on overall fluid flow behaviour. The thin section analysis showed that thrombolites are predominantly characterised by growth-framework porosity. Consequently, the growth forms and patterns of the microbial communities define the fluid flow crucial heterogeneities. This is a key observation because it implies that microbial reservoir

quality and performance can potentially be predicted in a sequence stratigraphic context by means of analysing the sediment associations in the inter-bioherm areas. Field observations revealed that bioherm evolution follows a simple model of progradational and aggradational phase according to the background sedimentation. Aggradation phases are accompanied with reduced porosity values due to the infill of mud-sized sediments in the pores. Therefore, gamma-ray logs can potentially serve as a proxy to estimate the quality of microbial reservoir facies. However, a deeper understanding of the response of microbialites to changing environmental conditions, such as background sedimentation, water-depths or light conditions is needed to accurately predict porosity characteristics in the microbialites.

The syn-depositional fracturing of microbialites has not been incorporated in the fluid flow simulation due to computational constraints. However, the microbial system is prone to early fracturing without the necessity of regional tectonic events. Therefore, this potential fluid flow network has to be incorporated in future flow simulations. The difficulty of this lies, however, in the prediction and modelling of this fracture system. How can we estimate the intensity or orientation of the open-mode fractures? The fracture system is essentially linked to the geometry of the bioherms and does not follow regional or yet predictable patterns. Thus, future research on this topic has to focus on possibilities to accurately quantify this fracture system, which has the potential to significantly impact reservoir performance.

The streamline forecasting analysis is based on simplified reservoir boundary conditions and essentially circumvents main aspects of reservoir engineering. However, the fluid flow simulation significantly contributed to a better understanding of the analogue microbial system and focused the attention to the critical variables. Additionally, recent research on fluid flow in ramp carbonates has shown that even with simplified and approximated dynamic models under different production scenarios, the main uncertainties affecting reservoir performance can be accurately identified (Fitch *et al.*, 2014). In reservoir performance prediction, a bottom-up modelling approach is typically used, which seeks to develop highly complex dynamic models incorporating all available data. The development of such models is difficult and time-consuming. Additionally, it is complicated to define the crucial parameters influencing reservoir performance. Thus, Williams *et al.* (2004) advocate a top-down reservoir modelling approach. This is a relatively new philosophy in dynamic reservoir modelling, developed by BP's research and

development division. The authors suggest starting dynamic reservoir studies with the simplest possible models and suitable simulator. Complexities are added step-by-step and as appropriate. Therefore, monitoring and recognising the impact factor of each added property level. This allows detailed ranking of each property or property set to accurately assess their importance on fluid flow behaviour. Using this approach resulted in up to 20% increase of estimated net present value of some of BP's major oilfields, through better predicting hydrocarbon reservoir performance Williams *et al.* (2004).

The same modelling philosophy can be applied to the developed streamline simulation model. It constitutes a base model and additional levels of complexities can and have to be added on a case-by-case basis to predict microbial reservoir performance. Nevertheless, the first main factor, the porosity distribution within the microbialites has been identified. Thus, future research should target to gain a better understanding of the palaeo-ecological factors influencing the growth patterns and thus the porosity characteristics of microbial communities.

### 8.3.3 Summary

In summary, based on the presented integrated reservoir characterisation, the analogue system of the Zebra River Canyon is classified as **hybrid 3** type carbonate reservoirs after the classification of Ahr (2008). The overall architecture and heterogeneities of this system are defined by depositional processes and influenced by syn-depositional fracture development. The latter has important implications for this type of microbial carbonates because this early fracture and fluid flow network is intrinsic to the microbial system and does not need an external driver to develop. Thus, fractures have to be expected and considered in microbial subsurface reservoir characterisation. The dynamic performance modelling showed that the majority of bioherm structures would be produced during secondary production. Although, the dynamic model constitutes the simplest model it focused the attention on the critical variables of the system: the **permeability contrast** of microbial carbonates and connecting grainstone horizon. This contrast is inherently connected to the evolution of the microbial carbonates. Therefore, future research should focus on a better understanding of the dynamics of microbial carbonates from micro to macro scale from a palaeo-ecological point of view in order to accurately predict porosity distribution and thus, reservoir quality and performance.

## 8.4 Conclusions

The main research outcomes of the investigation of Neoproterozoic strata in Namibia from a petroleum point of view are as follows:

- A total of four sections along the southern edge of the Owambo Basin were investigated to determine their source rock potential. None of the collected samples can be classified as potential source rock.
- The absence of organic enriched sediments in the Maieberg Formation, north of Tsumeb demonstrates that the Maieberg post-glacial sequences do not constitute a basin wide source rock horizon. The post-glacial source rock depositional system is defined by tectonically controlled sub-basins with anoxic conditions of the Otavi carbonate platform in concert with glacial induced palaeorelief.
- The outcome of the source rock evaluation shows that a profound understanding of the regional geology, in terms of structural history, sedimentology and sequence stratigraphy is needed to accurately evaluate Cryogenian post-glacial horizons. This emphasis the need of a better understanding of Neoproterozoic geology, on a global and in particular on a regional scale.
- A multidisciplinary analogue reservoir characterisation of an Ediacaran-aged microbial carbonate system has been presented. This system is the Omkyk Member of the Kuibis carbonate ramp in the Nama Basin, SW Namibia. Detailed sedimentological and structural characterisation of the microbialites was supplemented by acquisition of digital outcrop data by means of a lidar survey. Virtual outcrop interpretations served as input for geocellular modelling for the development of a static reservoir model. The final step of analogue reservoir characterisation constitutes dynamic performance analyses by means of streamline forecasting analyses.
- Microbial bioherm evolution has been analysed in detail and a generic model describing bioherm evolution has been proposed. Consequently, a new bioherm nomenclature to describe bioherm geometries has been introduced. Subsequently, a regional model of the depositional system of the microbial carbonates has been developed. Furthermore, petrophysical

properties of the microbial carbonates have been investigated by means of thin-section analyses.

- An important phase of fracture development in the microbialites has been recognised, summarised in chapter 5 and in Winterleitner et al (in press), which is attached in APPENDIX VII. Syn-depositional fractures are *intrinsic* to the microbial carbonates due to body forces of an early lithified, fragile microbial framework. Therefore no external driver is needed for the development of this fracture network. This has an important implication for microbial reservoir characterisation because fractures have to be considered in potential microbial reservoirs, independent form the regional setting. The syn-depositional network has the potential to significantly impact reservoir performance due to providing a preferred fluid flow pathway.
- Lidar was used to acquire 3D digital outcrop data from the Zebra River Canyon for subsequent reservoir modelling. Detailed interpretations of bioherm internal geometries were, however, hampered because outcrops in the Zebra River area are partly covered with shrub-size vegetation resulting in difficulties during triangulation of the point-cloud. Photogrammetry might be a better option to perform high detailed interpretations of the microbial structures.
- The lidar virtual outcrop model served as basic framework for the development of a static geocellular model. Two modelling approaches were used to simulate the laterally discontinuous bioherm structures: (1) object based numerical modelling and (2) multiple-point facies modelling. Comparison of facies cross-section with the virtual outcrop model validated the models. Furthermore, volumetric calculations of the microbial facies are in line with published data from the same section.
- Dynamic reservoir performance was tested by means of a streamline forecasting analyses, following a top-down modelling philosophy. Fluid flow results focused the attention on the critical variable affecting fluid flow in the analogue system: the permeability contrast between microbialites and connecting grainstone. Future research should target to

better understand porosity and consequently permeability heterogeneities to better understand and predict microbial reservoir performance.

- Based on the integrated reservoir characterisation the analogue microbial system is classified as hybrid 3 type reservoir after the carbonate reservoir classification of Ahr (2008). Reservoir heterogeneity and geometry is constrained by depositional processes in combination with syn-depositional fractures. However, the diagenetic history of the Omkyk Sequence 2 has not been studied. Selective dolomitisation of microbialites indicate that diagenetic alterations have affected the carbonate system. Therefore, future research might refine or overturn this classification.

# References


Aarnes, J. E., Kippe, V. and Lie, K.-A. (2005). "Mixed multiscale finite elements and streamline methods for reservoir simulation of large geomodels." Advances in Water Resources **28**(3): 257-271.

Adams, E. W., Grelaud, C., Pal, M., Csoma, A. E., Al Ja'aidi, O. S. and Hinai, R. A. (2011). "Improving reservoir models of Cretaceous carbonates with digital outcrop modelling (Jabal Madmar, Oman): static modelling and simulating clinoforms." Petroleum Geoscience **17**(3): 309-332.

Adams, E. W., Grotzinger, J. P., Watters , W. A., Schröder, S., McCormick, D. S. and Al-Siyabi, H. A. (2005). "Digital characterization of thrombolite-stromatolite reef distribution in a carbonate ramp system (terminal Proterozoic, Nama Group, Namibia)." AAPG Bulletin **89**(10): 1293-1318.

Adams, E. W. and Hasler, C.-A. (2010). "The intrinsic effect of shape on the retrogradation motif and timing of drowning of carbonate patch reef systems (Lower Frasnian, Bugle Gap, Canning Basin, Western Australia)." Sedimentology **57**(4): 956-984.

Adams, E. W., Schröder, S., Grotzinger, J. P. and McCormick, D. S. (2004). "Digital reconstruction and stratigraphic evolution of a microbial-dominated, isolated carbonate platform (terminal Proterozoic, Nama Group, Namibia)." Journal of Sedimentary Research **74**(4): 479-497.

Agada, S., Chen, F., Geiger, S., Toigulova, G., Agar, S., Shekhar, R., Benson, G., Hehmeyer, O., Amour, F., Mutti, M., Christ, N. and Immenhauser, A. (2014). "Numerical simulation of fluid-flow processes in a 3D high-resolution carbonate reservoir analogue." Petroleum Geoscience **20**(1): 125-142.

Agar, S. M., Geiger-Boschung, S., Matthai, S. K., Alway, R., Tomas, S., Immenhauser, A., Shekhar, R., Paul, J., Benson, G., Karcz, Z. and Kabiri, L. (2010). The Impact of Hierarchical Fracture Networks on Flow Partitioning in Carbonate Reservoirs: Examples Based on a Jurassic Carbonate Ramp Analog from the High Atlas. SPE Annual Technical Conference and Exhibition. Florence, Italy Society of Petroleum Engineers.

Ahr, W. M. (2008). Geology of carbonate reservoirs: the identification, description and characterization of hydrocarbon reservoirs in carbonate rocks. Hoboken, NJ, USA, John Wiley & Sons.

Ahr, W. M. and Hammel, B. S. (1999). "Identification and mapping of flow units in carbonate reservoirs an example from the happy spraberry (permian) field Garza County, Texas USA." Energy exploration & exploitation **17**(3-4): 311-334.

Ahrendt, H., Hunziker, J. and Weber, K. (1978). "Age and degree of metamorphism and time of nappe emplacement along the southern margin of the Damara Orogen/Namibia (SW-Africa)." Geologische Rundschau **67**(2): 719-742.

Al Haddad, S. and Mancini, E. A. (2013). "Reservoir characterization, modeling, and evaluation of Upper Jurassic Smackover microbial carbonate and associated facies in Little Cedar Creek field, southwest Alabama, eastern Gulf coastal plain of the United States." AAPG Bulletin **97**(11): 2059-2083.

Alkmim, F. F., Marshak, S., Pedrosasoares, A., Peres, G., Cruz, S. and Whittington, A. (2006). "Kinematic evolution of the Araçuaí-West Congo orogen in Brazil

and Africa: Nutcracker tectonics during the Neoproterozoic assembly of Gondwana." Precambrian Research **149**(1-2): 43-64.
Alkmim, F. F., Marshak, S., Fonseca, M.A. (2001). "Assembling West Gondwana in the Neoproterozoic: Clues from the Sao Francisco craton region, Brazil." Geology **29**(4): 319-322.
Allen, P. A. and Etienne, J. L. (2008). "Sedimentary challenge to Snowball Earth." Nature Geoscience **1**(12): 817-825.
Amour, F., Mutti, M., Christ, N., Immenhauser, A., Benson, G. S., Agar, S. M., Tomás, S. and Kabiri, L. (2013). "Outcrop analog for an oolitic carbonate ramp reservoir: A scale-dependent geologic modeling approach based on stratigraphic hierarchy." AAPG Bulletin **97**(5): 845-871.
Arpat, G. B. and Caers, J. (2007). "Conditional simulation with patterns." Mathematical Geology **39**(2): 177-203.
Astin, T. R. and Rogers, D. A. (1991). ""Subaqueous shrinkage cracks" in the Devonian of Scotland reinterpreted." Journal of Sedimentary Research **61**(5): 850-859.
Ayeni, G., Huck, A. and de Groot, P. (2008). "Extending reservoir property prediction with pseudo-wells." First break **26**(11): 11-29.
Aziz, A. and Ghnia, S. (2009). "Distribution of Infracambrian rocks and the hydrocarbon potential within the Murzuq and Al Kufrah basins, NW Africa." Geological Society, London, Special Publications **326**(1): 211-219.
Baker, R. (2001). "Streamline Technology: Reservoir History Matching and Forecasting= Its Success Limitations and Future." Journal of Canadian Petroleum Technology **40**(04): 23-27.
Barnaby, R. J. and Ward, W. B. (2007). "Outcrop Analog for Mixed Siliciclastic-Carbonate Ramp Reservoirs-Stratigraphic Hierarchy, Facies Architecture, and Geologic Heterogeneity: Grayburg Formation, Permian Basin, U.S.A." Journal of Sedimentary Research **77**(1): 34-58.
Basei, M. A. S., Nutman, A., Siga Jenior, O., Passarelli, C. R. and Drukas, C. O. (2009). The Evolution and Tectonic Setting of the Luis Alves Microplate of Southeastern Brazil: An Exotic Terrane during the Assembly of Western Gondwana. *In:* Developments in Precambrian Geology. (Eds) Gaucher, C., Sial, A. N., Frimmel, H. E. and Halverson, G. P., Elsevier. **Volume 16:** 273-291.
Batycky, R. P., Blunt, M. J. and Thiele, M. R. (1996). A 3d field scale streamline simulator with gravity and changing well conditions. SPE annual technical conference. Denver, USA**:** 467-476.
Bechstädt, T., Jager, H., Spence, G. and Werner, G. (2009). "Late Cryogenian (Neoproterozoic) glacial and post-glacial successions at the southern margin of the Congo Craton, northern Namibia: facies, palaeogeography and hydrocarbon perspective." Geological Society, London, Special Publications **326**(1): 255-287.
Beglinger, S. E., Doust, H. and Cloetingh, S. (2012). "Relating petroleum system and play development to basin evolution: Brazilian South Atlantic margin." Petroleum Geoscience **18**(3): 315-336.
Behr, H., Ahrendt, H., Schmidt, A. and Weber, K. (1981). "Saline horizons acting as thrust planes along the southern margin of the Damara Orogen (Namibia/SW-Africa)." Geological Society, London, Special Publications **9**(1): 167-172.

Belayneh, M., Geiger, S. and Matthäi, S. K. (2006). "Numerical simulation of water injection into layered fractured carbonate reservoir analogs." AAPG Bulletin **90**(10): 1473-1493.

Bellian, J. A. (2005). "Digital Outcrop Models: Applications of Terrestrial Scanning Lidar Technology in Stratigraphic Modeling." Journal of Sedimentary Research **75**(2): 166-176.

Bellian, J. A., Beck, R. and Kerans, C. (2007). "Analysis of hyperspectral and lidar data: Remote optical mineralogy and fracture identification." Geosphere **3**(6): 491-500.

Bellian, J. A., Kerans, C. and Jennette, D. C. (2005). "Digital Outcrop Models: Applications of Terrestrial Scanning Lidar Technology in Stratigraphic Modeling." Journal of Sedimentary Research **75**(2): 166-176.

Benson, G. S., Franseen, E. K., Goldstein, R. H. and Li, Z. (2014). "Workflows for incorporating stratigraphic and diagenetic relationships into a reservoir-analogue model from outcrops of Miocene carbonates in SE Spain." Petroleum Geoscience **20**(1): 55-78.

Benson, J. D., Pultz, L. M. and Bruner, D. (1996). "The influence of paleotopography, sea level fluctuation, and carbonate productivity on deposition of the Smackover and Buckner Formations, Appleton field, Escambia County, Alabama." Gulf Coast Association of Geological Societies Transactions **46**: 15-23.

Berra, F. and Carminati, E. (2012). "Differential compaction and early rock fracturing in high-relief carbonate platforms: numerical modelling of a Triassic case study (Esino Limestone, Central Southern Alps, Italy)." Basin Research **24**(5): 598-614.

Bhat, G. M., Ram, G. and Koul, S. (2009). "Potential for oil and gas in the Proterozoic carbonates (Sirban Limestone) of Jammu, northern India." Geological Society, London, Special Publications **326**(1): 245-254.

Blanco, G., Germs, G. J. B., Rajesh, H. M., Chemale, F., Dussin, I. A. and Justino, D. (2011). "Provenance and paleogeography of the Nama Group (Ediacaran to early Palaeozoic, Namibia): Petrography, geochemistry and U–Pb detrital zircon geochronology." Precambrian Research **187**(1): 15-32.

Blanco, G., Rajesh, H. M., Germs, G. J. B. and Zimmermann, U. (2009). "Chemical Composition and Tectonic Setting of Chromian Spinels from the Ediacaran-Early Paleozoic Nama Group, Namibia." The Journal of Geology **117**(3): 325-341.

Blunt, M. J., Liu, K. and Thiele, M. R. (1996). "A generalized streamline method to predict reservoir flow." Petroleum Geoscience **2**(3): 259-269.

Borgomano, J., Masse, J. P., Fenerci-Masse, M. and Fournier, F. (2013). "Petrophysics of lower cretaceous platform carbonate outcrops in Provence (SE France): Implications for carbonate reservoir characterisation." Journal of Petroleum Geology **36**(1): 5-41.

Borgomano, J. R. F., Fournier, F. o., Viseur, S. and Rijkels, L. (2008). "Stratigraphic well correlations for 3-D static modeling of carbonate reservoirs." AAPG Bulletin **92**(6): 789-824.

Boro, H., Bertotti, G. and Hardebol, N. J. (2012). "Distributed fracturing affecting isolated carbonate platforms, the Latemar Platform Natural Laboratory (Dolomites, North Italy)." Marine and Petroleum Geology **40**: 69-84.

Bosak, T., Lahr, D. J. G., Pruss, S. B., Macdonald, F. A., Dalton, L. and Matys, E. (2011). "Agglutinated tests in post-Sturtian cap carbonates of Namibia and Mongolia." Earth and Planetary Science Letters **308**(1-2): 29-40.

Bosence, D. (2005). "A genetic classification of carbonate platforms based on their basinal and tectonic settings in the Cenozoic." Sedimentary Geology **175**(1-4): 49-72.

Bouougri, E. and Porada, H. (2007). "Siliciclastic biolaminites indicative of widespread microbial mats in the Neoproterozoic Nama Group of Namibia." Journal of African Earth sciences **48**(1): 38-48.

Brandsäter, I., Wist, H. T., Nüss, A., Lia, O., Arntzen, O. J., Ringrose, P. S., Martinius, A. W. and Lerdahl, T. R. (2001). "Ranking of stochastic realizations of complex tidal reservoirs using streamline simulation criteria." Petroleum Geoscience **7**(5): 53-63.

Bryant, I., Carr, D., Cirilli, P., Drinkwater, N., McCormick, D., Tilke, P. and Thurmond, J. (2000). "Use of 3D digital analogues as templates in reservoir modelling." Petroleum Geoscience **6**(2): 195-201.

Buckley, S., Vallet, J., Braathen, A. and Wheeler, W. (2008a). "Oblique helicopter-based laser scanning for digital terrain modelling and visualisation of geological outcrops." International Archives of the Photogrammetry, Remote Sensing and Spatial Information Sciences **37**(B4): 493-498.

Buckley, S. J., Howell, J. A., Enge, H. D. and Kurz, T. H. (2008b). "Terrestrial laser scanning in geology: data acquisition, processing and accuracy considerations." Journal of the Geological Society **165**(3): 625-638.

Budd, D. A., Frost, E. L., Huntington, K. W. and Allwardt, P. F. (2013). "Syndepositional deformation features in high-relief carbonate platforms: long-lived conduits for diagenetic fluids." Journal of Sedimentary Research **83**(1): 12-36.

Burchette, T. P. (2012). "Carbonate rocks and petroleum reservoirs: a geological perspective from the industry." Geological Society, London, Special Publications **370**(1): 17-37.

Burchette, T. P. and Wright, V. P. (1992). "Carbonate ramp depositional systems." Sedimentary Geology **79**(1): 3-57.

Burton, D., Dunlap, D. B., Wood, L. J. and Flaig, P. P. (2011). "Lidar Intensity as a Remote Sensor of Rock Properties." Journal of Sedimentary Research **81**(5): 339-347.

Burton, D. and Wood, L. J. (2011). "Quantitative shale characterization of the tidally influenced Sego Sandstone." AAPG Bulletin **95**(7): 1207-1226.

Busfield, M. E. and Le Heron, D. P. (2013). "Glacitectonic deformation in the Chuos Formation of northern Namibia: implications for Neoproterozoic ice dynamics." Proceedings of the Geologists' Association **124**(5): 778-789.

Butterfield, N. J. (2009). "Macroevolutionary turnover through the Ediacaran transition: ecological and biogeochemical implications." Geological Society, London, Special Publications **326**(1): 55-66.

Caers, J. and Zhang, T. (2004). Multiple-point geostatistics: a quantitative vehicle for integrating geologic analogs into multiple reservoir models. *In:* Integration of outcrop and modern analogs in reservoir modeling. (Eds) Grammer, G. M., Harris, P. M., Eberli, G. P. **Am. Assoc. Petrol.Geol., Memoir:** 384-394.

Carle, S. F. and Fogg, G. E. (1996). "Transition probability-based indicator geostatistics." Mathematical Geology **28**(4): 453-476.

Carpenter, D. G., Guidry, S. A., Degraff, J. D. and Collins, J. (2006). Evolution of Tengiz rim/flank reservoir quality: new insights from systematic, integrated core fracture and diagenesis investigations. Giant hydrocarbon reservoirs of the world: From rocks to reservoir characterization and modeling: AAPG Annual Meeting. Abstracts. **15:** 18.

Clayton, V. D. (2002). Geostatistical reservoir modeling. New York, Oxford university press.

Collins, J., Kenter, J., Harris, P., Kuanysheva, G., Fischer, D. and Steffen, K. (2006). Facies and Reservoir-quality Variations in the Late Visean to Bashkirian Outer Platform, Rim, and Flank of the Tengiz Buildup, Precaspian Basin, Kazakhstan. *In:* Giant Hydrocarbon Reservoirs of The World: From Rocks to Reservoir Characterization and Modeling. (Eds) Harris, P. M. and Weber, L. J. Tulsa, American Association of Petroleum Geologists Memoir. **88:** 55-95.

Coniglio, M. and James, N. P. (1985). "Calcified algae as sediment contributors to early Paleozoic limestones: evidence from deep-water sediments of the Cow Head Group, Western Newfoundland." **55**: 748-754.

Corbeanu, R. M., Soegaard, K., Szerbiak, R. B., Thurmond, J. B., McMechan, G. A., Wang, D., Snelgrove, S., Forster, C. B. and Menitove, A. (2001). "Detailed Internal Architecture of a Fluvial Channel Sandstone Determined from Outcrop, Cores, and 3-D Ground-Penetrating Radar: Example from the Middle Cretaceous Ferron Sandstone, East-Central Utah." AAPG Bulletin **85**(9): 1583-1608.

Cozzi, A. (2000). "Synsedimentary tensional features in Upper Triassic shallow-water platform carbonates of the Carnian Prealps (northern Italy) and their importance as palaeostress indicators." Basin Research **12**(2): 133-146.

Cozzi, A., Grotzinger, J. P. and Allen, P. A. (2004). "Evolution of a terminal Neoproterozoic carbonate ramp system (Buah Formation, Sultanate of Oman): Effects of basement paleotopography." Geological Society of America Bulletin **116**(11): 1367-1384.

Craig, J., Biffi, U., Galimberti, R. F., Ghori, K. A. R., Gorter, J. D., Hakhoo, N., Le Heron, D. P., Thurow, J. and Vecoli, M. (2013). "The palaeobiology and geochemistry of Precambrian hydrocarbon source rocks." Marine and Petroleum Geology **40**: 1-47.

Craig, J., Thurow, J., Thusu, B., Whitham, A. and Abutarruma, Y. (2009). "Global Neoproterozoic petroleum systems: the emerging potential in North Africa." Geological Society, London, Special Publications **326**(1): 1-25.

Cressie, N. and Hawkins, D. M. (1980). "Robust estimation of the variogram: I." Journal of the International Association for Mathematical Geology **12**(2): 115-125.

David, M. (2012). Geostatistical ore reserve estimation. Amsterdam, Elsevier.

De Boever, E., Swennen, R. and Dimitrov, L. (2006). "Lower Eocene carbonate cemented chimneys (Varna, NE Bulgaria): Formation mechanisms and the (a)biological mediation of chimney growth?" Sedimentary Geology **185**(4): 159-173.

De Waele, B., Johnson, S. P. and Pisarevsky, S. A. (2008). "Palaeoproterozoic to Neoproterozoic growth and evolution of the eastern Congo Craton: Its role in the Rodinia puzzle." Precambrian Research **160**(1-2): 127-141.

De Wit, M. J., de Brito Neves, B. B., Trouw, R. A. J. and Pankhurst, R. J. (2008). "Pre-Cenozoic correlations across the South Atlantic region: (the ties that bind)." Geological Society, London, Special Publications **294**(1): 1-8.

Delaunay, B. N. (1934). "Sur la sphère vide." Izvestia Akademii Nauk SSSR, Otdelenie Matematicheskikh i Estestvennykh Nauk(7): 793-800.

Demaison, G. and Moore, G. T. (1980). "Anoxic environments and oil source bed genesis." AAPG Bulletin **64**(8): 1179-1209.

Deveugle, P. E. K., Jackson, M. D., Hampson, G. J., Farrell, M. E., Sprague, A. R., Stewart, J. and Calvert, C. S. (2011). "Characterization of stratigraphic architecture and its impact on fluid flow in a fluvial-dominated deltaic reservoir analog: Upper Cretaceous Ferron Sandstone Member, Utah." AAPG Bulletin **95**(5): 693-727.

Deynoux, M., Affaton, P., Trompette, R. and Villeneuve, M. (2006). "Pan-African tectonic evolution and glacial events registered in Neoproterozoic to Cambrian cratonic and foreland basins of West Africa." Journal of African Earth sciences **46**(5): 397-426.

Dibenedetto, S. and Grotzinger, J. (2005). "Geomorphic evolution of a storm-dominated carbonate ramp ( c. 549 Ma), Nama Group, Namibia." Geological Magazine **142**(5): 583-604.

Domack, E. W. and Hoffman, P. F. (2011). "An ice grounding-line wedge from the Ghaub glaciation (635 Ma) on the distal foreslope of the Otavi carbonate platform, Namibia, and its bearing on the snowball Earth hypothesis." Geological Society of America Bulletin **123**(7-8): 1448-1477.

Dovera, L., Caers, J. and Borgomano, J. (2006). MPG Simulation of Facies Thicknesses Interpreted through Sequence Stratigraphy-Application on a Carbonate Outcrop. 10th European Conference on the Mathematics of Oil Recovery.

Dupraz, C., Reid, R. P., Braissant, O., Decho, A. W., Norman, R. S. and Visscher, P. T. (2009). "Processes of carbonate precipitation in modern microbial mats." Earth-Science Reviews **96**(3): 141-162.

Dupraz, C. and Visscher, P. (2005). "Microbial lithification in marine stromatolites and hypersaline mats." Trends in Microbiology **13**(9): 429-438.

Dürr, S. B. and Dingeldey, D. P. (1996). "The Kaoko belt (Namibia): Part of a late Neoproterozoic continental-scale strike-slip system." Geology **24**(6): 503-506.

Eiler, J. M. (2007). "“Clumped-isotope” geochemistry—The study of naturally-occurring, multiply-substituted isotopologues." Earth and Planetary Science Letters **262**(3-4): 309-327.

Enge, H. D., Buckley, S. J., Rotevatn, A. and Howell, J. A. (2007). "From outcrop to reservoir simulation model: Workflow and procedures." Geosphere **3**(6): 469-490.

Enge, H. D. and Howell, J. A. (2010). "Impact of deltaic clinothems on reservoir performance: Dynamic studies of reservoir analogs from the Ferron Sandstone Member and Panther Tongue, Utah." AAPG Bulletin **94**(2): 139-161.

Eyles, N. (1993). "Earth's glacial record and its tectonic setting." Earth-Science Reviews **35**: 1-248.

Eyles, N. and Januszczak, N. (2004). "'Zipper-rift': a tectonic model for Neoproterozoic glaciations during the breakup of Rodinia after 750 Ma." Earth-Science Reviews **65**(1-2): 1-73.

Eyles, N. and Januszczak, N. (2007). "Syntectonic subaqueous mass flows of the Neoproterozoic Otavi Group, Namibia: where is the evidence of global glaciation?" Basin Research **19**(2): 179-198.

Fabuel-Perez, I., Hodgetts, D. and Redfern, J. (2009). "A new approach for outcrop characterization and geostatistical analysis of a low-sinuosity fluvial-dominated succession using digital outcrop models: Upper Triassic Oukaimeden Sandstone Formation, central High Atlas, Morocco." AAPG Bulletin **93**(6): 795-827.

Fabuel-Perez, I., Hodgetts, D. and Redfern, J. (2010). "Integration of digital outcrop models (DOMs) and high resolution sedimentology-workflow and implications for geological modelling: Oukaimeden Sandstone Formation, High Atlas (Morocco)." Petroleum Geoscience **16**(2): 133-154.

Fairchild, I. J. (1991). "Origins of carbonate in Neoproterozoic stromatolites and the identification of modern analogues." Precambrian Research **53**: 281-299.

Falivene, O., Arbues, P., Gardiner, A., Pickup, G., Munoz, J. A. and Caberra, L. (2006). "Best practice stochastic facies modeling from a channel-fill turbidite sandstone analog (the Quarry outcrop, Eocene Ainsa basin, northeast Spain)." AAPG Bulletin **90**(7): 1003-1029.

Feldmann, M. and MacKenzie, J. (1998). "Stromatolite-Thrombolite associations in a modern environment, Lee Stocking Island, Bahamas." PALAIOs **13**(2): 201-212.

Fitch, P. J. R., Jackson, M. D., Hampson, G. J. and John, C. M. (2014). "Interaction of stratigraphic and sedimentological heterogeneities with flow in carbonate ramp reservoirs: impact of fluid properties and production strategy." Petroleum Geoscience **20**(1): 7-26.

Flügel, E. (2004). Microfacies of carbonate rocks: analysis, interpretation and application. Amsterdam, Springer.

Frimmel, H. E. (2009). Configuration of Pan-African Orogenic Belts in Southwestern Africa. *In:* Developments in Precambrian Geology. (Eds) Gaucher, C., Sial, A. N., Frimmel, H. E. and Halverson, G. P., Elsevier. **Volume 16:** 145-151.

Frimmel, H. E., Basei, M. S. and Gaucher, C. (2010). "Neoproterozoic geodynamic evolution of SW-Gondwana: a southern African perspective." International Journal of Earth Sciences **100**(2-3): 323-354.

Frimmel, H. E., Foelling, P. G. and Eriksson, P. G. (2002). "Neoproterozoic tectonic and climatic evolution recorded in the Gariep Belt, Namibia and South Africa." Basin Research **14**: 55-67.

Frimmel, H. E. and Miller, R. M. (2009). Continental Rifting. *In:* Developments in Precambrian Geology. (Eds) Gaucher, C., Sial, A. N., Frimmel, H. E. and Halverson, G. P., Elsevier. **Volume 16:** 153-159.

Frost, E. L. (2007). "Facies heterogeneity, platform architecture and fracture patterns of the Devonian reef complexes, Canning Basin, Western Australia [unpublished Ph.D. dissertation]: University of Texas at Austin, Austin, Texas, 156 ".

Frost, E. L., Budd, D. A. and Kerans, C. (2012). "Syndepositional Deformation In A High-Relief Carbonate Platform and Its Effect On Early Fluid Flow As Revealed By Dolomite Patterns." Journal of Sedimentary Research **82**(12): 913-932.

Frost, E. L. and Kerans, C. (2009). "Platform-margin trajectory as a control on syndepositional fracture patterns, Canning Basin, Western Australia." Journal of Sedimentary Research **79**(2): 44-55.

Frost, E. L. and Kerans, C. (2010). "Controls on syndepositional fracture patterns, Devonian reef complexes, Canning Basin, Western Australia." Journal of Structural Geology **32**(9): 1231-1249.

Ganqing, J., Martin, J. K. and Nicholas, C.-B. (2003). "Stable isotopic evidence for methane seeps in Neoproterozoic postglacial cap carbonates." Nature **426**(6968): 822-826.

Gaucher, C., Frimmel, H. E. and Germs, G. J. B. (2009). Tectonic Events and Palaeogeographic Evolution of Southwestern Gondwana in the Neoproterozoic and Cambrian. *In:* Developments in Precambrian Geology. (Eds) Gaucher, C., Sial, A. N., Frimmel, H. E. and Halverson, G. P., Elsevier. **Volume 16:** 295-316.

Germs, G. J. B. (1972). "The stratigraphy and paleontology of the lower Nama Group, South West Africa." Bulletin, Precambrian Research **12**: 1-250.

Germs, G. J. B. (1974). "The Nama Group in South West Africa and Its Relationship to the Pan-African Geosyncline." The Journal of Geology **82**(3): 301-317.

Germs, G. J. B. (1983). "Implications of sedimentary facies and depositional environmental analysis of the Nama Group in South West Africa/Namibia." Geological Society of South Africa, Special Publication **11**: 89-114.

Germs, G. J. B. (1995). "The Neoproterozoic of southwestern Africa, with emphasis on platform stratigraphy and paleontology." Precambrian Research **73**: 137-151.

Germs, G. J. B., Knoll, A. H. and Vidal, G. (1986). "LATEST PROTEROZOIC MICROFOSSILS FROM THE NAMA GROUP, NAMIBIA (SOUTH WEST AFRICA)." Precambrian Research **32**: 45-62.

Ghori, K. A. R., Craig, J., Thusu, B., Luning, S. and Geiger, M. (2009). "Global Infracambrian petroleum systems: a review." Geological Society, London, Special Publications **326**(1): 109-136.

Gigli, G. and Casagli, N. (2011). "Semi-automatic extraction of rock mass structural data from high resolution LIDAR point clouds." International Journal of Rock Mechanics and Mining Sciences **48**(2): 187-198.

Gilbert, R., Liu, Y., Abriel, W. and Preece, R. (2004). "Reservoir modeling: Integrating various data at appropriate scales." The Leading Edge **23**(8): 784-788.

Glaessner, M. F. (1963). "Zur Kenntnis der Nama-Fossilien Suedwest-Afrikas." Annalen Naturhistorisches Museum Wien **66**: 113-120.

Gomes, P. O., Kilsdonk, B., Minken, J., Grow, T. and Barragan, R. (2009). The outer high of the Santos Basin, Southern São Paulo Plateau, Brazil: pre-salt exploration outbreak, paleogeographic setting, and evolution of the syn-rift structures. AAPG International Conference and Exhibition Cape Town, South Africa **10193**.

Gorter, J., Grey, K. and Hocking, R. (2007). "The petroleum exploration potential of the Australian Infracambrian (Ediacaran) of the Amadeus and Officer Basins." Australian Petroleum Production and Exploration Association (APPEA): 391-392.

Gradstein, F. M., Ogg, G. and Schmitz, M. (2012). The Geologic Time Scale 2012 2-Volume Set, Elsevier.

Gradstein, F. M., Ogg, J. G. and Smith, A. G. (2004). A geologic time scale 2004, Cambridge University Press.

Grasmueck, M., Weger, R. and Horstmeyer, H. (2004). "Three-dimensional ground-penetrating radar imaging of sedimentary structures, fractures, and archaeological features at submeter resolution." Geology **32**(11): 933-936.

Gresse, P. G. and Germs, G. J. B. (1993). "The Nama foreland basin: sedimentation, major unconformity bounded sequences and multisided active margin advance." Precambrian Research **63**: 247-272.

Grosjean, E., Love, G., Stalvies, C., Fike, D. and Summons, R. (2009). "Origin of petroleum in the Neoproterozoic–Cambrian South Oman Salt Basin." Organic Geochemistry **40**(1): 87-110.

Grotzinger, J. P., Adams, E. W. and Schröder, S. (2005). "Microbial–metazoan reefs of the terminal Proterozoic Nama Group (c. 550–543 Ma), Namibia." Geological Magazine **142**(05): 499-517.

Grotzinger, J. P., Bowring, S. A., Saylor, B. Z. and Kaufman, A. J. (1995). "Biostratigraphic and Geochronologic Constraints on Early Animal Evolution." Science **270**(5236): 598-604.

Grotzinger, J. P. and Miller, R. M. (2008). The Nama Group. *In:* The Geology of Namibia. (Eds) Miller, R. M. Windhoek, Namibia, Minestry of Mines and Energy, Geological Survey **2:** 13.229-213.272.

Grotzinger, J. P., Watters, W. A. and Knoll, A. H. (2000). "Calcified metazoans in thrombolite-stromatolite reefs of the terminal Proterozoic Nama Group, Namibia." Paleobiology **26**(3): 334-359.

Guidry, S. A., Grasmueck, M., Carpenter, D. G., Gombos, A. M., Bachtel, S. L. and Viggiano, D. A. (2007). "Karst and early fracture networks in carbonates, turks and caicos islands, British West Indies." Journal of Sedimentary Research **77**(6): 508-524.

Gupta, S. and Allen, P. A. (2000). "Implications of foreland paleotopography for stratigraphic development in the Eocene distal Alpine foreland basin." Geological Society of America Bulletin **112**(4): 515-530.

Hagadorn, J. W. and Bottjer, D. J. (1997). "Wrinkle structures: Microbially mediated sedimentary structures common in subtidal siliciclastic settings at the Proterozoic-Phanerozoic transition." Geology **25**(11): 1047-1050.

Hahn, G. and Pflug, H. (1985). "Polypenartige Organismen aus dem Jung-Präkambrium (Nama-Gruppe) von Namibia." Geologica et Palaeontologica **19**(1): 13-27.

Halverson, G. P., Hoffman, P.F., Schrag, D.P. and Kaufman, A.J. (2002). "A major perturbation of the carbon cycle before the Ghaub glaciation (Neoproterozoic) in Namibia: Prelude to snowball Earth?" Geochem. Geophys. Geosystems **3**(6): 1-24.

Halverson, G. P., Maloof, A. C. and Hoffman, P. F. (2004). "The Marinoan glaciation (Neoproterozoic) in northeast Svalbard." Basin Research **16**(3): 297-324.

Haneberg, W. (2008). "Using close range terrestrial digital photogrammetry for 3-D rock slope modeling and discontinuity mapping in the United States." Bulletin of Engineering Geology and the Environment **67**(4): 457-469.

Hedberg, R. (1979). "Stratigraphy of the Owamboland Basin, South West Africa Bulletin." Precambrian Research Unit Bulletin **24**: 325p.

Heijlen, W., Banks, D. A., Muchez, P., Stensgard, B. M. and Yardley, B. W. D. (2008). "The Nature of Mineralizing Fluids of the Kipushi Zn-Cu Deposit, Katanga, Democratic Repubic of Congo: Quantitative Fluid Inclusion

Analysis using Laser Ablation ICP-MS and Bulk Crush-Leach Methods." Economic Geology **103**(7): 1459-1482.
Hodgetts, D. (2013). "Laser scanning and digital outcrop geology in the petroleum industry: A review." Marine and Petroleum Geology **46**(0): 335-354.
Hoffman, P. and Halverson, G. (2008). Otavi Group of western Northern Platform, the eastern Kaoko Zone and western Northern Margin Zone. *In:* The Geology of Namibia. (Eds) Miller, R. M. Windhoek, Namibia, Minestry of Mines and Energy, Geological Survey **2:** 13.69-13.134.
Hoffman, P., Halverson, G., Domack, E., Husson, J., Higgins, J. and Schrag, D. (2007). "Are basal Ediacaran (635 Ma) post-glacial "cap dolostones" diachronous?" Earth and Planetary Science Letters **258**(1-2): 114-131.
Hoffman, P. F. (1991). "Did the breakout of laurentia turn gondwanaland inside-out?" Science **252**(5011): 1409-1412.
Hoffman, P. F. (1998). "A Neoproterozoic Snowball Earth." Science **281**(5381): 1342-1346.
Hoffman, P. F. (2011). "Strange bedfellows: glacial diamictite and cap carbonate from the Marinoan (635 Ma) glaciation in Namibia." Sedimentology **58**(1): 57-119.
Hoffman, P. F., Hawkins, D.P., Isachsen, C.E., Bowring, S.A. (1996). "Precise U–Pb zircon ages for early Damaran magmatism in the Summas Mountains and Welwitschia Inlier, northern Damara belt, Namibia." Geological Survey of Namibia Communications **11**(47-52).
Hoffman, P. F. and Li, Z.-X. (2009). "A palaeogeographic context for Neoproterozoic glaciation." Palaeogeography, Palaeoclimatology, Palaeoecology **277**(3-4): 158-172.
Hoffmann, K. H., Condon, D. J., Bowring, S. A. and Crowley, J. L. (2004). "U-Pb zircon date from the Neoproterozoic Ghaub Formation, Namibia: Constraints on Marinoan glaciation." Geology **32**(9): 817-820.
Honarpour, M. M., Koederitz, F. and Herbert, A. (1986). Relative permeability of petroleum reservoirs. Boca Raton, CRC Press.
Horsfield, B., Curry, D. J., Bohacs, K., Littke, R., Rullkötter, J., Schenk, H. J., Radke, M., Schaefer, R. G., Carroll, A. R., Isaksen, G. and Witte, E. G. (1994). "Organic geochemistry of freshwater and alkaline lacustrine sediments in the Green River Formation of the Washakie Basin, Wyoming, U.S.A." Organic Geochemistry **22**(3-5): 415-440.
Howell, J. A., Martinius, A. W. and Good, T. R. (2014). "The application of outcrop analogues in geological modelling: a review, present status and future outlook." Geological Society, London, Special Publications **387**(1): 1-25.
Hu, L. Y., Liu, Y., Scheepens, C., Shultz, A. W. and Thompson, R. D. (2013). "Multiple-Point Simulation with an Existing Reservoir Model as Training Image." Mathematical Geosciences **46**(2): 227-240.
Huang, W., Di Donato, G. and Blunt, M. J. (2004). "Comparison of streamline-based and grid-based dual porosity simulation." Journal of Petroleum Science and Engineering **43**(1-2): 129-137.
Hunt, D. W., Fitchen, W. M. and Kosa, E. (2003). "Syndepositional deformation of the Permian Capitan reef carbonate platform, Guadalupe Mountains, New Mexico, USA." Sedimentary Geology **154**(3): 89-126.
Huntington, K. W., Eiler, J. M., Affek, H. P., Guo, W., Bonifacie, M., Yeung, L. Y., Thiagarajan, N., Passey, B., Tripati, A., Daëron, M. and Came, R. (2009). "Methods and limitations of 'clumped' CO2isotope (Δ47) analysis by gas-

source isotope ratio mass spectrometry." Journal of Mass Spectrometry **44**(9): 1318-1329.

Jackson, M. D., Hampson, G. J. and Sech, R. P. (2009). "Three-dimensional modeling of a shoreface-shelf parasequence reservoir analog: Part 2. Geologic controls on fluid flow and hydrocarbon recovery." AAPG Bulletin **93**(9): 1183-1208.

Janson, X. and Madriz, D. D. (2012). "Geomodelling of carbonate mounds using two-point and multipoint statistics." Geological Society, London, Special Publications **370**(1): 229-246.

Jennings, J. W., Jr. and Ward, W. B. (2000). "Geostatistical Analysis of Permeability Data and Modeling of Fluid-Flow Effects in Carbonate Outcrops." SPE Reservoir Eval. & Eng. **3**(4): 291-303.

Jensen, S. R., Droser, M. L. and Gehling, J. G. (2006). A Critical Look at the Ediacaran Trace Fossil Record. *In:* Neoproterozoic Geobiology and Paleobiology. (Eds) Xiao, S. and Kaufman, A., Springer Netherlands. **27:** 115-157.

Jiang, G., Wang, X., Shi, X., Zhang, S., Xiao, S. and Dong, J. (2010). "Organic carbon isotope constraints on the dissolved organic carbon (DOC) reservoir at the Cryogenian–Ediacaran transition." Earth and Planetary Science Letters **299**(1-2): 159-168.

Johnson, J. and Grotzinger, J. P. (2006). "Affect of Sedimentation on Stromatolite Reef Growth and Morphology, Ediacaran Omkyk Member (Nama Group), Namibia." South African Journal of Geology **109**: 87-96.

Johnson, S. P., Rivers, T. and De Waele, B. (2005). "A review of the Mesoproterozoic to early Palaeozoic magmatic and tectonothermal history of south-central Africa: implications for Rodinia and Gondwana." Journal of the Geological Society **162**(3): 433-450.

Jones, R. R., Pringle, J. K., McCaffrey, K. J., Imber, J., Wightman, R., Guo, J. and Long, J. (2011). "Extending digital outcrop geology into the subsurface." SEPM Special Publication **Outcrops Revitalized: Tools, Techniques and Applications". SEPM Concepts in Sedimentology and Paleontology, 10** 31-50.

Jung, A. and Aigner, T. (2012). "CARBONATE GEOBODIES: HIERARCHICAL CLASSIFICATION AND DATABASE – A NEW WORKFLOW FOR 3D RESERVOIR MODELLING." Journal of Petroleum Geology **35**(1): 49-65.

Jung, A., Fenwick, D. H. and Caers, J. (2013). "Training image-based scenario modeling of fractured reservoirs for flow uncertainty quantification." Computational Geosciences **17**(6): 1015-1031.

Kamona, A. and Gunzel, A. (2007). "Stratigraphy and base metal mineralization in the Otavi Mountain Land, Northern Namibia—a review and regional interpretation." Gondwana Research **11**(3): 396-413.

Kaufman, A. J., Hayes, J. M., Knoll, A. H. and Germs, G. J. B. (1991). "Isotopic compositions of carbonates and organic carbon from upper Proterozoic successions in Namibia: stratigraphic variation and the effects of diagenesis and metamorphism." Precambrian Research **49**(3-4): 301-327.

Kendall, B., Creaser, R. A., Calver, C. R., Raub, T. D. and Evans, D. A. D. (2009). "Correlation of Sturtian diamictite successions in southern Australia and northwestern Tasmania by Re–Os black shale geochronology and the ambiguity of "Sturtian"-type diamictite–cap carbonate pairs as

chronostratigraphic marker horizons." Precambrian Research **172**(3-4): 301-310.
Kendall, B., Creaser, R. A. and Selby, D. (2006). "Re-Os geochronology of postglacial black shales in Australia: Constraints on the timing of "Sturtian" glaciation." Geology **34**(9): 729-732.
Kennard, J. M. and James, N. P. (1986). "Thrombolites and Stromatolites: Two Distinct Types of Microbial Structures." PALAIOs **1**(5): 492-503.
Kennedy, M., Mrofka, D. and von der Borch, C. (2008). "Snowball Earth termination by destabilization of equatorial permafrost methane clathrate." Nature **453**(7195): 642-645.
Kennedy, M. J., Christie-Blick, N. and Prave, A. R. (2001). "Carbon isotopic composition of Neoproterozoic glacial carbonates as a test of paleoceanographic models for snowball Earth phenomena." Geology **29**(12): 1135-1138.
Kennedy, M. J., Christie-Blick, N., Sohl L.E. (2001). "Are Proterozoic cap carbonates and isotopic excursions a record of gas hydrate destabilization following Earth's coldest intervals?" Geology **29**(5): 443-446.
Kirschvink, J. (1992). "Late Proterozoic low-latitude global glaciation: the snowball Earth." The Proterozoic Biosphere: 51-52.
Klise, K. A., Weissmann, G. S., McKenna, S. A., Nichols, E. M., Frechette, J. D., Wawrzyniec, T. F. and Tidwell, V. C. (2009). "Exploring solute transport and streamline connectivity using lidar-based outcrop images and geostatistical representations of heterogeneity." Water Resources Research **45**(5): 1-11.
Knoll, A. (2000). "Learning to tell Neoproterozoic time." Precambrian Research **100**(1): 3-20.
Koralegadara, G. and Parcell, W. C. (2008). Reservoir Characterization of Microbial Reef Reservoirs at Little Cedar Creek Field, Conecuh County, Alabama. 4th Annual Symposium on Graduate Research and Scholarly Projects (GRASP). Hughes Metropolitan Complex, Wichita State University**:** 57-58.
Korn, H. and Martin, H. (1959). "GRAVITY TECTONICS IN THE NAUKLUFT MOUNTAINS OF SOUTH WEST AFRICA." Geological Society of America Bulletin **70**(8): 1047-1078.
Kosa, E. and Hunt, D. W. (2005). "Growth of syndepositional faults in carbonate strata: Upper Permian Capitan platform, New Mexico, USA." Journal of Structural Geology **27**(6): 1069-1094.
Kosa, E. and Hunt, D. W. (2006). "Heterogeneity in Fill and Properties of Karst-Modified Syndepositional Faults and Fractures: Upper Permian Capitan Platform, New Mexico, USA." Journal of Sedimentary Research **76**(1): 131-151.
Kurtzman, D., El Azzi, J. A., Lucia, F. J., Bellian, J., Zahm, C. and Janson, X. (2009). "Improving fractured carbonate-reservoir characterization with remote sensing of beds, fractures, and vugs." Geosphere **5**(2): 126-139.
Labourdette, R., Crumeyrolle, P. and Remacha, E. (2008). "Characterisation of dynamic flow patterns in turbidite reservoirs using 3D outcrop analogues: Example of the Eocene Morillo turbidite system (south-central Pyrenees, Spain)." Marine and Petroleum Geology **25**(3): 255-270.
Lapponi, F., Casini, G., Sharp, I., Blendinger, W., Fernandez, N., Romaire, I. and Hunt, D. (2011). "From outcrop to 3D modelling: a case study of a dolomitized carbonate reservoir, Zagros Mountains, Iran." Petroleum Geoscience **17**(3): 283-307.

Larsen, B., Grunnaleite, I. and Gudmundsson, A. (2010a). "How fracture systems affect permeability development in shallow-water carbonate rocks: An example from the Gargano Peninsula, Italy." Journal of Structural Geology **32**(9): 1212-1230.

Larsen, B., Gudmundsson, A., Grunnaleite, I., Sælen, G., Talbot, M. R. and Buckley, S. J. (2010b). "Effects of sedimentary interfaces on fracture pattern, linkage, and cluster formation in peritidal carbonate rocks." Marine and Petroleum Geology **27**(7): 1531-1550.

Le Ber, E., Le Heron, D. P., Winterleitner, G., Bosence, D. W. J., Vining, B. A. and Kamona, F. (2013). "Microbialite recovery in the aftermath of the Sturtian glaciation: Insights from the Rasthof Formation, Namibia." Sedimentary Geology **294**(0): 1-12.

Le Heron, D., Busfield, M., Le Ber, E. and Kamona, A. (2013a). "Neoproterozoic ironstones in northern Namibia: Biogenic precipitation and Cryogenian glaciation." Palaeogeography, Palaeoclimatology, Palaeoecology **369**(0): 48-57.

Le Heron, D. P. (2012). "The Cryogenian record of glaciation and deglaciation in South Australia." Sedimentary Geology **243**: 57-69.

Le Heron, D. P., Busfield, M. E. and Kamona, F. (2013b). "An interglacial on snowball Earth? Dynamic ice behaviour revealed in the Chuos Formation, Namibia." Sedimentology **60**(2): 411-427.

Le Heron, D. P., Cox, G., Trundley, A. and Collins, A. (2011). "Sea ice-free conditions during the Sturtian glaciation (early Cryogenian), South Australia." Geology **39**(1): 31-34.

Le Heron, D. P. and Craig, J. (2012). "Neoproterozoic deglacial sediments and their hydrocarbon source rock potential." Geological Society, London, Special Publications **368**(1): 381-393.

Le Heron, D. P., Craig, J. and Etienne, J. L. (2009). "Ancient glaciations and hydrocarbon accumulations in North Africa and the Middle East." Earth-Science Reviews **93**(3-4): 47-76.

Leinfelder, R. R. and Hartkopf-Fröder, C. (1990). "In situ accretion mechanism of concavo-convex lacustrine oncoids ('swallow nests' ) from the Oligocene of the Mainz Basin, Rhineland, FRG." **37**: 287-301.

Li, Z. X., Bogdanova, S. V., Collins, A. S., Davidson, A., De Waele, B., Ernst, R. E., Evans, D. A. D., Fitzsimons, I. C. W., Fuck, R. A., Gladkochub, D. P., Jacobs, J., Karlstrom, K. E., Lu, S., Natapov, L. M., Pease, V., Pisarevsky, S. A., Thrane, K. and Vernikovsky, V. (2009). "How not to build a supercontinent: A reply to J.D.A. Piper." Precambrian Research **174**(1-2): 208-214.

Li, Z. X., Bogdanova, S. V., Collins, A. S., Davidson, A., De Waele, B., Ernst, R. E., Fitzsimons, I. C. W., Fuck, R. A., Gladkochub, D. P. and Jacobs, J. (2008). "Assembly, configuration, and break-up history of Rodinia: A synthesis." Precambrian Research **160**(1-2): 179-210.

Li, Z. X., Evans, D. A. D. and Zhang, S. (2004). "A 90° spin on Rodinia: possible causal links between the Neoproterozoic supercontinent, superplume, true polar wander and low-latitude glaciation." Earth and Planetary Science Letters **220**(3-4): 409-421.

Lipinski, C. J., Franseen, E. K. and Goldstein, R. H. (2013). "Reservoir analog model for oolite-microbialite sequences, Miocene terminal carbonate complex, Spain." AAPG Bulletin **97**(11): 2035-2057.

Littke, R. and Welte, D. (1992). Hydrocarbon source rocks. *In:* Understanding the earth. (Eds) Brown, G., Hawkesworth, CJ, Wilson, C. . Cambridge, Cambridge University Press**:** 364-374.

Liu, X. and Zhang, Z. (2008). "LIDAR data reduction for efficient and high quality DEM generation." International Society for Photogrammetry and Remote Sensing and Spatial Information Sciences **37**: 173-178.

Liu, Y., Harding, A., Abriel, W. and Strebelle, S. (2004). "Multiple-point simulation integrating wells, three-dimensional seismic data, and geology." AAPG Bulletin **88**(7): 905-921.

Lowe, D. (1992). Major events in the geological development of the Precambrian Earth. *In:* The Proterozoic Biosphere, A Multidisciplinary Study. (Eds) Schopf, J. W. and Klein, C. Cambridge, Cambridge University Press**:** 67-73.

Lucia, F. J. (2007a). Carbonate Reservoir Characterization: An Integrated Approach. Berlin Heidelberg, Springer.

Lucia, F. J. (2007b). Limestone Reservoirs. *In:* Carbonate Reservoir Characterization: An Integrated Approach, Springer Berlin Heidelberg**:** 181-215.

Lüning, S., Craig, J., Fitches, B., Mayouf, J., Busrewil, A., Dieb, M. E., Gammudi, A., Loydell, D. and McIlroy, D. (1999). "Re-evaluation of the petroleum potential of the Kufra Basin (SE Libya, ne Chad): does the source rock barrier fall?" Marine and Petroleum Geology **16**(7): 693-718.

Lüning, S., Craig, J., Loydell, D. K., Storch, P. and Fitches, B. (2000). "Lower Silurian `hot shales' in North Africa and Arabia: regional distribution and depositional model." Earth-Science Reviews **49**(1): 121-200.

Macdonald, F. A., Schmitz, M.D., Crowley, J.L., Roots, C.F., Jones, D.S., Maloof, A.C., Strauss, J.V., Cohen, P.A., Johnston, D.T., Schrag, D.P. (2010). "Calibrating the Cryogenian." Science **327**: 1241-1243.

Mahan, K. H., Wernicke, B. P. and Jercinovic, M. J. (2010). "The-U-total Pb geochronology of authigenic monazite in the Adelaide rift complex, South Australia, and implications for the age of the type Sturtian and Marinoan glacial deposits." Earth and Planetary Science Letters **289**(1-2): 76-86.

Mancini, E. A. and Parcell, W. C. (2001). "Outcrop Analogs for Reservoir Characterization and Modeling of Smackover Microbial Reefs in the Northeastern Gulf of Mexico Area." Gulf Coast Association of Geological Societies Transactions **LI**: 207-218.

Mancini, E. A., Parcell, W. C., Ahr, W. M., Ramirez, V. O., Llinás, J. C. and Cameron, M. (2008). "Upper Jurassic updip stratigraphic trap and associated Smackover microbial and nearshore carbonate facies, eastern Gulf coastal plain." AAPG Bulletin **92**(4): 417-442.

Mantovani, M. S. M. and Brito Neves, B. B. d. (2009). The Paranapanema Lithospheric Block: Its Nature and Role in the Accretion of Gondwana. *In:* Developments in Precambrian Geology. (Eds) Gaucher, C., Sial, A. N., Frimmel, H. E. and Halverson, G. P., Elsevier. **Volume 16:** 257-272.

Martin, H., Porada, H. and Wittig, R. (1983). The root zone of the Naukluft nappe complex: Geodynamic implications. *In:* Intracontinental Fold Belts, Springer**:** 679-698.

Matejovic, I. (1993). "Determination of carbon, hydrogen, and nitrogen in soils by automated elemental analysis (dry combustion method)." Communications in Soil Science & Plant Analysis **24**(17-18): 2213-2222.

Matheron, G. (1989). Estimating and choosing, Springer.

McCaffrey, K. J. W., Jones, R. R., Holdsworth, R. E., Wilson, R. W., Clegg, P., Imber, J., Holliman, N. and Trinks, I. (2005). "Unlocking the spatial dimension: digital technologies and the future of geoscience fieldwork." Journal of the Geological Society **162**(6): 927-938.

McNeill, D. F. and Eberli, G. P. (2012). "Early Load-Induced Fracturing in a Prograding Carbonate Margin." Perspectives in Carbonate Geology: A Tribute to the Career of Robert Nathan Ginsburg (Special Publication 41 of the IAS) **98**: 327-336.

Meert, J. G. and Lieberman, B. S. (2004). "A palaeomagnetic and palaeobiogeographical perspective on latest Neoproterozoic and early Cambrian tectonic events." Journal of the Geological Society **161**(3): 477-487.

Miller, J. A., Viola, G. and Mancktelow, N. S. (2008). "Oxygen, carbon and strontium isotope constraints on the mechanisms of nappe emplacement and fluid-rock interaction along the subhorizontal Naukluft Thrust, central Namibia." Journal of the Geological Society **165**(3): 739-753.

Miller, R. M. (1997). Chapter 11 The owambo basin of northern namibia. *In:* Sedimentary Basins of the World. (Eds) Selley, R. C., Elsevier. **Volume 3:** 237-268.

Miller, R. M. (2008). Otavi Group. *In:* The Geology of Namibia. (Eds) Miller, R. M. Windhoek, Namibia, Ministry of Mines and Energy, Geological Survey. **2:** 13.48-13.69.

Miller, R. M., Frimmel, H. E. and Halverson, G. P. (2009a). Passive Continental Margin Evolution. *In:* Developments in Precambrian Geology. (Eds) Gaucher, C., Sial, A. N., Frimmel, H. E. and Halverson, G. P., Elsevier. **Volume 16:** 161-181.

Miller, R. M., Frimmel, H. E. and Will, T. M. (2009b). Geodynamic Synthesis of the Damara Orogen Sensu Lato. *In:* Developments in Precambrian Geology. (Eds) Gaucher, C., Sial, A. N., Frimmel, H. E. and Halverson, G. P., Elsevier. **Volume 16:** 231-235.

Mirowski, P. W., Tetzlaff, D. M., Davies, R. C., McCormick, D. S., Williams, N. and Signer, C. (2008). "Stationarity Scores on Training Images for Multipoint Geostatistics." Mathematical Geosciences **41**(4): 447-474.

Moore, L. S. and Burne, R. (1994). The modern thrombolites of Lake Clifton, western Australia. *In:* Phanerozoic stromatolites II, Springer**:** 3-29.

Mostafa, M. Y. (2013). "Reservoir simulation and evaluation of the Upper Jurassic Smackover microbial carbonate and grainstone-packstone reservoirs in Little Cedar Creek field, Conecuh County, Alabama." Master Thesis **Texas A&M University, College Station, Texas**: 98.

Myers, K. J. and Wignall, P. B. (1987). Understanding Jurassic organic-rich mudrocks-new concepts using gamma-ray spectrometry and palaeoecology: examples from the Kimmeridge Clay of Dorset and the Jet Rock of Yorkshire. *In:* Marine clastic sedimentology, Springer**:** 172-189.

Narbonne, G. M. (2005). "THE EDIACARA BIOTA: Neoproterozoic Origin of Animals and Their Ecosystems." Annual Review of Earth and Planetary Sciences **33**(1): 421-442.

Narr, W., Fischer, D., Harris, P. M. M., Heidrick, T., Robertson, B. and Payrazyan, K. (2004). Understanding and Predicting Fractures at Tengiz – A Giant, Naturally Fractured Reservoir in the Caspian Basin of Kazakhstan. American

Association of Petroleum Geologists, Hedberg Conference, Abstracts. El Paso, Texas, March 14-18.

Nedelec, A., Affaton, P., Francelanord, C., Charriere, A. and Alvaro, J. (2007). "Sedimentology and chemostratigraphy of the Bwipe Neoproterozoic cap dolostones (Ghana, Volta Basin): A record of microbial activity in a peritidal environment." Comptes Rendus Geosciences **339**(3-4): 223-239.

Nelson, R. (2001). Geologic analysis of naturally fractured reservoirs. Houston,, Gulf Professional Publishing.

Noffke, N., Knoll, A. H. and Grotzinger, J. P. (2002). "Sedimentary Controls on the Formation and Preservation of Microbial Mats in Siliciclastic Deposits: A Case Study from the Upper Neoproterozoic Nama Group, Naibia." PALAIOS **17**: 533-544.

Nose, M., Schmid, D. U. and Leinfelder, R. R. (2006). "Significance of microbialites, calcimicrobes, and calcareous algae in reefal framework formation from the Silurian of Gotland, Sweden." Sedimentary Geology **192**(3-4): 243-265.

Olariu, M. I., Ferguson, J. F., Aiken, C. L. V. and Xu, X. (2008). "Outcrop fracture characterization using terrestrial laser scanners: Deep-water Jackfork sandstone at Big Rock Quarry, Arkansas." Geosphere **4**(1): 247-259.

Olcott, A. N., Sessions, A.L., Corsetti, F.A., Kaufman, A.J., de Oliviera, T.F. (2005). "Biomarker Evidence for Photosynthesis During Neoproterozoic Glaciation." Science **310**: 471-474.

Ortega, O. J., Gale, J. F. and Marrett, R. (2010). "Quantifying diagenetic and stratigraphic controls on fracture intensity in platform carbonates: An example from the Sierra Madre Oriental, northeast Mexico." Journal of Structural Geology **32**(12): 1943-1959.

Parcell, W. C. (2002). "Sequence stratigraphic controls on the development of microbial fabrics and growth forms-implications for reservoir quality distribution in the Upper Jurassic (Oxfordian) Smackover Formation, eastern Gulf Coast, USA." Carbonates and Evaporites **17**(2): 166-181.

Parcell, W. C. (2003). "Evaluating the Development of Upper Jurassic Reefs in the Smackover Formation, Eastern Gulf Coast, U.S.A. through Fuzzy Logic Computer Modeling." Journal of Sedimentary Research **73**(4): 498-515.

Parrish, J. T. and Curtis, R. L. (1982). "Atmospheric circulation, upwelling, and organic-rich rocks in the Mesozoic and Cenozoic eras." Palaeogeography, Palaeoclimatology, Palaeoecology **40**(1): 31-66.

Pearce, M. A., Jones, R. R., Smith, S. A. F. and McCaffrey, K. J. W. (2011). "Quantification of fold curvature and fracturing using terrestrial laser scanning." AAPG Bulletin **95**(5): 771-794.

Pedrosa-Soares, A. C., Alkmim, F. F., Tack, L., Noce, C. M., Babinski, M., Silva, L. C. and Martins-Neto, M. A. (2008). "Similarities and differences between the Brazilian and African counterparts of the Neoproterozoic Aracuai-West Congo orogen." Geological Society, London, Special Publications **294**(1): 153-172.

Penny, A. M., Wood, R., Curtis, A., Bowyer, F., Tostevin, R. and Hoffman, K. H. (2014). "Early animals. Ediacaran metazoan reefs from the Nama Group, Namibia." Science **344**(6191): 1504-1506.

Phelps, R. M. and Kerans, C. (2007). "Architectural Characterization and Three-Dimensional Modeling of a Carbonate Channel Levee Complex: Permian

San Andres Formation, Last Chance Canyon, New Mexico, U.S.A." Journal of Sedimentary Research **77**(11): 939-964.
Pickard, N. A. H. (1992). "Depositional controls on Lower Carboniferous mifrobial buildups, eastern Midland Valley of Scotland." **39**: 1081-1100.
Piper, J. D. A. (2009). "Comment on "Assembly, configuration, and break-up history of Rodinia: A synthesis" by Li et al. [Precambrian Res., 160 (2008) 179–210]." Precambrian Research **174**(1-2): 200-207.
Playton, T., Kenter, J., Levy, M., Pierre, A., Jones, G. D. and Harris, P. M. (2010). Strategies for Modeling Depositional Heterogeneity of Carbonate Ramps Using Outcrop Analogs and Multiple Point Statistics. GEO 2010. EAGE.
Pollard, D. D. and Fletcher, R. C. (2005). Fundamentals of structural geology Cambridge Cambridge University Press.
Pollock, D. W. (1988). "Semianalytical Computation of Path Lines for Finite-Difference Models." Ground Water **26**(6): 743-750.
Pöppelreiter, M. C., Balzarini, M. A., Hansen, B. and Nelson, R. (2008). "Realizing complex carbonate facies, diagenetic and fracture properties with standard reservoir modelling software." Geological Society, London, Special Publications **309**(1): 39-49.
Pranter, M. J., Ellison, A. I., Cole, R. D. and Patterson, P. E. (2007). "Analysis and modeling of intermediate-scale reservoir heterogeneity based on a fluvial point-bar outcrop analog, Williams Fork Formation, Piceance Basin, Colorado." AAPG Bulletin **91**(7): 1025-1051.
Prave, A., R., (1996). "Tale of three cratons: tectonostratigraphic anatomy of the Damara orogen in northwestern Namibia and the assembly of Gondwana " Geoloogy **24**(12): 1115-1119.
Pringle, J., Howell, J., Hodgetts, D., Westerman, A. and Hodgson, D. (2006). "Virtual outcrop models of petroleum reservoir analogues: a review of the current state-of-the-art." First break **24**(3): 33-42.
Pruss, S. B., Bosak, T., Macdonald, F. A., McLane, M. and Hoffman, P. F. (2010). "Microbial facies in a Sturtian cap carbonate, the Rasthof Formation, Otavi Group, northern Namibia." Precambrian Research **181**(1-4): 187-198.
Pyrcz, M. J., Catuneanu, O. and Deutsch, C. V. (2005). "Stochastic surface-based modeling of turbidite lobes." AAPG Bulletin **89**(2): 177-191.
Qassab, H., Pavlas, M. K. R., Afaleg, N., Ali, H., Kharghoria, A., He, Z., Lee, S. and Datta-Gupta, A. (2003). Streamline-based production data integration under realistic field conditions: Experience in a giant Middle-Eastern reservoir. SPE Annual Technical Conference and Exhibition, Society of Petroleum Engineers.
Raiswell, R. and Berner, R. A. (1985). "Pyrite formation in euxinic and semi-euxinic sediments." American Journal of Science **285**(8): 710-724.
Rarity, F., van Lanen, X. M. T., Hodgetts, D., Gawthorpe, R. L., Wilson, P., Fabuel-Perez, I. and Redfern, J. (2013). "LiDAR-based digital outcrops for sedimentological analysis: workflows and techniques." Geological Society, London, Special Publications **387**(1): 153-183.
Riding, R. (2000). "Microbial carbonates: the geological record of calcified bacterial–algal mats and biofilms." Sedimentology **47**: 179-214.
Riding, R. (2002). "Structure and composition of organic reefs and carbonate mud mounds: concepts and categories." Earth-Science Reviews **58**(1-2): 163-231.

Riding, R. (2008). "Abiogenic, microbial and hybrid authigenic carbonate crusts: components of Precambrian stromatolites." Geologia Croatia **61**(2-3): 73-103.

Riding, R. (2011). Microbialites, Stromatolites, and Thrombolites. *In:* Encyclopedia of Geobiology. (Eds) Reitner, J. and Thiel, V., Springer Netherlands**:** 635-654.

Rittersbacher, A., Buckley, S. J., Howell, J. A., Hampson, G. J. and Vallet, J. (2013). "Helicopter-based laser scanning: a method for quantitative analysis of large-scale sedimentary architecture." Geological Society, London, Special Publications **387**: 1-19.

Roberts, H. H. and Moore, C. H., Eds. (1971). Recently cemented aggregates (Grapestones), Grand Cayman Island, B.W.I. Baltimore.

Rose, C. V. and Maloof, A. C. (2010). "Testing models for post-glacial 'cap dolostone' deposition: Nuccaleena Formation, South Australia." Earth and Planetary Science Letters **296**(3-4): 165-180.

Rotevatn, A., Buckley, S. J., Howell, J. A. and Fossen, H. (2009). "Overlapping faults and their effect on fluid flow in different reservoir types: A LIDAR-based outcrop modeling and flow simulation study." AAPG Bulletin **93**(3): 407-427.

Russo, F., Gautret, P., Mastandrea, A. and Perri, E. (2006). "Syndepositional cements associated with nannofossils in the Marmolada Massif: Evidences of microbially mediated primary marine cements? (Middle Triassic, Dolomites, Italy)." Sedimentary Geology **185**: 267-275.

Sami, T. T. and James, N. P. (1993). "Evolution of an early Proterozoic foreland basin carbonate platform, lower Pethei Group, Great Slave Lake, north-west Canada." Sedimentology **40**(3): 403-430.

Samier, P., Quettier, L. and Thiele, M. (2002). "Applications of Streamline Simulations to Reservoir Studies." SPE Reservoir Evaluation & Engineering **5**(4): 324 - 332.

Saylor, B. Z. (2003). "SEQUENCE STRATIGRAPHY AND CARBONATE–SILICICLASTIC MIXING IN A TERMINAL PROTEROZOIC FORELAND BASIN, URUSIS FORMATION, NAMA GROUP, NAMIBIA." Journal of Sedimentary Research **73**(2): 264-279.

Saylor, B. Z., Grotzinger, J. P. and Germs, G. J. B. (1995). "Sequence stratigraphy and sedimentology of the Neoproterozoic Kuibis and Schwarzrand Subgroups (Nama Group), southwestern Namibia." Precambrian Research **73**: 153-171.

Schalk, K. and Germs, J. (1980). "The geology of the Mariental area. Explanation of Sheet 2416 (scale 1:250 000)." Geological Survey of Namibia, Windhoek.

Schieber, J. r. (1998). "Possible indicators of microbial mat deposits in shales and sandstones: examples from the Mid-Proterozoic Belt Supergroup, Montana, U.S.A." Sedimentary Geology **120**(1): 105-124.

Schneider, J., Boni, M., Laukamp, C., Bechstadt, T. and Petzel, V. (2008). "Willemite (Zn2SiO4) as a possible Rb–Sr geochronometer for dating nonsulfide Zn–Pb mineralization: Examples from the Otavi Mountainland (Namibia)." Ore Geology Reviews **33**(2): 152-167.

Schoenherr, J., Littke, R., Urai, J. L., Kukla, P. A. and Rawahi, Z. (2007). "Polyphase thermal evolution in the Infra-Cambrian Ara Group (South Oman Salt Basin) as deduced by maturity of solid reservoir bitumen." Organic Geochemistry **38**(8): 1293-1318.

Schoenherr, J., Reuning, L., Kukla, P. A., Littke, R., Urai, J. L., Siemann, M. and Rawahi, Z. (2009). "Halite cementation and carbonate diagenesis of intra-salt reservoirs from the Late Neoproterozoic to Early Cambrian Ara Group (South Oman Salt Basin)." Sedimentology **56**(2): 567-589.

Schröder, S., Grotzinger, J., Amthor, J. and Matter, A. (2005). "Carbonate deposition and hydrocarbon reservoir development at the Precambrian–Cambrian boundary: The Ara Group in South Oman." Sedimentary Geology **180**(1-2): 1-28.

Scotese, C. R. (2009). "Late Proterozoic plate tectonics and palaeogeography: a tale of two supercontinents, Rodinia and Pannotia." Geological Society, London, Special Publications **326**(1): 67-83.

Sech, R. P., Jackson, M. D. and Hampson, G. J. (2009). "Three-dimensional modeling of a shoreface-shelf parasequence reservoir analog: Part 1. Surface-based modeling to capture high-resolution facies architecture." AAPG Bulletin **93**(9): 1155-1181.

Seifert, D. and Jensen, J. (2000). "Object and pixel-based reservoir modeling of a braided fluvial reservoir." Mathematical Geology **32**(5): 581-603.

Shapiro, R. S. (2000). "A Comment on the Systematic Confusion of Thrombolites." PALAIOs **15**(2): 166-169.

Shekhar, R., Sahni, I., Benson, G., Agar, S., Amour, F., Tomas, S., Christ, N., Alway, R., Mutti, M., Immenhauser, A., Karcz, Z. and Kabiri, L. (2014). "Modelling and simulation of a Jurassic carbonate ramp outcrop, Amellago, High Atlas Mountains, Morocco." Petroleum Geoscience **20**(1): 109-123.

Shen, B., Dong, L., Xiao, S. and Kowalewski, M. Ç. (2008). "The Avalon explosion: evolution of Ediacara morphospace." Science **319**(5859): 81-84.

Shields, G. A. (2005). "Neoproterozoic cap carbonates: a critical appraisal of existing models and the plumeworld hypothesis." Terra Nova **17**(4): 299-310.

Shinn, E. A. (1969). "Submarine lithification of Holocene carbonate sediments in the Persian Gulf." **12/1-2**: 109-144.

Shinn, E. A., Robbin, D. M., Lidz, B. H. and Hudson, J. H. (1983). "Influence of deposition and early diagenesis on porosity and chemical compaction in two Paleozoic buildups: Mississippian and Permian age rocks in the Sacramento Mountains, New Mexico." SEPM Core Workshop **4**: 182-222.

Sial, A. N., Dardenne, M. A., Misi, A., Pedreira, A. J., Gaucher, C., Ferreira, V. P., Silva Filho, M. A., Uhlein, A., Pedrosa-Soares, A. C., Santos, R. V., Egydio-Silva, M., Babinski, M., Alvarenga, C. J. S., Fairchild, T. R. and Pimentel, M. M. (2009). The Sao Francisco Palaeocontinent. *In:* Developments in Precambrian Geology. (Eds) C. Gaucher, A., N. Sial, H. E. Frimmel, and Halverson, G. P., Elsevier. **Volume 16:** 31-69.

Sloan, R. (2003). Quantification of Uncertainty in Recovery Efficiency Predictions: Lessons Learned from 250 Mature Carbonate Fields. SPE Annual Technical Conference and Exhibition,. Denver, Colorado, 5-8 October, Society of Petroleum Engineers.

Smith, A. G. (2009). "Neoproterozoic timescales and stratigraphy." Geological Society, London, Special Publications **326**(1): 27-54.

Stern, R. J. (2008). "Neoproterozoic crustal growth: The solid Earth system during a critical episode of Earth history." Gondwana Research **14**(1-2): 33-50.

Strebelle, S. (2002). "Conditional simulation of complex geological structures using multiple-point statistics." Mathematical Geology **34**(1): 1-21.

Strebelle, S. and Levy, M. (2008). "Using multiple-point statistics to build geologically realistic reservoir models: the MPS/FDM workflow." Geological Society, London, Special Publications **309**(1): 67-74.

Szilas, A. P. (2010). Production and transport of oil and gas. Amsterdam, Elsevier.

Taware, S. V., Park, H.-y., Datta-Gupta, A., Bhattacharya, S., Tomar, A., Kumar, M. and Rao, H. (2012). Well placement optimization in a mature carbonate waterflood using streamline-based quality maps. SPE Oil and Gas India Conference and Exhibition, Society of Petroleum Engineers.

Thiele, M. R., Batycky, R. P., Blunt, M. J. and Orr, F. M., Jr. (1996). "Simulating Flow in Heterogeneous Systems Using Streamtubes and Streamlines." SPE Reservoir Engineering **11**(1): 5-12.

Thiele, M. R., Batycky, R. P. and Fenwick, D. H. (2010). "Streamline Simulation for Modern Reservoir-Engineering Workflows." Journal of Petroleum Technology **62**(1): 64 - 70.

Tissot, B. and Welte, D. (1978a). Identification of Source Rocks. *In:* Petroleum Formation and Occurrence. Berlin Heidelberg, Springer 429-471.

Tissot, B. and Welte, D. (1978b). Kerogen: Composition and Classification. *In:* Petroleum Formation and Occurrence. Berlin Heidelberg, Springer 123-147.

Tissot, B. P. and Welte, D. H. (1978c). Production and Accumulation of Organic Matter The Organic Carbon Cycle. *In:* Petroleum Formation and Occurrence. Berlin Heidelberg, Springer**:** 3-13.

Tojo, B., Katsuta, N., Takano, M., Kawakami, S. and Ohno, T. (2007). "Calcite dolomite cycles in the Neoproterozoic Cap carbonates, Otavi Group, Namibia." Geological Society, London, Special Publications **286**(1): 103-113.

Tomás, S., Zitzmann, M., Homann, M., Rumpf, M., Amour, F., Benisek, M., Marcano, G., Mutti, M. and Betzler, C. (2009). "From ramp to platform: building a 3D model of depositional geometries and facies architectures in transitional carbonates in the Miocene, northern Sardinia." Facies **56**(2): 195-210.

Tucker, M. E. and Wright, V. P. (1990). Carbonate sedimentology. Oxford, Blackwell.

Underwood, C. A., Cooke, M. L., Simo, J. A. and Muldoon, M. A. (2003). "Stratigraphic controls on vertical fracture patterns in Silurian dolomite, northeastern Wisconsin." AAPG Bulletin **87**(1): 121-142.

Vasconcelos, C., Warthmann, R., McKenzie, J. A., Visscher, P. T., Bittermann, A. G. and van Lith, Y. (2006). "Lithifying microbial mats in Lagoa Vermelha, Brazil: Modern Precambrian relics?" Sedimentary Geology **185**(3): 175-183.

Verwer, K., Merino-Tome, O., Kenter, J. A. M. and Della Porta, G. (2009). "Evolution of a High-Relief Carbonate Platform Slope Using 3D Digital Outcrop Models: Lower Jurassic Djebel Bou Dahar, High Atlas, Morocco." Journal of Sedimentary Research **79**(6): 416-439.

Vieira, L. C., Trindade, R. I. F., Nogueira, A. C. R. and Ader, M. (2007). "Identification of a Sturtian cap carbonate in the Neoproterozoic Sete Lagoas carbonate platform, Bambuı Group, Brazil." Comptes Rendus Geosciences **339**(1-4): 240-258.

Viola, G., Kounov, A., Andreoli, M. A. G. and Mattila, J. (2012). "Brittle tectonic evolution along the western margin of South Africa: More than 500Myr of continued reactivation." Tectonophysics **514-517**: 93-114.

Viola, G., Mancktelow, N. S. and Miller, J. A. (2006). "Cyclic frictional-viscous slip oscillations along the base of an advancing nappe complex: Insights into brittle-ductile nappe emplacement mechanisms from the Naukluft Nappe Complex, central Namibia." Tectonics **25**(3): TC3016.

Wilkinson, B. H. and Drummond, C. N. (2004). "Facies Mosaics Across the Persian Gulf and Around Antigua - Stochastic and Deterministic Products of Shallow-Water Sediment Accumulation." Journal of Sedimentary Research **74**(4): 513-526.

Williams, G., Mansfield, M., MacDonald, D. and Bush, M. (2004). Top-down reservoir modelling. SPE Annual Technical Conference and Exhibition. Houston, Texas, Society of Petroleum Engineers.

Williams, H. D., Burgess, P. M., Wright, V. P., Della Porta, G. and Granjeon, D. (2010). "Investigating Carbonate Platform Types: Multiple Controls and a Continuum of Geometries." Journal of Sedimentary Research **81**(1): 18-37.

Wilson, C. E., Aydin, A., Durlofsky, L. J., Boucher, A. and Brownlow, D. T. (2011a). "Use of outcrop observations, geostatistical analysis, and flow simulation to investigate structural controls on secondary hydrocarbon migration in the Anacacho Limestone, Uvalde, Texas." AAPG Bulletin **95**(7): 1181-1206.

Wilson, C. E., Aydin, A., Karimi-Fard, M., Durlofsky, L. J., Sagy, A., Brodsky, E. E., Kreylos, O. and Kellogg, L. H. (2011b). "From outcrop to flow simulation: Constructing discrete fracture models from a LIDAR survey." AAPG Bulletin **95**(11): 1883-1905.

Winland, H. D. and Matthews, R. K. (1974). "Origin and significance of grapestones, Bahama Islands." **44/3**: 921-927.

Winterleitner, G., Le Heron, D. P., Mapani, B., Vining, B. A. and McCaffrey, K. J. W. (2014). "Styles, origins, and implications of syn-depositional deformation structures in Ediacaran microbial carbonates (Nama Basin, Namibia)." Geological Society, London, Special Publications **In press**.

Wolf, K. H. (1965). "Petrogenesis and paleoenvironment of Devonian algal limestones of New South Wales." **4/1-2**: 113-178.

Wood, R. A. (2011). "Paleoecology of the earliest skeletal metazoan communities: Implications for early biomineralization." Earth-Science Reviews **106**(1): 184-199.

Wood, R. A., Grotzinger, J. P. and Dickson, J. A. D. (2002). "Proterozoic Modular Biomineralized Metazoan from the Nama Group, Namibia." Science **296**(5577): 2383-2386.

Wright, V. P. (2012). "Lacustrine carbonates in rift settings: the interaction of volcanic and microbial processes on carbonate deposition." Geological Society, London, Special Publications **370**(1): 39-47.

Xiao, S. and Laflamme, M. (2009). "On the eve of animal radiation: phylogeny, ecology and evolution of the Ediacara biota." Trends in Ecology & Evolution **24**(1): 31-40.

Xu, H., Dai, J. and Dutta, N. (2003). Using rock physics for pseudo well log construction. *In:* SEG Technical Program Expanded Abstracts 2003**:** 1680-1683.

Zhang, T., Bombarde, S., Strebelle, S. B. and Oatney, E. (2006). "3D Porosity Modeling of a Carbonate Reservoir Using Continuous Multiple-Point Statistics Simulation." SPE Journal **11**(3): pp. 375-379.

# Appendices

# APPENDIX I

Sedimentary Geology 294 (2013) 1–12

Contents lists available at ScienceDirect

Sedimentary Geology

journal homepage: www.elsevier.com/locate/sedgeo

# Microbialite recovery in the aftermath of the Sturtian glaciation: Insights from the Rasthof Formation, Namibia

Erwan Le Ber [a,*], Daniel P. Le Heron [a], Gerd Winterleitner [a], Dan W.J. Bosence [a], Bernie A. Vining [a,b], Fred Kamona [c]

[a] Earth Sciences Department, Queen's Building, Royal Holloway University of London, Egham, Surrey TW20 0EX, UK
[b] Baker Hughes, Bentley Hall, Blacknest, Alton, Hampshire GU34 4PU, UK
[c] Geology Department, University of Namibia, Windhoek, Namibia

ARTICLE INFO

*Article history:*
Received 6 February 2013
Received in revised form 1 May 2013
Accepted 8 May 2013
Available online 16 May 2013

Editor: B. Jones

*Keywords:*
Cap carbonate
Stromatolites
Cryogenian

ABSTRACT

Ice sheet meltback in the aftermath of the Sturtian (mid Cryogenian) glaciation was accompanied or followed by deposition of thick carbonate successions. In northern Namibia, the Rasthof Formation is a 200–400 m thick cap carbonate sequence divided into (1) a basal cap dolostone, (2) a microbial member and (3) an epiclastic member. This subdivision applies for >100 km along strike at the southern and western edges of the Owambo Basin. In this paper we focus essentially on macrofacies of the cap dolostone and the microbial member. Cap dolostones are commonly interpreted as subtidal to deep water deposits, with delicate mm thick laminae. We describe well-preserved, ungraded hummocky cross-stratification in the cap dolostone, expected to occur no deeper than the offshore transition zone. The overlying microbial member contains thickly laminated microbialites with folded and contorted intervals interpreted as soft-sediment deformation structures. The thickly laminated microbialites are followed by more thinly laminated microbialites, with "roll-up" structures and more unusual individual, vertical stromatolite morphologies. We interpret the vertical growths in the microbial member as a direct response to the changing environment. The new observations and interpretations presented in this paper contrast with previous work on the Rasthof Formation. We recognise a relatively shallower setting associated with a trend in the geometries of the microbial member.



## 1. Introduction

The style and intensity of glaciation, together with the nature of post-glacial climatic recovery, from the Sturtian icehouse event remain vigorously debated (e.g. Eyles and Januszcak, 2004, 2007; Fairchild and Kennedy, 2007; Allen and Etienne, 2008; Eyles, 2008; Le Heron et al., 2011; Le Heron, 2012). At least two glacial events punctuated the Neoproterozoic, the older Sturtian (750 Ma) and the younger Marinoan (635 Ma) event, sediments from which are preserved worldwide, including northern Namibia. The glaciogenic sediments are sharply overlain by a ~10 m cap dolostone unit, with mm thick laminae (Hoffman and Schrag, 2002; Shields, 2005; Hoffman et al., 2007). The cap dolostones deposited after the Marinoan glacial event have unusual features such as sheet-crack cements, low angle cross stratification, tube structures, tepee-like structures, giant wave ripples and seafloor crystal fans (Corsetti and Grotzinger, 2005; Corkeron, 2007; Hoffman et al., 2007; Hoffman and MacDonald, 2010; Rose and Maloof, 2010). They are more widely studied than the post Sturtian cap dolostones, in which these features are absent. Cap dolostones represent a real challenge in terms of interpreting sedimentation processes, timing of deposition and paleoenvironment interpretation (Hoffman et al., 2007; Loyd and Corsetti, 2010; Rose and Maloof, 2010; Kennedy and Christie-Blick, 2011). The cap dolostones often represent the base of what is termed the "cap carbonate sequence" (Hoffman and Schrag, 2002); sediments overlying the cap dolostone can include massive carbonates, transgressive shales or siltstones (Shields, 2005). In this study, we describe and interpret a cap carbonate sequence – the Rasthof Formation – preserved above a Sturtian glacial succession in Namibia. The scope of our study includes both the cap dolostone and its overlying microbialites.

Several recent studies focused on the Rasthof Formation in north-west Namibia with observations made on the cap dolostone and the microbialites. Publications cover several disciplines, encompassing outcrop studies (Hedberg, 1979; Hoffman and Halverson, 2008; Pruss et al., 2010), isotopic analyses (Yoshioka et al., 2003; Tojo et al., 2007; Pruss et al., 2010) and microscopic investigation (Pruss et al., 2010; Bosak et al., 2011, 2012). The Rasthof Formation was initially named the Rasthof Member (Hedberg, 1979). It is interpreted as a shoaling-upward succession, with the cap dolostone deposited in the deepest environment followed by sublittoral stromatolites (Halverson et al., 2005). An abundance of soft sediment deformation structures has been described (Hoffman and Halverson, 2008; Pruss et al., 2010), creating a chaotic aspect despite continuous laminae. Most recently the

* Corresponding author.
*E-mail addresses:* e.leber@es.rhul.ac.uk, leber.erwan@gmail.com (E. Le Ber).

0037-0738/$ – see front matter 
http://dx.doi.org/10.1016/j.sedgeo.2013.05.003

microbial member has been interpreted as a deep-water microbial ecosystem in the Warmquelle–Okaaru area (Fig. 1A) (Pruss et al., 2010), on account of the lack of bedforms, scour marks and intraclasts. Petrographic studies have revealed the occurrence of possible early agglutinated foraminifera in the microbial member (Bosak et al., 2012; Dalton et al., 2013). The aim of the present paper is to describe the Rasthof Formation at the Rasthof Farm locality. New sedimentological observations from the type area are presented, they suggest that the cap carbonate was deposited in substantially shallower water than suggested elsewhere. This interpretation has major implications both for facies models on the post-Sturtian carbonate platform and, potentially, for the interpreted magnitude of postglacial sea level rise.

## 2. Study area and stratigraphy

The Rasthof Formation was deposited on the Northern Platform and is well exposed along the edges of the Kamanjab Inlier, north-west Namibia (Fig. 1A). A regional model suggests that the Kamanjab Inlier is a basement high that created ridges separating platform facies to the north from slope facies to the south (Hoffman and Halverson, 2008). This paper presents data from the type section at Rasthof Farm, north of the Kamanjab Inlier and, therefore, on the platform.

Detailed previous studies of the platform were focused more than 50–100 km to the north-west and west. The cap dolostone and/or the microbial member were examined in the vicinity of Warmquelle, Okaaru and Ongongo localities (Yoshioka et al., 2003; Tojo et al., 2007; Hoffman and Halverson, 2008; Pruss et al., 2010; Bosak et al., 2011, 2012; Dalton et al., 2013). Hoffman and Halverson, 2008 also described the Rasthof Formation in the Northern Margin Zone, south of the Kamanjab Inlier. The type area of the unit ("Rasthof Member": Hedberg, 1979) in Rasthof Farm has, surprisingly, not been subject to detailed investigations.

In northern Namibia the Otavi Group (Fig. 1B) was deposited after the break-up of Rodinia (recorded by syn-rift sediments of the Nosib Group) and prior to the Pan African Orogen (recorded by molasse deposits of the Mulden Group) (Frimmel et al., 2011). The Otavi Group accumulated on an extensive carbonate platform lining the southern edge of the Congo Craton. It starts with the Ombombo Subgroup, consisting of mixed carbonate and siliciclastic sediments. These deposits are overlain by glacial sediments of the Chuos Formation, which are in turn followed by the Rasthof, Gruis and Ombaatjie formations; forming the Abenab Subgroup. A second glacial succession, the Ghaub Formation, is overlain by carbonate sediments, forming the Tsumeb Subgroup (Hoffmann and Prave, 1996).

On the Northern Platform, the Chuos Formation bears evidence of direct ice contact (subglacial shear zones, dropstones, ice-contact fans) with two glacial cycles preserved (Le Heron et al., 2013). The overlying 200–400 m thick Rasthof Formation rests in sharp contact,

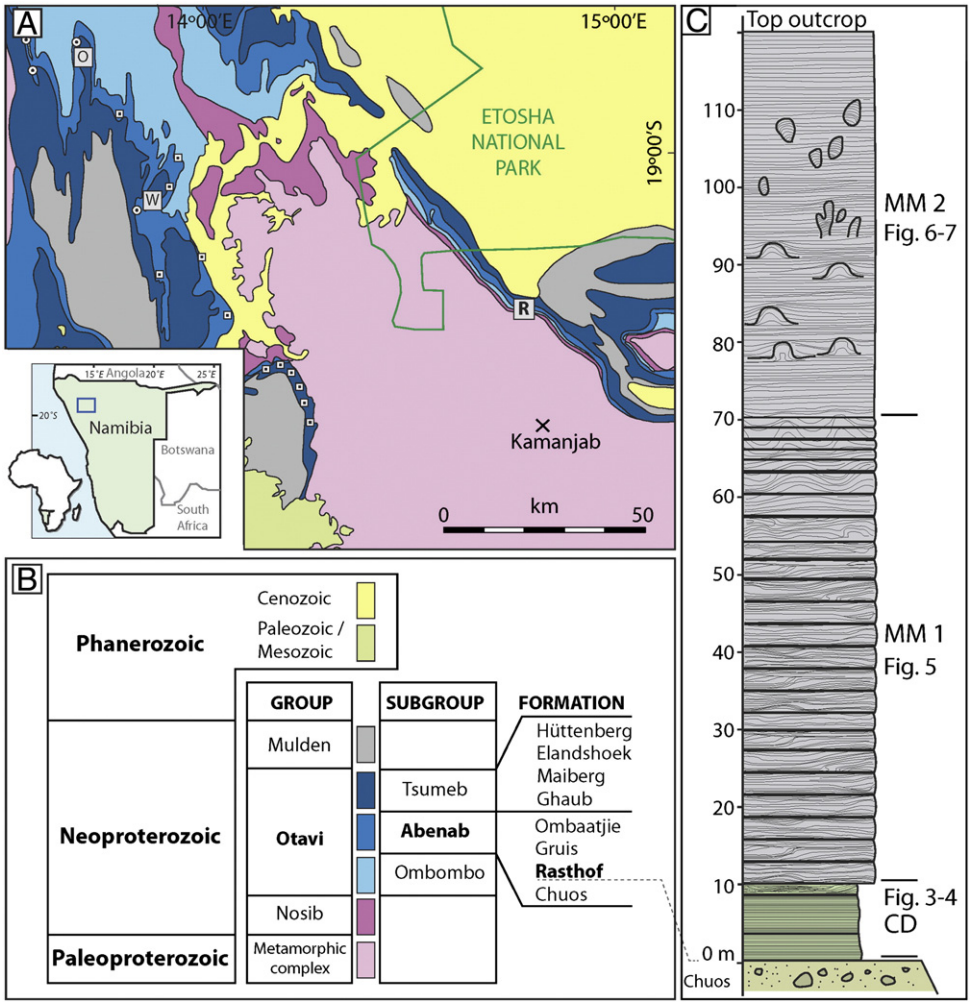


**Fig. 1.** Outcrop location and lithostratigraphy of the Otavi Group. A. Simplified geological map of the area (modified from Hoffman and Halverson, 2008), "R" is the location of the Rasthof Farm, ⊡ are the sections described by Hoffman and Halverson, 2008, ʘ are sections described by Pruss et al. (2010). "O" and "W" indicate Okaaru and Warmquelle areas. B. Stratigraphy of the Otavi Group, from Hoffman and Halverson, 2008. C. Idealized log of the section at Rasthof Farm, with references to others figures: Figs. 3–4 (deformation and hummocky cross-stratification, top cap dolostone); Fig. 5 (facies of MM1); and Figs. 6 and 7 (facies of MM2).

but without any evident unconformity, on the Chuos Formation. It starts with a "cap dolostone" also locally termed "rhythmite" or "abiotic member" (Hoffman and Halverson, 2008; Pruss et al., 2010), in which cm to dm thick allodapic beds alternate with m thick delicately laminated dolostone (Yoshioka et al., 2003; Tojo et al., 2007; Hoffman and Halverson, 2008). The cap dolostone is concordantly overlain by the microbial member (Hoffman and Halverson, 2008). Pruss et al. (2010) differentiated two types of facies in the microbial member: thickly and thinly laminated microbial mats, both exhibiting unusual styles of deformations interpreted as synsedimentary. Thickly laminated mats are characterised by several dm to m wide folds/dome like structures and more chaotic intervals. The thinly laminated mats are generally flat but still exhibit cm scale roll-up structures (Pruss et al., 2010).

In the Warmquelle–Khowarib area, the cap dolostone has previously been interpreted to record sub-storm wave base deposition (Yoshioka et al., 2003; Tojo et al., 2007). The microbial member was first interpreted by Hedberg (1979), on the northern flank of the Kamanjab Inlier, as a shallow water formation. This hypothesis is supported by the observation of microbial mats, oolites and intraformational breccias. The precise locations of Hedberg's observations are, however, unclear. Our study is located in the vicinity of where Hedberg first described the Rasthof Formation. The microbial member has more recently been recognised in the Warmquelle–Okaaru area (Fig. 1A, "W" and "O") of Pruss et al. (2010). There, it is interpreted as a deep water sub-storm wave base microbialite where fluid escape generated sedimentary dykes associated with soft-sediment deformation. Formation of the dykes may have been facilitated by tectonic activity.

## 3. Field observations

### 3.1. Outcrop overview

The Rasthof Formation is described at Rasthof Farm, where it is subvertical, dipping steeply north-east into the Owambo Basin. The log presented in Fig. 1C is idealized and represents observations compiled from along the outcrop. Lateral variability of the observed facies is still to be established. The contact with the underlying Chuos Formation is not apparent at this section, with the cap dolostone occupying low terrain and the microbial member present as a hill-forming unit. From afar (Fig. 2) the lower part of the outcrop exhibits a layer cake character; overlying strata are more massive in character with a less bedded aspect. Careful examination reveals that the layer cake character corresponds to the thickly laminated microbialites and the most continuous succession to the thinly laminated microbialites. We will refer to the thickly and thinly laminated microbialites respectively as the microbial member 1 (MM1) and microbial member 2 (MM2). In the following, we describe the cap dolostone, and both microbial members (Fig. 1C).

### 3.2. Cap dolostone

The contact with the Chuos Formation is concealed, but exposure quality improves upsection. The ~10 m thick unit is dominated by delicate, mm scale horizontal parallel laminae. However, rare 1–10 cm thick beds of non-laminated, white to grey beds punctuate this facies. These beds pinch out laterally over 100 m and probably correspond to the allodapic beds described by Hoffman and Halverson, 2008. Overlying laminae show subtle downlap relationships onto the top surface of these beds (Fig. 3A). The latter deposits also exhibit deformation structures. These include 1) dm scale overturned folds, with wavelengths <20 cm and short limbs dipping at 45–90° and 2) 10 cm wide fault-bend folds, with a low angle thrust ramp (Fig. 3B, D). An undeformed, hummocky cross-stratified interval occurs in the upper 2 m of the cap dolostone (Fig. 4), forming low angle, concave and convex bounding surfaces. Laminae in these bedforms are approximately parallel to the bounding surfaces, with subtle lateral variation in dip angles and lamina thicknesses. Dip directions are scattered.

At Rasthof Farm, the contact with the overlying deposits (which we describe as microbial member 1) is locally abrupt (Fig. 3C). Cap

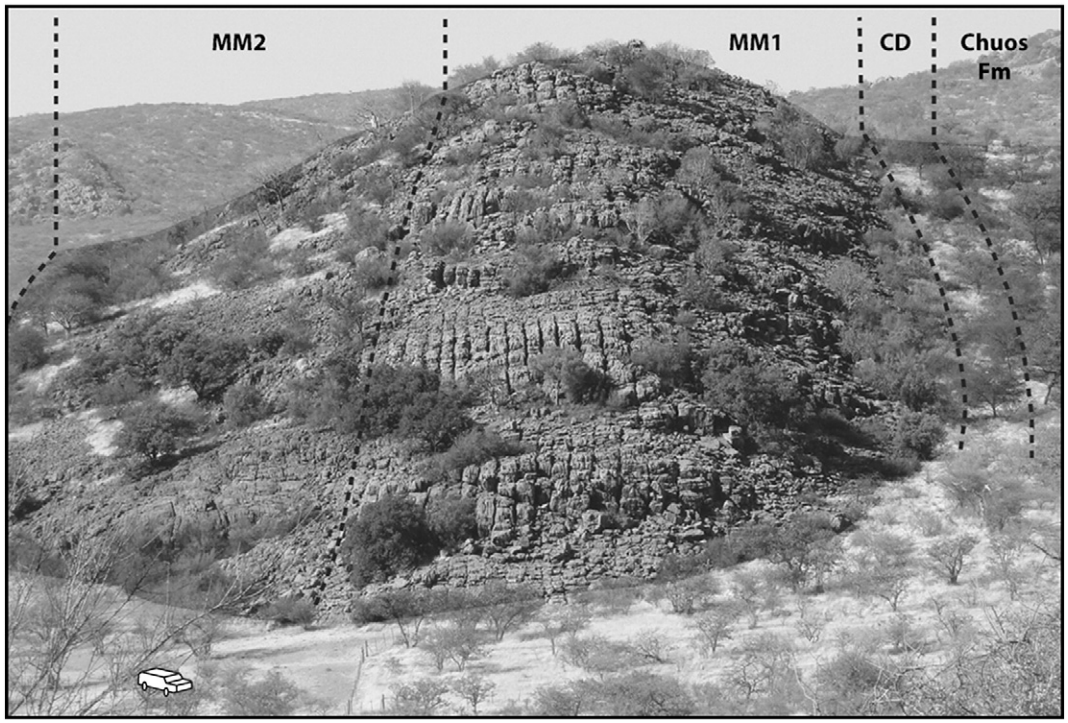


**Fig. 2.** A. View of the outcrop, looking southeast. Note the distinctions between the cap dolostone (CD), the microbial member 1 (MM1) and the microbial member 2 (MM2). MM1 is organised into 2–4 m thick beds and MM2 is more continuous. The white car is approximately 5 m long.

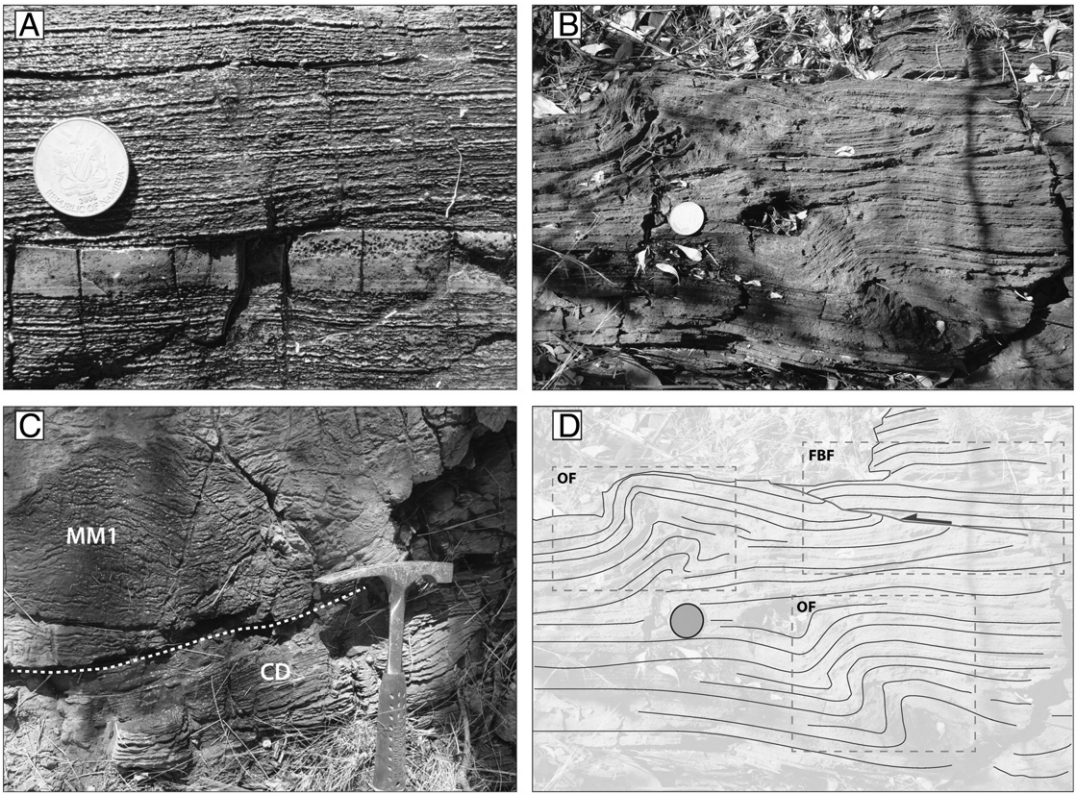


**Fig. 3.** Cap dolostone facies. Panel A shows thin and flat laminae, downlapping onto a white, non-laminated interval. Panels B and D show soft-sediment deformation structures in the cap dolostone. Two types of folds are observed: overturned folds (OF) and fault-bend folds (FBF). Note that the folds have the same orientation and probably represent different stages of deformation. Panel C shows sharp contact between the cap dolostone and MM1.

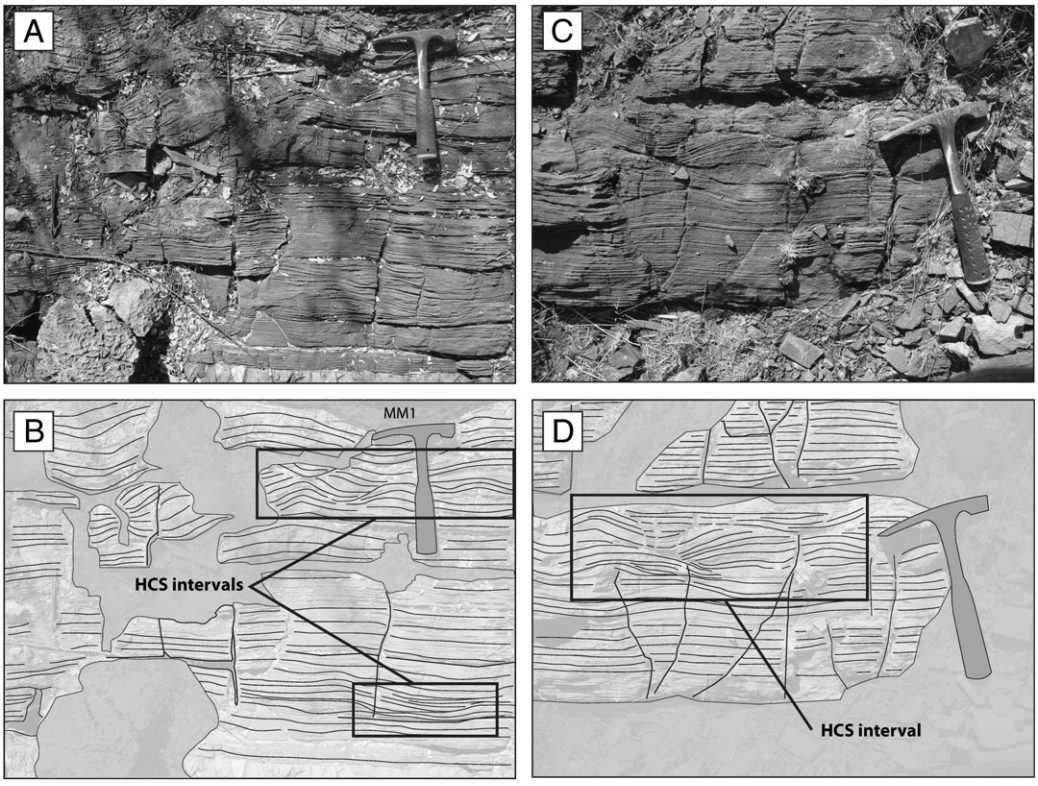


**Fig. 4.** Hummocky cross stratification (HCS): panels A, C (photos) and panels B, D (sketches), in the upper 2 m of the cap dolostone. The squares in panels B and D indicate the HCS intervals. Grey areas denote parts of the outcrop where facies are obscure as a result of weathering etc. On B, note the base of MM1 immediately above the HCS interval.

dolostone laminae generally change in thickness and become more crinkly and undulated. Recent weathering can lend a brecciated aspect to the upper few centimetres of the cap dolostone.

### 3.3. Microbial member 1 (MM1)

The microbial member 1 (MM1) is a ~60 m thick succession of thickly laminated microbialites. The facies consists of thin, sub-mm thick dark laminae, alternating with thicker (1–5 mm), crystalline laminae (Fig. 5A). Dolomitization of the formation makes observation of the primary textures complicated. Dark laminae consist of dolomicrite: these are generally continuous with local cloth-like thickenings. The light laminae are represented by an equigranular mosaic of subhedral dolomite. A similar type of crinkly laminae was described and analysed by Pruss et al. (2010) in the Rasthof Formation: they interpret thick light coloured laminae to record intervals of carbonate sedimentation outpacing the growth of microbial mats, whilst darker laminae result from microbially-induced precipitation. However, the same authors explain that no individual filaments are preserved.

The very base of this unit is characterised by crinkly laminae that grow on the top of the cap dolostone, sometime rising vertically with respect to bedding. When horizontal, undulation of the sets of laminae creates a series of weakly defined, laterally linked hemispheroids. The hemispheroids do not exceed 10 cm amplitude and wavelength. Laminae tend generally to form these undulating sets but are commonly deformed (Fig. 5B, C). Deformation consists of complex dm to m scale folds or contorted structures that do not show any preferential orientation. Rare break-up of sets can be observed at a dm scale (Fig. 5B), whilst discontinuities and thinning out of the laminae can be observed at a mm scale. These deformation structures are restricted to MM1 and are contained within individual intervals, with microbial laminae that recover a more horizontal aspect upsection. After 50 m, laminae tend to be less chaotic and flatter. They locally start to develop clear, 10 to 20 cm amplitude cone structures (Fig. 5D) indicating the arrival into microbial member 2 (MM2).

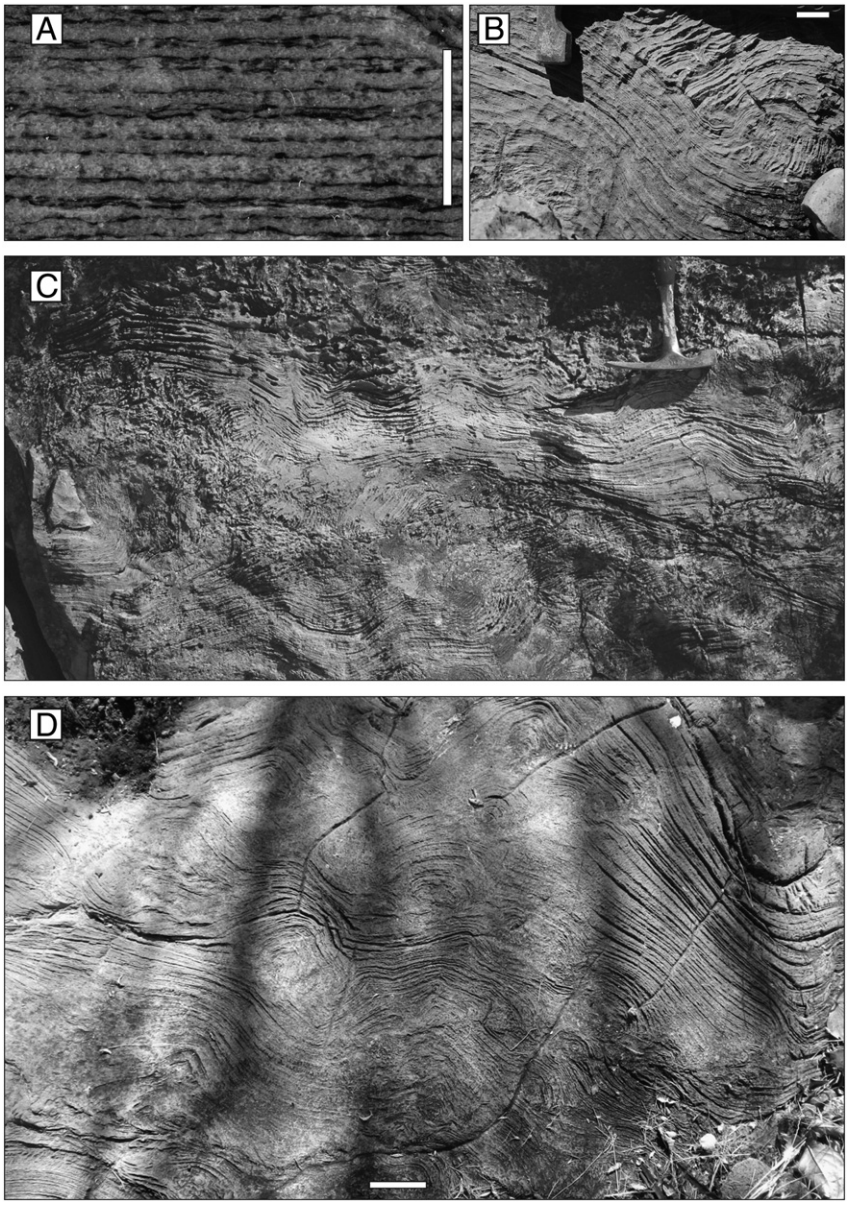


**Fig. 5.** MM1 facies. A. Mesoscale, showing thickly laminated microbialites. Thick, white equigranular mosaic of subhedral dolomite alternating with thin micritic laminae. Dark laminae are interpreted as microbial in origin (scale is 1 cm). B. Folded set of laminae (half bottom left) with angular contact with another set of laminae (top right corner). C. Typical MM1 facies with undulated bedsets. D. Upper facies found in MM1, with clearly differentiated, 10–20 cm high cones (scale is 10 cm).

### 3.4. Microbial member 2 (MM2)

The thinly laminated microbial mats of MM2 are organised differently to underlying deposits: light laminae are thinner (<1 mm), generally flat and parallel (i.e. no undulation). Locally, structures akin to roll-ups are recognised (Fig. 6): these consist of cm scale contorted intervals and can be fragmented. They lack a preferred orientation within beds, and occur adjacent to individual growths described below. Laminae above and below the contorted structures are perfectly flat and parallel.

In the lower part of MM2, horizontal laminae gradually increase in dip angle upward, approaching subvertical angles to form the flanks of 20–40 cm wide/high symmetrical dome structure (Fig. 7A and B). Above the domes, laminae recover a horizontal organisation, passing upward and gradationally into an overlying set of domes. These can be closely spaced laterally and vertically (<1 m). In other intervals upsection, very different structures occur: including up to 30 cm large columns, 10 cm large branching columns (Fig. 7C and D) or 10–20 cm wide individual morphologies probably part of a dense branching network (Fig. 7E and F). The laminae in these geometries are convex upward, whilst laminae between (where present) are concave upward (Fig. 7F) or almost horizontal. Local roll-up structures are observed close to the interface with the growth (Fig. 6B). In the geometries described above, laminated facies is obvious to a dm scale but more difficult to observe to a cm scale. This is due to an alternation of partly micro-clotted and discontinuous dark laminae with more continuous light laminae.

Sediments deposited between the columns and branching columns range between undisturbed, and different degrees of rolled-up and broken laminae. Where intergrowth laminae are broken, they form mm to cm diameter intraclasts and cm diameter void cement. Sedimentation around the individual growths can be complex and heterogeneous, with laminae on one side and intraclastic facies on the other side of the growth (Fig. 7F).

The thickness of the exposed microbial member 2 is ~50 m. A few metres from the top of the exposed section, individual microbial geometries disappear. The overlying facies of the Rasthof Formation are not exposed in the area. Previous studies done elsewhere on the Northern Platform mention a regional transition to grainstones and cross-bedded facies, with local tepee structures (Hoffman and Halverson, 2008; Pruss et al., 2010).

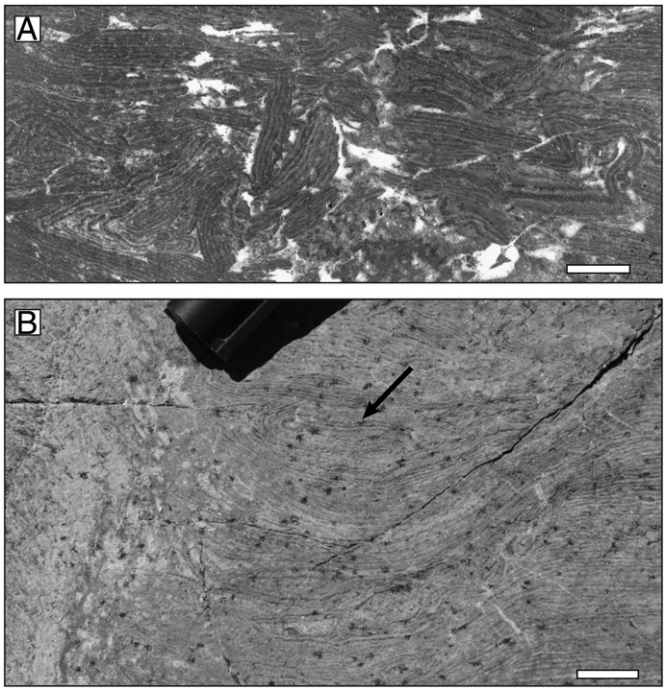


**Fig. 6.** Roll-up structures in MM2. A. Mix of rolled-up facies (left, right) and broken sets in the centre (scale is 1 cm). B. Rolled-up facies (arrow) sitting to the right side of a column formed of convex upward laminae (scale is 1 cm).

## 4. Petrographic description

Examination of thin sections in the cap dolostone, MM1 and MM2 have been undertaken to assess and compare grain sizes, with the aim to deduce variations in depositional energy between the different facies. Dolomitization occludes the detail of thin sections that we examined under a standard petrographic microscope. To resolve this, we placed a sheet of paper (80 gsm) under the thin sections to reveal the primary texture (Delgado, 1977). Photomicrographs were captured with a Nikon DS-5M camera. This approach reveals that sediments are laminated from the base to top, with lamina thicknesses in the range of <1 mm and <8 mm. Sub-mm thick, dark, fine grained laminae alternate with thicker light laminae. The latter contains grains and intraclasts.

In the cap dolostone (Fig. 8A, B), tens of μm thick, micritic dark laminae alternate with mm thick wackestone textures. Perfect rhombohedral crystals growing around or replacing initial grains are <20 μm. In the cap dolostone, several relatively large ovoid to circular morphologies occur (up to 100 μm, Fig. 8A), similar to those initially observed by Pruss et al. (2010). Non-laminated intervals found in the cap dolostone usually do not show any grain texture, yet infrequently reveal a packstone texture, with 20 to 100 μm "ghosts" of grains.

Upsection, grains size increases (Fig. 8B) to reach a size <75 μm. These grains probably consist of rolled material derived from the dark, fine-grained laminae, forming wackestone–packstone textures. In the deformed microbialites of MM1 (Fig. 8C, D), grains are slightly larger than in the cap dolostone. Textures vary between wackestone and grainstone and sporadic, mm scale intraclasts of well-preserved dark laminae can be found in the light laminae (Fig. 8D). Finally, in MM2 (Fig. 8E, F), facies found between the columns and branching columns exhibit large intraclasts (>100 μm).

## 5. Interpretations

### 5.1. Cap dolostone

The mm scale laminae in the cap dolostone compare well with that described from the basal Rasthof Formation elsewhere in Namibia (Yoshioka et al., 2003; Tojo et al., 2007; Hoffman and Halverson, 2008; Pruss et al., 2010), and more broadly to cap dolostones of different ages worldwide (Hoffman and Schrag, 2002; Shields, 2005). The fault-bend folds and monoclinal folds encountered in the upper part of this unit are interpreted as soft sediment deformation structures. This interpretation is supported by their intra-bed occurrence. We tentatively invoke a seismic origin for these soft-sediment deformations, possibly triggered by a post-glacial rebound after ice-melting (cf. Nogueira et al., 2003).

Allodapic beds are reported from elsewhere in the cap dolostone: a 1 m thick interval is recorded in the Warmquelle–Omutirapo area (Tojo et al., 2007 and personal observations). This turbidite contains dm-sized rip-up clasts, mud clasts, grading, and convolute bedding. On the foreslope of the platform, south of the Kamanjab Inlier, Hoffman and Halverson, 2008 report rhythmite facies associated with debris flows derived from the Northern Platform. No such facies are observed at Rasthof Farm. The non-laminated <10 cm layers are rare and do not exhibit any typical turbidite or allodapic sequence (Flügel, 2004). The packstone–wackestone textures imply comparatively energetic transport of sand-sized particles as bedload at intervals. Such energy levels might be attributable to 1) currents or more proximal storms events or 2) transport of material during seismic shocks.

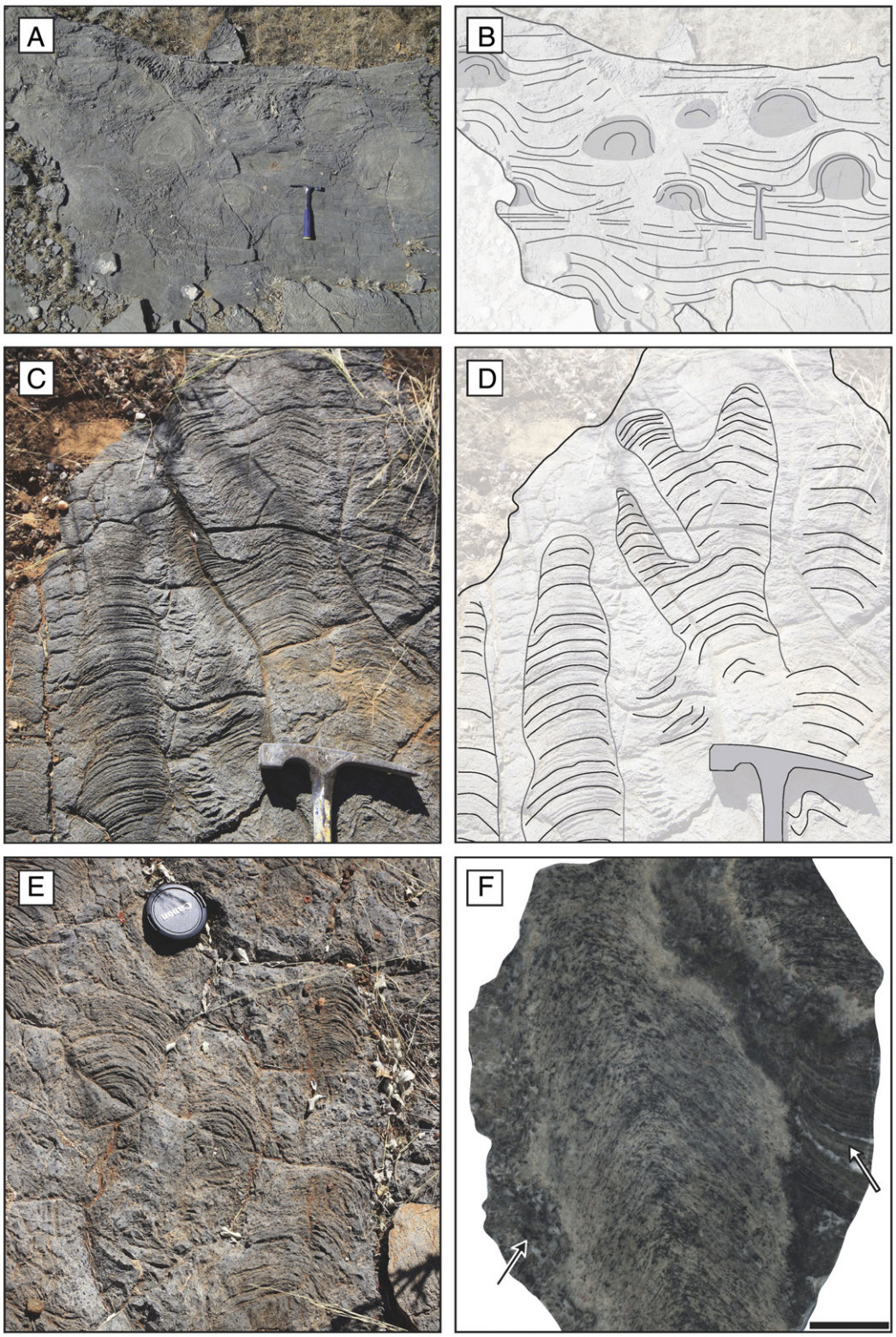


**Fig. 7.** Individual stromatolites morphologies in MM2. In panels A (photo) and B (sketch), thin laminae rise up to 90° to form individual dome geometries. Grey areas represent what was probably the "core" of these individual morphologies. Panels C (photo) and D (sketch) show branching columns. Another example of branching columns can also be observed as shown in panel E. Panel F is a polished sample from panel E, note the grainy facies (black arrow) and the laminated facies (white arrow) around the same growth. Scale is 2 cm.

At Rasthof Farm, the recognition of hummocky cross-stratification (HCS) is important because this structure confirms sedimentation in an energetic, comparatively shallow setting. HCS bedforms are recognised in a range of settings from outer shelf to intertidal environments (Cheel and Leckie, 1993), forming from the interaction of oscillatory gravity waves and possibly "combined" flows with geostrophic component superimposed (e.g. Dumas and Arnott, 2006). On the outcrop, the bases of the swales seem erosional, the absence of migrating ripples and soft-sediment deformation structures in HCS beds, coupled with the lack of massive grainstones underlying them, discounts a genesis

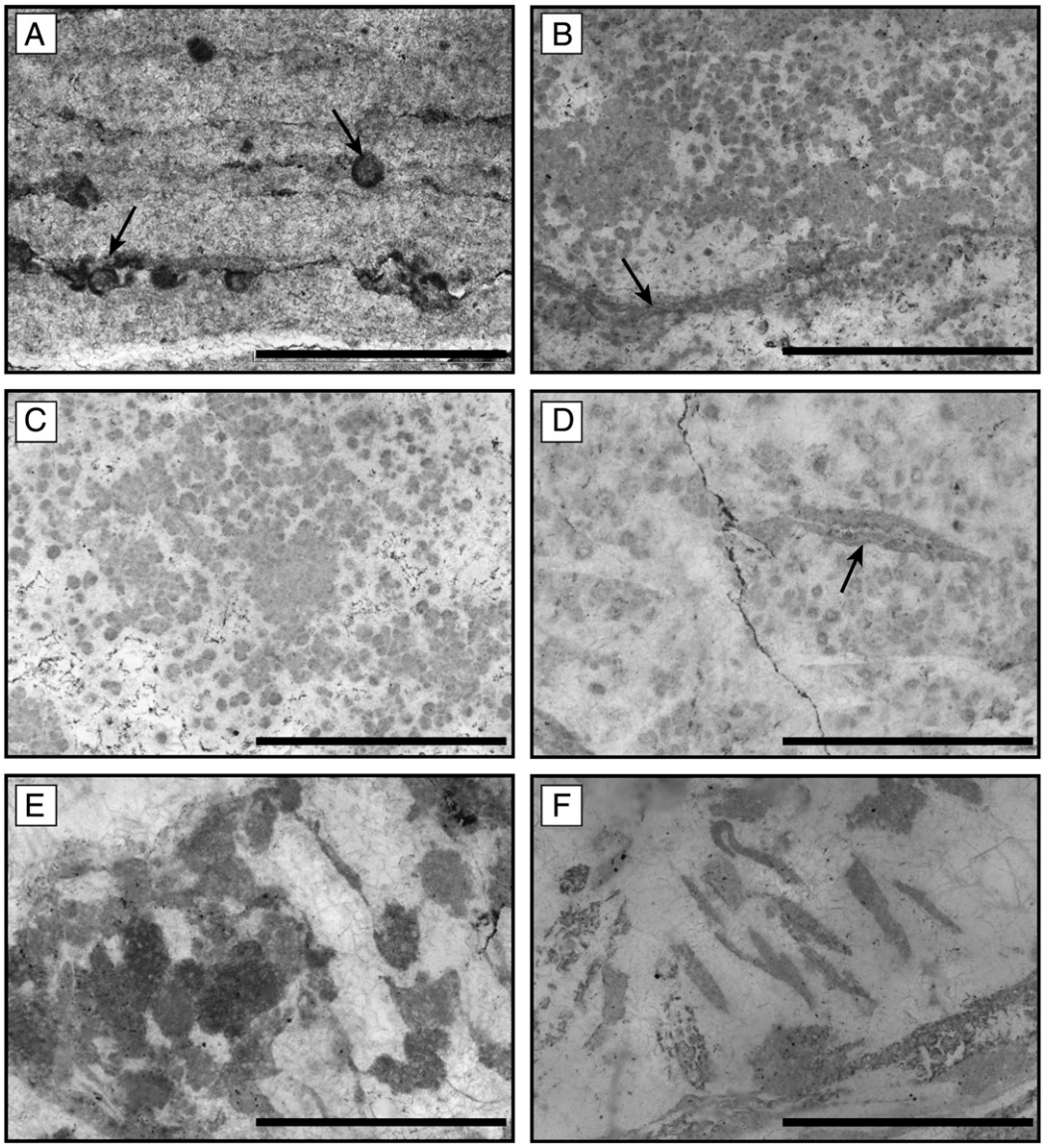


**Fig. 8.** Microfacies of the Rasthof Formation. Scale bar is 1 mm. A. Fine-grained cap dolostone facies and walled structures (arrows). B. Packstone–grainstone above a thin dark lamination (arrow). C Packstone–grainstone in MM1. D Packstone–grainstone in MM1, with an intraclast of dark lamination (arrow). E and F. Inter-columnar facies consisting of coarse intraclasts.

by turbidity currents (Mulder et al., 2009). The accumulation of at least the uppermost part of the cap dolostone, therefore, is interpreted to record deposition from storm wave activity.

The cap dolostone is described as the "abiotic member" by Hoffman and Halverson, 2008, meaning it is not biologically influenced and we agree. Occurrence of HCS at Rasthof Farm indicates that grains are not bound or trapped by microbial mats. Facies from the cap dolostone are only influenced by physical and chemical factors. Biogenic grains might be present as reworked material, but their incorporation does not imply a biogenic accumulation mechanism for the cap dolostone itself. For example, rounded and sometimes walled elements are observed (Fig. 8A). They compare in size and shape to those described and interpreted as putative eukaryotes by Pruss et al. (2010), Bosak et al. (2011, 2012) and Dalton et al. (2013) in the microbial member (80–100 km WNW from Rasthof Farm). The crinkly appearance of laminae less than 1 m above the HCS beds (basal MM1) marks the onset of microbial precipitation. We thus suggest that storm events and sea floor currents might have stimulated microbial colonization, distributing and seeding microbial communities with nutrients.

### 5.2. Microbial member 1 (MM1)

A microbial origin for MM1 is consistent with previously published interpretations (Hoffman and Halverson, 2008; Pruss et al., 2010), though no microbial filaments are preserved. Specifically, the recognition of "macroscopically layered authigenic microbial sediments with or without interlayered abiogenic precipitates" (Riding, 2011, p31) classifies them as stromatolites. The microbial origin of the unit coupled with 1) folds and contorted intervals and 2) the lack of thrust structures indicate that the stromatolites were cohesive but not lithified at the time of deformation. Under a stress regime, their rheology is more likely to be compared to a textile fabric or a rubbery material than a paper sheet.

At Rasthof Farm, no preferential orientation of the folds and no slump structures were observed, indicating a very low angle slope. Deformation styles range from gentle dm to m scale folds, contorted laminae and occasional break-up of the lamina sets (Fig. 5B). The scale of the structures and their occurrence between non deformed intervals, may suggest recurrent episodes of deformation. Cycles of quiescence to moderate energy (deposition of flat to undulated

laminae) punctuated by deformation episodes (folded and contorted strata) are thus recognised.

In previously studied outcrops (Fig. 1A), the deformation is assigned to early fluid escape during the sediment compaction, which also produced 0.5–1 m wide sedimentary dykes (Pruss et al., 2010). At Rasthof Farm, no such sedimentary dykes are observed; another process must have deformed the mats at this location. Sediments of the Rasthof Farm were also probably isolated from siliciclastic input and dominated by microbial mats. We can expect most of the grains to be trapped on the seafloor by these mats. Wave action can then shape and deform the cohesive mats with no resultant bedform. Deformed sets are >dm thick, limiting their breaking up. Furthermore, given the supposed cohesive nature of the mats upon deposition, no scour marks would be expected. To support this hypothesis at Rasthof Farm, we emphasise the occurrence of hummocky cross stratification in the underlying cap dolostone. HCS was formed in granular, non-biologically influenced sediments. In MM1, cohesive mats and trapping of grains prevented the generation of bedforms.

Thin section analysis demonstrates that grain size increases from the base to the top of the formation, consistent with a shoaling upward sequence as suggested by Halverson et al. (2005). Therefore, these data strongly imply that MM1 was deposited above the storm wave base. Furthermore, sedimentological evidence such as oolites (Hedberg, 1979) suggests that a shallow, high energy environment was present during Rasthof time in the area. At Rasthof Farm, the sediments might have been deposited between the storm wave base and an intertidal environment.

Whilst recurrent intervals of soft sediment deformation are inferred, pinpointing the trigger mechanism is challenging (e.g. Owen et al., 2011). Below, we consider two factors for the deformation in MM: storm wave impact and seismic shocks. Facies comparable to those of MM1 are unusual in the sedimentological record. The absence of sedimentary dykes excludes a fluid escape origin, whilst the lack of consistent orientation to the deformation structures likely excludes slope or gravity movements. However, since MM1 was deposited above the storm wave base, we argue that storm activity deformed the microbial mats. Also, given the depositional context of the Rasthof cap carbonate in the aftermath of the Chuos glacial event, fault re-activation during postglacial rebound cannot be excluded. For example, Nogueira et al. (2003) observed soft-sediment deformation in equivalent cap carbonates in Brazil, with rebound-induced earthquakes suggested. Soft-sediment deformation in microbial beds is commonly interpreted as a product of seismic activity (Kahle, 2002; Nogueira et al., 2003; Martín-Chivelet et al., 2011). However, a characteristic suite of deformation structures described in those papers (boudinages, pinch-and-swell structures, faults, kink bands, microbreccias) is missing from MM1. Note that a difference in lithology, with implications for rheology and cohesion, may also explain the restricted range of deformation structures and facies in the Rasthof Formation, compared to analogous deformed microbial mats from elsewhere.

Toward the top of MM1, laminae appear less chaotic and rise as dm high conical structures (Fig. 5D). Cones point upward and we do not interpret these structures as soft sediment deformations: rather, we interpret them as a stage of vertical microbial growth. Such a change compared to the underlying facies can be explained by overall increase in energy levels.

### 5.3. Microbial member 2 (MM2)

MM2 consists of thinly laminated microbialites (<1 mm) with local, cm scale, roll-up structures. Pruss et al. (2010) interpreted these geometries as the result of fluid escape perforating the sets of laminae. In the Rasthof Farm area, no dykes were observed below or nearby the roll-up structures; another process must be invoked at this location. Similar structures are described and interpreted in shelfal marine, possibly sub-photic settings (Simonson and Carney, 1999), in supra- to shallow subtidal environments (Schieber et al., 2007; Harwood and Sumner, 2011), and in lacustrine settings where they are interpreted as slope-generated slump structures (Dean and Fouch, 1983). Roll-up structures are not restricted to a single depositional environment. The occasionally broken sets of laminae in the roll-up structures form cm-sized intraclasts, and thus result from a relatively high energy event, strong enough to break the laminae.

The size of the rolled-up intervals (<dm) differs from the deformations in MM1 (>dm to m scale. To explain the different deformation styles and scales between MM1 and MM2, we can invoke: 1) different rheologies; 2) different rates of lithification of the sediments; 3) influence of solid vertical stromatolites (columns, domes) on water movement in MM2; 4) lack of seismic shock during the deposition of MM2. The second point is important: in MM1 sediments might not be lithified as quickly as in MM2. As a result, thick (>10 cm) sets of laminae can be deformed in MM1. In MM2, a more rapid lithification only allowed the deformation of the first few centimetres (e.g. 1–2 cm) of the seafloor. Thicknesses of deformed sets have a direct result on the rheology and deformation style, with large folds in MM1 and much smaller roll-up structures in MM2. Thinner deformed intervals also allowed easier breaking up of the sediments in MM2 (Fig. 6A). A more rapid lithification in MM2 is also supported by the occurrence of vertical growths. Laminae were locally able to stack for tens of centimetres and form solid geometries. Water energy (current, waves, storms) and paths were influenced by these growths, possibly also influencing abrasion power of water.

MM2 exhibits microbial morphologies not hitherto described from the Rasthof Formation in north-west Namibia. Other stromatolite morphologies occur (Cloud and Semikhatov, 1969; Miller, 2008) in the Berg Aukas Formations: lateral equivalent of the Rasthof Formation in north-east Namibia. Hedberg (1979) may have observed what we describe as dome structures: reference to “a peculiar algal growth which resembles the structure found in pillow lava” is made in his description of facies variations along the northern flank of the Kamanjab Inlier. Also, void-filling thrombolites are noted by Hoffman et al. (1998) on the Northern Platform.

The domes, column and branching column geometries are interpreted as individual stromatolite forms. Analysis of MM2 clearly demonstrates the co-occurrence of individual stromatolite geometries and inter-stromatolite sediments (non-laminated coarse material, thinly laminated facies with roll-up structures). Between the depositions of MM1 and MM2, a change in environmental parameters and lithification rate may have stimulated the development of well-established stromatolite geometries. In MM2, some microbial communities were able to develop into vertical and solid-structured stromatolites. Meanwhile, microbial communities between individual growths also flourished, producing flat horizontal laminae. At least the topmost of these in the succession were poorly lithified, readily deformable and fragmented shortly after deposition (producing roll-up structures, intraclasts).

It is often suggested that local vertical development of microbial laminae is related to increasing wave energy (Wright, 1990; Flügel, 2004). However, stromatolite geometries are influenced by many parameters (Grotzinger and Knoll, 1999; Dupraz et al., 2006), and there is no unequivocal correlation between morphologies and paleodepth or paleoenvironment. Thus, whilst using analogue stromatolite geometries from the literature may be problematic, analysis of inter-microbialite sediments (grain size, bedforms) may be more revealing. At Rasthof Farm, we observe intraclasts between or next to individual stromatolite mounds (Fig. 7F). Intraclasts record syndepositional events that were sufficiently energetic to break and rework non-lithified and cohesive sediments. Interestingly, we have observed completely reworked sediments on one side and preserved laminae on the other side of a vertical same growth (Fig. 7F). This means that energy in the environment is highly influenced by the relief of the stromatolites. Laminae deposited between the vertical growths can not only be well protected from current energy, but can also be destroyed and reworked.

## 6. Depositional model

A regional view of the carbonate platform during deposition of the Rasthof Formation was proposed by Hoffman and Halverson, 2008 and is adapted in Fig. 9A. In this model, the Rasthof Farm facies belong to the Northern Platform. Sediments possibly accumulated in a large lagoon or intra-shelf basin setting, not far from the ridges separating the platform from the foreslope, located southward (Fig. 9A). Observations of in situ oolites intervals by Hedberg (1979) indicate a high energy, shallow, probably intertidal environment in quite close proximity to Rasthof Farm, north of the Kamanjab Inlier. South of the same Inlier, Hoffman and Halverson, 2008 also described oolitic blocks derived from the Northern Platform at Rasthof time. No oolites were observed at Rasthof Farm, indicating a relatively deeper, quieter environment of possible upper subtidal character. A simple proximal to distal facies model (Fig. 9B) places MM2 as the most shoreward microbialite assemblage. The observation of intraclasts around the individual growths of MM2 and break-up of the laminae within the roll-up structures suggests a relatively constant high energy setting, associated to the rise of individual geometries. The setting was probably quiescent during deposition of MM1: no individual growths developed, and sedimentation was dominated by (initially) slightly undulating microbial beds. Occasional high energy events across the platform locally stimulated the soft-sediment deformation of stromatolites. Note that we interpret MM1, MM2 and the cap dolostone to be laterally adjacent, as well as stratigraphically transitional deposits. At Rasthof Farm, MM1 is characterised by folded sets of laminae and rare cone structures toward the top, whilst MM2 exhibits a variety of individual growths as well as roll-up structures. Changing environmental controls, associated with different rheologies and faster lithification in MM2, probably led to the formation of individual microbial geometries.

Intercalated siliciclastic deposits are notably absent at every level at Rasthof Farm. Their absence may be attributable to either protection of the studied area from siliciclastic dilution, or an absence of siliciclastic input altogether. This might explain the generally rare occurrence of bedforms, even if favourable water depths might have allowed their formation during Rasthof time. In the microbial member, the microbial nature of the sediments implies trapping of carbonate grains, which inhibits the genesis of bedforms.

At Rasthof Farm, the deformation structures in MM1 do not appear to be associated with sedimentary dykes. Whilst early compaction probably played a part in determining the final geometry of soft-sediment deformation structures, we emphasise the likely role of storm wave activity and possible seismic shocks. The microbial laminae were formed on a very low angle slope, isolated from siliciclastic input, forming extensive cohesive mats.

## 7. Discussion: stromatolite patterns

Several approaches have been used to describe and understand stromatolite geometries (Bosak et al., 2013 and references therein). It is widely accepted that, stromatolites and more generally microbialites are the result of an interaction between microbial communities and external, environmental factors (e.g. sediment input, wave energy). From these interactions, microbial communities can create different patterns, with some examples from the Cryogenian (Tucker, 1977; Planavsky and Grey, 2008).

Few publications focus on the sedimentology of post-Sturtian cap carbonate sequences and stromatolite descriptions from this specific interval are rare. Considering microbial sediments as the result of an interaction between environmental and microbial controls, we suggest that the different morphologies observed at the Rasthof Farm follow a trend. The succession can be idealized, with 6 different geometries distinguished (Fig. 10). The first half of the microbial member is characterised by undulating to chaotic laminae (1). In the middle of the microbial member local solid cores are formed, creating dm high cones (2). This might imply increasing energy levels. The following forms are considered to result from this increasing energy, with concomitant intraclastic input. In MM2, a differing rheology allied to changing environmental controls allowed the development of greatly diversified geometries. Upsection, cone geometries are succeeded by

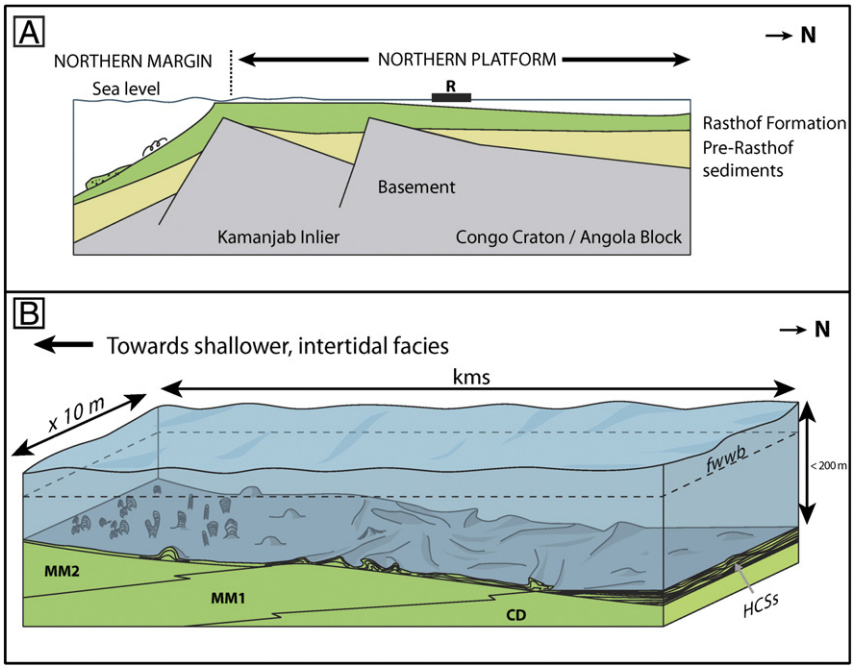


**Fig. 9.** Model for the Rasthof Formation, Rasthof Farm. Panel A represents a transect of the platform, "R" is the location of the Rasthof Farm. Panels B shows that the cap dolostone (CD) records the deepest facies of the Rasthof Formation (Hoffman and Halverson, 2008) but HCS indicates that it was deposited above the storm wave base. The microbial member 1 (MM1) was deposited on a very low slope and deformed by seismic shocks and/or waves. The microbial member 2 (MM2) was deposited when tectonic activity stopped and/or in a shallower setting. Increasing energy levels present in this environment led to the development of vertical growth.

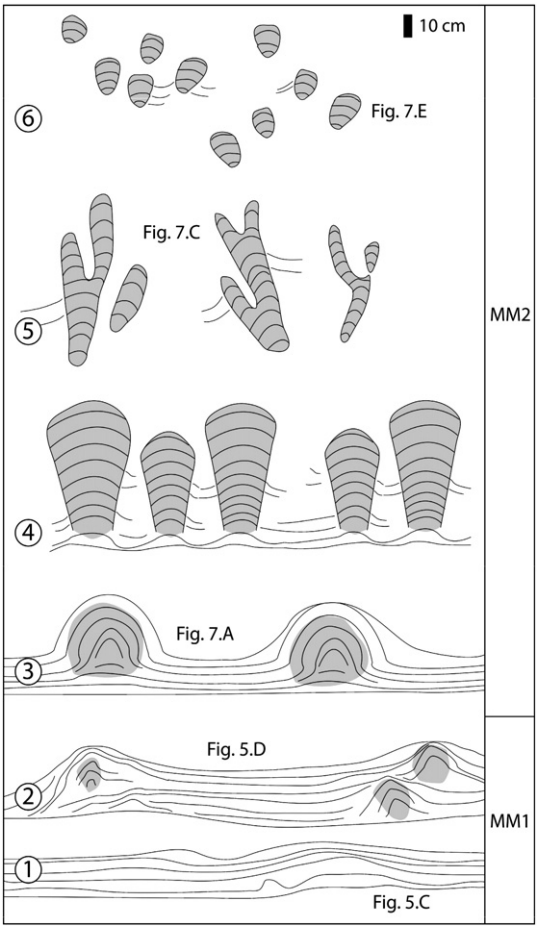


**Fig. 10.** Idealized vertical succession of stromatolite geometries observed at Rasthof Farm. The succession charts the responses of the microbial communities to a changing postglacial environment. 1. Crinkly and undulating stromatolites. 2. Crinkly and undulating stromatolites with local development of cones. 3. Domes. 4. Large columns. 5. Branching columns. 6. Extreme degree of branching.

rounded domes (3), followed by large columns (4). Inter-growth laminae tend to disappear, possibly as a result of destruction and reworking by wave processes. Nevertheless, these intergrowth laminae are preserved where they are protected in the lee of vertical growths (Fig. 7F). Throughout MM2, geometries continue to change to branching columns (5), a geometry that is developed to the extreme at the top of the succession (6).

Upsection, stromatolites become rarer to absent. We suggest that microbial communities lost their competition versus the environment. The top the Rasthof Formation is not exposed at Rasthof Farm but Hoffman and Halverson, 2008 note that, to a regional scale, the top of the formation is characterised by shallow water facies and local subaerial exposure on the Northern Platform. This is consistent with the trend observed in the microbial member at Rasthof Farm. Increasing energy in the environment led to the arrival of high energy, very shallow water facies. Microbial communities were overtaken by these facies.

## 8. Conclusions

- The cap dolostone and microbial member of Rasthof Formation were collectively interpreted to record sub-storm wave base deposition by previous authors (Tojo et al., 2007; Pruss et al., 2010). At Rasthof Farm, a shallower setting is recognised from a new dataset;
- The Rasthof Farm succession commences with a non microbially-influenced, cap dolostone unit, comprising laminites punctuated by hummocky cross stratification (HCS) intervals at the top. Formation of HCS indicates that grains were not cohesive during the deposition of the cap dolostone. HCS records storm wave agitation of the carbonate platform;
- A locally sharp contact marks the juncture between the cap dolostone and overlying microbialites. The microbial laminae of MM1 were modified by a possible association of storm wave agitation and seismic shocks. Above, well differentiated stromatolite (columns and domes morphologies) of MM2 may record deposition in a shallower high energy setting;
- Facies models for Cryogenian carbonate platforms, and in particular those on which the post-Sturtian cap carbonates were deposited, are comparatively few. By proposing a simple depositional model for the facies from the Rasthof Farm, a trend in the organisation of microbial communities can be highlighted. This has major implications for understanding the recovery patterns of microbial communities in the aftermath of the Sturtian snowball Earth event, and possibly in other stromatolitic outcrops.

## Acknowledgments

Erwan Le Ber wants to thanks the owners of the Rasthof Farm: Smit and Erika Meyer for welcoming us on their land; the Department of Geology of the University of Namibia; Marie Busfield (RHUL). This work was generously supported by a grant from Sonangol to Daniel P. Le Heron, supporting the doctoral research of the first author. We are grateful for their permission to publish here. The authors are grateful to the editor, Brian Jones, and the two reviewers, Sara Pruss and Stefan Schroeder for their comments and suggestions that greatly improved the manuscript.

## References

Allen, P.A., Etienne, J.L., 2008. Sedimentary challenge to Snowball Earth. Nature Geoscience 1, 817–825.
Bosak, T., Lahr, D.J.G., Pruss, S.B., MacDonald, F.A., Dalton, L., Matys, E.D., 2011. Agglutinated tests in post-Sturtian cap carbonates of Namibia and Mongolia. Earth and Planetary Science Letters 308, 28–40.
Bosak, T., Lahr, J.G., Pruss, S.B., MacDonald, F.A., Gooday, A.J., Dalton, L., Matys, E.D., 2012. Possible early foraminiferans in post-Sturtian (713–636 Ma) cap carbonates. Geology 40, 67–70.
Bosak, T., Knoll, A.H., Petroff, A.P., 2013. The meaning of stromatolites. Annual Review of Earth and Planetary Sciences 41, 3.1–3.24.
Cheel, R.J., Leckie, D.A., 1993. Hummocky cross-stratification. In: Wright, V.P. (Ed.), Sedimentary Review. Wiley Blackwell, London, pp. 103–122.
Cloud, P.E., Semikhatov, M.A., 1969. Proterozoic stromatolite zonation. American Journal of Science 267, 1017–1061.
Corkeron, M., 2007. 'Cap carbonates' and Neoproterozoic glacigenic successions from the Kimberley region, north-west Australia. Sedimentology 54, 871–903.
Corsetti, F.A., Grotzinger, J.P., 2005. Origin and Significance of tube structures in Neoproterozoic post-glacial cap carbonates. Example from noonday dolomite, Death Valley, United States. Palaios 20, 348–362.
Dalton, L.A., Bosak, T., Macdonald, F.A., Lahr, D.J.G., Pruss, S.B., 2013. Preservational and morphological variability of assemblages of agglutinated eukaryotes in Cryogenian cap carbonates of northern Namibia. Palaios 28, 67–79.
Dean, W.E., Fouch, T.D., 1983. Lacustrine environment. In: Scholle, P.A., Bedout, D.G., Moore, C.H. (Eds.), Carbonate Depositional Environments: AAPG Memoir, 33, pp. 97–130.
Delgado, F., 1977. Primary textures in dolostones and recrystallized limestones: a technique for their microscopic study. Journal of Sedimentary Petrology 47, 1339–1341.
Dumas, S., Arnott, R.W.C., 2006. Origin of hummocky and swaley cross-stratification-The controlling influence of unidirectional current strength and aggradation rate. Geology 34, 1073–1076.
Dupraz, C., Pattisina, R., Verrecchia, E.P., 2006. Translation of energy into morphology: simulation of stromatolites morphospace using a stochastic model. Sedimentary Geology 185, 185–203.
Eyles, N., 2008. Glacio-epochs and the supercontinent cycle after 3.0 Ga: tectonic boundary conditions for glaciation. Palaeogeography, Palaeoclimatology, Palaeoecology 258, 89–129.
Eyles, N., Januszcak, N., 2004. 'Zipper-rift': a tectonic model for Neoproterozoic glaciations during the breakup of Rodinia after 750 Ma. Earth-Science Reviews 65, 1–73.
Eyles, N., Januszczak, N., 2007. Syntectonic subaqueous mass flows of the Neoproterozoic Otavi Group, Namibia: where is the evidence of global glaciation? Basin Research 19, 179–198.
Fairchild, I.J., Kennedy, M.J., 2007. Neoproterozoic glaciation in the Earth System. Journal of the Geological Society of London 164, 895–921.

Flügel, E., 2004. Microfacies of Carbonate Rocks: Analysis, Interpretation and Application. Springer (976 pp.).
Frimmel, H.E., Basei, M.S., Gaucher, C., 2011. Neoproterozoic geodynamic evolution of SW-Gondwana: a southern African perspective. International Journal of Earth Sciences 100, 323–354.
Grotzinger, J.P., Knoll, A.H., 1999. Stromatolites in Precambrian: evolutionary mileposts or environmental dipsticks? Annual Review of Earth and Planetary Science 27, 313–358.
Halverson, G.P., Hoffman, P.F., Schrag, D.P., Maloof, A.C., Rice, A.H.N., 2005. Toward a Neoproterozoic composite carbon-isotope record. GSA Bulletin 117, 1181–1207.
Harwood, C.L., Sumner, D.Y., 2011. Microbialites of the Neoproterozoic Beck Spring Dolomite, Southern California. Sedimentology 58, 1648–1673.
Hedberg, R.M., 1979. Stratigraphy of the Ovamboland Basin South West Africa. Chamber of Mines Precambrian Research Unit. : Bulletin, 24 (325 pp.).
Hoffmann, K.H., Prave, A.R., 1996. A preliminary note on a revised subdivision and regional correlation of the Otavi Group based on glaciogenic diamictites and associated cap dolostones. Communications of the Geological Survey of Namibia 11, 77–82.
Hoffman, P.F., Halverson, G.P., 2008. Otavi Group of the western Northern Platform, the Eastern Kaoko Zone and the western Northern Margin Zone. In: Miller, R.McG. (Ed.), The Geology of Namibia, 2, pp. 13.69–13.134.
Hoffman, P.F., Macdonald, F.A., 2010. Sheet-crack cements and early regression in Marinoan (635 Ma) cap dolostones: regional benchmarks of vanishing ice-sheets? Earth and Planetary Science Letters 300, 374–384.
Hoffman, P.F., Schrag, D.P., 2002. The snowball Earth hypothesis: testing the limits of global change. Terra Nova 14, 129–155.
Hoffman, P.F., Kaufman, A.J., Halverson, G.P., 1998. Comings and goings of global glaciations on the Neoproterozoic tropical platform in Namibia. GSA Today 8, 1–9.
Hoffman, P.F., Halverson, G.P., Domack, E.W., Husson, J.M., Higgins, J.A., Schrag, D.P., 2007. Are basal Ediacaran (635 Ma) post-glacial "cap dolostones" diachronous? Earth and Planetary Science Letters 258, 114–131.
Kahle, C.F., 2002. Seismogenic deformation structures in microbialites and mudstones, Silurian Lockport Dolomite, northwestern Ohio. U.S.A. Journal of Sedimentary Research 72, 201–216.
Kennedy, M.J., Christie-Blick, N., 2011. Condensation origin for Neoproterozoic cap carbonates during deglaciation. Geology 37, 319–322.
Le Heron, D.P., 2012. The Cryogenian record of glaciation and deglaciation in South Australia. Sedimentary Geology 243–244, 57–69.
Le Heron, D.P., Cox, G.M., Trundley, A.E., Collins, A., 2011. Sea-ice free conditions during the early Cryogenian (Sturt) glaciation, South Australia. Geology 39, 31–34.
Le Heron, D.P., Busfield, M.E., Kamona, F., 2013. An interglacial on snowball Earth? Dynamic ice behaviour revealed in the Chuos Formation, Namibia. Sedimentology 60, 411–427.
Loyd, S.J., Corsetti, F.A., 2010. The origin of the millimetre scale lamination in the Neoproterozoic Lower Beck Spring Dolomite: implication for widespread, fine-scale, layer-parallel diagenesis in Precambrian carbonates. Journal of Sedimentary Research 80, 678–687.
Martín-Chivelet, J., Palma, R.M., López-Gómez, J., Kietzmann, D.A., 2011. Earthquake-induced soft-sediment deformation structures in Upper Jurassic open-marine microbialites (Neuquén Basin, Argentina). Sedimentary Geology 235, 210–221.
Miller, R.McG., 2008. The geology of Namibia. Neoproterozoic to Lower Palaeozoic, volume 2. Ministry of mines and energy, Windhoek, Namibia.
Mulder, T., Razin, P., Faugeres, J.C., 2009. Hummocky cross-stratification-like structures in deep-sea turbidites: Upper Cretaceous Basque basins (Western Pyrenees, France). Sedimentology 56, 997–1015.
Nogueira, A.C.R., Riccomini, C., Sial, A.N., Moura, C.A.V., Fairchild, T.R., 2003. Soft-sediment deformation at the base of the Neoproterozoic Puga cap carbonate (southwestern Amazon craton, Brazil): Confirmation of rapid icehouse to greenhouse transition in snowball Earth. Geology 31, 613–616.
Owen, G., Moretti, M., Alfaro, P., 2011. Recognising triggers for soft-sediments deformations: current understanding and future directions. Sedimentary Geology 235, 133–140.
Planavsky, N., Grey, K., 2008. Stromatolite branching in the Neoproterozoic of the Centralian Superbasin, Australia: an investigation into sedimentary microbial control of stromatolite morphology. Geobiology 6, 33–45.
Pruss, S.B., Bosak, T., Macdonald, F.A., Mclane, M., Hoffman, P.F., 2010. Microbial facies in a Sturtian cap carbonate, the Rasthof Formation, Otavi Group, northern Namibia. Precambrian Research 181, 187–198.
Riding, R., 2011. The nature of stromatolites: 3,500 million years of history and a century of research. In: Reitner, J., Queric, N.V., Arp, G. (Eds.), Advances in Stromatolite Geobiology: Lecture Notes in Earth Sciences, 131, pp. 29–74.
Rose, C.V., Maloof, A.C., 2010. Testing models for post-glacial 'cap dolostone' deposition: Nuccaleena Formation, South Australia. Earth and Planetary Science Letters 296, 165–180.
Schieber, J., Bose, P.K., Eriksson, P.G., Banerjee, S., Sarkar, S., Altermann, W., Catuneanu, O., 2007. Atlas of Microbial Mat Features Preserved Within the Clastic Record. Elsevier (288 pp.).
Shield, G.A., 2005. Neoproterozoic cap carbonates: a critical appraisal of existing models and the plumeworld hypothesis. Terra Nova 17, 299–310.
Simonson, M., Carney, K.E., 1999. Roll-up structures: evidence of in situ microbial mats in Late Archean Deep Shelf environments. Palaios 14, 13–24.
Tojo, B., Katsuta, N., Takano, M., Kawakami, S., Ohno, T., 2007. Calcite–dolomite cycles in the Neoproterozoic Cap carbonates, Otavi Group, Namibia. Geological Society, London, Special Publication 286, 103–113.
Tucker, M.E., 1977. Stromatolite biostromes and associated facies in the late Precambrian Porsanger Dolomite Formation of Finnmark, Arctic Norway. Palaeogeography, Palaeoclimatology, Palaeoecology 21, 55–83.
Wright, P., 1990. Carbonate depositional systems I: marine shallow-water and lacustrine carbonates. In: Tucker, M.E., Wright, V.P., Dickson, J.A.D. (Eds.), Carbonate Sedimentology, pp. 137–163.
Yoshioka, H., Asahara, Y., Tojo, B., Kawakami, S., 2003. Systematic variations in C, O, and Sr isotopes and elemental concentrations in Neoproterozoic carbonates in Namibia: implications for a glacial to interglacial transition. Precambrian Research 124, 69–85.

# APPENDIX II

# Leco Carbon and Sulphur Elemental Analyses

| Location | Sample | TC | TS | Sample | TOC | TS | TIC (TC-TOC) | $Cc_{eq}$ |
|---|---|---|---|---|---|---|---|---|
| | | %C | %S | | %C | %S | %C | % Carbonate |
| Halali Waterhole | HAL1.1 | **11.31** | 0.02 | HAL1.4 | **0.24** | 0.03 | 11.07 | **92.22** |
| Halali Waterhole | HAL2.1 | **2.30** | 0.02 | HAL2.4 | **0.29** | 0.03 | 2.01 | **16.74** |
| Halali Waterhole | HAL3.1 | **11.88** | 0.03 | HAL3.4 | **0.12** | 0.02 | 11.76 | **97.99** |
| Halali Waterhole | HAL4.1 | **12.03** | 0.02 | HAL4.4 | **0.10** | 0.03 | 11.92 | **99.37** |
| Halali Waterhole | HAL5.1 | **11.64** | 0.03 | HAL5.4 | **0.18** | 0.03 | 11.45 | **95.42** |
| Halali Waterhole | HAL6.1 | **11.74** | 0.04 | HAL6.4 | **0.10** | 0.02 | 11.64 | **96.98** |
| Halali Waterhole | HAL7.1 | **11.48** | 0.03 | HAL7.4 | **0.09** | 0.02 | 11.38 | **94.85** |
| Halali Waterhole | HAL8.1 | **11.93** | 0.02 | HAL8.4 | **0.15** | 0.02 | 11.78 | **98.20** |
| Halali Waterhole | HAL9.1 | **11.77** | 0.03 | HAL9.4 | **0.13** | 0.02 | 11.64 | **97.04** |
| Halali Waterhole | HAL10.1 | **11.86** | 0.03 | HAL10.4 | **0.12** | 0.02 | 11.74 | **97.82** |
| Halali Waterhole | HAL1.2 | **12.13** | 0.03 | HAL1.5 | **0.27** | 0.04 | 11.86 | **98.86** |
| Halali Waterhole | HAL2.2 | **2.36** | 0.03 | HAL2.5 | **0.27** | 0.03 | 2.09 | **17.40** |
| Halali Waterhole | HAL3.2 | **11.71** | 0.02 | HAL3.5 | **0.11** | 0.02 | 11.60 | **96.69** |
| Halali Waterhole | HAL4.2 | **11.81** | 0.02 | HAL4.5 | **0.11** | 0.02 | 11.70 | **97.49** |
| Halali Waterhole | HAL5.2 | **11.67** | 0.03 | HAL5.5 | **0.23** | 0.03 | 11.43 | **95.28** |
| Halali Waterhole | HAL6.2 | **11.49** | 0.03 | HAL6.5 | **0.10** | 0.03 | 11.39 | **94.88** |
| Halali Waterhole | HAL7.2 | **11.33** | 0.03 | HAL7.5 | **0.09** | 0.03 | 11.24 | **93.65** |
| Halali Waterhole | HAL8.2 | **11.84** | 0.02 | HAL8.5 | **0.14** | 0.03 | 11.70 | **97.50** |
| Halali Waterhole | HAL9.2 | **11.76** | 0.03 | HAL9.5 | **0.12** | 0.03 | 11.64 | **97.03** |
| Halali Waterhole | HAL10.2 | **11.80** | 0.03 | HAL10.5 | **0.12** | 0.03 | 11.68 | **97.32** |
| Halali Waterhole | HAL11.1 | **11.78** | 0.02 | HAL11.4 | **0.13** | 0.04 | 11.65 | **97.06** |
| Halali Waterhole | HAL12.1 | **11.39** | 0.03 | HAL12.4 | **0.10** | 0.03 | 11.29 | **94.06** |
| Halali Waterhole | HAL13.1 | **11.54** | 0.04 | HAL13.4 | **0.18** | 0.04 | 11.36 | **94.63** |
| Halali Waterhole | HAL14.1 | **10.60** | 0.04 | HAL14.4 | **0.17** | 0.03 | 10.43 | **86.93** |
| Halali Waterhole | HAL11.2 | **11.80** | 0.02 | HAL11.5 | **0.10** | 0.03 | 11.70 | **97.51** |
| Halali Waterhole | HAL12.2 | **11.43** | 0.03 | HAL12.5 | **0.09** | 0.03 | 11.34 | **94.48** |
| Halali Waterhole | HAL13.2 | **11.53** | 0.05 | HAL13.5 | **0.17** | 0.04 | 11.37 | **94.71** |
| Halali Waterhole | HAL14.2 | **10.57** | 0.05 | HAL14.5 | **0.15** | 0.03 | 10.42 | **86.79** |
| Bulk Halali WH | | **10.94** | **0.03** | | **0.15** | **0.03** | **10.80** | **89.96** |
| Tsumeb Mine | MIN3.1 | **11.98** | 0.02 | MIN3.4 | **0.12** | 0.03 | 11.85 | **98.78** |
| Tsumeb Mine | MIN2.1 | **0.18** | 0.01 | MIN2.4 | **0.07** | 0.02 | 0.12 | **0.99** |
| Tsumeb Mine | MIN3.2 | **11.88** | 0.03 | MIN3.5 | **0.13** | 0.03 | 11.75 | **97.88** |

# Leco Carbon and Sulphur Elemental Analyses

| | | | | | | | | |
|---|---|---|---|---|---|---|---|---|
| Tsumeb Mine | MIN2.2 | 0.19 | 0.02 | MIN2.4 | **0.08** | 0.04 | 0.11 | **0.96** |
| Bulk Tsumeb Mine | | **6.06** | **0.02** | | **0.10** | **0.03** | **5.96** | **49.65** |
| Tsumeb Road Cut | TSU2.1 | **8.89** | 0.02 | TSU2.4 | **0.06** | 0.03 | 8.83 | **73.62** |
| Tsumeb Road Cut | TSU3.1 | **8.75** | 0.04 | TSU3.4 | **0.06** | 0.06 | 8.69 | **72.44** |
| Tsumeb Road Cut | TSU4.1 | **8.20** | 0.03 | TSU4.4 | **0.07** | 0.04 | 8.13 | **67.77** |
| Tsumeb Road Cut | TSU5.1 | **10.16** | 0.03 | TSU5.4 | **0.05** | 0.03 | 10.11 | **84.24** |
| Tsumeb Road Cut | TSU2.2 | **8.80** | 0.03 | No second measurment due to problems with LECO measurement system | | | | |
| Tsumeb Road Cut | TSU3.2 | **8.72** | 0.04 | No second measurment due to problems with LECO measurement system | | | | |
| Tsumeb Road Cut | TSU4.2 | **8.21** | 0.03 | No second measurment due to problems with LECO measurement system | | | | |
| Tsumeb Road Cut | TSU5.2 | **10.12** | 0.03 | No second measurment due to problems with LECO measurement system | | | | |
| Tsumeb Road Cut | TSU8.1 | **6.44** | 0.10 | TSU8.5 | **0.16** | 0.10 | 6.27 | **52.27** |
| Tsumeb Road Cut | TSU9.1 | **9.02** | 0.06 | TSU9.5 | **0.11** | 0.05 | 8.91 | **74.28** |
| Tsumeb Road Cut | TSU10.1 | **8.88** | 0.06 | No second measurment due to problems with LECO measurement system | | | | |
| Tsumeb Road Cut | TSU13.1 | **9.68** | 0.05 | No second measurment due to problems with LECO measurement system | | | | |
| Tsumeb Road Cut | TSU8.2 | **6.41** | 0.11 | TSU8.4 | **0.18** | 0.11 | 6.23 | **51.95** |
| Tsumeb Road Cut | TSU9.2 | **9.03** | 0.06 | TSU9.4 | **0.09** | 0.05 | 8.93 | **74.44** |
| Tsumeb Road Cut | TSU10.2 | **8.91** | 0.05 | TSU10.4 | **0.06** | 0.04 | 8.85 | **73.73** |
| Tsumeb Road Cut | TSU13.2 | **9.68** | 0.04 | TSU13.4 | **0.05** | 0.04 | 9.64 | **80.30** |
| Bulk Road Cut | | **8.74** | **0.05** | | **0.09** | **0.06** | **8.46** | **70.50** |
| Kamanjab | KAM5.1 | **12.38** | 0.02 | KAM5.4 | **0.61** | 0.02 | 11.77 | **98.06** |
| Kamanjab | KAM7.1 | **12.15** | 0.02 | KAM7.4 | **0.05** | 0.02 | 12.10 | **100.81** |
| Kamanjab | KAM8.1 | **12.21** | 0.02 | KAM8.4 | **0.08** | 0.03 | 12.13 | **101.12** |
| Kamanjab | KAM9.1 | **11.82** | 0.02 | KAM9.4 | **0.41** | 0.03 | 11.41 | **95.08** |
| Kamanjab | KAM10.1 | **12.20** | 0.02 | KAM10.4 | **0.19** | 0.03 | 12.01 | **100.05** |
| Kamanjab | KAM11.1 | **11.67** | 0.03 | KAM11.4 | **0.51** | 0.03 | 11.16 | **92.96** |
| Kamanjab | KAM5.2 | **12.50** | 0.02 | KAM5.5 | **1.01** | 0.03 | 11.49 | **95.78** |
| Kamanjab | KAM7.2 | **12.23** | 0.02 | KAM7.5 | **0.07** | 0.03 | 12.16 | **101.36** |
| Kamanjab | KAM8.2 | **12.26** | 0.02 | KAM8.5 | **0.07** | 0.03 | 12.18 | **101.53** |
| Kamanjab | KAM9.2 | **12.09** | 0.02 | KAM9.5 | **0.07** | 0.03 | 12.02 | **100.14** |
| Kamanjab | KAM10.2 | **12.26** | 0.03 | KAM10.5 | **1.78** | 0.04 | 10.48 | **87.32** |
| Kamanjab | KAM11.2 | **12.00** | 0.02 | KAM11.5 | **0.12** | 0.04 | 11.88 | **99.04** |
| Kamanjab | KAM12.1 | **12.31** | 0.02 | KAM12.5 | **1.06** | 0.03 | 11.25 | **93.71** |
| Kamanjab | KAM14.1 | **12.58** | 0.02 | KAM14.5 | **0.07** | 0.03 | 12.51 | **104.26** |
| Kamanjab | KAM15.1 | **12.58** | 0.02 | KAM15.5 | **1.32** | 0.02 | 11.25 | **93.79** |

# Leco Carbon and Sulphur Elemental Analyses

| | | | | | | | | |
|---|---|---|---|---|---|---|---|---|
| Kamanjab | KAM16.1 | **12.51** | 0.02 | KAM16.5 | **0.77** | 0.03 | 11.74 | **97.81** |
| Kamanjab | KAM17.1 | **12.43** | 0.02 | KAM17.5 | **0.14** | 0.03 | 12.30 | **102.46** |
| Kamanjab | KAM18.1 | **12.56** | 0.02 | KAM18.5 | **1.26** | 0.03 | 11.30 | **94.13** |
| Kamanjab | KAM19.1 | **12.47** | 0.02 | KAM19.5 | **0.99** | 0.03 | 11.49 | **95.72** |
| Kamanjab | KAM20.1 | **12.34** | 0.02 | KAM20.5 | **0.11** | 0.03 | 12.23 | **101.90** |
| Kamanjab | KAM21.1 | **12.33** | 0.03 | KAM21.5 | **0.15** | 0.03 | 12.18 | **101.46** |
| Kamanjab | KAM23.1 | **12.58** | 0.01 | KAM23.5 | **0.41** | 0.02 | 12.17 | **101.38** |
| Kamanjab | KAM12.2 | **12.43** | 0.02 | KAM12.4 | **0.42** | 0.03 | 12.01 | **100.10** |
| Kamanjab | KAM14.2 | **12.55** | 0.02 | KAM14.4 | **1.72** | 0.02 | 10.83 | **90.26** |
| Kamanjab | KAM15.2 | **12.24** | 0.02 | KAM15.4 | **0.07** | 0.03 | 12.16 | **101.35** |
| Kamanjab | KAM16.2 | **12.71** | 0.02 | KAM16.4 | **0.42** | 0.02 | 12.29 | **102.43** |
| Kamanjab | KAM17.2 | **12.71** | 0.02 | KAM17.4 | **1.53** | 0.02 | 11.18 | **93.16** |
| Kamanjab | KAM18.2 | **12.53** | 0.02 | KAM18.4 | **0.11** | 0.03 | 12.42 | **103.52** |
| Kamanjab | KAM19.2 | **12.47** | 0.02 | KAM19.4 | **1.95** | 0.02 | 10.52 | **87.63** |
| Kamanjab | KAM20.2 | **12.30** | 0.02 | KAM20.4 | **0.40** | 0.03 | 11.90 | **99.15** |
| Kamanjab | KAM21.2 | **12.46** | 0.02 | KAM21.4 | **0.57** | 0.03 | 11.89 | **99.06** |
| Kamanjab | KAM23.2 | **12.37** | 0.02 | KAM23.4 | **2.10** | 0.02 | 10.27 | **85.54** |
| Bulk Kamanjab | | **12.35** | **0.02** | | **0.64** | **0.03** | **11.71** | **97.56** |

# APPENDIX III

# East section

| Acquisition | | | | Processing | | | | | | | |
|---|---|---|---|---|---|---|---|---|---|---|---|
| Scans acquired | Date | Size (pts) | Purpose | Photo linked | Georef data | Colour scans | Image editing | Fracture editing | 3D fractures | Google Earth Loc. | Cleaned (Polydata) |
| ScanPos01 - Pan01 | 28/06/2011 | 1,998,000 | Panorama scan Tripod position 1 | No photos as problem with camera | | | | | | √ | √ |
| ScanPos01 - Scan01 | 28/06/2011 | 24,344 | Find relector | No photos as problem with camera | | | | | | | |
| ScanPos01 - Scan02 | 28/06/2011 | 26,724 | Find relector | No photos as problem with camera | | | | | | | |
| ScanPos01 - Scan03 | 28/06/2011 | 17,334 | Find relector | No photos as problem with camera | | | | | | | |
| ScanPos01 - Scan04 | 28/06/2011 | 87,870 | Find relector | No photos as problem with camera | | | | | | | |
| ScanPos01 - Scan05 | 28/06/2011 | 32,112 | Find relector | No photos as problem with camera | | | | | | | |
| ScanPos01 - Scan06 | 28/06/2011 | 12,870 | Find relector | No photos as problem with camera | | | | | | | |
| ScanPos01 - Scan07 | 28/06/2011 | 4,495,147 | Scan of cliff face | No photos as problem with camera | | | | | | √ | √ |
| ScanPos01 - Scan08 | 28/06/2011 | 3,222,690 | Detailed scan of lower cliff face | No photos as problem with camera | | | | | | √ | √ |
| | | | | | | | | | | | |
| ScanPos02 - Pan01 | 29/06/2011 | 1,998,000 | Panorama scan Tripod position 2 | √ | √ | √ | √ | √ | √ | √ | √ |
| ScanPos02 - Scan01 | 29/06/2011 | 154 | ? | | | | | | | | |
| ScanPos02 - Scan02 | 29/06/2011 | 5,832 | Find reflector | | | | | | | | |
| ScanPos02 - Scan03 | 29/06/2011 | 18,486 | Find Reflector | | | | | | | | |
| ScanPos02 - Scan04 | 29/06/2011 | 2,137,674 | Detailed scan - East Cliff | √ | √ | √ | √ | √ | √ | √ | √ |
| ScanPos02 - Scan05 | 29/06/2011 | 3,594,530 | Detailed scan - East Cliff - central section | √ | √ | √ | √ | √ | √ | √ | √ |
| | | | | | | | | | | | |
| ScanPos03 - Pan01 | 29/06/2011 | 1,998,000 | Panorama scan Tripod position 3 | √ | √ | √ | √ | √ | √ | √ | √ |
| ScanPos03 - Scan01 | 29/06/2011 | 62,700 | Find Reflectors | | | | | | | | |
| ScanPos03 - Scan02 | 29/06/2011 | 5,508,870 | Detailed scan - East Cliff | √ | √ | √ | √ | √ | √ | √ | √ |
| | | | | | | | | | | | |
| ScanPos04 - Pan02 | 29/06/2011 | 1,998,000 | Panorama scan Tripod position 3 | √ | √ | √ | √ | √ | √ | √ | √ |
| ScanPos04 - Scan01 | 29/06/2011 | 2,184 | Find reflector | | | | | | | | |
| ScanPos04 - Scan02 | 29/06/2011 | 26,268 | Find reflector | | | | | | | | |
| ScanPos04 - Scan03 | 29/06/2011 | 6,354,126 | Detailed scan - East Cliff from river bed | √ | √ | √ | √ | √ | √ | √ | √ |

Linking Section

| Acquisition | | | | Processing | | | | | | | |
|---|---|---|---|---|---|---|---|---|---|---|---|
| **Scans acquired** | **Date** | **Size (pts)** | **Purpose** | **Photo linked** | **Georef data** | **Colour scans** | **Image editing** | **Fractures editing** | **3D fractures** | **Google Earth Loc.** | **Cleaned (Polydata)** |
| ScanPos01 - Pan01 | 03/07/2011 | 1,998,000 | Panorama scan Tripod position 1 | √ | √ | √ | √ | √ | x | √ | √ |
| ScanPos01 - Scan01 | 03/07/2011 | 22,264 | Find reflector | | | | | | | | |
| ScanPos01 - Scan02 | 03/07/2011 | 7,446 | Find reflector | | | | | | | | |
| ScanPos01 - Scan03 | 03/07/2011 | 9,994,790 | Detailed scan to south-west of scan position | √ | √ | √ | √ | √ | x | √ | √ |
| ScanPos01 - Scan04 | 03/07/2011 | 5,288,633 | Detailed scan to south-west of scan position | √ | √ | √ | √ | √ | x | √ | √ |
| ScanPos01 - Scan05 | 03/07/2011 | 806,300 | Find reflector | | | | | | | | |
| ScanPos01 - Scan06 | 03/07/2011 | 842,438 | Find reflector | | | | | | | | |
| | | | | | | | | | | | |
| ScanPos02 - Pan01 | 03/07/2011 | 1,998,000 | Panorama scan Tripod position 2 | √ | √ | √ | √ | √ | x | √ | √ |
| ScanPos02 - Scan01 | 03/07/2011 | 9,150 | Find reflector | | | | | | | | |
| ScanPos02 - Scan02 | 03/07/2011 | 6,000 | Find reflector | | | | | | | | |
| ScanPos02 - Scan03 | 03/07/2011 | 3,192,480 | Detailed scan to south of scan position | √ | √ | √ | √ | √ | x | √ | √ |
| ScanPos02 - Scan04 | 03/07/2011 | 2,329,064 | Detailed scan to south-west of scan position | √ | √ | √ | √ | √ | x | √ | √ |

# West Sections

| Acquisition | | | | | Processing | | | | | | | |
|---|---|---|---|---|---|---|---|---|---|---|---|---|
| Scans acquired | Date | Size (pts) | Purpose | Section | Photo linked | Georef data | Colour scans | Image editing | Fracture editing | 3D fractures | Google Earth Loc. | Cleaned (Polydata) |
| ScanPos01 - Pan01 | 30/06/2011 | 1,998,000 | Panorama scan Tripod position 1 | Scans in the western part | √ | √ | √ | √ | √ | √ | √ | √ |
| ScanPos01 - Scan01 | 30/06/2011 | 10,560 | Find reflector | | | | | | | | | |
| ScanPos01 - Scan02 | 30/06/2011 | 36,680 | Find reflector | | | | | | | | | |
| ScanPos01 - Scan03 | 30/06/2011 | 14,790 | Find reflector | | | | | | | | | |
| ScanPos01 - Scan04 | 30/06/2011 | 18,490 | Find reflector | | | | | | | | | |
| ScanPos01 - Scan05 | 30/06/2011 | 3,003,613 | Detailed scan to south of scan position | | √ | √ | √ | √ | √ | √ | | √ |
| ScanPos01 - Scan06 | 30/06/2011 | 3,236,024 | Detailed scan to west of scan position | | √ | √ | √ | √ | √ | √ | | √ |
| | | | | | | | | | | | | |
| ScanPos02 - Pan01 | 30/06/2011 | 1,998,000 | Panorama scan Tripod position 2 | | √ | √ | √ | √ | √ | √ | √ | √ |
| ScanPos02 - Scan01 | 30/06/2011 | 4,750 | Find reflector | | | | | | | | | |
| ScanPos02 - Scan02 | 30/06/2011 | 6,384 | Find reflector | | | | | | | | | |
| ScanPos02 - Scan03 | 30/06/2011 | 3,905,495 | Detailed scan of lvl 2 Build ups | | √ | √ | √ | √ | √ | √ | | √ |
| ScanPos02 - Scan04 | 30/06/2011 | 1,340,570 | Detailed scan to north-west of scan position | | √ | √ | √ | √ | √ | √ | | √ |
| | | | | | | | | | | | | |
| ScanPos03 - Pan01 | 30/06/2011 | 1,998,000 | Panorama scan Tripod position 3 | | √ | √ | √ | √ | √ | √ | √ | √ |
| ScanPos03 - Scan01 | 30/06/2011 | 32,776 | Find reflector | | | | | | | | | |
| ScanPos03 - Scan02 | 30/06/2011 | 8,256 | Find reflector | | | | | | | | | |
| ScanPos03 - Scan03 | 30/06/2011 | 24,160 | Find reflector | | | | | | | | | |
| ScanPos03 - Scan04 | 30/06/2011 | 35,404 | Find reflector | | | | | | | | | |
| ScanPos03 - Scan05 | 30/06/2011 | 7,056 | Find reflector | | | | | | | | | |
| ScanPos03 - Scan06 | 30/06/2011 | 18,232 | Find reflector | | | | | | | | | |
| ScanPos03 - Scan07 | 30/06/2011 | 4,113,120 | Detailed scan to north of scan position | | √ | √ | √ | √ | √ | √ | √ | √ |
| ScanPos03 - Scan08 | 30/06/2011 | 2,569,018 | Detailed scan (strip) to north of scan position | | √ | √ | √ | √ | √ | √ | √ | √ |
| | | | | | | | | | | | | |
| ScanPos04 - Pan01 | 30/06/2011 | 1,998,000 | Panorama scan Tripod position 4 | Linking Scan | **No photos - linking scan** | | | | | | √ | √ |
| ScanPos04 - Scan01 | 30/06/2011 | 159,999 | Find reflector | | | | | | | | | |
| ScanPos04 - Scan02 | 30/06/2011 | 21,216 | Find reflector | | | | | | | | | |
| ScanPos04 - Scan03 | 30/06/2011 | 6,586 | Find reflector | | | | | | | | | |
| ScanPos04 - Scan04 | 30/06/2011 | 21,816 | Find reflector | | | | | | | | | |
| ScanPos04 - Scan05 | 30/06/2011 | 9,401 | Find reflector | | | | | | | | | |
| ScanPos04 - Scan06 | 30/06/2011 | 37,422 | Find reflector | | | | | | | | | |
| ScanPos04 - Scan07 | 30/06/2011 | 1,088 | Find reflector | | | | | | | | | |

# West Sections

| Acquisition | | | | | Processing | | | | | | | |
|---|---|---|---|---|---|---|---|---|---|---|---|---|
| Scans acquired | Date | Size (pts) | Purpose | Section | Photo linked | Georef data | Colour scans | Image editing | Fracture editing | 3D fractures | Google Earth Loc. | Cleaned (Polydata) |
| ScanPos05 - Pan01 | 01/07/2011 | 1,998,000 | Panorama scan Tripod position 5 | Scans in the eastern part | √ | √ | √ | √ | √ | √ | √ | √ |
| ScanPos05 - Scan01 | 01/07/2011 | 7,140 | Find reflector | | | | | | | | | |
| ScanPos05 - Scan02 | 01/07/2011 | 13,943 | Find reflector | | | | | | | | | |
| ScanPos05 - Scan03 | 01/07/2011 | 17,762 | Find reflector | | | | | | | | | |
| ScanPos05 - Scan04 | 01/07/2011 | 7,488 | Find reflector | | | | | | | | | |
| ScanPos05 - Scan05 | 01/07/2011 | 9,052 | Find reflector | | | | | | | | | |
| ScanPos05 - Scan06 | 01/07/2011 | 2,645,508 | Detailed scan to south-west of scan pos | | √ | √ | √ | √ | √ | √ | √ | √ |
| ScanPos05 - Scan07 | 01/07/2011 | 1,899,230 | Detailed scan to north of scan position | | √ | √ | √ | √ | √ | √ | √ | √ |
| ScanPos05 - Scan08 | 01/07/2011 | 7,752 | Find reflector | | | | | | | | | |
| | | | | | | | | | | | | |
| ScanPos06 - Pan01 | 01/07/2011 | 1,998,000 | Panorama scan Tripod position 6 | | √ | √ | √ | √ | √ | √ | √ | √ |
| ScanPos06 - Scan01 | 01/07/2011 | 2,880 | Find reflector | | | | | | | | | |
| ScanPos06 - Scan02 | 01/07/2011 | 21,112 | Find reflector | | | | | | | | | |
| ScanPos06 - Scan03 | 01/07/2011 | 7,552 | Find reflector | | | | | | | | | |
| ScanPos06 - Scan04 | 01/07/2011 | 8,760 | Find reflector | | | | | | | | | |
| ScanPos06 - Scan05 | 01/07/2011 | 8,316 | Find reflector | | | | | | | | | |
| ScanPos06 - Scan06 | 01/07/2011 | 2,410,415 | Detailed scan to south-east (Log-canyo | | √ | √ | √ | √ | √ | √ | √ | √ |
| ScanPos06 - Scan07 | 01/07/2011 | 3,941,080 | Detailed scan to north (Leaning-towers) | | √ | √ | √ | √ | √ | √ | √ | √ |
| ScanPos06 - Scan08 | 01/07/2011 | 21,504 | Find reflector | | | | | | | | | |
| | | | | | | | | | | | | |
| ScanPos07 - Pan01 | 01/07/2011 | 1,998,000 | Panorama scan Tripod position 7 | | √ | √ | √ | √ | | | √ | √ |
| ScanPos07 - Scan01 | 01/07/2011 | 37,338 | Find reflector | | | | | | | | | |
| ScanPos07 - Scan02 | 01/07/2011 | 3,011,360 | Panorama of log section | | √ | √ | √ | √ | √ | √ | √ | √ |
| ScanPos07 - Scan03 | 01/07/2011 | 7,952,892 | Detailed Scan of Log section | | √ | √ | √ | √ | √ | √ | √ | √ |
| | | | | | | | | | | | | |
| ScanPos08 - Pan01 | 01/07/2011 | 1,998,000 | Panorama scan Tripod position 8 | | **No photos as problem with camera** | | | | | | √ | √ |
| ScanPos08 - Scan01 | 01/07/2011 | 14,208 | Find reflector | | | | | | | | | |
| ScanPos08 - Scan02 | 01/07/2011 | 12,000 | Find reflector | | | | | | | | | |
| ScanPos08 - Scan03 | 01/07/2011 | 4,508 | Find reflector | | | | | | | | | |
| ScanPos08 - Scan04 | 01/07/2011 | 7,072 | Find reflector | | | | | | | | | |
| ScanPos08 - Scan05 | 01/07/2011 | 2,425,104 | Detailed Scan | | **No photos as problem with camera** | | | | | | √ | √ |

# Reflector positions

## East section

| GPS locations of reflectors (UTM) | | | |
|---|---|---|---|
| X | Y | Z | LABEL |
| 627240 | 7287580 | 1308.188 | R1 |
| 627262.5 | 7287653 | 1303.131 | R2 |
| 627013.1 | 7287656 | 1281.186 | R3 |
| 627013.1 | 7287656 | 1282.666 | R31 |
| 627005.7 | 7287624 | 1285.937 | R4 |
| 626981.3 | 7287515 | 1288.94 | R5 |

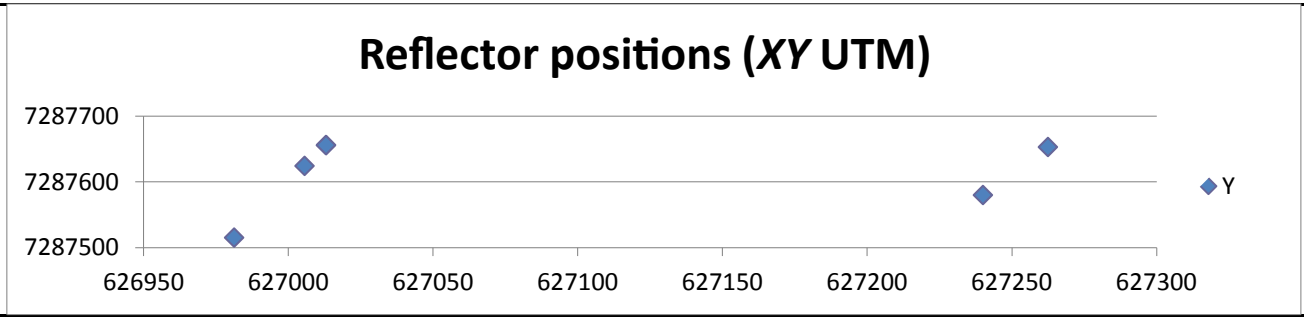


## Linking section

| GPS locations of reflectors (UTM) | | | |
|---|---|---|---|
| X | Y | Z | LABEL |
| 626817.2 | 7287241 | 1274.785 | G1 |
| 626958.2 | 7287262 | 1288.811 | G2 |
| 627108.1 | 7287044 | 1281.231 | G3 |
| 627044.8 | 7286993 | 1286.482 | G4 |
| 626918.8 | 7287188 | 1276.326 | G5 |

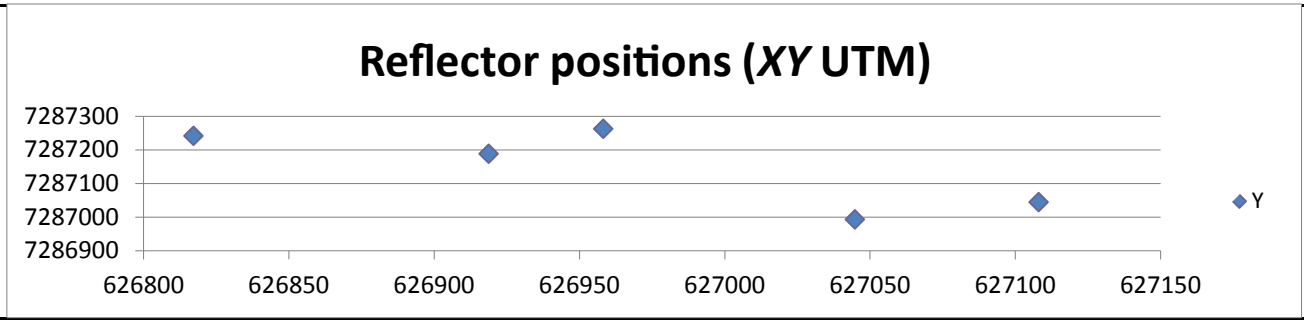


## West section

| GPS locations of reflectors (UTM) | | | |
|---|---|---|---|
| X | Y | Z | LABEL |
| 625908.4 | 7287222 | 1311.895 | Z1 |
| 626246.7 | 7287642 | 1286.802 | Z10 |
| 626318.9 | 7287669 | 1284.606 | Z11 |
| 625721.5 | 7287417 | 1250.722 | Z2 |
| 625755 | 7287532 | 1272.952 | Z3 |
| 625638 | 7287616 | 1271.341 | Z4 |
| 625423.2 | 7287517 | 1272.495 | Z5 |
| 625943.9 | 7287480 | 1275.138 | Z6 |
| 625865.4 | 7287410 | 1260.889 | Z7 |
| 626418.8 | 7287329 | 1335.278 | Z8 |
| 626217.7 | 7287334 | 1274.889 | Z9 |

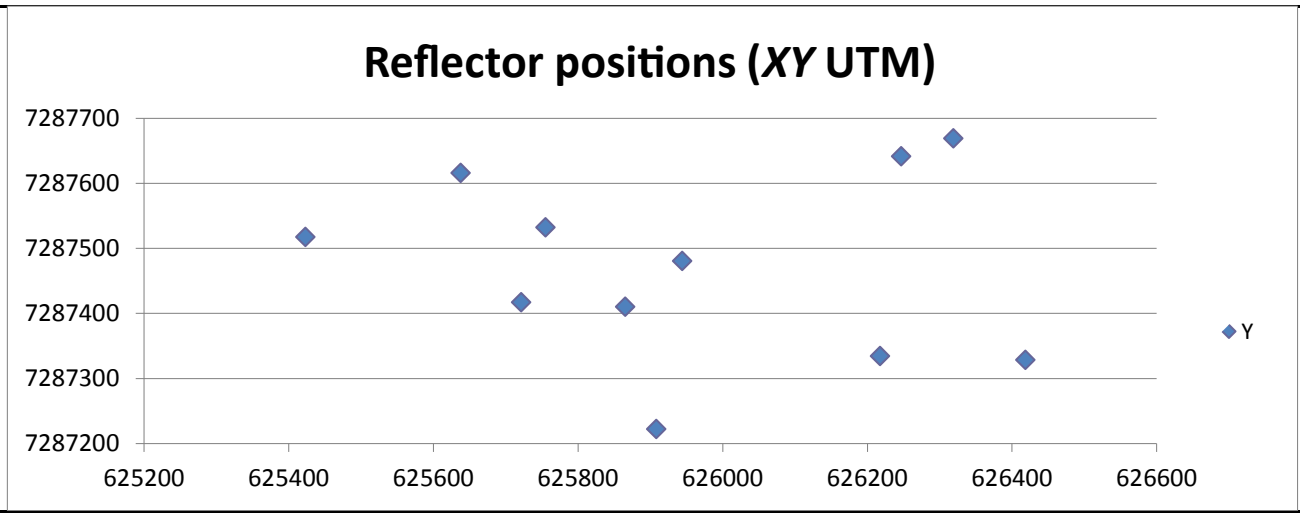

# APPENDIX IV

# Lidar Workflow

LiDAR based Fieldwork

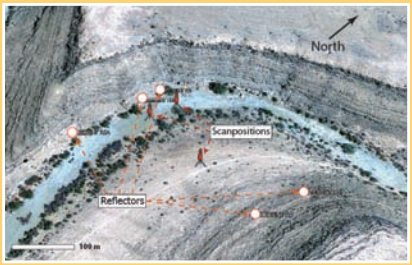


Scanning

Panorama Scans

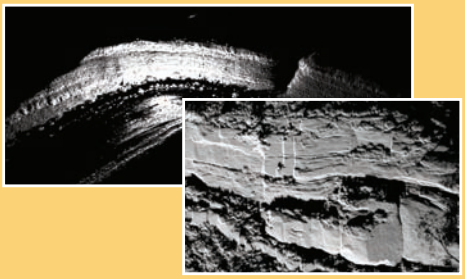

Detailed Scans

Postprocessing

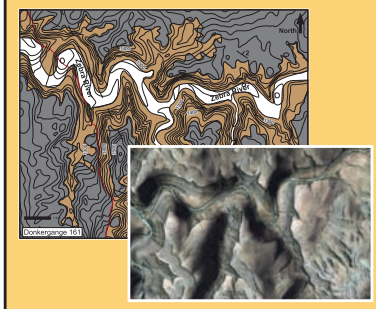

Define Scansections

Photo Editing & Texturing

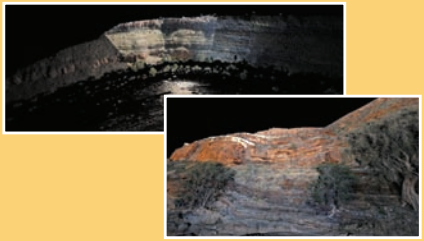

Merging Images on Point Cloud

Data Cleaning

Merge Single Scans

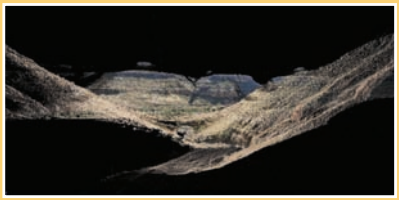

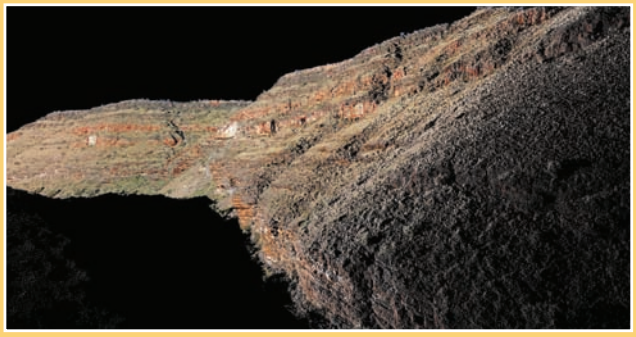

3D Photorealistic Virtual Outcrop Model

# APPENDIX V

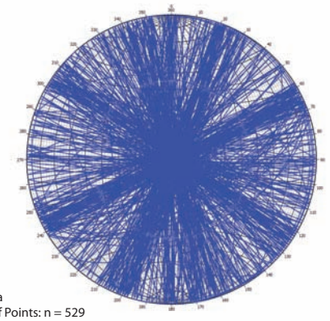

Entire Data
Number of Points: n = 529

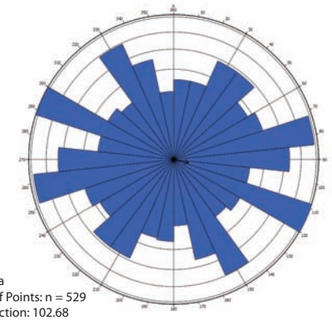

Entire Data
Number of Points: n = 529
Mean direction: 102.68
Interval size: 12

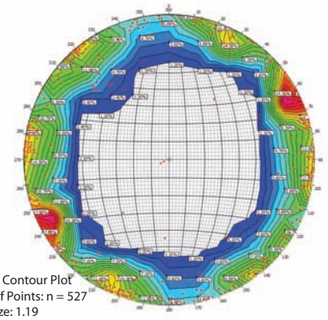

Field Data Contour Plot
Number of Points: n = 527
Interval size: 1.19

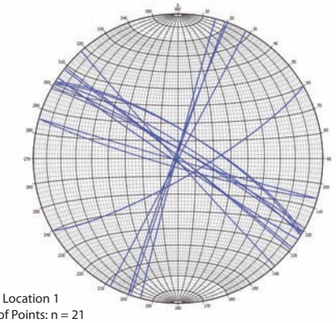

Fractures Location 1
Number of Points: n = 21

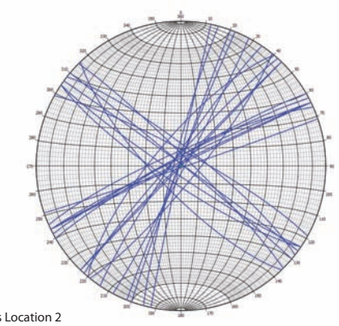

Fractures Location 2
Number of Points: n = 26

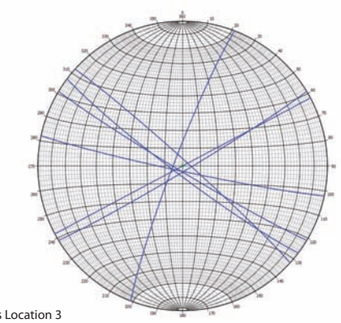

Fractures Location 3
Number of Points: n = 7

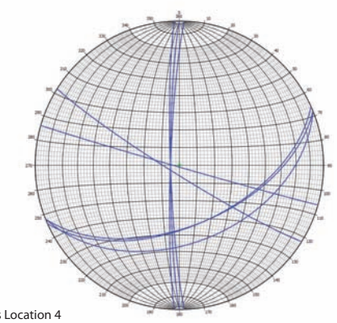

Fractures Location 4
Number of Points: n = 8

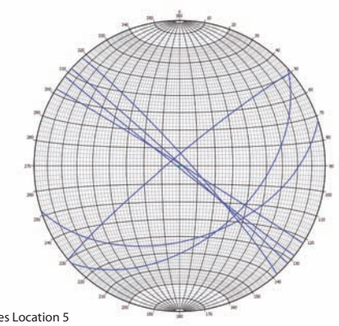

Fractures Location 5
Number of Points: n = 7

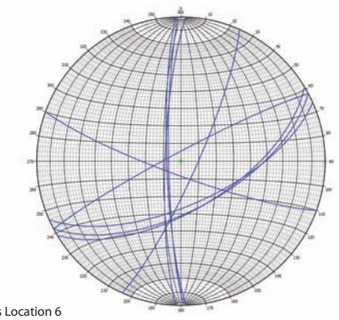

Fractures Location 6
Number of Points: n = 9

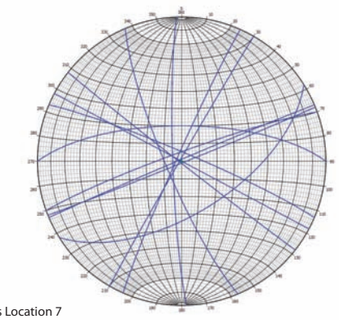

Fractures Location 7
Number of Points: n = 12

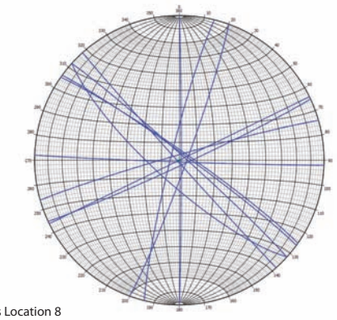

Fractures Location 8
Number of Points: n = 12

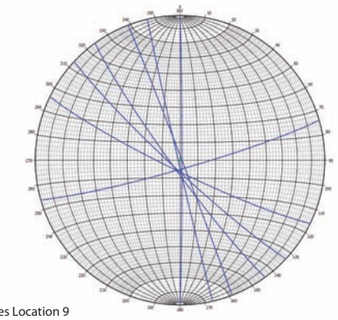

Fractures Location 9
Number of Points: n = 7

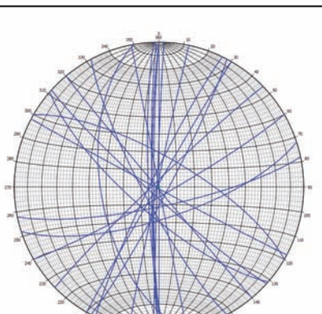

Fractures Location 10
Number of Points: n = 22

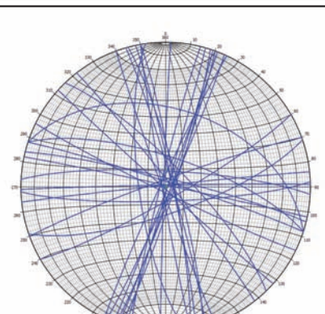

Fractures Location 11
Number of Points: n = 34

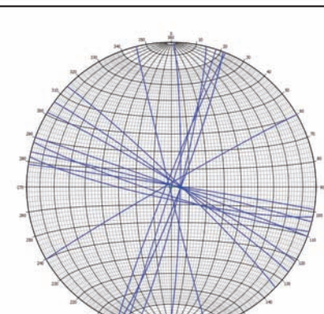

Fractures Location 12
Number of Points: n = 16

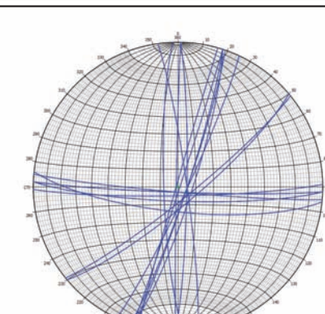

Fractures Location 13
Number of Points: n = 18

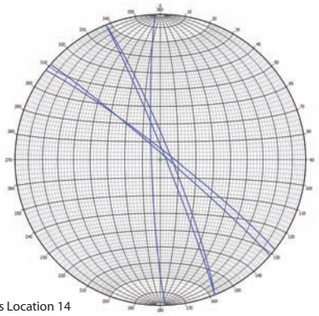

Fractures Location 14
Number of Points: n = 5

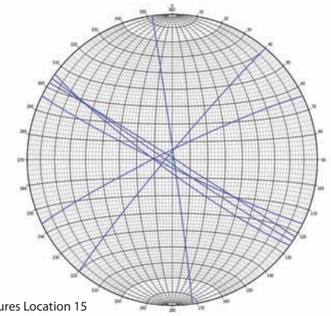

Fractures Location 15
Number of Points: n = 7

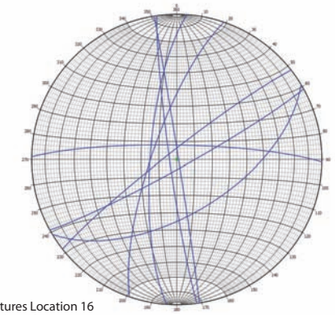

Fractures Location 16
Number of Points: n = 8

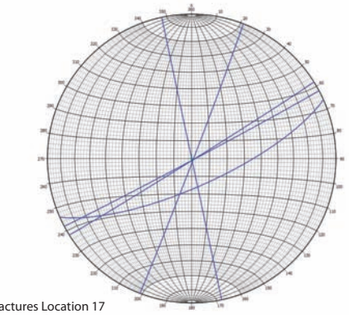

Fractures Location 17
Number of Points: n = 5

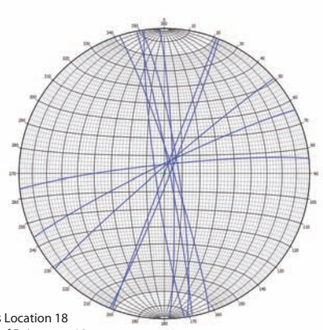

Fractures Location 18
Number of Points: n = 10

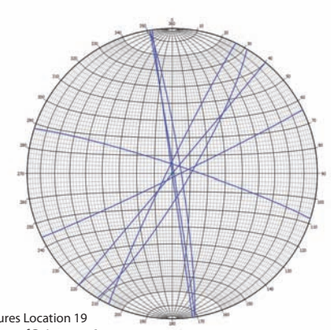

Fractures Location 19
Number of Points: n = 8

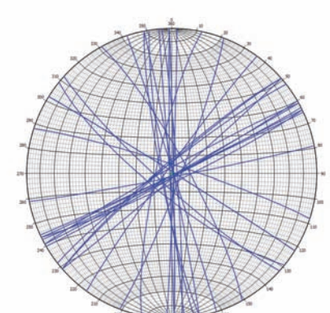

Hoogland Fractures Location 20
Number of Points: n = 31

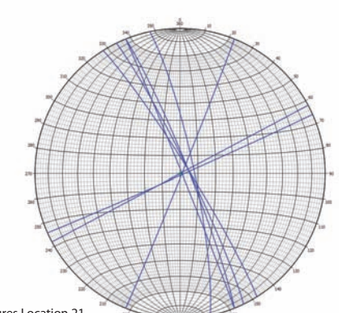

Fractures Location 21
Number of Points: n = 8

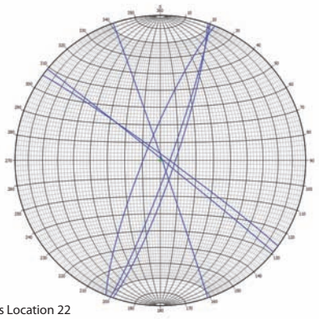

Fractures Location 22
Number of Points: n = 6

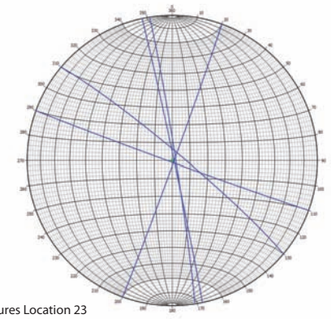

Fractures Location 23
Number of Points: n = 5

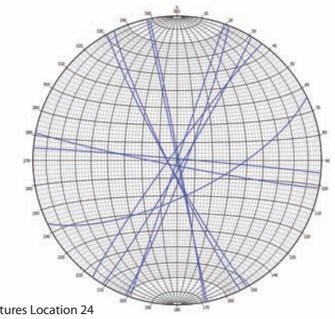

Fractures Location 24
Number of Points: n = 11

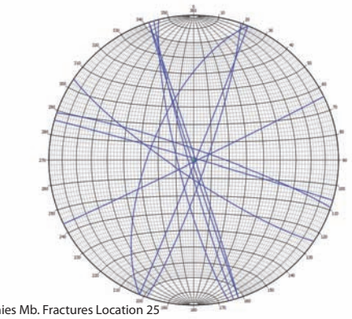

Kanies Mb. Fractures Location 25
Number of Points: n = 11

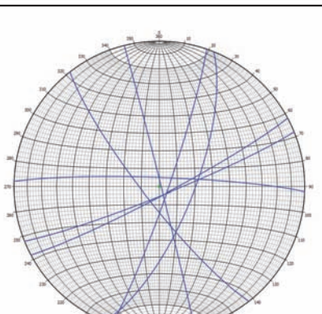

Fractures Location 26
Number of Points: n = 7

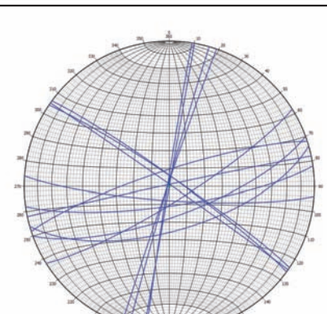

Fractures Location 27
Number of Points: n = 14

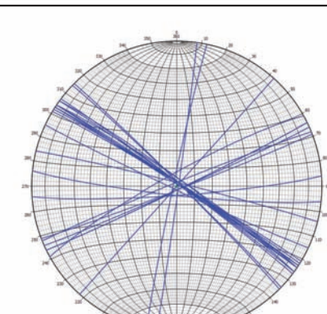

Fractures Location 28
Number of Points: n = 26

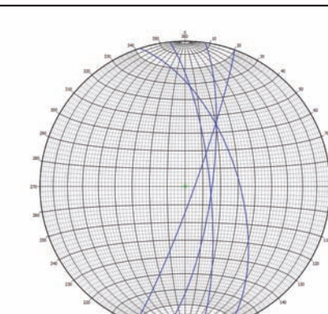

Bioherm 1 Fractures Location 29
Number of Points: n = 4

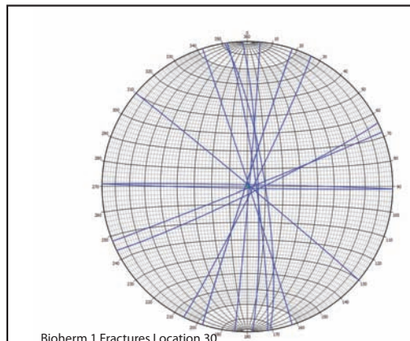

Bioherm 1 Fractures Location 30
Number of Points: n = 13

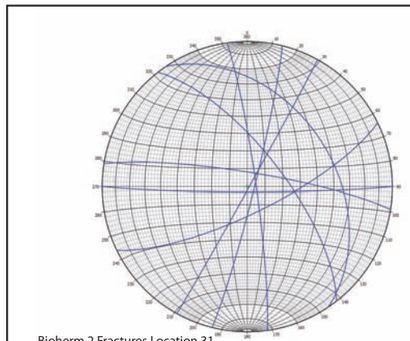

Bioherm 2 Fractures Location 31
Number of Points: n = 8

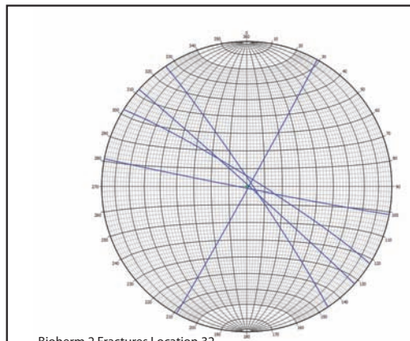

Bioherm 2 Fractures Location 32
Number of Points: n = 5

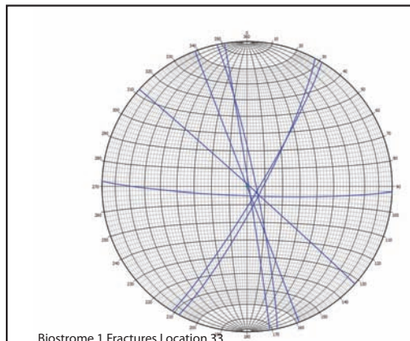

Biostrome 1 Fractures Location 33
Number of Points: n = 7

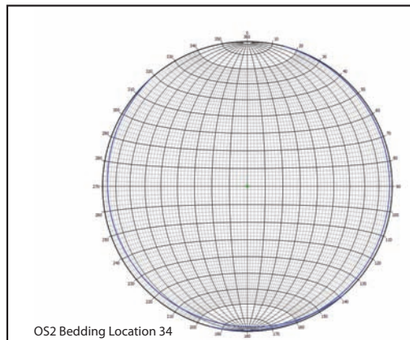

OS2 Bedding Location 34
Number of Points: n = 2

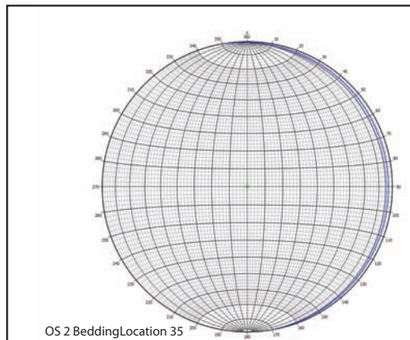

OS 2 BeddingLocation 35
Number of Points: n = 2

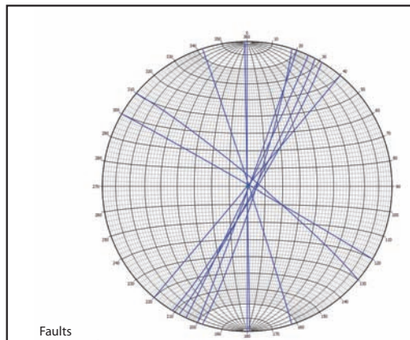

Faults
Number of Points: n = 11

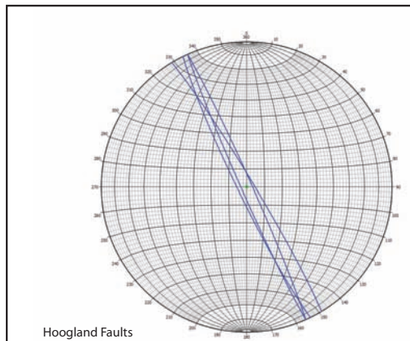

Hoogland Faults
Number of Points: n = 4

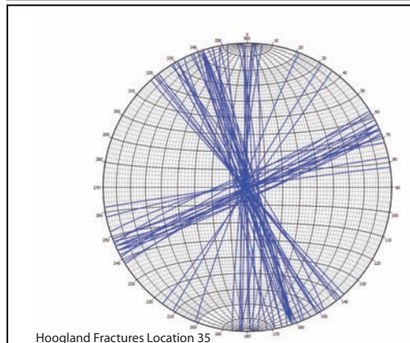

Hoogland Fractures Location 35
Number of Points: n = 59

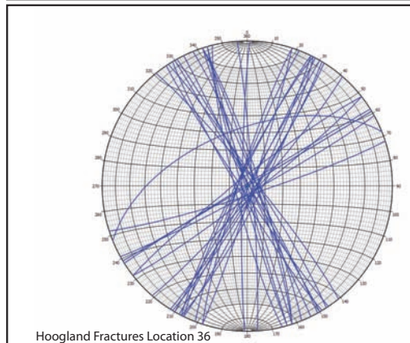

Hoogland Fractures Location 36
Number of Points: n = 36

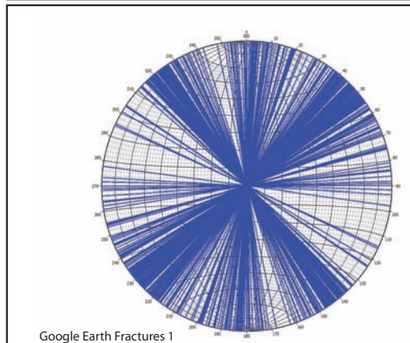

Google Earth Fractures 1
Number of Points: n = 295

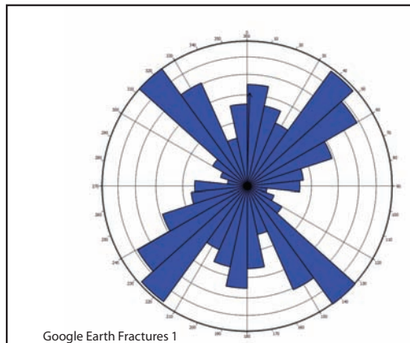

Google Earth Fractures 1
Number of Points: n = 295

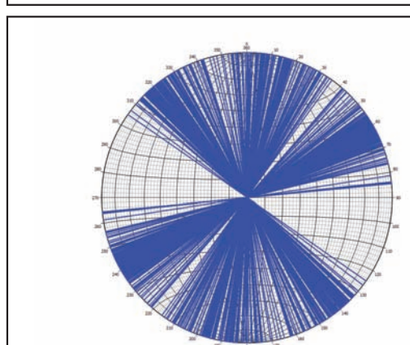

Google Earth Fractures 2
Number of Points: n = 446

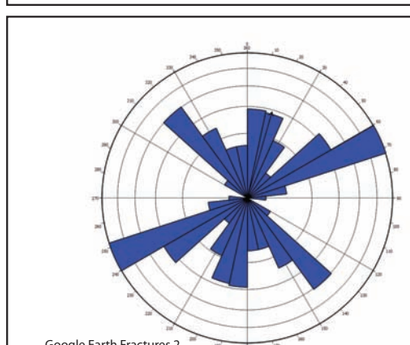

Google Earth Fractures 2
Number of Points: n = 446

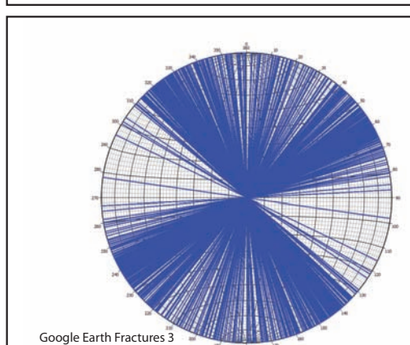

Google Earth Fractures 3
Number of Points: n = 428

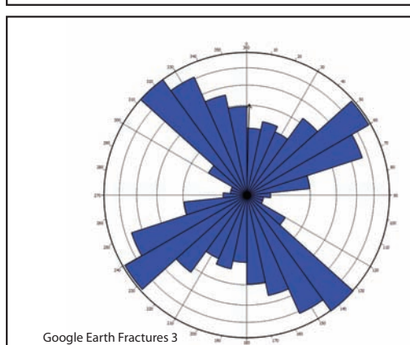

Google Earth Fractures 3
Number of Points: n = 428

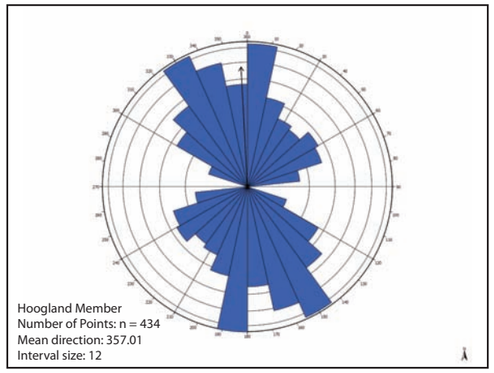

Hoogland Member
Number of Points: n = 434
Mean direction: 357.01
Interval size: 12

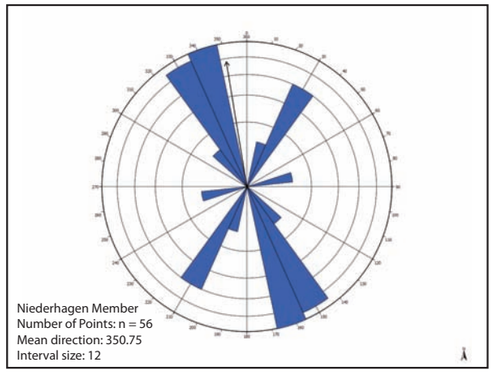

Niederhagen Member
Number of Points: n = 56
Mean direction: 350.75
Interval size: 12

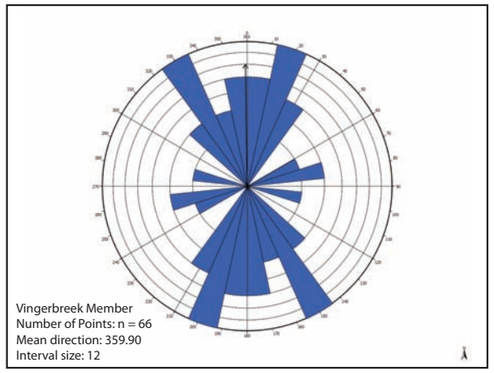

Vingerbreek Member
Number of Points: n = 66
Mean direction: 359.90
Interval size: 12

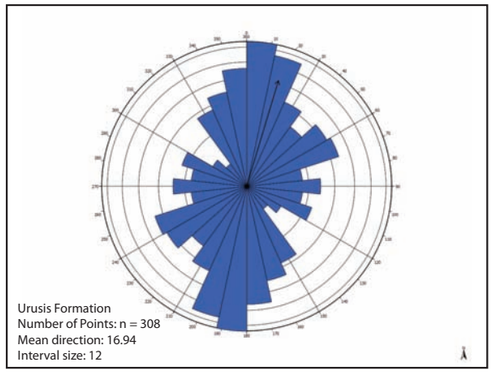

Urusis Formation
Number of Points: n = 308
Mean direction: 16.94
Interval size: 12

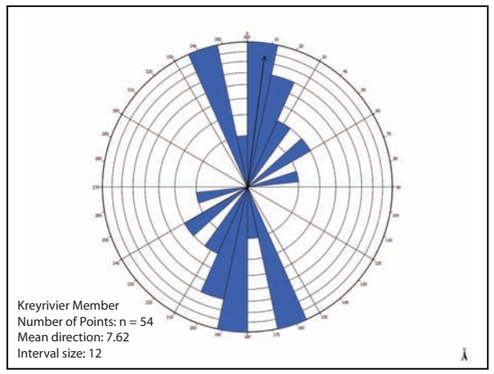

Kreyrivier Member
Number of Points: n = 54
Mean direction: 7.62
Interval size: 12

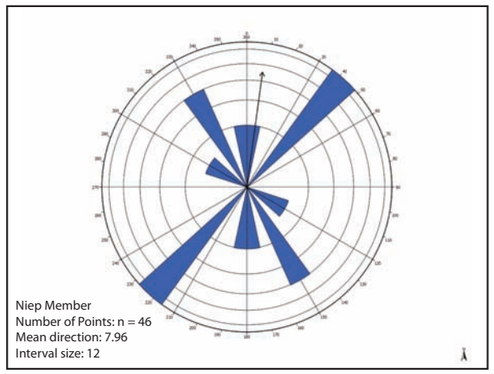

Niep Member
Number of Points: n = 46
Mean direction: 7.96
Interval size: 12

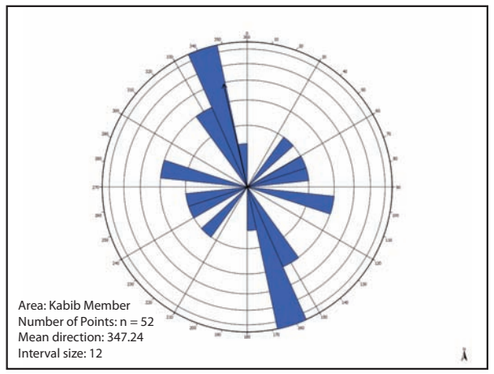

Area: Kabib Member
Number of Points: n = 52
Mean direction: 347.24
Interval size: 12

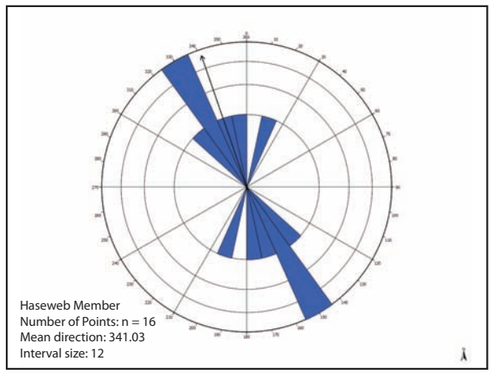

Haseweb Member
Number of Points: n = 16
Mean direction: 341.03
Interval size: 12

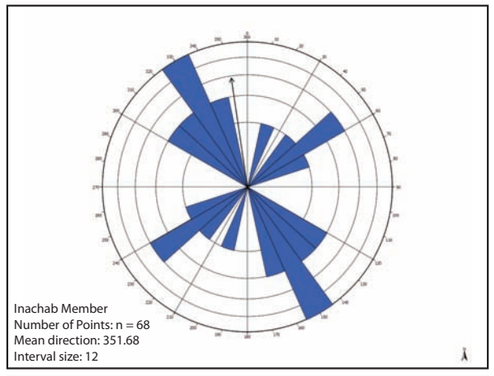

Inachab Member
Number of Points: n = 68
Mean direction: 351.68
Interval size: 12

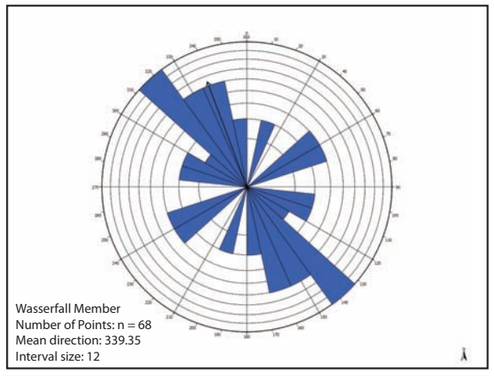

Wasserfall Member
Number of Points: n = 68
Mean direction: 339.35
Interval size: 12

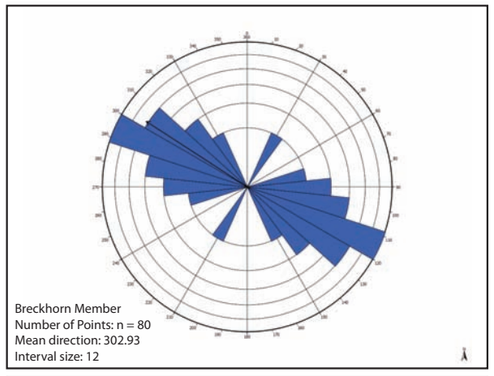

Breckhorn Member
Number of Points: n = 80
Mean direction: 302.93
Interval size: 12

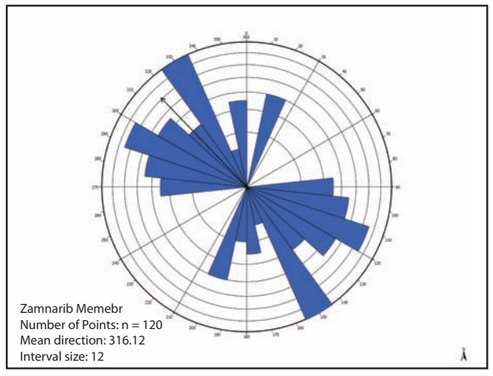

Zamnarib Memebr
Number of Points: n = 120
Mean direction: 316.12
Interval size: 12

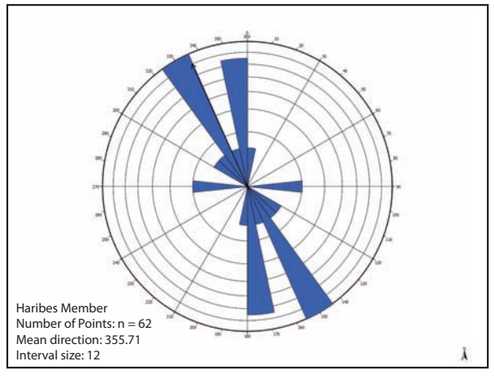

Haribes Member
Number of Points: n = 62
Mean direction: 355.71
Interval size: 12

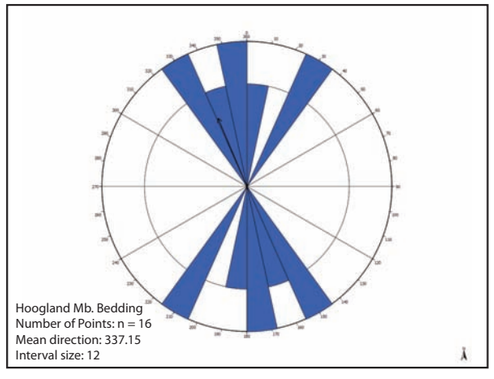

Hoogland Mb. Bedding
Number of Points: n = 16
Mean direction: 337.15
Interval size: 12

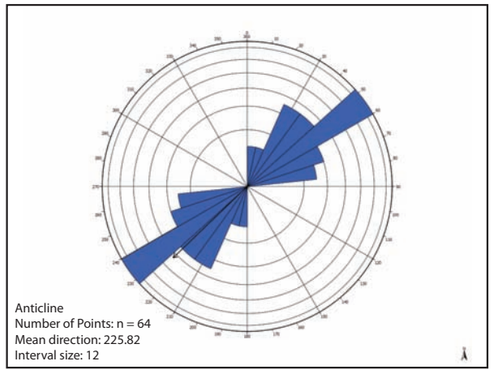

Anticline
Number of Points: n = 64
Mean direction: 225.82
Interval size: 12

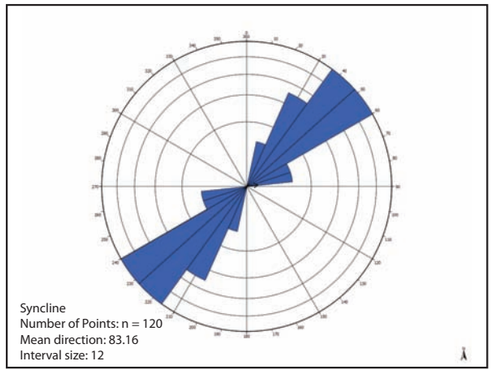

Syncline
Number of Points: n = 120
Mean direction: 83.16
Interval size: 12

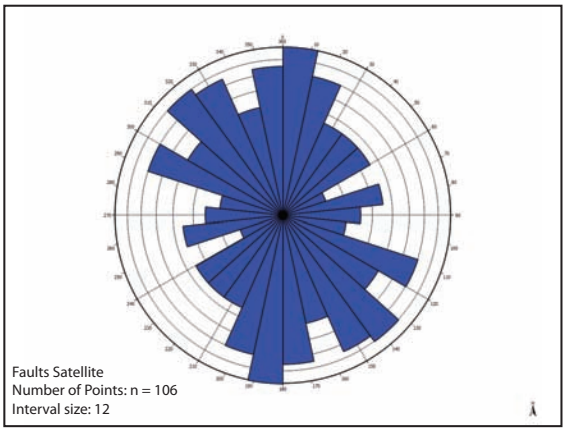

Faults Satellite
Number of Points: n = 106
Interval size: 12

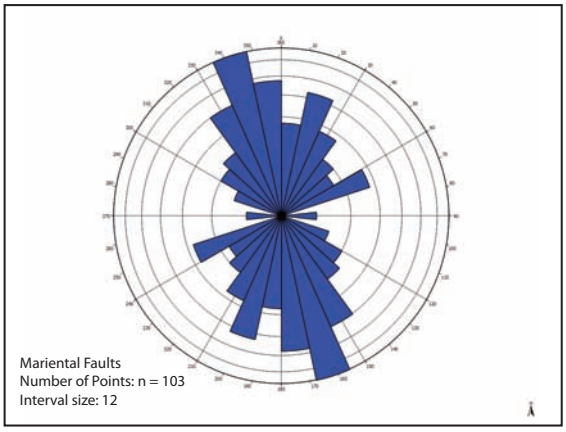

Mariental Faults
Number of Points: n = 103
Interval size: 12

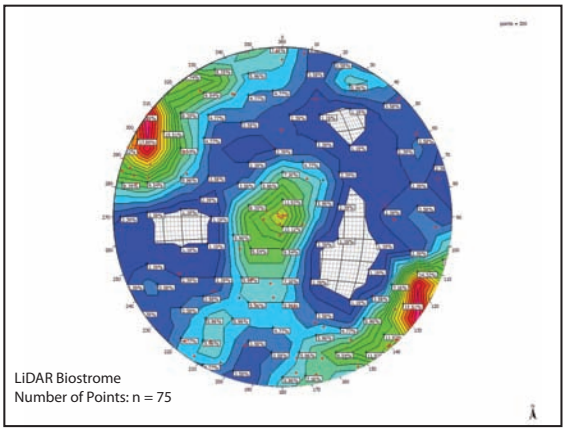

LiDAR Biostrome
Number of Points: n = 75

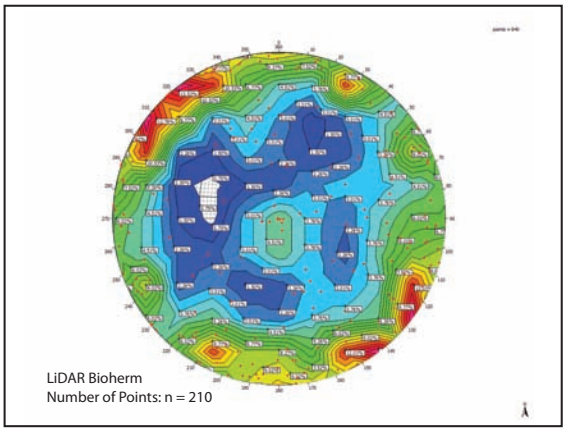

LiDAR Bioherm
Number of Points: n = 210

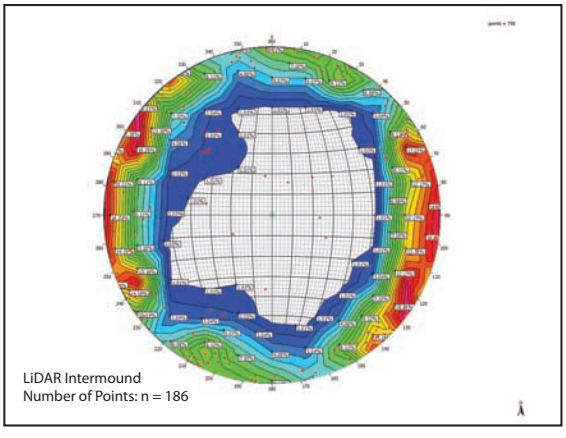

LiDAR Intermound
Number of Points: n = 186

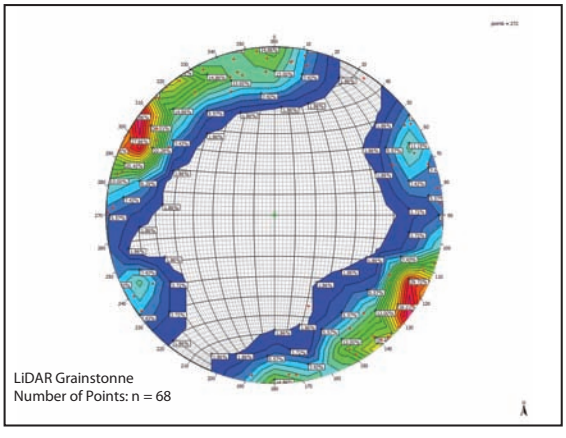

LiDAR Grainstonne
Number of Points: n = 68

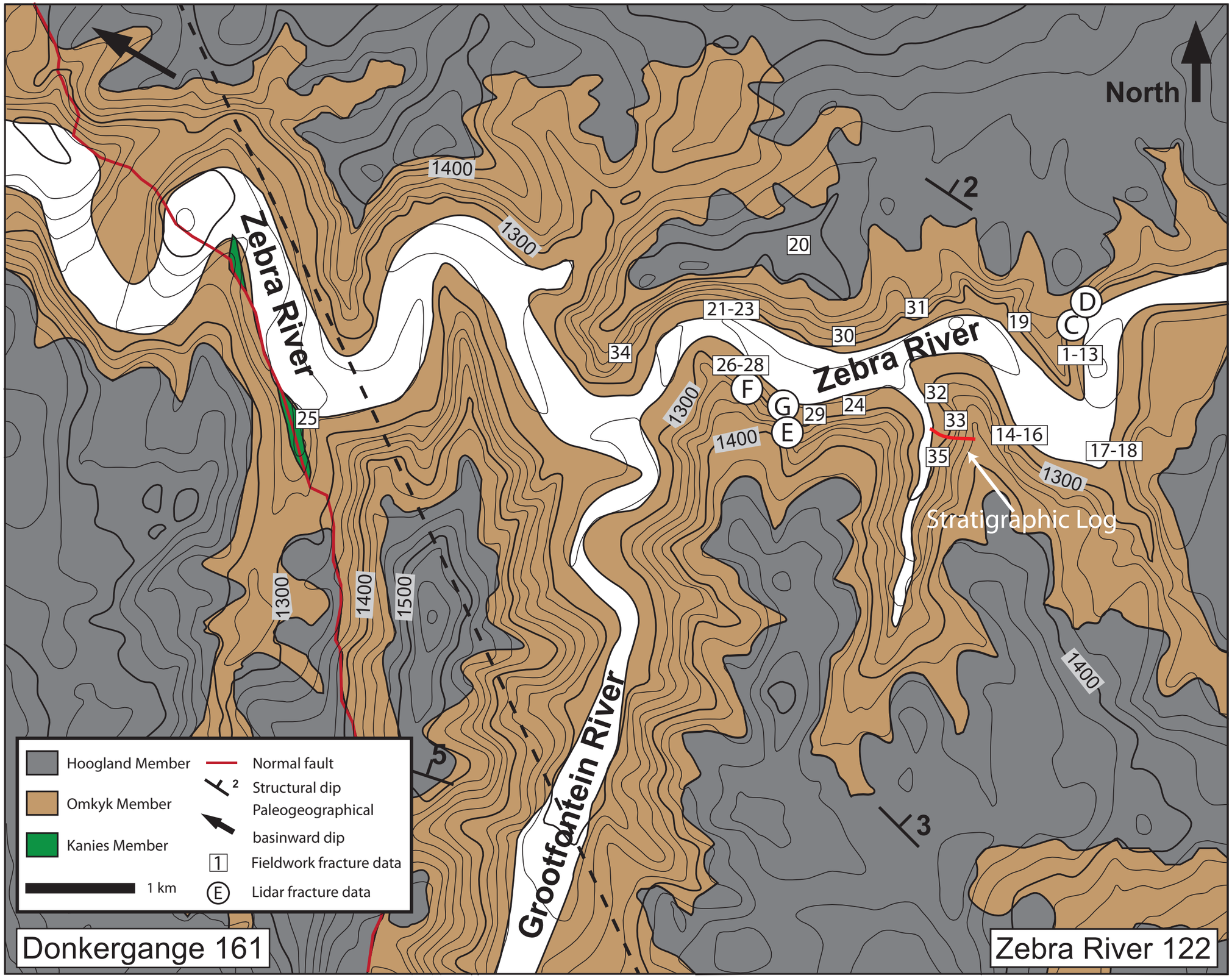
North
Zebra River
Zebra River
Grootfontein River
1400
1300
1500
20
2
21-23
31
30
34
19
D
C
1-13
26-28
F
G
E
29
24
32
33
14-16
17-18
35
25
Stratigraphic Log
5
3
Hoogland Member
Omkyk Member
Kanies Member
1 km
Normal fault
Structural dip
Paleogeographical basinward dip
Fieldwork fracture data
Lidar fracture data
Donkergange 161
Zebra River 122

# APPENDIX VI

# The matlab source-code

```
clear
%% Input
method = 'efficient';
num = 2000;
l = 1150;
w = 2400;
h = 60;
maxr = 37;
minr = 2;
min_dist = 22;

alpha = 0:10:360;
beta = 0:10:90;

save_q = 'y';
save_file = 'bioherm.txt';

%% Main
xo = zeros(1,num);
yo = zeros(1,num);

if min_dist == 0
    xo = rand(1,num)*w;
    yo = rand(1,num)*l;
else
    counter = 1;
    xo(1) = rand(1,1)*w;
    yo(1) = rand(1,1)*l;
    for k = 2:num
        dist = min_dist-1;
        while min(dist)<min_dist
            xo_new = rand(1,1)*w;
            yo_new = rand(1,1)*l;

            dist = sqrt((xo_new-xo(1:k)).^2 + (yo_new-yo(1:k)).^2);
        end
        xo (k) = xo_new;
        yo (k) = yo_new;
        disp(k)
    end
end

r = rand(1,num)*(maxr-minr)+minr;
zo = zeros(1,num);

alphaN = repmat(alpha,length(beta),1);
alphaN = alphaN'; alphaN = alphaN(:);

betaN = repmat(beta, length(alpha),1);
betaN = betaN(:);

alphaNN = repmat(alphaN',num,1);
betaNN = repmat(betaN', num, 1);
xoNN = repmat(xo',1,length(alpha)*length(beta));
yoNN = repmat(yo',1,length(alpha)*length(beta));
```

```
zoNN = repmat(zo',1,length(alpha)*length(beta));
rNN = repmat(r',1,length(alpha)*length(beta));

X = xoNN + rNN.*cosd(alphaNN).*sind(betaNN);
Y = yoNN + rNN.*sind(alphaNN).*sind(betaNN);
Z = zoNN + rNN.*cosd(betaNN);

% Check intersect
index_inter = zeros(num,num);
for j = 1:num
    dist_o = sqrt((xo(j)-xo).^2 + (yo(j)-yo).^2);
    sum_r = r(j)+r;
    index_inter(j,:) = dist_o < sum_r;
end
index_inter = index_inter - diag(diag(index_inter));
index_inter = index_inter == 1;

% Remove points in the intersections
num_inter = sum(index_inter,2);
for j = 1:num
    ui = find(index_inter(j,:));
    for u = 1:num_inter(j)
        dist_p = sqrt((xo(j)-X(ui(u),:)).^2+(yo(j)-
Y(ui(u),:)).^2+(zo(j)-Z(ui(u),:)).^2);
        X(ui(u),dist_p < r(j)) = NaN;
        Y(ui(u),dist_p < r(j)) = NaN;
        Z(ui(u),dist_p < r(j)) = NaN;
    end
end

X = X(:);
Y = Y(:);
Z = Z(:);

X(isnan(X)) = [];
Y(isnan(Y)) = [];
Z(isnan(Z)) = [];



%% Plot

plot(X,Y,'.') % 2D
%plot3(X,Y,Z,'o') % 3D
axis equal

%% Save
switch save_q
    case 'y'
        disp('Saving')
        save_f = [X Y Z];
        save(save_file,'save_f','-ascii')
end
```

# APPENDIX VII

# Styles, origins and implications of syndepositional deformation structures in Ediacaran microbial carbonates (Nama Basin, Namibia)

G. WINTERLEITNER[1]*, D. P. LE HERON[1], B. MAPANI[2], B. A. VINING[1] & K. J. W. MCCAFFREY[3]

[1]*Department of Earth Sciences, Royal Holloway University of London, Egham, Surrey, TW20 0BY, UK*

[2]*Geology Department, University of Namibia, Windhoek, Namibia*

[3]*Department of Earth Sciences, Durham University, Durham, DH1 3LE, UK*

**Corresponding author (e-mail: gerd.winterleitner@gmail.com)*

**Abstract:** Outstanding exposures of Ediacaran-aged thrombolite–stromatolite bioherms and biostromes crop out in the Nama Basin, SW Namibia. Fieldwork, dovetailed with remote sensing and a terrestrial laser scanning (LiDAR) survey, allow the fracture network of this succession to be characterized, and the relative age of fracture sets and families to be determined. The results show that the microbial carbonates were affected by intense syndepositional brittle and ductile deformation. Early brittle fracturing was favoured where early lithification of microbialites took place upon deposition. Such deposits were prone to gravitational collapse due to internal weaknesses during early lithification. Timing of syndepositional fracturing of bioherms and biostromes is demonstrated by contemporaneous microbial overgrowth over brecciated material in open-mode fractures. Ductile deformation occurs preferentially around massive thrombolite domes and columns, represented by folding of mud-dominated sediments in inter-column fill. Secondary fractures developed during the long-lived structural history of the Nama Basin, resulting in a complex fracture network of syndepositional fractures overprinted by secondary fractures. These findings have important implications for carbonate reservoir characterization in microbial reservoirs and subsurface fluid-flow estimations. The observed syndepositional fractures form due to body forces that are intrinsic to the microbial system and thus do not require an external tectonic driver.

Since their first description in the literature (Kalkowsky 1908), microbial carbonates have been subject to intense investigation. Much attention has focused on Precambrian and Cambrian microbialites (Aitken 1967; Fairchild 1991; Glumac & Walker 1997; Grotzinger & Knoll 1999; Riding 2000). They represent the first record of life on Earth extending back some 3.4 Ga (Allwood *et al.* 2007). Organo-sedimentary structures produced by bacterial communities give insight into earliest biological evolution and serve as proxy for the chemical and physical conditions during the Precambrian (Fairchild *et al*. 1990; Summons *et al.* 1999; Schröder *et al.* 2004; Le Heron *et al.* 2013). Following the destruction of carbonate platforms during the Cryogenian glaciations, these robust communities were rapidly re-established, flourishing with complex forms (Le Ber *et al.* 2013).

Huge oil reserves, hosted in microbial carbonates, were discovered by Petrobras and BG Group in the Santos Basin of Brazil in 2006 (Gomes *et al.* 2009; Beglinger *et al.* 2012; Wright 2012). **EDQ1** This has stimulated a resurgence of interest in microbial carbonates more generally from two perspectives: (1) to establish facies models from around the world, including Neoproterozoic strata (e.g. Le Ber *et al.* 2013) and (2) to understand the patterns of deformation that cross-cut microbial build-ups. In the case of the former, microbial carbonates are notoriously heterogeneous, and thus efforts to understand their sequence-stratigraphic context, reservoir architecture and heterogeneity are required (Parcell 2003; Mancini *et al.* 2004; Schröder *et al.* 2005; Al Haddad & Mancini 2013). Such study aims to understand pore geometries and their influence on fluid-flow performance. With regard to their deformation many carbonates are natural fractured reservoirs. The fracture system has an important role in reservoir performance, as fractures can either significantly enhance or retard fluid flow, depending on local context. This aspect is the topic of the present paper, in which we present a

*From*: BOSENCE, D. W. J., GIBBONS, K. A., LE HERON, D. P., MORGAN, W. A., PRITCHARD, T. & VINING, B. A. (eds) *Microbial Carbonates in Space and Time: Implications for Global Exploration and Production*. Geological Society, London, Special Publications, **418**, http://doi.org/10.1144/SP418.12

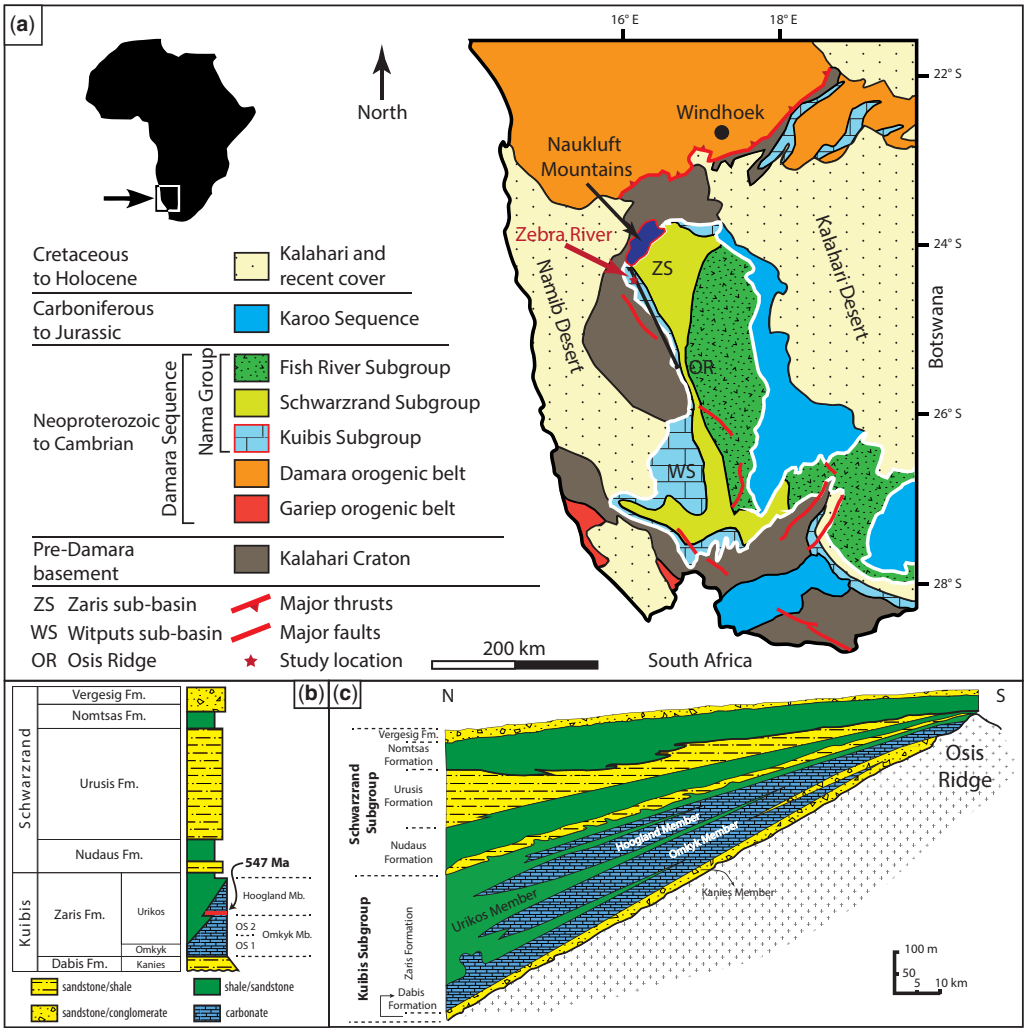


**Fig. 1.** (**a**) Geological map of south Namibia. White outline indicates extent of the Nama Basin. Modified after Adams *et al.* (2005). (**b**) Stratigraphy of the Zaris sub-basin. Modified after Blanco *et al.* (2011). Red line in the lower Hoogland Member indicates dated ash bed with a U–Pb zircon age date of 547.32 ± 0.65 Ma (Narbonne *et al.* 2012). (**c**) Schematic cross-section of the Kuibis and Schwarzrand Subgroups in the Zaris sub-basin. Location of cross-section see Figure 1a. Modified after Gresse & Germs (1993).

**Colour online/ colour hardcopy**

high quality, outcrop case study of both brittle and ductile deformation affecting a carbonate platform of Ediacaran age in the Nama Basin, Namibia (Fig. 1a).

In this paper, we present a detailed description of the carbonates of the Nama Basin, Namibia (Fig. 1a), focusing on structural characteristics. Our objective is to provide a framework of the response of microbialites to deformation during early compaction and lithification. We will link different fracture patterns to individual growth forms and geometries of the microbial carbonate system, presenting a valuable analogue dataset for fracture systems in microbial reservoirs.

## Study area, geological background and outcrop overview

The study area is located in the Zebra River Canyon system at the NW edge of the Nama Basin, in south-central Namibia (Fig. 1a). The terminal Neoproterozoic–early Cambrian Nama Basin has been interpreted as a foreland basin fill, which formed

during the final stages of the Pan-African Damara and Gariep orogenic events (Germs 1974). The advancing nappe fronts of the Damara and Gariep belts submerged the northwestern part of the Kalahari craton, which initiated the deposition of the mixed carbonate-siliclastic Nama sediment succession on the Kalahari craton at *c.* 550 Ma (Grotzinger & Miller 2008). The age of the sediment succession is constrained by several dated ash beds in addition to Ediacaran body fossils *Namacalathus* and *Cloudina* (Grotzinger *et al.* 2000; Wood *et al.* 2002; Wood 2011). The Cambrian boundary in the Nama Basin is situated in the Nomtas Formation of the upper Schwarzrand Subgroup, constrained between two dated ash beds with U–Pb zircon ages of 542.68 $\pm$ 2.80 Ma and 540.61 $\pm$ 0.88 Ma (Narbonne *et al.* 2012) (Fig. 1b). A detailed description of the geodynamic evolution of the Pan-African system in SW Gondwana is given by Frimmel *et al.* (2002, 2010), Alkmim *et al.* (2006), De Wit *et al.* (2008), Li *et al.* (2008), Pedrosa-Soares *et al.* (2008) and Scotese (2009).

The general architecture and stratigraphy of the Nama foreland basin fill has been outlined in a series of papers (Germs 1972, 1974, 1995; Gresse & Germs 1993). The Nama is subdivided into two sub-basins, namely the Zaris sub-basin in the north and Witputs sub-basin in the south (Fig. 1a). The two sub-basins are separated by the Osis ridge, which is interpreted as a peripheral forebulge in the foreland basin. The sediment successions thicken from the Osis ridge (1 km thickness) towards the deeper parts of the sub-basins (3 km thickness): to the north in the Zaris sub-basin (Fig. 1c) and to the south in the Witputs sub-basin respectively.

The Nama Group is divided into three subgroups. In ascending stratigraphic order, these are the Kuibis, Schwarzrand and Fish River subgroups. The general trend of the subgroups characterizes a typical foreland basin fill represented by an overall decrease in sediment maturity upsection. The lowermost Kuibis Subgroup is characterized by a shallow marine, mixed carbonate clastic succession. The first deepening of the basin resulted in the deposition of fluvial to shallow marine siliciclastic sediments, which exhibit a cratonic interior provenance (Blanco *et al.* 2011). Following this first transgressive event, extensive carbonate platforms developed in both sub-basins: the Kuibis platform in the Zaris sub-basin (Adams *et al.* 2004, 2005; Dibenedetto & Grotzinger 2005) and the Huns platform in the Witputs sub-basin (Saylor *et al.* 1995; Saylor 2003). With the ongoing deepening of the Nama Basin and an increased input of siliciclastic material carbonate production came to a halt, at first in the Zaris sub-basin and subsequently in a later stage in the Witputs sub-basin (Grotzinger & Miller 2008). This succession is summarized in the Schwarzrand Subgroup, represented by flysch sediments derived from the advancing orogenic fronts of the Damara and Gariep belts. The molasse sediments are found at the uppermost part of the Schwarzrand Subgroup representing continental collision at *c.* 542 Ma (Blanco *et al.* 2009). The youngest Nama subgroup, the Fish River Subgroup, represents the final filling of the basin, characterized by more proximal molasse-type sediments originating from the unroofing of the Damara and Gariep orogens (Blanco *et al.* 2011).

The location of the Nama outcrops within the southern part of the Namib Desert, in concert with gentle regional dips of a few degrees, make them ideal for studying both sedimentology and structure. A deeply dissected topography (Fig. 2) characterizes the Zebra River area. The canyonlands, some following regional faults and others forming more locally developed fracture sets, have been excavated by flash-flood processes. The network of canyons yields exposures in excess of 100 m high, allowing sedimentology and structural phenomena to be mapped in 3 D (Fig. 3a).

### *The Kuibis Subgroup*

The study interval is situated in the lower parts of the Kuibis Subgroup, which is the basal unit of the Nama Group (Fig. 1b). Excellent exposures of the Kuibis carbonate platform can be found in the Zebra River Canyon system of the Zaris Mountains of south-central Namibia (Fig. 1a). The superb quality of the outcrops in the dendritic canyon systems provides an exceptional opportunity to study the Omkyk and Hoogland members of the Kuibis carbonate platform (Fig. 3a).

The Subgroup is divisible into the Dabis and overlying Zaris formations (Fig. 1b). The basal unit of the Kuibis succession, the Dabis Formation, unconformably overlies pre Nama basement strata and is represented in the study area by the Kanies Member. The Kanies Member has been interpreted as the first flooding event on the Kalahari Craton in the Nama Basin and is characterized by brown to greenish immature sandstones, which reach a maximum thickness of 1–3 m. These are interpreted as braided fluvial deposits (Germs 1983). With the ongoing deepening of the basin, this succession grades upward into the Zaris Formation, which encompasses three members: Urikos, Omkyk and Hoogland members. The latter two members have been interpreted as a carbonate ramp system (Burchette & Wright 1992) with a palaeogeographic dip towards the NW (Germs 1983). The age of the Kuibis platform is directly constrained by a U–Pb zircon date of 547.32 $\pm$ 0.65 Ma in the lowermost part of the Hoogland Member (Fig. 1b) (Narbonne *et al.* 2012).

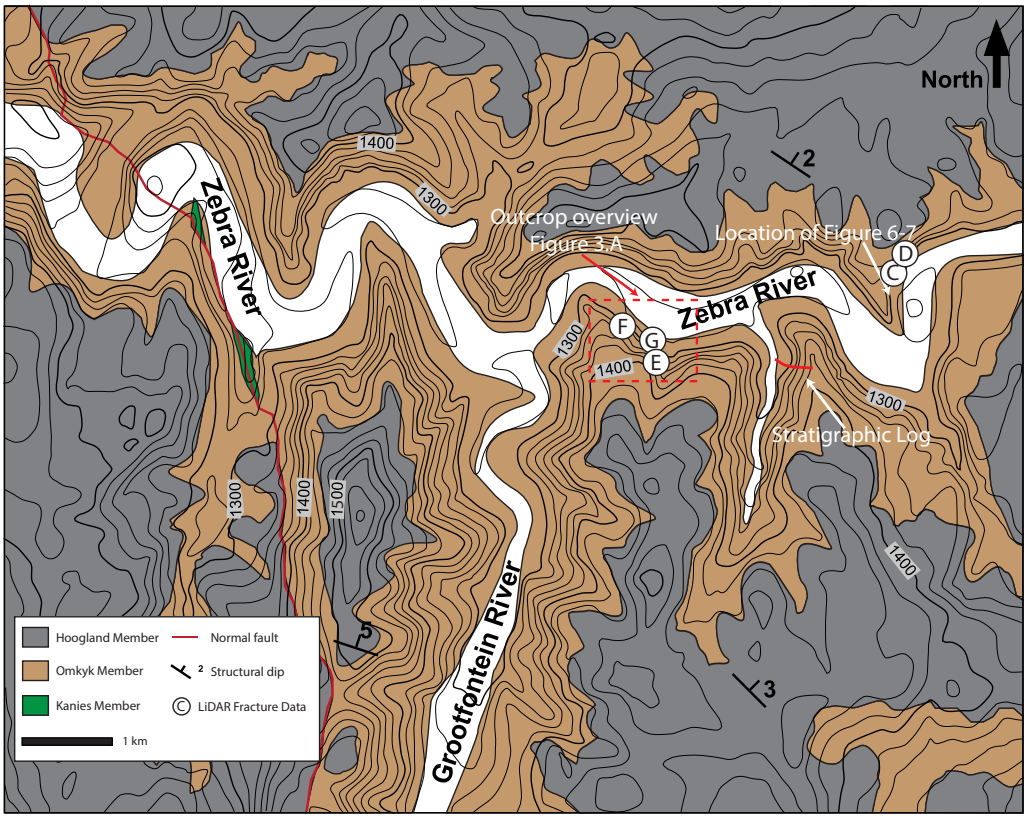


**Fig. 2.** Geological map of the Zebra River Canyon system in the study area. Modified after Adams *et al.* (2005).

**Colour online/ colour hardcopy**

The carbonate strata downlap onto the clastics of the Urikos Member towards the NW. The Urikos Member represents distal facies and is characterized by basinal shales and outer- to mid-ramp mudstones. Up-dip, the Urikos Member interfingers with the proximal carbonate-dominated successions of the Omkyk and Hoogland members. These latter two members comprise the Kuibis carbonate platform of the Zaris sub-basin. The platform has a thickness of *c.* 150 m near the Osis ridge and thickens to more than 500 m northward to the Naukluft Mountains (Germs 1983; Grotzinger *et al.* 2005). The Kuibis carbonate platform exhibits a ramp geometry: it has been interpreted as a storm- and wave-dominated carbonate ramp, subdivided into inner-, mid- and outer-ramp facies (Dibenedetto & Grotzinger 2005). In this paper, we present a detailed log section through part of the Omkyk Member (Fig. 4). The inner-ramp facies was deposited above fairweather wave-base and represents the shallowest facies. It consists of thrombolitic and stromatolitic biostromes and bioherms associated with medium- to coarse-grained packstones and grainstones, regarded as interbioherm facies (Fig. 4, 37–52 m). Back-barrier and peritidal deposits of the inner ramp include mudstones, calcisiltite and minor shale. Mid-ramp facies, deposited between storm and fairweather wave-base is characterized by mudstones, calcilutite and minor shale. Graded storm beds with hummocky cross-stratification (Fig. 4, 13 m) are common. The outer-ramp succession, deposited below storm wave-base, marks the transition zone to the basinal shale of the Urikos Member and consists mainly of greenish shales and minor mudstones, interbedded with a few storm deposits. Microbial carbonates are found throughout the entire Zaris Formation but are best developed in the upper half of the Omkyk Member.

### *Omkyk Member*

The Omkyk Member was examined in some detail by a group of researchers led by John Grotzinger (Grotzinger *et al.* 2000; Adams *et al.* 2004, 2005; Dibenedetto & Grotzinger 2005; Grotzinger

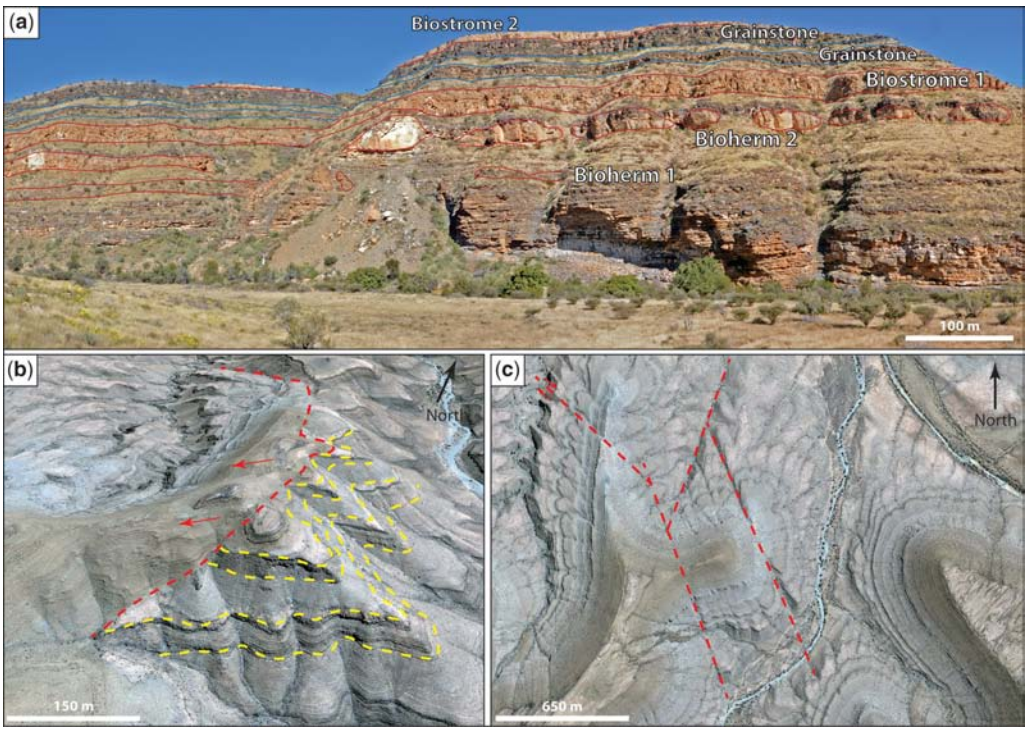


**Colour online/ colour hardcopy**

**Fig. 3.** (**a**) Outcrop overview of Zebra River Canyon system with stratigraphic interpretations. (**b**) Google Earth satellite image of the normal fault in the west of the study area (oblique view from the SE). See Figure 2 for location. The normal fault can be easily recognized due to the vertical offset. Yellow dotted lines indicate horizontal bedding of the Omkyk Member. The Hoogland Member (to the west of the normal fault) shows a vertical offset of *c.* 120 m. (**c**) Example of identified strike-slip faults on Google Earth imagery. Note visible dextral displacement of NW–SE-trending fault.

*et al.* 2005). Figure 4 is a new sedimentary log of the Omkyk Member in the Zebra River area, *c.* 1 km along-strike from that of Adams *et al.* (2005). The following is a resume of the key sedimentological and stratigraphic aspects of this succession. Whilst the observations are those of the first author of the present paper, it is recognized that inevitably several of these features overlap with those described in Adams *et al.* (2005) along-strike. Ramp carbonates of the Omkyk Member form two coarsening-upward shoaling sequences, Omkyk Sequence 1 (OS1) and Omkyk Sequence 2 (OS2) (Grotzinger *et al.* 2005). The lower part of OS1is characterized by mid-shoreface hummocky cross-bedded grainstones, intercalated with storm-generated shale and mudstone beds. It overlies fluvial sandstones of the Dabis Formation and represents the first occurrence of carbonates in the Zaris sub-basin. OS1 grades upward into wave-influenced, shoreface grainstones, which are typically coarse-grained and cross-bedded. The second shoaling-upward sequence is OS2, which is split into five further sequence-stratigraphic units (Adams *et al.* 2005) (Fig. 4); these are labelled Units 1 to 5 in this paper. Three facies associations represent each of these five units of OS2: (1) mud-dominated facies, (2) grain-dominated facies and (3) thrombolite–stromatolite facies. The mud-dominated facies consists of siliciclastic shales, lime mudstone, intraclast breccias and irregular laminate. The grain-dominated facies is represented by coarse-grained grainstones and minor fine- to medium-grained grainstones. Grainstones are composed of millimetre-scaled peloids, intraclasts and coated grains (Adams *et al.* 2005). Thrombolite–stromatolite facies thus represent the microbial carbonates, developed as bioherms and biostromes, respectively.

Thrombolite–stromatolite carbonates are found at several stratigraphic levels within the Omkyk Member (Grotzinger *et al.* 2000; Adams *et al.* 2004, 2005). Four levels of microbial carbonates are found in the OS2 and comprise both bioherms (Fig. 3a, Bioherms 1 & 2) and biostromes (Fig. 3a, Biostrome 1) within the Zebra River Farm outcrops. A laterally extensive thrombolitic biostrome started to develop in the latest stages of OS2

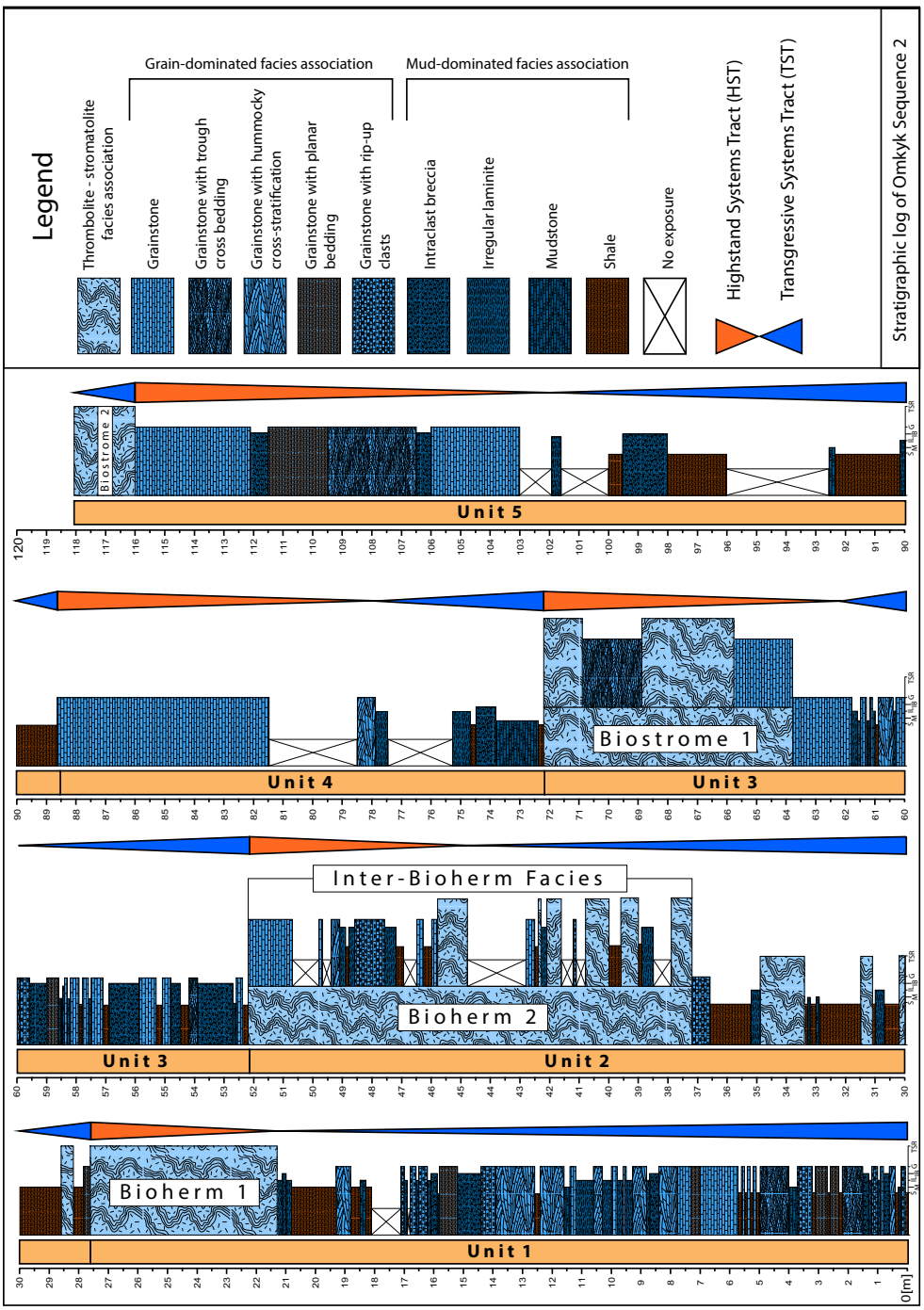


**Fig. 4.** Sedimentary log of Omkyk Sequence 2. The location of the measured section is indicated in Figure 2.

**Colour online/ colour hardcopy**

and marks the top of the Omkyk Member (Fig. 3a, Biostrome 2).

Bioherms exhibit a mound-like geometry in cross-section view and are laterally discontinuous (Fig. 3a). The bioherms range from *c.* 1–20 m in height, and several tens of metres in width. The individual mounds are separated by inter-bioherm facies and the plan-view shape of the bioherms has been interpreted to be circular (Adams *et al.* 2005). The internal architecture of the bioherms is predominately defined by domal to columnar thrombolites. In general the cores of the individual domes and columns are thrombolitic and tend to become stromatolitic towards the margins. The plan-view shape is circular to elliptic, being several decimetres along the short axes and several metres along the long axes. Inter-column fill is variable and depending on the stratigraphic position it may comprise, shale, mudstone and cross-stratified pack- to grainstone, associated with *Namacalathus* and *Cloudina* fragments (Grotzinger *et al*. 2000; Wood *et al*. 2002; Wood 2011).

The onset of the bioherm growth is interpreted to represent the late stages of the transgressive unit systems tract (Fig. 4, 37–45 m). In this stage the bioherms are aggradational and are associated with mud-dominated facies, such as shale and mudstones. Thus, the nucleation of the bioherms was interpreted to have occurred during times of maximum accommodation space and reduced background sedimentation (Adams *et al.* 2005; Grotzinger *et al.* 2005). During the highstand systems tracts (HST) and times of decreasing accommodation, the bioherms became progressively more associated with grain-dominated facies and subsequently started to prograde. The increasing sediment input at the latest stages of Unit 2 terminated the microbial growth and grainstones covered the bioherms.

Biostromes are characterized by a tabular, sheet-like geometry and are lateral continuous geobodies (up to several kilometres across) (Fig. 3a). Their thickness in the Zebra River area is *c.* 11–13 m. The internal structure is defined by coalesced thrombolitic, fine-scaled columns (centimetres to a few decimetres in height). Both biostromes in the study area are associated with grain-dominated facies, indicating shallow water depths and high-energy conditions. Therefore the evolution of the biostromes was interpreted to have formed during times of reduced accommodation space and high sediment input during the unit HST (Fig. 4, 64–72 m & 116–118 m) (Adams *et al.* 2005).

The microbial carbonates in OS2 show no evidence of karstification. Biostromes and bioherms are both affected by intense selective dolomitization. Carbonates in the study area are in general limestone and are only partly dolomitized in the vicinity of the microbial carbonates.

## Methods

The Zebra River Canyon system was placed into its structural regional context by means of a basic remote sensing study using Google Earth imagery and digitizing lineaments and fracture data from the geological map of Mariental (Schalk & Germs 1980). Lineaments were mapped onscreen without applying a minimum length rule. The excellent high resolution of the Google Earth images and absence of vegetation in the Zaris Mountains made it possible to trace faults (Fig. 3b, c) and fractures. A total of 278 fractures (Fig. 5a, b) and 108 lineaments (Fig. 5f) on the geological map and 723 fractures (Fig. 5c, d) and 106 faults (Fig. 5e) on the satellite imagery were mapped and analysed. It should be noted that this is a preliminary structural analysis of the area, and there was no attempt to analyse the structural history. The purpose of the remote sensing was to define the regional trend of the faults and fractures.

At outcrop, fieldwork was targeted on the description of geometry, morphology and on the internal structure of the microbial carbonates in the Zebra River Canyon system. Thus, a detailed investigation of the microbial framework development in a sequence-stratigraphic context was carried out. In addition to sedimentological observations a comprehensive analyses of the structural characteristics of the carbonate system in the Zebra River Canyon was conducted. This included detailed description of brittle and ductile deformation of microbialites and inter-bioherm facies in relation to the microbial architecture. More than 500 strike-and-dip measurements of fractures were collected (Fig. 5g), focused on the inter-bioherm areas (Fig. 5h) and grainstone horizons. The microbial carbonates form steep almost vertical cliffs and only a few reliable field-based fracture measurements could be obtained. In order to obtain accurate fracture data from the microbialites a LiDAR survey was carried out using a terrestrial laser scanner (Riegl Z420i) with a nominal range of 800 m (see Jones *et al.* (2010) for a review of methodologies). The resulting digital outcrop model has an average resolution of 10 cm. Sections of interests were scanned in detail with a resolution of 2 cm. Fracture mapping was directly carried out on the meshed fracture surfaces of the virtual outcrop model following the manual method outlined by Wilson *et al.* (2011). A total of four sections were digitally mapped: (1) inter-bioherm area (182 fractures, Fig. 5l), (2) grainstone horizon (74 fractures, Fig. 5k), (3) bioherms of Unit 2 (210 fractures, Fig. 5j) and (4) part of the biostrome in Unit 3 (75 fractures, Fig. 5i).

High-resolution photos were taken of selected bioherms and biostromes (Figs 6 & 7). Fracture interpretation was carried out on panorama

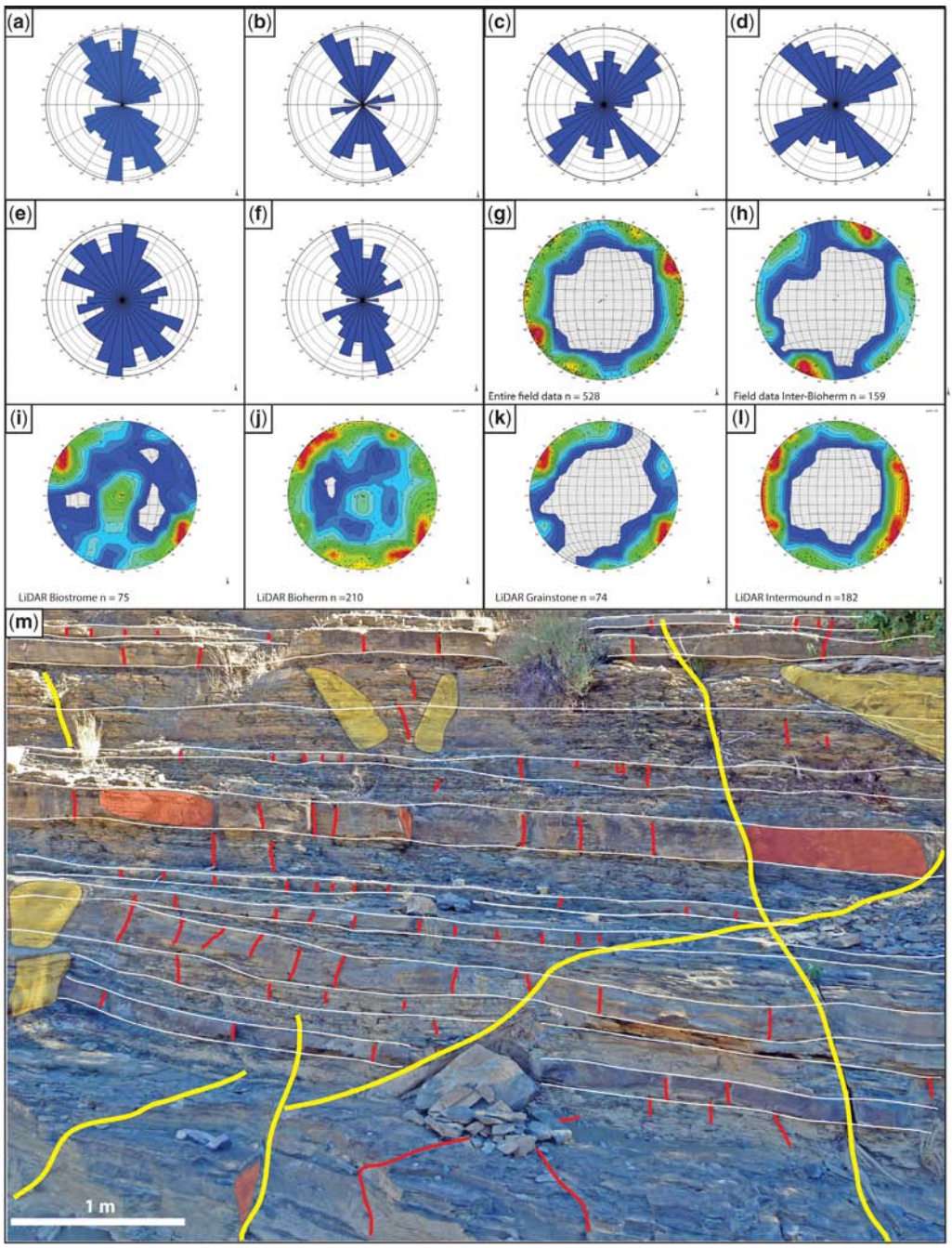


**Colour online/ colour hardcopy**

**Fig. 5.** (**a**) Rose diagram of fractures in the Hoogland Member. Digitized from the geological map of Mariental. Interval size 12, $N = 217$. (**b**) Rose diagram of fractures in the Naudus Formation. Digitized from the geological map of Mariental. Interval size 12, $N = 61$. (**c**) Rose diagram of fractures in the Hoogland Member. Digitized from Google Earth satellite imagery. Interval size 12, $N = 295$. (**d**) Rose diagram of fractures in the Hoogland Member. Digitized from Google Earth satellite imagery. Interval size 12, $N = 428$. (**e**) Rose diagram of faults. Digitized from Google Earth satellite imagery. Interval size 12, $N = 106$. (**f**) Rose diagram of faults. Digitized from the geological map of Mariental. Interval size 12, $N = 108$. (**g**–**l**) Contour plots of fracture data poles. The colour coding indicates relative

photomosaic images and subsequently ground-truthed with the LiDAR datasets to obtain accurate geometries. A total of 628 fracture traces were mapped on the photomosaic (Fig. 6). These were subsequently grouped and their cross-cutting relationships and fracture terminations analysed. A simple linear fracture density analysis (number of fractures per unit length) was conducted by applying a horizontal scanline (length 101 m) on the spatially referenced fracture traces (Fig. 6).

## Sedimentological overview

Fieldwork results and photomosaic interpretations revealed a complex system of stacking patterns and internal architecture of the microbial carbonate system. This can be observed at several scales throughout the entire sequence in the Zebra River Canyon system. The following focuses on three scales of observation: (1) at the level of the entire OS2 and the various stacking patterns of the microbialites; (2) at the level of the microbial horizons and the distinctive differences between the microbialites and their interactions with each other; and (3) at the level of the scale of the internal structure of the microbialites with respect to changing growth forms during the evolution of the microbialites.

### *Bioherms*

Due to limited outcrop of bioherms in Unit 1, the following descriptions derive mainly from observations of bioherms in Unit 2 of the OS2. Previous authors interpreted shutdown of bioherm growth in Unit 1 at the latest stages of the HST (Adams *et al.* 2005). Thus, bioherms have been interpreted to be restricted to each unit. However, several bioherms have been observed which kept up with the increasing sediment input during Unit 1 HST and early Unit 2 transgressive systems tract. These remaining mound structures formed topographic highs and subsequently served as preferential growth locations for bioherms during the onset of microbial growth in Unit 2 (Fig. 7). This in turn led to the formation of stacked bioherms where one mound grew over rigid topographies of the remaining underlying mounds (Fig. 7).

During the onset of the bioherm evolution, the microbialites are associated with mud-dominated facies, and bioherms only aggrade. At that stage, microbial carbonates are best described as microbial patches. These small-scaled mounds are characterized by an association of massive columns (Fig. 8a), domes and goblet-shaped thrombolitic structures. These structures are isolated and in general neither branch nor merge. Inter-column widths attain several metres, and distances between the mounds range from $<10$ m to $>100$ m. The first input of grain-dominated material allowed the microbialites to spread out laterally over the inter-column fills as well as over entire inter-bioherm areas. In cases of close-spaced microbial patches the lateral spreading zones merge together (Fig. 7). These 'merging zones' are defined by offlap and onlap geometries. An alternating change from mud-dominated to grain-dominated background sedimentation is common in the lower half of Unit 2. During times of carbonate sedimentation microbialites tend to spread out laterally and merge together. In contrast to that, shale and lime-mud deposition appear to be associated with aggradation. In such cases microbialites grow vertically and no lateral spreading occurs. Shale and mud beds can be traced over entire bioherm bodies but are preferentially deposited in local topographic lows, like the merging zones. The input of mud-dominated sediments locally terminates microbial activity and growth is restricted to topographic highs (e.g. bioherm cores). The microbial structural framework evolution is thus directly related to background sedimentation and can be subdivided into aggradational phases during mud-dominated sedimentation and lateral spreading phases during grain-dominated sedimentation.

Given sufficient time, these processes eventually lead to amalgamation of the individual microbial structures to bioherms and on a bigger scale to composite bioherms. The lateral spreading, bioherm amalgamation and growth termination is repeated up to three times resulting in a complex bioherm and composite bioherm internal stacking pattern in the lower half of Unit 2 (Fig. 7).

**Fig. 5.** (*Continued*) abundance of fracture poles: red corresponds to high density, blue to low density. Location of fracture measurements is indicated in Figure 2. The contour plots are as follows. (g) Entire fracture data derived from field measurement. $N = 528$. (h) Fracture data derived from field measurement at inter-bioherm facies at location C. $N = 159$. (i) Fracture data derived from LiDAR interpretation of the biostrome horizon at location G. $N = 75$. (j) Fracture data derived from LiDAR interpretation of the bioherm horizon at location F. $N = 210$. (k) Fracture data derived from LiDAR interpretation of the grainstone horizons at location E. $N = 74$. (l) Fracture data derived from LiDAR interpretation of the inter-bioherm facies at location D. $N = 182$. (**m**) Photointerpretation of fracture traces and fracture planes in the inter-bioherm facies at location D. Yellow fracture traces and fracture planes correspond to secondary fractures of category 1. Note that these fractures cross-cut several bedding planes (white horizontal lines). Red fracture traces and fracture planes indicate category 2 fractures of the secondary fractures which predominately abut at bedding planes. For locations, see Figure 2.

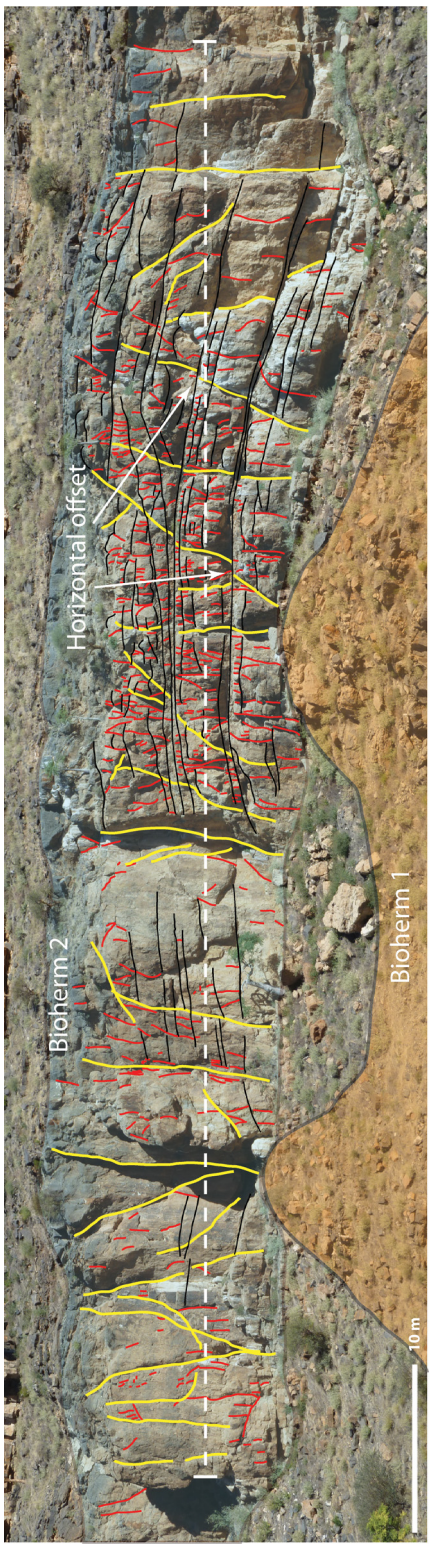


**Colour online/ colour hardcopy**

**Fig. 6.** Photomosaic image and fracture interpretation of a composite bioherm structure. For location see Figure 2. The blue shaded area indicates the composite mounds in Unit 2 and the orange shaded area outlines an underlying bioherm of Unit 1. Yellow lines are primary fractures, red are secondary fractures and black lines are shale and mud beds. White dotted line indicates the position of the scanline (length is 101 m). Note the higher secondary fracture density in the bioherm area above Unit 1 bioherm and the offset of primary fracture against shale gliding horizons.

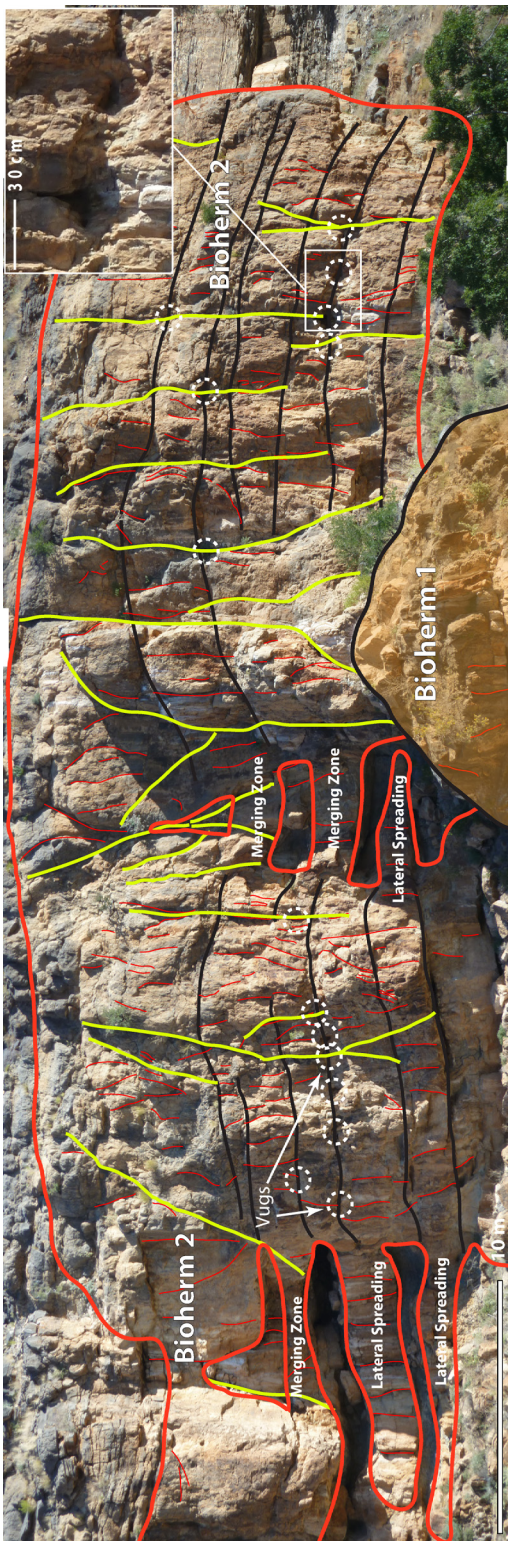


**Fig. 7.** Photomosaic image and fracture interpretation of a composite bioherm structure. For location see Figure 2. The image shows the lateral spreading and merging zones within a composite bioherm structure of Bioherm 2 unit, which partly started to grow over a mound of Bioherm 1. Yellow fracture traces indicate primary fractures. Black horizontal lines are shale and mud beds. Note the dissolution cavities and vugs at the intersection of primary fractures and shale and mud beds.

**Colour online / colour hardcopy**

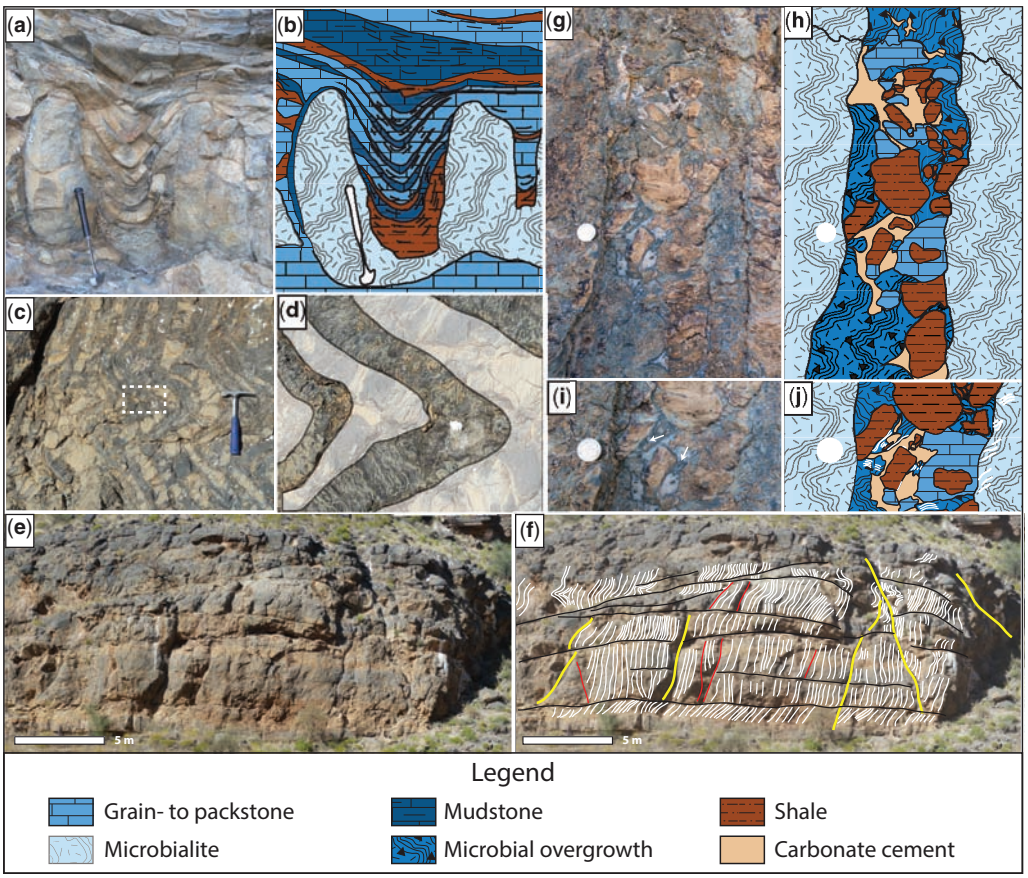


**Colour online/ colour hardcopy**

**Fig. 8.** (**a**) & (**b**): (a) Outcrop photo of syn-depositional deformation around massive thrombolite columns. Note the 'wrapping around' of inter-column sediment layers forming inter-column folds. (b) Redrawn structures of outcrop photo. Geological hammer for scale. (**c**) & (**d**): (c) Outcrop photo showing brittle deformation of microbial carbonates. Geological hammer for scale. (d) Enlarged section of outcrop photo. White shaded area represents inter-column fill. White rectangle in (c) indicates size and location of enlarged area. Note broken and rotated small scaled thrombolitic columns. (**e**) & (**f**): (e) Outcrop photo of a bioherm in Unit 2 and (f) photo interpretation. White lines indicate thrombolite and stromatolite columns. Note different orientation of column-folds at the top of the mound. Black lines are shale and mud beds, yellow lines are primary fractures and red lines are secondary fractures. (**g**) & (**h**): (g) Outcrop photo of an open mode fracture in Bioherm 2 and (h) redrawn structures. The fracture is filled with mudstone and grain- to packstone clasts with microbial over-growth, surrounded by a thin dark layer of dolomite cement and blocky white calcite cement. Coin for scale (diameter of coin is 2.5 cm). (**i**) & (**j**): Zoomed-in section of (g) and redrawn structures. Note the microbial overgrowth indicated by arrows in (i) and white lines in (j). Coin for scale (diameter of coin is 2.5 cm).

The upper half of Unit 2 is characterized by grain-dominated background sedimentation and the growth form of the microbialites changes to smaller scaled columns (Fig. 8c). The columns have diameters of 1–2 dm at the middle of Unit 2 HST but get continuously smaller (1–5 cm) when reaching the top of Unit 2. This growth form tends to branch laterally and forms continuous coalesced bodies within the mounds and composite bioherms. Sediment pockets, filled with packstones and grainstones, are common. A schematic illustration of a composite bioherm is given in Figure 9a.

### *Biostromes*

The microbial carbonates forming the lateral continuous biostrome of Unit 3 are in general more homogeneous than the microbialites of Unit 2. Biostrome 1 is associated with grainstones throughout the entire HST sequence of Unit 3 and the

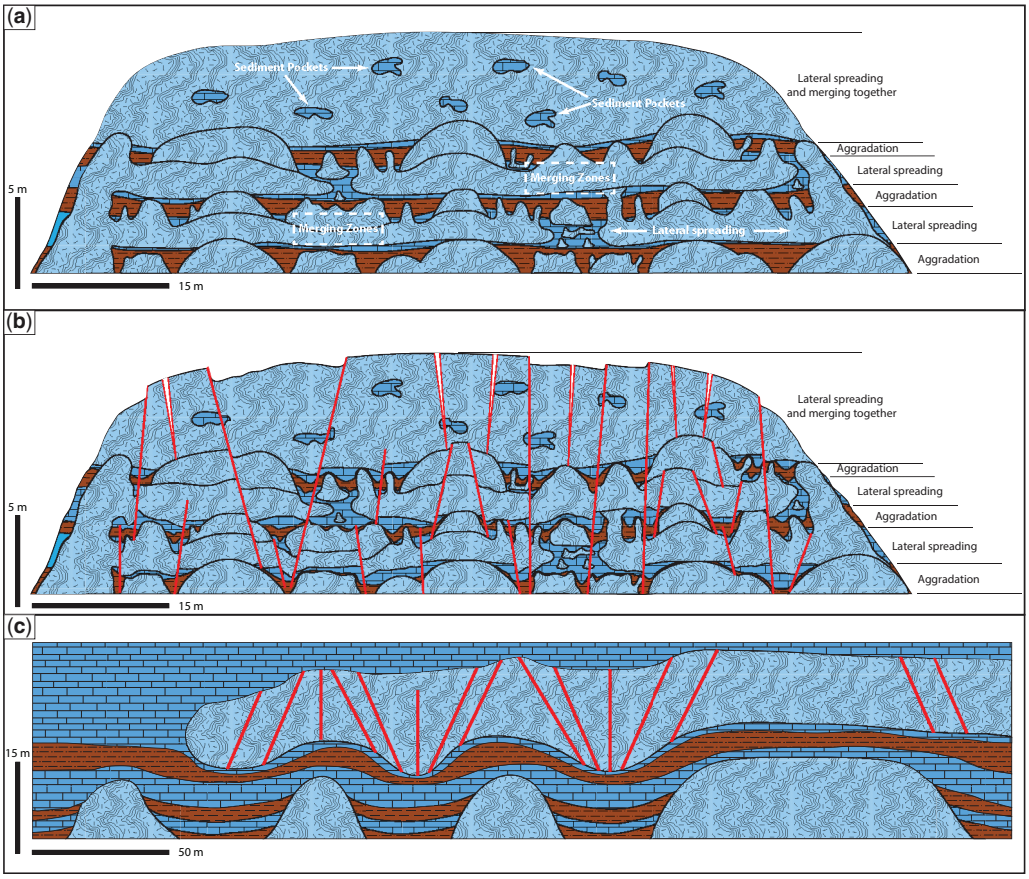


**Fig. 9.** (**a**) Schematic model of a composite bioherm. (**b**) Schematic model of syndepositional deformation within a composite bioherm. (**c**) Cartoon illustrating syndepositional fracturing in a biostrome due to differential compaction in underlying bioherm horizon.

**Colour online/ colour hardcopy**

dominant growth forms are fine-scaled branching columns. Biostrome 2, which caps the OS2, started to develop in the latest stages of Unit 5 HST. In that stage the biostrome is defined by branching thrombolite columns. This changes with increased mud-dominated sediment influx to domal and goblet-shaped thrombolites at the top of the biostrome and the onset of the first transgression in the Hoogland Member.

The structural framework of the bioherms is characterized by a dendritic architecture formed by thrombolite columns with abundant grainstone sediment pockets and dissecting grainstone channels.

## Structures

### *Remote sensing*

Two main lineament directions in the Omkyk and Hoogland members were identified from the geological map, which are NNE–SSW and SSE–NNW. Two subsets have an orientation NE–SW and SW–NW (Fig. 5f). The satellite image interpretations show the same four main orientations (Fig. 5e). The absence of vegetation and the near-horizontal bedding of the Nama Group in the study area, allowed the majority of the mapped lineaments to be identified as steep strike-slip faults (no visible vertical offset on the satellite images: cf. Fig. 3c). A few normal faults could be identified based on the visible vertical offset of the sub-horizontal bedding in the area. The normal fault in the west of the study area shows an offset of *c.* 120 m of the Hoogland Member against the Omkyk Member and can easily be recognized on the satellite imagery (Fig. 3b). The analysis of the fracture traces from the satellite image interpretation show that the main fracture sets are orthogonal, and strike NE–SW and SW–NW, with subordinate sets trending north–south and

SSE–NNW (Fig. 5c, d). Digitized fractures of the Hoogland Member from the geological map show a predominant direction of SSE–NNW and north–south (Fig. 5a).

### *Field-based fracture data*

The field analyses revealed two categories of fractures – primary and secondary – defined by their cross-cutting relationships. Primary fractures are only found in the microbial carbonates and cross-cut entire bioherms and biostromes, as well as shale and mud horizons within the microbialites. The fractures are typically open (of centimetre to decimetre scale), filled with brecciated inter-column material. They show no consistent orientation and the dip is primarily steep to vertical. In areas above topographic highs (e.g. stacked bioherms) primary fractures are inclined towards the antecedent topography, resulting in medium to high dip angles (60–85°) (Fig. 10a). Centimetre to decimetre offset of fractures can be observed where fractures cross-cut mud and shale horizons (Fig. 6). Fractures are filled with brecciated material and cement (Fig. 8g). Prominent examples of primary fractures were observed in stacked bioherm complexes and in biostrome areas overlying inter-bioherm facies. In these cases, the fractures are inclined towards the underlying bioherm and inter-bioherm facies zones and cross-cut the entire microbial carbonates (Fig. 7). These fractures show a wedge-shaped geometry in cross-section (Fig. 10a). Vugs and dissolution cavities are common where primary fractures cross-cut shale and mud beds within the bioherms (Fig. 7). These features are open and circular to elliptic in cross-section and are several centimetres to a few decimetres wide. Vugs are restricted to the microbial carbonates and have not been observed in the inter-bioherm facies or overlying grainstone horizons.

A total of nine secondary fracture sets could be identified which are grouped according to four main directions: (1) north–south; (2) NE–SW; (3) east–west; and (4) SE–NW. All fractures are vertical to subvertical with dip of 80–90° (Fig. 5g, h; Table 1). The age and relative age of the individual secondary fracture sets is problematic owing to numerous tectonic events and likely intervals of reactivation throughout the Phanerozoic (Viola *et al.* 2012). However, two categories of fracture sets could be identified: (1) throughgoing fractures (5–20 m in height) which cross-cut several bedding planes and (2) strata-bound fractures which terminate at bedding planes and at fracture surfaces of category 1 (Table 1; Fig. 5m). We therefore argue that fractures of category 1 are the older, since fracture planes of category 2 fractures abut at fracture surfaces of category 1.

### *LiDAR fracture data*

LiDAR fracture mapping has been carried out at two locations and fractures were mapped in the inter-bioherm facies, bioherm and biostrome horizon and in the grainstone horizon of Unit 4–5 (Fig. 5i–k). All nine fracture sets from the field observation were identified in the LiDAR interpretation in the inter-bioherm area at locations C and D (see Fig. 2). At locations E, F and G (see Fig. 2) only five of the fracture sets could be identified. The reason for that is most likely the lower resolution (10 cm point cloud spacing to 2 cm spacing in the inter-bioherm area of digital outcrop model) of the LiDAR scan.

Primary fractures were detected in the bioherm and biostrome horizon (note the lower dip angles in the contour plots I and J of Fig. 5). No consistent orientation of primary fractures in the microbial carbonates is apparent. Primary and secondary fractures have been identified on the photomosaic interpretation (Fig. 6). A distinct difference in secondary fracture abundance occurs: a higher density of secondary fractures is noted (1) in stacked bioherm complexes and (2) where several mud and shale beds are present within the mound structure (Fig. 6). In the case of the latter, secondary fracture termination occurs at shale horizons. In order to quantify relative fracture abundance, fractures were merged onto the virtual outcrop model and a scanline analysis was carried out (see Fig. 6 for scanline location). The total fracture density of the entire composite bioherm is 0.664 fractures per metre whereas the density in the stacked bioherm interval with abundant shale beds is almost double with 1.155 fractures per metre.

### *Competency of microbial carbonates*

From a structural perspective, an understanding of the external morphology and internal structure of thrombolite–stromatolite build-ups is crucial as a means of understanding brittle and ductile deformation and the development of complex fracture patterns within the microbialites.

The structural behaviour of the microbialites is predominately affected by the geometry of the microbial framework. Bioherms and biostromes are internally heterogeneous and the microbial framework, as described above, is prone to early deformation due to internal weakness (Fig. 9b). Furthermore, the stacking patterns of the microbialites affect the early deformation. This is documented at two situations: (1) where a biostrome overlies bioherms and (2) in stacked bioherm complexes. In the first case prominent features within the biostrome are differential compaction structures (Fig. 9c). The underlying mounds are less

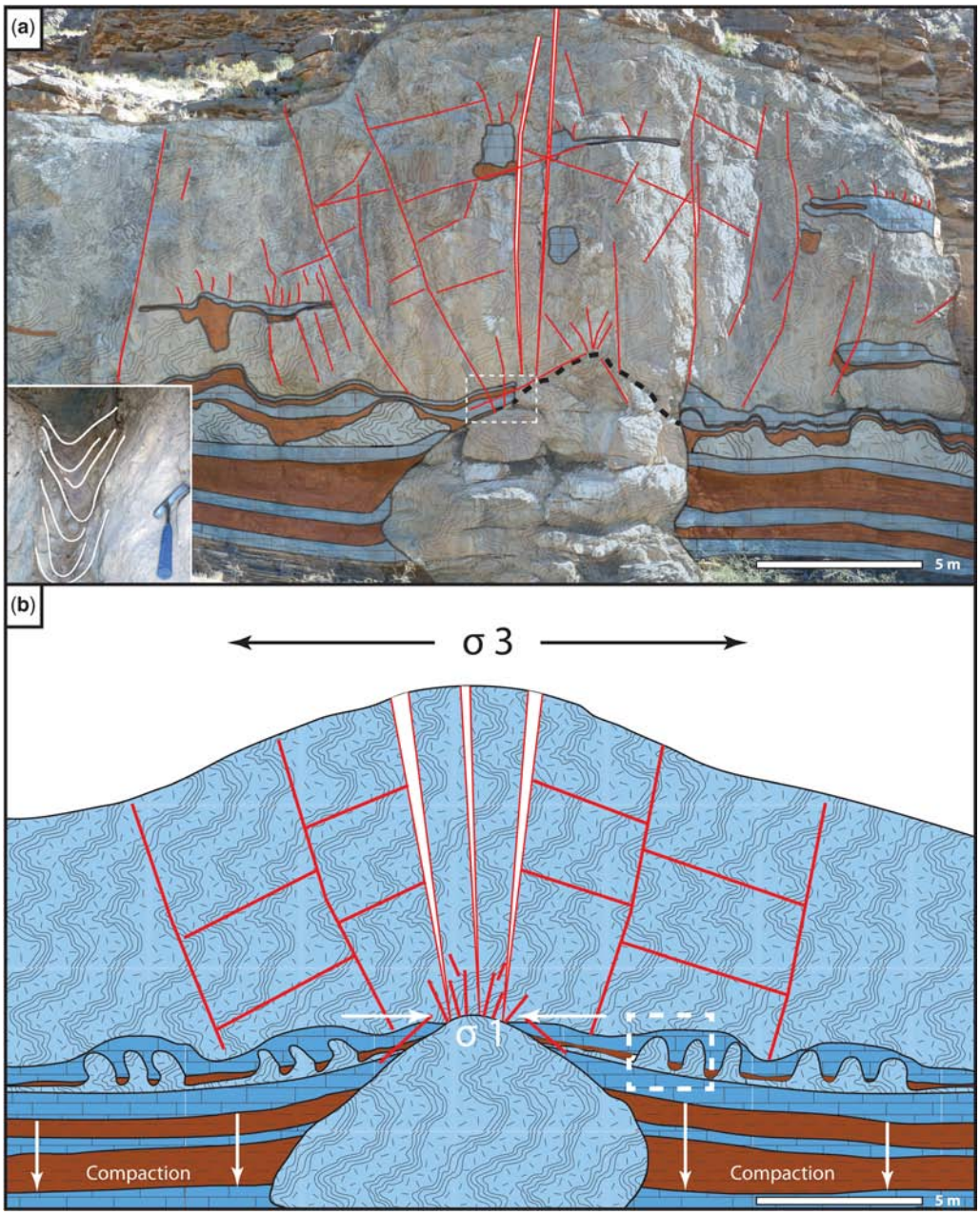


**Colour online/ colour hardcopy**

**Fig. 10.** (**a**) Photo interpretation of a stacked bioherm structure in Units 1 and 2: note the mapped sediment pockets within the mound structure. The black dotted line indicates the upper margin of the mound structure originated in Unit 1. Note the first lateral spreading of the microbialites near the top of the underlying mound structure, which gets terminated by shale input. Red lines are mapped fractures. White filling of the fractures above the underlying bioherm indicates the wedge-shaped geometry. Enlarged picture shows folding of fine-grained sediments at the contact zone within the stacked bioherm (white dotted rectangle indicates location). (**b**) Conceptual cartoon showing syndepositional fracture development due to differential compaction and the formation of antecedent topographic highs. White dashed rectangle indicates the location of Figure 8a, d.

**Table 1.** *Identified fracture sets with average strike direction and grouping*

| Fracture set | Orientation (strike) | Category |
|---|---|---|
| Fracture set 1 | *c.* 5° | 1 |
| Fracture set 2 | *c.* 30° | 2 |
| Fracture set 3 | *c.* 45–50° | 1 |
| Fracture set 4 | *c.* 75° | 2 |
| Fracture set 5 | *c.* 90° | 2 |
| Fracture set 6 | *c.* 110° | 2 |
| Fracture set 7 | *c.* 135° | 1 |
| Fracture set 8 | *c.* 155° | 1 |
| Fracture set 9 | *c.* 165–170° | 2 |

compressible than the inter-bioherm sediments during compaction resulting in deformed zones in the biostrome over inter-bioherm facies. These areas are characterized by increased primary fracturing, orientated towards the depression, and rotated thrombolite blocks and columns (Fig. 9c).

In the second case of stacked bioherms, an increased primary fracturing and deformation is apparent in the overgrowing bioherm (Fig. 10a, b). Dissecting open-mode fractures are orientated towards the top of the underlying antecedent topographic highs. The contact zones between the mounds show intense deformation, such as fracturing and folding (Fig. 10a). An additional zone of deformation occurs on the flanks of the stacked mounds where they overlie inter-bioherm facies represented by vertical to subvertical primary fractures in the bioherms (Fig. 10a, b) and folding around small-scaled thrombolite columns in the inter-bioherm facies (Fig. 8a, b).

Brittle and ductile deformation structures characterize the internal disintegration of the microbial framework. There is a distinct difference in the competency of the various microbial growth forms. Isolated, massive thrombolite columns and domes associated with mud-dominated facies are competent whereas fine-scaled columns tend to have an incompetent behaviour. Differentiation between isolated massive domes and inter-column sediments reveals that the latter typically drape the thrombolite dome topography, thicken laterally into it, and onlap the dome margins (Fig. 8a, b). The enlarged section in Figure 10a showcases an example of this ductile, compactional folding at the contact zone of a stacked bioherm complex. Many of the thrombolites exhibit column structures orientated subnormal to bedding, which show evidence of brittle deformation. Figures 8c and 8d show broken and rotated thrombolite columns within a bioherm, forming thrombolite column fold structures. A consistent inclination or trend of these folds has not been observed. On the contrary, photomosaic interpretation of a bioherm in Unit 2 shows that different fold directions occur within one mound and are preferentially found above shale and mud beds (Fig. 8e, f).

The thicknesses of shale and mud beds can reach up to several centimetres and are the lateral equivalents of mud-dominated inter-bioherm sediments. They are characterized by stylolites with several centimetres of amplitude, and small-scale fold structures are common. Primary open-mode fractures cross-cut these shale beds whereas secondary fractures are terminated (Fig. 6). A subhorizontal offset of primary fractures, ranging from several centimetres to a few decimetres, at these beds occurs. This demonstrates that gliding along the shale beds, indicated by the fold structures, happened after primary fracture development.

Open-mode fractures are common throughout the microbial carbonates (Fig. 8g, h). The fractures are filled with brecciated material of inter-bioherm sediments. At several locations microbial overgrowths around clasts in the fractures were observed. Note the white arrows in Figure 8i and the white lines in Figure 8j indicating the microbialites. The overgrowth occurs as laminated microbial fabric around clasts, growing into the cavities of the fracture. This indicates that the open-mode fractures developed in an actively depositing carbonate platform. The overgrowth is followed by a thin layer of dark dolomitic rim cement and blocky marine calcite cement (Fig. 8g, h).

## Discussion

### *Regional fractures*

Two main orientations of structural features have been identified from the combined results of remote sensing analyses and fieldwork. The predominant orientations in the northwestern part of the Zaris sub-basin are NE–SW and NW–SE. The majority of the mapped lineaments are steep, subvertical strike-slip faults. Only a few normal faults could be identified. All secondary fracture sets are subvertical and show the same main orientations with subsets north–south and east–west. A detailed structural interpretation has not hitherto been undertaken in the NW part of the Nama Basin.

A recent study, focusing on the tectonic brittle evolution of the Namaqualand metamorphic complex at the southwestern edge of the Nama Basin, was conducted by Viola *et al.* (2012), from whom the following summary derives. The authors identified a total of ten deformational events, which have taken place between the start of the Pan-African orogenic cycle and the present day. Pan-African events are represented by four compressional episodes, each defined by steep strike-slip

faulting: an initial NW–SW event (D1) is followed by a clockwise rotation of the stress field (D2 and D3, to the NNW–SSE and north–south, respectively). The latest compressional event in the Precambrian (D4) has a main compressional direction ESE–WSW. These first four events have been linked to the development of the Damara orogen to the north, and the Gariep Belt to the west. Phanerozoic extensional events relate to opening of the South Atlantic: the main extensional direction was NE–SW and east–west, and this was associated with subsequent margin uplift.

Recognizing that the Zebra River study area is *c.* 450 km to the north of Namaqualand, the study of Viola *et al.* (2012) provides evidence that the northwestern edge of the Nama Basin is most likely to have undergone a similar long-lived structural history. However, it is not possible at the moment to link individual faults or fracture sets in the Zebra River area to individual tectonic events in SW Africa. The purpose of the remote study and fracture analyses was not to unravel the structural history of the Zaris sub-basin, but rather to provide a basis for the differentiation of primary and secondary fractures. Nevertheless, as the results show, all subvertical secondary fracture sets with their consistent orientations and dip angles can be tentatively linked to more regionally recognized deformational events in SW Africa.

### *Early fractures*

By clear contrast, primary fractures with their lower dip angles, random orientations and restriction to microbialites cannot be linked to the regional structural events. A key observation is the recognition of microbial overgrowth in open-mode fractures, which illustrates early development of primary fractures during deposition. Additionally, primary fractures cross-cut and are offset at shale and mud beds within the microbialites. This indicates that primary fracture development predates: (1) the bedding-plane gliding at these beds; and (2) the evolution of mechanical boundaries within the bioherm where secondary fractures abut. Evidence of syndepositional deformation in the microbialites of the Omkyk Member has also been reported by the occurrence of the sponge-like metazoan *Namapoikia rietoogenesis,* which preferentially grew in the protection of open-mode joints (Wood *et al.* 2002). Furthermore, evidence of early brittle deformation of thrombolite columns and block rotation in the Zebra River area was reported by Johnson & Grotzinger (2006). Korn & Martin (1959) reported synsedimentary faulting and fracturing from the Kanies Member in the northwestern part of the Nama Basin. Based on these reports, and on our own observations, we therefore argue that primary fractures are syndepositional and are the oldest structural features observed in the Zebra River area.

Syndepositional deformation and fracture development in carbonates is increasingly recognized as an important process (Cozzi 2000; Hunt *et al.* 2003; Underwood *et al.* 2003; Frost & Kerans 2009, 2010; Berra & Carminati 2012; McNeill & Eberli 2012). Syndepositional fracture development in carbonates has been categorized into three groups: (1) gravitationally controlled fractures; (2) antecedent-topography-controlled fractures; and (3) tectonically controlled fractures (Frost 2007; Guidry *et al.* 2007). Mechanisms for gravitationally controlled fractures include: overstepping of platform margins and related instabilities, basinwards tilting due to compaction of basinal sediments, and sliding along dipping bedding planes (e.g. Kosa & Hunt 2005, 2006).

Processes involved with the formation of antecedent-topography-related fractures are due to differential compaction of slope and basinal sediments. The resulting deformational features have been described where early-cemented strata are deformed over rigid topographic highs such as: platform escarpments, bioherm complexes, drowned reef spines and crystalline basement highs (e.g. Frost & Kerans 2009; Boro *et al.* 2012). Tectonically controlled syndepositional fractures are related to the local faulting and folding process and are genetically related to the local stress field. An important difference between these three groups of fracture development is that the main driver for gravitational and antecedent-topography-related fractures is its intrinsic nature. This means that fractures form due to architecture and geometry of the carbonates whereas tectonically related fractures need an extrinsic force in order to develop.

A significant factor for all three syndepositional fracture groups is early cementation and lithification of carbonate sediments, which enables the brittle deformation of carbonates from early stages onward. These processes might be important factors, especially for microbial carbonates. Microbial carbonates form by definition through trapping and binding of sediment grains and through the precipitation of calcium carbonate (Fairchild 1991; Riding 2000, 2008; Dupraz & Visscher 2005; Nose *et al.* 2006; Russo *et al.* 2006; Dupraz *et al.* 2009). The precipitation strengthens the microbial deposit by providing a rigid structure that allows the microbial community to keep up with the surrounding sedimentation. Therefore, lithification occurs instantly in microbial carbonates, and hence typically before that in surrounding sediments. Thus, an early-lithified, rigid microbial framework is established. From the outcrop-scale to the micro-scale, this becomes prone to internal weaknesses and failure owing to later compaction of inter-bioherm

sediments, along with sediments trapped inside bioherms itself.

### *Bioherm fractures*

Adams *et al.* (2005) interpreted the bioherms to be simple, hemispheroidal constructions. This assumption was necessary by those authors who required such approximations to develop a geocellular reservoir model. However, we wish to emphasize some caution with this approach. The composite architecture of the bioherms suggests that these constructions are unlikely to exhibit a simple circular or elliptical map expression as a general rule, even if such morphologies can be mapped out in limited exposures. Our observations of the microbialites in cross-section suggest a simple three-stage model: (1) incipient bioherms were an initial loose association of dome- and goblet-shaped thrombolite domes (Fig. 8a); (2) during progradation the incipient bioherms began to branch and expand laterally (Figs 7 & 9a); (3) given sufficient time, lateral amalgamation of these incipient forms produced merged and composite bioherms. This preliminary model has important implications, because merged and composite bioherms are likely to develop into highly irregular microbial complexes. Whether predictable bioherm geometries do occur remains to be tested. In addition to the consequences for the mound geometry this model has implications for the bioherm internal architecture. Merged bioherms and composite bioherms (Fig. 9a) are the result of recurrent phases of aggradation and lateral microbial spreading, eventually leading to the development of a complex microbial framework. This fragile system is prone to instability due to internal weaknesses (Fig. 9b).

Johnson & Grotzinger (2006) studied the response of microbial growth morphology regarding changing background sedimentation in the Zebra River area. The authors showed that the microbial communities tend to form individual separated domes and large columns during shale sedimentation. Carbonate sedimentation instead favours the development of smaller scaled columns, which tend to branch and form a dendritic, coalesced network.

Incorporating these observations into our model results in thrombolite dome development during aggradational phases and coalesced columns during spreading phases. Therefore, within merged bioherms and composite bioherms, both ductile and brittle deformation occurs. Folds of mud-dominated sediments around domes and goblet-shaped thrombolites demonstrate ductile deformation. The 'wrapping' of shale and mud layers around microbial build-ups has been reported and interpreted as a syndepositional feature (Goldhammer *et al.* 1985). The differential compaction and syndepositional deformation of the aggradational microbial system affects in turn the coalesced microbial bodies. The thrombolite domes form topographic highs within the mounds during compaction, which causes instability and fracturing in the flanks of the overgrowing coalesced microbialites due to differential compaction. Sediment pockets within the coalesced column bodies are a further source of internal instability resulting in increased fracture zones and rotated columns in the overlying strata. A conceptual model illustrating syndepositional deformation within a composite bioherm is given in Figure 9b.

On the larger scale, antecedent-topography-related syndepositional fractures can be observed at two different situations in the sequence: (1) within bioherms of Unit 2, which started to grow over bioherms from Unit 1 (stacked bioherms); and (2) at biostromes in Unit 3 where the biostrome is overlying bioherm structures. In the first case of stacked bioherms, differential compaction of surrounding and underlying sediments leads to syndepositional deformation (Fig. 10a). Johnson & Grotzinger (2006) measured in detail the inter-bioherm sediments and the contemporaneous bioherm layers at the location of Figure 10. A total compaction rate of more than 40% was calculated for the inter-bioherm sediments and only *c.*10% in the bioherm itself. As a consequence of this differential compaction, the mound is affected by a horizontal deformation ($\sigma 3$) at the upper part of the structure and a compressional deformation (local $\sigma 1$) at the contact zone. Cross-cutting, syndepositional opening mode fractures develop due to this flexural stress pattern and are inclined towards the underlying bioherm-top (Fig. 10a, b). The same process can also be seen in composite bioherms where only a part of these amalgamated structures are above bioherms (cf. Fig. 6). In addition to that, mud and shale beds within composite bioherms act as gliding horizons as indicated by the small-scaled folds. The gliding follows the local topography as indicated by the lack of trend of the folds of the deformed and broken microbial columns. This eventually leads to the gravitational breakdown of entire composite bioherm bodies during compaction. In the case of biostromes overlying bioherms, primary fracture development and block rotation are observed in sinkhole-like structures (Fig. 9c). Since the inter-bioherm facies compacts more than the rigid microbial mounds, the bioherms form antecedent highs.

The features described above are clearly related to gravitationally induced deformation for two reasons: (1) a gravitationally driven breakdown of the rigid early-cemented microbial framework and (2) breakdown of bioherms through the

development of gliding horizons in the mud and shale beds. These also explain why there is no consistent orientation of primary fractures because primary fracture development follows internal architecture and local topographic morphology. Both features are intrinsic to the microbial system and therefore randomly orientated. However, it should be noted here that there is no clear separation between the gravitational and antecedent-topographic-high-controlled fractures since they influence and condition each other. For instance, the differential compaction in a stacked bioherm causes space in the inter-bioherm facies, which in turn enables bedding-plane gliding at the shale horizons. It can be regarded as a feedback loop where one event causes the other and vice versa.

The temporal evolution of mechanical layering in carbonates is also important (Frost & Kerans 2010). A mechanical layer is generally defined as a unit with the same mechanical properties (for instance rigidity) but it does not necessarily correlate with lithological boundaries or bedding planes. These mechanical boundaries develop over time and fractures are generally terminating at these boundaries. During early lithification and burial in particular, boundaries can shift. This temporal evolution of mechanical layering is apparent in Bioherm 2. Early syndepositional fractures cross-cut entire mounds in various directions and secondary post-depositional fractures terminate at the shale and mud beds within the mounds (Fig. 6). The shale beds therefore influence the mechanical layer. This implies that the bioherms acted as one mechanical layer during early lithification and primary fracture development. The evolution of multiple mechanical layers in the mounds, bounded by shale and mud beds, formed at a later stage.

### *Dissolution features*

Vugs occur preferentially at the intersections of primary fractures, are restricted to the microbial carbonates and are here interpreted as dissolution features. The surrounding inter-bioherm facies and overlying grainstones do not show evidence of dissolution or karstification and no vugs have been observed. Furthermore, none of the secondary fracture sets is affected by dissolution. Thus, we interpret the formation of vugs at primary fracture intersections as the result of an early fluid-flow network through the microbialites. The importance of syndepositional fracture networks, contributing to an early fluid-flow system is increasingly recognized (Guidry *et al.* 2007; Ortega *et al.* 2010; Frost *et al.* 2012) and in particular for carbonate hydrocarbon reservoirs (Narr *et al.* 2004; Carpenter *et al.* 2006; Collins *et al.* 2006). Furthermore, it has been shown that this network can act as a long-lived conduit for diagenetic fluids and is likely to be reactivated during regional tectonic events (Frost *et al.* 2012; Budd *et al.* 2013). This observation has important implications for the subsurface flow behaviour of microbial carbonates. Microbial carbonate systems are likely to be affected by intense early fracture network development and therefore this network can potentially significantly enhance or undermine fluid flow.

It is intriguing that only the microbialites and the carbonates in close vicinity of the microbialites in the study area are affected by selective dolomitization. The syndepositional fractures might have provided an early pathway for dolomitizing fluids, which only affected the bioherms and biostromes but not the surrounding strata. However, this hypothesis requires confirmation by detailed diagenetic studies of the Omkyk Member. Currently, therefore, microbial dolomitization cannot be discounted (Vasconcelos *et al.* 2006).

## Conclusions

(1) Microbial carbonates of the Nama Basin, Namibia comprise a variety of bioherm, biostrome and intermound facies. Microbialites comprise a suite of stromatolite and thrombolite mounds, whilst intermound facies include grainstone-packstones produced from crestal collapse, wave-rippled and cross-bedded strata. Understanding the vertical and lateral distribution of the mounds is essential because this influences the nature and distribution of fracture networks.

(2) An important syndepositional phase of structure development is recognized. A primary fracture system developed during the early stages of lithification, as a result of differential compaction and formation of antecedent topographic highs. The primary fractures are confined to the microbialites and immediately adjacent and supra-adjacent packages. Large dissolution vugs at intersections of primary fractures and extensive cementation of primary open-mode fractures demonstrate that this fracture network acted as an early fluid-flow system. Primary fractures form due to intrinsic body forces and internal weakness and geometries of the microbial system. Thus, no external driver is needed.

(3) Nine subvertical secondary fracture sets developed during the long-lived structural evolution of the Nama Basin of more than 500 Ma. The overprint of primary and secondary fractures resulted in a complex fracture network system in the bioherms and biostromes.

(4) These observations have implications for reservoir characterization in microbial carbonates because primary, open-mode fractures have the potential to significantly enhance reservoir performance through providing preferred fluid-flow pathways. Furthermore, the syndepositional fractures are most likely to be reactivated during later deformation. Additionally, the syndepositional fracture network develops separately from the regional tectonic history and can be overlooked or underestimated in areas with minor or no expected fracturing. Therefore, a careful characterization of this early syndepositional fracture system is needed in order to accurate predict fluid flow in microbial carbonate reservoirs.

The authors are very grateful to our industry partners Sonangol and NAMCOR for jointly sponsoring this research in two grants to DPLeH. We are also grateful to them for granting the release of this outcrop dataset for publication.

## References

Adams, E. W., Schröder, S., Grotzinger, J. P. & McCormick, D. S. 2004. Digital reconstruction and stratigraphic evolution of a microbial-dominated, isolated carbonate platform (terminal Proterozoic, Nama Group, Namibia). *Journal of Sedimentary Research*, **74**, 479–497, http://doi.org/10.1306/122903740479

Adams, E. W., Grotzinger, J. P., Watters, W. A., Schröder, S., McCormick, D. S. & Al-Siyabi, H. A. 2005. Digital characterization of thrombolite-stromatolite reef distribution in a carbonate ramp system (terminal Proterozoic, Nama Group, Namibia). *AAPG Bulletin*, **89**, 1293–1318, http://doi.org/10.1306/06160505005

Aitken, J. D. 1967. Classification and environmental significance of cryptalgal limestones and dolomites, with illustrations from the Cambrian and Ordovician of southwestern Alberta. *Journal of Sedimentary Research*, **37**, 1163–1178, http://doi.org/10.1306/74d7185c-2b21-11d7-8648000102c1865d

Al Haddad, S. & Mancini, E. A. 2013. Reservoir characterization, modeling, and evaluation of Upper Jurassic Smackover microbial carbonate and associated facies in Little Cedar Creek field, southwest Alabama, eastern Gulf coastal plain of the United States. *AAPG Bulletin*, **97**, 2059–2083, http://doi.org/10.1306/07081312187

Alkmim, F. F., Marshak, S., Pedrosasoares, A., Peres, G., Cruz, S. & Whittington, A. 2006. Kinematic evolution of the Araçuaí-West Congo orogen in Brazil and Africa: Nutcracker tectonics during the Neoproterozoic assembly of Gondwana. *Precambrian Research*, **149**, 43–64, http://doi.org/10.1016/j.precamres.2006.06.007

Allwood, A. C., Walter, M. R., Burch, I. W. & Kamber, B. S. 2007. 3.43 billion-year-old stromatolite reef from the Pilbara Craton of Western Australia: ecosystem-scale insights to early life on Earth. *Precambrian Research*, **158**, 198–227, http://doi.org/10.1016/j.precamres.2007.04.013

Beglinger, S. E., Doust, H. & Cloetingh, S. 2012. Relating petroleum system and play development to basin evolution: Brazilian South Atlantic margin. *Petroleum Geoscience*, **18**, 315–336, http://doi.org/10.1144/1354-079311-022

Berra, F. & Carminati, E. 2012. Differential compaction and early rock fracturing in high-relief carbonate platforms: numerical modelling of a Triassic case study (Esino Limestone, Central Southern Alps, Italy). *Basin Research*, **24**, 598–614.

Blanco, G., Rajesh, H. M., Germs, G. J. B. & Zimmermann, U. 2009. Chemical composition and tectonic setting of Chromian Spinels from the Ediacaran–Early Paleozoic Nama Group, Namibia. *The Journal of Geology*, **117**, 325–341, http://doi.org/10.1086/597366

Blanco, G., Germs, G. J. B., Rajesh, H. M., Chemale, F., Dussin, I. A. & Justino, D. 2011. Provenance and paleogeography of the Nama Group (Ediacaran to early Palaeozoic, Namibia): petrography, geochemistry and U–Pb detrital zircon geochronology. *Precambrian Research*, **187**, 15–32, http://doi.org/10.1016/j.precamres.2011.02.002

Boro, H., Bertotti, G. & Hardebol, N. J. 2012. Distributed fracturing affecting isolated carbonate platforms, the Latemar Platform Natural Laboratory (Dolomites, North Italy). *Marine and Petroleum Geology*, **40**, 69–84.

Budd, D. A., Frost, E. L., Huntington, K. W. & Allwardt, P. F. 2013. Syndepositional deformation features in high-relief carbonate platforms: long-lived conduits for diagenetic fluids. *Journal of Sedimentary Research*, **83**, 12–36.

Burchette, T. P. & Wright, V. P. 1992. Carbonate ramp depositional systems. *Sedimentary Geology*, **79**, 3–57.

Carpenter, D. G., Guidry, S. A., Degraff, J. D. & Collins, J. 2006. Evolution of Tengiz rim/flank reservoir quality: new insights from systematic, integrated core fracture and diagenesis investigations. Giant hydrocarbon reservoirs of the world: From rocks to reservoir characterization and modeling. AAPG Annual Meeting, **15**, 18.

Collins, J., Kenter, J., Harris, P., Kuanysheva, G., Fischer, D. & Steffen, K. 2006. Facies and reservoir-quality variations in the Late Visean to Bashkirian Outer Platform, Rim, and Flank of the Tengiz Buildup, Precaspian Basin, Kazakhstan. *In*: Harris, P. M. & Weber, L. J. (eds) *Giant Hydrocarbon Reservoirs of The World: From Rocks to Reservoir Characterization and Modeling*. AAPG Memoir, Tulsa, OK, **88**, 55–95.

Cozzi, A. 2000. Synsedimentary tensional features in Upper Triassic shallow-water platform carbonates of the Carnian Prealps (northern Italy) and their importance as palaeostress indicators. *Basin Research*, **12**, 133–146.

De Wit, M. J., De Brito Neves, B. B., Trouw, R. A. J. & Pankhurst, R. J. 2008. Pre-Cenozoic correlations across the South Atlantic region: (the ties that bind). *In*: Pankhurst, R. J., Trouw, R. A. J., De Brito

Neves, B. B. & De Wit, M. J. (eds) *West Gondwana: Pre-Cenozoic Correlations Across the South Atlantic Region*. Geological Society, London, Special Publications, **294**, 1–8, http://doi.org/10.1144/sp294.1

Dibenedetto, S. & Grotzinger, J. 2005. Geomorphic evolution of a storm-dominated carbonate ramp (*c.* 549 Ma), Nama Group, Namibia. *Geological Magazine*, **142**, 583–604, http://doi.org/10.1017/s0016756805000890

Dupraz, C. & Visscher, P. T. 2005. Microbial lithification in marine stromatolites and hypersaline mats. *Trends in Microbiology*, **13**, 429–438, http://doi.org/10.1016/j.tim.2005.07.008

Dupraz, C., Reid, R. P., Braissant, O., Decho, A. W., Norman, R. S. & Visscher, P. T. 2009. Processes of carbonate precipitation in modern microbial mats. *Earth-Science Reviews*, **96**, 141–162, http://doi.org/10.1016/j.earscirev.2008.10.005

Fairchild, I. J. 1991. Origins of carbonate in Neoproterozoic stromatolites and the identification of modern analogues. *Precambrian Research*, **53**, 281–299.

Fairchild, I. J., Marshall, J. D. & Bertrand-Sarafati, J. 1990. Stratigraphic shifts in carbon isotopes from Proterozoic stromatolitic carbonates (Mauretania): influences of primary mineralogy and diagenesis. *American Journal of Science*, **290-A**, 46–79.

Frimmel, H. E., Foelling, P. G. & Eriksson, P. G. 2002. Neoproterozoic tectonic and climatic evolution recorded in the Gariep Belt, Namibia and South Africa. *Basin Research*, **14**, 55–67.

Frimmel, H. E., Basei, M. S. & Gaucher, C. 2010. Neoproterozoic geodynamic evolution of SW-Gondwana: a southern African perspective. *International Journal of Earth Sciences*, **100**, 323–354, http://doi.org/10.1007/s00531-010-0571-9

Frost, E. L. 2007. *Facies Heterogeneity, Platform Architecture and Fracture Patterns of the Devonian Reef Complexes, Canning Basin, Western Australia*. PhD thesis, University of Texas at Austin, Texas.

Frost, E. L. & Kerans, C. 2009. Platform-margin trajectory as a control on syndepositional fracture patterns, Canning Basin, Western Australia. *Journal of Sedimentary Research*, **79**, 44–55.

Frost, E. L. & Kerans, C. 2010. Controls on syndepositional fracture patterns, Devonian reef complexes, Canning Basin, Western Australia. *Journal of Structural Geology*, **32**, 1231–1249.

Frost, E. L., Budd, D. A. & Kerans, C. 2012. Syndepositional deformation in a high-relief carbonate platform and its effect on early fluid flow as revealed by dolomite patterns. *Journal of Sedimentary Research*, **82**, 913–932.

Germs, G. J. B. 1972. The stratigraphy and paleontology of the lower Nama Group, South West Africa. *Bulletin, Precambrian Research*, **12**, 1–250.

Germs, G. J. B. 1974. The Nama Group in South West Africa and its relationship to the Pan-African geosyncline. *The Journal of Geology*, **82**, 301–317.

Germs, G. J. B. 1983. Implications of sedimentary facies and depositional environmental analysis of the Nama Group in South West Africa/Namibia. *Geological Society of South Africa, Special Publication*, **11**, 89–114.

Germs, G. J. B. 1995. The Neoproterozoic of southwestern Africa, with emphasis on platform stratigraphy and paleontology. *Precambrian Research*, **73**, 137–151.

Glumac, B. & Walker, K. R. 1997. Selective dolomitization of Cambrian microbial carbonate deposits: a key to mechanisms and environments of origin. *PALAIOS*, **12**, 98–110.

Goldhammer, R. K., Hardie, L. A. & Nguyen, C. 1985. Compactional features in Cambro-Ordovician Carbonates of Central Appalachians and their significance. *AAPG Bulletin*, **69**, 257–258.

Gomes, P. O., Kilsdonk, B., Minken, J., Grow, T. & Barragan, R. 2008. *The outer high of the Santos Basin, Southern São Paulo Plateau, Brazil: pre-salt exploration outbreak, paleogeographic setting, and evolution of the syn-rift structures*. AAPG International Conference and Exhibition, Cape Town, South Africa, October 26–29, 2008, Abstracts CD. http://www.searchanddiscovery.net/documents/2009/10193gomes/images/gomes.pdf (last accessed 17/09/2011).

Gresse, P. G. & Germs, G. J. B. 1993. The Nama foreland basin: sedimentation, major unconformity bounded sequences and multisided active margin advance. *Precambrian Research*, **63**, 247–272.

Grotzinger, J. P. & Knoll, A. H. 1999. Stromatolites in Precambrian carbonates: evolutionary mileposts or environmental dipsticks? *Annual Review of Earth and Planetary Sciences*, **27**, 313–358, http://doi.org/10.1146/annurev.earth.27.1.313

Grotzinger, J. P. & Miller, R. M. 2008. The Nama Group. *In*: Miller, R. M. (ed.) *The Geology of Namibia.* Ministry of Mines and Energy, Geological Survey Windhoek, Namibia, **13**, 229–272.

Grotzinger, J. P., Watters, W. A. & Knoll, A. H. 2000. Calcified metazoans in thrombolite-stromatolite reefs of the terminal Proterozoic Nama Group, Namibia. *Paleobiology*, **26**, 334–359.

Grotzinger, J. P., Adams, E. W. & Schröder, S. 2005. Microbial–metazoan reefs of the terminal Proterozoic Nama Group (*c.* 550–543 Ma), Namibia. *Geological Magazine*, **142**, 499–517, http://doi.org/10.1017/s0016756805000907

Guidry, S. A., Grasmueck, M., Carpenter, D. G., Gombos, A. M., Bachtel, S. L. & Viggiano, D. A. 2007. Karst and early fracture networks in carbonates, Turks and Caicos Islands, British West Indies. *Journal of Sedimentary Research*, **77**, 508–524.

Hunt, D. W., Fitchen, W. M. & Kosa, E. 2003. Syndepositional deformation of the Permian Capitan reef carbonate platform, Guadalupe Mountains, New Mexico, USA. *Sedimentary Geology*, **154**, 89–126.

Johnson, J. & Grotzinger, J. P. 2006. Affect of sedimentation on stromatolite reef growth and morphology, Ediacaran Omkyk Member (Nama Group), Namibia. *South African Journal of Geology*, **109**, 87–96.

Jones, R. R., Pringle, J. K., McCaffrey, K. J., Imber, J., Wightman, R., Guo, J. & Long, J. 2010. Extending digital outcrop geology into the subsurface. *In*: Martinsen, O. J., Pulham, A. J., Haughton, P. & Sullivan, M. D. (eds) *Outcrops Revitalized: Tools, Techniques and Applications*. Society for Sedimentary Geology, **10**, 31–50.

KALKOWSKY, E. 1908. Oolith und Stromatolith im norddeutschen Buntsandstein. *Zeitschrift der deutschen geologischen Gesellschaft*, **60**, 68–125.

KORN, H. & MARTIN, H. 1959. Gravity tectonics in the Naukluft Mountains of South West Africa. *Geological Society of America Bulletin*, **70**, 1047–1078, http://doi.org/10.1130/0016-7606(1959)70[1047:gtitnm]2.0.co;2

KOSA, E. & HUNT, D. W. 2005. Growth of syndepositional faults in carbonate strata: Upper Permian Capitan platform, New Mexico, USA. *Journal of Structural Geology*, **27**, 1069–1094, http://doi.org/10.1016/j.jsg.2005.02.007

KOSA, E. & HUNT, D. W. 2006. Heterogeneity in fill and properties of karst-modified syndepositional faults and fractures: Upper Permian Capitan Platform, New Mexico, USA. *Journal of Sedimentary Research*, **76**, 131–151.

LE BER, E., LE HERON, D. P., WINTERLEITNER, G., BOSENCE, D. W. J., VINING, B. A. & KAMONA, F. 2013. Microbialite recovery in the aftermath of the Sturtian glaciation: insights from the Rasthof Formation, Namibia. *Sedimentary Geology*, **294**, 1–12, http://doi.org/10.1016/j.sedgeo.2013.05.003

LE HERON, D. P., BUSFIELD, M. E., LE BER, E. & KAMONA, A. F. 2013. Neoproterozoic ironstones in northern Namibia: biogenic precipitation and Cryogenian glaciation. *Palaeogeography, Palaeoclimatology, Palaeoecology*, **369**, 48–57, http://doi.org/10.1016/j.palaeo.2012.09.026

LI, Z. X., BOGDANOVA, S. V. *ET AL.* 2008. Assembly, configuration, and break-up history of Rodinia: a synthesis. *Precambrian Research*, **160**, 179–210, http://doi.org/10.1016/j.precamres.2007.04.021

MANCINI, E. A., LLINAS, J. C., PARCELL, W. C., AURELL, M., BADENAS, B., LEINFELDER, R. R. & BENSON, D. J. 2004. Upper Jurassic thrombolite reservoir play, northeastern Gulf of Mexico. *AAPG Bulletin*, **88**, 1573–1602, http://doi.org/10.1306/06210404017

MCNEILL, D. F. & EBERLI, G. P. 2012. Early load-induced fracturing in a prograding carbonate margin. *In*: SWART, P. K., EBERLI, G. P. & MCKENZIE, J. A. (eds) *Perspectives in Carbonate Geology: A Tribute to the Career of Robert Nathan Ginsburg (Special Publication 41 of the International Association of Sedimentologists)*. Wiley-Blackwell, Chichester, UK, 327–336.

NARBONNE, G. M., XIAO, S., SHIELDS, G. A. & GEHLING, J. G. 2012. The Ediacaran Period. *In*: GRADSTEIN, F. M., SCHMITZ, J. G. O. D. & OGG, G. M. (eds) *The Geologic Time Scale*. Elsevier, Boston, 413–435.

NARR, W., FISCHER, D., HARRIS, P. M. M., HEIDRICK, T., ROBERTSON, B. & PAYRAZYAN, K. 2004. *Understanding and predicting fractures at Tengiz giant, naturally fractured reservoir in the Caspian Basin of Kazakhstan*. AAPG Hedberg Conference, Abstracts. El Paso, Texas, March 14–18.

NOSE, M., SCHMID, D. U. & LEINFELDER, R. R. 2006. Significance of microbialites, calcimicrobes, and calcareous algae in reefal framework formation from the Silurian of Gotland, Sweden. *Sedimentary Geology*, **192**, 243–265, http://doi.org/10.1016/j.sedgeo.2006.04.009

ORTEGA, O. J., GALE, J. F. & MARRETT, R. 2010. Quantifying diagenetic and stratigraphic controls on fracture intensity in platform carbonates: an example from the Sierra Madre Oriental, northeast Mexico. *Journal of Structural Geology*, **32**, 1943–1959.

PARCELL, W. C. 2003. Evaluating the development of Upper Jurassic reefs in the Smackover Formation, Eastern Gulf Coast, U.S.A. through fuzzy logic computer modeling. *Journal of Sedimentary Research*, **73**, 498–515, http://doi.org/10.1306/122002730498

PEDROSA-SOARES, A. C., ALKMIM, F. F., TACK, L., NOCE, C. M., BABINSKI, M., SILVA, L. C. & MARTINS-NETO, M. A. 2008. Similarities and differences between the Brazilian and African counterparts of the Neoproterozoic Aracuai-West Congo orogen. *In*: PANKHURST, R. J., TROUW, R. A. J., DE BRITO NEVES, B. B. & DE WIT, M. J. (eds) *West Gondwana: Pre-Cenozoic Correlations Across the South Atlantic Region*. Geological Society, London, Special Publications, **294**, 153–172, http://doi.org/10.1144/sp294.9

RIDING, R. 2000. Microbial carbonates: the geological record of calcified bacterial–algal mats and biofilms. *Sedimentology*, **47**, 179–214, http://doi.org/10.1046/j.1365-3091.2000.00003.x

RIDING, R. 2008. Abiogenic, microbial and hybrid authigenic carbonate crusts: components of Precambrian stromatolites. *Geologia Croatia*, **61**, 73–103.

RUSSO, F., GAUTRET, P., MASTANDREA, A. & PERRI, E. 2006. Syndepositional cements associated with nannofossils in the Marmolada Massif: evidences of microbially mediated primary marine cements? (Middle Triassic, Dolomites, Italy). *Sedimentary Geology*, **185**, 267–275, http://doi.org/10.1016/j.sedgeo.2005.12.017

SAYLOR, B. Z. 2003. Sequence stratigraphy and carbonate–siliciclastic mixing in a terminal Proterozoic foreland basin, Urusis Formation, Nama Group, Namibia. *Journal of Sedimentary Research*, **73**, 264–279.

SAYLOR, B. Z., GROTZINGER, J. P. & GERMS, G. J. B. 1995. Sequence stratigraphy and sedimentology of the Neoproterozoic Kuibis and Schwarzrand Subgroups (Nama Group), southwestern Namibia. *Precambrian Research*, **73**, 153–171.

SCHALK, K. & GERMS, J. 1980. *The Geology of the Marienta area. Explanation of Sheet 2416 (scale 1:250 000)*. Geological Survey of Namibia, Windhoek.

SCHRÖDER, S., SCHREIBER, B. C., AMTHOR, J. E. & MATTER, A. 2004. Stratigraphy and environmental conditions of the terminal Neoproterozoic– Cambrian Period in Oman: evidence from sulphur isotopes. *Journal of the Geological Society, London*, **161**, 489–499, http://doi.org/10.1144/0016-764902-062

SCHRÖDER, S., GROTZINGER, J., AMTHOR, J. & MATTER, A. 2005. Carbonate deposition and hydrocarbon reservoir development at the Precambrian–Cambrian boundary: the Ara Group in South Oman. *Sedimentary Geology*, **180**, 1–28, http://doi.org/10.1016/j.sedgeo.2005.07.002

SCOTESE, C. R. 2009. Late Proterozoic plate tectonics and palaeogeography: a tale of two supercontinents, Rodinia and Pannotia. *In*: CRAIG, J., THUROW, J., THUSU, B., WITHAM, A. & ABUTARRUMA, Y. (eds) *Global Neoproterozoic Petroleum Systems: The Emerging Potential in North Africa*. Geological Society, London, Special Publications, **326**, 67–83, http://doi.org/10.1144/sp326.4

Summons, R. E., Jahnke, L. L., Hope, J. M. & Logan, G. A. 1999. 2-Methylhopanoids as biomarkers for cyanobacterial oxygenic photosynthesis. *Nature*, **400**, 554–557.

Underwood, C. A., Cooke, M. L., Simo, J. A. & Muldoon, M. A. 2003. Stratigraphic controls on vertical fracture patterns in Silurian dolomite, northeastern Wisconsin. *AAPG Bulletin*, **87**, 121–142, http://doi.org/10.1306/072902870121

Vasconcelos, C., Warthmann, R., McKenzie, J. A., Visscher, P. T., Bittermann, A. G. & van Lith, Y. 2006. Lithifying microbial mats in Lagoa Vermelha, Brazil: modern Precambrian relics? *Sedimentary Geology*, **185**, 175–183, http://doi.org/10.1016/j.sedgeo.2005.12.022

Viola, G., Kounov, A., Andreoli, M. A. G. & Mattila, J. 2012. Brittle tectonic evolution along the western margin of South Africa: more than 500 Myr of continued reactivation. *Tectonophysics*, **514–517**, 93–114, http://doi.org/10.1016/j.tecto.2011.10.009

Wilson, C. E., Aydin, A. *et al.* 2011. From outcrop to flow simulation: constructing discrete fracture models from a LIDAR survey. *AAPG Bulletin*, **95**, 1883–1905, http://doi.org/10.1306/03241108148

Wood, R. A. 2011. Paleoecology of the earliest skeletal metazoan communities: Implications for early biomineralization. *Earth-Science Reviews*, **106**, 184–190, http://doi.org/10.1016/j.earscirev.2011.01.011

Wood, R. A., Grotzinger, J. P. & Dickson, J. A. D. 2002. Proterozoic modular biomineralized metazoan from the Nama Group, Namibia. *Science*, **296**, 2383–2386, http://doi.org/10.1126/science.1071599

Wright, V. P. 2012. Lacustrine carbonates in rift settings: the interaction of volcanic and microbial processes on carbonate deposition. *In*: Garland, J., Neilson, J. E., Laubach, S. E. & Whidden, K. J. (eds) *Advances in Carbonate Exploration and Reservoir Analysis*. Geological Society, London, Special Publications, **370**, 39–47, http://doi.org/10.1144/SP370.2

# APPENDIX VIII